Ductile Fuses for Special Concentrically Braced Frames

By

Santiago Bonetti

Submitted to the graduate degree program in Civil Engineering and the Graduate Faculty of the University of Kansas School of Engineering in partial fulfillment of the requirements for the degree of Doctor of Philosophy.

_____	_____
Adolfo B. Matamoros (Chair)	**JoAnn Browning**
_____	_____
Stanley T. Rolfe	**Francis M. Thomas**
_____	
Richard Hale	

Date Submitted: _____

The Dissertation Committee for Santiago Bonetti certifies
That this is the approved Version of the following dissertation:

Ductile Fuses for Special Concentrically Braced Frames

Committee:

_____
Adolfo B. Matamoros
(Chair)

Date approved: _____

Abstract

The behavior of Fuse Elements subjected to load reversals is explored for potential use in Steel Concentrically Braced Frames. Two fuse elements are investigated through experimental and computational analyses. The use of these fuse elements allows the braces to yield in a ductile manner while limiting the damage to the brace elements and the connections.

Both fuse elements are intended to maintain frame strength under repeated cycles beyond yield both in tension and compression, providing balance between the tensile and compressive lateral load resistance across the building in the direction of the braced frame which helps prevent the accumulation of inelastic drifts in one direction.

The first fuse element system consists of a reduced brace section with oval cutouts and is designated by the letters RXS. The tensile capacity of the fuse element is mainly a function of the cross sectional area whereas the fuse compressive capacity depends not only on the fuse cross sectional area but also on the fuse length. Experimental results showed that the response of the RXS fuse to the loading history was rather poor mainly because of its limited energy dissipation capacity. This fuse system is highly sensitive to eccentricities on axial loading and it is not suitable for the intended applications, although it provided valuable information for the development of the second fuse system presented.

The second fuse element is a brace composite element that consists of steel bars embedded in a polymer matrix that is confined by carbon fiber reinforced polymer. The letters BCE designate this second system. The tensile capacity is provided by the steel bars, similarly the buckling capacity is also provided by the steel bars but due to the slenderness of the bars, a confined polymer matrix is provided to improve the stiffness of the system under compressive loads. The polymer matrix is confined by a Carbon Reinforced Polymer layer.

The BCE fuse system has the ability to dissipate energy without loss in strength up to very large inelastic deformations. Experimental results showed that damage to the BCE fuse was very limited even at unit deformations beyond 3%, indicating that the fuse has remarkable toughness under load reversals.

The BCE fuse exhibited great potential as an energy dissipation device. The biggest benefit of the composite fuse is its inherent toughness. The fact that the fuse bars can be easily replaced after large inelastic deformations is another significant advantage. Even though the fuse was subjected to large inelastic deformations, there was virtually no loss in strength in tension and compression, and there was no meaningful overstrength in compression.

Keywords: fuse, composite, brace, steel, earthquake.

Acknowledgments

I would like to express my sincere appreciation to my advisor and mentor Dr. Adolfo B. Matamoros for his invaluable guidance, encouragement and support throughout this research. Without his enormous effort it would have been impossible to complete this research and put together this dissertation. Special thanks are due to Dr. Stanley T. Rolfe and Dr. Richard Hale, both members of my doctoral committee, whose numerous critical suggestions have been very valuable. I would also like to thank Dr. JoAnn Browning and Dr. Francis M. Thomas (also members of my doctoral committee) for reviewing this dissertation and for their helpful suggestions and Jim Weaver for his help and support.

I would also like to thank my family, specially my mother Maria Luisa and my aunt Maria Margarita, for their moral and financial support, and Beatriz for her dedication to help me finish this dissertation and for her keen interest, and encouragement.

I would like to acknowledge Builders Steel Company from Kansas City which kindly donated materials for the study

Table of Content

List of Tables

List of Figures

1 Introduction

1.1 Problem Statement

Because of their relatively large lateral stiffness bracing systems reduce the drift demand on structures due to earthquake loads. Older seismic design provisions require that braces be proportioned to remain within their elastic range of response for the design earthquake [FEMA, NEHRP 1994], although it was expected that brace elements may deform beyond the buckling and yield displacements under severe dynamic excitations. Limit states such as safety (collapse) and serviceability were addressed implicitly. New design provisions [AISC, 2005] are beginning to explicitly address critical parameters of structural response under severe earthquake motions such as inelastic deformations, drift capacities, and over-strength.

Concentrically braced frames (CBF) are among the most commonly used structural systems to provide lateral seismic resistance for low- and medium-rise buildings due to their structural efficiency, and because they are simple to build. CBF's are defined as those braced frames in which the centerlines of members that meet at a joint intersect at a point to form a vertical truss system that resists lateral loads [AISC, 2005, C13.1].

The seismic performance of ordinary CBF's has been investigated extensively [Astaneh-Asl and Goel 1982; Walpole 1985; Redwood and Channagiri 1991; Kim and Goel 1992; Tremblay, Archambault, and Filiatrault 1995]. Results from these investigations and damage of CBF's during past earthquakes have raised some concerns with respect to the drift capacity of braces due to damage incurred as they

deform inelastically while subjected to strong ground motions. Severe local buckling and early net fracture of the brace in the connection areas have been found to significantly diminish the effectiveness of CBF's within its inelastic range of behavior. Furthermore, large drift demands due to early brace fracture induce excessive ductility demands to beams and columns, or their connections. Research has demonstrated that adequate design parameters such as width/thickness ratios and special detailing of end connections greatly improve the inelastic behavior of CBF's; new design requirements for concentrically braced frames are based on those developments.

Since the initial adoption of CBF's in seismic resistant design, increasing brace strength and stiffness has been the emphasis of code provisions [FEMA, NEHRP 1994]. In recent years seismic design provisions have added requirements for ductility and energy dissipation capability [AISC, 2005, C13.1]. Accordingly, provisions for special concentrically braced frames (SCBF's) were developed and earlier design provisions were retained as ordinary concentrically braced frames (OCBF's). SCBF is a new category of concentrically braced frame that was introduced in the 1997 AISC seismic provisions [Malley, 2003] incorporating many of the recommendations resulting from testing at The University of Michigan [Goel, 1993; Astaneh, 1985].

Current AISC seismic design provisions [AISC, 2005] limit the use of ordinary concentrically braced frames (OCBF's) in seismically active regions because tests have showed that they sustain significant damage when deforming in the

inelastic range and because they have limited drift capacity. These provisions require the use of special concentrically braced frames (SCBF's) in regions of high seismicity because these systems are intended to provide stable and ductile behavior when deforming in the inelastic range of response.

Provisions for SCBF's require that braces be proportioned to prevent net section fracture failure within the connection because that type of failure compromises the drift capacity of the frame. In many instances this requirement implies the need for reinforcing the brace at the connection. The drawback of such reinforcement is that it adds significant cost to the connection.

To address this problem it is proposed to have yielding over a reduced strength section of the brace as the tension governing limit state so that braces yield in a ductile manner instead of having a brittle failure at the connection. The strength of the brace is reduced near the connection using fuse elements that do not compromise the overall performance, and prevent local connection failure modes such as net-section fracture and block shear rupture. To accomplish this goal, two different types of fuse elements are investigated:

a) The first fuse element consists of reducing the net cross section of the brace by introducing oval shaped cutouts. Due to this approach being similar to the "dog-bone" [Plumier, 1997] or Reduced Beam Section (RBS) used in Special Moment Frames (SMF), the Reduced Brace Section fuse is designated by the letters "RXS".

b) The second fuse element consists of a high performance composite element made with metal bars embedded in a polymer matrix that is confined by a fiber reinforced polymer layer. This composite element fuse has been designated by the letters “BCE”.

Both fuse systems are intended to provide a cost-effective method to improve the performance of steel special concentrically braced frames (SCBF’s) under earthquake loads. One of the benefits of these fuses is the reduction of size and cost of connections. By allowing the fuse to yield and by providing balance between the tensile and compressive lateral load resistance across the building a significant improvement in the performance of the structural system may be achieved.

This study describes the experimental and analytical work during the development of these alternative design and construction methods and is intended to explore the feasibility of these fuse systems and their applications in the real world.

1.2 Objectives and Scope of Research

The main objectives of this study are:

a. To experimentally determine the hysteretic behavior of round hollow steel bracing (HSS) members with the RXS and BCE fuse elements, and to develop design procedures and fabrication methods based on experimental results and computational analyses.

b. To develop an understanding of the structural behavior of concentrically braced frames with these alternative novel methods of design and construction.

The following tasks were carried out in order to achieve the stated objectives:

i. Two round hollow structural sections (HSS) with the RXS fuse system were tested under monotonic loads and a third specimen was tested under cyclic loading to determine the hysteretic behavior of axially loaded steel bracing members with the first proposed fuse element. The effect of the following design parameters was investigated: hole aspect ratio, percentage of reduction in area, and the controlling failure limit state.

ii. Twenty one brace composite elements were tested, one under monotonic tension, one under monotonic compression and nineteen under cyclic loading to determine the local hysteretic behavior of axially loaded steel bracing members with this second fuse element. The following parameters were experimentally investigated: bar slenderness, confinement ratio, fuse connection end conditions, polymer matrix durometer, axial load eccentricity, and number of bars embedded in the polymer matrix.

iii. The experimental hysteresis loops were compared with those obtained from the hysteresis model proposed by earlier studies on steel braced frames [Jain, Goel, and Hanson, 1978], and were modified based on experimental and computational results.

iv. The deformation capacity of concentrically braced frames with the RXS system was computationally analyzed for different frame geometries.

v. The behavior of the fuse elements was characterized by relating the level of damage with the drift ratio, and by establishing limits for the drift demand at which safe behavior of the system is expected to occur.

This report contains ten chapters.

Chapter 2 describes recent updates to the AISC Seismic Provisions, implications of these updates with respect to brace connections, and compliance of the proposed fuse elements with the latest AISC Seismic Provisions [AISC, 2005].

Chapter 3 contains a literature review on the performance of concentrically braced frames in past earthquakes, hysteretic behavior and analytical modeling of braces, fracture life of braces subjected to load reversals, CBF's novel systems, and presents an overview of the design criteria used for CBF's.

In Chapter 4 the design strength criteria and the design parameters for the RXS fuse are described in detail. In Chapter 5 the experimental program for the RXS fuse is described and experimental results from the tests carried out are presented. Chapter 6 presents an analysis of the experimental results for the RXS fuse and a discussion of the implications of these results on the viability of this type of fuse to improve the performance of CBF's under earthquake loading.

In Chapter 7 the basic configuration of high performance composite element or Brace Composite Element (BCE) fuse is presented. Chapter 8 presents the

experimental program for the BCE fuse which comprises a preliminary test series and a second series with full-scale fuses. The implications of the experimental results for the BCE fuse are discussed. In Chapter 9 the experimental results are verified and further analyzed in detail through the use of finite element analyses. In addition, Chapter 9 also includes phenomenological models to represent the observed force-displacement relationship of the BCE fuse, and establishes a design reference for this type of fuse.

Chapter 10 presents final conclusions from and recommendations on the implementation of these alternative methods of design and construction for concentrically braced frames.

2 Structural Systems with Fuse Elements

Recent modifications to the AISC seismic provisions [AISC, 2005] have incorporated requirements and recommendations from research and damage from past earthquakes to improve the behavior of concentrically braced frames. The development, feasibility and compliance of the proposed fuse elements with current seismic design provisions are based on the stated intent of those modifications.

2.1 Recent Updates to the AISC Seismic Provision

The 1997 AISC Seismic Provisions for Structural Steel Buildings [AISC, 1997] incorporated many of the recommendations resulting from the FEMA/SAC research program related to seismic design of steel buildings [FEMA, 1997; SAC, 1994]. The 1997 AISC seismic provision acknowledged variations between minimum yield strength and expected yield strength of different materials. The recognition of these variations was essential for situations where the provisions required comparison of member strengths to control the location of inelastic deformations.

When this project initially started the AISC Seismic Design Provision that was in effect at the time was the 2002 version [AISC, 2002], published in 2003. This seismic provision included recommendations resulting from investigations of the FEMA/SAC project [FEMA, 2000; SAC, 1997]. It incorporated a set of modifications to the 1997 AISC Seismic Provision [AISC, 1997], which included a new commentary to alert designers about potential net-section weakness for hollow

structural braces connected through a single gusset plate in concentrically braced steel frames.

The most recent AISC Seismic Provision [AISC, 2005] was completed in 2005 and published in the second quarter of 2006. Compared to its preceding seismic design provision, this 2005 updated version provided a more conservative approach to estimate the expected yield strength. Furthermore, the 2005 provision acknowledged that not only there are variations between the minimum yield strength and the expected yield strength, but also between the minimum ultimate strength and the expected ultimate strength. Similar to the 2002 provision [AISC, 2002], values of expected yield strength and expected ultimate strength different from those provided in the norm are permitted by the 2005 provision [AISC, 2005] if determined by testing conducted in accordance with the requirements for the specified grade of steel.

2.2 Implications of Recent Provision Updates

This dissertation was written following the third edition of the AISC LRFD Manual of Steel Construction [LRFD, 2002] and the 2002 AISC Seismic Provision [AISC, 2002]. By the time both manuals were published, this dissertation was almost completed. The thirteenth edition of the AISC Manual of Steel Construction [LRFD/ASD, 2005] was published in spring 2006, whereas the 2005 AISC Seismic Provision [ASIC, 2005] was published during the summer of 2006.

In the thirteenth edition of the AISC Manual of Steel Construction [LRFD/ASD, 2005] the resistance factor for compression members was increased from 0.85 to 0.9. This is the only variation on that affects design calculations for the fuse elements presented in this thesis. The resistance factor for compression had the effect of increasing the nominal buckling capacity of the fuse elements by 5% compared with the original calculations based on the third edition [LRFD, 2002]. This increment in the resistance factor reflects confidence on compression member design procedures; it also reflects that the buckling capacity of a steel section is not as critical of a limit state as it was assumed in previous versions of the manual.

There are few changes that are relevant to the design of concentrically braced frames between the current 2005 seismic design provision [AISC, 2005] and the preceding 2002 version of the provision [AISC, 2002]. These changes, for the most part, do not affect the fuse element design calculations described in chapters 4 and 7. Among those changes, the only one that is pertinent to the design of both types of fuse elements presented in this thesis is the ratio of the expected yield strength to the minimum specified yield strength $\boldsymbol{R_y}$ which was increased for some applications in the 2005 provision [AISC, 2005]. Through the experimental portion of this study it was demonstrated that values of $\boldsymbol{R_y}$ given by the 2002 seismic design provision [AISC, 2002] were already conservative enough to avert brittle failures at the brace connections, and that the more conservative approach adopted by the current provision, which requires greater $\boldsymbol{R_y}$ ratios, demonstrates the importance given to preventing overstressed brace connections during a seismic event. Design calculations

were checked and updated for the latest 2005 provision [AISC, 2005] when necessary on Chapter 5. Only when those changes between the two provisions apply to the fuse element a reference to the 2005 provision was provided.

The AISC "Seismic Provisions for Structural Steel Buildings" [AISC, 2002] states in the section for design of SCBF [AISC, 2002, 13.3a] the following:

> "The required strength of bracing connections … shall be the lesser of the following:
>
> (a) The nominal axial tensile strength of the bracing member, determined as $R_y F_y A_g$.
>
> (b) The maximum force, indicated by analysis that can be transferred to the brace by the system."

Compliance with this strength requirement is conservatively met by using the nominal tensile strength as the starting point for the design of the connection design.

$$FCC > R_y * F_y * A_g \qquad \text{<Eq. 2.1>}$$

where:

FCC= Factored Connection Capacity

R_y = Ratio of the Expected Yield Strength to the minimum specified yield strength $\boldsymbol{F_y}$. Values for $\boldsymbol{R_y}$ depend on member type [AISC, 2002, table I-6-1]. $\boldsymbol{R_y}$ is 1.3 for HSS ASTM A500, A501. $\boldsymbol{R_y}$ was increased to 1.4 in the 2005 provision [AISC, 2005].

F_y = Specified minimum yield stress of the type of steel to be used, ksi

A_g = Gross area, $in.^2$

In other words, the factored capacity of a brace connection, such as the knife-plate connection between gusset plates and round hollow brace sections, shall not be larger than the yield capacity of any brace that is connected to the frame through the gusset plate. To comply with the AISC seismic requirement, the brace connection in this particular case shown in Fig. 2.1 has to be strong enough so that failure will occur along the connected element, and not at the connection.

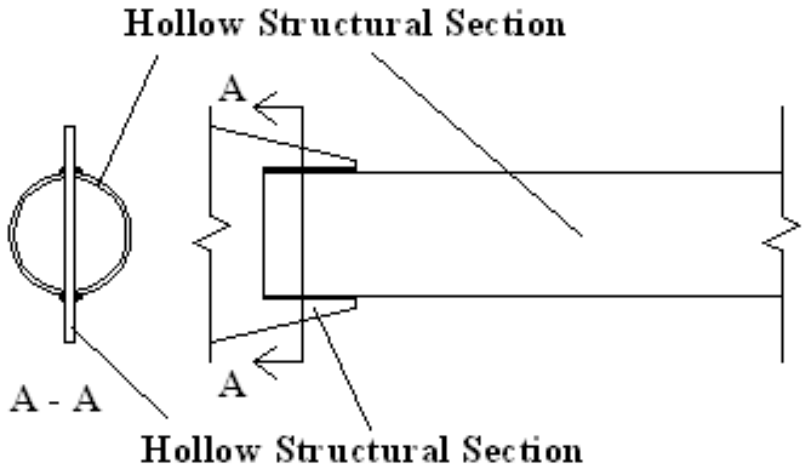

Fig. 2.1- Typical HSS Gusset Plate Connection.

The commentary of the AISC "Seismic Provisions for Structural Steel Buildings" [AISC, 2002] state in regards to the Tensile Strength [AISC, 2002, C13.3b] the following:

> "It should be noted that some, if not all, steel materials commonly used for braces have Expected Yield Strengths significantly higher than their specified minimum yield strengths; some have Expected Yield Strengths almost as high as their tensile strength. For such cases, no significant reduction of the brace

section is permissible and connections may require local reinforcement of the brace section. This is the case for knife-plate connections between gusset plates and A53 or A500 braces (e.g. pipe braces or square, rectangular, or round hollow structural steel tube braces), where the over-slot of the brace required for erection leaves a reduced section. If this section is left un-reinforced, net-section fracture will be the governing limit state and brace ductility may be significantly reduced [Korol, 1996; Cheng, Kulak, and Khoo, 1998]. Reinforcement may be provided in the form of steel plates welded to the tube, increasing the effective area at the reduced brace section."

The currently used practice of welding reinforcing steel plates around the brace section at the connection is shown in Fig. 2.2. The drawback is that such reinforcement adds significant cost. Furthermore, recommended practices by the AISC seismic provisions [AISC, 2005] for welding reinforcing plates around the tube may be difficult to implement in field conditions and may create a potential stress riser that could lead to crack initiation.

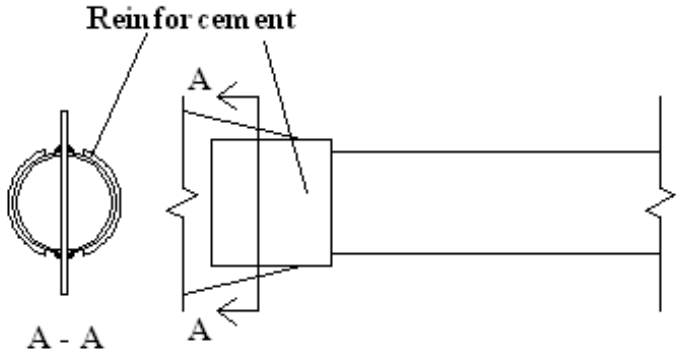

Fig. 2.2 - HSS Gusset Plate Connection Reinforcement.

The 2005 provision [ASIC, 2005] introduced the ratio of the Expected Ultimate Strength to the minimum specified ultimate strength $\boldsymbol{R_t}$. The addition of this ratio adds another element to the design procedure to confirm if reinforcement of the brace at the connection is required.

$$A_e = R_y * F_y * A_g / (0.75 * R_t * F_u) \qquad \text{<Eq. 2.2>}$$

$$\text{If } A_e > A_g,$$

$\therefore$ Connection requires local reinforcement of the brace section.

where:

R_t = Ratio of the expected ultimate strength to the minimum specified ultimate strength $\boldsymbol{F_u}$ ($\boldsymbol{R_t}$=1.3 by AISC 2005).

R_y = Ratio of the expected yield strength to the minimum specified yield strength $\boldsymbol{F_y}$. Values for $\boldsymbol{R_y}$ depend on member type [AISC, 2002, table I-6-1].

F_y = Brace specified minimum yield stress.

F_u = Brace specified minimum ultimate stress.

A_g = Brace gross area, $in.^2$

A_e = Brace effective area, $in.^2$

2.3 Fuse Elements

An alternative solution to the reinforced connection is to reduce the brace section at a distance away from the connection using fuse elements to allow yielding over the reduced section as the tension governing limit state, so that the braces yield in a ductile manner instead of having a brittle failure at the connection. Although C13.3b includes the phrase "no significant reduction of the brace section is permissible", this is made in the context of the brace section at the connection. The stated intent of having gross-section tension yielding as the tension governing limit state of the brace is that the brace yields in a ductile manner. Therefore, reduction of the brace at a short distance away from the connection, allowing the brace to yield in a ductile manner, would be consistent with the intent of the provision so long as brittle failure of the fuse is prevented prior to significant inelastic deformations.

Under compressive loads failure at the connection is very unlikely. Gusset plates are typically proportioned conservatively enough to resist the maximum force indicated by analysis that can be transferred to the brace [LRFD, 1999]. However, the connection compressive capacity could be compromised by brace post-buckling deformations which induce significant rotations at the connection. The fuse elements are intended to keep buckling limit states away from the connection and suppress second order effects from the gusset plate during brace post-buckling deformations.

Two types of fuse elements were investigated in this study. Both systems provide a method for performance improvement for steel concentrically braced frames (CBF's) under earthquake loads and allow reducing size and cost of the

connection while permitting the brace to yield. Providing balance between the tensile and compressive lateral load resistance across the building in the direction of the braced frame has the benefit of preventing the accumulation of inelastic drifts in one direction.

2.3.1 Reduced Braced Section Fuse Element "RXS"

The first fuse element consists of reducing the section of the brace with oval cutouts, and is designated by the letters "RXS". The tensile capacity of the fuse element is mainly a function of the net cross sectional area, whereas the compressive capacity depends not only on the cross sectional area of the fuse but also on the length of the fuse. Design parameters and construction procedures for the RXS fuse element are explained in detail in Chapter 4.

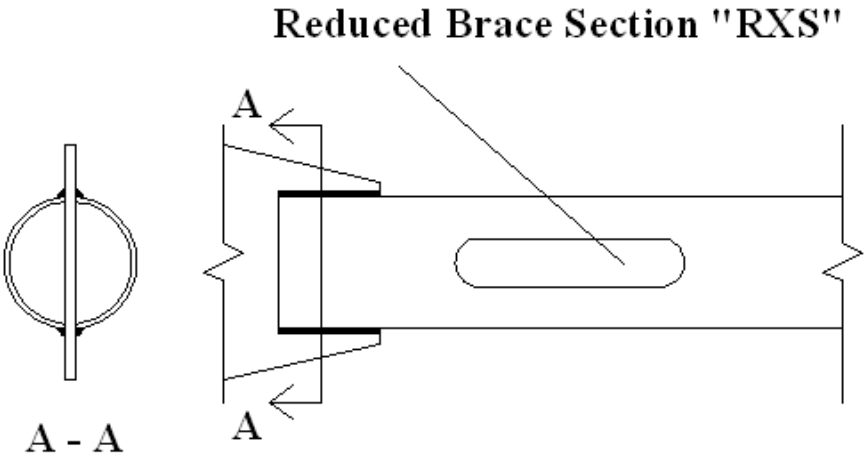

Fig. 2.3 - RXS Fuse Element System.

2.3.2 Brace Composite Element "BCE" Fuse Element

The second fuse element is a brace composite element that consists of metal bars embedded in a polymer matrix, which is confined by carbon fiber reinforced polymer. The letters "BCE" are used to designate this second system. The tensile strength is equal to that of the metal. The compressive strength is defined by the buckling capacity of the metal bars. Due to the slenderness of the bars, a confined polymer matrix is used to provide lateral restraint and maintain the axial stiffness of the bars under compressive loads. The polymer matrix is confined by a Carbon Reinforced Polymer layer (Fig. 2.4). Design parameters and construction procedures for the RXS fuse element are explained in detail in Chapter 7.

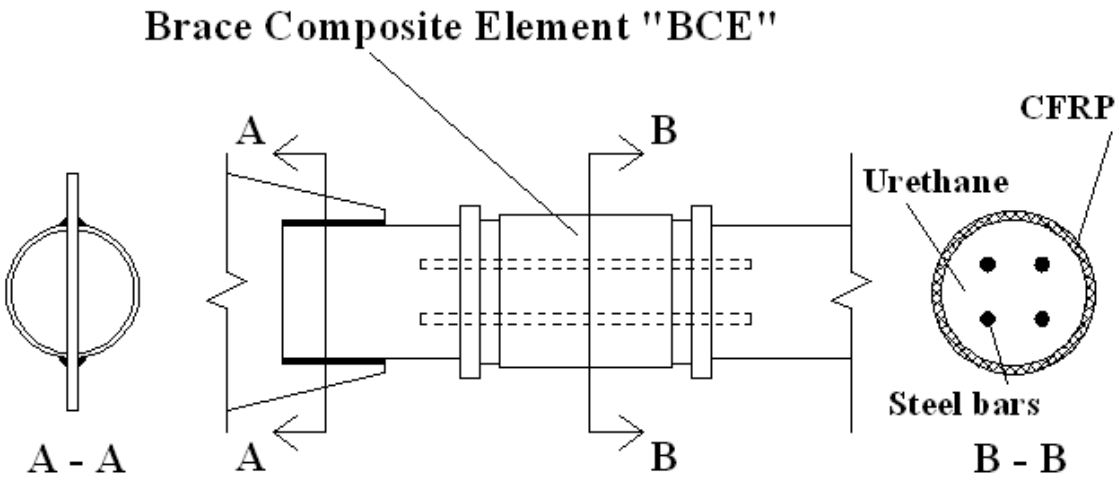

Fig. 2.4 - BCE Fuse System.

3 Literature Review

The inelastic response of Concentrically Braced Frames (CBF's) under seismic loads is dominated by the hysteretic behavior of the brace. For this reason the modeling of brace behavior when subjected to axial load reversals should be accurate and fully understood in order to effectively design or model CBF's. This chapter presents a discussion on the performance of CBF's in past earthquakes; previous studies investigating the experimental behavior and analytical modeling of braces; and general design criteria of CBF's.

There has been increasing interest in the development of novel systems to enhance the performance of CBF's. Some of these novel systems intended for use in earthquake resistant design are also presented in this section, including similar fuse elements studied by other researchers and shape memory alloy composite materials with applications in Civil Engineering.

3.1 Performance of CBF's in Past Earthquakes

The performance of steel buildings in eleven major earthquakes that occurred over the past three decades was documented by The American Iron and Steel Institute [Yanev, Gillengerten, and Hamburger, 1991]. In general, most of the damage was in minor structures that had rod or angle sections as tension braces. Among the failure patterns observed were buckling of braces, fracture of brace members at welded splices, fracture at the net section of bolted connections, and fracture in gusset plates.

Collapse of an entire building due to failure of CBF's was rare, and damage to CBF's was considered to be mainly a result of poor detailing, and inadequate design of connections.

Tremblay et al. (1995) investigated the performance of CBF's during the Northridge earthquake in 1994. Many of the braced frames damaged during the Northridge earthquake were rather old and most likely belonged to the ordinary braced frame category. Braced frames with some degree of ductile detailing were also found to have exhibited considerable damage. Although no collapse of steel buildings occurred, numerous failures and evidence of inelastic response were observed by the authors in elements other than the bracing members along the lateral load path of CBF's. These occurred as cracks in floor diaphragms, failures of brace connections, torsional deformations of beams, and tensile fracture of anchor bolts or base plates. Many of the failures observed were brittle in nature.

After the 1995 Hyogo-ken Nanbu (Kobe) earthquake Tremblay et al. (1996) carried out an investigation to examine the behavior of steel buildings during the earthquake. Contrary to preliminary observations made by damage reconnaissance teams from the outside of buildings shortly after the earthquake, a large number of modern steel buildings proportioned in accordance to the latest building codes had suffered significant damage. Most of the buildings examined had tension-only X-bracing or chevron bracing with different steel shapes. In general, fracture of bracing members or their connections was commonly found in CBF's. Damage was clearly more severe in members with smaller cross sections. However, some tension-only

braces with well-designed brace connections performed well. Tension-compression braces showed signs of fatigue fracture at plastic hinge locations, fracture at bolted brace to gusset connections, and failure of the welded connections between the gusset and the frame. This investigation confirmed the need for well-designed connections in CBF's and encouraged the use of highly redundant lateral load resisting systems.

3.2 Modeling the Hysteretic Behavior

Proper modeling of the hysteretic behavior of braces subjected to cyclic loads is vital for the accurate analysis of braced frames. Several analytical models have been developed to characterize the cyclic behavior of axially loaded steel elements. These models can be divided into three types according to the modeling technique: finite element models, phenomenological brace models, and physical theory models.

3.2.1 Finite Element Models

The finite element approach generally subdivides the brace longitudinally into a series of elements. The cross section geometry and material properties of each element are usually defined to match those of the steel section. The biggest advantage of this approach is that is applicable to many types of problems, and that only the member geometry and material properties need to be defined. Goel, and Rai (1997) used the finite element approach to confirm the experimental local failure reproduced in test specimens.

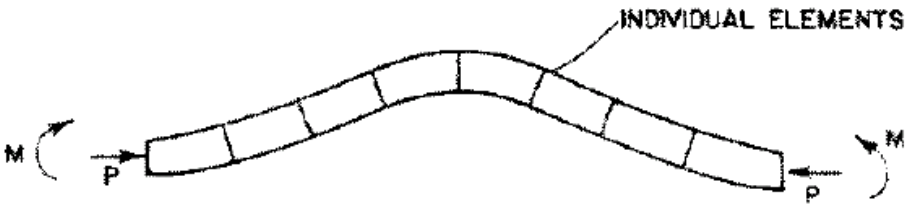

Fig. 3.1 - Finite Element Models [Hassan, and Goel, 1991].

3.2.2 Phenomenological Brace Models

Phenomenological models are based on simplified hysteretic rules that only mimic the observed force-displacement curves of a brace member. Accurate representation of member cyclic behavior is possible with this approach when the shape of the hysteretic loops is known. The use of this modeling method requires specification of numerous empirical input parameters for each element analyzed.

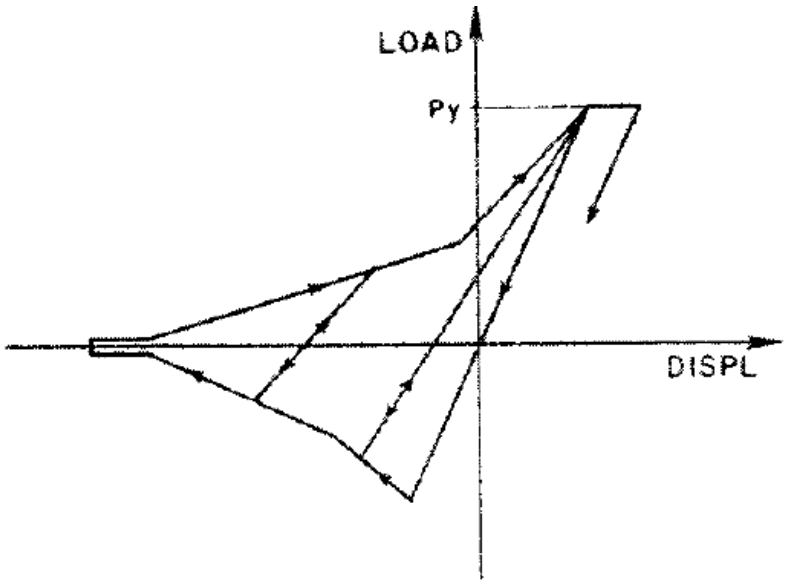

Fig. 3.2 - Phenomenological Models [Hassan, and Goel, 1991].

Some of the most important phenomenological models that have been developed are presented in the following:

3.2.2.1 Higginbotham (1973)

Higginbotham (1973) developed one of the very first analytical models of the axial hysteretic behavior of steel members. He proposed a cyclic force-deformation pattern using the exact curvature of the buckling member together with the following assumptions: (1) The member was initially perfectly straight, of uniform stiffness, supported at the ends by frictionless pins, and bent about a principal axis of the cross section, (2) the axial forces were applied at the ends of the member through the center of mass of the cross section, (3) plastic displacement at constant force $\boldsymbol{P_y}$ takes place, (4) buckling initiates at the Euler critical load with the member remaining straight until that force is reached, and (5) the moment curvature relationship is assumed elastic-perfectly plastic with reduction associated with the axial load effects.

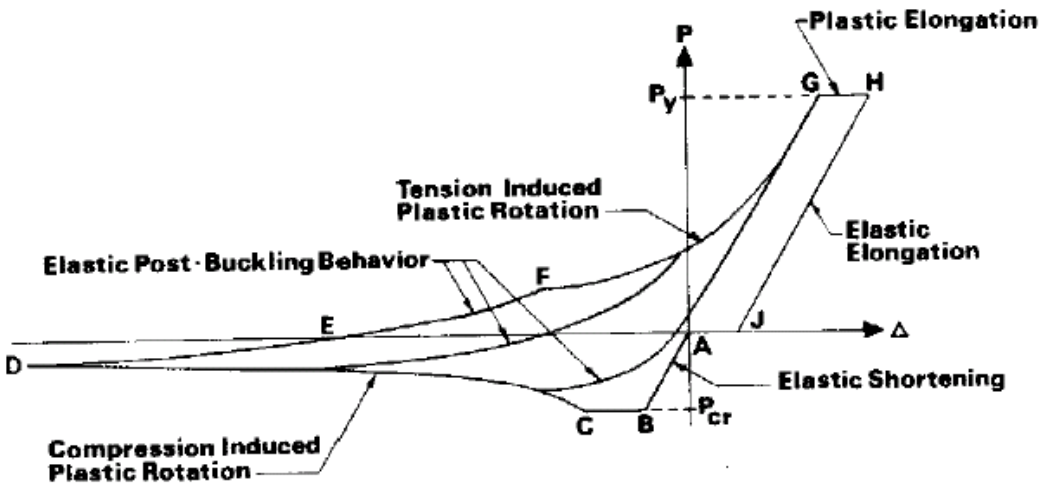

Fig. 3.3 - Cyclic Force-Deformation Pattern [Higginbotham, 1973].

3.2.2.2 Kahn and Hanson (1976)

In one of the earliest experimental investigations on hysteretic characteristics of axially loaded members subject to alternating tension and compression loads, Kahn and Hanson (1976) tested sixteen steel bars made from a rectangular cross section of 1 in. x ½ in. and four different lengths: 24in., 34 in., 49 in., and 59 in. The effective slenderness ratio ***KL/r*** ranged from 85 to 210. The cyclic behavior of a pin-ended steel member (bars welded to steel plates at the ends) was traced using the model analytically obtained by Higginbotham (1973) to define specific areas of concern such as the limit between linear and non-linear range of behavior due to compressive loads. It was observed from this experimental study that the maximum compressive load decreased with increasing cycles, and that the largest decrement was observed between the first and second cycles. It was also observed that with increasing number

of cycles the maximum compressive load became almost constant, for a given effective slenderness ratio. Members with shorter lengths exhibited greater hysteretic energy dissipation than longer specimens. The dynamic hysteretic response was nearly identical to the static response although the dynamic response was slightly stiffer in the tension region.

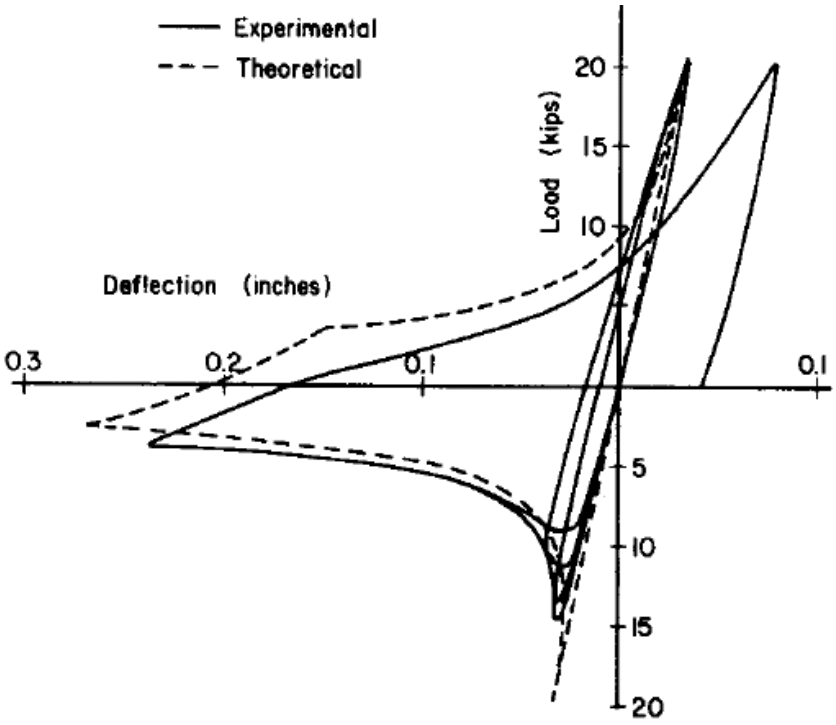

Fig. 3.4 - Comparison of Experimental and Theoretical Axial Load-Deflection for Column with KL/r = 85 [Kahn and Hanson, 1976].

3.2.2.3 Singh (July 1977)

The buckling model proposed by Singh (1977) was based on theoretical and experimental data obtained by Prathuangist (1976) and by Kahn and Hanson (1976). The mathematical buckling model was a simple multi-linear force-displacement function that utilized straight lines to simplify the relationship between axial force and axial deformation. The model was an adequate representation of pin-ended bracing members with slenderness ratio greater than 60, but it did not take into account the decrement in the buckling capacity of bracing members that takes place in subsequent compression cycles after the first buckling cycle.

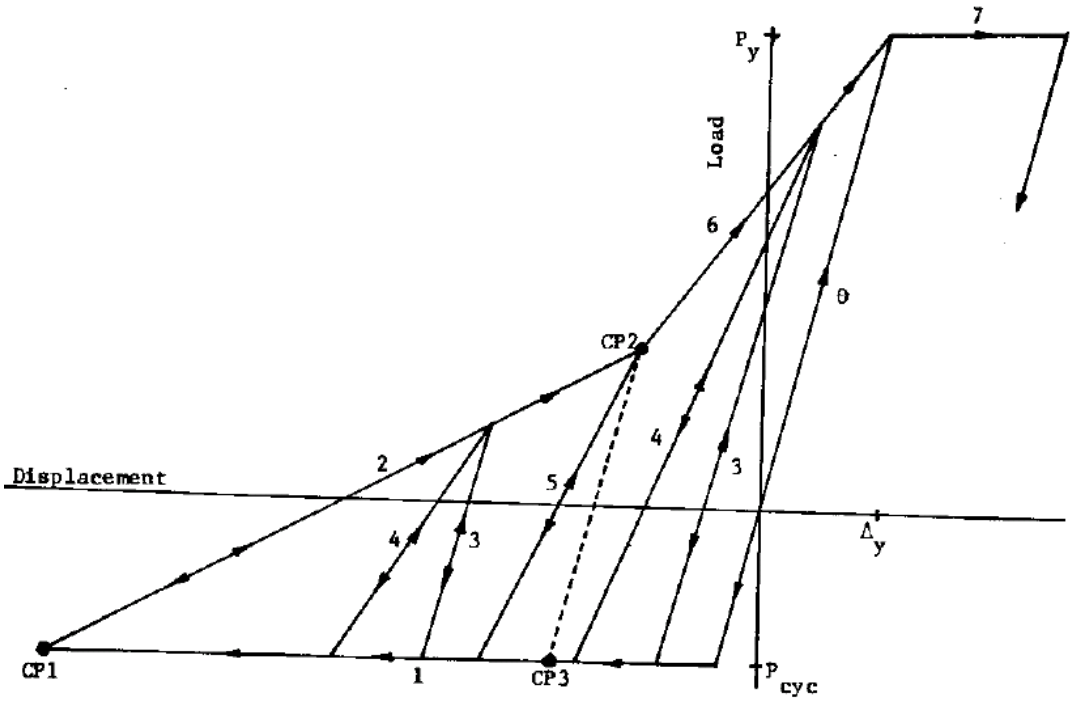

Fig. 3.5 - Mathematical Model [Singh, 1977].

3.2.2.4 Jain, Goel, and Hanson (1978)

Jain, Goel, and Hanson (1978) tested twenty-four specimens made from 1 in. x 1 in. cold rolled steel tubes and eight specimens made from 1”x1”x1/4” to 1-1/2”x1-1/2”x1/8” hot rolled single angle section under static and dynamic loading conditions to determine the hysteretic behavior of axially loaded steel bracing members. Each specimen was welded to two end plates, which were bolted to the support blocks of the test reaction frame. Effective slenderness ratio of tube specimens ranged from 30 to 140, whereas the effective slenderness ratio of the angles ranged from 85 to 120. The purpose of the static tests in angles and tubes was to study the influence of connection flexural strength and stiffness, and the influence of cross-sectional shape on the response of the brace. The purpose of the dynamic tests was to study the influence of rate of loading, local buckling and repeatability of the hysteretic loops.

Hysteretic curves obtained from tests were compared to previous hysteretic models proposed by other authors: the theoretical model of Prathuangsit [Prathuangsit, 1976], empirical coefficients of Wakabayashi [Wakabayashi, 1977], and the buckling model of Singh [Singh, 1977]. This comparison helped in understanding the limitations of each of those models and was the basis for developing a new model to represent the hysteretic behavior of bracing members, which was a modification of the buckling model developed by Singh. One drawback

is that control points developed to define this model were only applicable to tubular bracing members.

A brace element was developed and incorporated into a computer program; the behavior of this element was based on a multi-linear phenomenological model intended to reproduce the hysteretic behavior of a brace.

The study found that the effective slenderness ratio ***KL/r*** was the most influential parameter in determining the hysteretic behavior of bracing members, and that the connection stiffness had a significant influence on behavior because it affected the effective length factor ***K***.

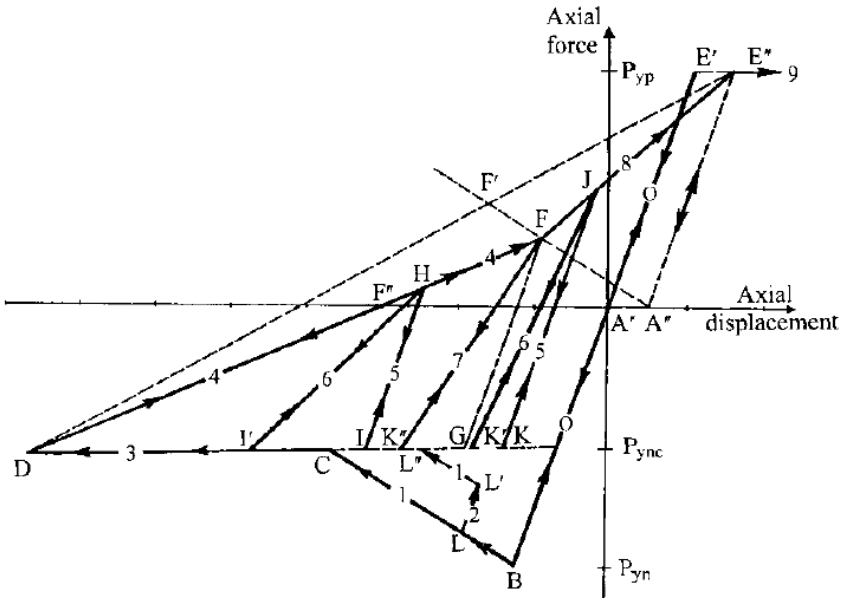

Fig. 3.6 - Axial Hysteretic Behavior in Post-Buckling Region
[Jain, Goel, and Hanson, 1978].

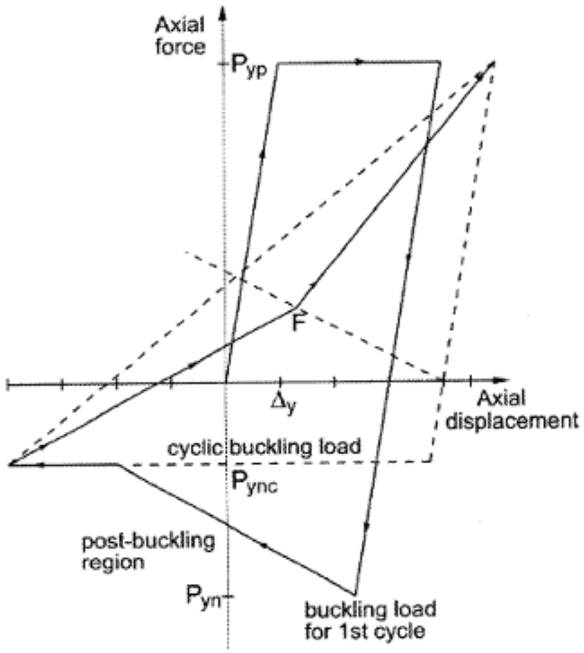

Fig. 3.7 - Overall Behavior [Jain, Goel, and Hanson,1978].

3.2.2.5 Popov and Maison (1980)

Popov and Maison (1980) carried out an analytical and experimental study on half-scale K-braced building frames subject to severe cyclic loading. The analytical cyclic behavior model proposed was developed based on several characteristic zones in a typical hysteretic loop such as the post-buckling zone. Based on the analytical cyclic behavior model an algorithm was developed to be incorporated into a computer program.

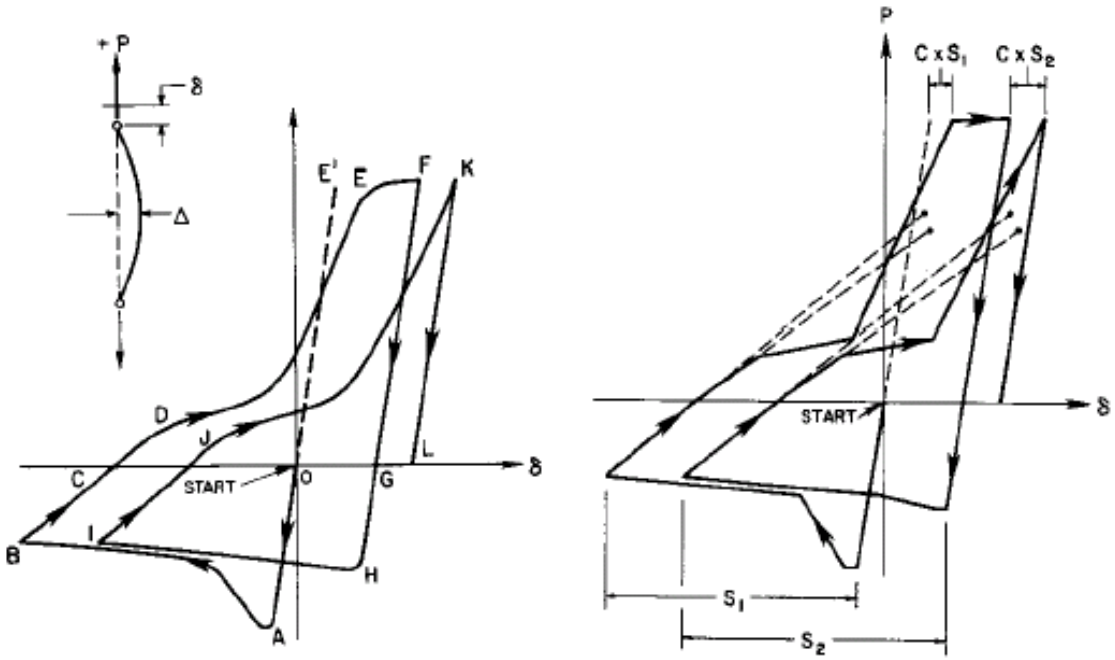

a) Idealized strut hysteretic behavior. b) Computer algorithm.

Fig. 3.8 - Hysteretic Behavior [Popov and Maison, 1980].

Experimental results from the half-scale K-braced building frame test were compared with computer simulations using the algorithm and conclusions demonstrated agreement between the experimental and analytical results.

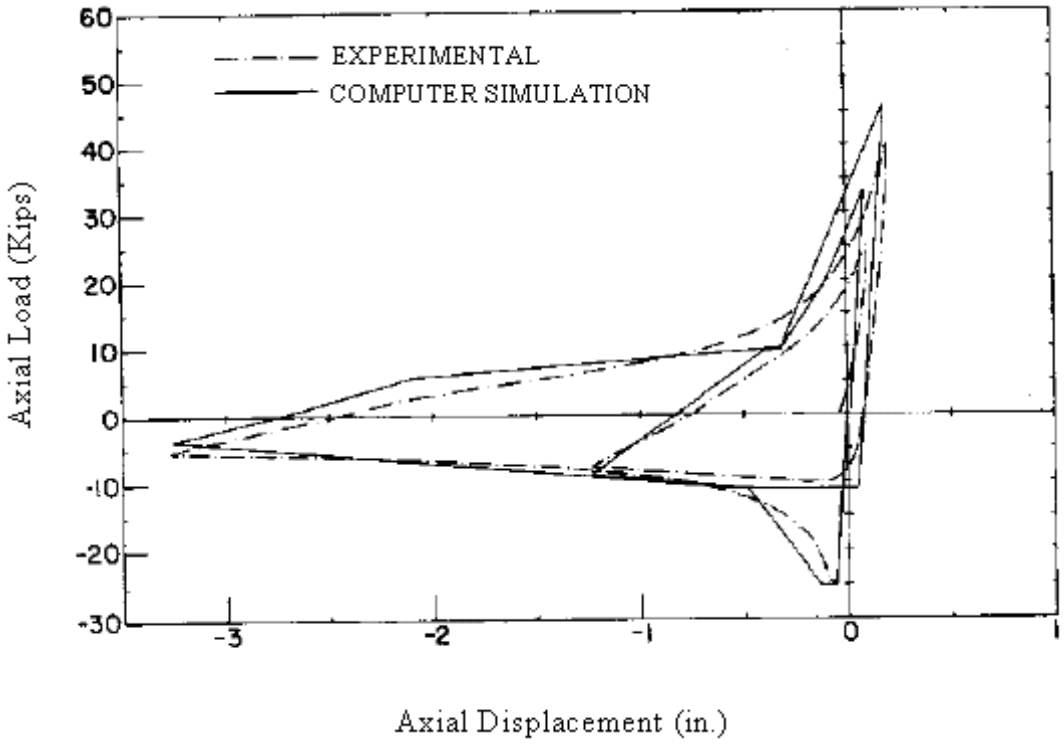

Fig. 3.9 - Analytical and Experimental Hysteretic Behavior
[Popov and Maison, 1980].

3.2.2.6 Popov and Black (1981)

Popov and Black (1981) conducted an experimental study of the hysteretic behavior of twenty-four struts of different steel shapes and sizes employed in practice. The effective slenderness ratio of specimens ranged from 40 to 120, and they had either a pinned-pinned or a pinned-fixed end condition. In addition they suggested an approach for calculating the deteriorating capacity of struts under extreme load reversals. The model by Popov and Black was based on the two main causes that contribute to the decrease in column capacity under repeated cycles of

inelastic behavior in compression, which are the Bauschinger effect and the effect of residual curvature in the column element resulting from plastic hinge rotations during previous cycles. Each of these effects was approximately accounted for by means of reduction factors applied to the nominal initial capacity of a straight column.

Among the findings from this study was that the cross sectional shape had little influence on the hysteretic behavior, and that for a given ***KL/r***, the end condition of the specimen had a minor influence on the hysteretic behavior. The effective slenderness ratio ***KL/r*** was found to have the largest influence on the hysteretic behavior, and members with effective slenderness ratio of 80 and 120 exhibited pinched hysteretic loops. Other parameters that affected behavior were lateral-torsional buckling, local buckling, and web buckling between stitch fasteners (in built-up members). The different shapes used on this study were ranked in order of decreasing performance: tube, wide flange, structural *T*, double channels, and finally double angles.

The study found that there was a decrease in the compressive load-carrying capacity during consecutive cycles. After the first cycle the compressive capacity was reduced to only half of the initial value. Because of the Bauschinger effect, the compressive capacity was reduced by as much as 25%.

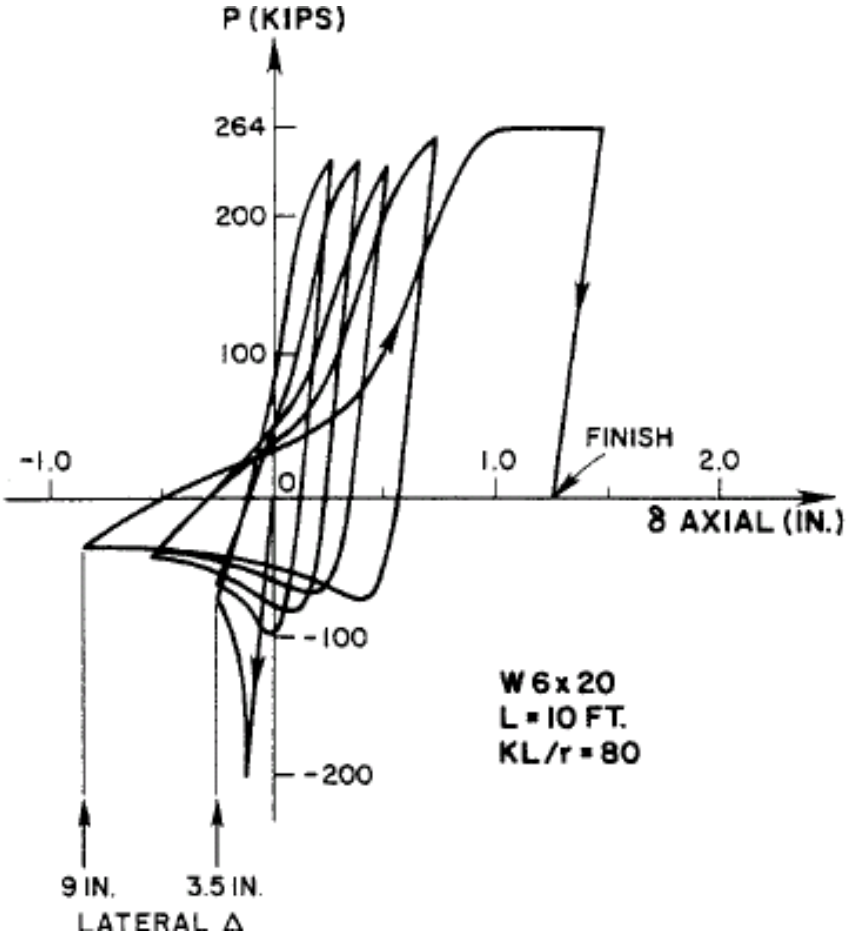

Fig. 3.10 - Axial Force-Displacement Hysteretic Loops for a Strut [Popov and Black, 1981].

It was concluded that calculating buckling loads using the analytical approach with the reduction factors was satisfactory and useful in developing algorithms for determining the deterioration of the cyclic buckling capacity of struts.

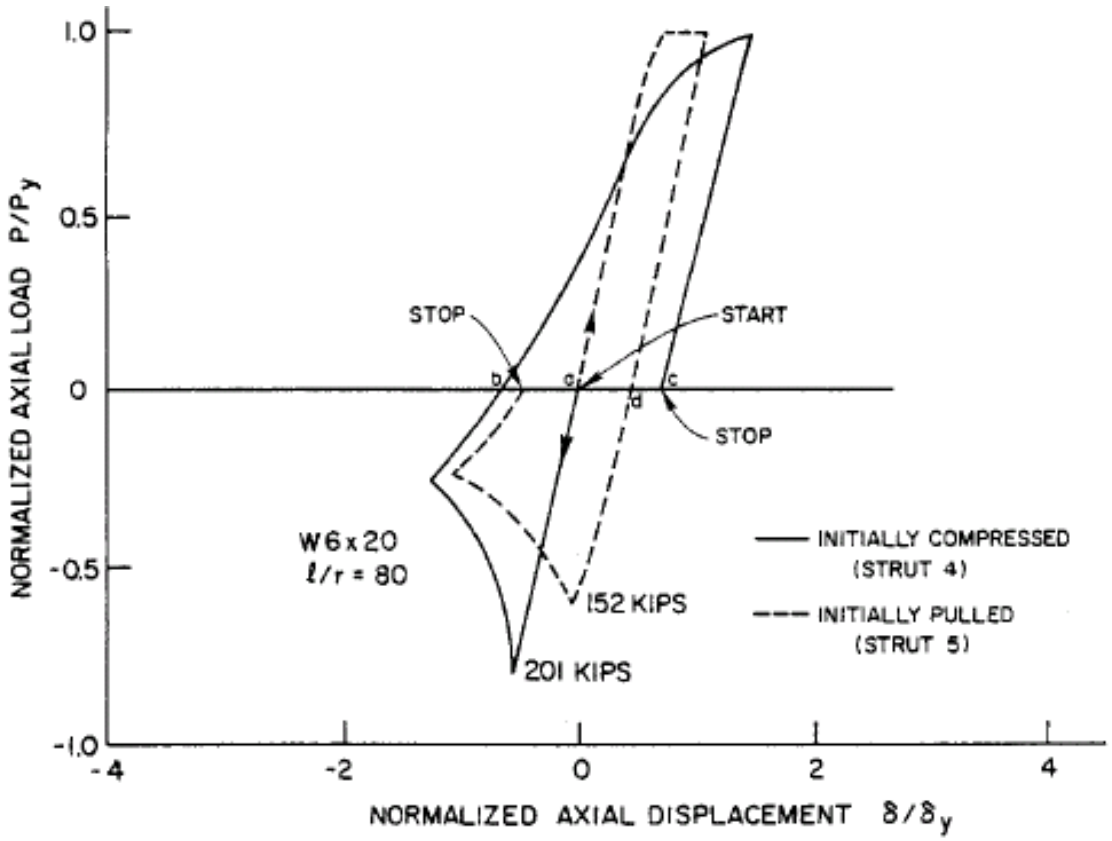

Fig. 3.11 - Loss of Compressive Capacity of Strut initially Strained into Tensile Yield [Popov and Black, 1981].

3.2.2.7 Astaneh-Asl and Goel (1985)

Astaneh-Asl and Goel (1985) investigated the behavior of nine full-size double angle braces subject to in-plane buckling and out-of-plane buckling due to severe cyclic load reversals. The angles were stitched together and were connected to end gusset plates with bolts or fillet welds. Five of the nine test specimens were proportioned according to code requirements in place at that time. The remaining specimens were proportioned based on experimental observations from the first five tests and analysis of the behavior of these specimens. New design procedures were developed for improved ductility and energy dissipation capacity. This new design procedure included three major criteria: a) excessive local yielding should be avoided in the connection and stitch areas; b) the strength and ductility of connections should be sufficient to withstand large post buckling deformations; and c) the strength of connections should not be less than that of the braces.

The last four test specimens, designed following the new proposed criteria, showed significant improvement in their performances. For bolted connections it was suggested reinforcing the net section such that plastic hinges at the ends of the member formed outside the net section, in the gross section of the double angles.

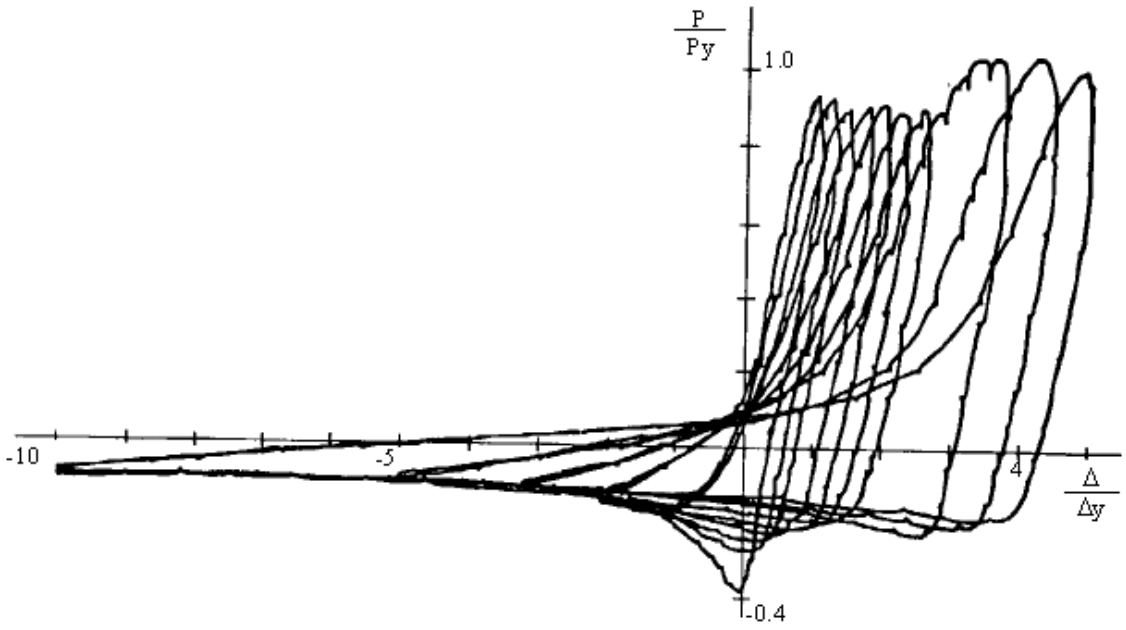

Fig. 3.12 - Hysteretic Loops from Test [Astaneh-Asl and Goel, 1985].

3.2.3 Physical Theory Models

The third type of analytical model is the physical theory model. These models incorporate simplified theoretical formulations based on physical considerations that allow the cyclic inelastic behavior to be computed. Unlike the phenomenological models, the input data for physical theory models is based on the material and geometric properties of a member. These models usually consist of elastic beam segments with an elastic-plastic cell representing the assumed location of a plastic hinge.

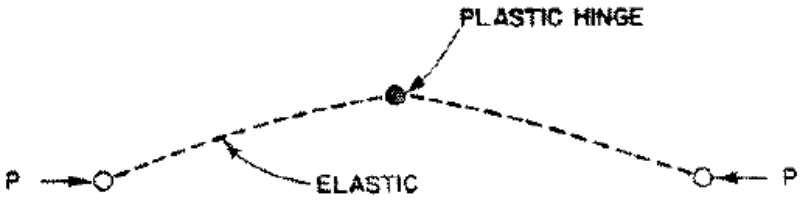

Fig. 3.13 - Physical Theory Model.

The most important physical theory models that have been developed are presented in the following:

3.2.3.1 Prathuangsit (1976)

The theoretical model for axially loaded members developed by Prathuangsit (1976) consists basically of two straight segments with equal initial rotations at mid-span and at the ends as shown in Fig 3.14. The ends were restrained by symmetrical rotational springs that represented the property of semi-rigid connections.

Among the assumptions made by Prathuangsit in his model were: lateral torsional or local buckling would not occur and members had an elastic-perfectly plastic stress-strain relationship.

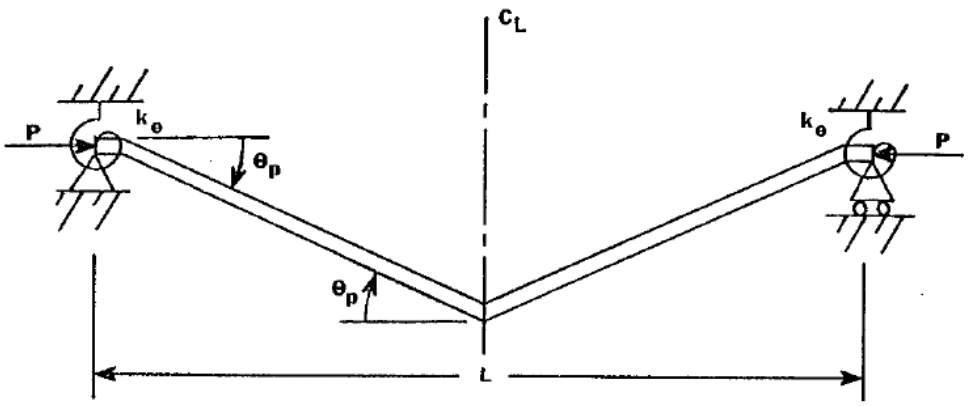

Fig. 3.14 - Theoretical Member with Initial Imperfections [Prathuangsit, 1976].

An approximate expression for curvature ($\phi=\partial^2 y/\partial x^2$) was used to obtain force-deformation relations to generate hysteretic curves for bracing members (shown in Fig. 3.15).

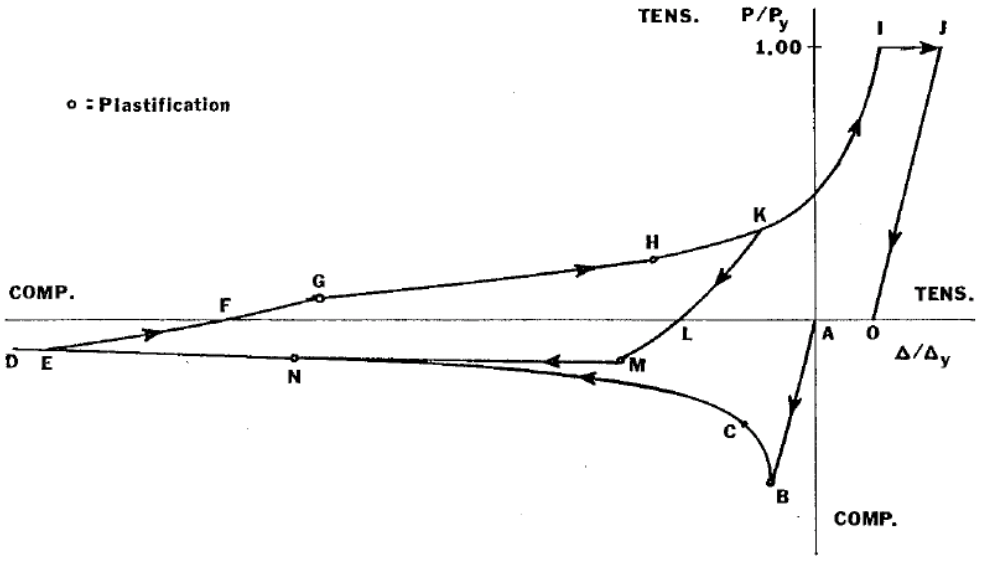

Fig. 3.15 - Typical Theoretical Axial Load Displacement Curve [Prathuangsit, 1976].

3.2.3.2 Wakabayashi (1977)

Wakabayashi et al. (1977) investigated the cyclic behavior of a restrained brace under an eccentric load both experimentally and analytically. They proposed four empirical coefficients to describe the hysteretic behavior of axially loaded steel bracing members as shown in Fig. 3.16. These coefficients are: the maximum compressive load, compressive load at maximum compressive displacement, tensile load at maximum tensile displacement, and area of the hysteretic loop.

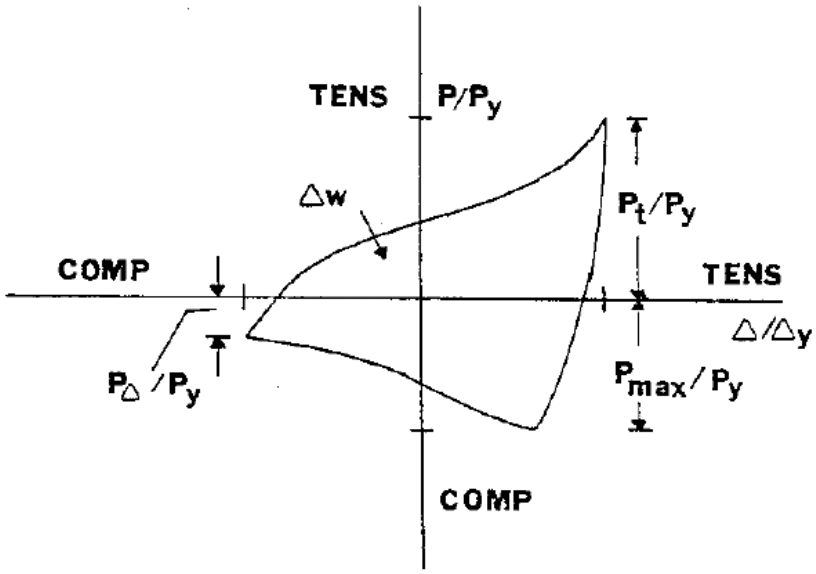

Fig. 3.16 - Hysteretic Model [Wakabayashi, 1977].

The model analyzed in their study consisted of a bar of length L restrained at both ends by elastic rotational springs of stiffness k_θ subjected to an axial force P at an eccentricity e as shown in Fig. 3.17. Some of the assumptions in the analysis were: the bar deflects when the compression load reaches the smaller of elastic buckling

load or the yield load, and moment curvature relation of the cross-section was elastic perfectly-plastic. Wakabayashi et al. tested twenty-one specimens with square cross-section and eight specimens with H-shape cross-section, and then he compared experimental results with the analytical results and concluded that the effect of elastic end restraints on the hysteretic behavior of a bracing member could be evaluated in terms of the effective slenderness ratio.

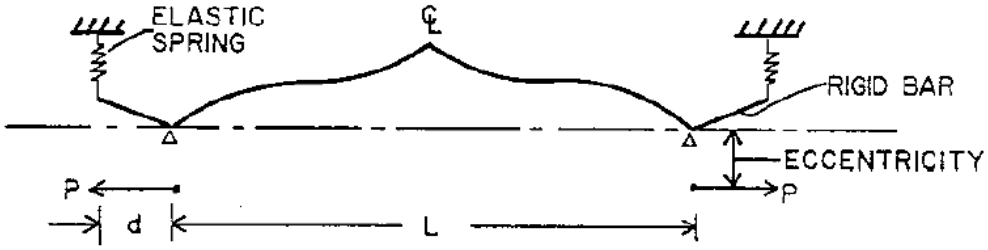

Fig. 3.17 - Theoretical Model [Wakabayashi, 1977].

3.2.3.3 Gugerli and Goel (1982)

Gugerli and Goel (1982) studied the inelastic behavior of steel bracing members under severe axial deformations to verify mathematical models proposed by several investigators in the past. They used a combined experimental and analytical approach. First, a theoretical model was proposed based on a multi-linear approximation of the hysteretic loops, and then it was modified empirically to provide closer agreement to experimental results. A model of a pin-ended brace member with a plastic hinge at mid-span and elastic brace segments was the basis for the theoretical investigation.

Simulating the reduction in compressive strength led to significantly better agreement between the analytical model and experimental results. The experimental study consisted of nine commercially-available wide-flange shapes and structural tubes with different slenderness and width-thickness ratios, diagonally mounted with rigid end connections subjected to horizontal cyclic displacements.

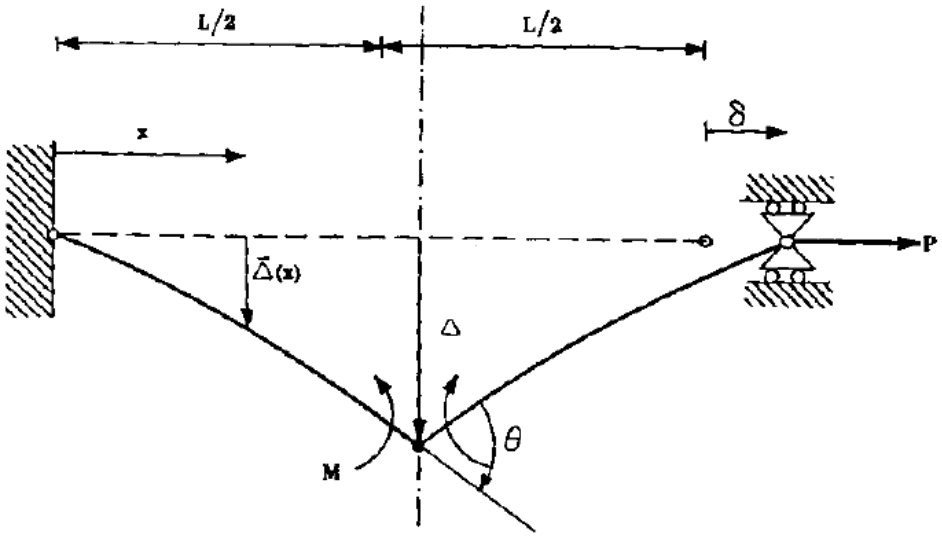

Fig. 3.18 - Member Geometry of Point Hinge Model [Gugerli and Goel, 1982].

As found by previous investigators, it was observed from the behavior of test specimens that the effective slenderness ratio ***KL/r*** was the most influential parameter on the hysteretic behavior. In addition, ***KL/r*** affected the fracture life of the specimens. The influence of different cross-sectional shapes on the hysteretic behavior was more notable than that of width-thickness ratio. The fracture life decreased with increasing width-thickness ratio and increased as the slenderness ratio

increased. Experimental results also indicated that the level of local buckling was inversely proportional to the slenderness ratio.

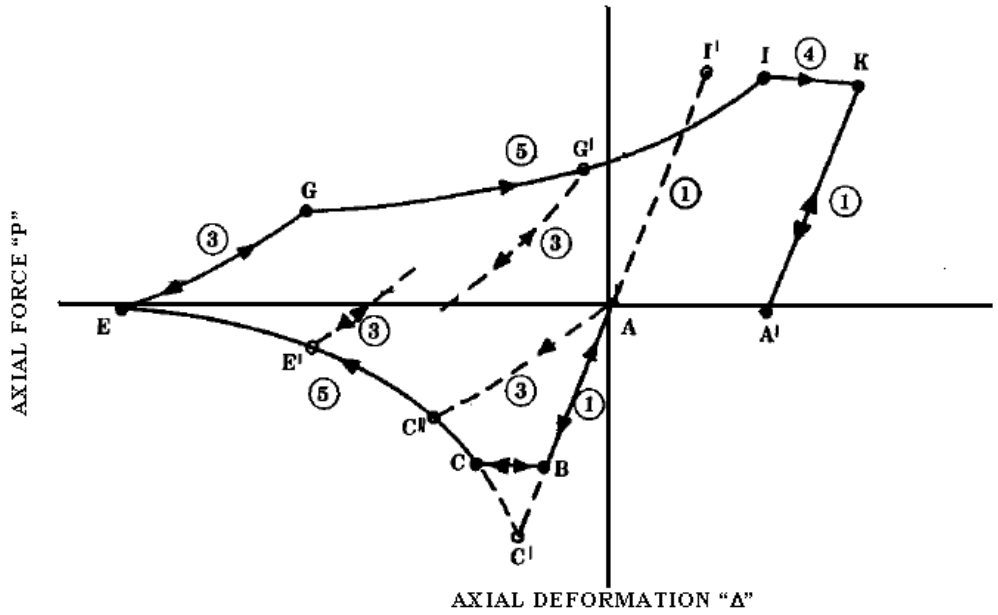

Fig. 3.19 - Typical Hysteretic Loop with Different Regimes of Member Behavior [Gugerli and Goel, 1982].

3.2.3.4 Ikeda and Mahin (1984)

Ikeda and Mahin (1984) developed a refined physical theory brace model for inelastic response analysis of braced steel structures. Their model combined analytical formulations describing plastic hinge behavior with empirical formulas based on studies of experimental data. This model was derived from the basic approach taken by Gugerli and Goel (1982). In the refined model, the initial modulus of elasticity E was replaced by the tangent modulus of elasticity E_t in order to improve the simulation of material nonlinearities. The brace was idealized as pin-

ended member with a plastic hinge located at its mid-span. The properties of the plastic hinge were defined by a specific interaction curve relating axial force and plastic hinge moment. While analytical expressions formed the basis of the model, several empirical parameters to represent behavioral characteristics were implemented in this model in order to achieve better representation of observed cyclic inelastic behavior. Among these behavioral characteristics were: the variation of tangent modulus of elasticity during cycles, the gradual plastification process of the plastic hinge, and the residual displacement due to material nonlinearities. Verification of the model was performed on the basis of quasi-static analyses of individual struts and dynamic response analyses of a three-story X-braced steel frame. Based on this verification it was concluded that the refined model was able to simulate the cyclic inelastic buckling of braces very well both in quasi-static and dynamic analyses. Moreover, the authors concluded that the refined model showed better performance than the model by Gugerli et al. [Gugerli and Goel, 1982].

3.2.4.5 Ballio and Perotti (1985)

Ballio and Perotti (1985) studied the cyclic behavior of axially loaded members in order to assess the performance of bracing systems under strong seismic actions. They proposed a numerical model to describe the cyclic behavior of axially loaded members. They tested six specimens with double angles and double channels, using single diagonal and double diagonal braces. They proposed a model based on a

two-degrees of freedom system (axial and flexural), which consisted of a two rigid elements connected by a deformable cell. The restoring moment and axial force in the cell were computed by dividing the section into strips and by assuming that the material had an elasto-plastic response, including strain hardening.

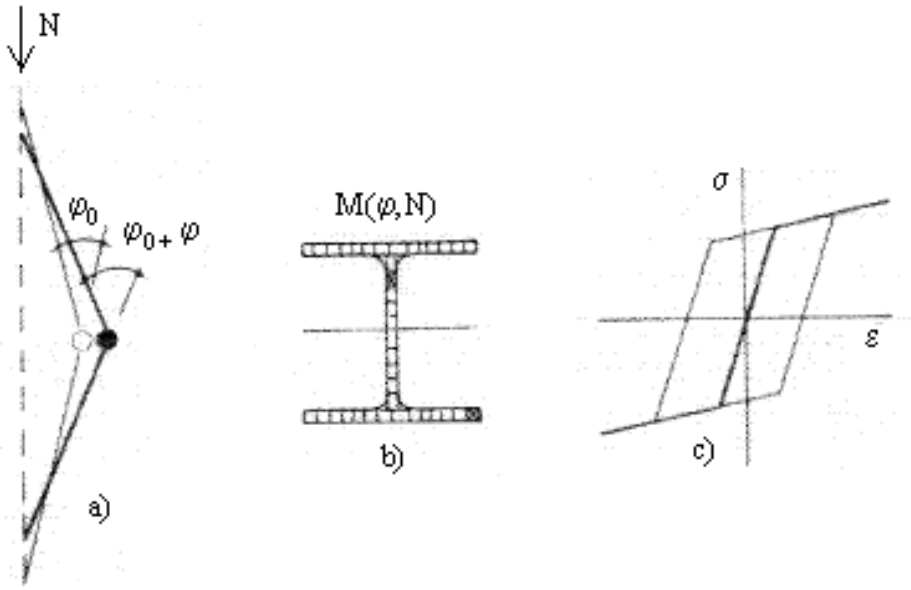

Fig. 3.20 - Theoretical Model Assumptions [Ballio and Perotti, 1985].

Results from the numerical analysis based on the proposed model were compared with experimental results. Among the findings the authors concluded that the proposed numerical model of axially loaded bars can simulate with good accuracy the various facets of the experimental behavior of the bars, up to high values of plastic deformation (errors within 10%).

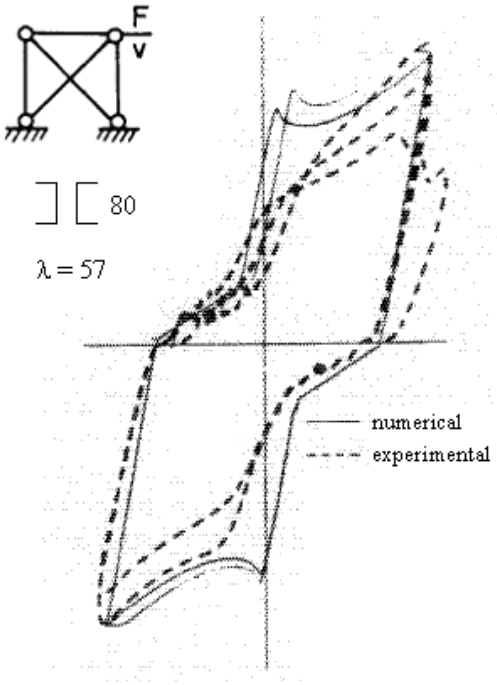

Fig. 3.21 - Superimposed Numerical and Experimental Load-Deflection Ccurves [Ballio and Perotti, 1985].

The two diagonal systems obviously showed a more symmetrical behavior (Fig. 3.21). At low displacements it was observed that results obtained with the numerical model were conservative when compared with the experimental results, while for higher amplitudes the opposite trend was observed.

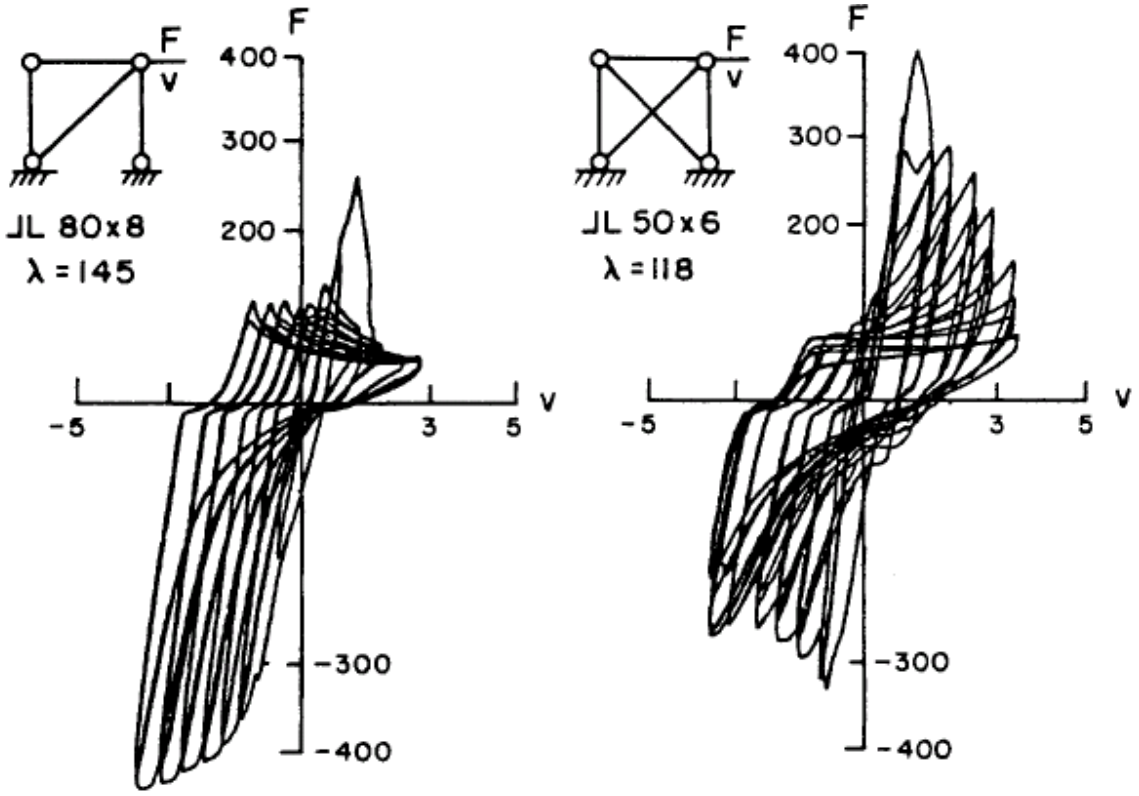

Force = KN; displacement = cm.

Fig. 3.22 - Experimental Hysteretic Behavior [Ballio and Perotti, 1985].

3.2.3.6 Walpole and Remennikov (1995)

Walpole and Remennikov (1995) used the refined physical theory model proposed by Ikeda and Mahin (1984) to further develop an incremental analytical model for estimating the strain hardening hysteretic behavior of steel brace members subjected to cyclic loading. Similar to the previous model, they modeled the brace as a pin-ended member with a plastic hinge located at mid-span. An incremental

solution procedure was employed where the incremental axial force ***dP*** was related to the incremental axial deformation $d\delta$ by means of a tangent stiffness coefficient K_t. The member was loaded with an axial load ***P***, that caused an internal plastic hinge moment ***M***, an axial deformation δ, and a plastic hinge rotation ϕ.

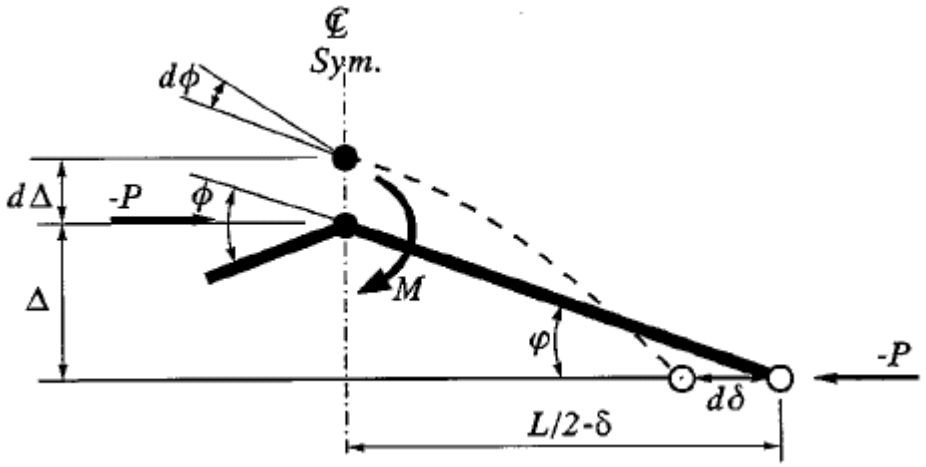

Fig. 3.23 - Deformed Shape of a Brace Member [Remennikov and Walpole, 1995].

This model presents a better implementation of the Bauschinger effect, which enables the model to represent the strain hardening and strain softening effects. The analytical formulation of the plastic hinge behavior was combined with empirical formulas developed on the basis of experimental data, confirming the validity of the inelastic model.

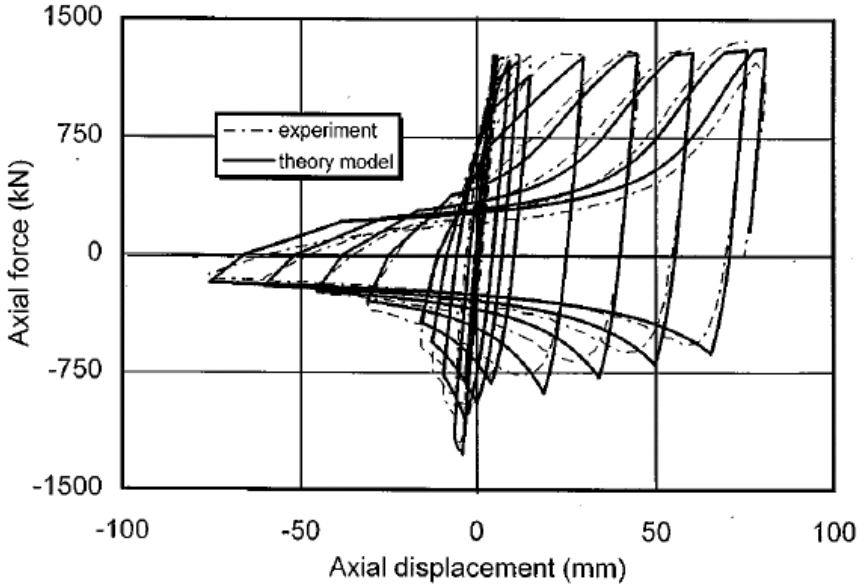

Fig. 3.24 - Comparison of Analytical and Experimental P-δ Curves for Fixed-Fixed Brace Members [Remennikov and Walpole, 1995].

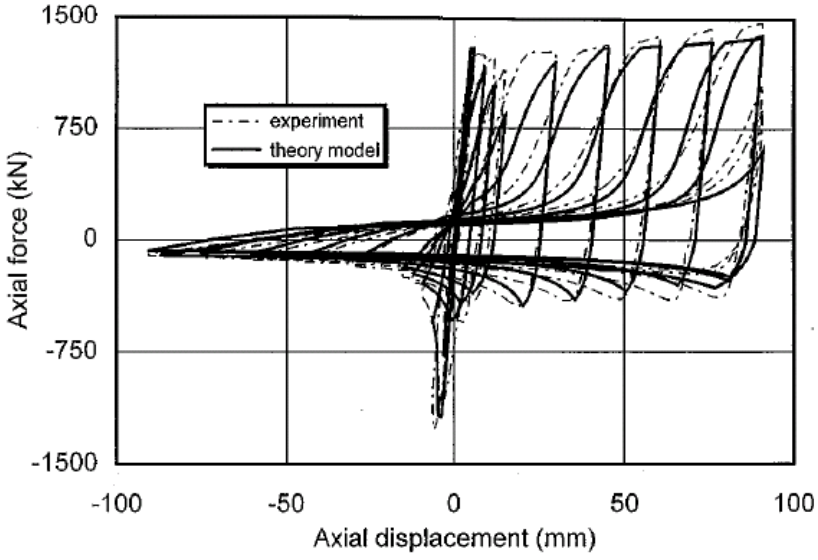

Fig. 3.25 - Comparison of Analytical and Experimental P-δ Curves for Pinned-Pinned Brace Members [Remennikov and Walpole, 1995].

3.3 Calculating Fracture Life Based on Hysteretic Behavior

Brace elements in CBF's are expected to undergo large inelastic deformations during severe ground motions that can cause early fracture. Based on results from experimental investigations on the hysteretic behavior of braces, the fracture life of braces can be calculated in terms of prior deformations. The most important investigations related to the fracture life of braces are presented in the following.

3.3.1 Tang and Goel (1987)

Tang and Goel (1987) presented an empirical criterion to estimate the fracture life of rectangular tubular bracing members in terms of standard cycles. The method involved converting general deformation cycles of a brace into an equivalent number of standard cycles N_s:

$$N_s = \frac{\sum(\Delta_t - \Delta_c)}{\Delta_y} \qquad \text{<Eq. 3.1>}$$

Δ_y = yield deformation of the brace

Δ_c = compression deformation of the brace

Δ_t = tension deformation of the brace

Test results on square and rectangular tubular section braces conducted by Liu (1987) and Lee (1987) showed that the fracture life of braces was very sensitive to width-to-thickness ratios, slenderness ratio, width-to-depth ratio and the mechanical properties of steel. The following empirical formula was proposed by Tang and Goel to calculate the fracture life:

$$N_f = C_s \cdot \frac{(b/d)(KL/r)}{[(b-2t)/t]^2} \qquad \text{KL/r>60} \qquad \text{<Eq. 3.2>}$$

$$N_f = C_s \cdot \frac{(b/d)(60)}{[(b-2t)/t]^2} \qquad \text{KL/r} \leq 60 \qquad \text{<Eq. 3.3>}$$

N_f = fracture life in terms of standard cycles

C_s = 262, numerical constant obtained from test results

d = gross depth of the section

When N_s exceeded N_f the brace was considered to have fractured.

3.3.2 Tremblay (2002)

Tremblay (2002) surveyed past experimental studies on the inelastic response of diagonal steel bracing members to collect data for the seismic design of concentrically braced frames. In total he examined 9 experimental studies that included 76 tested specimens [Archambault, Tremblay, Filiatrault 1995; Black, Wegner, Popov 1980; Gugerli 1982; Lee, Goel 1987; Leowardi, Walpole 1996; Liu 1987; Wakabayashi, Nakamura, Yoshida 1977; Remennikov, A., and Walpole, W. 1996]. He examined the buckling strength, post-buckling behavior at various ductility levels, maximum tensile strength including strain hardening effects, and the lateral deformations of the braces upon buckling. He proposed equations for each of those parameters. In addition he also surveyed the fracture life of braces made with rectangular hollow sections (RHS). He proposed a simple approach to estimate the fracture life of these braces by relating the total ductility reached at fracture μ_f with

the brace slenderness parameter λ. A linear relationship between these two parameters was obtained from a linear regression for the 38 RHS brace specimens examined (Fig. 3.26).

$$\mu_f = a + b\lambda \qquad ; \qquad \{a = 2.4;\ b = 8.3\} \qquad \text{<Eq. 3.4>}$$

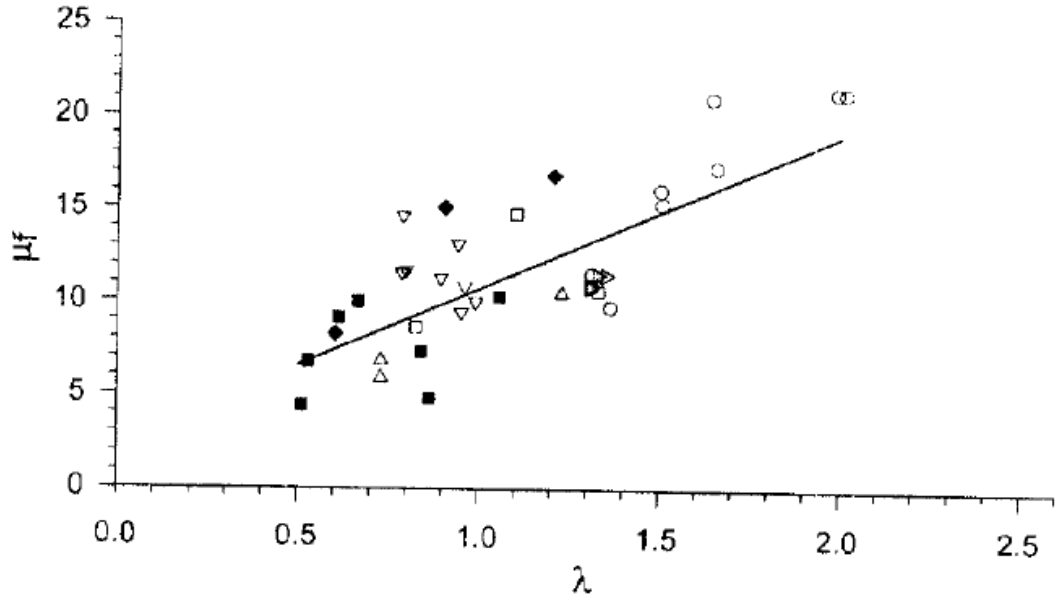

Fig. 3.26 - Prediction of Peak Ductility at Fracture μ_f [Tremblay, 2001].

The total ductility reached at fracture μ_f was defined as the sum of the peak ductility reached in tension and the peak ductility attained in compression in any cycle before the half-cycle in tension in which failure of the brace was observed. The author indicated that additional test data were needed to improve the accuracy of the proposed model.

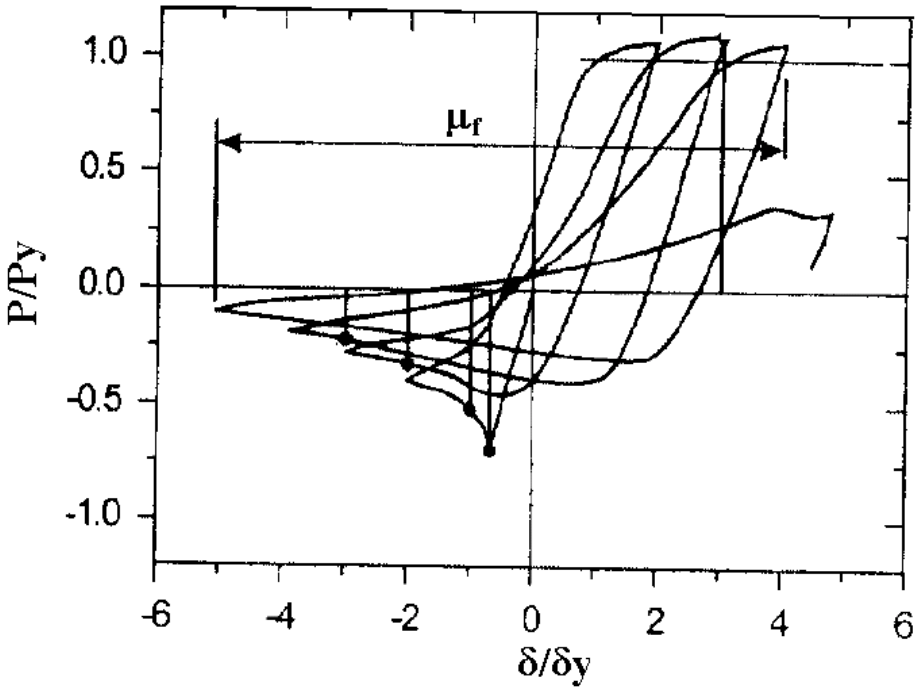

Fig. 3.27 - Definition of the Total Ductility Reached at Fracture μf [Tremblay, 2001].

3.4 General Design Criteria for CBF's

The main objective of earthquake resistant design provisions is to prevent the collapse of structures under severe earthquakes. Many of these provisions require that CBF's be proportioned to remain in the elastic range of response for the design earthquake. In the UBC provision [UBC, 1994] the design strength is expressed as a base shear force, which is distributed along the height of the building to obtain the design force at each story. UBC seismic provisions [UBC, 1994] are based on elastic design spectra and a response reduction factor R_w. By definition a response spectrum is a plot of the maximum response of a single-degree-of-freedom oscillator with

different frequencies to a specific ground motion [Naeim 1989]. Design spectra are smooth representations of the earthquake demands expected at a site.

Examination and re-evaluation of the design practice was carried out by Goel (1993). An alternate design philosophy was proposed in his study, which allowed designing concentric braced frames for ductile behavior. Goel concluded that earthquake resistant design of concentric braced structures should emphasize ductility of bracing members rather than specify increased design forces in order to compensate for lack of ductility.

Frame elements other than the braces should be proportioned to perform within their elastic range of response when acting together with the braces during severe earthquakes. Seismic provisions for CBF's require that beams and columns be protected from yielding under the designed earthquake in order to maintain the structural integrity of the system [Tremblay 2002]. Braces are the primary lateral load resistant elements of the frame and they should be able to undergo inelastic deformations while other elements of the frame remain elastic during a major earthquake.

Factors that significantly affect the inelastic response of CBF's are:

1. Type of brace cross-section. For instance, it was shown by Tang and Goel (1987) that rectangular HSS shapes were more vulnerable to premature local buckling and early fracture. Single-symmetric braces such as T-shapes were less efficient than doubly symmetric shapes such as W-shapes [Black and Popov 1981].

2. Behavior of the braces in compression. The effective slenderness ratio ***KL/r*** is the single most important parameter that affects the compressive capacity and the shape of the hysteretic loops [Jain, Goel and Hanson 1978; Black and Popov 1981; Gugerli and Goel 1992]. Kahn and Hanson (1976) observed from experimental studies that braces with shorter lengths exhibited greater hysteretic energy dissipation than longer specimens. Braces with an effective slenderness ratio ***KL/r*** exceeding 80 generally present pinched hysteretic loops, and a greater ***KL/r*** ratio also results in a lower compressive resistance.
3. Configuration of the concentrically braced frame system. Bracing configuration is also of prime importance in the inelastic response of CBF's. There are basically four types on concentrically braced frame configurations. The first ones are bracing systems in which the lateral load is shared equally between tension and compression acting braces (Fig 3.28a). The second type are the tension-only braces, which are basically slender braces designed to resist the story shear entirely acting in tension (Fig. 3.28b). Diagonal brace configurations are the third type (Fig. 3.28c), the shear is resisted by only one brace or braces oriented in a single direction (tension or compression). The last three types are the Chevron (Fig. 3.28d), V-braces (Fig. 3.28e) and the K-braces (Fig. 3.28f). These configurations are very popular because they allow openings to be easily created within the braced frames. The difference between the two is that Chevron and V-braces behave in a manner such that there is an unbalanced brace load at mid-span of the beam that creates plastic

hinges at mid-span even before the braces reach their yield capacity, whereas the unbalanced brace load is applied horizontally to the columns at mid height of K-braces.

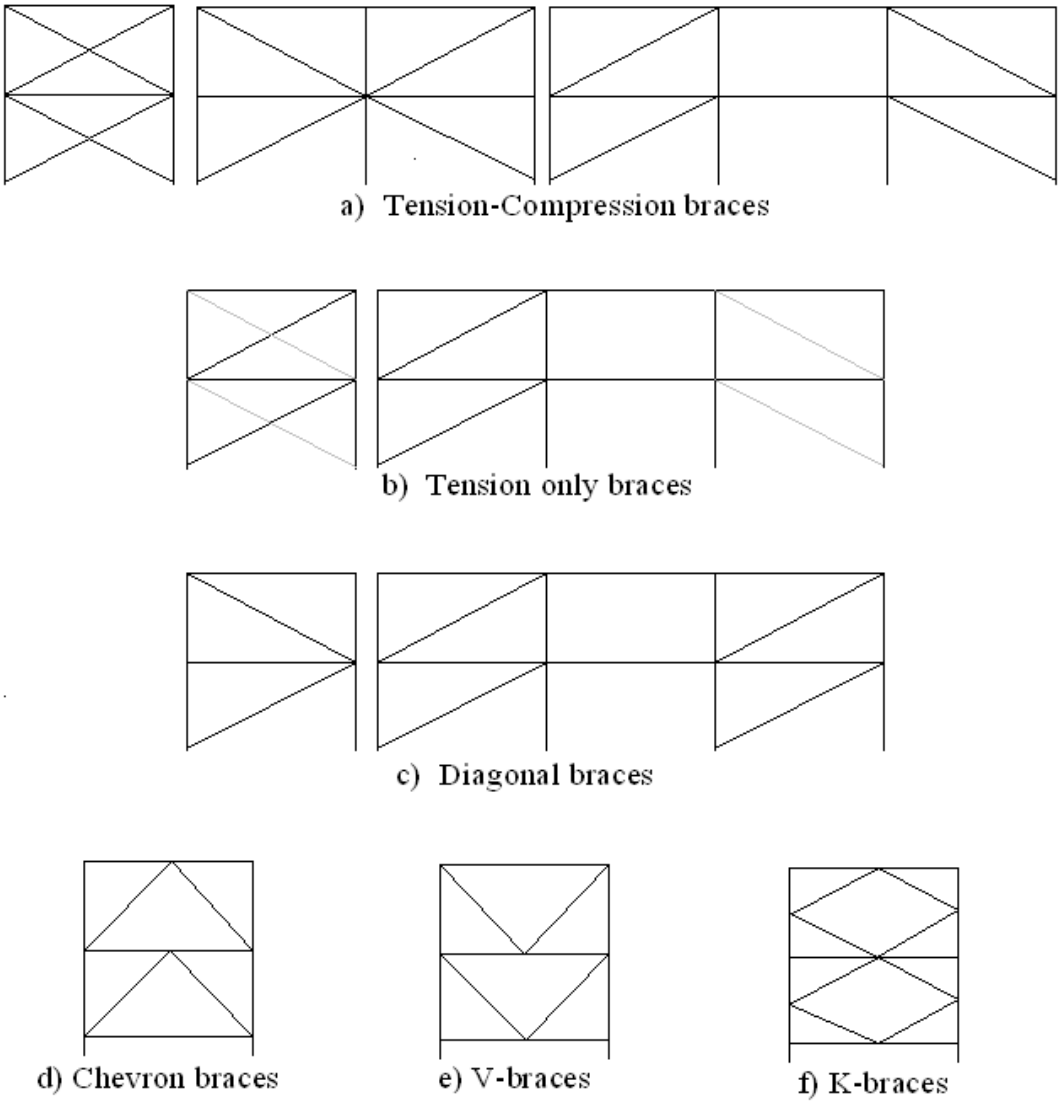

Fig. 3.28 - Concentrically Braced Frame Configurations.

4. Detailing of the brace connection. The brace connections should be proportioned with adequate strength to avoid brittle failures. Failure at the brace connection results in poor inelastic behavior of the brace.

3.5 Concentrically Braced Frames Novel Systems

Extensive efforts have been dedicated to develop systems where the inelastic action would be restricted to structural elements other than the braces in concentrically braced frames [Aristizabal-Ochoa 1986; Balendra, Sam, and Liaw 1995; Tremblay, 1993; Blakeborough, and Bourahla 2002]. The most important novel concentrically braced frame systems recently proposed are presented in the following.

3.5.1 Knee-Brace-Frames (KBF)

Aristizabal-Ochoa (1986) presented a lateral brace system for single and multi-story steel frame construction to overcome the deficiencies of concentrically braced frames. The system was initially called Disposable Knee Bracing (DKB), but today is also known as knee-brace-frame (KBF). In this KBF system one end of the diagonal brace is connected to a knee anchor instead of the beam-column joint. The knee anchor is a fuse-like element that yields in flexure and dissipates energy during severe lateral loads, while the diagonal brace element provides the required lateral stiffness and remains in the elastic range at all times. The knee element is a disposable beam element that can be replaced after its energy dissipation capacity has been utilized. Based on experimental results from various authors [Balendra et al.,

1995; Blakeborough, and Bourahla 2002] it was found that with an appropriate design of knee anchors, the KBF system can be an efficient ductile energy dissipation system for steel concentrically braced frames during severe earthquakes.

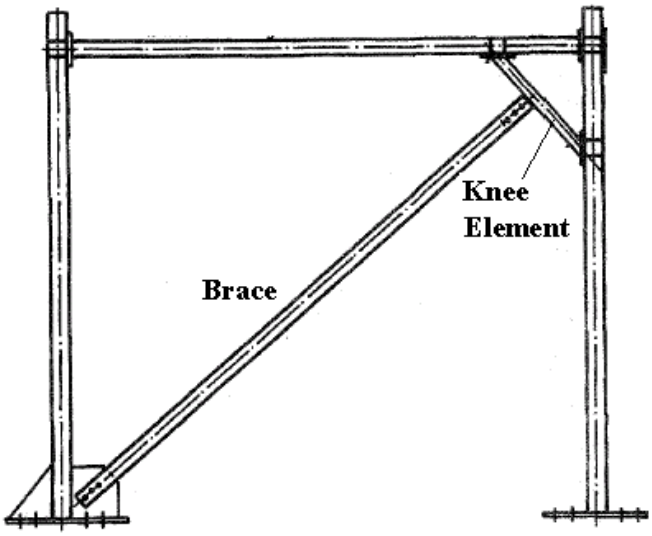

Fig. 3.29 - Knee Brace Frame "KBF" [Aristizabal-Ochoa, 1986].

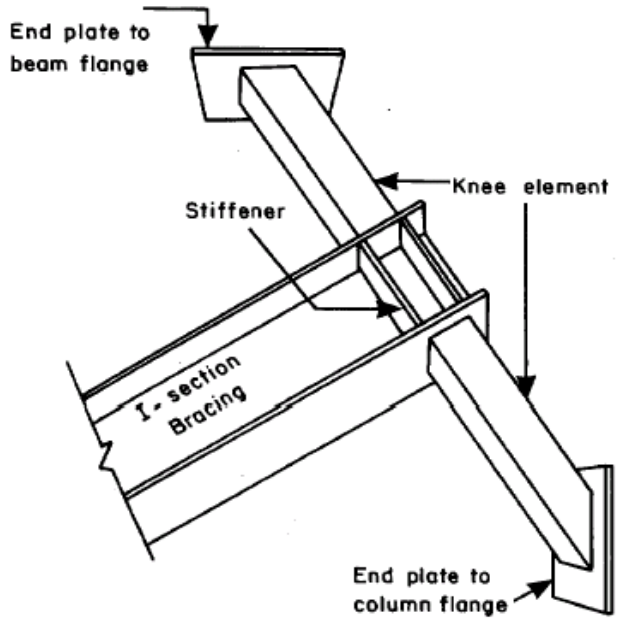

Fig. 3.30 - "KBF" Connection Detail [Aristizabal-Ochoa, 1986].

3.5.2 Friction Concentrically Braced Frames (FCBF)

Tremblay and Stiemer (1993) carried out an experimental study to investigate the performance of concentrically braced frames including friction-type bolted brace connections. This system is known as Friction Concentrically Braced Frame (FCBF). This approach of slotted bolted connections, which was previously studied by other authors [Elsesser 1986; Fitzgerald et al., 1989], consists of a connection at one end of the brace that would slip at a predetermined load level. During severe seismic loads, energy would be absorbed and dissipated by friction upon sliding of these connections, with no damage to the surrounding structural elements. The specimens tested in this study consisted of 203x203x13 hollow tubular brace with a connection that included A325 ¾" bolts, and gusset plates with 5/8"-3/4" thickness. The slotted

holes were able to accommodate a maximum slip equal to approximately 2 in. in each direction. Such amount of slip could easily be experienced in typical braced frame configurations undergoing lateral story drift equal to 2% of the story height, which was current Canadian Code [CSA, 1994] limitation for drift due to seismic loads at the time. The experimental study showed that the FCBF system exhibited very high-energy dissipation capabilities under extreme loading conditions. This system could be used for new buildings or existing braced structures.

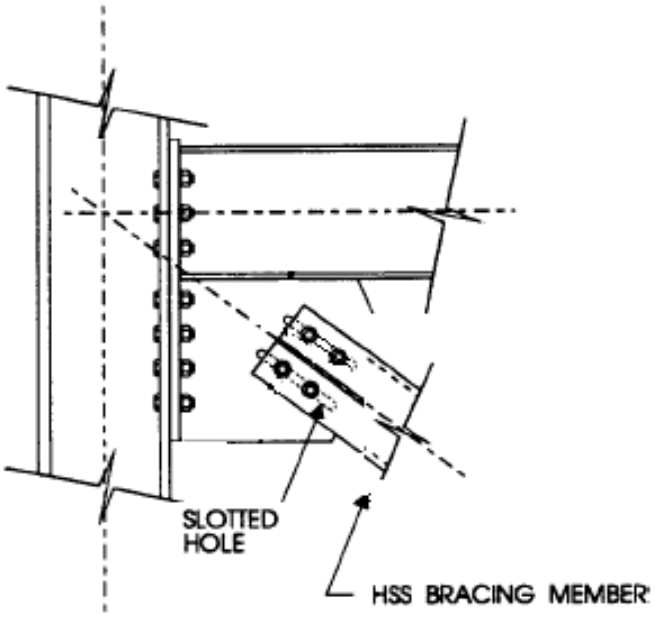

Fig. 3.31 - Friction Concentrically Braced Frame System "FCBF"
[Tremblay and Stiemer, 1993].

3.5.3 Fuse Configurations Intended for HSS Bracing Elements

Tremblay, Bouatay, Rezai, and Prion (1999) investigated the inelastic cyclic load-deformation hysteresis curves of various fuse configurations intended for HSS bracing elements. They performed a pilot experimental study to determine the potential of reducing the disparity between the tension and compression capacities of typical brace components in concentrically braced frames. HSS brace elements with different fuse detail configurations were tested. Some specimens made of HSS 102x102x4.8 included fuse elements consisting of a cross sectional area reduction by the removal of a 55-mm wide elliptical shape from all sides of the HSS brace element. The elliptical cutout was chosen to avoid stress concentrations and high strain zones at sharp rectangular corners. The length of the ellipse (yield zone) was selected as 125-mm and 175-mm, as shown in Fig. 3.32.

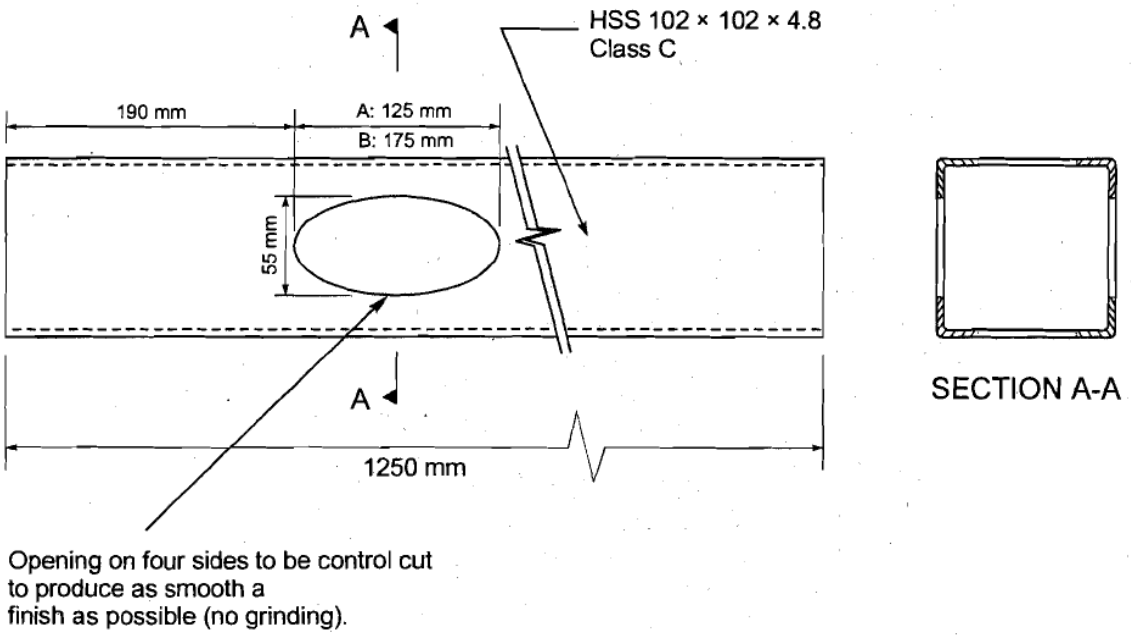

Fig. 3.32 - HSS Wall Elliptical Cutout Detail [Tremblay et al., 1999].

The specimens were intended to be subjected to concentric axial cyclic loading, but it was noted that upon installation of the specimen in the loading frame a small deviation was measured (less than a few hundreds of an inch) between the specimen and the line of action of the actuator. A ductile load-deformation behavior with a maximum post-yield axial deformation of four times yield displacement was recorded from some specimens as can be seen in Fig. 3.33.

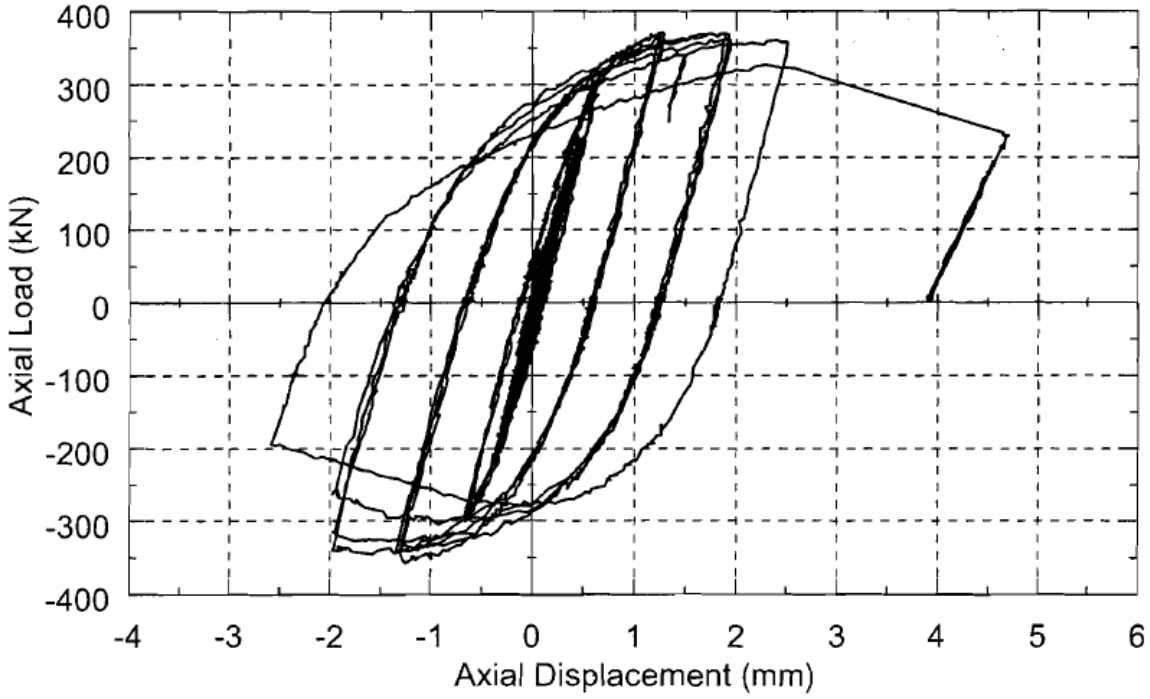

Fig. 3.33 - Axial Load vs. Axial Displacement Response of Elliptical Fuse Element [Tremblay et al., 1999].

Experimental results indicated that even though the yield zone was distributed over the entire ellipse length, the plastic strains were mainly concentrated over a relatively short length of the fuse (around mid-fuse length), as can be seen in Fig. 3.34. An expected fracture occurred in the narrowest portion of the fuse. This implies that for a structure that could undergo large story displacements during an earthquake the length of the fuse detail should be increased considerably to ensure the braces do not rupture under large axial displacement demands.

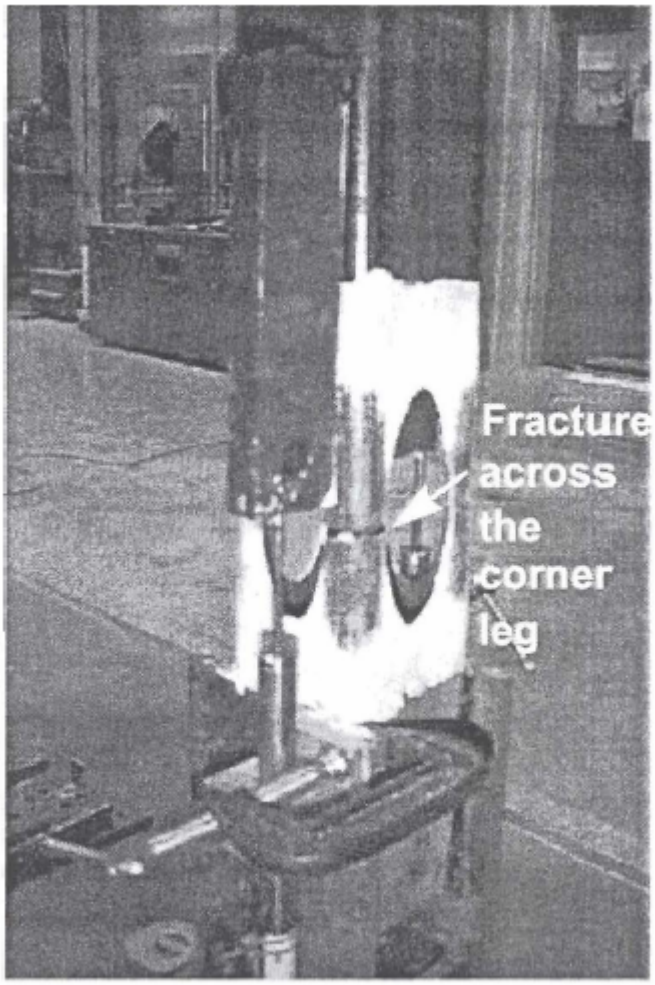

Fig. 3.34 - Fracture Failure of Elliptical Fuse Element [Tremblay et al., 1999].

3.5.4 Buckling-Restrained Braced Frames (BRBF)

Black, Makris, and Aiken (2004) performed a comprehensive testing program on buckling-restrained braced frames "BRBF" also known as unbonded braces. BRBF is a relatively new type of concentrically braced frame system that has had extensive use in Japan as hysteretic dampers within moment-resisting frames. The introduction to the US design practice occurred in 1999, and its use in this country has primarily been as a main seismic-load resisting system for buildings [Sabelli and Lopez, 2004].

Buckling-restrained braced frames offer strength and energy dissipation while at the same time exhibit well-distributed yielding. This system has full, balanced hysteretic behavior with compression yielding similar to tension yielding behavior [Tremblay, 1999]. It utilizes the ductility of steel much more effectively than do conventional braced frames such as Special Concentrically Braced Frames (SCBF's) or Ordinary Concentrically Braced Frames (OCBF's), which depend on brace buckling for their ductility.

The buckling-restrained brace tested consisted of a steel core encased in a steel tube filled with concrete, shown in Fig. 3.35. The steel core carries the axial load while the outer tube, via the concrete, provides lateral support to the core and prevents global buckling. A thin layer of material along the steel core/concrete interface eliminates shear transfer during the elongation and contraction of the steel core and also accommodates its lateral expansion when in compression. It is the

ability of the steel core to contract and elongate freely within the confining steel/concrete-tube assembly that leads to the name unbonded brace.

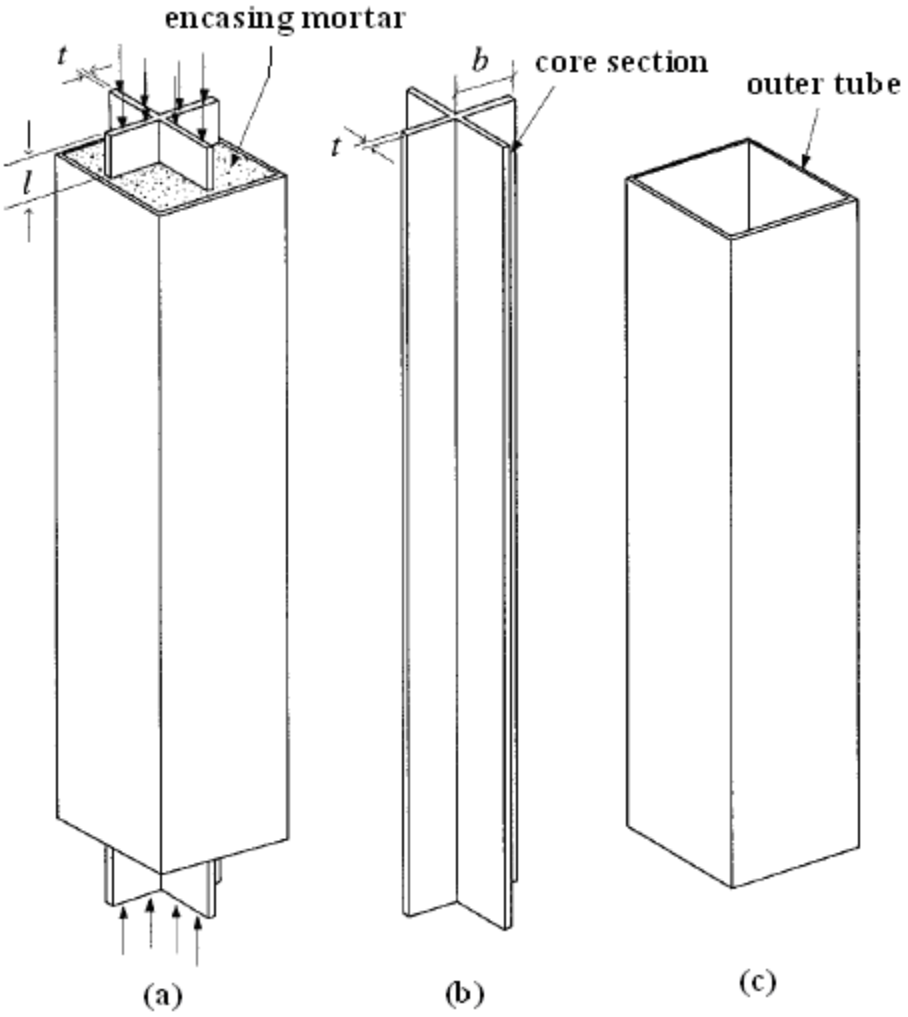

Fig. 3.35 - (a) Buckling-Restrained Brace, (b) Core Member, and (c) Outer Tube [Black et al., 2004].

Three distinct buckling modes are identified in the stability analysis of BRB's: (1) global flexural buckling of the entire brace; (2) buckling of the inner core in higher modes; (3) plastic torsional buckling of the portion of the steel core which extends outside the confining tube.

The BRB specimens tested by Black et al., were subjected to cyclic loading. Additional tests that included large-deformation, low cycle fatigue tests and simulated earthquake displacement tests. The BRB specimens exhibited stable hysteretic behavior for all displacement amplitudes as can be seen in Fig. 3.36. The loops from the displacement at each end are nearly identical indicating that yielding happens uniformly throughout the member. The maximum brace force was 3,005-KN (675.6 Kips) in tension and 3,400-KN (764.3 Kips) in compression, a difference of 13%.

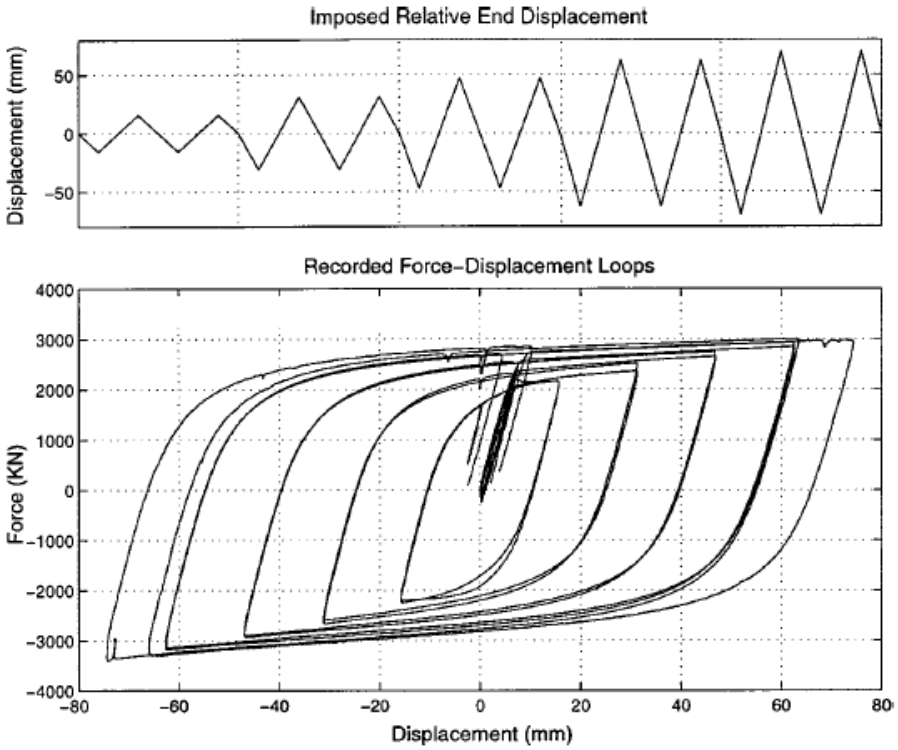

Fig. 3.36 - Cyclic Loading Test: (Top) Loading History; (Bottom) Recorded Force versus Overall Displacement of Yielding Portions
[Black et al., 2004].

The force-displacement loops resulting from the low-cycle fatigue test performed are shown in Fig. 3.37. The brace exhibited stable hysteretic behavior for the entire test consisting of 31 cycles. The initial intention was to conduct the test to failure, which was anticipated to occur at roughly 20 cycles. This value was exceeded and subsequently the test was stopped at 31 cycles (without failure) in order to avoid potential damage to the instrumentation or test setup.

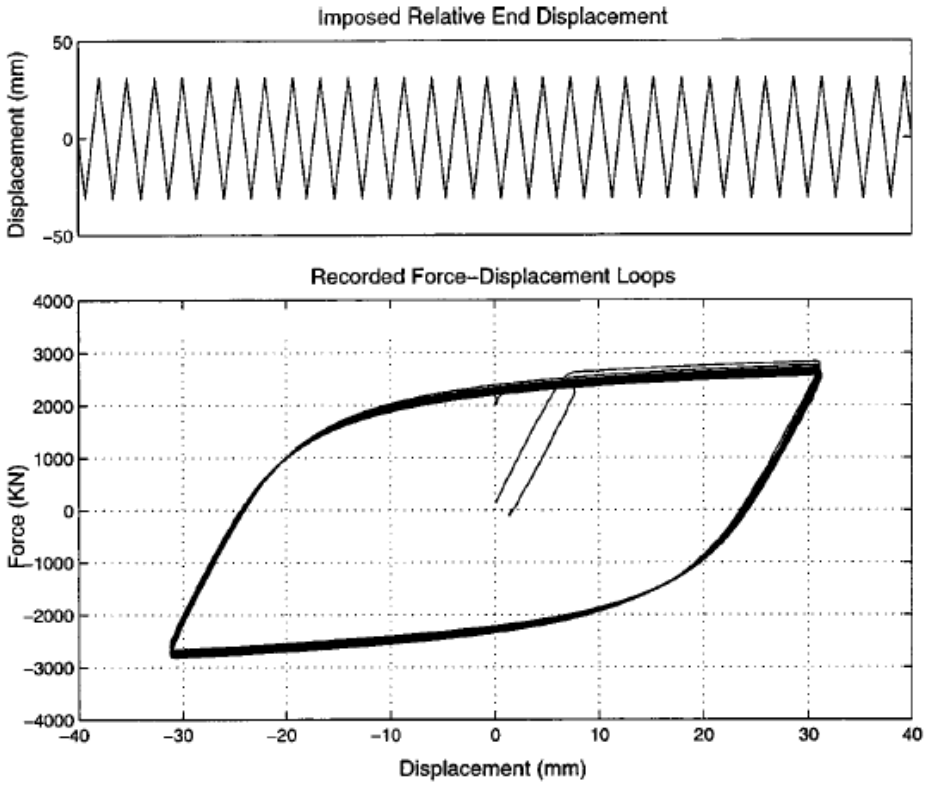

Fig. 3.37 - Low Cycle Fatigue test: (Top) Loading History; (Bottom) Recorded Force versus Overall Displacement of Yielding Portions
[Black et al., 2004].

From the experimental results it was found that the plastic torsional buckling in the inner core is the most critical stability mode. It was concluded that if the yielding portion extends outside of the confining tube, the flanges of the yielding portion should have a small width to thickness ratio, approximately less than five. It was also demonstrated that buckling-restrained braced frames (BRBF's) are a reliable and practical alternative to conventional framing systems to enhance the earthquake resistance of new and existing structures, capable of providing the rigidity needed to

satisfy structural drift limits, while delivering a substantial and repeatable energy absorption capability.

3.6 Smart Materials in Civil Engineering

The work of civil engineers is becoming more challenging due to the increasing demand for slender, wide spanned structures with high adaptability to changes in use, and also the increasing demand for a reduction of the structural mass for economical purposes. Civil engineers are seeking new materials and technologies and are going beyond their habitual way of thinking. One of these new materials are shape memory alloys, which are often regarded as "smart materials". This section presents a brief description of shape memory alloys, some of the applications of shape memory alloys in civil engineering structures, previous studies on composite materials reinforced with shape memory alloys that are well suited for civil engineering applications, and a preliminary study on a High Performance Composite Element (HPCE), which constitutes the foundation of one of the fuse elements evaluated in this dissertation.

3.6.1 Shape Memory Alloys (SMA)

Shape Memory Alloys (SMA's) are a class of alloy that exhibit thermo-mechanical characteristics that make them useful for seismic applications. The main advantage of SMA's is that, unlike other metals, the nonlinear deformation is

reversible. They have the ability to dissipate significant energy with little permanent deformation.

The only two types of SMA that have achieved a commercial exploitation level are Nitinol alloys (Nickel Titanium Naval Ordnance Laboratory) and copper-based alloys [Barnes, 1999]. The nickel-titanium alloys are capable of strain recovery of up to 8% to 8.5%, large pseudo-elastic hysteresis, they tend to be more thermally stable than copper-based alloys, and also have better corrosion resistance and higher ductility at low temperatures. Copper-based alloys are capable of strain recovery of up to 4.5%, are susceptible to stress-corrosion cracking, but are much less expensive. Copper-based alloys can be melted and extruded in air with ease, and have a wider range of potential transformation temperatures.

Shape memory alloys have two unique properties: Pseudo-Elasticity or Super-Elasticity (SE), and Shape Memory Effect (SME). These two unique properties are made possible through a solid-state phase change or molecular rearrangement in which molecules remain closely packed so that the substance remains solid. The two phases, which occur in SMA's are:

- Martensite: is the soft and ductile, easily deformed, lower temperature phase.
- Austenite: the stronger, high temperature phase.

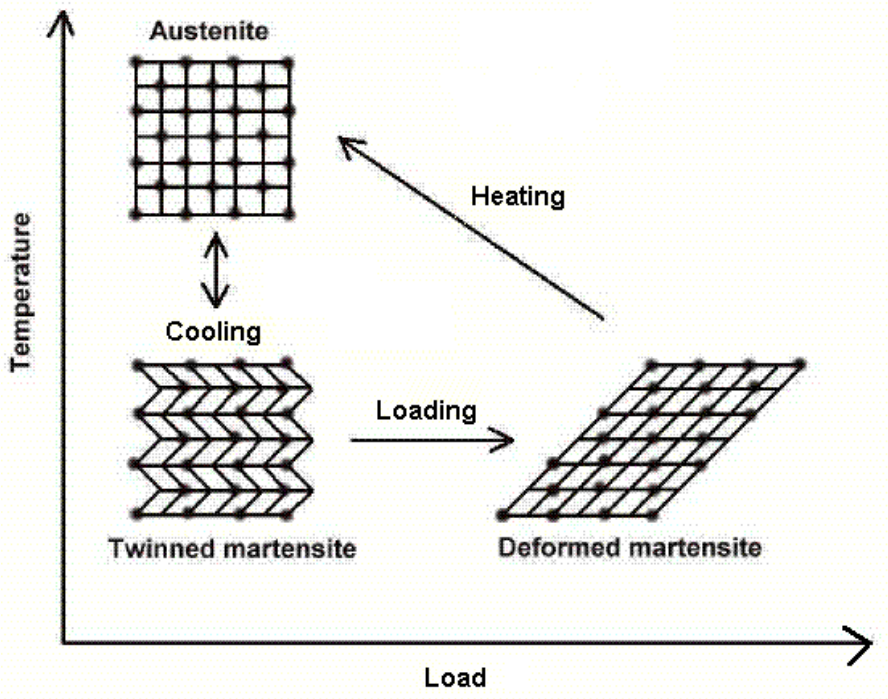

Fig. 3.38 - Schematic of Thermo-Elastic Martensitic Austenitic Phase Transformation of SMAs [Jorma Ryhänen, 2000].

.

3.6.1.1 Pseudo-Elasticity Effect (SE)

Pseudo-Elasticity or Super-Elasticity "SE" is an almost rubber-like flexibility of some SMAs. The super-elasticity of SMAs occurs without a change in temperature, but this property is not an isothermal phenomenon because as load is applied and strain increases there is a stress induced transformation due to self heating of the material (Fig. 3.39). In Fig. 3.39 M_s is the temperature at which the Martensite phase begins forming, M_f is the temperature at which the Martensite phase

finishes forming, A_s is the temperature at which the Austenite phase begins forming, and A_f is the temperature at which the austenite phase finishes forming.

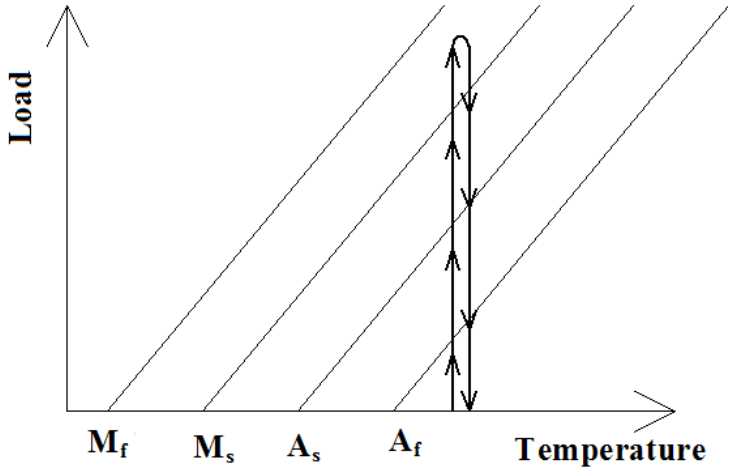

Fig. 3.39 - Stress Induced Phase Transformation Load-Temperature Diagram.

Nickel-Titanium is one type of SMA known for its pseudo-elastic properties. For Nitinol alloys, the phase change can be stress induced at room temperature if the alloy has the appropriate formulation and treatment [Barnes, 1999]. Nitinol starts its loading cycle in the stiff Austenitic phase. When it reaches a certain stress it transforms to the Martensitic phase. This initial phase change from Austenite to Martensite results in a plateau in the stress-strain curve that resembles yielding. The load is absorbed by the softer Martensite phase as the specimen deforms within its inelastic range of behavior. The loading plateau is followed by a significant increase in stiffness similar to an exaggerated strain hardening effect that is considerably valuable because it aids in limiting displacements. Upon unloading, the Martensite phase becomes unstable and reverts back to Austenite. This transformation occurs at a

lower stress than the forward transformation, creating a hysteresis, which results in energy dissipation, as shown in Fig. 3.40. Furthermore, upon unloading, the alloy springs back to its original shape with little residual strain, generally less than 2%. This leads to the possibility of dissipating energy over the course of a cyclic or dynamic loading, such as during a seismic event.

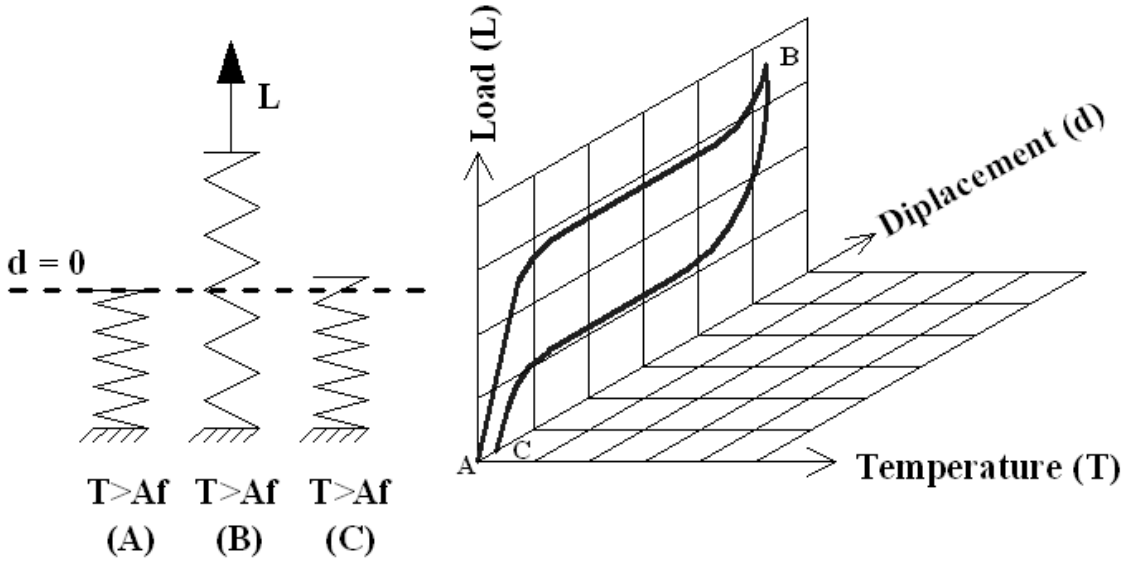

Fig. 3.40 - Three Dimensional Load-Displacement-Temperature Showing The Super-Elasticity "SE" Property of SMAs.

Since SE only occurs at some temperatures, to be useful in civil engineering applications, the super-elastic range of the SMA must be as wide as possible.

3.6.1.2 Shape Memory Effect (SME)

The Shape Memory Effect "SME" is the unique ability of SMAs to be deformed and then returned to their original shape simply by applying heat to the alloy. Unlike Pseudo-Elasticity, the phase change is temperature induced rather than stress induced. The loading cycle of the shape memory effect is similar to that of Pseuso-Elasticity until unloading. Upon unloading there is some inelastic deformation recovery, but most of the residual deformation is only restored during heating to a temperature above that of the Austenite phase temperature A_f.

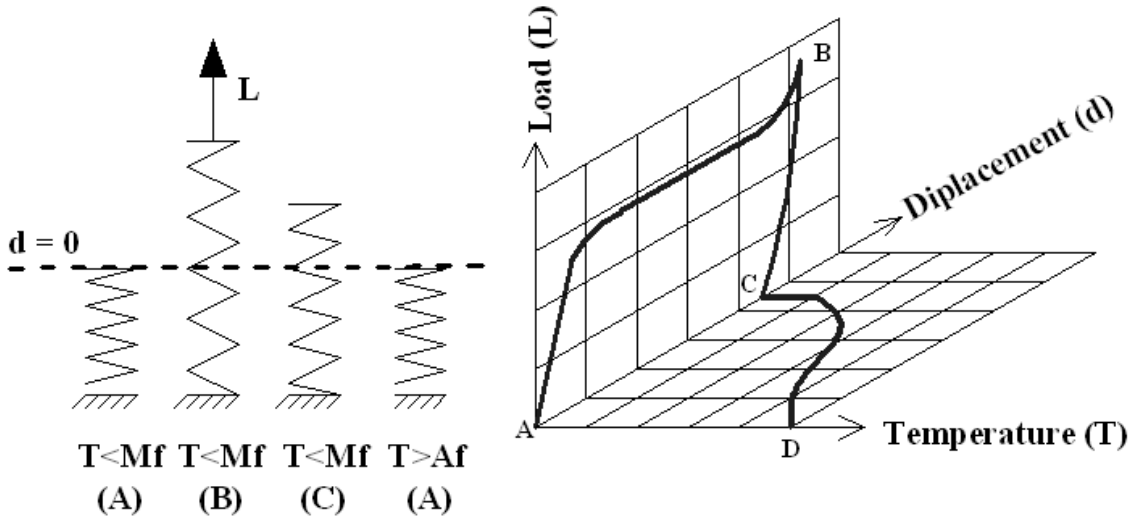

Fig. 3.41 - Three Dimensional Load-Displacement-Temperature Showing the Shape Memory Effect "SME" Property of SMAs.

3.6.2 Shape Memory Alloys in Civil Engineering Structures

Further improvements to conventional seismic protection strategies in reducing structural damage can be achieved using new materials endowed with better mechanical properties such as shape memory alloys. Some studies on SMA's and their applications in civil engineering structures are presented in the following.

3.6.2.1 Higashimo (1996)

Higashimo (1996) carried out an analytical study to evaluate the effectiveness of an eccentric bracing shape memory alloy device for multistory buildings. The device consists of multiple loops of SMA wires incorporated into eccentric braced frames at each level of the buildings, as shown in Fig. 3.42.

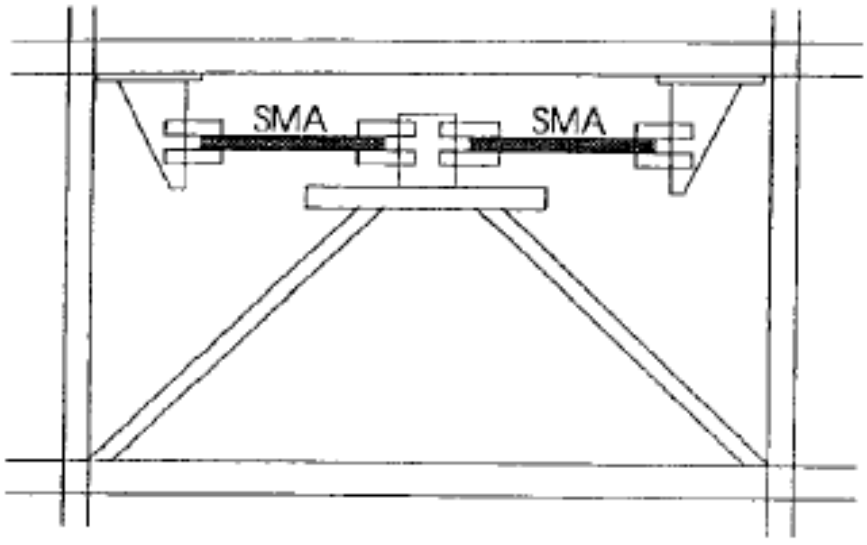

Fig. 3.42 - Schematic of a Bay Modeled with Two Isolation Devices Composed of Multiple Loops of Nitinol Were Wrapped Around Two Posts [Higashimo, 1996].

The model was subjected to a Northridge ground motion record scaled to 0.2g, 0.4g, and 0.6g. It was found that interstory drift decreased by almost 50% for each of the three levels of input, while the first-floor interstory drift was reduced even further. The energy absorbed by the frame was reduced to about 15% compared to the frame without the devices. The one noted drawback was the increase in acceleration, as high as 200% in some stories, attributed to an increase in initial stiffness due to austenite phase of the hysteretic behavior. Although initially all of the SMA devices were designed to be identical, it was discovered that the most effective control strategy was to use devices on the first floor having twice the yield capacity of those on the upper floors. Using this approach, the devices on the first five floors were effective in dissipating energy through hysteretic behavior, but there was no energy dissipation at the top floor, even for the 0.6g ground motion.

3.6.2.2 Wilde, Zheng, Gardoni, and Fujino (1998)

Wilde, Zheng, Gardoni, and Fujino (1998) conducted an experimental study on tension-compression and bending of Nitinol bars with different heat treatment to evaluate their response under cyclic loading with various amplitudes and determine the feasible application of shape memory alloy damper devices. First a tension-compression test was carried out. Then, experiments of SMA subjected to uniform bending moment were performed. Additionally, a fatigue test was conducted to determine the cyclic properties of the specimens. Finally the experimental results

were verified by simple 3D numerical simulation by FEM. The SMA specimens used for the experiments are shown in Fig. 3.43.

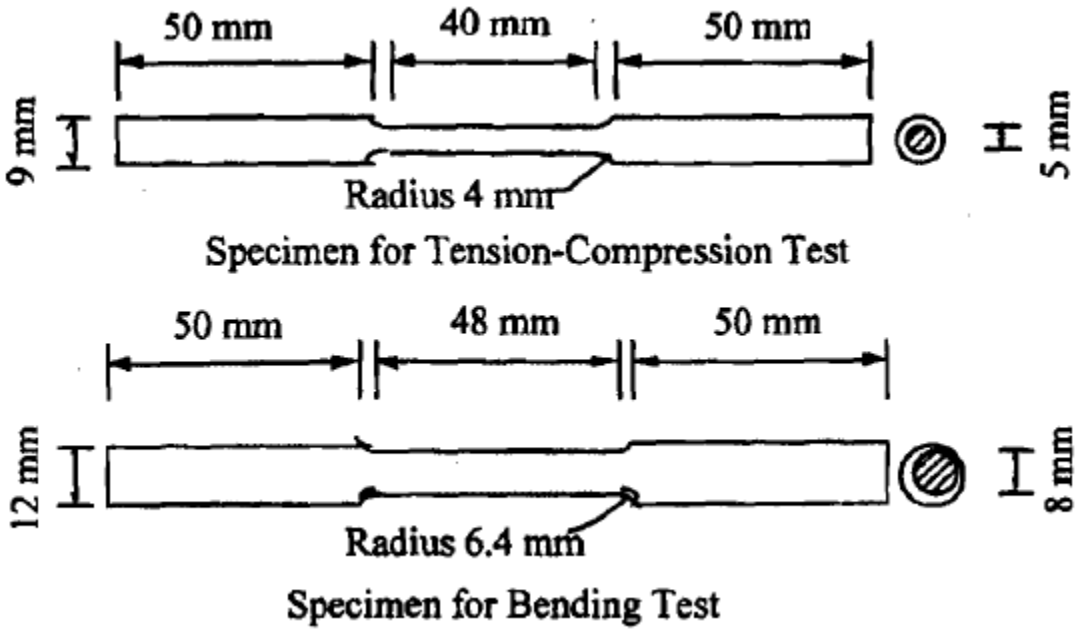

Fig. 3.43 - Tension-Compression and Bending Test Specimens [Wilde et al., 1998].

The specimens were machined from a round section. The central portion of the specimen had a smaller cross section than the end portions in order to force deformations to concentrate at a section where the stresses are not affected by the loading equipment-gripping device. The radius between the two cross sections was on the order of one to two times the diameter of the bar to reduce the stress concentration caused by the abrupt change in section area. For tension and compression tests, the length to diameter ratio of the specimen yield zone was limited to avoid several

undesirable conditions that may happen during compression, such as a very weak buckling capacity compared to the tensile capacity of the specimen. A height-diameter ratio of 10 was suggested as a practical limit by the authors. However, it is important to note that as the length of the specimen decreases, the effect of boundary conditions at the ends becomes relatively important. Therefore for tension and compression test, a height-diameter ratio of 8 was chosen. The bars were cut with an abrasive wheel and machined to the desired cylindrical dimensions. The machining step was quite crucial, as it should be performed as slow as possible to avoid any significant temperature increase that could result in a modification of the super-elastic properties.

Test results confirmed a large hysteretic response of Nitinol damper devices and its variable response at different displacement levels. The specimen thermally treated at 400˚C for 600 seconds (type 1) had smaller residual displacements and more stable hysteresis than the specimen thermally treated at the same temperature but for 1800 seconds (type 2).

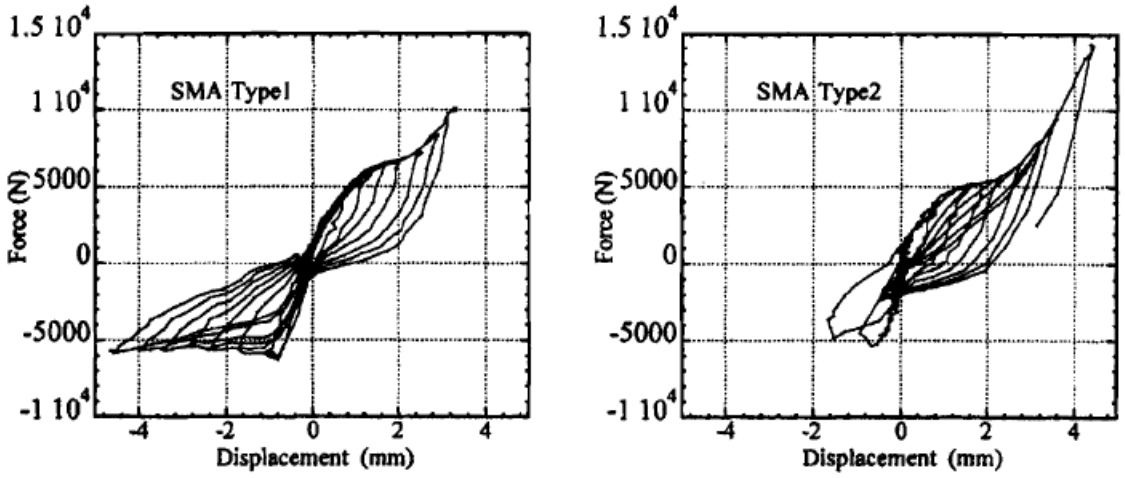

Fig. 3.44 - Force-Displacement Curves for Tension-Compression Tests

[Wilde et al., 1998].

Both type of specimens showed long fatigue life. It was observed during the tests that the hysteresis loops did not deteriorate with the increase of number of input cycles.

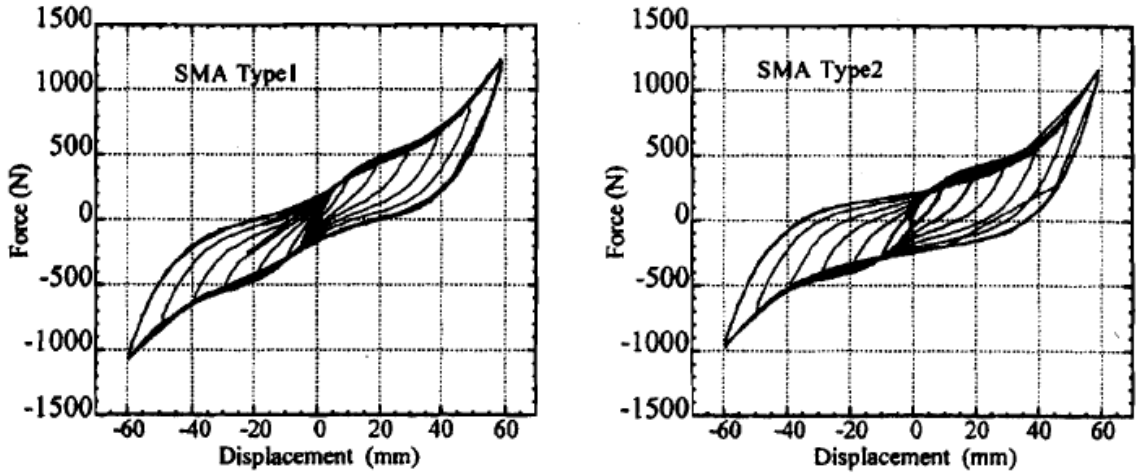

Fig. 3.45 - Force-Displacement Curver for Simple Harmonic Bending Tests

[Wilde et al., 1998].

3.6.2.3 DesRoches (1999)

DesRoches (1999) investigated the efficiency of using "smart restrainers" to reduce the seismic vulnerability of bridges. The use of shape memory alloys (SMA) devices as replacement for conventional restrainers was investigated as a method for improving the seismic response of bridges. Analytical studies showed that these devices, used as passive dampers, are effective in both limiting the relative displacement between frames, and reducing the negative effects of pounding of bridge decks. In addition, by concentrating damage and energy in controlled locations, these devices can be used to reduce the demand on individual frames in multiple-frame bridges. Comparisons with conventional restrainers showed that the shape memory alloy restrainers reduced the relative hinge opening between bridge frames 20-25% of that of conventional restrainers.

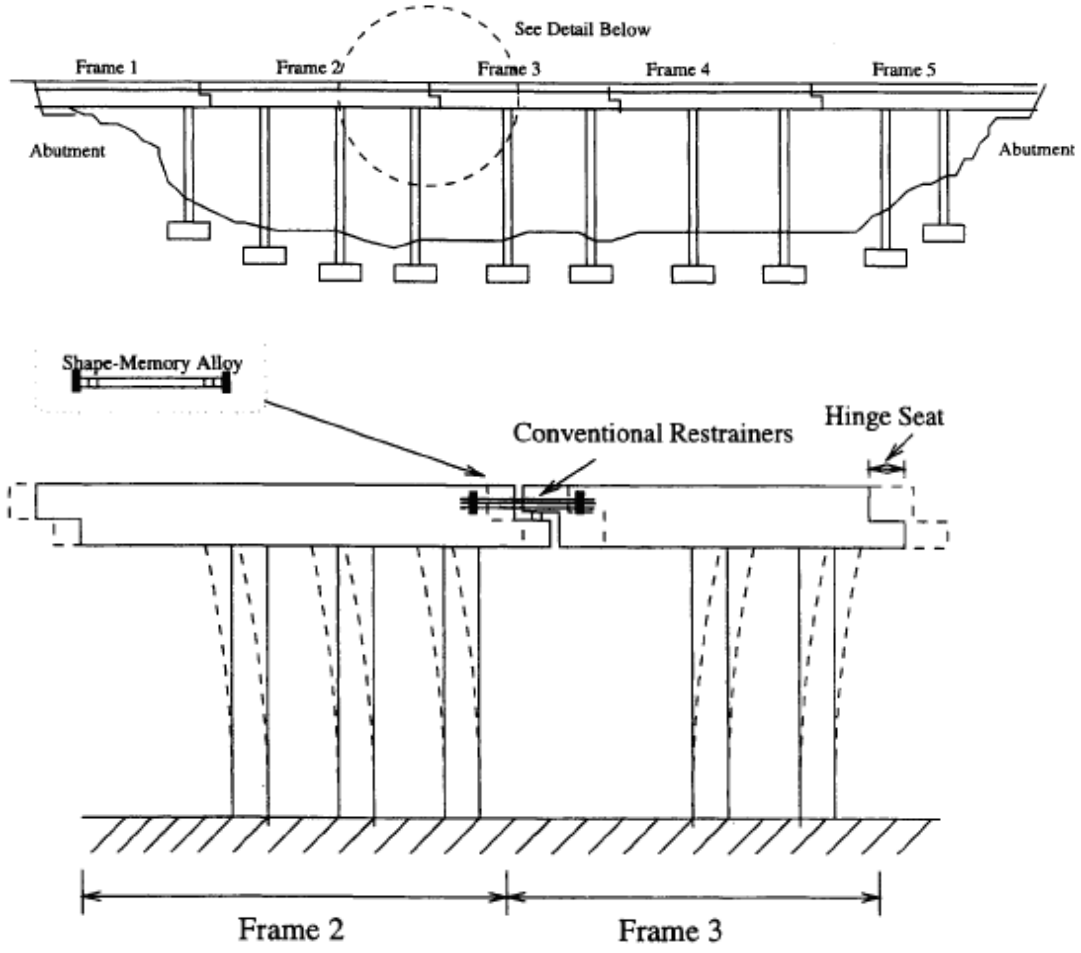

Fig. 3.46 – Typical Multiple-Frame Bridge with Intermediate Hinge and Restrainer [DesRoches, 1999].

3.6.2.4 Tamai and Kitagawa (2002)

Tamai and Kitagawa (2002) developed a novel type of seismic resisting members with shape memory alloy (SMA) wires. The elements developed by Tamai and Kitagawa were intended for use as hysteretic dampers for building structures with concentrically braced frames and exposed-type column base. Pulsating tension loading tests were performed with constant, increasing and decreasing strained

amplitude to investigate restoring force characteristics of the SMA wires by taking advantage of their super-elastic properties. Test results showed spindle shaped hysteresis loops without residual deformation; they also showed good fatigue toughness and absorbed energy, which makes the systems good candidates for hysteretic dampers in buildings. The exposed-type column base-plate was fastened to the base with anchor bolts consisting of SMA and ordinary steel bolts as can be seen in Fig. 3.47. A sheath encloses the SMA bolts to enable repair after an earthquake.

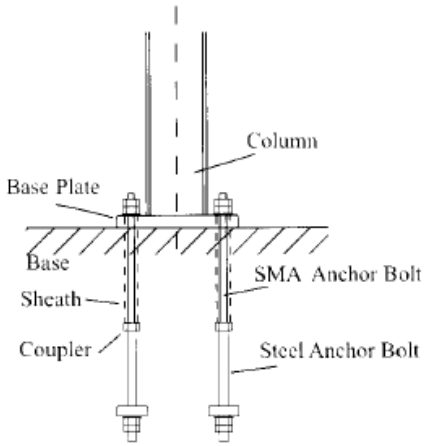

Fig. 3.47 - Exposed-Type Column Base with SMA Anchorage

[Tamai, and Kitagawa, 2002].

The braced frame with the SMA damper is shown in Fig. 3.48. The two diagonal braces are fastened to the corner of the beam-to-column connection. Similar to the base plate anchor bolts the brace consists of SMA and ordinary steel braces. The tension connected braced frame with the SMA damper has a good mechanism that prevents compressive axial force in the brace, and consequently brace buckling even if the brace has a relatively large slenderness ratio.

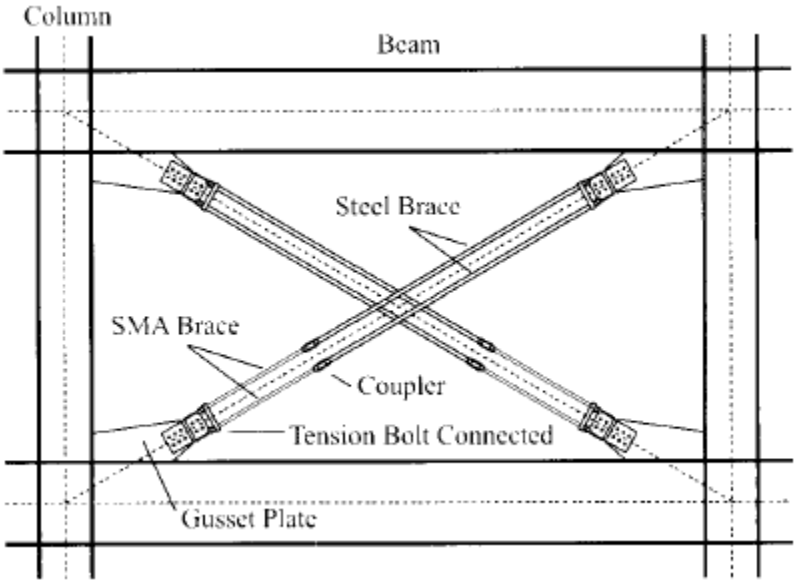

Fig. 3.48 - Concentrically Braced Frame with SMA Damper [Tamai, and Kitagawa, 2002].

In both structural systems, the initial elastic limit displacement and strength are adjustable by changing the length and cross sectional area of the ordinary steel and SMA members. The seismic energy is absorbed effectively in the SMA, which makes it possible to reduce the responses of the building frame and prevent serious damage to the frame under severe earthquakes, and also enables the frame to be easily repaired by simply renewing the SMA members after the earthquake.

3.6.2.5 DesRoches and Delemont (2002)

DesRoches and Delemont (2002) investigated the effectiveness of a different type of "smart restrainers" to reduce the seismic vulnerability of bridges due to excessive movement at the intermediate hinges and abutments during earthquakes. This "smart restrainer" was intended as a retrofit for a simply supported bridge by replacing conventional restrainer cables and bars that were also initially designed to reduce the possibility of collapse due to unseating at the supports. Full-scale SMA restrainer bars were tested. The restrainers were 280-mm long, and 25.4-mm diameter Nitinol shape memory alloy bars as shown in Fig. 3.49.

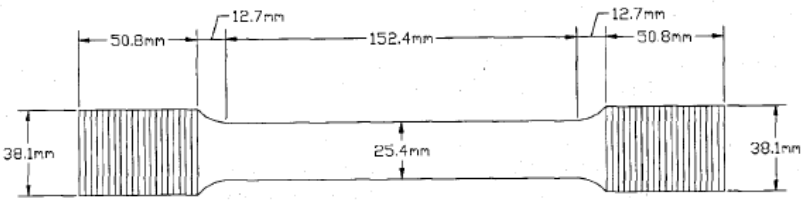

Fig. 3.49 - Nitinol SMA Restrainer Bar Used in Experimental Test [DesRoches, and Delemont, 2002].

The bars were subjected to cyclical strains up to 8% with minimum residual deformation. The relative hinge displacement in a bridge using conventional steel restrainer cables was compared with the displacement using smart restrainers. Results showed that the SMA restrainers reduced relative hinge displacements at the abutment much more effectively than conventional steel cable restrainers. The large

elastic strain range of the SMA restrainers allowed them to undergo large deformations while remaining within their elastic range of behavior. Additionally, the super-elastic property of the SMA restrainers resulted in energy dissipation at the hinges.

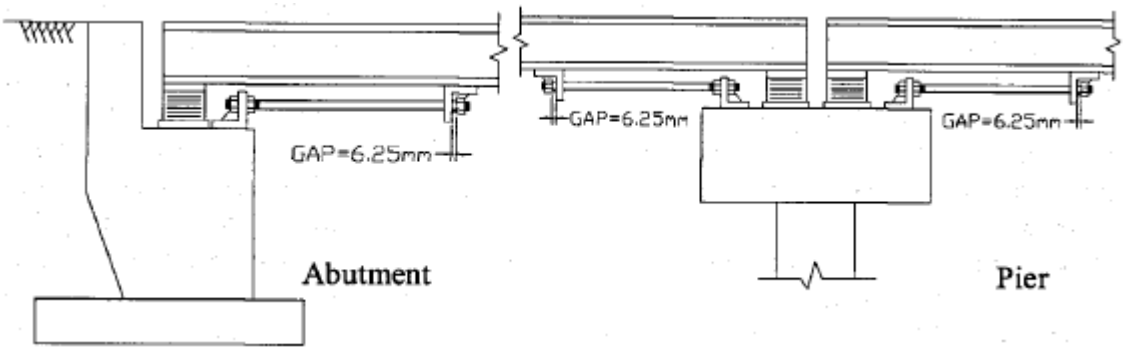

Fig. 3.50 - Configuration of SMA Restrainer Bar in Multi-Span Simply Supported Bridge [DesRoches, and Delemont, 2002].

3.6.2.6 Leon, DesRoches, Ocel and Hess (2001-2004)

Leon, DesRoches, Ocel and Hess (2001-2004) evaluated the application of Nitinol shape memory alloy tendons in a semi-rigid steel beam-column connection. Two full-scale beam-column connections were tested with and without the tendon devices according to the SAC testing protocol. The beam-column connection consisted of a W24x94 beam, W14x159 column, all of A572 Grade 50 steel, and four 1 ½ inch diameter SMA rods connected from the flanges of the beam to the column, as shown in Fig. 3.51.

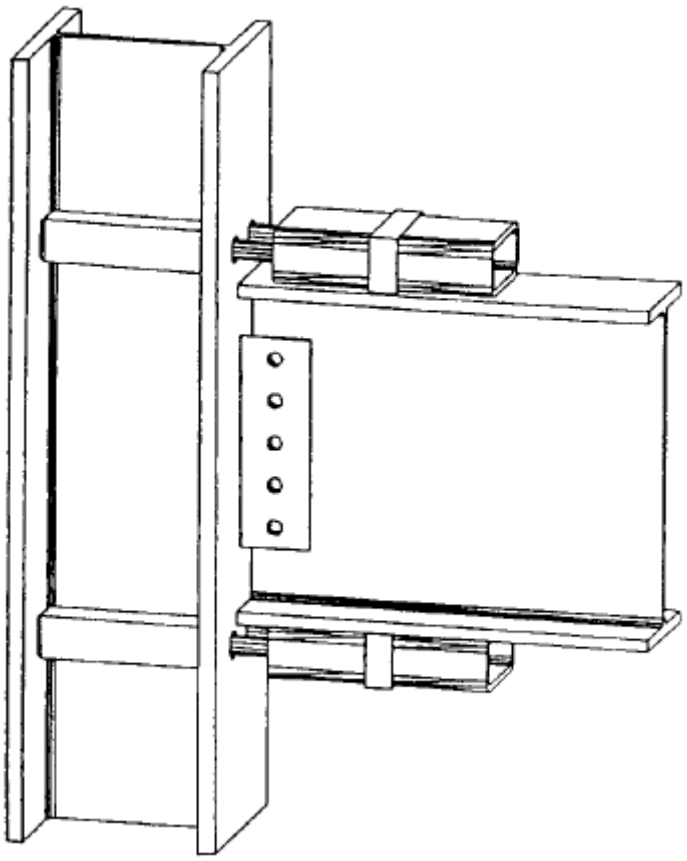

Fig. 3.51 - Innovative Beam-Column Connection Using Shape Memory Alloy Tendons [DesRoches et al., 2004].

Because the tendons were designed to act in the shape memory mode (purely martensitic behavior), the tendons were heated upon the end of cycling to restore the connection to its original configuration. The initial test was halted because the shear tab weld fractured on each end. After repairing and reinforcing the shear welds, the specimens were retested. The tendons showed that at repeated 4% drift, the hysteretic

loops were nearly identical, leading to the conclusion that the SMA connection was able to undergo repeated large deformations without strength degradation. Further, the hysteretic loops of a second set of test were nearly identical to those of the first set, indicating that the tendons were able to recover their properties following heating to restore their original shape. The connection failed after approximately 8 cycles at 4% drift due to a stress concentration above the termination point of the fillet weld. Due to this failure, the connection did not exhibit stable behavior for many more cycles at drifts of 4% or greater.

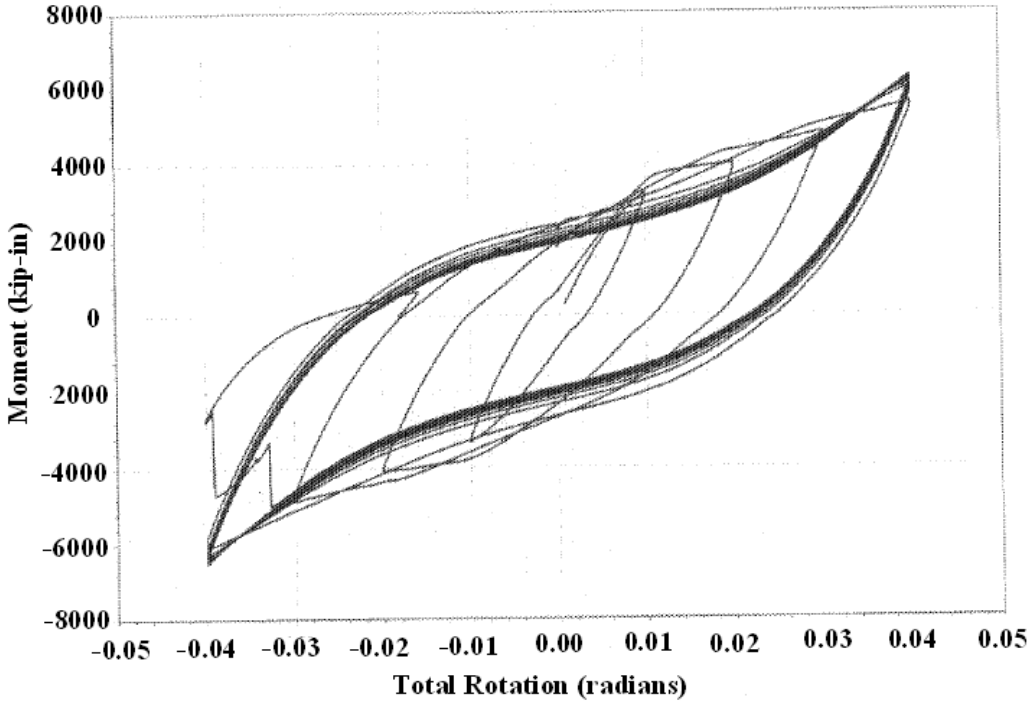

Fig. 3.52 - Moment vs. Total Rotation of SMA Beam-Column Connection [DesRoches et al., 2004].

In 2004, they carried out similar tests to further evaluate the feasibility of such new class or partially restrained moment connection using shape memory alloys. Besides the quasi-static test according to the SAC loading protocol, a test was also performed under dynamic loads to examine the strain rate effects on the performance of the connection. The dynamic tests showed similar behavior, except for a decrease in energy dissipation capacity when compared to the quasi-static test. Details of this second connection tested are shown in Fig. 3.53. This second connection utilized the same design philosophy as the first connection, but the detailing of various elements was slightly altered to address deficiencies found during testing of the first connection in 2001.

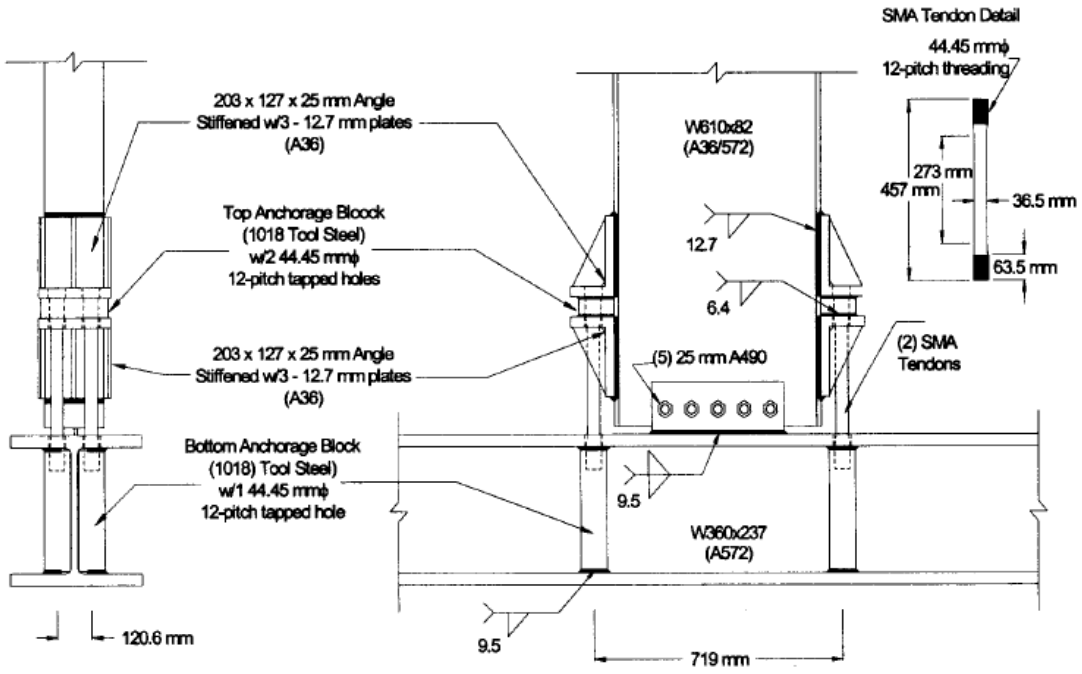

Fig. 3.53 - Details of Second SMA Beam-Column Connection

[DesRoches et al., 2004].

The connection was tested and then the tendons were heated to initiate the shape memory effect, then the connection was re-tested showing nearly identical hysteretic behavior during the retest. The hysteresis loops of the eighth 4% drift cycle were identical, with no loss in strength, stiffness, or any signs of fatigue. This implies that these hybrid connections could be reused following a seismic event, if the tendons can be appropriately heated to initiate the shape memory effect.

A comparison of the moment versus rotation relationship for the first cycle with a peak rotation of 3-rads. is shown in Fig. 3.54 for the initial, retest, and dynamic tests. The most obvious feature of the dynamic hysteresis was the pronounced difference in energy dissipation between the initial and the retest. The energy dissipated during the dynamic test was approximately 1/3 that of the initial test, signifying that the martensitic tendons display obvious strain rate effects.

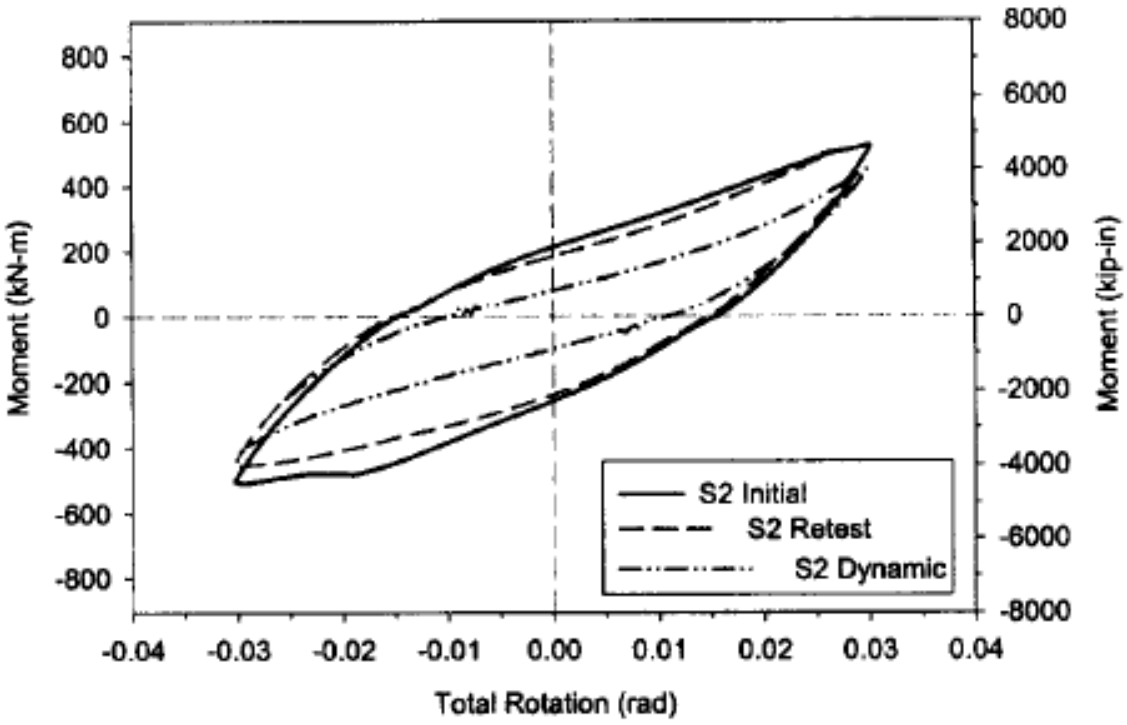

Fig. 3.54 - Moment versus Total Rotation Comparisons for Connection [DesRoches et al., 2004].

3.6.2.7 Moumni, Van Herpen, and Riberty (2005)

Moumni, Van Herpen, and Riberty (2005) studied the fatigue behavior of Nitinol shape memory alloys through a series of fatigue uniaxial tensile-compressive tests performed at a temperature and deformation regime in which the alloy exhibited pseudo-elasticity. Based on experimental results numerical calculations were performed to predict the mechanical fatigue behavior of SMA's. Two types of fatigue were considered: (a) Classical mechanical fatigue due to mechanical cyclic in the pseudo-elastic domain of SMA's, in which the objective was to determine the number

of cycles before failure, (b) Thermal fatigue or amnesia of the material due to degradation of the material characteristics responsible for the shape memory effect, where the objective was to determine if the material remained able to remember its initial shape. The Nitinol specimens used are shown in Fig. 3.55.

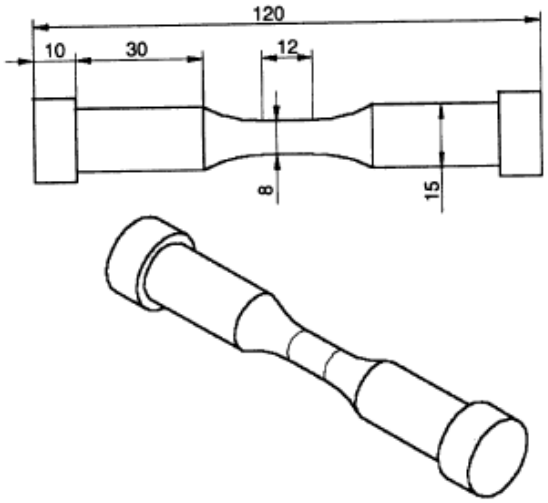

Fig. 3.55 - Fatigue Test Nitinol Bar Specimen

[Moumni et al., 2005].

Under the stress-controlled fatigue cyclic loading, the strain-stress response of the material presented a hysteresis loop that varied but stabilized after a small number of cycles. The starting point of the stress-strain curves deviated upon cycling. This deviation can be explained by the accumulation residual strain, which increases for the first few cycles and tends to saturate. When the residual strain stopped increasing (saturation) the hysteresis loop stabilized, as can be seen in Fig. 3.56.

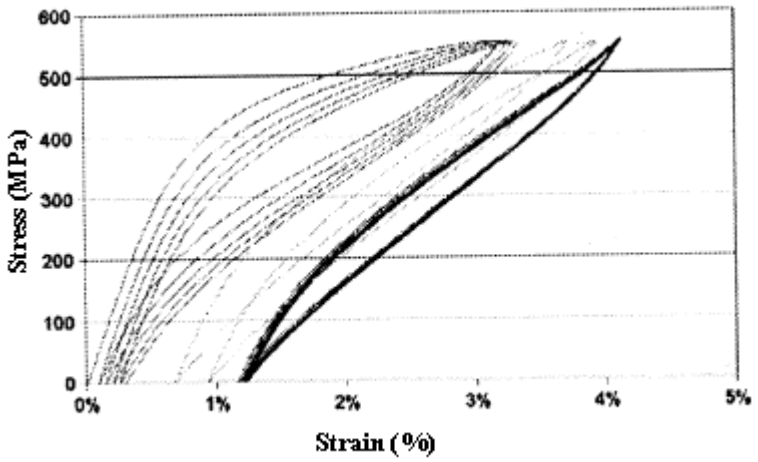

Fig. 3.56 - Cyclic Pseudo-Elasticity [Moumni et al., 2005].

For the test conducted, an example of the evolution of the dissipated energy, which is equal to the surface of the hysteresis loop in the stress-strain curve, versus the number of cycles to failure is shown in Fig. 3.57.

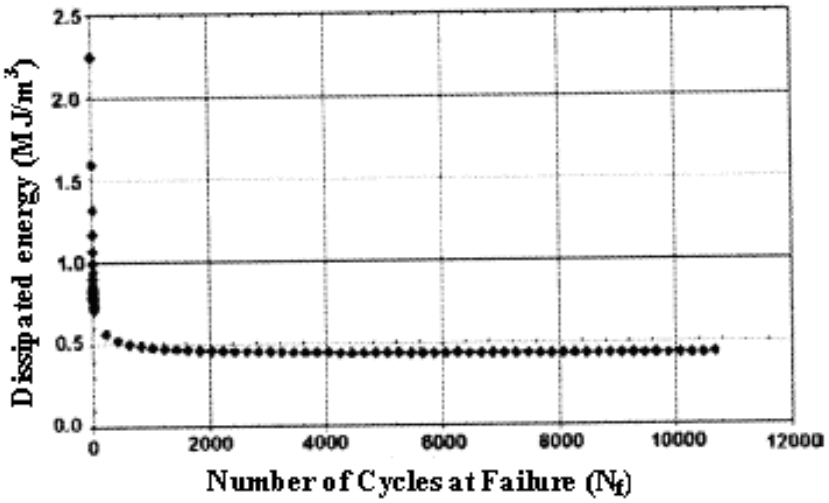

Fig. 3.57 - Stabilization of The Dissipated Energy

[Moumni et al., 2005].

After a rapid decrease, the dissipated energy per cycle stabilizes at about 60 cycles. This stabilized dissipated energy per cycle was used to numerically represent the fatigue behavior using the following equation:

$$D = \alpha N_f^{\beta}$$ <Eq. 3.5>

where:

D = dissipated energy

α and β = material parameters

N = number of cycles at failure

3.6.3 Composite Elements

In recent years there has also been considerable interest not only in shape memory alloys alone but also in the area of shape memory alloy composites, which are basically SMA actuators embedded into a polymer matrix. Considerable attention has been devoted, during the past few years, to the development of Nitinol-reinforced composite structures that have built-in shape control capabilities. Some studies on SMA composite materials are presented in the following.

3.6.3.1 Furuya (1999)

Furaya (1999) investigated the behavior of two types of composite materials with shape memory alloys. One composite material was a Nitinol (TiNi) fiber reinforced aluminum matrix plate, where the shape memory shrinkage and recovery

stresses of embedded pre-strained Nitinol fibers at higher temperatures were utilized to enhance mechanical properties such as tensile strength and fatigue resistance.

When the SMA fibers were embedded in the aluminum matrix, the composite was pre-strained in the direction of the fibers at low temperature, and then heated to the SMA phase state to introduce a compressive residual stress into the composite due to the fact that the SMA fibers had more shrinkage than the aluminum matrix. This compressive residual stress is very useful for closing the micro-crack of the composite because it can effectively partly decrease environmental stresses, which in turn increases the fatigue life of the composite element.

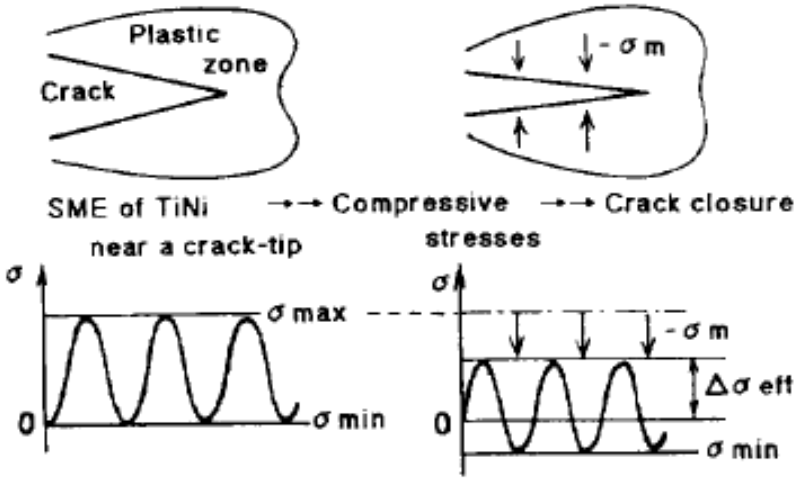

Fig. 3.58 - Residual Compressive Stress and Crack-Closure [Furuya, 1999].

Test results from this first type of approach showed that the tensile yield stress increased at higher temperatures, as shown in Fig. 3.59.

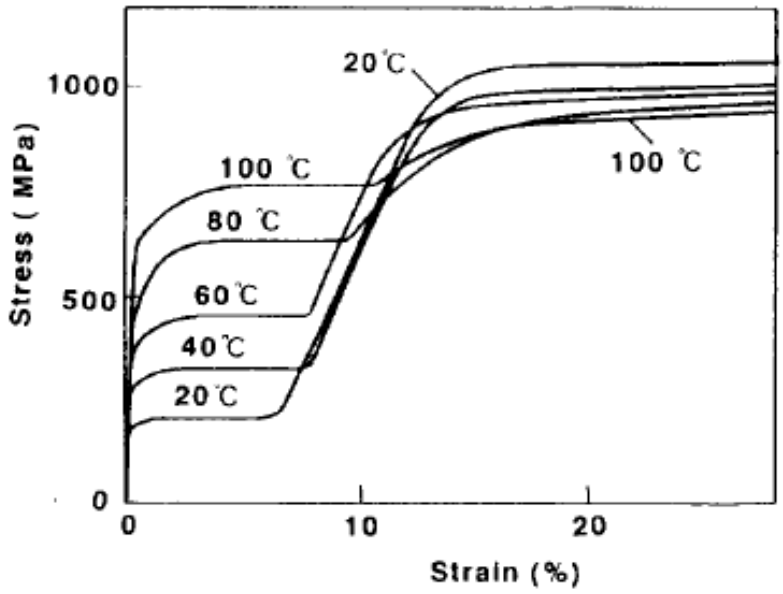

Fig. 3.59 - Tensile Stress-Strain Curves of Nitinol Fibers at Different Temperatures [Furuya, 1999].

Test results also showed that at higher temperatures the resistance to fatigue crack propagation increased.

The second composite material was a Nitinol (TiNi) fiber reinforced and Nitinol powder particle mixed plaster matrix. This second type of composite was used to study the resistance to fracture (fracture toughening) and vibration damping. Both improved by the use of the Nitinol fibers and powder. After a three point bending test, the plaster-only sample showed brittle fracture, whereas the plaster sample with Nitinol showed very ductile fracture.

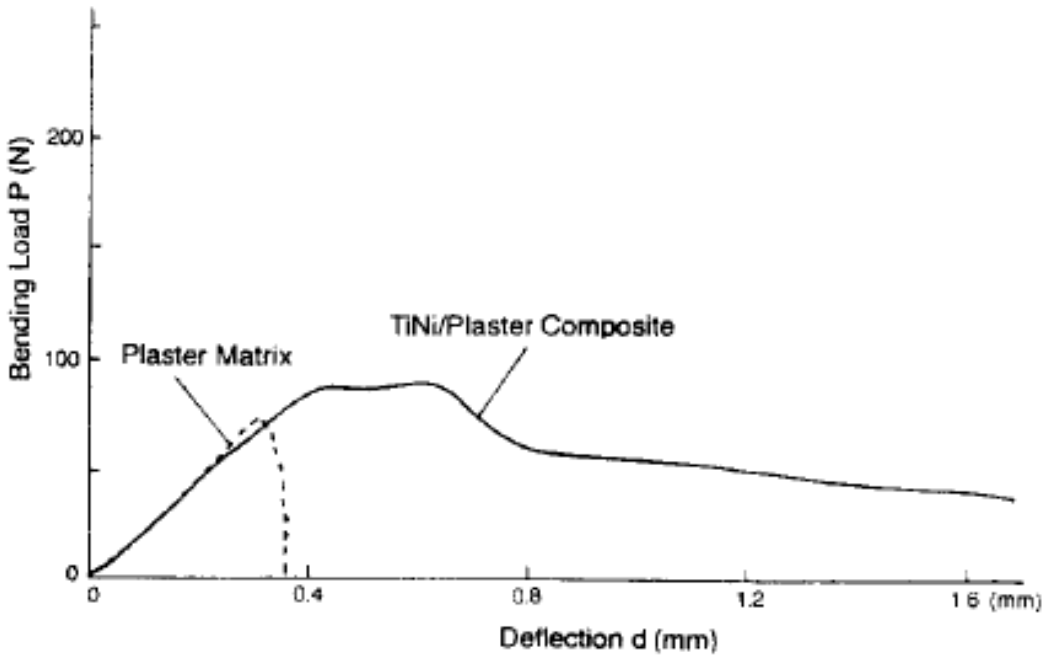

Fig. 3.60 - Bending Load versus Deflection Curves of Plaster Matrix and Nitinol/Plaster Composite after Three Point Bending Test [Furuya, 1999].

3.6.3.2 Gotthardt and Parlinska (2002)

Gotthardt and Parlinska (2002) investigated the behavior of a smart material made by embedding pre-strained 0.15-mm diameter SMA wires into a Polymer matrix consisting of Kevlar-fiber reinforced epoxy-matrix. The goal of their study was to develop an SMA composite that could shift the vibrational frequency of the smart material away from damaging input frequencies by an activation of the SMA wires.

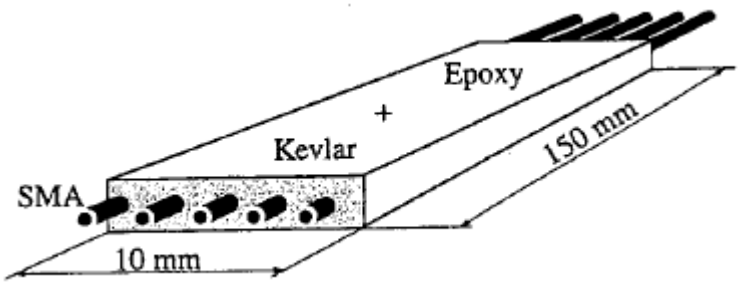

Fig. 3.61 - SMA Composite Material Specimen Tested

[Gotthardt, and Parlinska, 2002].

They found that incorporating the SMA wires into the polymer matrix changed the vibration frequency of the smart material in a reversible way with temperatures changes. The stress generated in the "activated" composite resulted in a frequency shift, which increased with the volume fraction of the embedded SMA wires and decreased with increasing composite thickness. It was also observed that the frequency shift had a linear dependence with stress for all tested samples regardless whether the stress was induced by phase transformation or by straining the specimen at room temperature. They concluded that the SMA wire composite is suitable for applications in adaptive vibration control.

3.6.3.3 Moore and Bruck (2002)

Moore and Bruck (2002) studied the repeatable bending actuation of polyurethanes using embedded SMA wires exhibiting large deformation recovery. For their investigation simple beam specimens were fabricated by embedding Nitinol

wires in a flexible industrial matrix. The specimen was 85.4-mm long, 9.6-mm wide and 6-mm thick. Shape Memory Alloy wires were embedded near the central axis of the specimen at a depth of approximately 1.5 wire diameters from the specimen surface.

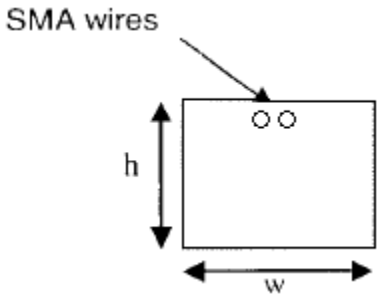

Fig. 3.62 - Specimen Geometry Used for the Actuation Characterization Experiment [Moore, and Black, 2002].

Test results indicated high repeatable bending actuation of the composite element. It was concluded that the level of bending actuation depends on the constraint of the SMA wires imposed by the stiffness of the polyurethane matrix.

As part of this investigation on SMA wires embedded in a polyurethane matrix, Moore and Bruck carried out standard wire pullout tests to study the bond strength of the SMA wire-matrix interface. Specimens were fabricated by casting each matrix material around a single wire that had been previously positioned at the center of a plastic mounting cup with the axis of the cup and the axis of the wire being coincident. The polymer was mixed to the proper proportions and then carefully poured into the mounting cup. Results from the pullout test showed good

bond strength between the embedded SMA wire and the flexible polyurethane matrix. As expected, the level of interfacial adhesion significantly influenced the maximum wire displacement and stress induced actuation.

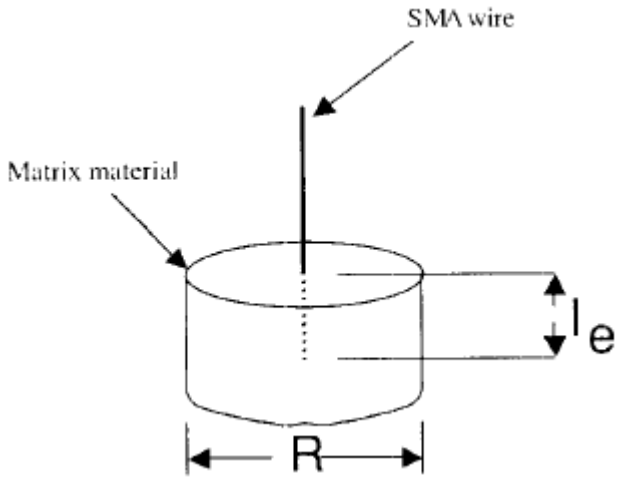

Fig. 3.63 - Specimen Configuration for Wire Pullout Tests [Moore, and Black, 2002].

3.6.3.4 Murasawa, Tohgo, and Ishii (2004)

Murasawa, Tohgo, and Ishii (2004) examined the behavior of composites containing shape memory alloy fibers or Titanium fibers in a Polycarbonate (PC) matrix and also in an epoxy matrix to evaluate the potentiality of SMA composites as structural and functional materials. Both pre-strained and non-pre-strained fibers were used. Shape memory alloy fiber composites were subjected to uniaxial tension up to fracture. They also tested the SMA composite specimens under tensile loading-unloading to study their thermo-mechanical deformation properties.

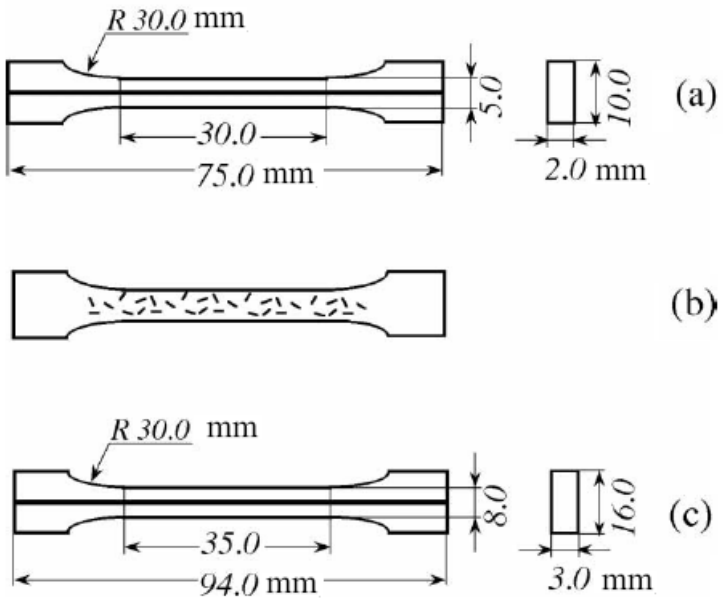

Fig. 3.64 - Specimen Configurations: (a) Long Fiber Reinforced Composite (Nitinol/PC); (b) Short Fiber Reinforced Composite (Nitinol/PC); Long Fiber Reinforced Composite (Nitinol/Epoxy) (Pre-Strained Fiber) [Murasawa et al., 2004].

Test results showed that the strain for the initiation of necking and the strain for the fiber or matrix fracture in the SMA composites were higher than those in the Titanium composites. This is attributed to the unique stress-strain relations accompanied by the stress-induced martensitic transformation of the SMA fibers. The SMA composites containing shape memory effect fibers and polycarbonate exhibited a large contraction by heating after tensile loading-unloading, but these compressive residual stresses were not significant.

3.6.4 Preliminary Study on High Performance Composite Element "HPCE"

A preliminary study on the response of High Performance Composite Elements "HPCE" subjected to cyclic loading was carried out in 2004 at the Civil, Environmental, and Architectural Engineering Department of The University of Kansas [Lambrecht, 2004]. This preliminary study was intended to develop a novel partially restraint beam-to-column connection by using a HPCE consisting of Shape Memory Alloy rods embedded in a Urethane Cylinder matrix confined by a Carbon Fiber Reinforced Polymer wrap.

The beam-to-column connection proposed from this preliminary study is composed of two steel plates with one hinge connection at the center, one HPCE at the top of the connection and another one at the bottom. The hinge connections are intended to transfer shear loads, and allow for rotation, whereas the HPCEs restraint rotations between the beam and the column and consequently transfer moment. Even though this system was initially thought as a partially restrained moment connection, a fully restrained moment connection can also be accomplished by increasing the stiffness of the HPCEs in compression and tension.

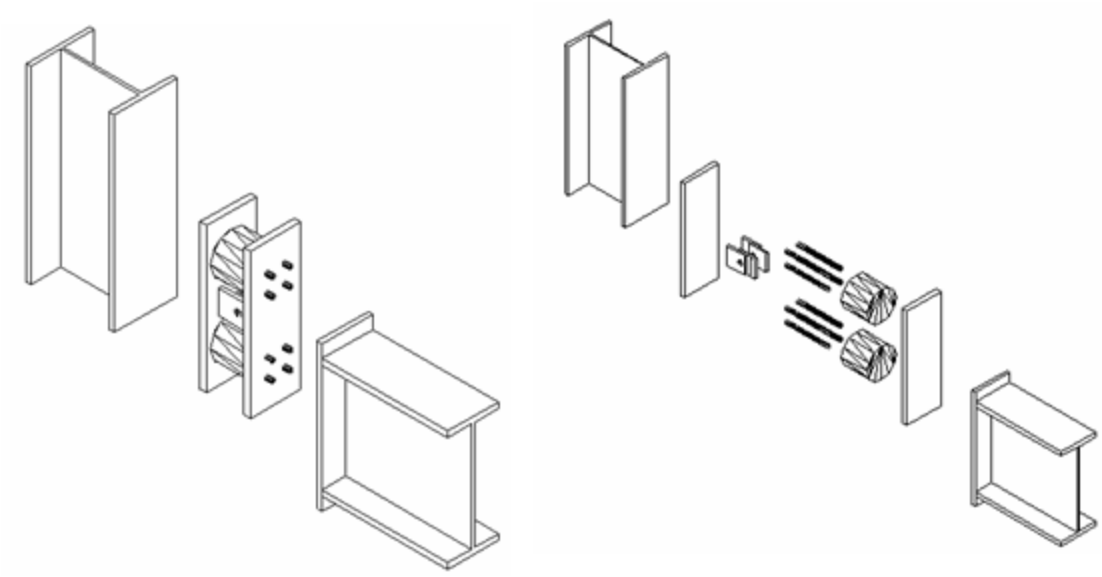

Fig. 3.65 - High Performance Composite Element with Shear Hinge for use in Beam-Column Connection.

The HPCE specimens tested had four 0.197 in.-diameter Nickel-Titanium Shape Memory Alloy rods embedded in a 5in.-diameter 6in.-long 70-durometer urethane cylinder matrix. Two different configurations were tested with the urethane matrix confined by 3in.-wide and 4.5in.-wide Carbon Fiber Reinforced Polymer layers 0.09-in. thick, respectively.

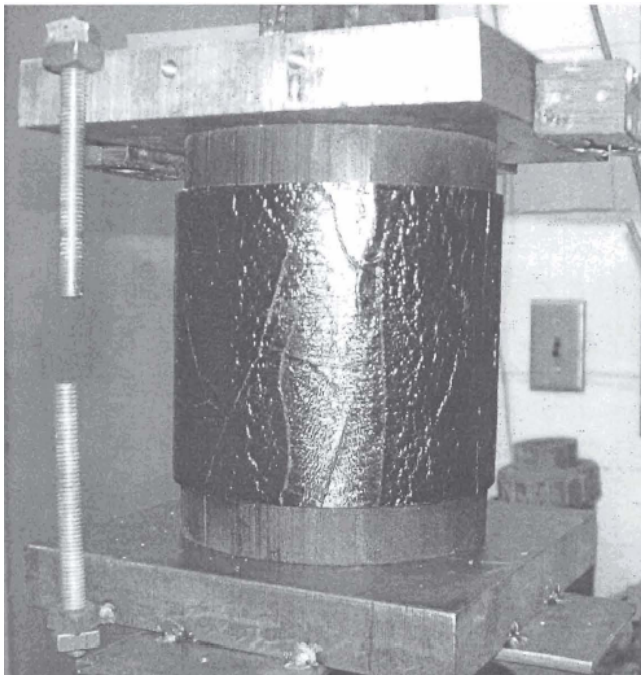

Fig. 3.66 - High Performance Composite Element

[Matamoros, and Lambretch, 2004].

Initial testing results showed limited yield deformation of the SMA rods due to stress concentrations at the cut threaded ends. These threads were necessary for specimen assembly purposes. Early fracture of the rods occurred at the initial stages of the loading history under tensile loads right at the cut threaded ends. Consequently, rolled threads were used in an effort to reduce stress concentrations but there was not any major improvement on the performance of the SMA rods. Since the stress concentration persisted, the cross section area of the rod was reduced between the threaded ends to ensure a yield zone between those threaded areas at the end of the

SMA rods and avoid early fracture. This last solution considerably improved the behavior of the HPCE since it allowed the SMA rods to withstand deformations beyond yielding. As expected, the wider the Carbon FRP confinement the stiffer the HPCE under compressive loads.

In general, experimental results from this preliminary study showed that HPCE was a promising system able to withstand large inelastic deformations under cyclic loads. Additionally the HPCE proved to be an efficient energy dissipation system due to the use of Nitinol Shape Memory Alloys that allowed the system to deform within its inelastic range of response without permanent deformations. Even though the specimens with reduced rod sections were able to undergo deformations beyond buckling and yielding under cyclic loading, the behavior of the HPCE can still be improved by better detailing and fabrication of the rods. An improved uniform yield zone between the threaded ends can help avoid early fracture of the rods due to stress concentrations at the cut threads.

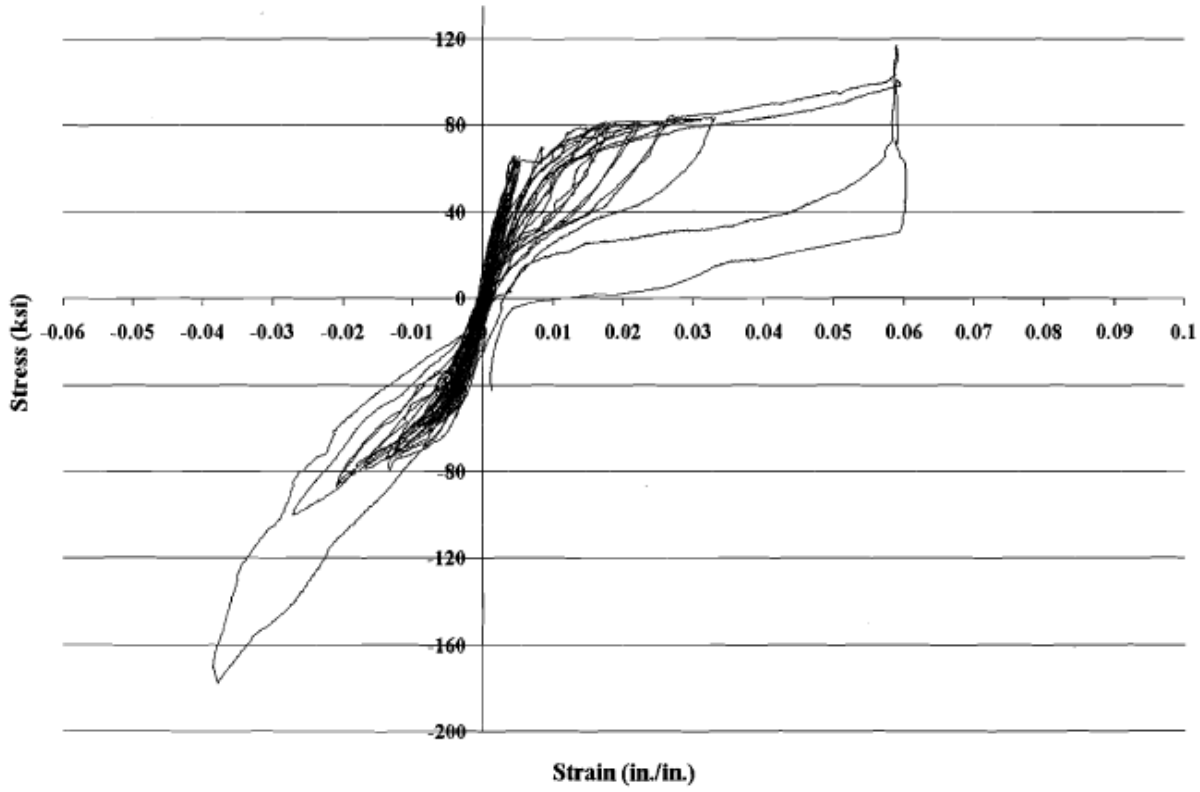

Fig. 3.67 - HPCE Stress Strain Curve / SMA Rods with rolled threads and Reduced Section [Matamoros, and Lambretch, 2004].

4 RXS Fuse Design

Basic criteria to proportion the reduced brace section fuse (RXS) are discussed in this chapter. The influence of reduced section cutout shape and the number of cutouts on the behavior of the RXS fuse are discussed. Criteria to calculate the design strength of the RXS fuse are presented. The overall goals of the design are to provide flexibility with respect to the brace size and to develop a system with adequate drift capacity. Design parameters that define the size of the reduced section cutout are also described in this chapter.

4.1 RXS Fuse Configuration

The basic configuration of the RXS fuse is discussed in this section. Rationale for selecting the shape of the reduced section cutouts and the number of cutouts are explicitly discussed, and a fabrication method is described. The basic RXS fuse configuration selected was developed using computational models.

4.1.1 Reduced Section Shape

The RXS fuse is composed of several oval cutouts. An oval-shaped cutout was selected for use in the RXS fuse instead of the elliptical shape used by Tremblay et al. [Tremblay, et al., 1999] because this configuration provides more ductility under tension loads. An oval cutout would be able to elongate more over a longer yield zone instead of having plastic strains concentrated over the relatively short mid-length of the ellipse. Additionally, an oval shape is easier to fabricate.

The behavior of the RXS fuse is sensitive to the shape of the oval cutouts. As much as possible the shape of multiple cutouts should be identical to avoid inducing an eccentricity. Shop fabrication is strongly recommended because the shape of the oval cutouts requires precision that can be difficult to accomplish on-site. The brace cross sectional area may be reduced by using a cutting torch system, which is proven technology that brings good performance and low fabrication cost because it makes fast and clean cuts through steel. This cutting technique, however, would not leave a desirable smooth surface. After torch cutting the oval shape, normal fabrication practice used in bridge structures which requires smooth edges is recommended to avoid discontinuities along the cutout edges left from the torch cut. Smooth edges would delay fracture failure allowing more of the desired ductile behavior of the RXS fuse.

Finite element model analyses of the reduced section were carried out with the assumption of isotropic-elastic material properties, and a 29000 ksi Young modulus of elasticity. The reduced section was modeled as elastic homogeneous solid material with a uniform stress applied on the top of the model and a fixed boundary condition on the bottom of the model. Various round hollow structural sections with the RXS fuse were compared to determine the optimal reduced section cutout shape. Two models, one with three oval cutouts and a second model also with three elliptical cutouts were studied. Spatial displacements and stress concentrations were compared between the two. Both cutout shapes were 10 in. long and 3.5 in. wide, and both specimens were subjected to a uniform stress in the tube of 50 ksi applied on the top

of the model with the bottom edges of the model restrained against both rotation and translation.

In terms of stress concentrations the oval cutout RXS fuse model performed better than the elliptical-shaped cutout fuse. The elliptical cutout FEM showed larger stress concentrations than those observed in the oval cutout FEM. Furthermore, in the model with elliptical cutouts stress concentrations were localized over a narrower portion of the reduced section right at the wider region of the elliptical shape. The model with the oval-shaped cutouts had a much better stress distribution, as can be seen in Fig. 4.1.

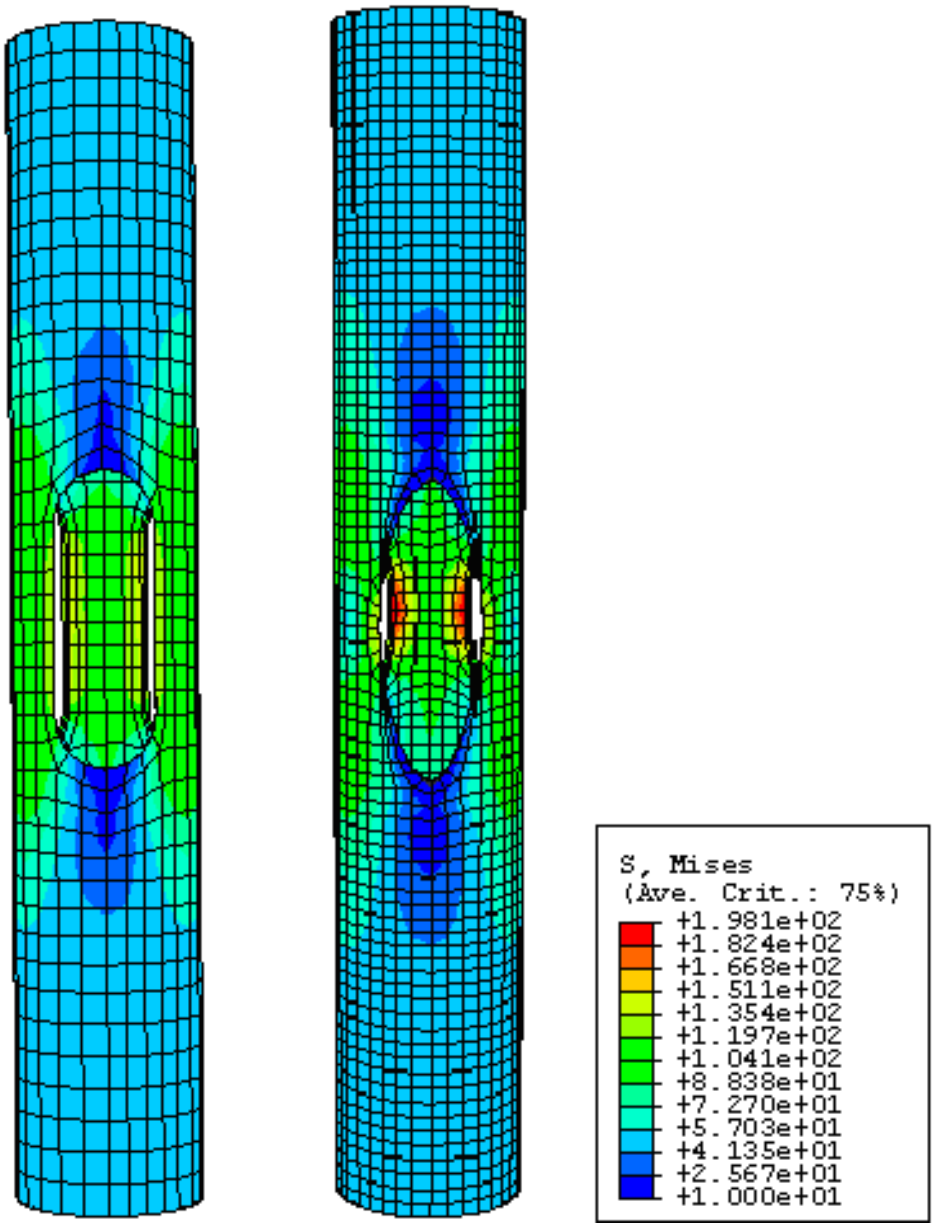

Oval Cutouts Elliptical Cutouts

Fig. 4.1 - Von Misses Stress FEM (Ksi) – Oval Cutout vs. Elliptical Cutout.

Specimen	Applied Stress (ksi)	Maximum Stress Concentration (ksi)
3 Elliptical Cutouts	50	198.05
3 Oval Cutouts	50	146.6

Table 4.1 - Shape of RXS Fuse Cutouts, Summary of FEM Results.

4.1.2 Number of Oval Cutouts

Another consideration for determining the optimal configuration of the fuse is the number of cutouts and their distribution around the brace cross-sectional area.

For a given reduction in area, fabrication cost increases with the number of cutouts for two reasons: first, the diameter of the cutouts decreases as the number of cutouts increases, adding difficulty to the fabrication process if the diameter becomes too small, and second, more cutouts means more time required during the fabrication process. As a general approach, the minimum possible number of cutouts should be used to optimize fabrication cost. Regardless of the number of cutouts used in the RXS there should be constant spacing between them to keep a uniform load distribution throughout the RXS fuse; otherwise the arms would have different sizes and there would be an undesired eccentricity induced by the unsymmetrical geometry.

The option of using one single oval cutout was initially rejected not only because it does not allow a uniform load transfer through the RXS fuse, but also because instability becomes the fuse limit state. This instability is more significant as the reduction in area increases.

As a general design criterion, three oval cutouts symmetrically placed around the cross section of the RXS are set as the minimum number necessary to provide enough stiffness to the RXS fuse system. The drawback of using this minimum criterion as a general rule is that as the diameter of the HSS increases, so does the force carried by each arm, and the lack of redundancy may affect the performance of the system. In order to study the effect of the number of cutouts a FEM was carried out for a fuse with four cutouts. Assumptions for the analysis were elastic material properties, and the same round hollow structural section size used in the model with three oval cutouts presented in section 4.1.1. Like in the case of the three oval cutout fuse the model with four oval cutouts was subjected to a uniform stress of 50 ksi. The oval cutouts were also 10 in. long, but the oval shape diameter was reduced to 2.625 in. to match the same percentage of area reduction used in the three oval cutouts model.

The longitudinal edges of the inner faces of the arms were the areas subjected to the largest stress demands, starting at the transition region between the straight and the circular parts of the arm, as shown in Fig. 4.2. It can be seen from the FEM results that the maximum stress at this particular area was slightly larger for the model with three oval cutouts. The maximum stress in the three oval cutout fuse was 146.6 ksi,

compared with 132.6 ksi for the four cutout fuse. Because the difference is small, and assuming that the edges of the reduced section are smooth (as recommended for fabrication of the fuse element), this increment in the peak stress is not expected to be a major factor on the performance of the RXS fuse.

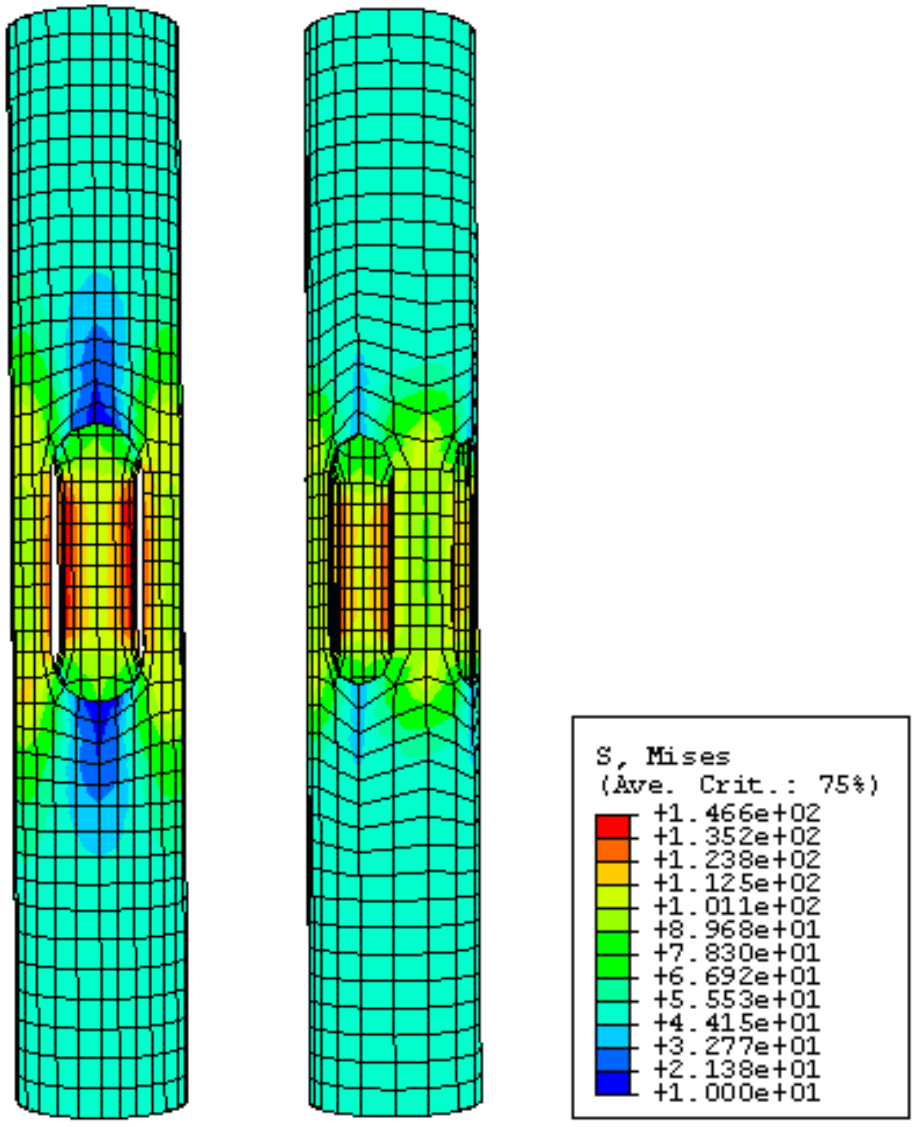

3 Oval Cutouts 4 Oval Cutouts

Fig. 4.2 - Von Misses Stress FEM (ksi).

Specimen	Applied Stress (ksi)	Maximum Stress Concentration (ksi)
3 Oval Cutouts	50	146.6
4 Oval Cutouts	50	132.6

Table 4.2 - Number of Cutouts, Summary of FEM Results.

4.2 Strength Criteria

The RXS system is proportioned using three different design criteria. The first two are based on the tensile capacity of the fuse, the connection capacity and the braced frame drift demand. The third design criterion is based on the compressive capacity of the fuse and the bracing member.

4.2.1 Fuse Element Tension Design Criteria

There are two important tension design criteria. The first design criterion requires that the capacity of the brace must be less than that of the connection to avoid connection failure.

$$FCC > R_y * F_y * A_g \qquad \text{<Eq. 4.1>}$$

When the capacity of the brace is greater than that of the connection, a fuse element is required so that the fuse tensile capacity becomes the tensile limit state.

If:

$$FCC < R_y * F_y * A_g \qquad \text{< Eq. 4.2>}$$

then:

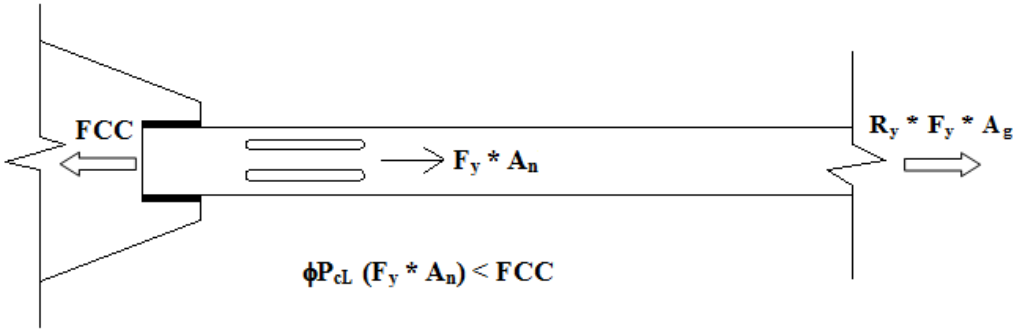

Fig. 4.3 - First Tension Design Criterion.

where:

FCC= Factored Connection Capacity

$R_y * F_y * A_g$ = The nominal axial tensile strength of the bracing member.

R_y = Ratio of the Expected Yield Strength to the minimum specified yield strength $\boldsymbol{F_y}$. Values for $\boldsymbol{R_y}$ depend on member type [AISC, 2002, table I-6-1]. $\boldsymbol{R_y}$ is 1.3 for HSS ASTM A500, A501. $\boldsymbol{R_y}$ was increased to 1.4 in the 2005 provision [AISC, 2005].

F_y = Specified minimum yield stress of the type of steel to be used, ksi

A_g = bracing member gross area, $in.^2$

A_n = Fuse reduced net area $in.^2$

The second design criterion requires that the length of the reduced section must provide sufficient inelastic deformation to satisfy drift demands of the braced frame.

Braced frame drift demand < Braced frame drift capacity <Eq. 4.3>

where:

braced frame drift capacity = function (total brace axial elongation) <Eq. 4.4>

The brace axial elongation is calculated as the summation of the total RXS axial deformation from two fuses (one fuse at each end of the brace) plus the brace non-reduced section axial deformation.

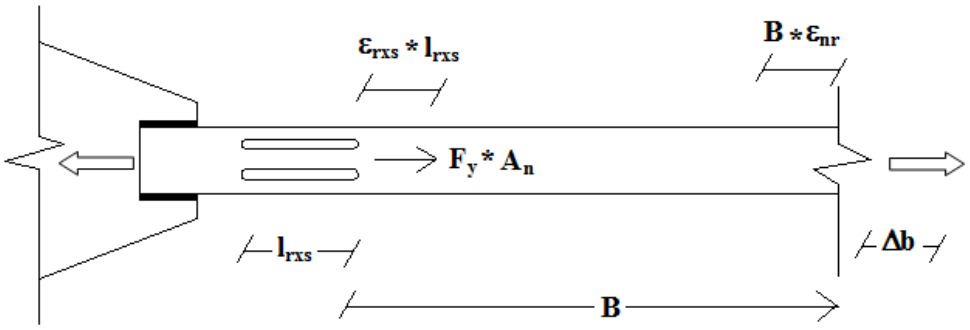

Fig. 4.4 – Second Tension Design Criterion.

$$\Delta b = \varepsilon_{nr} * B + 2(\varepsilon_{rxs} * l_{rxs}) \qquad \text{<Eq. 4.5>}$$

Δb = total brace elongation.

ε_{nr} = non-reduced section strain.

ε_{rxs} = reduced section strain.

l_{rxs} = oval cutout length.

4.2.2 Fuse Element Compression Design Criteria

The compression design criterion includes two important compression design parameters, global buckling capacity and local buckling capacity, being global capacity that of the brace without the fuse element and local capacity that provided by the fuse element. The bracing member may be proportioned so that either one controls.

4.2.2.1 Global Buckling Controls Member Size

The first compression design method is to proportion the brace so that global buckling is the controlling limit state (Fig. 4.5). To comply with this requirement the global effective slenderness ratio of the brace must be larger than the local effective slenderness ratio (Fig. 4.5).

By reducing the brace cross sectional area with the addition of the RXS fuse, the local tension capacity becomes the brace limit state under tensile loads. But the RXS fuse is to be subjected to cyclic loads and since compression is the brace global limit state, the second requirement of the third design criteria is fulfilled by the local

tension capacity being larger than the global buckling capacity as this implies that the global tension capacity also remains larger than the buckling capacities.

$\phi P_{cL} > \phi P_{cG}$ $(KL/r_{local} < KL/r_{global})$ <Eq. 4.6>

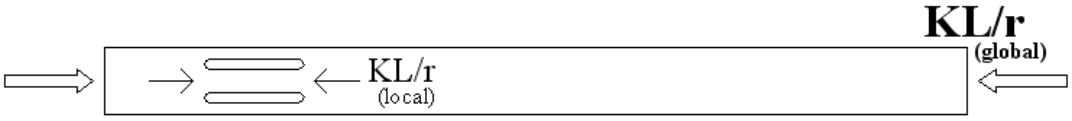

Fig. 4.5 - Strength Criterion: Global Buckling Controls Member Size.

where,

ϕP_{cL} = factored RXS buckling strength or local buckling strength.

ϕP_{cG} = factored bracing member buckling strength or global buckling strength.

KL/r = effective slenderness ratio.

4.2.2.2 Local Buckling Controls Member Size

The second compression design method requires that the global buckling capacity of the system shall be larger than the local buckling capacity (Fig. 4.6). Because local compression controls member size, a wider range of local slenderness ratios can be selected to allow the system comply with ductility requirements. This second approach is more flexible in terms of the system design; additionally, it keeps the brace global compressive behavior from buckling, which helps to prevent the undesirable brace out of plane buckling. The drawback of this second criterion is that

because braces are sized based on the local buckling capacity of the RXS, this could result in larger HSS brace sizes.

$\phi P_{cL} < \phi P_{cG}$ $(KL/r_{local} > KL/r_{global})$ <Eq. 4.7>

Fig. 4.6 - Strength Criterion: Local Buckling Controls Member Size.

where,

ϕP_{cL} = factored RXS buckling capacity or local buckling capacity.

ϕP_{cG} = factored bracing member buckling capacity or global buckling capacity.

KL/r = effective slenderness ratio.

4.3 Design Parameters

The local tensile capacity of the RXS is proportional to the reduction of the brace cross-sectional area with respect to the gross area, whereas the RXS local buckling capacity does not only depend on the reduction of the brace cross-sectional area, but also depends on the length of the oval cutout. There are two design parameters that define the geometry of the RXS oval cutouts. These parameters are:

f = area reduction coefficient.

HAR = hole aspect ratio.

The first parameter ***f*** determines the percentage of cross-sectional area reduction to limit the tensile strength of the brace so that the connection cannot be overloaded. The second parameter ***HAR*** determines the length of the reduced section, which defines the local buckling capacity of the brace and its ability to deform in the inelastic range of response.

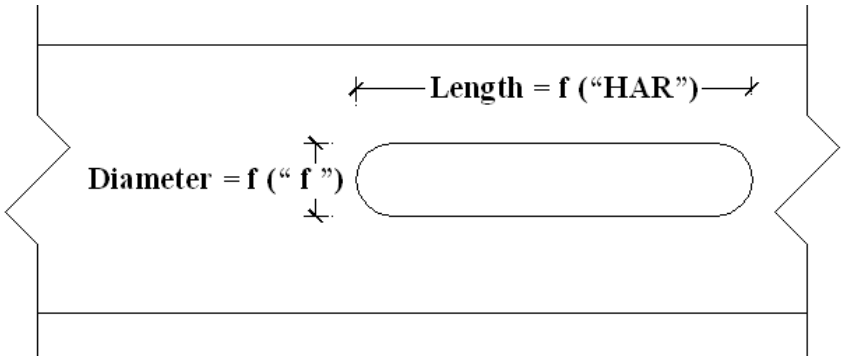

Fig. 4.7 Design Parameters.

4.3.1 Area Reduction Coefficient "f"

The area reduction coefficient is the primary design parameter to be selected for the RXS fuse element. It defines the reduction in cross-sectional area. The area reduction coefficient ***f*** must be selected to prevent net-section fracture at the brace connection,

The lower bound or minimum area reduction coefficient f_{min} is defined by the minimum reduction required to prevent net-section fracture at the brace connection. This lower bound applies to the two design approaches and it depends on the factored brace connection capacity and the factored brace yield capacity so that the factored

brace connection capacity does not become the limit state that controls the failure mechanism of the bracing system and it is determined by the following expression:

$$f_{min} = 1 - \frac{\text{factored brace connection capacity}}{\text{factored brace yield capacity}} > 0 \qquad \text{<Eq. 4.8>}$$

the design example included at the end of this chapter demonstrates how to calculate this lower bound for the area reduction coefficient ***f***.

Based on the first design criterion (Fig. 4.5) the brace section can be reduced as much as it does not affect the overall capacity of the brace member in compression. Therefore, the upper bound of the area reduction coefficient is mainly determined by the maximum brace section reduction allowed without compromising the overall strength of the brace. As mentioned before, the local tensile capacity and the local compressive capacity of the RXS should be larger than the global buckling capacity of the brace to comply with the first strength criteria.

The local buckling capacity of the RXS is affected by the reduction coefficient and the length of the oval cutouts. Assuming that the local compressive capacity is similar to the local tension capacity, but smaller (even for circular cutouts instead of oval cutouts) an upper bound of the area reduction coefficient can be estimated with the following expression:

$$f_{max} = 1 - \frac{\text{Global buckling capacity of brace}}{\text{Global tensile capacity of brace}} > 0 \qquad \text{<Eq. 4.9>}$$

the design example included at the end of this chapter demonstrates how to calculate this upperbound for the area reduction coefficient f.

If the area reduction coefficient is larger than this upper bound limit, the local buckling capacity of the system becomes the governing compressive limit state. Otherwise the global buckling capacity will be the controlling limit state.

If the brace is to be proportioned so that local buckling capacity is the limit state, there is no upper bound for the selection of the area reduction coefficient other than economy, because excessive area reduction coefficient might require the use of significantly large brace sizes.

The drift capacity of concentrically braced frames is expected to decrease as the area reduction coefficient increases and the local tensile capacity decreases. Therefore it is uneconomical to reduce the section up to a hypothetical maximum upper bound for the area reduction coefficient.

Specified steel properties by ASTM [ASTM, 2003] usually are substantially less than the actual material yield strength, F_y, and ultimate strength, F_u; some have expected yield strength almost as high as their ultimate tensile strength [AISC, 2005, C13.3b]. For this reason the calculated capacities based on ASTM material properties may be significantly lower than the actual capacities and consequently the lower and upper bound of the area reduction coefficient would vary too. In general area reduction coefficients in the proximity of the lower bound should be selected, but it is strongly recommended that design area reduction coefficients should be a little bit

larger than the minimum required to avoid major impact on design calculations due to excessive variations between provided and actual material properties.

4.3.2 Hole Aspect Ratio "HAR"

The length of the oval cutout is defined by the product of the hole aspect ratio ***HAR*** and the width of the cutout. Thus, the hole aspect ratio ***HAR*** is very important parameter for the local buckling capacity of the RXS fuse, and like the case of the area reduction coefficient, it has limitations. The oval cutout should be long enough to provide adequate brace ductility. If the first compression design parameter is adopted, the oval cutout should be short enough so that the local buckling capacity of the RXS fuse does not become the governing limit state over brace global buckling capacity (Fig. 4.5). If brace members were proportioned for local buckling capacity (Fig. 4.5), the only restriction on estimating ***HAR*** is the maximum ductility allowed by seismic provisions for concentrically braced frames. In other words, the length of the RXS should not be excessively long because the effective slenderness ratio of the fuse arms might become greater than the recommended 200 by AISC provisions [LRFD/ASD, 2005].

The ***HAR*** varies depending on the area reduction coefficient provided, the global buckling capacity of the brace, and the maximum story drift ratio allowed by seismic provisions for concentrically braced frames. It is difficult to establish mathematical expressions to estimate an upper and a lower bound for this parameter

because the ***HAR*** is selected through a trial and error method in which basically if the brace is sized for its global buckling capacity (first design philosophy, Fig. 4.5) one ***HAR*** is tried and checked for the strength criteria, if it does not comply with the condition, there is an error, and a smaller ***HAR*** should be tried in order to increase the local buckling capacity. This process is repeated iteratively until a selected ***HAR*** makes the RXS fuse comply with the design strength condition. Because the buckling capacity of the RXS fuse is highly sensitive to the ***HAR***, to start the *HAR* trial and error selection method it is recommended to initially try a first iteration with a ***HAR*** = 2 and then keep increasing the ***HAR*** as long as the fuse local buckling capacity does not go under the brace global buckling capacity and becomes the limit state.

For braces proportioned for their local buckling capacity (second design criteria, Fig. 4.6) there is more flexibility in the selection of the ***HAR*** parameter, but as mentioned the AISC provisions recommend effective slenderness ratios shall not exceed 200 since it might require special care to minimize inadvertent damage during construction.

As mentioned above it is difficult to establish mathematical expressions to estimate the ***HAR***, but the iterative trial and error selection process can be alleviated by expressing the ***HAR*** as a function of the RXS fuse two design philosophies restrictions in terms of the size and capacities.

For braces proportioned for their global buckling capacity the ***HAR*** can be established by complying with the following expression:

HAR = Function (f, ϕP_{cG}); $\phi P_{cG} < \phi P_{cL}$ <Eq. 4.10.>

where,

HAR = hole aspect ratio

f = area reduction coefficient

ϕP_{cG} = factored bracing member buckling capacity or global buckling capacity

ϕP_{cL} = factored RXS buckling capacity or local buckling capacity

For braces proportioned for their local buckling capacity the ***HAR*** can be established by complying with the following expression:

HAR = f (f, KL/r); KL/r<200 <Eq. 4.11.>

where,

HAR = hole aspect ratio

f = area reduction coefficient

KL/r = effective slenderness ratio

In general, if braces with the RXS fuse are proportioned for their global buckling capacity (Fig. 4.5) the only restriction is that an adequate ***HAR*** should be provided so that local buckling capacity is larger than the global buckling capacity and the addition of the RXS fuse does not affect brace size. A conservative approach criterion for this design philosophy would be to use a smaller ***HAR*** than the maximum permitted to allow a broader difference between the two buckling capacities. On the other hand, the largest ***HAR*** that allows the RXS to comply with ductility requirements should be selected to optimize the design if braces with the

RXS fuse are proportioned for their local buckling capacity (Fig. 4.6). By using the largest ***HAR*** possible the brace system cost is optimized since the local buckling capacity of the system will be the optimal smaller and therefore the required brace size will be optimal too.

4.4 RXS Design Parameter Selection

General design procedures for braces with the RXS fuse system are presented in appendix A. Calculations are shown for a brace sized for its global buckling capacity. All calculations were developed for a round HSS 6.625x0.500 A500 Grade B steel, which was the size chosen to experimentally reproduce local behavior at the laboratory. This section presents a discussion on the selection of the RXS fuse design parameters based on design procedures presented in Appendix A.

4.4.1 Area Reduction Coefficient (*f*) Selection

The provided area reduction coefficient, f, depends on the connection factored capacity and the connection demand. Based on design calculations, a minimum area reduction coefficient of approximately 40 percent is required for most HSS sizes made with A500 Grade B steel to avoid the use of reinforcement at the connection.

To set the minimum value of f, the actual material yield strength, F_y, and ultimate strength, F_u, must be considered. These material properties may be, and indeed usually are, substantially higher than the minimum values specified for A500 grade B steel. Therefore, the effect of expected variations in F_y and F_u, on f_{min} are studied for an HSS 6.625X0.25 by increasing the material yield strength, F_y, and

ultimate strength, F_u, calculating the respective connection capacity and connection demand for the given mechanical properties and finally calculating the area reduction coefficient (Appendix A).

It was found that if F_u is held constant, f_{min} increases as F_y increases and for F_y held constant, f_{min} decreases as F_u increases. Since the yield strength F_y is expected to have a significant increment compared to F_u, and since there is no major design impact if f_{min} decreases due to F_u increments because a lower limit value is being studied, attention focuses on the effect of F_y on f_{min}. Three variation patterns were considered:

F_y increases, F_u remains constant (continuous line Fig. 9).

F_y increases twice the amount of F_u increments (dotted line Fig. 9).

F_y and F_u increase the same amount (dashed line Fig. 9).

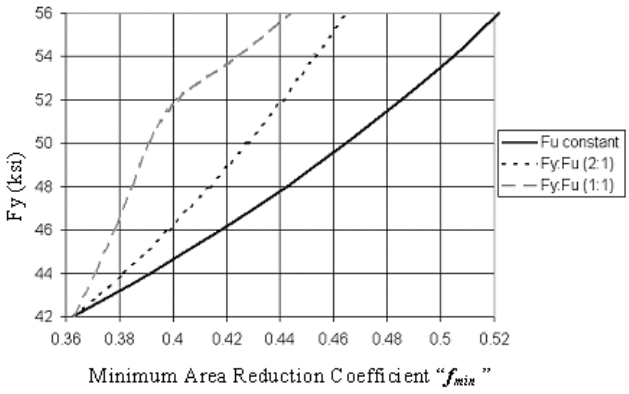

Fig. 4.8 - Effect of Tensile Strength Variations on Minimum Area Reduction Coefficient Study for a HSS 6.625x0.25.

Looking at Fig. 4.8 it can be seen that as the increment margin between F_y and F_u increases, the minimum area reduction coefficient f_{min} increases. The case where F_u is held constant as F_y increases is not realistic because as the actual F_y increases with respect to the minimum specified, the actual F_u also increases with respect to its minimum specified. But the increment margin between F_y and F_u is not known until test coupons are tested, and therefore this case is included in Fig. 4.8 as a theoretical referential worst-case scenario. Higher increments of F_y with respect to F_u are not included, because as mentioned before, the area reduction coefficient tends to decrease with F_u increments.

Based on the Ratio of the Expected Yield Strength to the minimum specified yield strength R_y equal to 1.3, and the specified minimum yield strength equal to 42 ksi, the expected yield strength is anticipated to be around 54.6 ksi. For F_y equal to 54.6 ksi, from Fig. 4.8 the minimum area reduction coefficient could be anywhere between 43 percent and a theoretical referential worst-case scenario of approximately 51 percent.

Therefore, in order to provide enough allowance for the minimum area reduction coefficient to increase beyond the initial calculated f_{min} without having a major impact on design calculations, and taking into account specimen fabrication simplicity a conservative and optimal solution is to use a provided area reduction coefficient of 50 percent instead of using f_{min} for this particular case.

4.4.2 Hole Aspect Ratio (HAR) Selection

For three cutouts, once the value of ***f*** is selected the value of ***HAR*** determines the length of the oval shaped cutout. ***HAR*** is thus a functional parameter for the local buckling capacity of the RXS. The ratio of nominal local to global buckling capacity and HAR for different HSS sizes was calculated following the design procedure shown in Appendix A, and can be seen in Fig. 4.9. For a constant brace element global length, and constant reduction coefficient ***f***, as ***HAR*** increases the buckling capacity ratio decreases for many round hollow structural section sizes.

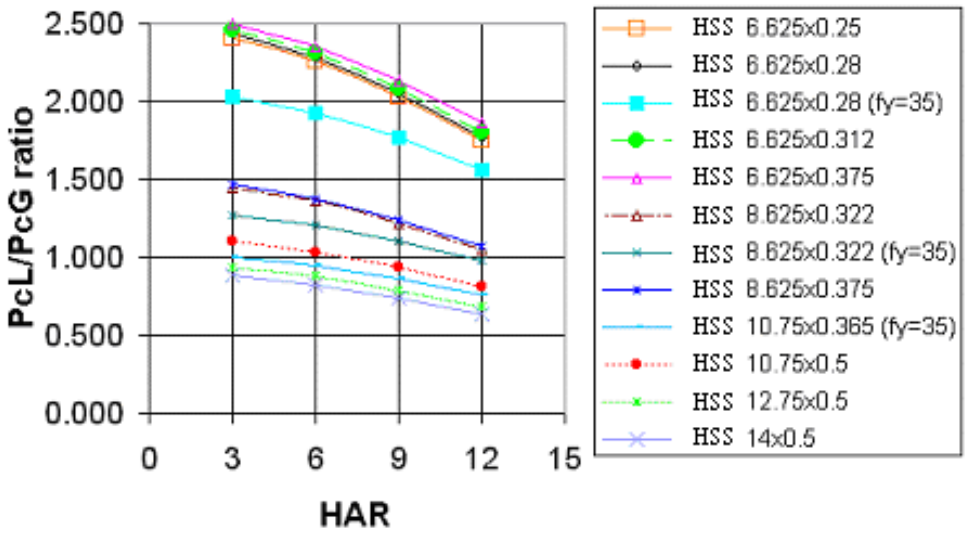

PcL = Local buckling capacity (Fuse compressive capacity).

PcG = Global buckling capacity (Brace compressive capacity).

HAR = Hole aspect ratio.

Fig. 4.9 - Effect of Hole Aspect Ratio on Fuse-Brace Buckling Capacity Ratio.

As previously stated, the intent of the RXS approach is to obtain the desired failure behavior in tension of gross-section yielding without adverse effect on failure behavior in compression. Thus the buckling capacity ratio should be larger than one to allow the global behavior to govern so the RXS does not introduce different compressive governing limit states.

Holding other parameters constant and using specimen parameters, the relationship between ***HAR*** and buckling capacity ratio for an HSS 6.625X0.25 can be seen in Fig. 4.10. ***HAR*** values with ratios of nominal local to global buckling capacity below the split threshold are to be discarded, and for this case, any HAR value smaller than 3 would work, in terms of local buckling capacity of the RXS. Keeping ***HAR*** as large as possible has the advantage of having the local buckling failure be more ductile for a long cutout than for a relatively shorter cutout. Thus an ***HAR*** of 3 is selected for the test specimens. This ***HAR*** of 3 results in a cutout length of 10 inches.

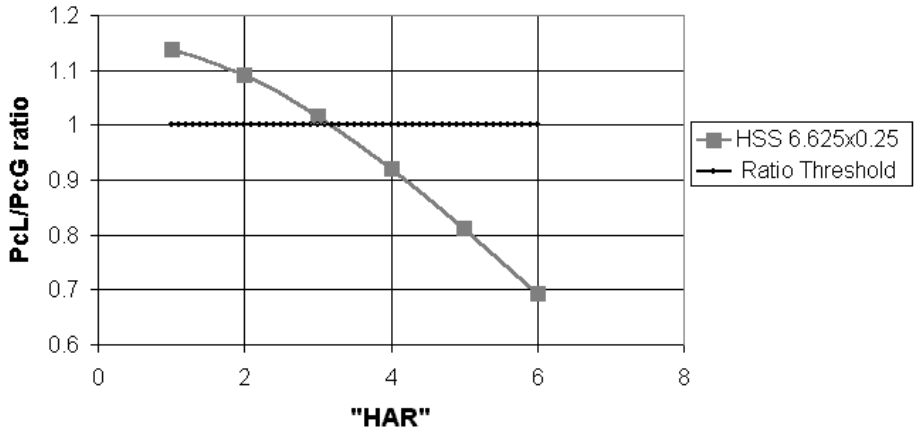

PcL = Local buckling capacity (Fuse compressive capacity).

PcG = Global buckling capacity (Brace compressive capacity).

HAR = Hole aspect ratio.

Fig. 4.10 - Design Hole Aspect Ratio Split Threshold.

5 Experimental Program for the RXS Fuse.

The experimental program was initially configured to include testing of fifteen hollow structural sections (HSS) under monotonic loads and different cyclic loading conditions to study the hysteretic behavior of axially loaded steel braces with the RXS fuse. The experimental matrix was divided into a local series or preliminary proof of concept study on the local behavior of the fuse and a global series intended to study the interaction between the fuse and a full-length brace. However, after preliminary experimental results it was found that the RXS fuse was too sensitive to damage to eccentric axial loads, and consequently the second portion of the experimental matrix was not carried out.

Even though experimental results indicated that the RXS fuse is not suitable for concentrically braced frames, since it does not perform well under eccentric axial loads, there are several valuable lessons learned from the experimental and computational studies for this first fuse element. Furthermore, this fuse could have other applications or even help in the development of other systems as it was the case during the development of the second brace composite element fuse element (BCE). For these reasons the preliminary experimental results for the RXS fuse and the entire experimental matrix as it was initially intended are presented in this chapter.

The effect of the following parameters was investigated: hole aspect ratio, percentage of reduction in area, and the controlling limit state. Local behavior of the RXS fuse was studied by testing three full-size specimens made with HSS

6.625x0.25. The first two specimens were subjected to one of the following loading profiles: monotonic compression and monotonic tension. The third specimen of the preliminary local series study was subjected to a cyclic loading pattern. The Global behavior of the RXS fuse was intended to be experimentally reproduced by testing nine specimens made with HSS 2.500x0.125, one specimen made with HSS 3.500x0.125 and two full size specimens with HSS 6.625x0.25, but as mentioned before due to results from the local behavior experimental series, the global series of the experimental program was not carried out.

5.1 Local Series

This series was carried out to test the proposed concept and consisted of three short specimens made with HSS 6.625x0.25 proportioned with a fifty one percent reduction of the gross cross-sectional area and a hole aspect ratio (HAR) of 3, resulting in a 42-in. long specimen with an oval-shaped cutout with a length of 10 in. and a hole diameter of 3-1/2 in. Each specimen was subjected to one of the following loading profiles: monotonic compression, monotonic tension, and a cyclic loading pattern.

5.1.1 Material Properties

Coupons from the oval cutouts of the HSS local series were prepared based on the ASTM standard test methods of tension testing [ASTM, 2003], and then subjected

to a tensile tests to determine the actual yield and ultimate strengths, and strain at fracture.

A pair of replicate specimens yielded similar results. Strain gages used for the first test coupon elongated up to approximately 5 percent. After 5 percent, the gages failed before the specimen reached its estimated ultimate tensile strength F_u of 64 ksi. Results from the second test coupon replicated stress-strain behavior, but elongated up to 12 percent, as shown in Fig. 5.1.

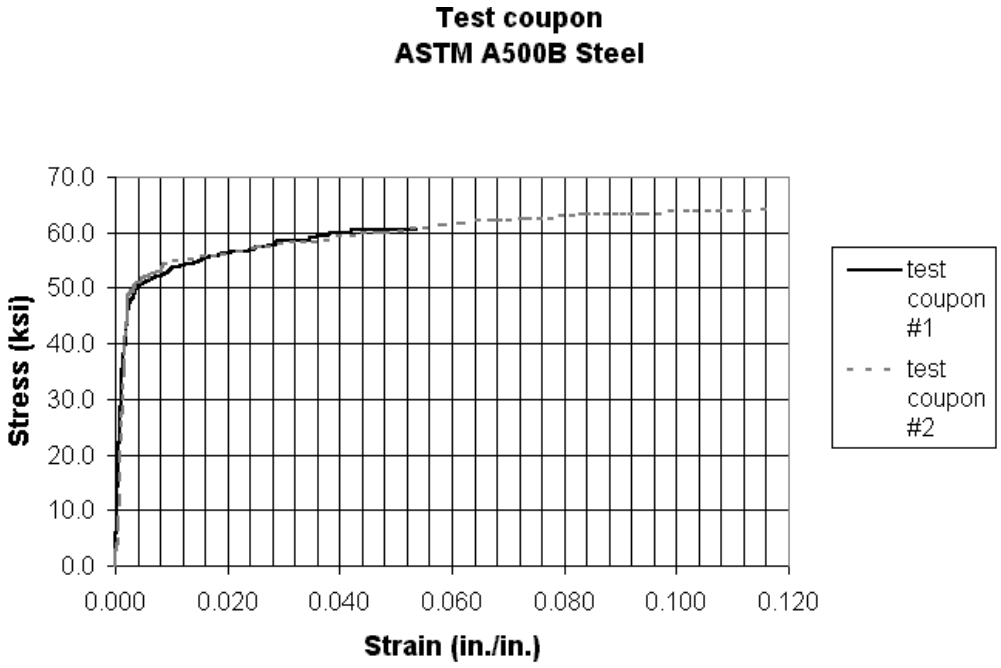

Fig. 5.1 - Test Coupons Stress-Strain Curve.

The stress-strain curves showed a well-defined linear elastic portion with modulus of elasticity of approximately 29,000 ksi and a yield plateau typical of

ductile steels. Visual inspection and the 0.2 percent offset method resulted on a yield strength F_y of 50 ksi, as shown in Fig. 5.2.

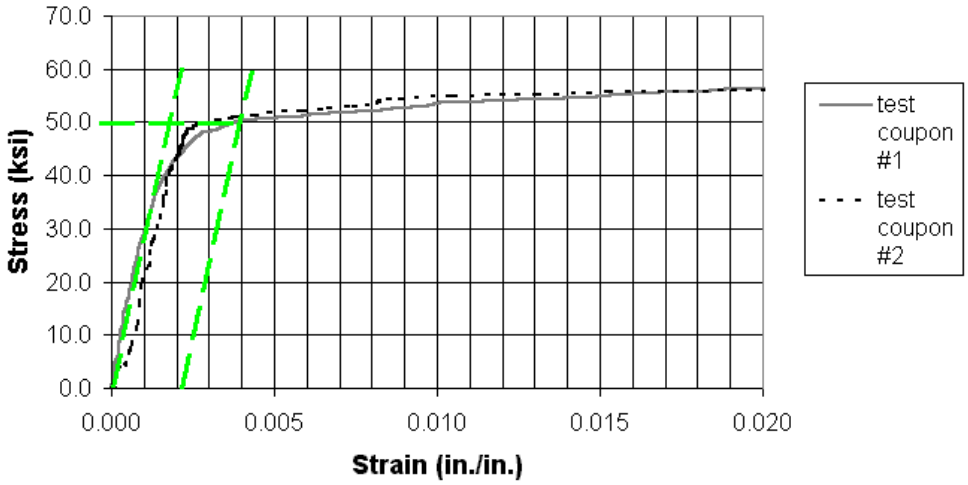

Fig. 5.2 - Test Coupons 0.2 Percent Offset Method.

	F_y (ksi)	F_u (ksi)
Test Coupon	50	64
Specified A500 grade B steel minimums by ASTM	42	58

Table 5.1 - Test Coupon vs. Specified Material Properties.

Thus actual ratios of expected to minimum specified strengths are:

$$R_{y,\ coupon} = F_{y,\ coupon}/F_{y,\ spec.} = 50ksi/42ksi = 1.19 \qquad \text{<Eq. 5.1>}$$

$$R_{t,\ coupon} = F_{u,\ coupon}/F_{u,\ spec.} = 64ksi/58ksi = 1.10 \qquad \text{<Eq. 5.2>}$$

The ratio of the expected yield strength to the minimum specified yield strength $\boldsymbol{F_y}$ for the test coupon was smaller than the $\boldsymbol{R_y}$=1.3 given by the AISC 2002 seismic provision [AISC, 2002]. The updated ratio of 1.4 from the latest AISC 2005 seismic provision [AISC, 2005] is even bigger than the $\boldsymbol{R_y}$ of the coupon. This lower value of $\boldsymbol{R_y}$ of the test specimen was rather beneficial for the overall performance of the brace because it allows the lower bound of the area reduction coefficient to be even smaller. Because the actual $\boldsymbol{R_y}$ was lower than the $\boldsymbol{R_y}$ provided by AISC seismic requirements [AISC, 2005], a broader range of provided area reduction coefficients is available.

The ratio of the expected ultimate strength to the minimum specified ultimate strength Fu was also smaller for the test coupon than the new $\boldsymbol{R_t}$=1.3 introduced by the latest AISC 2005 seismic provision [AISC, 2005]. Calculations using Eq. 2.2 (chapter 2) and the measured test coupon ratios confirmed that reinforcement of the brace at the connection was still required and therefore the RXS fuse was still a viable alternative to reinforcement.

$$A_e = R_{y,\ coupon} * F_y * A_g / (0.75 * R_{t,\ coupon} * F_u) \quad \text{<Eq. 2.2>}$$

$A_e = 1.19 * 42ksi * 4.68\ in2 / (0.75 * 1.1 * 58ksi) = 4.89\ in2$

Because $A_e = 4.89\ in2 > Ag = 4.68\ in^2$.

$\therefore$ Connection requires local reinforcement of the brace section.

where:

$R_{t,\ coupon}$ = Ratio of the expected ultimate strength to test coupon ultimate strength $\boldsymbol{F_u}$.

$R_{y,\ coupon}$ = Ratio of the expected yield strength to the minimum specified yield strength $\boldsymbol{F_y}$.

F_y = Brace specified minimum yield stress.

F_u = Brace specified minimum ultimate stress.

A_g = Brace gross area, in^2.

A_e = Brace effective area, in^2 calculated from Eq. 2.2.

5.1.2 Experimental Configuration for RXS Fuse

End fixtures were designed to fit the test specimens so that monotonic loads were uniformly distributed along the full specimen cross section. These fixtures were proportioned conservatively to resist the maximum calculated failure load of the local series test specimens. Among these fixtures were: 1-in. thick end plates connected with 5/16-in. fillet welds for both the monotonic compression test specimen (Fig 5.3) and the monotonic tension test specimens.

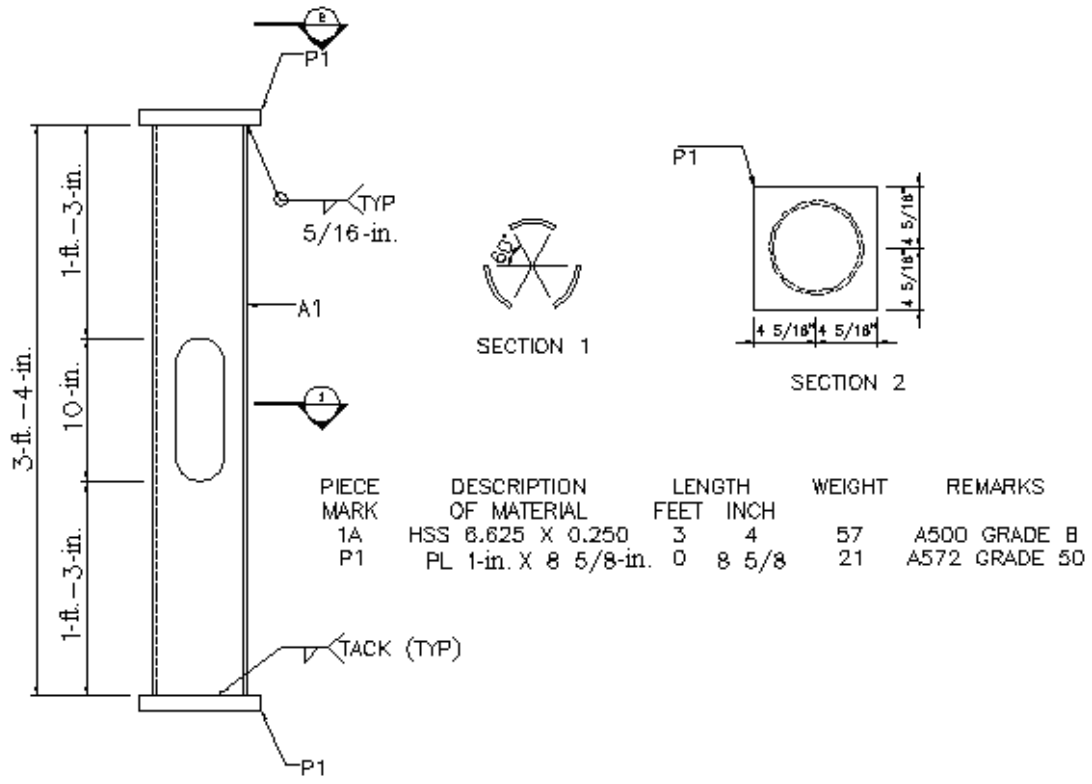

Fig. 5.3 - Monotonic Compression Test Specimen.

The monotonic tension test specimen also included 1 ½-in. diameter ASTM A490 bolts 8-in. long welded to the end plates as shown in Fig. 5.4.

The distance between the end plate and the oval cutout was set at 50 percent more than the oval cutout length of 10-in. This 15-in. distance provided to achieve a uniform stress distribution and avoid end effect in the test region.

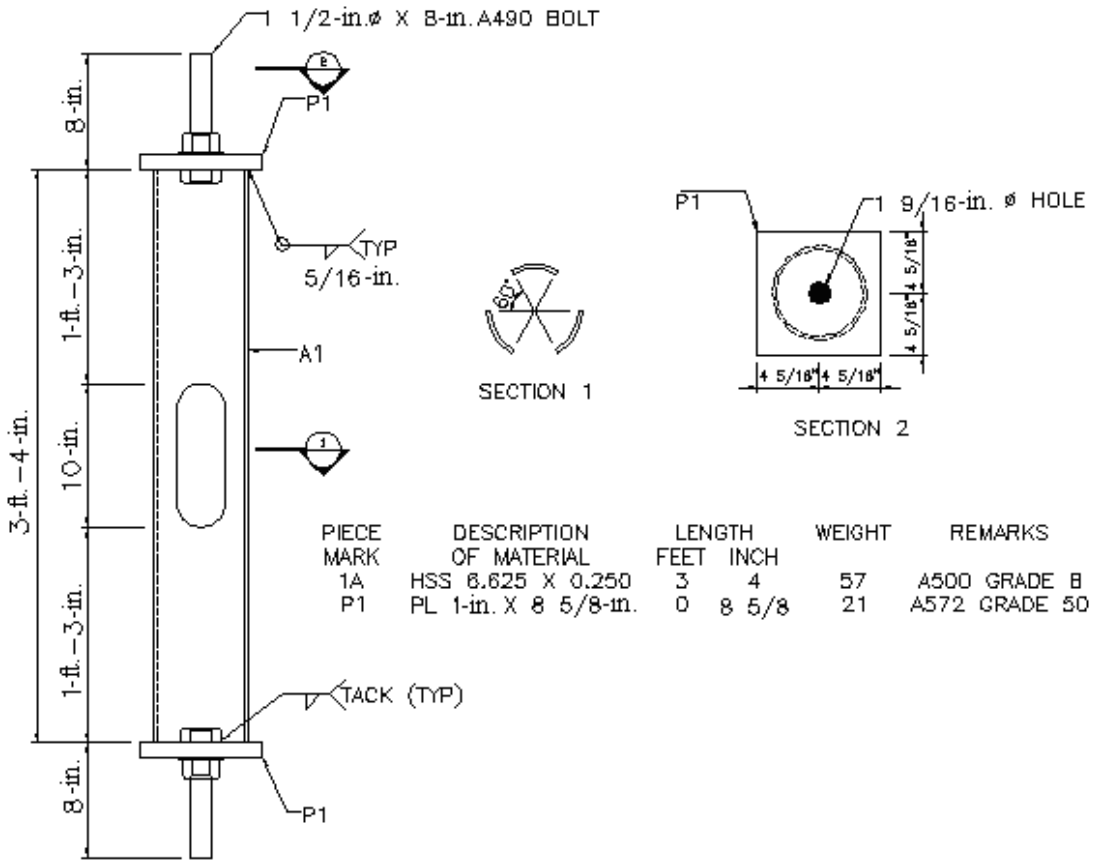

Fig. 5.4 - Monotonic Tension Test Specimen.

The fabrication of the test specimen used in the monotonic tests was conducted in accordance to normal building practice, with no special requirements for smooth edges at cuts.

Using the measured value of $F_{y,\ coupon}$ = 50 ksi, and $F_{u,\ coupon}$ = 64 ksi to update the initial spreadsheet calculations shown in Chapter 4, and neglecting the resistance factors established in the LRFD AISC Manual of Steel Construction [LRFD, 2002], the nominal strength of the test specimen was re-calculated as follows:

Local design nominal compressive strength	96.5 kips
Local design nominal tensile yield strength	114.4 kips
Local design nominal tensile ultimate strength	146.4 kips

Table 5.2 - Test Specimen Calculated Capacities.

5.1.2.1 Monotonic Compressive Test Results

The loading sequence for the monotonic compressive test was to approach a critical buckling load with a loading rate of approximately 3 ksi/min., continue to load in compression with a loading rate of approximately 1 ksi/min. up to the specimen critical buckling load, and then continue to load in compression to allow post-buckling deformations. The maximum applied load was 97,400 lb, which was very close the calculated critical nominal buckling load of 96,500 lb.

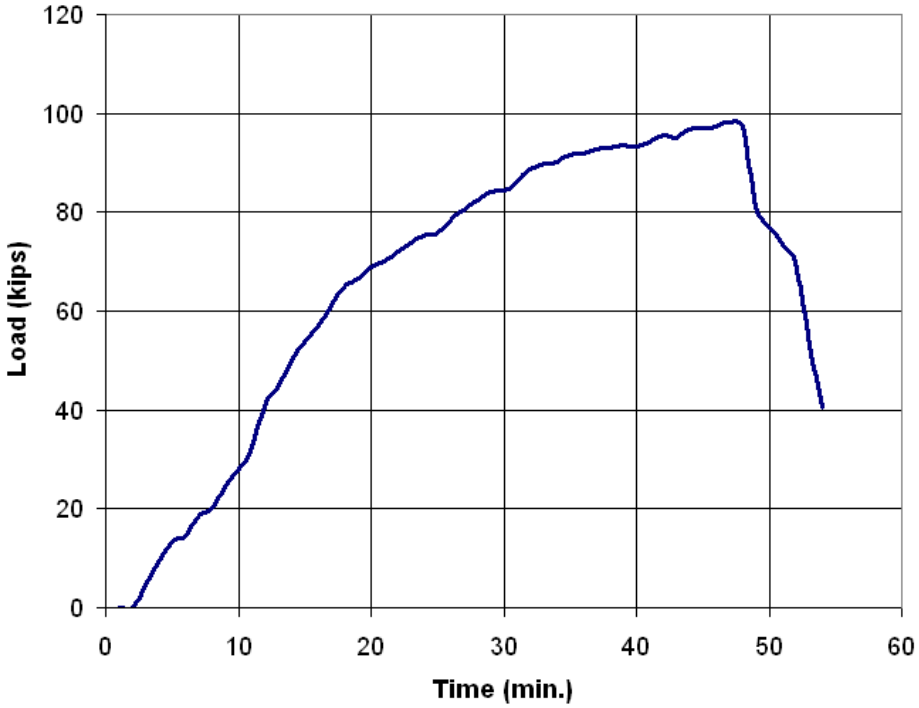

Fig. 5.5 - Monotonic Compression Test, Loading Profile.

A Universal (tension and compression) Testing Machine hydraulically applied monotonic compression load to the RXS fuse specimen. The frame of the testing machine consists of a lower fixed crosshead that works as the reaction head for compression testing, an upper crosshead, and a loading table under the lower crosshead. The upper crosshead moves together with the loading table. For compression testing, the RXS fuse specimen was placed between the loading table and the fixed lower crosshead.

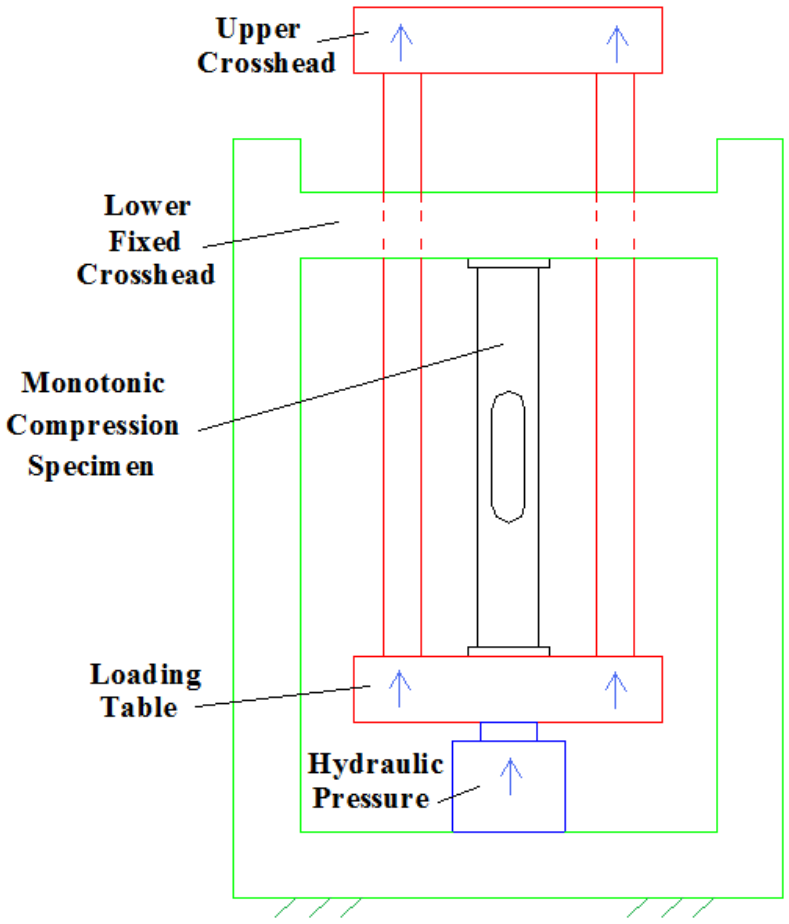

Fig. 5.6 - Sketch of the Monotonic Compression Testing Set Up Configuration.

Among the instruments employed for the monotonic compression test to measure displacement were LVDT's (Linear Variable Displacement Transformers), extensometers, and strain gages. These instruments, and other instrumentation and equipment employed are described in detail in section 5.3. Strain gage locations for first local series test, are shown in Fig. 5.7. Three strain gages were placed equally along two of the three arms, and two gages along the third arm. At the non-reduced

sections, strain gages were attached near the arm ends, in line with gages along the arms. Two strain gages were attached in line with an oval cutout.

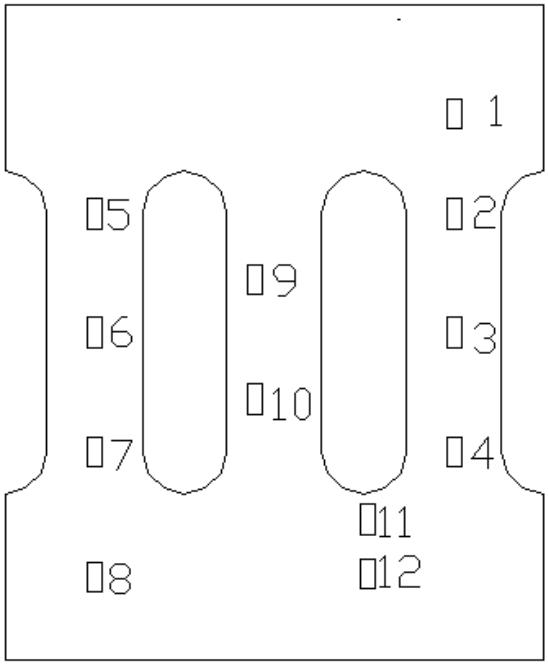

Fig. 5.7 - Strain Gage Locations on Monotonic Compression Specimen.

During the test no significant deformations were observed as the compressive load approached the calculated critical buckling load. Buckling was observed along the reduced section after the critical buckling load was reached. The load-deflection curve for the specimen is shown in Fig. 5.8, where the deflection was measured with an LVDT and the force from the Baldwin testing equipment readings. At critical buckling load the specimen shortened approximately 0.2-in. Post-buckling deformations were the specimen shortened a total of 0.3507-in. The specimen was

able to deform even more within its post-buckling behavior but it was decided to stop the test at that point.

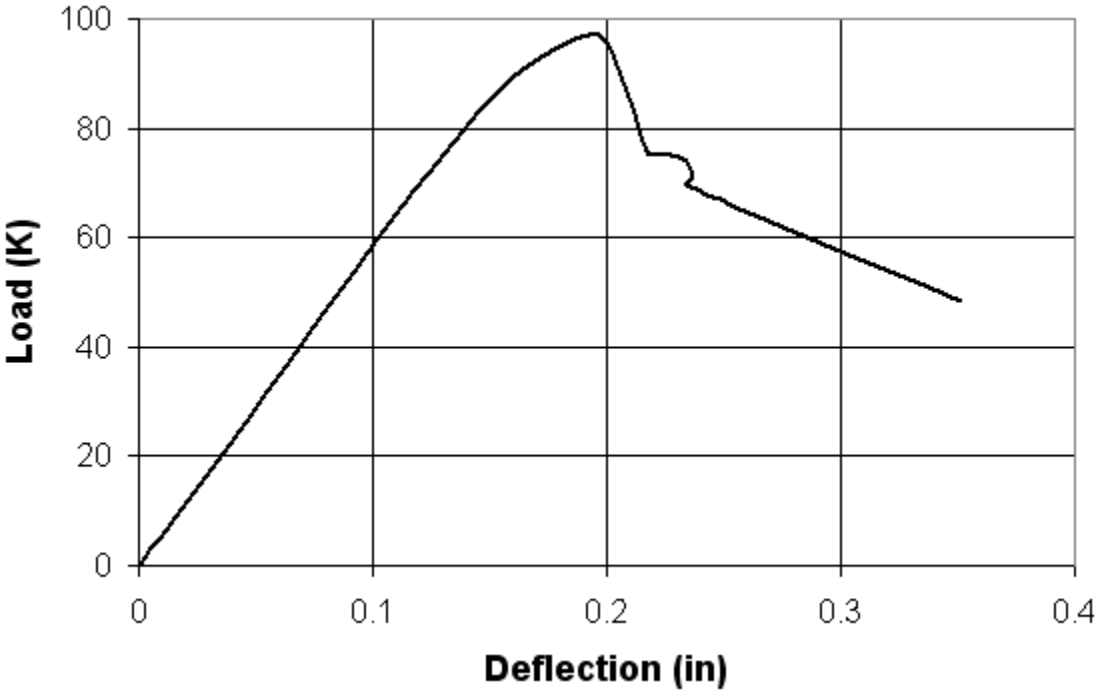

Fig. 5.8 - Load-Deflection Response Monotonic Compression Test.

After the critical buckling load was reached during test, the compressive capacity of the specimen started to decrease, and large buckling deformations were observed. The lateral deflection along the longitudinal axis increased towards the outside direction of the test specimen as seen in Fig. 5.9a and 5.9b. The outward buckling of all arms was expected because the shape of the arms, curved along the transversal axis, makes the inner face stiffer than the outer face.

Fig. 5.9a - Monotonic Compression, RXS after Buckling Failure.

Fig. 5.9b - Monotonic Compression, RXS after Buckling Failure.

Buckling deformations occurred along the reduced section, with slight differences between the arms. The lateral deflection of two arms was measured with dial gages during test until the compressive capacity of the specimen started to rapidly decrease after buckling. It was observed, as can be seen in Fig. 5.10, that buckling deformations along these two arms were different. Moreover, even before

reaching the critical buckling load, some lateral deformation along the arms was detected by the dial gage measurements.

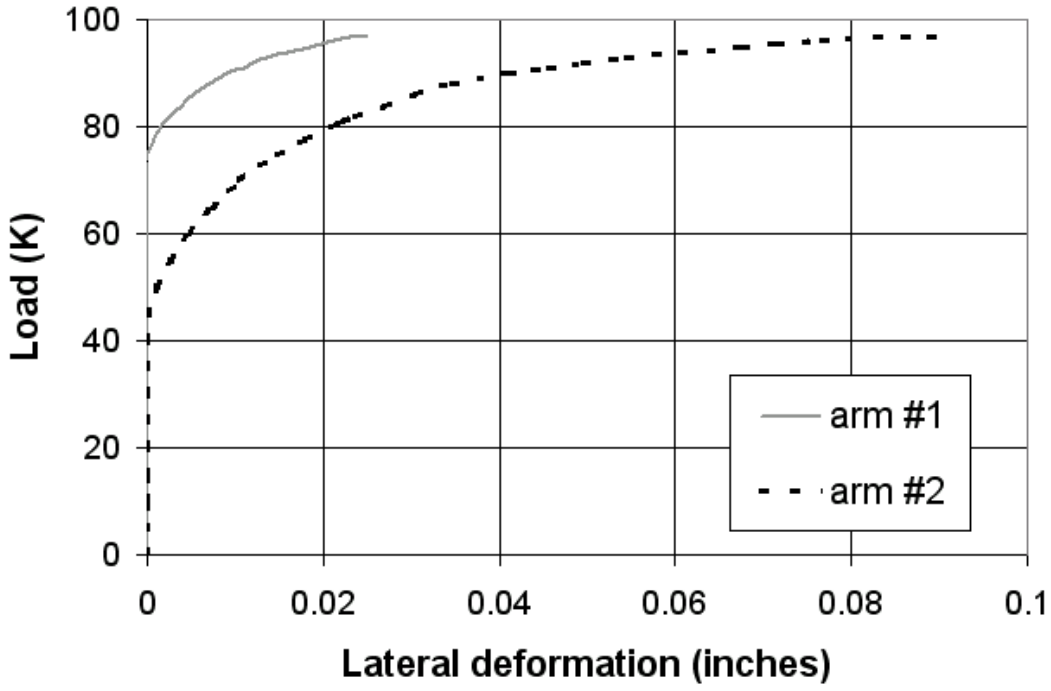

Fig. 5.10 – Monotonic Compression, Arm Lateral Deflection vs. Load.

Post-test shortening of the RXS fuse was measured: 1/8-in. arm #1, 3/8-in. arm #2, and ¼-in. arm #3. These measurements matched those calculated by multiplying the arm length of 10-in. by the maximum strain of each arm obtained from the load vs. reduced section strain curves shown in Fig. 5.11. This confirmed that the total shortening of 0.3507-in. occurred mostly, if not entirely, across the reduced section.

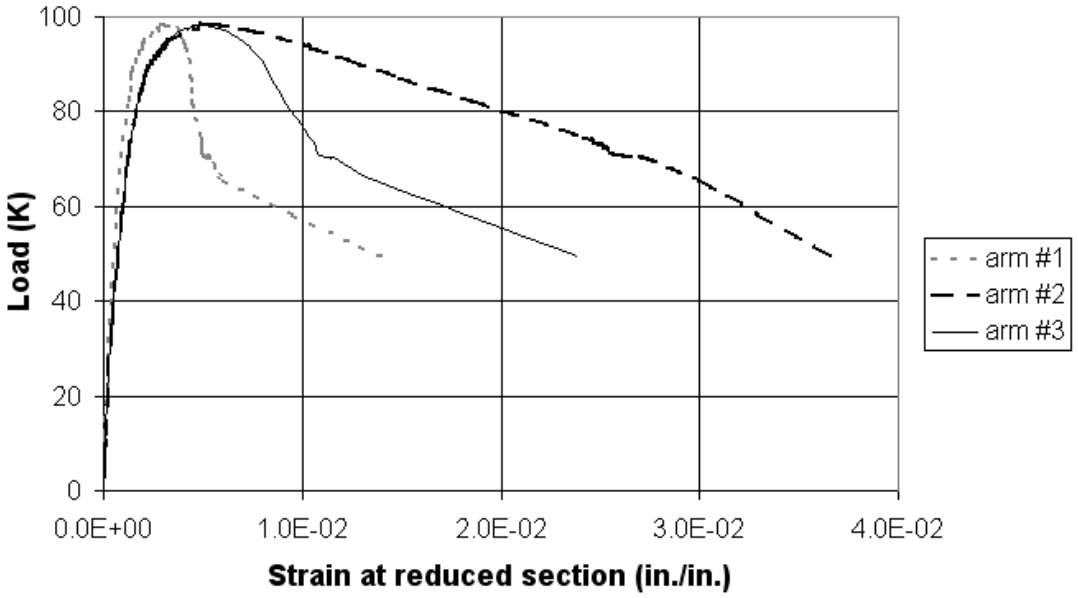

Fig. 5.11 - Monotonic Compression, Load vs. Strain at Three Arms.

The behavior of arm #1, which experienced the largest buckling deformation, is shown in Fig. 5.12. As the reduced section was subjected to compressive loads, similar behavior was detected along the arm. As the compressive load approached the critical buckling load, strains at mid-arm reversed. After reaching buckling loads, tensile strains were detected at the middle arm regions. Regions away from the mid-arm experienced compression strains even during the post-buckling behavior. These strains increased significantly after reaching the critical buckling load.

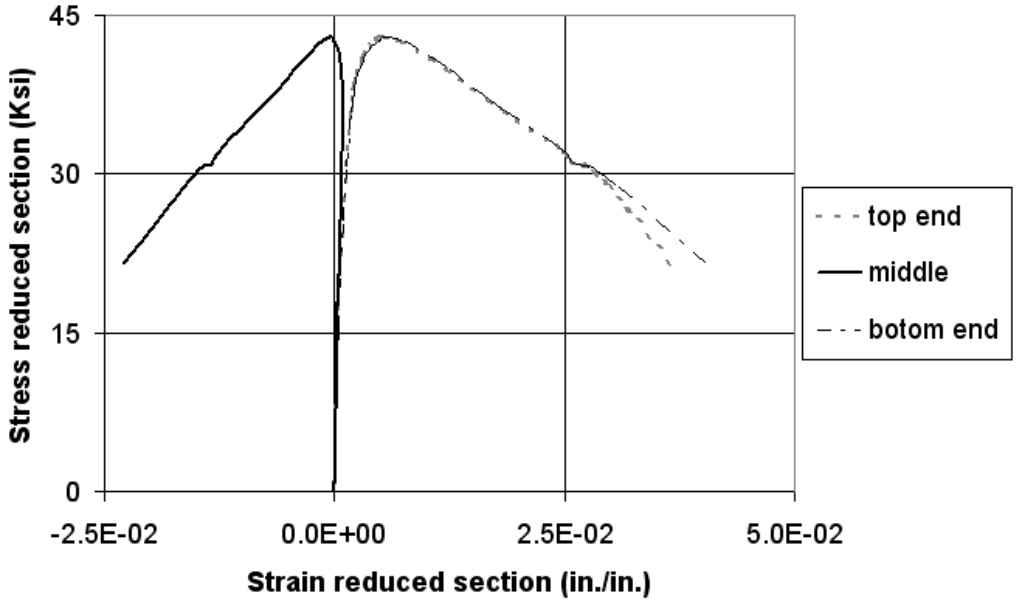

Fig. 5.12 - Monotonic Compression, Stress-Strains Curves Along One Single Arm.

5.1.2.2 Monotonic Tensile Test Results

The loading sequence for the monotonic tension test consisted of a uniformly increasing load, with a loading rate of approximately 1.5 ksi/min, until the specimen failed by fracture at the reduced section (Fig. 5.13).

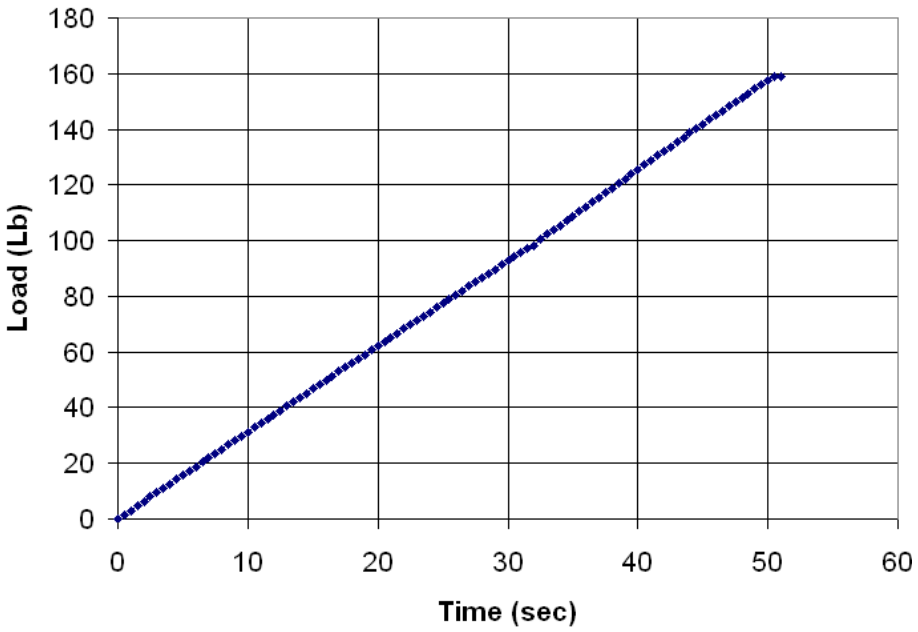

Fig. 5.13 - Monotonic Tension Test, Loading Profile.

A Universal (tension and compression) Testing Machine, similar to that used during the monotonic compression test, hydraulically applied monotonic tension load to the RXS fuse specimen. The frame of this testing machine also consists of a lower fixed crosshead that works as the reaction head for tension, an upper crosshead, and a loading table under the lower crosshead which moves together with the upper crosshead. For tension testing, the monotonic tension test specimen was placed between the fixed lower crosshead and the upper crosshead.

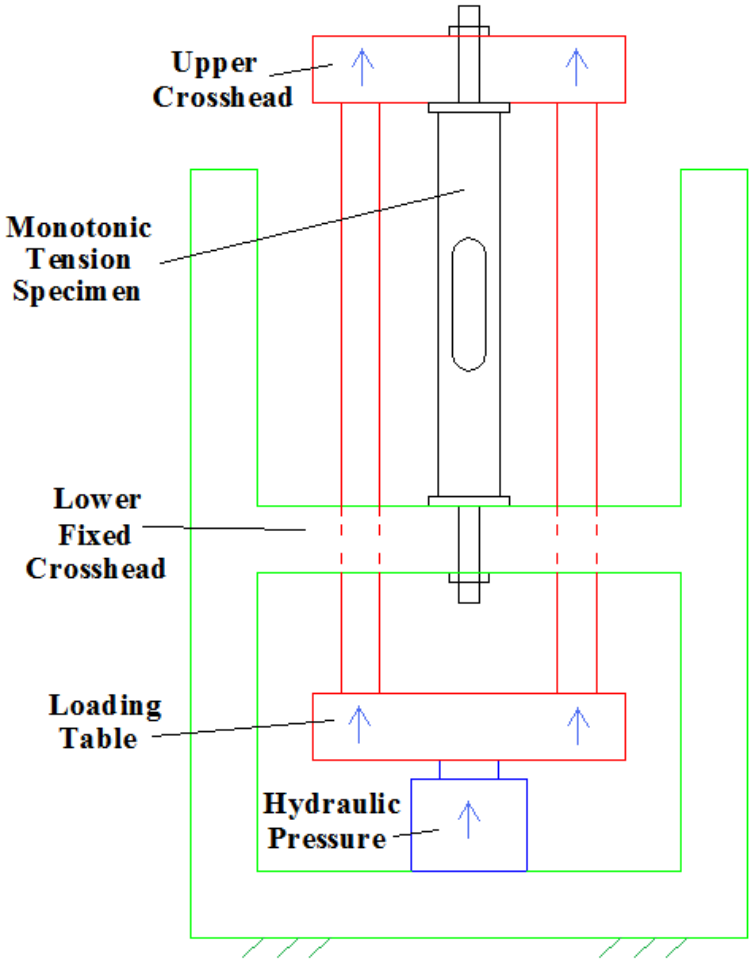

Fig. 5.14 - Sketch of the Monotonic Tension Testing Set Up Configuration.

Strain gage locations for the second local series test, are shown in Fig. 5.15. Three strain gages were placed equally along each arm. At the non-reduced sections, strain gage were attached near the arm ends, in line with gages along the arms. Two strain gages were attached in line with an oval cutout.

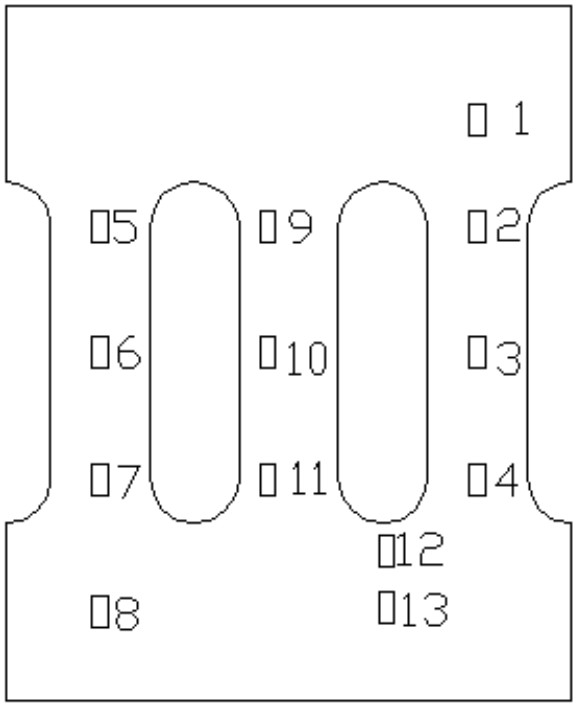

Fig. 5.15 - Strain Gage Locations on Monotonic Tension Specimen.

The maximum applied load was 158,900-lb., at a maximum stress of 69.5 ksi. The calculated nominal ultimate capacity of 146,400 lb. differs by 8.5 percent with respect to the maximum load measured during the test. No visible axial deformation occurred before fracture.

The specimen yielded at a load of approximately 126,000 lb., equivalent to a reduced section stress of 55 ksi (Fig. 5.16). The load-deflection curve shown in Fig 5.16 ends at a deflection of 0.06-in. because the extensometer was removed to protect it from damage due to specimen fracture failure.

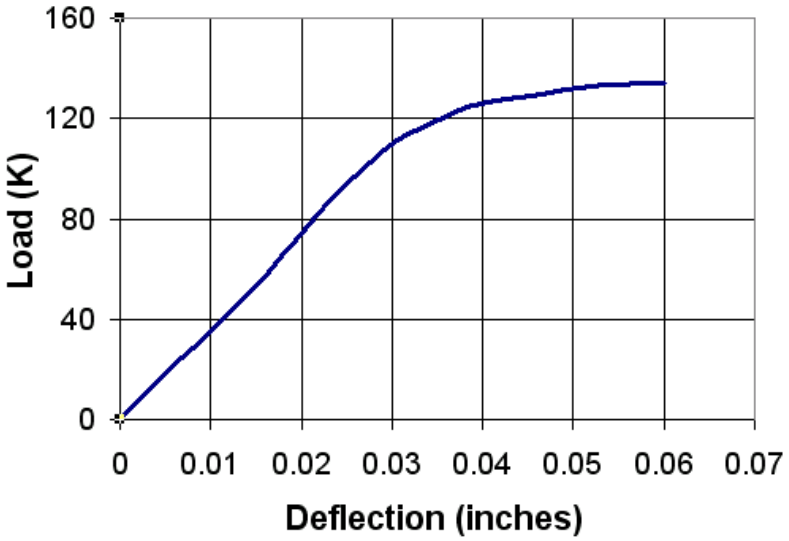

Fig. 5.16 - Monotonic Tension, Stress-Strain Extensometer.

Fracture failure occurred at the end of one arm as shown in Fig. 5.17, exactly at the location of strain gage 11. This strain gage was located where the semicircular cut transitions to the straight longitudinal cut.

Fig. 5.17 - Monotonic Tension, RXS after Fracture Failure.

Post-test elongation measurements indicated a total axial deformation of 5/8-in. These measurements matched well the overall elongation calculated from reduced section stress-strain curves, which confirmed that like the monotonic compression test the axial deformation during the monotonic tension test occurred mostly, if not entirely, along the reduced section.

The stress-strain curve of the RXS fuse under monotonic tension showed a well-defined linear elastic portion with a modulus of elasticity of approximately 29,000 ksi and a yield plateau typical of ductile steels. The curve was similar, although with a slightly higher stiffness than that obtained from test coupons as shown in Fig. 5.18.

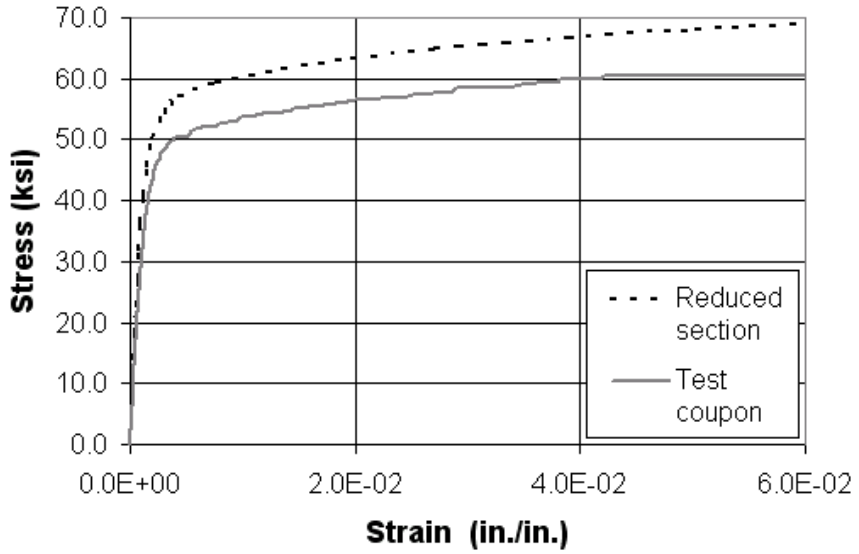

Fig. 5.18 - Stress-Strain Curve of Reduced Section and Test Coupon.

The behavior along the arm where fracture failure occurred is shown in Fig. 5.19. As the reduced section was subjected to tensile stresses within the elastic range, similar behavior was detected along all the arms. But as the tensile stresses approached the yield stress, regions away from the middle showed a larger stress than that measured at the middle region. Fracture failure occurred right at the location where the bottom end strain gage, Fig. 5.19, was installed (strain gage #11 from Fig 5.15).

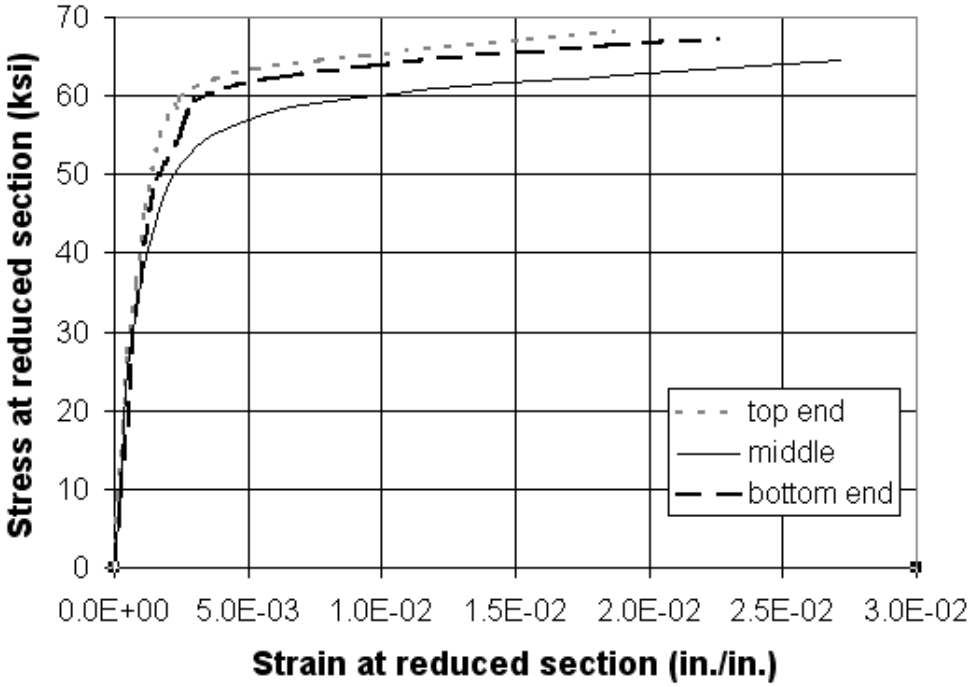

Fig. 5.19 - Monotonic Tension, Stress-Strains at Failure Arm.

5.1.2.3 Summary of Results for Monotonic Tests

Under tensile loads the test specimen elongated a maximum of 5/8-in. before it failed by fracture. The compression monotonic test specimen shortened 3/8-in. under compression loads. The relative axial displacement between the two specimens tested was measured and it confirmed the 1 in. residual inelastic deformation between the two specimens as shown in Fig. 5.20.

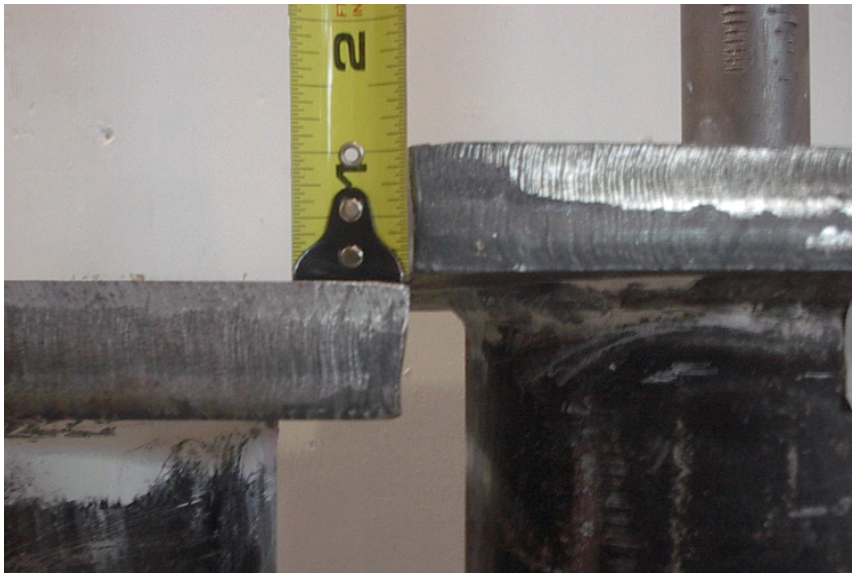

Fig. 5.20 - Relative Axial Displacement between Specimens.

5.1.2.3.1 Monotonic Compressive Test

The buckling load observed in the test matched the nominal local buckling load. Approximately 90% of the total axial deformation of the specimen occurred along the reduced section. Buckling deformations at the reduced section were slightly different between the three arms. Although this was not detrimental to the behavior of these short specimens, this asymmetry could have a detrimental effect on the behavior of a full-length brace with the RXS fuse.

Maximum load	97,400 Lb
Maximum stress	42.6 ksi
Critical buckling load specimen strain at reduced section	0.004771 in./in.
Maximum post-buckling strain reached at reduced section	0.00835in./in.
Total residual inelastic axial deformation	3/8 in.

Table 5.3 - Summary of Results, Monotonic Compression Test.

5.1.2.3.2 Monotonic Tensile Test

The maximum tensile load applied during test was 8.5 % larger than the nominal load at fracture. No visible axial deformation occurred before fracture at the end of one of the RXS fuse arms. Reduced section stress-strain curves showed that the specimen had ductile behavior during the test; it was able to undergo large deformations before it fractured. Similar to the monotonic compression test, most of the specimen axial deformation occurred along the RXS, with less than 10% of the deformation being estimated to occur along the non-reduced sections at failure.

Maximum load at fracture failure	158,900 Lb
Reduced section maximum stress at fracture failure	69.5 ksi
Arm strain at fracture	0.06 in./in.
Specimen strain at fracture	0.015 in./in.
Reduced section stress at yield	55 ksi
Arm strain at yield	0.003 in./in.
Specimen strain at yield	0.0011875 in./in.
Total residual inelastic axial deformation	5/8 in.

Table 5.4 - Summary of Results, Monotonic Tension Test.

5.1.3 RXS Cyclic Loading Test Results

Test specimens were initially fabricated using normal building fabrication practice with no special requirements for smooth edges cuts. Due to the location of the fracture of the specimen loaded in tension, normal bridge fabrication practice with smooth edge requirements was implemented for the specimen subjected to cyclic loading to delay fracture and improve the ductility of the RXS fuse.

Similar end fixtures to those used in the monotonic tension test specimens were used. The main difference is that the 1 ½-in. A490 bolts were replaced by 6-ft. and 3.5-ft. ASTM A193 threaded steel rods to attach the test specimen to the self-reacting frame.

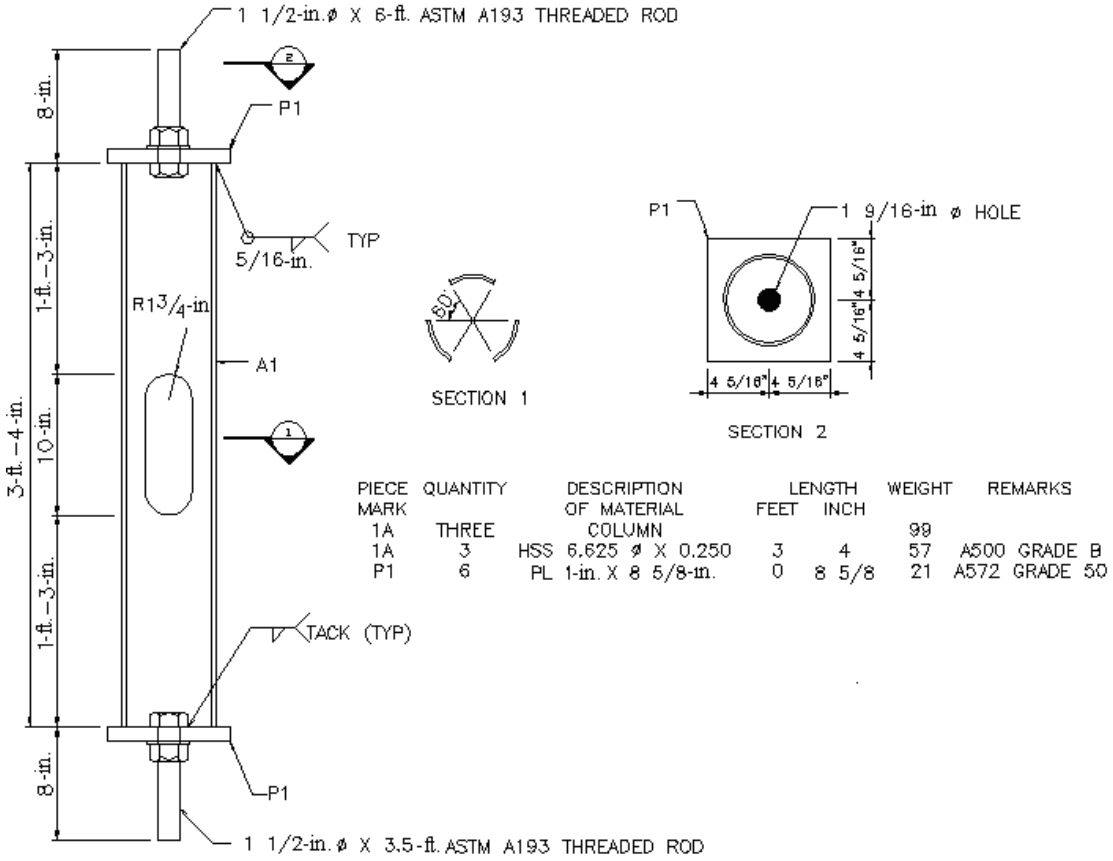

PIECE MARK	QUANTITY	DESCRIPTION OF MATERIAL	LENGTH FEET	LENGTH INCH	WEIGHT	REMARKS
1A	THREE	COLUMN			99	
1A	3	HSS 6.625 ø X 0.250	3	4	57	A500 GRADE B
P1	6	PL 1-in. X 8 5/8-in.	0	8 5/8	21	A572 GRADE 50

Fig. 5.21 - Cyclic Loading Test Specimen.

Strain gage locations are shown in Fig. 5.22. Like the monotonic tension test specimen, three strain gages were placed equally spaced along each arm. At the non-reduced sections, strain gages were attached near the arm end, in line with gages along the arms. Two strain gages were located in line with an oval cutout. In addition to the strain gages, two LVDT's (linear variable displacement transducer) were also used to measure linear displacement of the specimen.

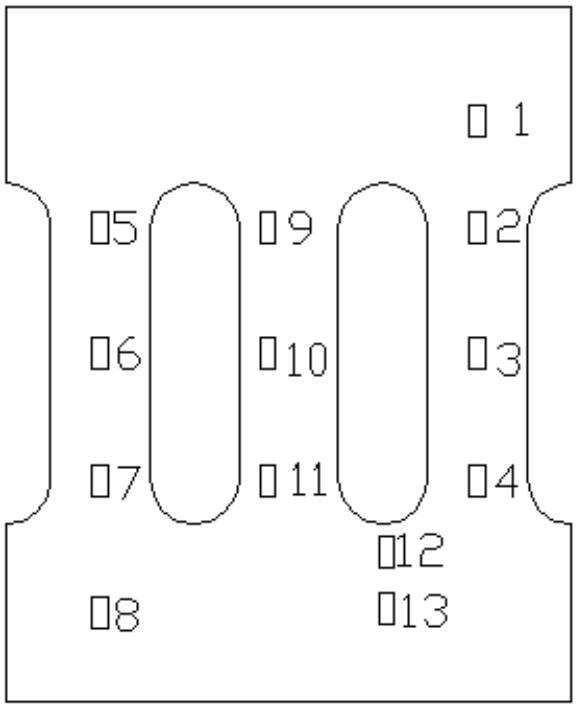

Fig. 5.22 - Strain Gage Locations on Cyclic Loading Test Specimen.

A self-reacting frame, such as that sketched in Fig. 5.23, was used to carry out this third local series test. It consisted of two vertical W12x58 columns and two cross-beams made with MC18x58. The double channels and the columns were connected through 16 bolts at each joint. Fig. 5.23 shows the self-reacting frame as it was initially sketched during the design stage.

Two double-acting hollow plungers were installed on one side of the self-reacting frame. Both hollow plungers moved equally during tension and compression cycles, but under the tension cycles the outermost hollow plunger applied tension to the specimen as it pushed against the MC18x58 cross-beam transferring the tensile load through the 6-ft. long ASTM A193 threaded steel rod to the specimen. On the other side of the specimen the tensile load was transferred from the specimen to the 3.5-ft. long ASTM A193 threaded steel rod connected to the outermost load cell. During the compression cycles the innermost hollow plunger applied compression directly to the specimen as it pushed against the MC18x58 cross-beam. On the other side of the specimen the innermost load cell took load readings as the specimen sustained compressive loads.

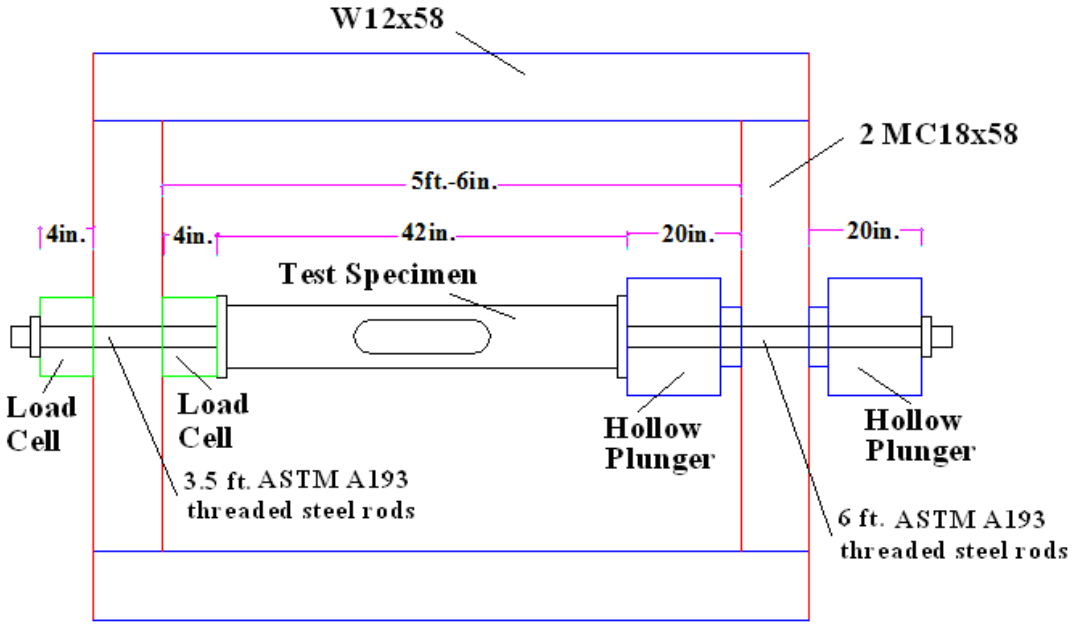

Fig. 5.23 - Sketch of Self-Reacting Frame Test Set Up.

5.1.3.1 Loading History

The cyclic behavior of test specimens is greatly influenced, among other factors, by the loading history [Tremblay, 2002]. The loading history used, shown in Fig. 5.24, is a symmetrical displacement pattern that was devised based on the SAC loading protocol [SAC, 1997] and results from the monotonic tests, to provide information concerning the elastic and inelastic behavior of the test specimen under load reversals. The deformation parameter used to control the loading history was the axial deformation divided by the displacement at yield measured during the monotonic tension test.

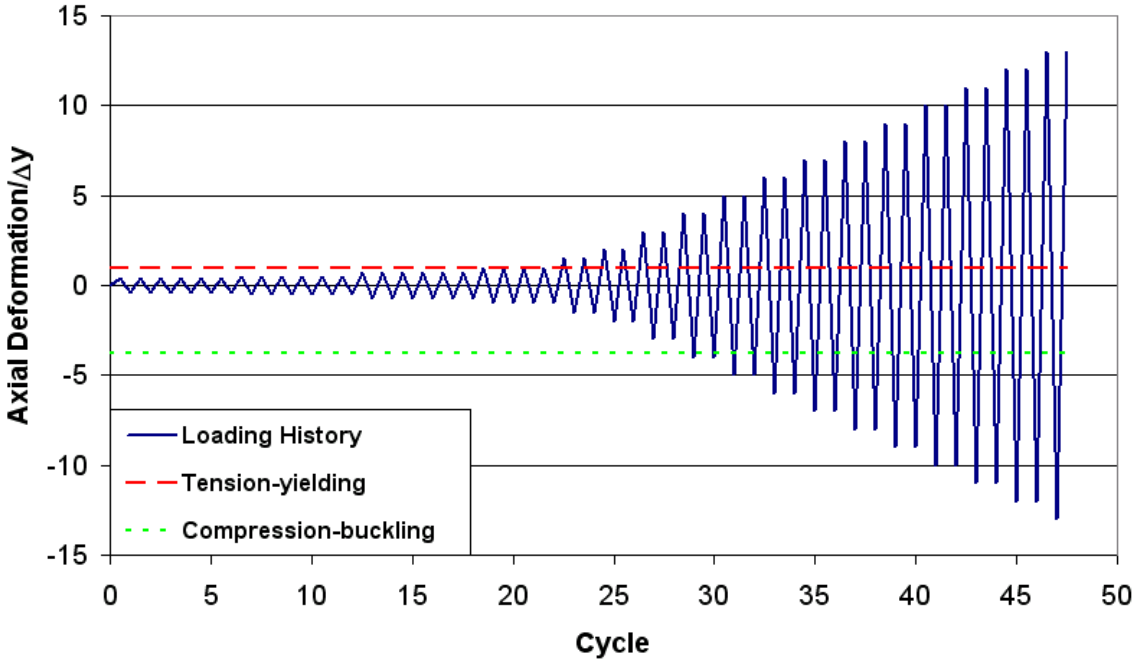

Fig. 5.24 - Loading History.

As can be seen in Fig 5.24 the displacement amplitude in tension and in compression increases stepwise at every sixth cycle within the linear-elastic range of behavior, at every fourth cycle at yielding Δy, and at every second cycle after yielding. The upper dashed line in Fig. 5.24 represents the displacement at yield measured in the monotonic tension test, whereas the dotted line represents the displacement at buckling measured in the monotonic compression test.

The loading history is presented in table 5.5, for a maximum of twenty-four load steps and sixty-two cycles. The estimated specimen strain per load step was calculated directly from peak deformation percentages defined by the SAC loading protocol [SAC, 1997]. The axial displacement and tension load were calculated using

those same peak deformation percentages in combination with results from the monotonic tension test.

Table 5.5 shows that at load step twenty-four and overall cycle sixty-two the specimen would have reached the maximum axial deformation from the monotonic tension test before fracture. Even though this maximum axial deformation was expected to be even higher than that due to the implementation of normal bridge fabrication practice with smooth edges, it was assumed that the fatigue produced by the load reversals would play an important factor too.

Load Step	cycles	Sum:cycles	Peak deformation	%	strain (in./in.) **strain gage** control	axial deformation/Δy	Axial displac. **LVDT** (in.) control	tension **LOAD** (Lb)
1	6	6	0.00375	37.5	1.13E-03	0.38	0.032	91000
2	6	12	0.005	50	1.50E-03	0.50	0.038	105500
3	6	18	0.0075	75	2.25E-03	0.75	0.049	120000
4	4	22	0.01	100	3.00E-03	1.00	0.058	125750
5	***2***	***24***	***0.015***	***150***	***4.50E-03***	***1.50***	***0.074***	***130600***
6	2	26	0.02	200	6.00E-03	2.00	0.089	133300
7	2	28	0.03	300	9.00E-03	3.00	0.120	137000
8	2	30	0.04	400	1.20E-02	4.00	0.151	139700
9	2	32	0.05	500	1.50E-02	5.00	0.181	141800
10	2	34	0.06	600	1.80E-02	6.00	0.212	143700
11	2	36	0.07	700	2.10E-02	7.00	0.242	145400
12	2	38	0.08	800	2.40E-02	8.00	0.272	146880
13	2	40	0.09	900	2.70E-02	9.00	0.303	148200
14	2	42	0.1	1000	3.00E-02	10.00	0.333	149450
15	2	44	0.11	1100	3.30E-02	11.00	0.363	150550
16	2	46	0.12	1200	3.60E-02	12.00	0.394	151570
17	2	48	0.13	1300	3.90E-02	13.00	0.424	152500
18	2	50	0.14	1400	4.20E-02	14.00	0.454	153400
19	2	52	0.15	1500	4.50E-02	15.00	0.484	154200
20	2	54	0.16	1600	4.80E-02	16.00	0.514	155400
21	2	56	0.17	1700	5.10E-02	17.00	0.544	156050
22	2	58	0.18	1800	5.40E-02	18.00	0.575	156650
23	2	60	0.19	1900	5.70E-02	19.00	0.605	157180
24	2	62	0.2	2000	6.00E-02	20.00	0.635	158900
Total cycles	62							

at tensile yield

right before critical buckling

maximum buckling deformation during monotonic compression test

maximum axial deformation during monotonic tension test before fracture

Table 5.5 - Loading History Calculations.

5.1.3.2 Expected Behavior

It was expected that under concentric loads the specimen would be subjected to yield deformations under tension after load step #4, and under compressive concentric loads the specimen would reach critical buckling after load step #5. In other words, the specimen was expected to behave within its elastic range of response until load step #4 under tension and load step #5 under compression.

After the specimen started to deform in the inelastic range of response, it was expected that under load reversals the nominal capacity would deteriorate due to the Bauschinger effect and the effect of residual curvature of the arms resulting from plastic rotations during previous cycles. Furthermore, based on previous experiments [Popov and Black, 1981] from other studies, it was expected that after the buckling load was reached, the compressive capacity at subsequent cycles would decrease to almost half of the initial critical buckling capacity.

It was also expected that the load-displacement response of the specimen would be adequate in terms of the energy dissipation capacity and that the peak deformation under tensile loads would be similar to the peak deformation before failure of the monotonic tension test.

The Bauschinger effect is defined as follows: when materials are loaded uniaxially in one direction (e.g. in tension) into the plastic regime, unloaded to zero stress level, and then reloaded in the reverse direction (e.g. in compression), they may yield during the reloading, at a stress level lower than if the reloading were carried out in the original direction. [Parker, and Underwood, 1997].

5.1.3.3 Observations During Test and Results

The specimens were loaded following the displacement history described in sec 5.1.3.1. The overall behavior of the specimen was significantly different to what initially was expected.

It was observed during the first cycle of the second load step (cycle #7 overall) that one of the RXS fuse three arms started to show signs of buckling deformations. Because it was unexpected to have inelastic deformations at such early stages of the loading history the experiment was interrupted and after further checks of the reaction system it was found that a small eccentricity was being applied towards the arm that initially buckled, as shown in Fig. 5.25. For this reason that arm was being subjected to higher stresses than the other two arms causing early buckling deformations on that particular arm. The other two arms did not show any signs of buckling deformations at that stage of the loading history. The eccentricity problem was fixed as the specimen was re-aligned with the hollow plungers and after the second load step of the first cycle the test continued and the applied load was almost concentric.

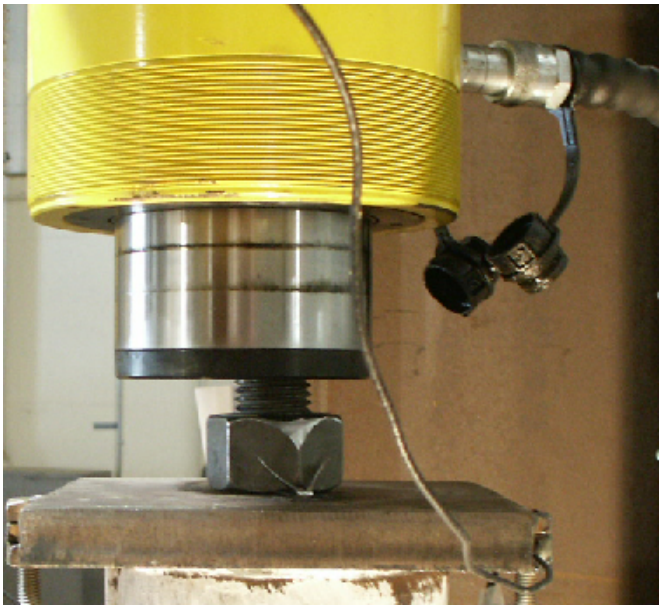

Fig. 5.25 - Initial Eccentricity on Axial Load.

Contrary to the initially expected behavior, yield deformations were not observed or recorded by the instrumentation during load step #4. For this reason it was decided to modify the loading history for subsequent load steps from 2 cycles per load step to 4 cycles, until yield deformations were recorded. However, inelastic deformations under tension loads were never observed or recorded by the instrumentation during subsequent load steps.

The other two arms that had not initially buckled, started to show inelastic deformations under compressive loads after load step #5, and the test continued after verifying that the load was still concentrically applied.

As the test progressed by increasing the displacement at every load step, severe buckling deformations were visually detected under compression. These buckling deformations accentuated with every subsequent cycle. After load step #6 it was observed that the thin coating of whitewash started to detach from the surface of the RXS, which was a clear sign of moderate steel deterioration. The deterioration became more evident as the test continued. The RXS fuse arms were severely deteriorated at the beginning of load step #12 before low cycle fatigue failure, as can be seen in Fig. 5.26.

Fig. 5.26 - RXS Fuse Arm Deterioration at Start of Load Step #12.

As mentioned before the specimen was never able to reach the yield displacement measured in the monotonic tension test. It was observed that at peak displacement under tension the arms never recovered their original straight shape, and instead a residual buckling deformation was observed.

During load step #12 of the first cycle, and fifty-first cycle overall, the arm that initially buckled failed in the form of a horizontal fatigue crack at the middle of the inner face of the arm. The crack initiated simultaneously at the center of the two longitudinal cuts, and propagated from the edges of the inner face of the arm towards its longitudinal center as the load increased. After that first arm failed, the other two arms had the same type of failure. The test concluded at load step #12 after fatigue failure was detected on all three arms.

Fig. 5.27 shows the load-displacement response of the specimen to the loading history up to load step #12 ($\Delta = \pm 8.0\ \Delta_y$), when fatigue failure occurred.

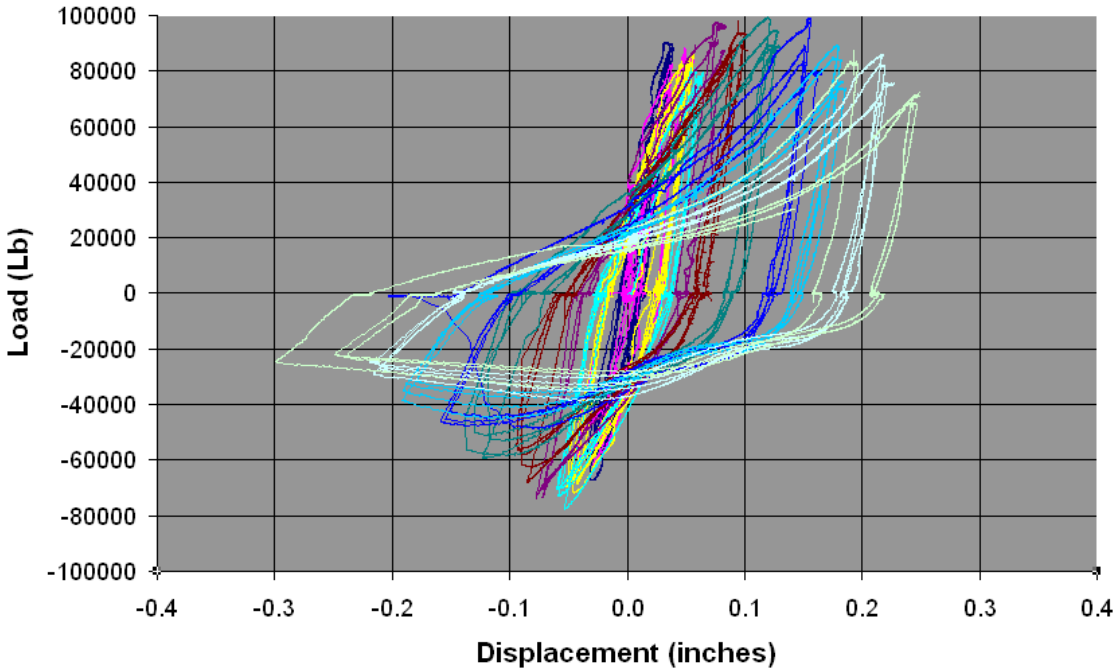

Fig. 5.27 - Axial load vs. Displacement Response.

As previously mentioned, under tension loads the specimen never reached inelastic deformations, and the tensile loads for every load step after the initial buckling deformation never matched those analytically calculated and were recorded well below the calculated capacities. Under compression loads the specimen was subjected to inelastic deformations from the very beginning of the test and even though the compressive loads were also well below the calculated capacities, it is considered that the performance of the specimen under compression was promising,

taking into account that the specimen was severely subjected to buckling deformations for approximately more than 44 cycles before fatigue failure.

5.2 Global Series

This series consisted of nine specimens made with HSS2.500x0.125, one specimen made with HSS 3.5x0.125, and two specimens made with HSS6.625x0.25 as can be seen in Table 5.6.

All test specimens made with HSS 2.500x0.125 are proportioned with a sixty percent area reduction of the gross cross-sectional area, specimen made with HSS 3.500x0.125 is proportioned with a forty two percent area reduction, and specimens made with HSS 6.625x0.25 are proportioned with the same fifty one percent area reduction used in the local series. All sections have a total length of 10-ft.

Size	HAR	Buckling	RXS	Loading sequence
HSS 2.500x0.125	-	Global	0	Monotonic compression
HSS 2.500x0.125	-	Global	0	Loading pattern L1
HSS 2.500x0.125	3.0	Global	1	Monotonic tension
HSS 2.500x0.125	3.0	Global	1	Monotonic compression
HSS 2.500x0.125	3.0	Global	1	Loading pattern L1
HSS 2.500x0.125	3.0	Global	1	Loading pattern L2
HSS 2.500x0.125	2.0	Global	1	Loading pattern L1
HSS 2.500x0.125	3.0	Global	2	Loading pattern L1
HSS 2.500x0.125	5.0	Local	2	Loading pattern L1
HSS 3.500x0.125	2.0	Global	2	Loading pattern L1
HSS 6.625x0.250	3.0	Local	1	Loading pattern L1
HSS 6.625x0.250	4.0	Local	1	Loading pattern L1

Table 5.6 - Experimental Program Global Series.

	HSS	HSS	HSS	HSS	HSS	HSS
Global	10.78	10.78	10.78	27.91	190.50	190.50
Local	13.00	11.24	7.05	29.21	97.30	83.30
Area	60%	60%	60%	42%	51 %	51%
Hole aspect	2.0	3.0	5.0	2.0	3.0	4.0
Hole	1-1/2	1-1/2	1-1/2	1-1/2	3-1/2	3-1/2
Hole length	3.0	4.5	7.5	3.0	10.0	14.0
Total length	10	10	10	10	10	10

Table 5.7 - Specimen Design Properties.

Variations in hole aspect ratios and member size were intended to be investigated in order to determine the behavior of the proposed system for different limit states, the number of RXS fuses along the same bracing member, and two loading patterns, including the same loading history used for the local series cyclic loading test, and a second loading history with major emphasis in post-buckling deformations labeled ***L2*** (Fig. 5.28), but as mentioned before, due to results from the experimental local series, the experimental global series program was not carried out.

The second displacement pattern labeled ***L2*** is unsymmetrical and it was devised based on previous studies [Goel, Aslani, 1992]. It is intended to induce considerable axial deformation in the post-buckling range of response. The amplitude of the excursions in tension increases stepwise at every cycle. In compression, the amplitude of the excursions increases stepwise at every cycle until it reaches a severe post-buckling axial deformation at -12Δy (Δy being the yield displacement in tension, and the negative sign being indicative of compressive deformations), it remains at that constant amplitude for five cycles, and then it increases up to –16Δy for the remaining cycles.

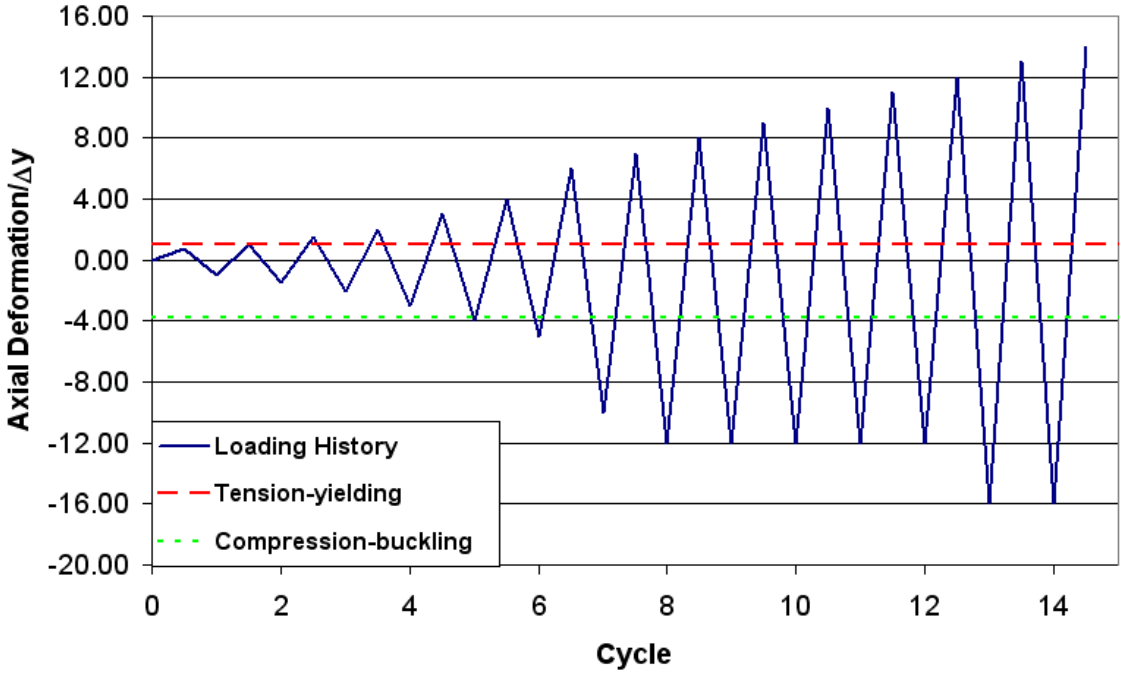

Fig. 5.28 - Loading History "L2".

A second more complex self-reacting frame was planned to be used as part of the global series test set-up. This self-reacting frame is similar to the one used by Dr. Subhash Goel in several bracing tests [Goel, Jain, and Hanson, 1980] and it is sketched in Fig. 5.29.

Test setup consists mainly of a four-hinged frame, a hydraulic actuator and a supporting frame. The specimen is placed in a diagonal position inside the four-hinged frame and secured to the lower beam of the reacting frame. As the actuator applies predetermined horizontal displacements to the upper beam of the four-hinged frame, the diagonal specimen is subjected to mainly push-pull loading simulating the actual loading of bracing members due to earthquakes.

The actuator reacts against one of the two of the supporting frame columns, and applies load the four-hinged frame horizontal beam that is free to translate in the horizontal direction as the diagonal specimen deforms. The diagonal specimen receives the load from the four-hinged horizontal beam and reacts against the lower horizontal beam of the supporting frame.

The test specimen forms an angle of 25 deg. with respect to the horizontal axis. Axial loads in test specimens should be calculated by taking into account the component of the force measured by the actuator load cell neglecting any small change in the 25 deg. angle during test as the diagonal deforms.

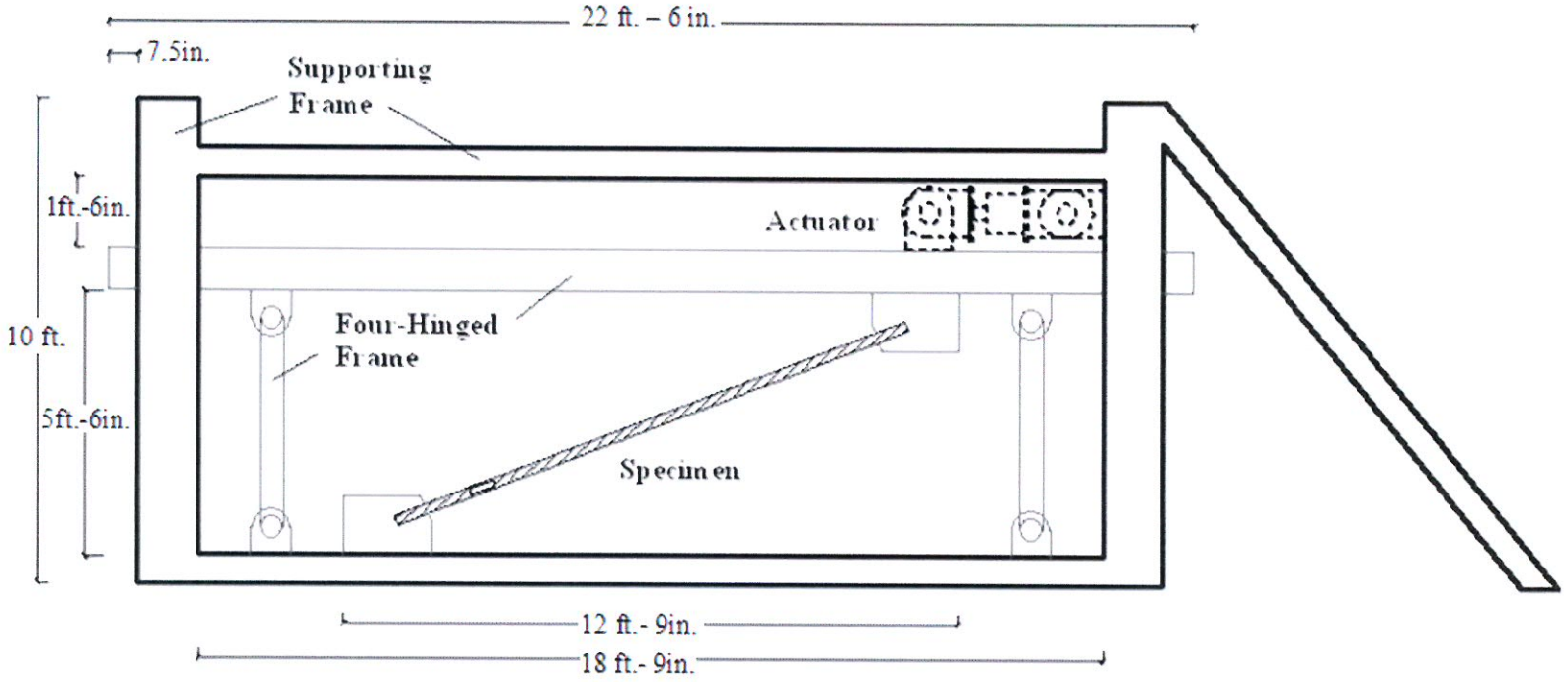

Fig. 5.29 - Global Series Self-Reacting Frame Sketch.

5.3 Instrumentation

Among the instruments employed in the experimental program are:

5.3.1 LVDT's

LVDT's (Linear Variable Displacement Transformers) measure linear displacement. They consist of a hollow cylindrical inductor body and a displaceable core that translates within the LVDT body so the output voltage varies as the core moves. This variation in voltage is linear over a specific range, and is related to a linear displacement through a scale factor based on the slope of Output Voltage vs. Linear Displacement plot. LVDT's were used to measure local test specimen axial displacement when subjected to monotonic compression and will be used to measure linear displacement for third local series test and for global series test specimens.

5.3.2 Extensometer

An Extensometer with a 4-in. gage length that measures linear displacement was used during local series monotonic tension test. This extensometer is a full Wheatstone bridge design transducer powered by 10 VDC (volts direct current). It has two halves that separate as the test specimen elongates making the output voltage vary. The variation in voltage is related to a linear displacement through a scale factor based on the slope of Output Voltage vs. Linear Displacement plot.

5.3.3 Strain Gages

A strain gage is a device used to measure the strain of an object. The most common type of strain gage consists of an insulating flexible backing which supports a metallic foil pattern. The gage is attached to the object by a suitable adhesive. As the object is deformed, the foil is deformed, causing its electrical resistance to change. This resistance change, usually measured using a Wheatstone bridge, is related to the strain by the quantity known as the gage factor.

Bondable strain gages adhered to the outer surface of the test specimen measured strain at specific locations across the RXS. Strain gage locations for first local series test, monotonic compression, are shown in Fig. 5.7. Strain gages locations for second local series test, monotonic tension, are shown in Fig. 5.15. The same strain gage configuration shown in Fig. 5.15 was used to locate strain gages for the third local series test, cyclic loading (Fig. 5.22).

5.3.4 Dial Gages

Dial gages were used during the local series monotonic compression test to measure the RXS lateral buckling deflection. They are commonly used to accurately measure movement of the test in progress. The magnetic gage base was placed on the

loading base of the testing machine with the dial gages placed perpendicular to the longitudinal axis of the arms.

5.3.5 Whitewash

A thin coat of whitewash, a mixture of Type ***S*** masonry lime and tap water, was applied to the first two local series tests, and will be applied to the third local series specimen. For the global series test specimens, a thin coat of whitewash will only be applies at the ends and middle regions of the specimens since these regions are prone to develop plastic hinges. Whitewash provides a brittle coating with a high color contrast useful in revealing the underlying bare steel local yielding as the light colored brittle whitewash (and any brittle mill scale) detaches from the specimen surface. The mixture, applied using different types of common paintbrushes, has a watery paint consistency and translucency during application, drying to opacity.

5.3.6 Handmade Load Cell

Handmade load cells were fabricated to measure loads from hydraulic hollow cylinders that will be used for third local series test and global series tests. These handmade load cells consist of small metal hollow cylinders with four strain gages located around the outer surface of the cylinder connected in a special manner to form a full Wheatstone bridge circuit.

A full Wheatstone bridge circuit is a divided bridge circuit with four active arms that results from connecting four strain gages (resistors) together in a diamond orientation (Fig. 5.26), these resistors are arranged so that the electric circuit is split into two paths.

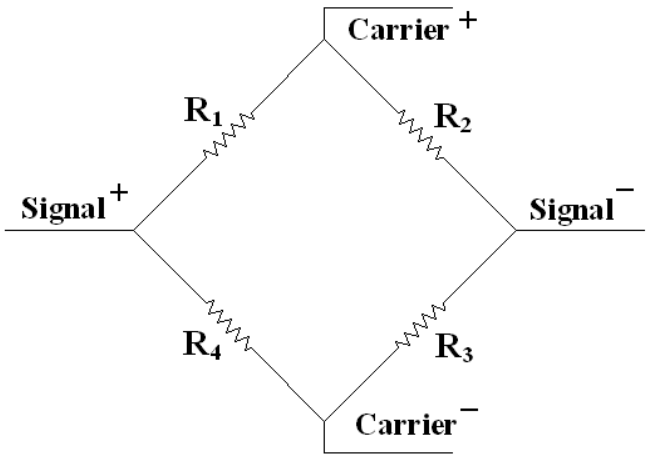

Fig. 5.30 - Full Wheatstone Bridge Electric Circuit.

When force is applied to the cylinder the output voltage from the full bridge circuit varies as the cylinder is subjected to compressive strains. This variation in voltage is linear over a specific range depending on the calibration, and is related to linear force through a scale factor based on the slope of Output Voltage vs. Linear force plot. The location of the strain gages and the wire distribution used to build the full Wheatstone bridge circuit around the hollow cylinder is graphically described by unfolding the cylinder outer surface to an equivalent plate as shown in Fig. 5.31.

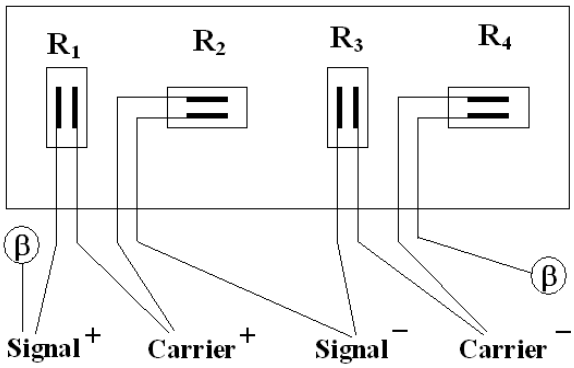

Fig. 5.31 - Full Wheatstone Bridge Configuration.

5.3.7 Pressure Transducer

One pressure transducer was used to measure load directly from the hydraulic hollow cylinders as a backup system for the handmade load cells. By connecting the pressure transducer to the hydraulic jack, as force is applied, the output voltage from the pressure transducer varies, this variation in voltage is linear over a specific range, and is related to pressure through a scale factor based on the slope of Output Voltage vs. Pressure and then correlated to Output Voltage vs. Load.

5.4 Loading Equipment and Data Acquisition

Among the loading equipment employed in the experimental program are:

5.4.1 Baldwin Universal Testing Machine

Baldwin Universal (tension and compression) Testing Machines were used to apply load to the local series monotonic test specimens. The frame of the hydraulic

testing machines consist of a lower fixed crosshead that works as the reaction head for tension and compression testing, an upper sensitive crosshead that applies load for tension testing, and a loading table under the lower crosshead that applies load for compression testing. The upper crosshead moves together with the loading table.

There is a console next to the testing machine that has controls for the hydraulic pump, and to raise or lower the fixed crosshead. It also has a load indicator with two needles, one for active load and one for peak load. This console also has an analog voltage output signal that is related to the applied load through a scale factor based on the slope of Output Voltage vs. Applied Load plot.

For tensions testing, the monotonic tension test specimen was placed between the fixed lower crosshead and the sensitive upper crosshead. A set of vee-cut wedge jaw grips transmitted the measured load. For compression testing, the monotonic compression test specimen was simply placed between the loading table and the fixed lower crosshead.

5.4.2 Data Acquisition System

The data acquisition is a Hewlett Packard (HP) VXI Plug and Play system on a Dell 100 MHz Pentium II personal computer with the HP DAC Express version 1.0 data acquisition software, configured to acquire data from any of the transducers (LVDT, Extensometer, load cell) or strain gages by entering the proper scale factor or gage factor respectively. This software has a variable scanning rate that ranges from 1

to 2500 scans/second with a maximum file size of 2-Gb to locate strain gages. A scanning rate of 10 scans/second was selected as more than sufficient.

5.4.3 Hollow Cylinders

Two double-acting hollow plungers ENERPAC RRH-10010 will be used in conjunction with self-reacting frames for the third local series test and global series tests. The hollow plungers have a maximum stroke range of 10 inches, and maximum load capacity of 206 kips advancing and 136 kips retracting.

6 Analysis of RXS Fuse Experimental Results

This chapter presents an analysis of the experimental results from the RXS fuse local series. The chapter includes a discussion on the mode of failure and drift capacity of concentrically braced frames with the RXS fuse. The local behavior of the RXS fuse under eccentric loads is evaluated using finite element analysis, and expected eccentricities in brace axial load are calculated by modeling several braced frame under lateral loads using finite element analysis.

6.1 Tensile Stress Field

The brittle behavior of the RXS fuse specimen subjected to monotonic tension prompted a detailed analysis to study the stress distribution through the transition region between the semicircular cut and the longitudinal cut. This analysis is based on a conceptual analogy of flow lines and stress trajectories that represents the stress field surrounding the oval cutout. This conceptual analogy is verified through computational models by the finite element method. The analysis was intended also to study other potential regions of the cutout that might also reduce the capacity of the RXS fuse to undergo deformations beyond yielding under tensile loads.

Figure 6.1 illustrates how the oval cutouts create a disruption of the uniform stress field parallel flow lines. The stresses between point ***B*** and the oval cutout are conceptually smaller than stresses at point ***A*** because the separation between the two flow lines at point ***B*** increases as they approach the oval cutout. At point ***C***, the upper

flow line joins other adjacent flow lines that are also disrupted by the oval cutout and need to adjust their trajectory to move around the circular obstacle.

The separation between disrupted flow lines is smaller at point ***C*** than the separation of uniformly spaced flow lines at point ***A***, and this separation between flow lines is even smaller at point ***C*** for flow lines with greater trajectory adjustment to move around the circular obstacle. Thus, the largest stresses are observed at point ***C***, where the semicircular cut transitions to the straight longitudinal cut. Theoretically this larger stress at point ***C*** remains constant along the longitudinal cut of the oval cutout until the longitudinal cut transitions back to the semicircular cut.

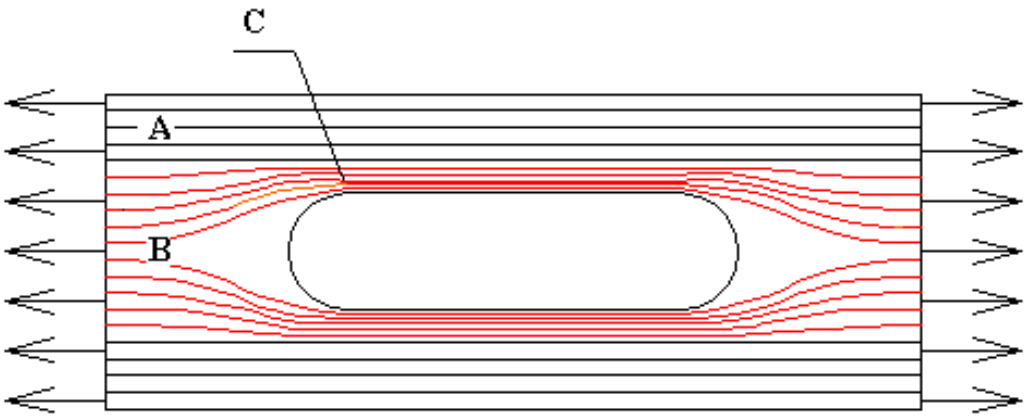

Fig. 6.1 - Monotonic Tension Conceptual Stress Flow Lines.

Figure 6.2 illustrates the behavior in the area surrounding the oval cutout. Figure 6.2 shows the arm at point ***C*** stretching much more than at point ***A*** due to the non-uniform distribution of stresses. The stress at point ***C***, σmax, is larger than the average stress in the region away from the cutout, σ_{nom}.

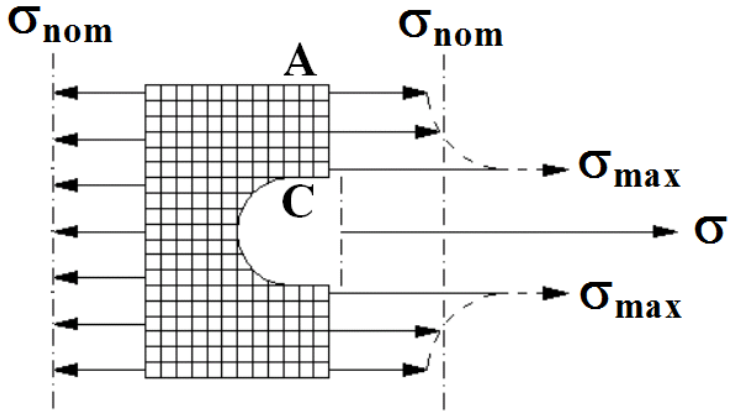

Fig. 6.2- Monotonic Tension, Conceptual Stress Concentration.

Figure 6.3 shows the Von Mises stress distribution along the RXS fuse calculated using finite element analysis. This FEM was modeled using the same properties described in Chapter 4 and it corroborates that stresses are higher at the edges of the longitudinal cut demands as illustrated in Fig. 6.1. The FEM revealed slightly higher stress demands where the semicircular cut transitions to the straight longitudinal cut, which is where the monotonic tension test specimen fractured. The stress concentration factor K_t is estimated based on this FEM results.

$$Kt = \frac{\sigma_{maximum}}{\sigma_{nominal}} = \frac{146.6\ ksi}{50\ ksi} = 2.93 \qquad \text{<Eq. 6.1>}$$

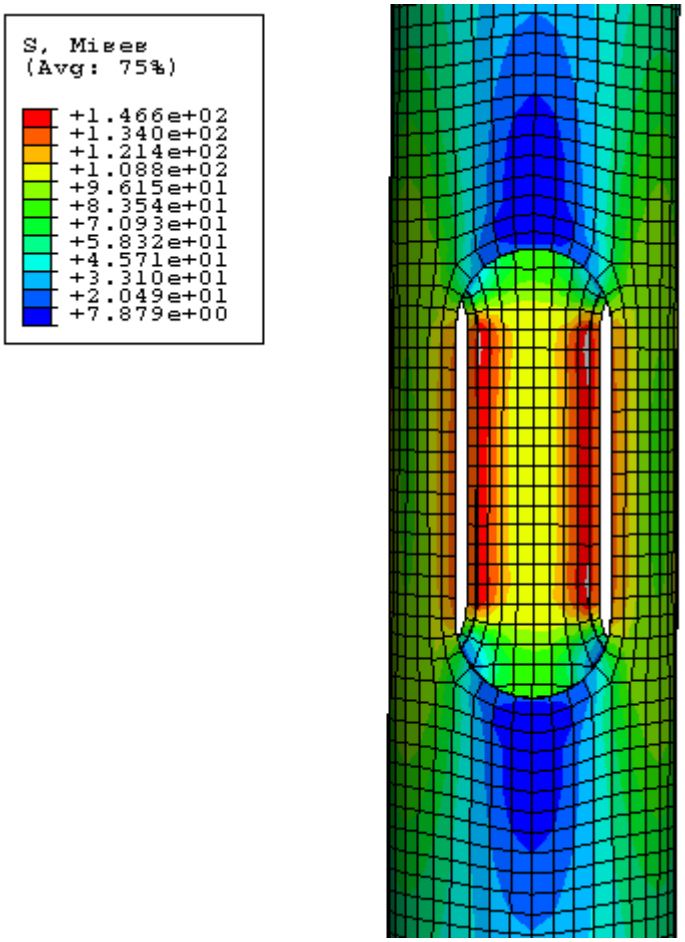

Fig. 6.3 - Von Misses Stress FEM (ksi) – RXS fuse Stress Concentrations.

Due to the observed mode of failure of the RXS fuse under monotonic tension, it is clear that normal BRIDGE fabrication practice with smooth edge requirements would delay fracture, incrementing the ductility of the fuse. Special

consideration should be given to the region where the semicircular cut, transitions to the longitudinal cut which is where fracture is expected to occur. This is important when the fuse is subjected to load reversals, because the specimen is expected to fail in tension at axial displacements smaller than those that might be obtained under compression loads.

6.2 Ductility Implications of Monotonic Test Results

The purpose of this analysis was to determine the maximum story drift ratio that the RXS fuse allows for diagonal bracing systems before fracture. This analysis determines an upper bound for maximum story drift.

This analysis was based on the braced frame geometry shown in Fig. 6.4 and the axial displacements obtained from the local series monotonic tension test. Beam and columns are assumed to be rigid, and only brace axial deformations are considered for story drift calculations. Connections were assumed as fully articulated.

The rotation of the frame results in a small change in the elevation of the beam, which is negligible compared with the remaining terms and is thus neglected in the calculations.

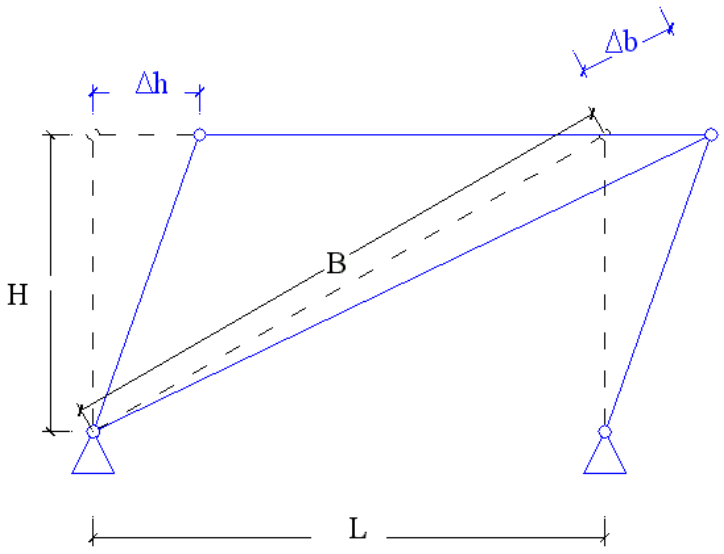

Fig. 6.4 - Brace Subjected to Tensile Loads.

H = column height.

B = brace length.

L = beam length.

Δ_h = frame horizontal displacement.

Δ_b = brace elongation.

The brace axial elongation is calculated as the summation of the total RXS axial deformation from the two fuses (one fuse at each end of the brace) plus the brace non-reduced section axial deformation.

$$\Delta b = \varepsilon_{nr} * B + 2(\varepsilon_{rxs} * l_{rxs}) \qquad \text{<Eq. 6.2>}$$

ε_{nr} = non-reduced section strain.

ε_{rxs} = reduced section strain.

l_{rxs} = oval cutout length.

The reduced section strain ε_{rxs} was assumed to be constant with a strain of 6 percent. This is the strain that was measured during the monotonic tension test at tensile fracture. Experimental results showed that the non-reduced section did not have nonlinear deformations when fracture occurred at the RXS. For this reason ε_{nr} was calculated based on linear-elastic behavior.

$$\varepsilon_{nr} = \frac{A_{rxs}}{A_g} \cdot f_r \cdot \frac{1}{E_s} \qquad \text{<Eq. 6.3>}$$

A_{rxs} = reduced section net area.

A_g = HSS gross area.

f_r = reduced section stress

E_s = steel modulus of elasticity of steel.

The horizontal frame displacement can be estimated using the following expression:

$$\Delta h = \sqrt{(B + \Delta b)^2 - H^2} - L \qquad \text{<Eq. 6.4>}$$

and the story drift ratio Δh/H is given by

$$\frac{\Delta h}{H} = \sqrt{\left(\frac{L}{H}\right)^2 + \frac{2*\Delta b}{H} * \left[\sqrt{\left(\frac{L}{H}\right)^2 + 1}\right] + \left(\frac{\Delta b}{H}\right)^2} - \frac{L}{H} \qquad \text{<Eeq. 6.5>}$$

Using the same parameters for the design of the monotonic test specimen, that is HAR = 3 and f = 51.13, the maximum story drift ratio before fracture was

computed to be 0.8% for frames with an L/H ratio of approximately 1.34 and story height of 22-ft (average values for major hangar structures that are known to used the type of bracing system investigated). By using a larger HAR this maximum drift capacity is expected to increase.

From Eq. 6.3:

$$\varepsilon_{nr} = \frac{2.29in^2}{4.68in^2} * 69.5ksi * \frac{1}{29000ksi} 1.173E-3 \frac{in}{in}.$$

$f_{r\ (before\ fracture)}$ = 69.5ksi (from section 5.1.2.2, chapter 5).

if,

$$B = \sqrt{(L^2 + H^2)} = 1.672 * H \quad for \quad {}^{L}/_{H} = 1.34 \qquad \text{<Eq. 6.6>}$$

From Eq. 6.2:

$\Delta b = \varepsilon_{nr} * B + 2(\varepsilon_{rxs} * l_{rxs}) =$ 1.173E-3*(1.672*22-ft.)+2(0.06*10-in.*1ft/12-in.)

$\Delta b = \varepsilon_{nr} * B + 2(\varepsilon_{rxs} * l_{rxs}) =$ = 0.143-ft.

From Eq. 6.5:

$$\frac{\Delta h}{H} = \sqrt{(1.34)^2 + \frac{2 * 0.143ft}{22ft} * \left[\sqrt{(1.34)^2 + 1}\right] + \left(\frac{0.143ft}{22ft}\right)^2} - 1.34$$

$$\frac{\Delta h}{H} = 0.008 = 0.8\%$$

Figure 6.5 shows the limiting drift ratio, L/H, as a function of the aspect ratio of the braced bay, with other parameters held constant, f = 51.13% , and HAR = 3. For bays that are twice as long as they are tall the drift capacity was the lowest, and

the limiting drift ratio increased with increasing aspect ratios L/H beyond 2. The limiting drift ratio increased at a higher rate as the L/H ratio decreased below 2.0.

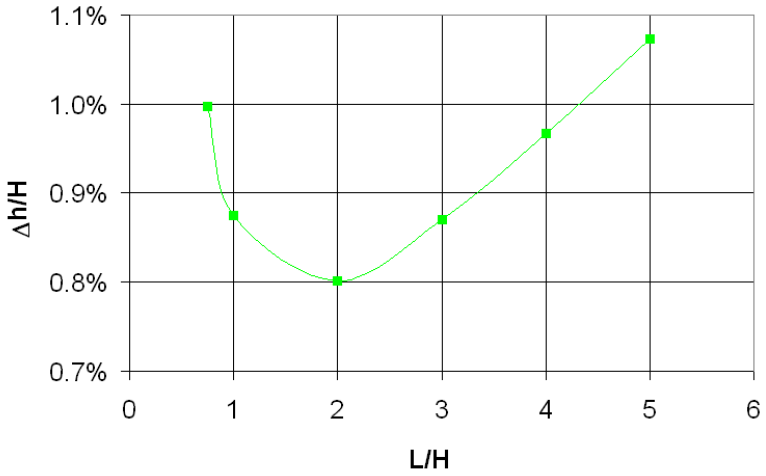

Fig. 6.5 - Story Drift vs. L/H Ratio for Varying H.

The variation in drift capacity with area reduction coefficients ***f*** is illustrated in Fig. 6.6. The curve labeled f = 51.13% repeats the curve shown in Fig.6.5. Figure 6.6 shows that the maximum story drift ratio increases as the value of ***f*** decreases. The area reduction coefficient had a greater influence on the drift capacity for frames with shallower angles respect to the horizontal (larger values of L/H).

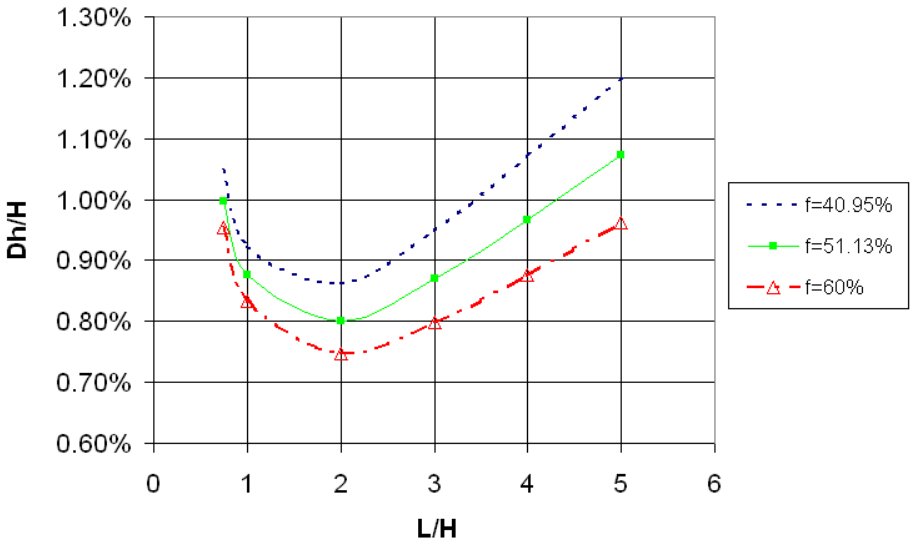

Fig. 6.6 - Story Drift vs. L/H Ratio for Varying f.

Braces in a typical concentrically braced frame without the RXS can be expected to yield and buckle at story drifts of about 0.3 percent to 0.5 percent [AISC, 2005, C13.1]. Using the current RXS design parameters and assuming an RXS fuse linear-elastic elongation, the maximum story drift at fuse yielding is 0.22%.

f_r = 55 ksi (from monotonic tension test results at yielding, chapter 5).

From Eq. 6.3:

$$\varepsilon_{nr} = \frac{2.29in^2}{4.68in^2} * 55ksi * \frac{1}{29000ksi} = \quad 9.28\text{E-}4\text{in./in.}$$

ε_{rxs}=0.003 in./in. (from monotonic tension test results at yielding, chapter 5).

From Eq. 6.2:

$$\Delta b = \varepsilon_{nr} * B + 2(\varepsilon_{rxs} * l_{rxs}) = \text{9.28E-4in./in.*(1.672*22ft)+2(0.003*10in*1ft/12in)}$$

$$\Delta b = \varepsilon_{nr} * B + 2(\varepsilon_{rxs} * l_{rxs}) = \text{3.91E-2 ft}$$

From Eq. 6.5:

$$\frac{\Delta h}{H} = \sqrt{(1.34)^2 + \frac{2 * 0.0391ft}{22ft} * \left[\sqrt{(1.34)^2 + 1}\right] + \left(\frac{0.0391ft}{22ft}\right)^2} - 1.34$$

$$\frac{\Delta h}{H} = 0.0022 = 0.22\%$$

The maximum story drift ratio recommended for concentrically braced frames before failure by the Federal Emergency Management Agency [FEMA, 1997] is 1.5 percent, whereas the National Building Code of Canada [NBCC, 1995] recommends a maximum of 2 percent. Research has demonstrated that under severe earthquakes, concentrically braced frames could undergo story drift ratios exceeding 2 percent and structural collapse soon after [Jain, Hanson, Goel 1978]. Other authors considered the 2% drift limit state of the NBCC as excessive for single story CBFs [Medhekar, Kennedy 1999].

The calculations so far indicate that under monotonic tension the RXS fuse system for a HSS 6.625x0.25 and design variables used may reach a story drift ratio of 0.22% within its linear-elastic range of response, and up to 1.2% before fracture. Because most of the total brace elongation occurs at the reduced section, the limiting drift ratio could be increased by increasing the length of the oval cutout.

If the first design philosophy is implemented (described in chapter 4), in which braces are proportioned in compression on the basis of their global buckling capacity, improving the story drift of a braced frame with the RXS fuse element

might require shallower angles and longer braces in some instances. For braces proportioned on the basis of their local buckling capacity, there are no restrictions with respect to the length of the oval cutout other than the maximum effective slenderness ratio "KL/r" recommended by AISC. Consequently larger story drift ratios than those using the first design approach can be accomplished.

6.3 Implications of Cyclic Loading Test Results

The behavior observed during the local cyclic test did not match the behavior of the two monotonic tests. The difference can be attributed to the eccentricity of the axial load, which created a non-uniform stress distribution along the reduced brace section. The load-displacement response of the specimen to the loading history was rather poor mainly because: (a) limited energy dissipation capacity of the specimen, (b) the specimen reduced section could not develop its yield capacity, and (c) strength deterioration due to early buckling deformations.

Both monotonic test results and the cyclic load test results were superimposed to illustrate the effect of the eccentricity on the performance of the RXS (Fig. 6.7). The measured buckling capacity during the monotonic compression test was 42.6 ksi, and the maximum compressive stress measured during the cyclic load test was 32 ksi., which is 75% of the buckling capacity.

$$\Delta\sigma_{tcompression} = F_{cr\,(monotonic\ compression\ test)} - \sigma_{compression,\ \ max\ (cylic\ load\ test)}$$

<Eq. 6.7>

$$\Delta\sigma_{tension} = 42.6\ ksi - 32\ ksi = 10.6\ ksi$$

The measured yield stress during the monotonic tension test was 55 ksi, and the cyclic load test measured maximum tensile stress before fatigue fracture failure during the compression cycle was 42.5 ksi, which is 77% of the measured F_y.

$$\Delta\sigma_{tension} = F_{y\ (monotonic\ tension\ test)} - \sigma_{tension,max\ \ (cylic\ load\ test)}$$ <Eq. 6.8>

$$\Delta\sigma_{tension} = 55\ ksi - 42.5\ ksi = 12.5\ ksi$$

The drift capacity of the RXS fuse was significantly affected by the eccentricity. The fuse arm strain at fracture was measured at 0.06 in./in. during the monotonic tension test. This strain capacity would be as high as 0.12 in./in. with normal bridge fabrication practice with smooth edge requirements. The maximum fuse arm strain during the cyclic load test was measured at 0.025 in./in. before fatigue fracture. This is less than half of the tensile strain capacity obtained during the monotonic tension test and 2% of the strain capacity obtained from the test coupons.

$$\Delta\varepsilon = \varepsilon_{(monotonic\ tension)} - \varepsilon_{(cyclic\ load)}$$ <Eq. 6.9>

$$\Delta\varepsilon = 0.06\text{in./in.} - 0.025\text{in./in.}$$

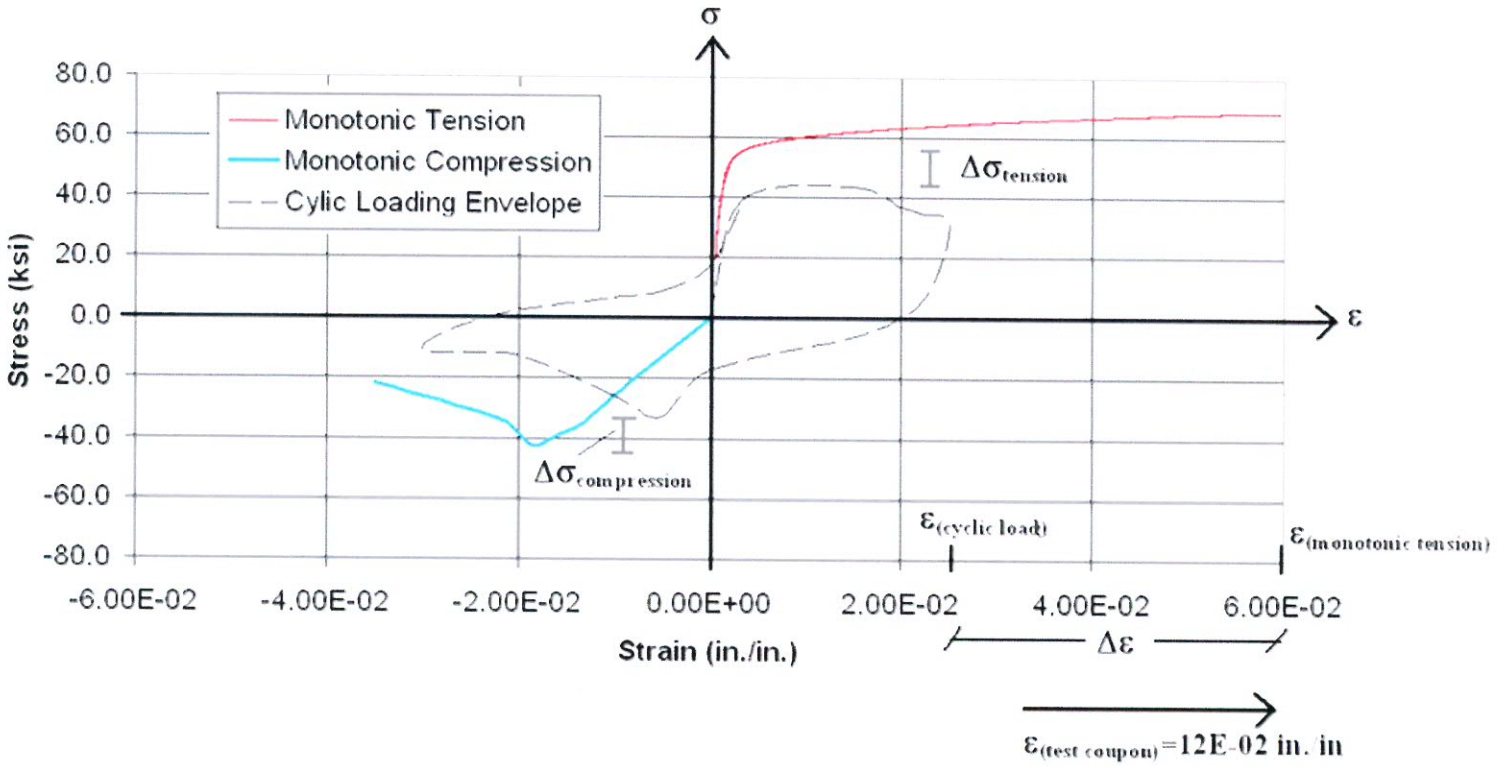

Fig. 6.7 - RXS Monotonic Test Results vs. RXS Cyclic Test Envelope.

Additional testing could be carried out on similar specimens even with different design properties to obtain more data on the inelastic seismic performance of the RXS fuse under cyclic loading. In particular the influence of different loading histories could be carefully examined to investigate if adequate seismic performance, without premature failure, can be achieved in the absence of eccentricity on the axial load. Due to the sensitivity of the RXS fuse to eccentricities in the brace axial load, any further testing was considered not worthy until the behavior of the RXS fuse under different eccentricities or the expected magnitude of these eccentricities were computationally analyzed using simple finite element models.

6.3.1 RXS Fuse Behavior under Eccentric Loads

Even though results from the cyclic loading test already showed that eccentric loads were very detrimental to the hysteretic behavior of the system, an analytical study was undertaken to gain a better understanding of why it was that the RXS fuse behavior was affected by eccentricities. This study was vital for the successful development of similar CBFs fuse systems such as the second system presented in this work at hand.

The effect of different levels of eccentricity on the performance of the RXS fuse was investigated by analyzing three different models of the system subjected to similar compressive loads in magnitude but applied at different eccentricities. Elastic material properties were assumed for the three models and a point load was applied at

the ends of the model. The specimens modeled were a replica of the three local series specimens tested under monotonic and cyclic loads from the preliminary proof of concept experimental program.

Figure 6.8 shows the Von Mises stress distribution of the RXS fuse subjected to concentric loads. The maximum stress was 146.6 ksi at the edge between the oval cutout and the straight longitudinal cut. The three arms showed a uniform stress distribution.

The second model is shown in Fig. 6.9. The same point load was applied at 1 in. from the center of the HSS cross sectional area, towards one of the three arms that composed the RXS. The maximum stress increased from 146.6 ksi to to 242 ksi on the RXS arm closer to the point load. The other two arms showed stresses even smaller than 50 ksi. As can be seen in Fig. 6.9 (c) the arm closer to the eccentric point load tends to buckle before the other two arms, which makes the RXS bend with respect to its longitudinal axis. This bending is considered highly damaging to the overall performance of the brace with the fuse because it will induce long inelastic deformations in the reduced section, which will have the effect of reducing the drift ratio at fracture.

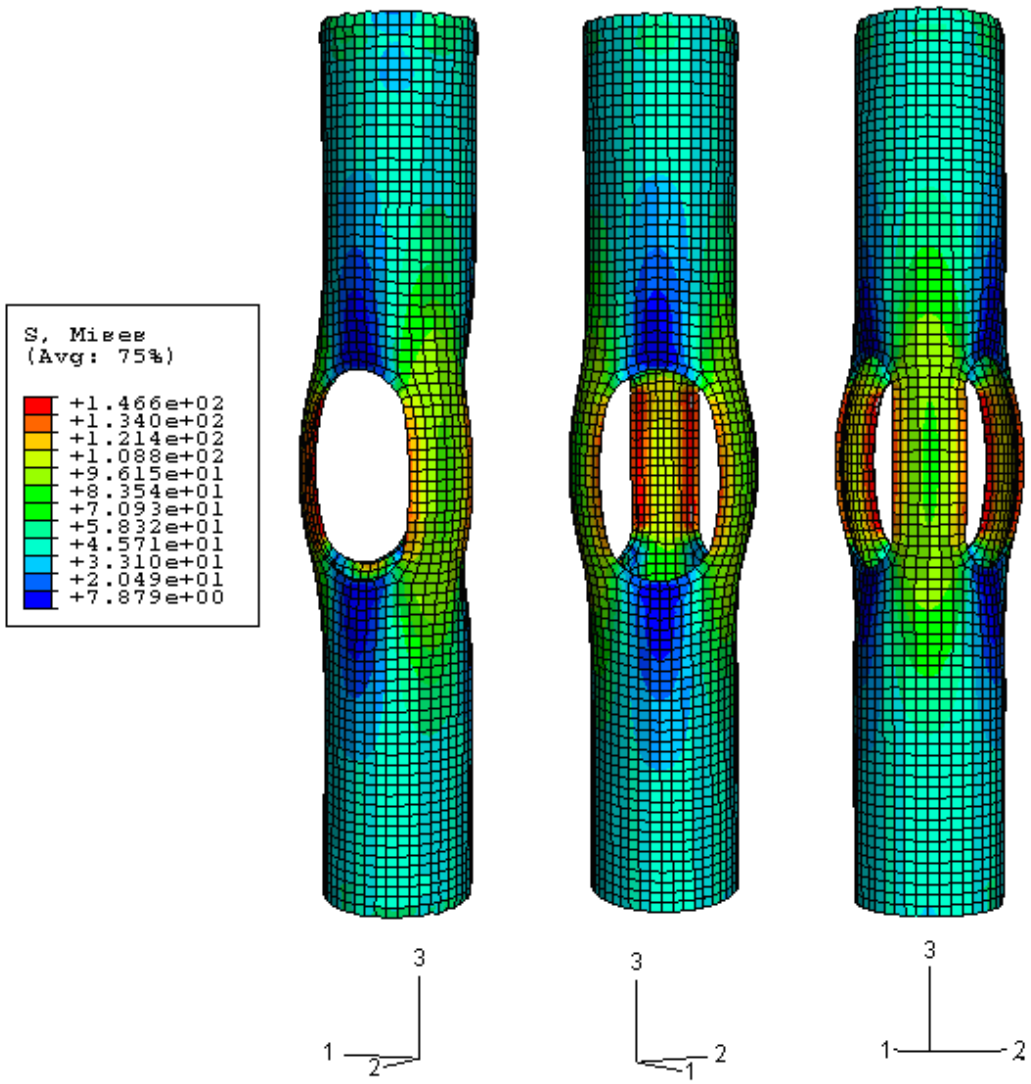

(a) (b) (c)

Fig. 6.8 - Von Mises Stress FEM (ksi), Concentric Load.

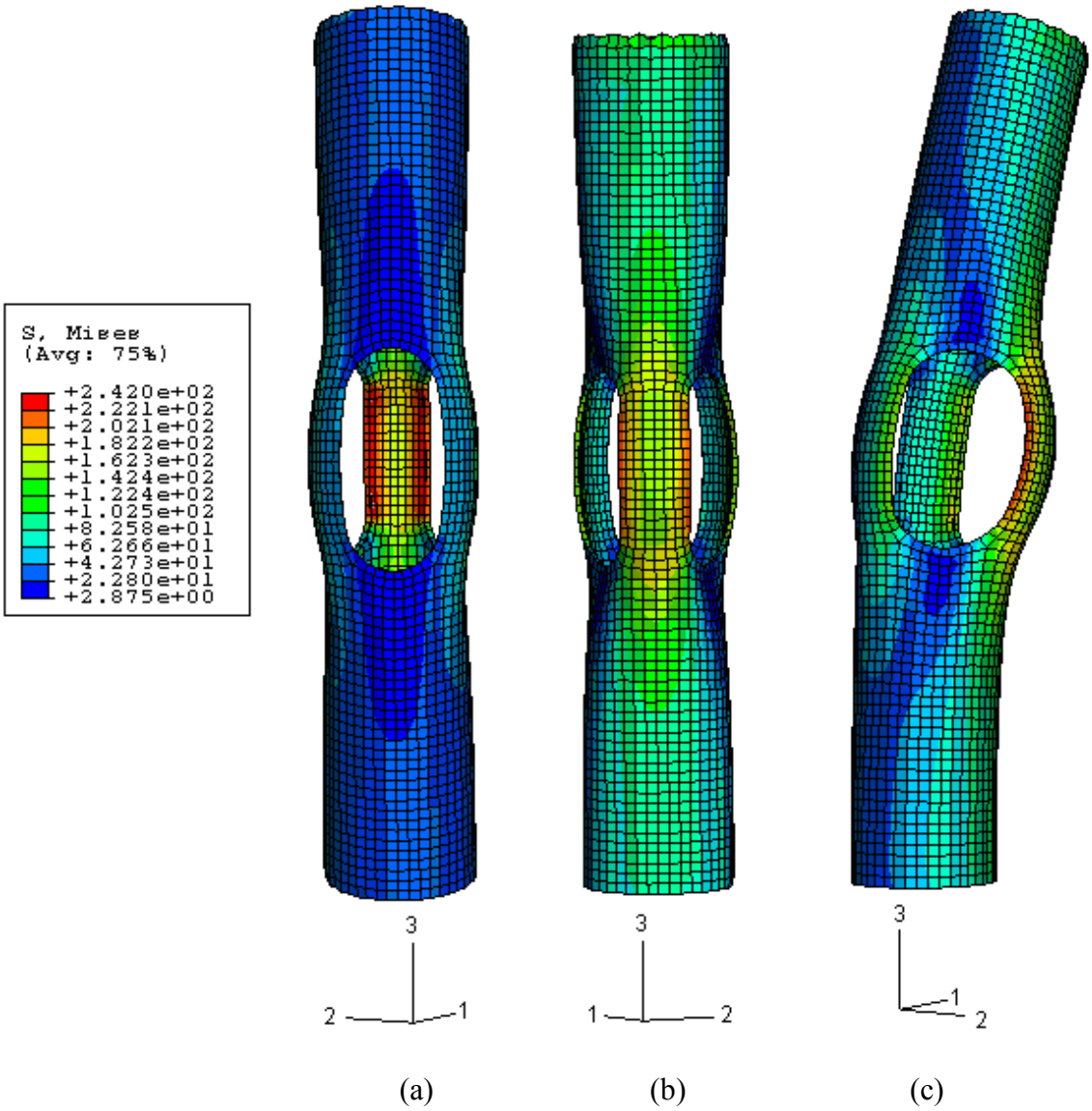

Fig. 6.9 - Von Mises Stress FEM (ksi), 1-in. Eccentric Load at RXS arm.

The third model is shown in Fig. 6.10. The point load was applied at 1-in. from the center of the HSS cross sectional area, towards the oval cutout. This third FEM resulted to be the worst case scenario because the maximum stress increased even more, from 146.6 ksi to 253 ksi. Bending of the specimen with respect to its longitudinal axis was also observed (Fig. 6.10(c)). Two arms are subjected to this maximum stress. Because the eccentric load is applied towards the oval cutout, there is no support directly under the point of application of the load. This is detrimental to the overall stiffness of the fuse and increases the damaging effects of bending with respect to the longitudinal axis of the brace.

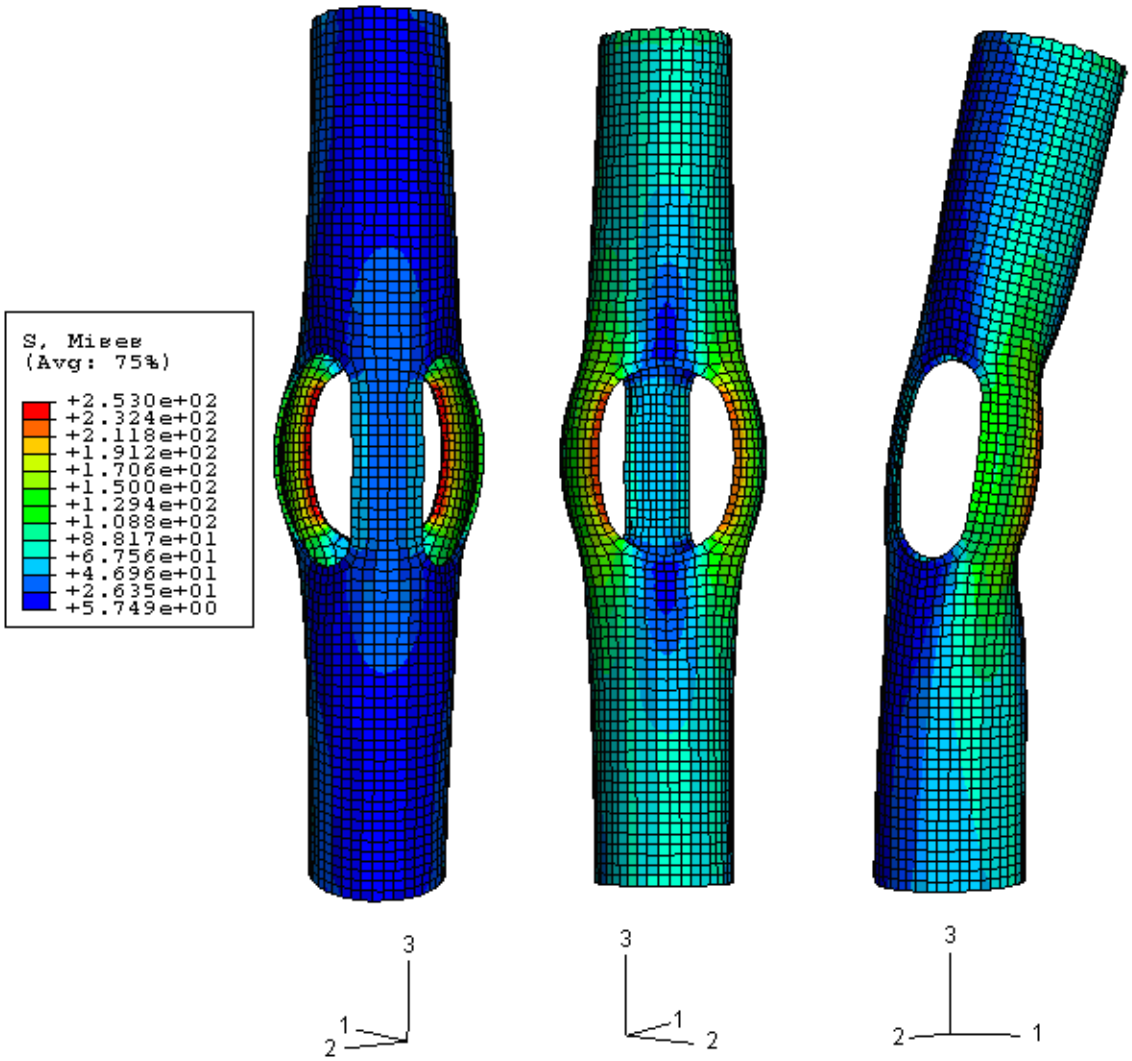

(a) (b) (c)

Fig. 6.10 - Von Mises Stress FEM (ksi), 1-in. Eccentric Load at RXS Oval Cutout.

The two eccentric load finite element models were analyzed for different values of eccentricity of the point load and a maximum stress vs. eccentricity relationship was plotted in Fig. 6.11. Two cases are shown in Fig. 6.11: (a) eccentricity towards the oval cutout, and (b) eccentricity towards the arm. The round HSS cross section diameter was 3 5/8 in. Although it is very unlikely that the fuse would be subjected to such a big eccentricity, a model subjected to a maximum eccentricity of 3 in. is included. The maximum stress vs. eccentricity relationship was found to be approximately linear for eccentricities towards one of the arms of the fuse. This relationship was similar for eccentricities towards one of the oval cutouts of the RXS fuse, although with slightly higher stresses. For eccentricities greater than 2 in. the slope of the stress concentration vs. eccentricity was found to increase with respect to the eccentricity for the case (a). This can be attributed to the instability created by the lack of support in the direction of the eccentricity, which accentuates when the point load is applied directly over the oval cutout.

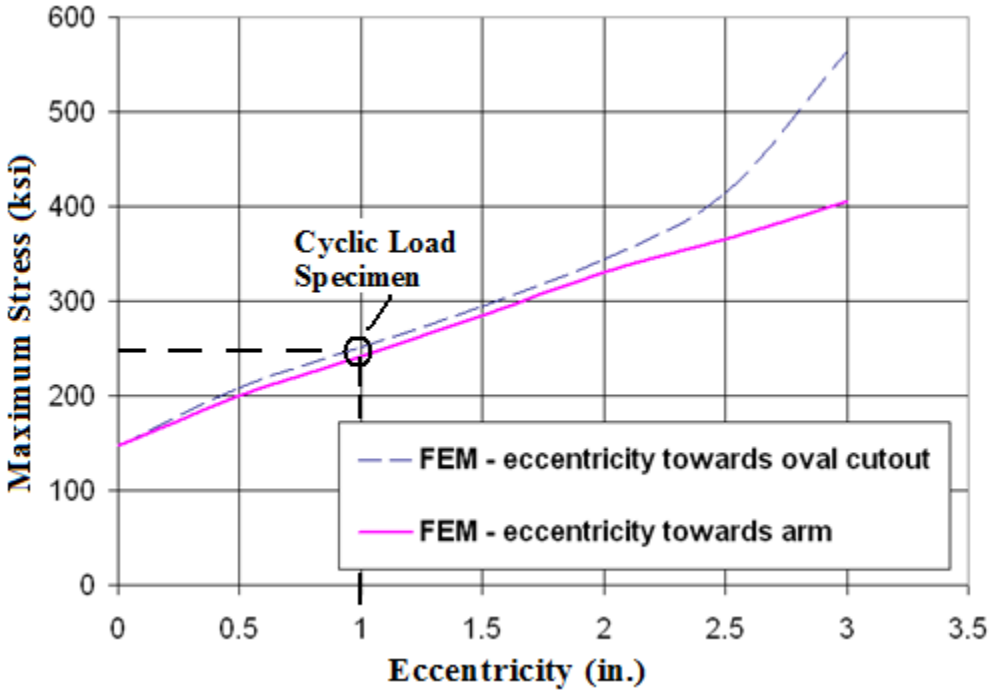

Fig. 6.11 - RXS Fuse - Eccentricity vs. Maximum Stress.

6.3.2 Expected Eccentricity in Brace Axial Load

Because the hysteretic behavior of the RXS fuse was significantly affected by non-uniform distributions of the load, eccentricities in the axial load of braces with the RXS fuse were computationally estimated by modeling several frames with finite element analysis (FEA). The goal of the analyses was to determine how much eccentricity can be expected in the axial load transferred from the frame to the brace, and how the frame characteristics influence the magnitude of these eccentricities in brace axial load at the fuse element. Variations in frame stiffness relative to the brace

and the angle of inclination of the brace are the two variables used to model several frames with same brace size, brace length and RXS fuse dimensions.

6.3.2.1 Braced Frames Model Setup

The frames created are 2-dimensional models and the stiffness of these braced frame models is estimated as a dependant variable of the beams and columns areas with respect to the plane of the frame. The stiffness of the frame elements relative to the brace is then calculated as a function of their depth. The ratio of beam to column depth is used as the first parameter that affects the lateral load transfer from the frame to the brace, and consequently the eccentricity of the brace axial load. The second parameter used to study brace load eccentricity was the brace angle ϕ with respect to the horizontal axis of the frame lower beam, as can be seen in Fig. 6.12.

Elastic material properties were assumed for these FEM's. Boundary conditions were defined so that the brace reacted against the lower beam. Translations and moments were prevented at the bottom of the lower beam by defining a fixed boundary condition. The rest of the braced frame including the diagonal brace was free to move and deform as load was applied. The magnitude of the applied load was 100 kips in all models, and it was placed at the top left corner of the frame. The brace length and the RXS fuse dimension was also a constant for all frames modeled.

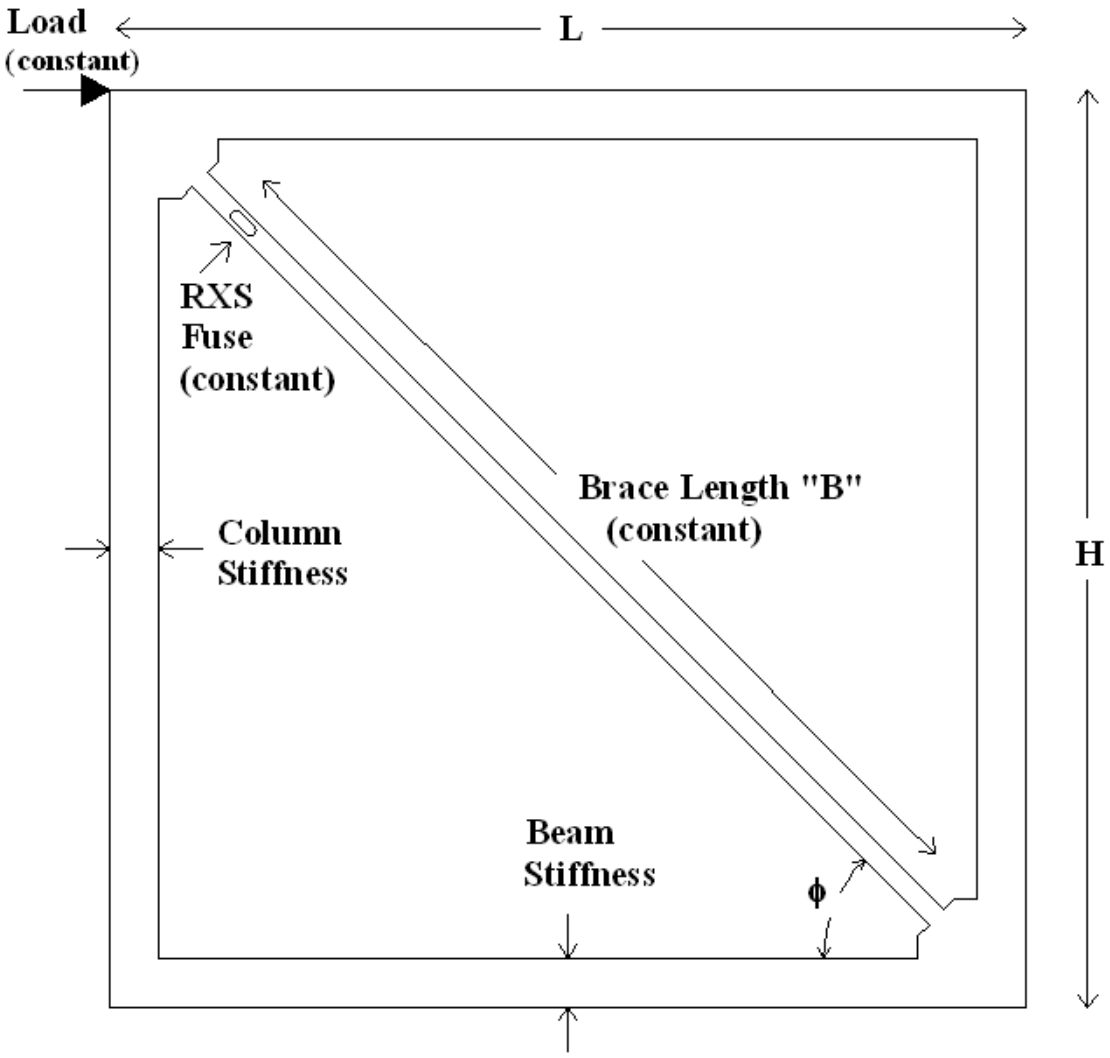

Fig. 6.12 - Braced Frame Model Setup.

Sixteen frames were modeled to study the eccentricities in the axial load of braces with the RXS fuse for different beam-to-column stiffness ratios and a constant brace angle ϕ of 45 deg. as shown in Table 6.1. The control frame "H" with beam/column stiffness ratio equal to one and brace angle ϕ equal to 45 deg. is highlighted. To evaluate the eccentricity for frames with beam/column stiffness ratios less than one, the column depth was kept constant at 16 in. and the beam depth was decreased every 2 in. per frame from the control beam until a depth equal to 2 in. (frame A). Similarly, to evaluate the eccentricity for frames with beam/column stiffness ratios greater than one, the beam depth was maintained constant at 16 in. and the column depth was decreased by 2 in. per frame from the control column, until frame "P" with a depth of 2 in. Frame "N", with a column depth of 5 in. was added to the list in order to optimize eccentricity calculation for beam/column stiffness ratios greater than one.

Frame	Beam/Column Length Ratio	Beam/Column Stiffness		Brace Angle "ϕ" (degrees)	P Lateral Load (Kips)
		Beam-depth/Column-depth	Ratio		
A	H/L = 1	2"/16"	***0.13***	45	100.00
B	H/L = 1	4"/16"	***0.25***	45	100.00
C	H/L = 1	6"/16"	***0.38***	45	100.00
D	H/L = 1	8"/16"	***0.50***	45	100.00
E	H/L = 1	10"/16"	***0.63***	45	100.00
F	H/L = 1	12"/16"	***0.75***	45	100.00
G	H/L = 1	14"/16"	***0.88***	45	100.00
H	H/L = 1	16"/16"	***1.00***	45	100.00
I	H/L = 1	16"/14"	***1.14***	45	100.00
J	H/L = 1	16"/12"	***1.33***	45	100.00
K	H/L = 1	16"/10"	***1.60***	45	100.00
L	H/L = 1	16"/8"	***2.00***	45	100.00
M	H/L = 1	16"/6"	***2.67***	45	100.00
N	H/L = 1	16"/5"	***3.20***	45	100.00
O	H/L = 1	16"/4"	***4.00***	45	100.00
P	H/L = 1	16"/2"	***8.00***	45	100.00

Table 6.1 - Beam/Column Stiffness Ratio Frame Properties.

To study the eccentricities in the axial load of braces with the RXS fuse for different diagonal bracing angles ϕ seven frames were modeled as shown in Table 6.2. The angle ϕ is increased and decreased from that of the control frame "H" highlighted in Table 6.2. Special consideration was given to angles of inclination smaller than 45 deg. In these frames as the brace angle ϕ increases the brace axial force, calculated as the component of the horizontal force, decreases. Consequently the brace takes less lateral load, while beams, columns, and connections become more active in resisting the lateral load. This is not the a desired behavior of the braced

frame because brace design theory dictates that beams and columns should remain relatively undamaged while the brace member yields in tension and buckles in compression in order to maintain the structural integrity of the gravity carrying system. It is assumed that angles ϕ greater than 55 deg. would result in improved behavior, not because the frame geometry is beneficial in terms of the eccentricities in the brace axial load, but because the brace does not take as much lateral load as those with shallower angles ϕ, for this reason a maximum angle of 55 deg. Was adopted in the study. A 25 deg. angle was intuitively assumed as small enough for this study assuming that for braced frames with brace angles ϕ shallower than 25 deg. the length of the brace relative to the frame geometry would be considered too long, and consequently not optimal in terms of the cost.

Frame	Beam/Column Length Ratio	Beam/Column Stiffness Ratio		Brace Angle "ϕ" (degrees)	**P** Lateral Load (Kips)
		Beam-depth/Column-depth	Ratio		
Q	1 < H/L	16"/16"	1.00	***55***	100.00
R	1 < H/L	16"/16"	1.00	***50***	100.00
H	H/L = 1	16"/16"	1.00	***45***	100.00
S	1 > H/L	16"/16"	1.00	***40***	100.00
T	1 > H/L	16"/16"	1.00	***35***	100.00
U	1 > H/L	16"/16"	1.00	***30***	100.00
V	1 > H/L	16"/16"	1.00	***25***	100.00

Table 6.2 - Bracing Angle "ϕ" Frame Properties.

6.3.2.2 Finite Element Analysis Results

The contour plots of the Von Mises stresses from the control frame "H" finite element analysis are shown in the following. The other twenty-one braced frame finite element model contour plots used in this study are presented in appendix D. The control frame "H" was modeled with the oval cutout reduced section to simulate eccentricities in axial loads for braces with the RXS fuse and also without any reduced section to simulate eccentricities in axial load with the second brace composite element (BCE) fuse element.

Since the addition of the RXS fuse to the brace disturbs the uniform stress field parallel stress flow lines deviate in areas of stress concentrations. For better display of the stress distribution along the brace and the area surrounding the RXS fuse the FEM's are presented using two different stress scales. The first stress scale goes up to 60 ksi and a second stress scale goes up to a maximum of 25 ksi.

The finite element model mesh of the control braced frame model "H" is shown in Fig. 6.13. The contour plot of the same control braced frame model "H" without the RXS fuse is shown in Fig. 6.14. There is a stress concentration where the point load is applied at the upper left corner of the frame, but this region is not of interest for this study. Frame beams and columns are subjected to a maximum of 10 ksi in some particular locations whereas the brace element is taking most of the lateral load and is subjected to a maximum stress of approximately 25 ksi.

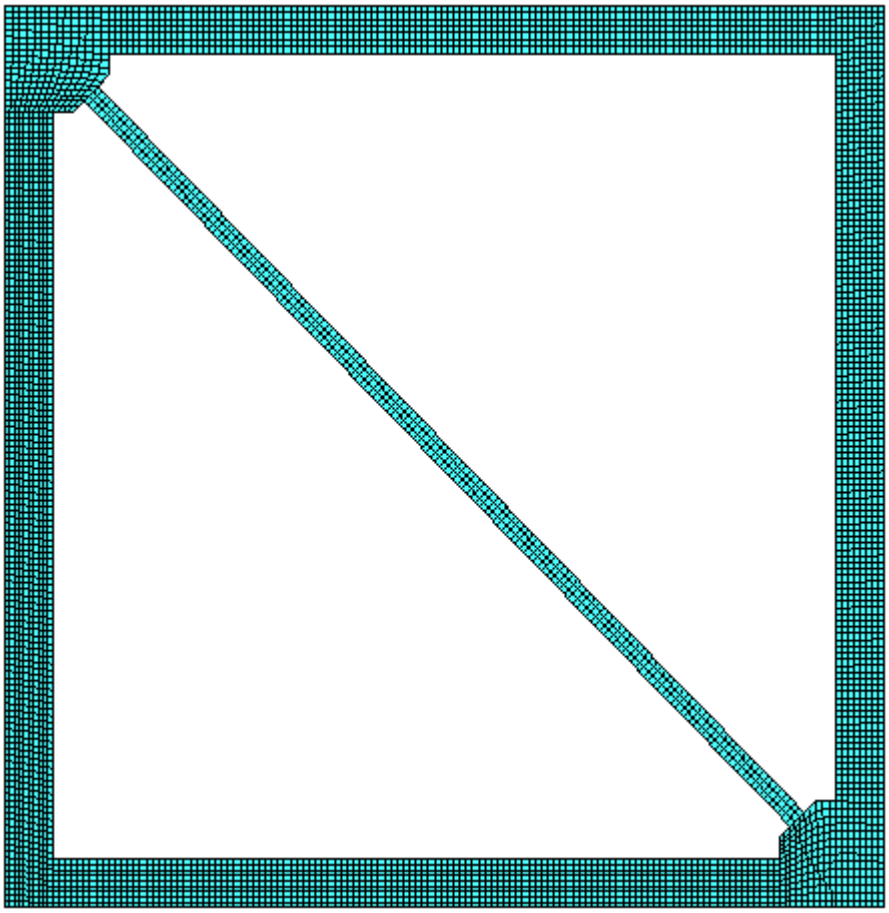

Fig. 6.13 - FEM Mesh – Frame “H” without Reduced Section.

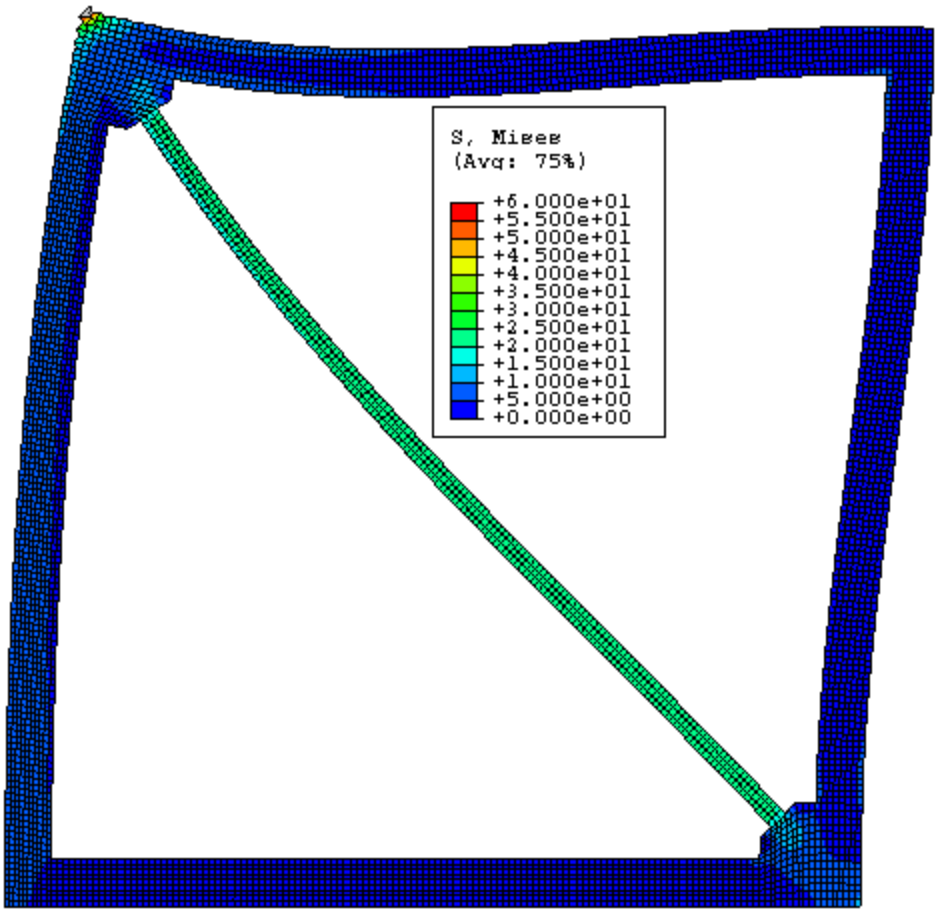

Fig. 6.14 - Von Mises Stress – Frame “H” without Reduced Section.

The contour plot shown in Fig. 6.14 shows a uniform stress distribution along the brace. A closer view at the gusset-plate-to-brace connection (Fig. 6.15) with the same stress scale up to 60 ksi shows that there is a non-uniform stress distribution, with a minimum of approximately 20 ksi and a maximum of approximately 25 ksi.

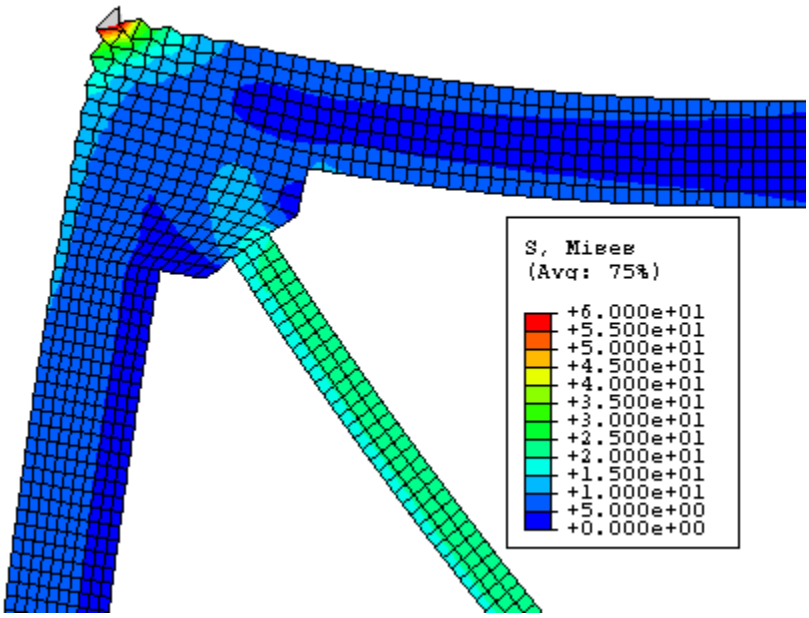

Fig. 6.15 - Von Mises Stress – Frame "H" without Reduced Section – Zoom.

A smaller stress scale of up to 25 ksi is shown in Fig. 6.16. The contour shows that this non-uniform stress distribution starts at the upper gusset-plate-to-brace connection and it reverses at approximately 2/3 of the brace length towards the lower part of the brace.

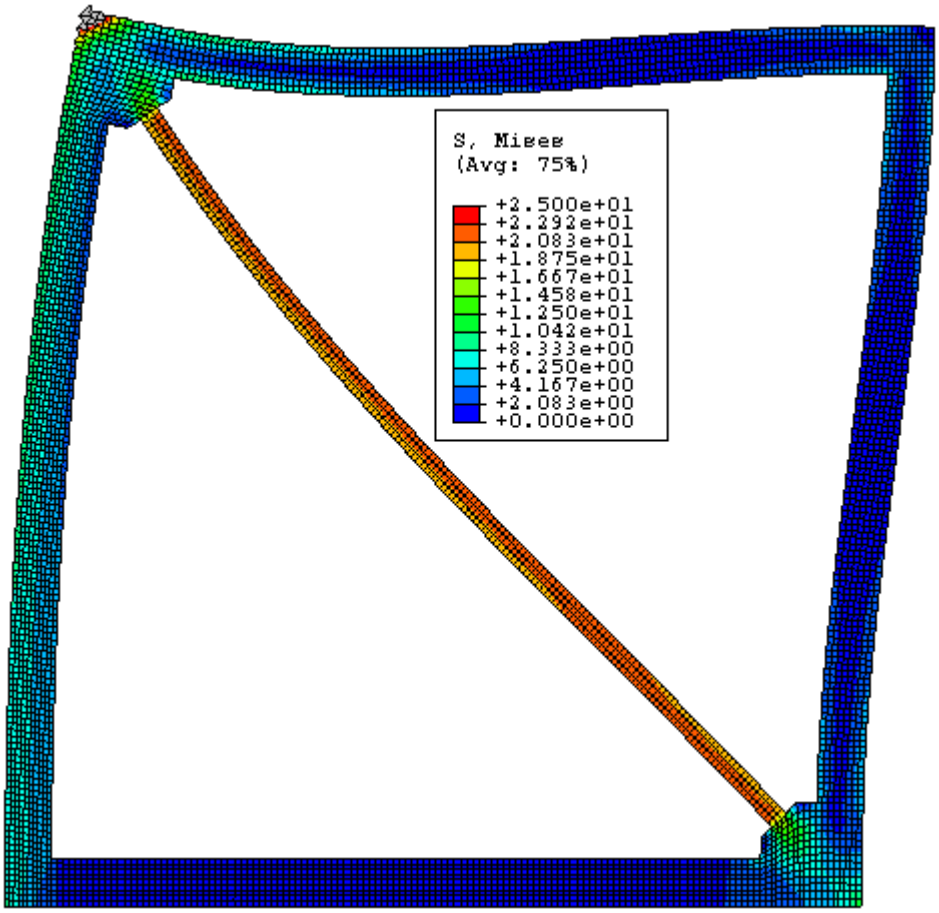

Fig. 6.16 - Von Mises Stress – Frame "H" without Reduced Section, Stress Scale #2.

The finite element model mesh of the control braced frame model "H" is shown in Fig. 6.17. The FEM Von Mises stress of frame "H" with the RXS fuse at the upper part of the diagonal brace is shown in Fig. 6.18. By comparing the behavior of the braced frame with and without the RXS fuse it appears that the addition of the

RXS fuse did not alter the behavior of the frame significantly because beams, columns, and the diagonal brace are subjected to similar stresses.

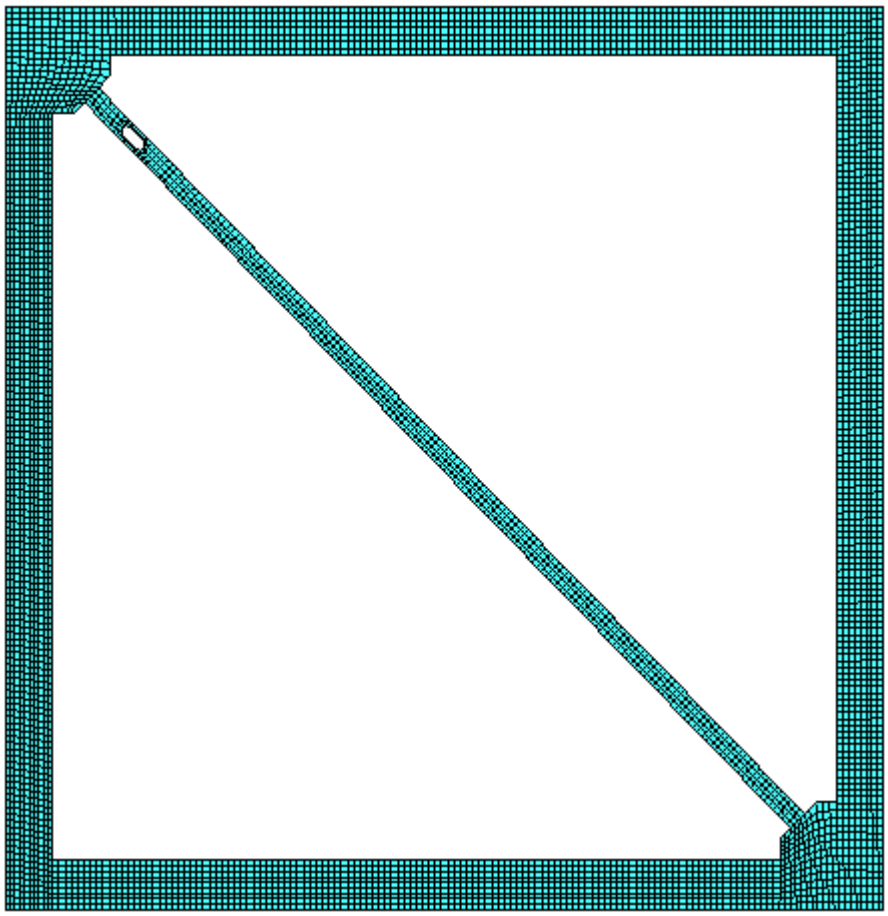

Fig. 6.17 - FEM Mesh Frame “H” with RXS Fuse.

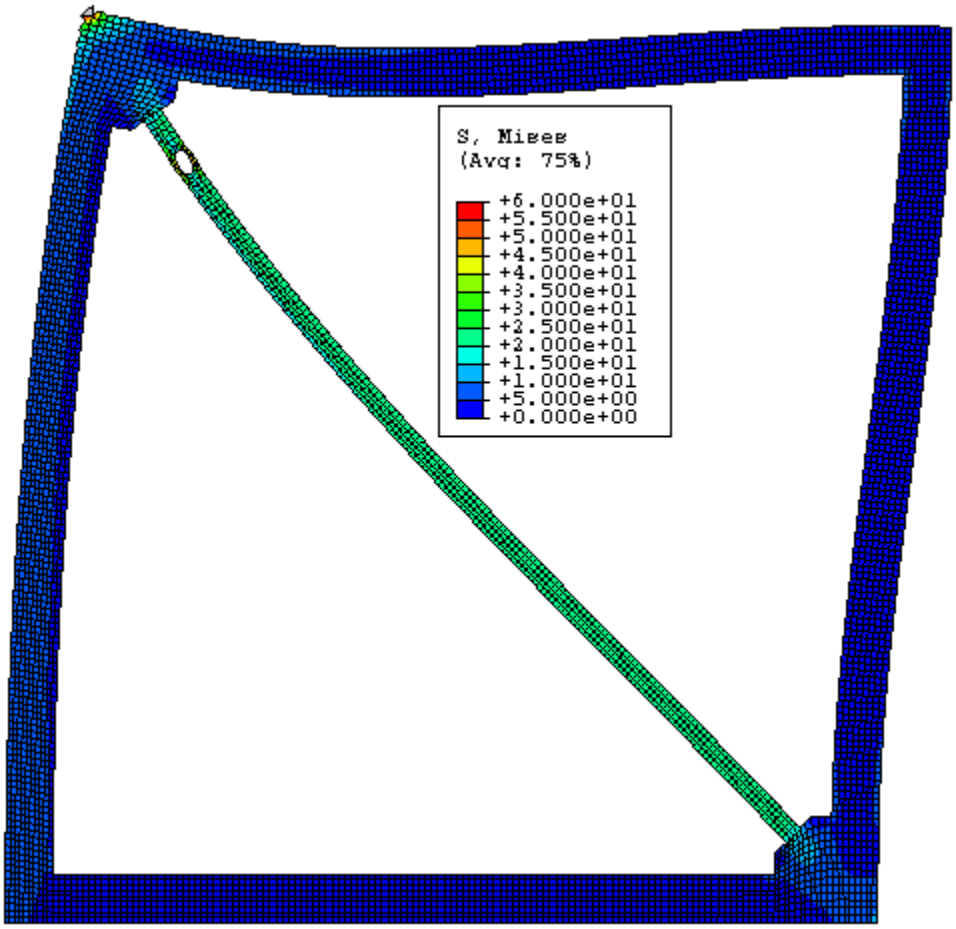

Fig. 6.18 - Von Mises Stress – Frame “H” with RXS Fuse.

A closer view right at the gusset-plate-to-brace connection with the same stress scale up to 60 ksi reveals that there are stress concentrations in the region surrounding the RXS fuse (Fig. 6.19).

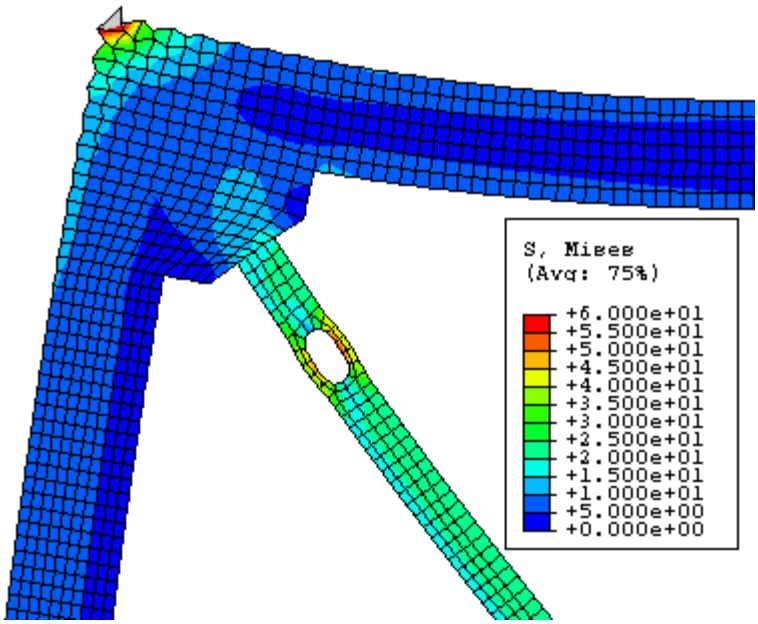

Fig. 6.19 - Von Mises Stress – Frame “H” with RXS Fuse – Zoom #1.

A detail of the RXS fuse stresses can be seen in Fig.6.20. The Von Mises stress contour plot with a stress scale up to 60 ksi shows that the upper right side of the RXS fuse is subjected to larger stresses than the lower left side.

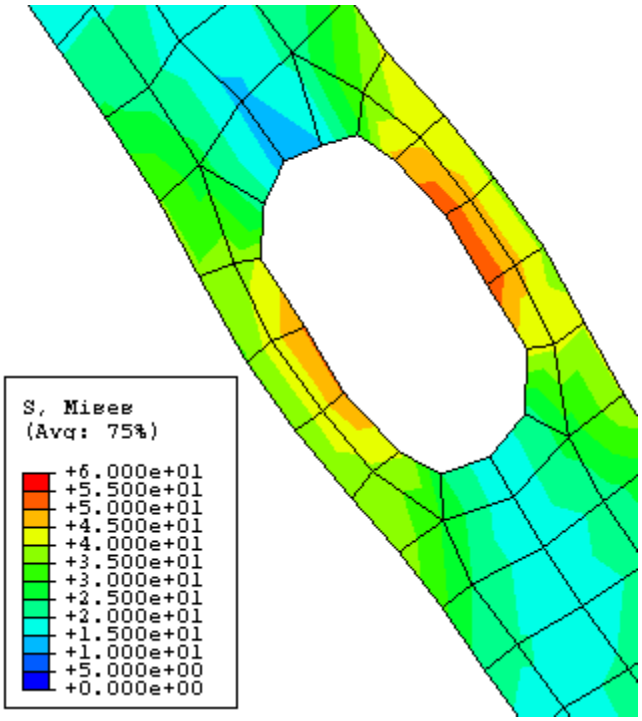

Fig. 6.20 - Von Mises Stress – Frame "H" with RXS Fuse – Zoom #2.

Using the same smaller stress scale up to 25 ksi as before it can be seen in Fig. 6.21 that, similar to the frame without the RXS fuse, the non-uniform stress distribution also reverses in the proximity of the frame lower right gusset-plate-to-brace connection.

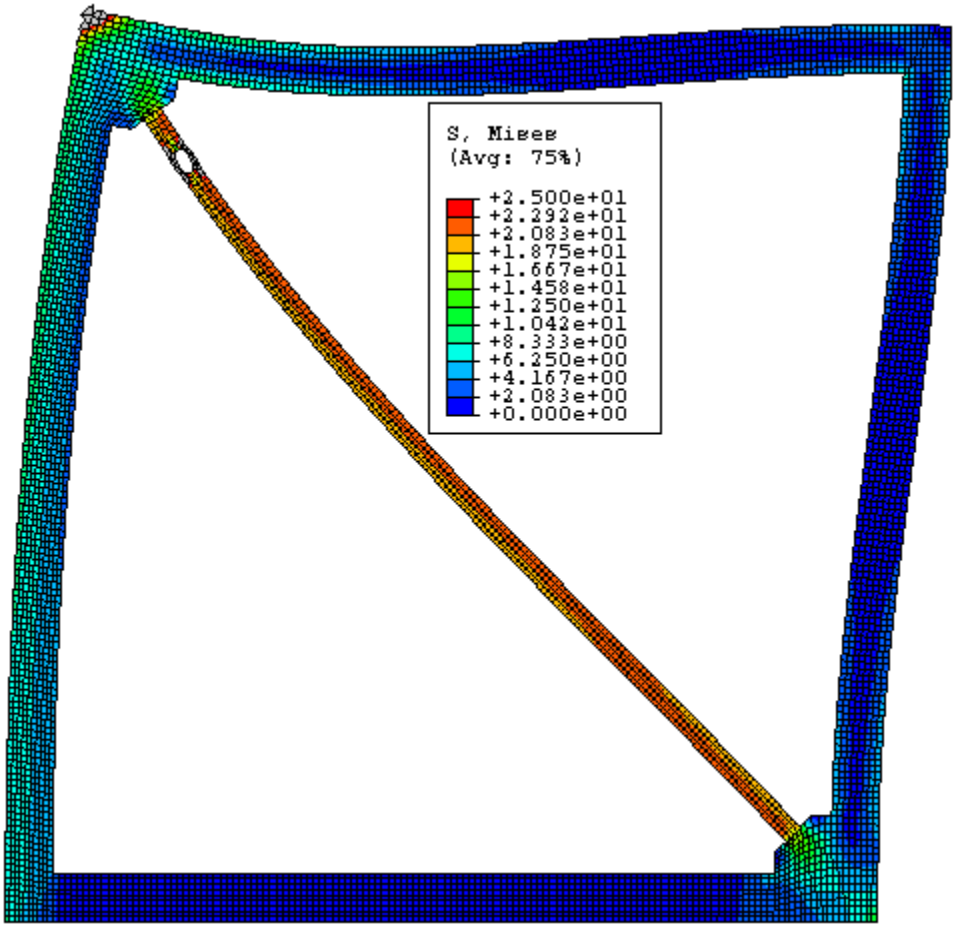

Fig. 6.21 - Von Mises Stress – Frame “H” with RXS Fuse – Stress Scale #2.

6.3.2.3 Eccentricity Computation Based on FEA Results

The non-uniform stress distribution along the RXS fuse induces a moment force that can be transformed into an eccentricity of the applied brace axial load. From FEA results is found that the upper right side of the brace at the RXS fuse, labeled side "a" in Fig. 6.21, is subjected to stresses between 60 ksi and 35 ksi, whereas the lower left side, labeled side "b" in Fig. 6.21, is subjected to smaller stresses with values that range between an approximate high 50 ksi and an approximate low 35 ksi. Thus, the greater eccentricity is expected towards the side "a" of the RXS.

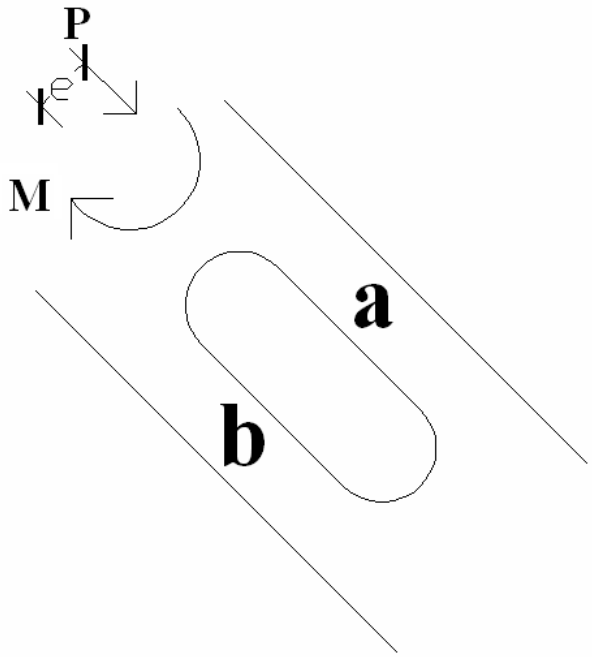

Fig. 6.22 - RXS Fuse Eccentricity Calculation – Diagram #1.

Taking the non-uniform stress distribution induced moment as the product of the brace axial load times the eccentricity Eq. 6.10 can be solved for the eccentricity once the moment and brace axial load are known.

$$e = M/P \qquad \text{<Eq. 6.10>}$$

where

e= eccentricity of applied brace axial load

M = induced moment to the RXS fuse due to the eccentricity

P = Brace axial load applied to the RXS fuse

The brace axial load at the RXS fuse is estimated from the Von Mises stress distribution and is calculated as the sum of the equivalent loads “Pa” and “Pb” on each side of the RXS fuse. For the control frame “H” the stress at three points (1) center, (2) inferior edge, and (3) superior edge of each arm is averaged and then multiplied by the depth of the arm “d”, equal to 1.5625 (Fig. 6.22). These stresses were estimated to be:

Stress (ksi)	Side “a”	Side “b”
Inferior	58.51	51.28
Center	43.95	43.95
Superior	36.63	36.63

Table 6.3 - Stress Distribution on Each Side of the RXS Fuse.

Average stress at “a” = (Inferior stress+ Center stress+ Superior stress)/3 <Eq. 6.11>

Average stress at “a” = (58.51 ksi +43.95 ksi +36.63 ksi)/3 = 46.36 ksi

Pa = (average stress at “a”) * d = 46.36 ksi * 1.5625 in = 72.44 kips/in <Eq. 6.12>

Average stress at “b” = (Inferior stress+ Center stress+ Superior stress)/3 <Eq. 6.11>

Average stress at “b” = (51.28 ksi +43.95 ksi +36.63 ksi)/3 = 42.95 ksi

Pb = (average stress at “b”) * d = 42.95 ksi * 1.5625 in = 68.68 kips/in <Eq. 6.12>

Therefore the total brace axial load applied to the RXS fuse on frame “H” is equal to:

P=Pa+Pb = 72.44 kips/in + 68.68 kips/in = 141.12 kips/in <Eq. 6.13>

The moment is calculated as the difference between loads “Pa” and “Pb” times the lever arm “x” equal to 2.5313 inches which goes from the center of the arm to the center of the oval cutout as shown in Fig.6.22.

$$M = (Pa - Pb)*x \quad \text{<Eq. 6.14>}$$

M = (72.44 kips/in – 68.68 kips/in) * 2.5313 in = 9.53 kips/in – in

Once the induced moment and the applied axial load are known, the eccentricity can be calculated using Eq. 6.10.

$$e = M/P = 9.53 \text{ kips/in} - \text{in} / 141.12 \text{ kips/in} = 0.068 \text{ in.} \quad \text{<Eq. 6.10>}$$

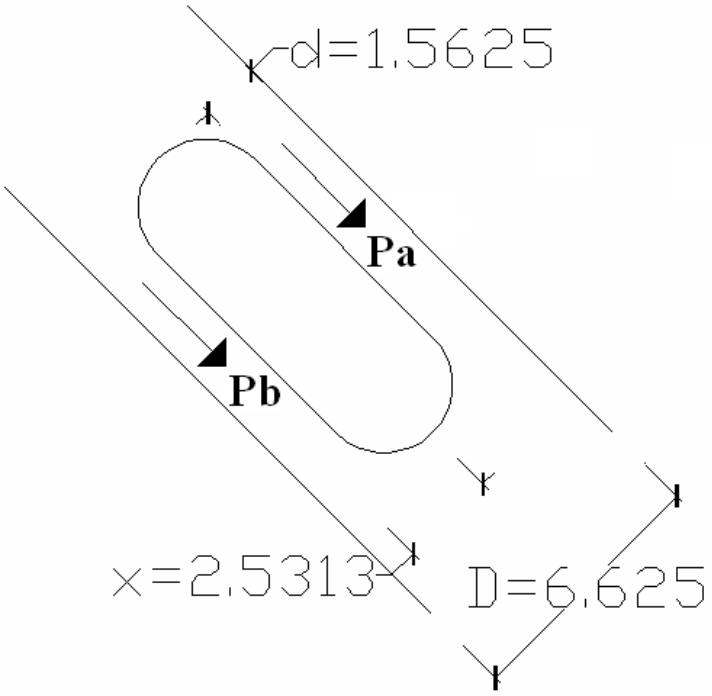

Fig. 6.23 - RXS Fuse Eccentricity Calculation – Diagram #2.

Results from similar calculations for the other braced frames modeled in the study are shown in Table 6.4. Calculations of the control frame "H" are highlighted.

Frame	Beam/Column Stiffness Ratio	σa Stress (ksi)	σb Stress (ksi)	Pa Load (K/in)	Pb Load (K/in)	P(a+b) Load (K/in)	M Moment (k/in-in)	e Eccentricity (in.)
A	***0.13***	49.15	40.63	76.79	63.48	140.27	33.70	0.240
B	***0.25***	47.59	39.45	74.35	61.64	135.99	32.18	0.237
C	***0.38***	46.61	39.07	72.83	61.05	133.88	29.83	0.223
D	***0.50***	46.73	39.93	73.01	62.40	135.41	26.87	0.198
E	***0.63***	50.45	43.90	78.83	68.59	147.42	25.91	0.176
F	***0.75***	45.08	40.10	70.43	62.65	133.08	19.70	0.148
G	***0.88***	46.64	43.06	72.87	67.27	140.14	14.16	0.101
H	***1.00***	46.36	43.95	72.44	68.68	141.12	9.53	0.068
I	***1.14***	46.80	44.50	73.13	69.53	142.66	9.10	0.064
J	***1.33***	46.20	43.76	72.18	68.38	140.56	9.62	0.068
K	***1.60***	49.63	43.38	77.55	67.78	145.33	24.72	0.170
L	***2.00***	46.81	39.04	73.15	61.00	134.15	30.74	0.229
M	***2.67***	46.04	37.32	71.94	58.31	130.25	34.49	0.265
N	***3.20***	50.51	39.67	78.93	61.98	140.90	42.91	0.305
O	***4.00***	50.42	38.79	78.78	60.60	139.39	46.01	0.330
P	***8.00***	50.91	35.24	79.54	55.06	134.60	61.96	0.460

Table 6.4 - Beam/Column Stiffness Ratio Frame Calculations.

Calculation for the other braced frames modeled to study the influence of the diagonal brace angles ϕ on the eccentricity are shown in Table 6.5. Calculations of the control frame "H" are also highlighted.

Frame	Brace Angle "ϕ" (degrees)	σa Stress (ksi)	σb Stress (ksi)	Pa Load (K/in)	Pb Load (K/in)	P(a+b) Load (K/in)	M Moment (k/in-in)	e Eccentricity (in.)
Q	***55***	50.59	45.80	79.04	71.56	150.60	18.94	0.126
R	***50***	43.83	40.85	68.49	63.83	132.32	11.80	0.089
H	***45***	46.36	43.95	72.44	68.68	141.12	9.53	0.068
S	***40***	46.66	43.07	72.91	67.30	140.20	14.20	0.101
T	***35***	51.39	44.05	80.30	68.83	149.13	29.03	0.195
U	***30***	49.81	40.32	77.83	63.00	140.83	37.55	0.267
V	***25***	47.62	38.09	74.40	59.52	133.91	37.67	0.281

Table 6.5 - Bracing Angle "ϕ" Frame Calculations.

Eccentricity variations due to different beam to column stiffness ratios are shown in Fig 6.24. The control frame "H" with a beam/column stiffness ratios equal to 1 and frames with beam/column stiffness ratios of approximately 1 induced smaller eccentricity in brace axial load. As the beam/column stiffness ratio decreases or increases from 1, the eccentricities increase on both sides of the curve. The eccentricity in axial load was more sensitive to the column stiffness since reducing the stiffness of the column resulted in greater eccentricities than those obtained by reducing the beam stiffness.

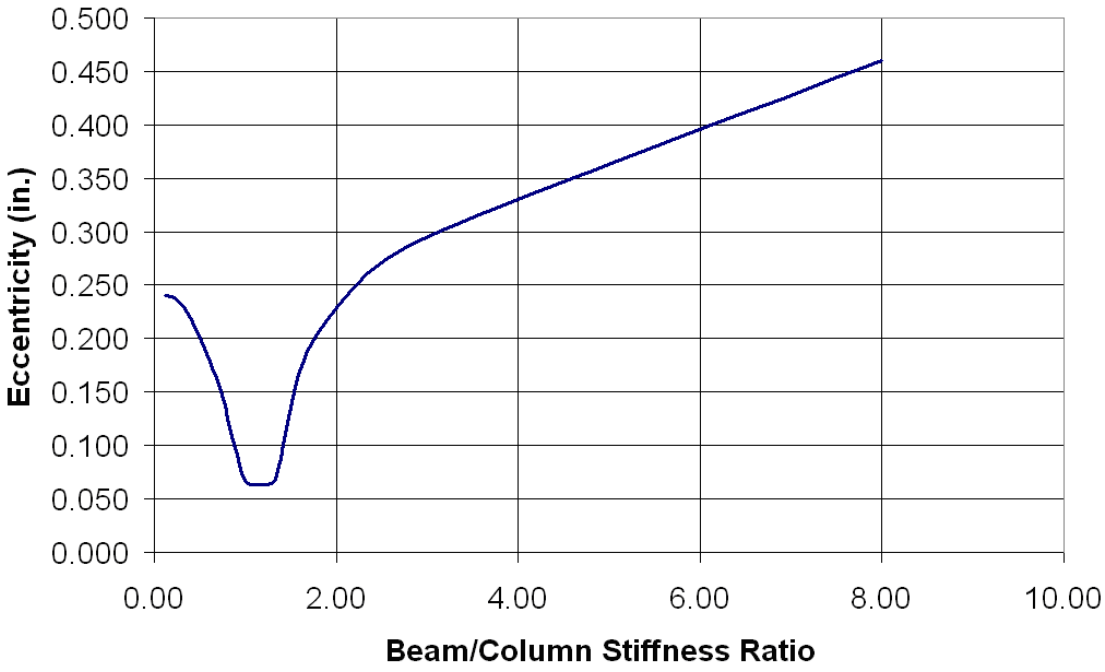

Fig. 6.24 - Eccentricity vs. Beam/Column Stiffness Ratio.

The same curve shown in Fig. 6.24 is shown in Fig. 6.25 with a different horizontal scale. This relationship shown in Fig. 6.25 confirms that symmetric frames with similar beam and column stiffness result in smaller eccentricities in brace axial load, and also it shows that column stiffness had a bigger effect on the eccentricity than that of the beams.

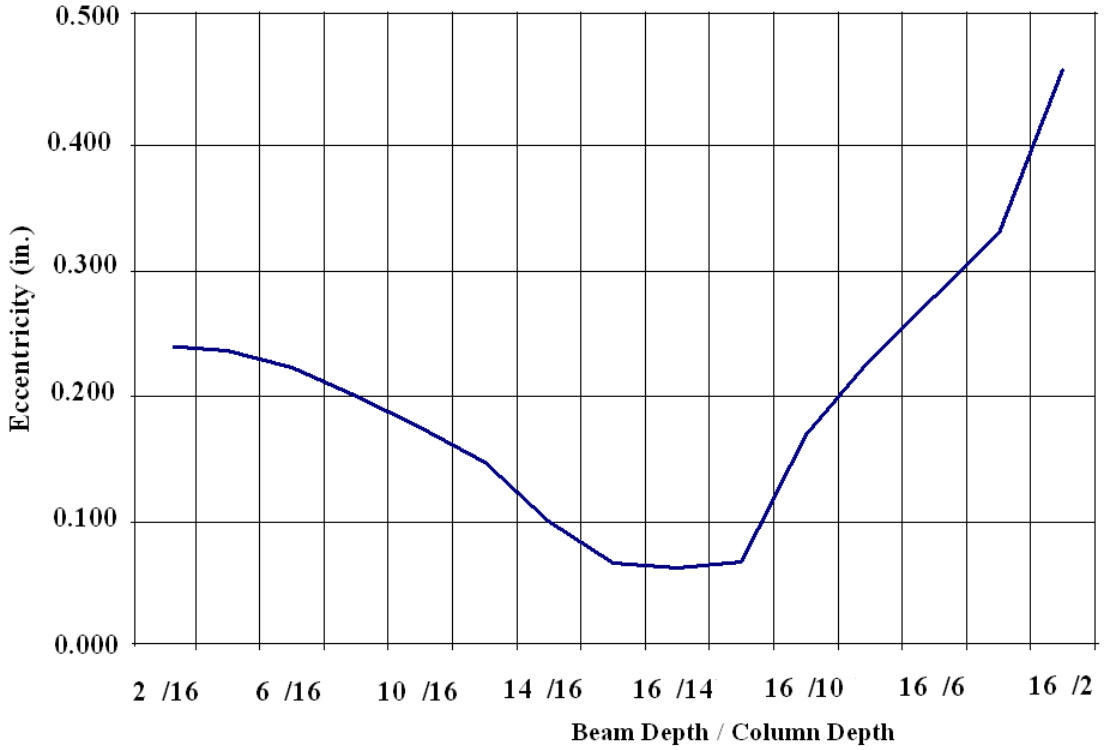

Fig. 6.25 - Eccentricity vs. Beam Depth / Column Depth.

Variations in eccentricity for different diagonal brace angles ϕ are plotted in Fig.6.26. For the study of this second parameter a stiffness ratio of one was used for all frames modeled. Similar to the case of the first parameter, frame "H", with a diagonal brace angle ϕ of 45 deg. induced the lowest eccentricity in the axial load. Increasing or decreasing the angle of the diagonal with respect to the horizontal has the effect of increasing eccentricity. This increment was bigger for shallower brace angles with respect to the horizontal. Increasing the angle of the control frame brace from 45 deg. to 55 deg. Resulted in an increase in the eccentricity from 0.068 in. to

0.126 in. Decreasing the angle from 45 deg. to 35 deg. Resulted in a more significant increment from 0.068 in. to 0.281 in.

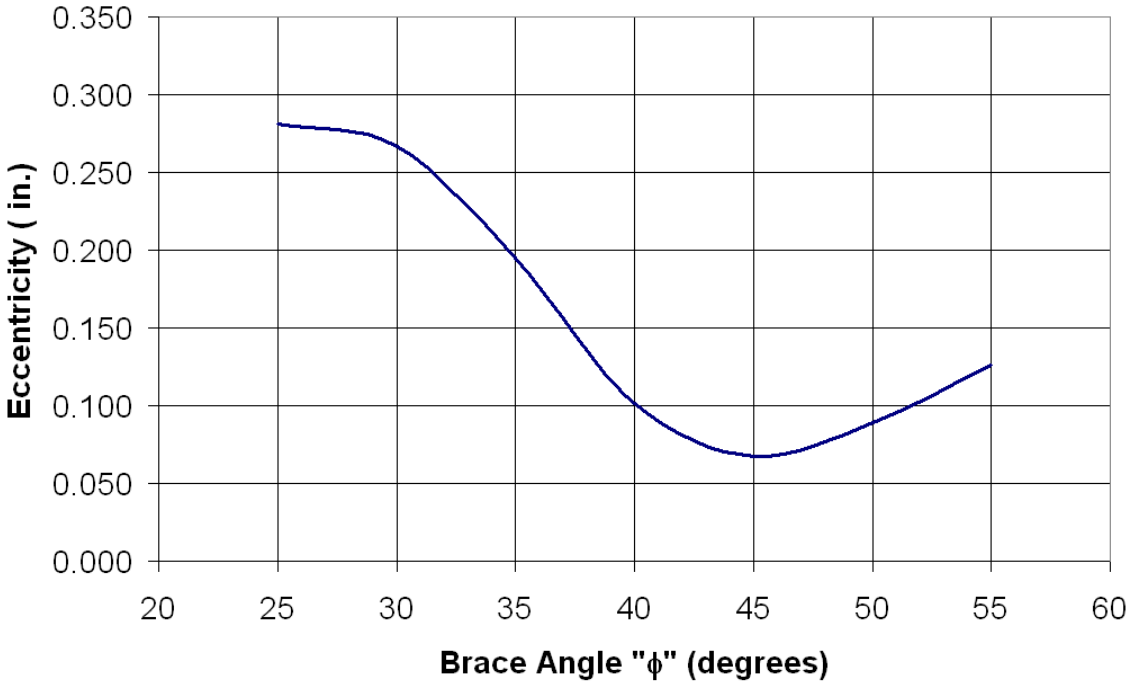

Fig. 6.26 - Eccentricity vs. Brace Angle “ϕ”.

7 BCE Fuse Configuration and Design

This chapter presents a description of the Brace Composite Element "BCE", its different components, and the basic concepts that define how this fuse system is proportioned. The BCE fuse design procedures are similar to those of the RXS fuse element presented in Chapters 4 and Appendix A, although there are some added complexities because this fuse system is made of multiple parts fabricated with three different materials. This complexity is what makes the BCE fuse a system with greater functionality and efficiency, well suited to sustain severe seismic events. A design calculation example is presented at the end of this chapter. Similar to the RXS fuse design example, the specimens were proportioned to meet the characteristics of the loading frame.

7.1 BCE Fuse Configuration

This section presents the basic configuration of the BCE fuse. The high performance composite fuse element is composed of three parts:

1) Metal.
2) Polymer matrix.
3) Fiber reinforced polymer.

The bars are the main load-bearing component of the BCE fuse. The capacity of the fuse and the characteristics of the confining system are driven by the bar material properties. The bars can be made of steel or shape memory alloys. The

confining system is made of a cylindrical polymer matrix, which is stiffened by a confining layer made of a carbon fiber reinforced polymer. The tensile strength of the fuse is provided by the bars. Similarly, the capacity in compression is closely related to the capacity of the metal bars. Due to the slenderness of the bars their capacity in compression is limited by buckling and the bars are not capable of resisting the amount of load when subjected to tension. To accommodate this weakness a buckling-restraint system is provided by embedding the bars in a cylindrical urethane matrix confined by a carbon fiber reinforced polymer layer (Fig. 7.1) which significantly increases the strength of the bars in compression.

The BCE fuse requires additional components that are essential to an adequate load transfer from the brace to the fuse element. For the case of a hollow round brace these components include steel plates at the top and bottom of the fuse. There are four steel plates, the outermost plates are welded to the round HSS brace, whereas the innermost plates are connected to the fuse element through load transfer nuts. The assembly between the fuse element and the brace is made possible by either welding or bolting the outermost steel plates with the innermost steel plates (Fig. 7.1).

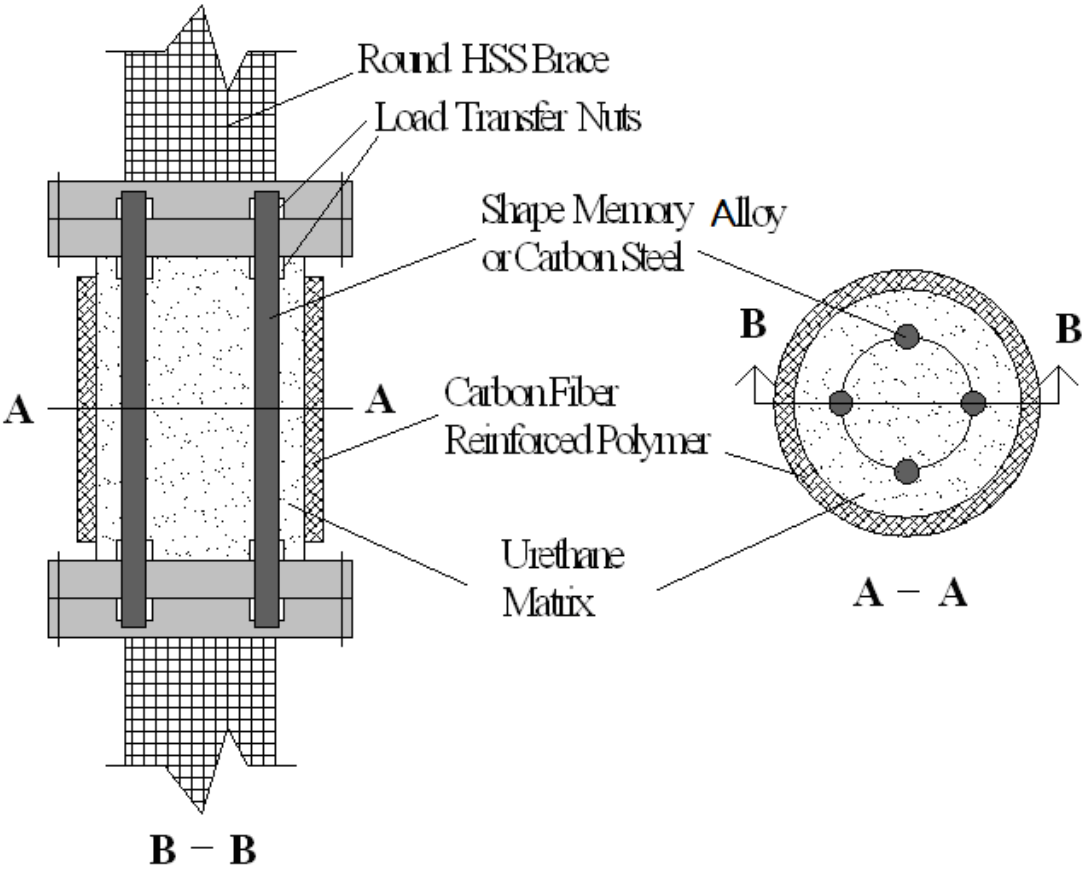

Fig. 7.1 - BCE Fuse Basic Configuration.

Methods for proportioning and fabricating each of the parts of the BCE fuse are explicitly discussed in the following pages. The basic BCE fuse configuration is supported by results from computational models.

7.2 Bar Material for BCE

For a preliminary study [Lambrecht, 2004] with reduced-scale models the bars of the brace-composite-element (BCE) were made of shape memory alloys (SMA). The material used was a Nickel-Titanium alloy (Nitinol) with unique properties (described in the literature review on Chapter 3) that make this alloy ideally suited for the intended fuse applications. However, the superior mechanical properties of SMA's also bring about difficulties in fabrication because machining of titanium based alloys requires special equipment and skilled/experienced labor. The fabrication cost added to the cost of the SMA material diminishes the economic feasibility of the BCE fuse.

Even though Nitinol is strongly recommended as ideally suited material to improve the performance of the BCE fuse, carbon steel was selected for the bar material for the fabrication of the full-scale BCE fuse specimens because this material is ductile, easy to machine, and does not cost as much as shape memory alloys. Considering the objectives of this investigation carbon steel was the most feasible material.

Although SMA's are not the most economic option for the BCE fuse bar material, there are some instances where SMAs would be a desirable alternative. The advantages of using SMA's is that they are less susceptible to being damaged and can dissipate energy without permanent deformations if the strain demands remain below damaging values for the material. From a long term economic perspective, using shape memory alloy bars could also be a feasible option since a BCE fuse with SMA

bars is less likely to require major repairs or even bar replacement after the system is subjected to a major seismic event and the bars are subjected to large inelastic displacements.

There are implications other than material and fabrication costs that must be considered before selecting shape memory alloys as the BCE fuse bar material. These implications are associated with technology development roadblocks caused by difficulties in the SMA manufacturing processes.

One of the major problems of machining Nitinol bars is the severe hardening of the material. Conventional mechanical machining procedures, such as using a computer numerical control (CNC), a mechanical device used to fabricate components by the selective removal of material, can significantly degrade the quality of machined surfaces and shorten the life of machine tools. Additionally, stress-induced martensitic transformation at the cutting front complicates the conditions of contact between tool and workpiece. Alternative methods employed to overcome these difficulties are energy-assisted machining processes.

The electro-discharge machining (EDM) method is among the energy-assisted machining processes exhibiting an adequate ability in machining Nitinol alloys. EDM is an established electro-thermal process for metals and a non-contact machining method, which would not cause any mechanically induced transformation. Tool wear is thus no longer an issue. However, a drawback of this energy-assisted machining method is that the process produces microscopically rough surfaces [Mamalis, 2004] and induces heat-affected zones. Both of these can affect the mechanical integrity and

the functional properties of Nitinol alloys since these rough surfaces create stress concentrations that could be significantly detrimental to the overall performance of the BCE fuse SMA when subjected to large inelastic deformations.

Although shape memory alloys were not used in the fabrication of the BCE fuse specimens, there are several important lessons learned from the preliminary study on BCE fuse elements with SMA's. These lessons played a key role in the development and optimization of the fuse assembly configuration.

The experimental preliminary study consisted of testing high performance composite elements with Nitinol wires 0.197-in. in diameter (5 mm.) and 8 ¾-in. long embedded in a 6-in. tall, 5-in. diameter cylindrical matrix made of 70-durometer urethane. A confining layer was placed around the urethane matrix. The layer was made of carbon fiber reinforced polymer (CFRP) CYCOM 5276-1 [Cytec, 2002] and it was approximately 0.095-in. thick (Fig. 7.3).

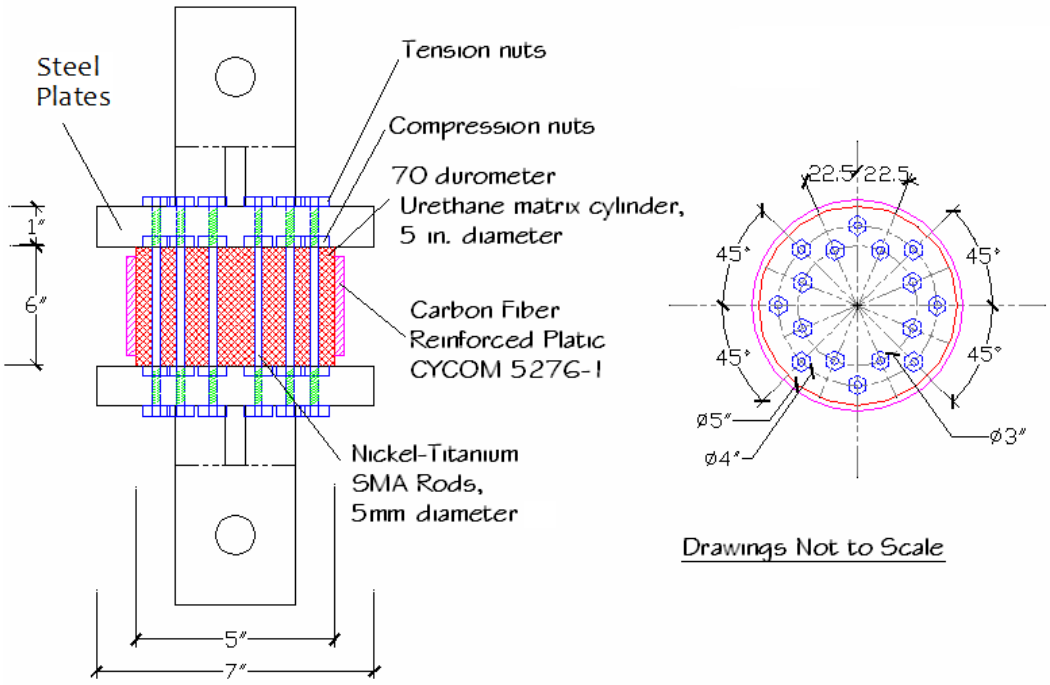

Fig 7.2 - High Performance Composite Element, Preliminary Study.

The 5-mm diameter Nitinol rods used on the High Performance Composite Element (HPCE) were anchored to steel plates through threaded ends that accommodated two nuts on each rod end, one on either side of the steel plates. The nuts on the outside face of the steel plate transferred tension loads from the plate to the Nitinol rods, and the nuts on the inside face of the steel plate (matrix side) transferred compression loads from the plates to the Nitinol rods.

During these preliminary tests it was observed that at the threaded area directly underneath the compression nut the SMA rods fractured as the HPCE was entering the inelastic range of response. The main reason for the failure were the presence of stress concentrations induced by the cut thread and rotation of the steel

plates with respect to the longitudinal axis of the fuse as the fuse was subjected to buckling deformations during the compression cycles.

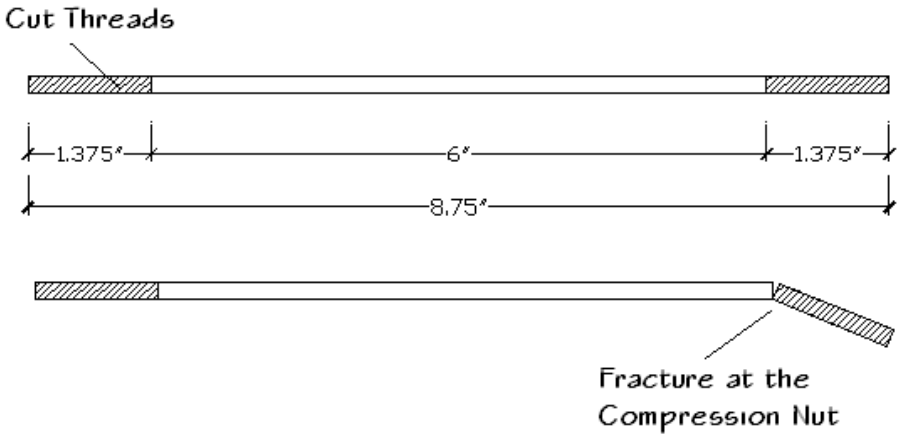

Fig. 7.3 - SMA/Nitinol Rods used on the HPCE, Dimensions and Fracture Failure.

To address this problem several alternatives were explored to improve the performance of the fuse in the inelastic range of response.

a) A first alternative was to introduce the use of rolled threads instead of cut threads. Even though the rolled threads improved the behavior of the fuse in the inelastic range of response, it did not fix the problem as fracture of the SMA Nitinol rods still occurred at the same location.

b) A second alternative was to reduce the SMA rod diameter by several U-shaped indentations to reduce the stress demands in the threaded area (Fig. 7.4).

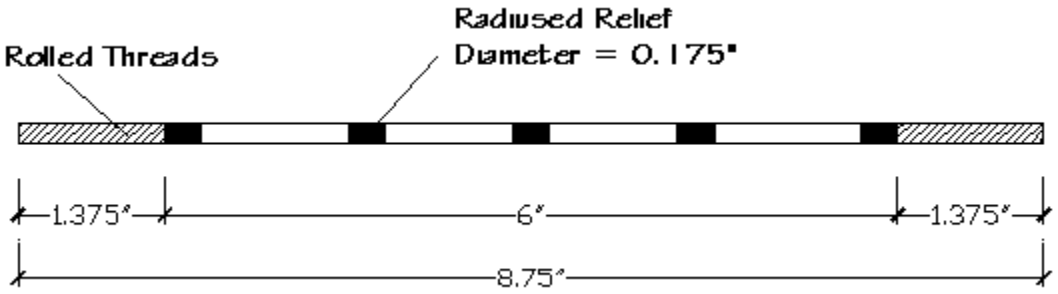

Fig. 7.4 - SMA/Nitinol Rods Notch Alternative Configuration.

c) A third approach (Fig. 7.5) was to reduce the diameter of the bar between the threaded ends. However, as mentioned before, Titanium is not an easy material to machine because it requires special equipment and labor. Although this solution provided better results, the performance of the fuse when subjected to large inelastic deformations was not satisfactory yet as the rods were not able to deform as much as expected within their inelastic range of response before fracture failure.

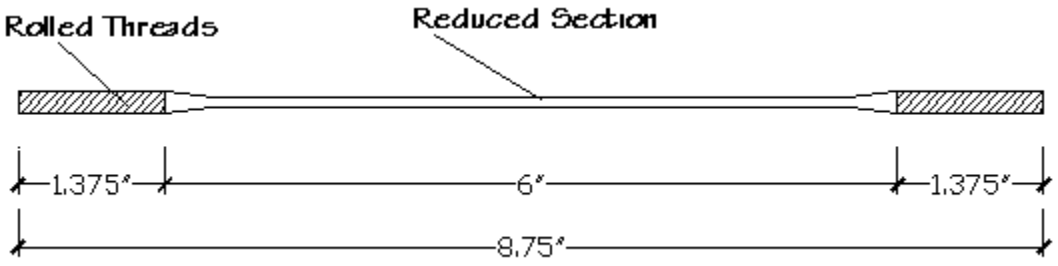

Fig. 7.5 - SMA/Nitinol Rods Reduced Area Alternative Configuration.

The BCE fuse configuration used a similar approach to the reduced section alternative but with carbon steel instead of SMA Nitinol rods. Other changes included

a different pre-preg Carbon Fiber Reinforced Polymer (CFRP) and a higher durometer urethane matrix. The other difference between the preliminary HPCE specimens and the BCE fuse was that the BCE represented a full-scale element as it would be implemented in a concentrically braced frame, whereas the HPCE was a small scale prototype.

Based on the preliminary study on fuses with SMA's rods it was concluded that fracture toughness was a property that was critical to the successful performance of the fuse when subjected to large inelastic deformations under cyclic loads. Therefore one of the most important criteria for selecting a carbon steel material was the notch toughness.

One of the methods implemented in ASTM standards to measure the fracture toughness of different types of steel is the Charpy V-Notch (CVN) impact test which is the most widely used test to measure notch toughness [Rolfe and Barsom, 1999].

Among the types of carbon steel available in the market, ASTM A709 steel was chosen due to its notch toughness properties, which are shown in Table 7.1. Fracture-critical materials are marked with the letter "F" by ASTM standards.

Grade	Minimum CVN Test Value (ft-lbf)	Minimum Average CVN Test Value (ft-lbf)		
		Zone 1	Zone 2	Zone 3
36 F	20	25 at 70˚F	25 at 40˚F	25 at 10˚F
50 F	20	25 at 70˚F	25 at 40˚F	25 at 10˚F
100 F	28	35 at 30˚F	35 at 0˚F	35 at -30˚F

Table 7.1 - Fracture-Critical A709 Materials Provided by ASTM Standards.

Among the three grades available in ASTM standards, 36F and 50F were initially chosen over grade 100F because high strength steels with higher carbon content usually provide less ductility (Fig. 7.6). Even though A709 - 100F steel provided higher CVN values, ductility was also a crucial bar property, as the bars must elongate as much as the BCE fuse system demands.

Both carbon steels grade 36F and grade 50F show similar CVN values and both grades also provide adequate ductility. Using grade 36F allowed for a wider range of fuse sizes that could be tested in the load frame available so ASTM A709 grade 36F steel was selected instead of grade 50F.

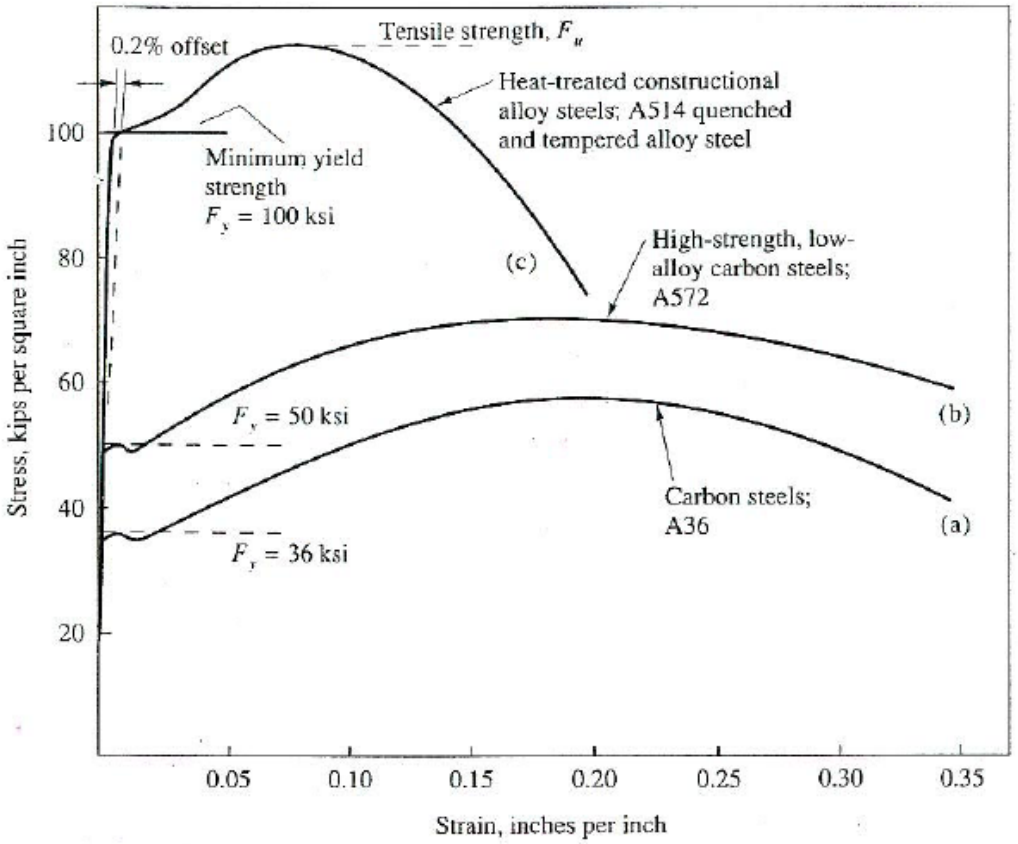

Fig. 7.6 - Stress-Strain Curves for Steel [Salmon and Johnson, 1999].

The ASTM standards also provide three zones for each of A709 steel grades. Even though Table 7.1 shows the same CVN values for each zone, these are given for different temperatures. The absorbed energy required before fracture of some common structural materials is higher as the temperature increases (Fig. 7.7) [Rolfe and Barsom, 1999]. This is not the case of some materials. For example, aluminum and very high-strength steels have low levels of notch toughness at all temperatures,

and 180 ksi yield strength alloy steel has high level of notch toughness at all temperatures.

The CVN values of lower strength steels, specifically 40 ksi structural steel, are higher as the temperature increases. At 140F the behavior of this type of lower strength structural steel is completely ductile, with high CVN values (Fig. 7.7). At -200F the behavior of the same material is completely brittle.

Taking into account that the specimens were going to be tested at room temperature, A709-36F zone 3 steel was selected, as it was expected that its CVN values would be more than the 25 ft-lbf specified by ASTM standards at -30 F.

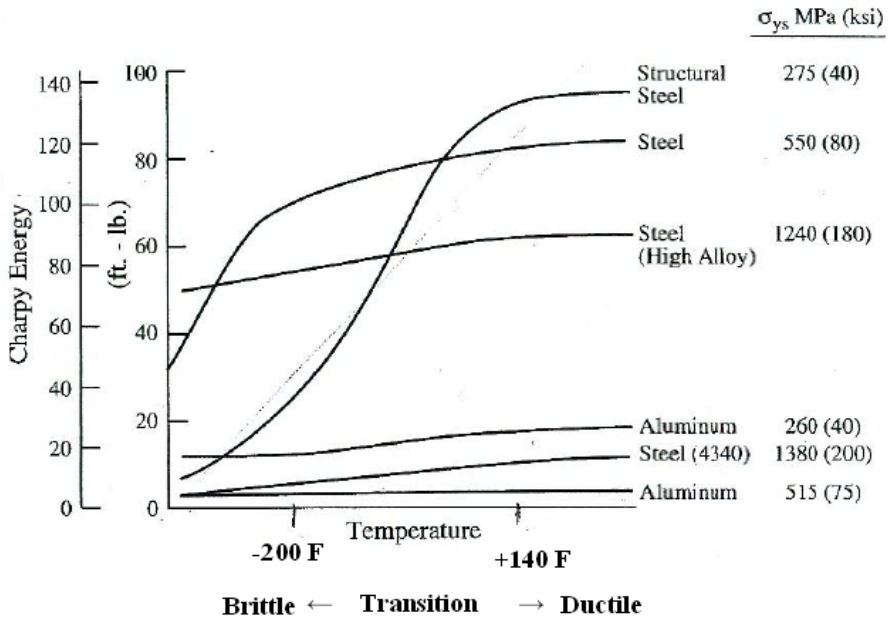

Fig 7.7 - Charpy V-Notch Impact Energy vs. Temperature from Rolfe and Barsom.

A fuse system with A709 grade 36F zone 3 steel bars does not provide residual deformation recovery as a fuse with shape memory alloy (SMA) bars does, but its ductility and notch toughness makes it suitable not only for this research but also for BCE fuse applications in practice. It is expected that the behavior of the BCE fuse with A709 grade 36F zone 3 carbon steel bars will still be adequate in terms of performance, and material, and fabrication cost savings make it a much more feasible option than SMAs.

7.3 Brace Composite Element Bar Shape

A different anchoring system was used in the full scale Brace Composite Element (BCE) with carbon steel bars as a result of the lessons learned from the study with SMA rods [Lambrecht, 2004]. The main change was the anchoring of the steel bars to the steel plates. This change was implemented because it was experimentally determined from the preliminary study that fracture failure occurred at the transition between the rod and the threaded ends, where the compression nut transfers the load from the steel plate to the bar.

This fracture failure was caused by stress concentrations induced by the addition of the threaded area, which disrupted the uniform stress flow. This condition was computationally verified for a ½-in. diameter bar through finite element analysis, as shown in Fig. 7.8. The finite element model material was defined by linear-Elastic properties with a 29000 ksi modulus of elasticity The bar was subjected to a uniform axial stress of 50 ksi. The FEM results show that at the threaded end and its

proximities (gray areas) stresses were greater than the applied 50 ksi axial stress (Fig. 7.8).

A closer look of the stress distribution calculated with the finite element model at the threaded end is presented in Fig. 7.9. The figure shows that the very first thread, where the bar transitions from a round cross section without any surface discontinuities to the threaded surface, is subjected to the highest stress of 80 ksi. This represents a 60 % stress increment with respect to the axial stress applied.

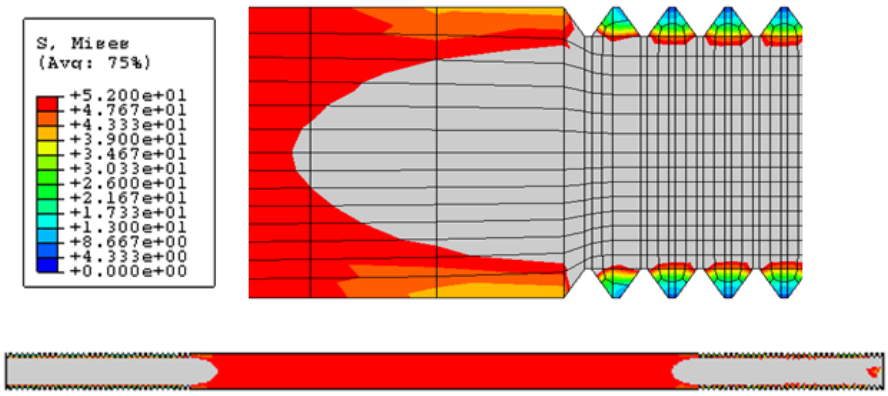

Fig 7.8 - Finite Element Analysis for a Plain Round ½-in. Diameter Bar with Threaded Ends (52 ksi scale).

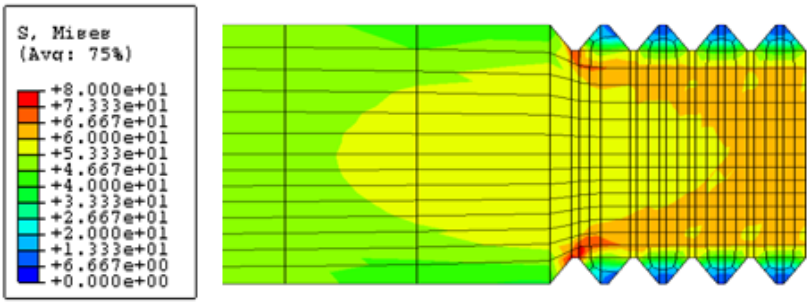

Fig 7.9 - Finite Element Analysis for a Plain Round ½-in. Diameter Bar with Threaded Ends (80 ksi scale).

Efforts for developing a new system were focused on reducing the stress demand in the threaded area to improve the performance of the bars when subjected to large inelastic deformations. To accomplish this goal, a bar yield zone was introduced between threads by reducing the diameter so that the non linear behavior would occur over a region with uniform stress distribution.

Other changes in the shape of the bar were introduced to improve performance. The transfer of compression load from the plate to the nut on the matrix side of the composite element was found to be a critical region because high stress demands caused early brittle failures. Therefore, another design consideration was that the compression-transfer threaded portion of the bar should be the strongest area by providing a larger diameter than that required at the yield zone and the tension-transfer portion of the threaded end.

It is important to highlight that the two nuts on each side of the plate were intended to keep a tight fit between the steel plate and the parts of the bar embedded in the steel plate so that this portion of the bar would not be subjected to bending stresses when the fuse is subjected to large inelastic deformations due to buckling. This tight fit also keeps the fuse system from having displacements at zero loads. Any anchoring system implemented should keep this tight fit and restrain this portion of the bar from any limit state that might compromise the fuse performance.

An alternative to the anchoring system used in the reduced-scale study is to replace the compression nut and threaded compression zone by an enlarged bar diameter or shoulder (Fig. 7.10). Adding the shoulder ensures that the stress demands

in the compression load transfer area are reduced. This configuration would still provide adequate and even simpler anchoring of the bar because the tension nut together with the bar shoulder would restrain the part of the bar embedded in the steel plate from any type of stresses other than those caused by axial load. The transition between the shoulder diameter and the yield zone with smaller diameter was chosen to have a circular radius in order to reduce stress demands caused by the change in geometry. The transition between the shoulder and the bar portion embedded in the steel plates was chosen to be a 90 deg. transition in other to provide a flat surface that would properly accommodate the steel plates.

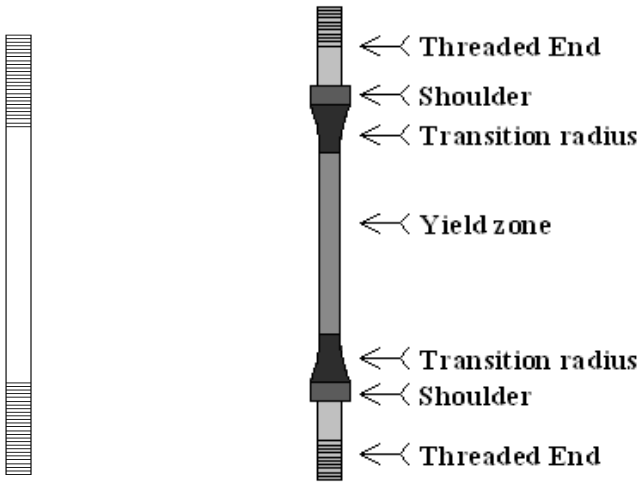

Fig. 7.10 - Preliminary HPCE Bar Shape vs. BCE Bar Shape.

Another consideration in optimizing the shape of the bar was that the threaded ends should have a larger diameter than the yield zone in order to avoid excessive

stress demands in the area surrounding the tension nut. Specs for typical thread sizes were reviewed to make sure that the minor diameter of the thread was slightly larger than the diameter of the yield zone.

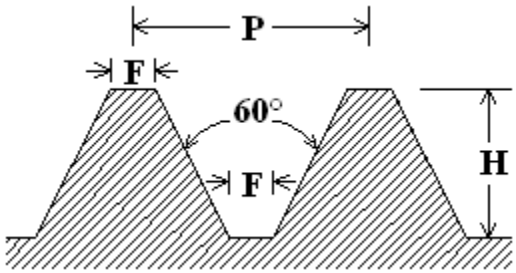

F = Basic width of flat

P = Pitch

H = Basic depth of thread

Fig 7.11 - American Standard Screw Threads.

Minor diameter of the thread = bar diameter – H * 2 <Eq. 7.1>

For a constant yield zone diameter, increasing the shoulder size implies the need for larger bars and greater machining costs as more material would have to be removed in the yield zone. Because material and fabrication costs increase with increasing shoulder diameter optimizing the shoulder size implies selecting the smallest diameter possible.

It was estimated that using 36 ksi steel a BCE fuse with four ½-in. diameter bars would have a failure load below the capacity of the testing equipment for a set of

½-in. diameter bars, the diameter of the treaded region should be a least 5/8-in. because it results in a thread minor diameter of 0.5069-in.

Thread Minor diameter = bar diameter – H * 2 > diameter of yield zone <Eq. 7.2>

Thread Minor diameter = 5/8-in. – 0.05905 in. *2

Thread Minor diameter = 0.5069 in. > ½-in. ∴OK.

A slightly smaller option that would allow fabricating a bar with a ½-in. diameter yield zone is using a 9/16-in. diameter in the threaded area. However, this diameter would provide a minor diameter of 0.45-in., which is less than the ½-in. yield zone diameter and could lead to early fracture. The next larger option is using a diameter of a ¾-in. threaded area. This size will reduce stress demands even more because this diameter is much larger than the ½-in. yield zone.

Stress demands were calculated through finite element analysis by modeling bars with 5/8-in. and ¾-in. thread diameters. Both bars were modeled with a constant 1 in. diameter shoulder, a ½-in. diameter yield zone, a circular radius transition between the yield zone and the shoulder, a 90 deg. transition between the shoulder and the thread, and a tensile stress equal to 50 ksi applied at the reduced section (Fig. 7.12).

Results from the 5/8-in. thread model (FEM) confirmed that the new bar configuration was likely to improve the performance of the fuse because the bars would be subjected to smaller stress demands due to the discontinuity induced by the thread. Calculated stress demands from the FEM with a 5/8-in. thread diameter,

shown in Fig 7.12, still show stress demands over 50 ksi at the 90 deg. transition between the shoulder and the threaded portion of the bar, and also at the first tension nut thread. However the magnitude of these stress demands are much smaller than those obtained from modeling the preliminary bar configuration. The ¾-in. diameter FEM showed a superior stress distribution as it does not show any stress demand over 50 ksi.

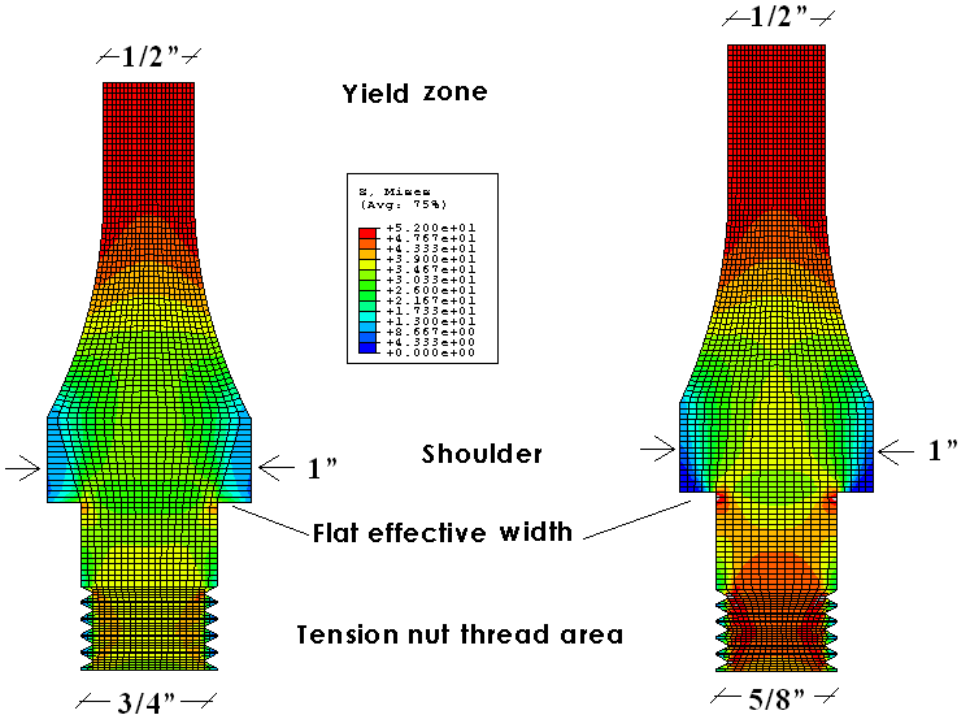

Fig. 7.12 - Tension Nut Load Transfer Area FEMs.

Using a ¾-in. diameter in the threaded area reduces stress demands at the bar ends. However, the larger diameter also implies that the flat portion of the bar that

makes contact with the plates and transfers the compression load to the bar will be smaller if the diameter of the shoulder remains constant at 1-in.

A fraction of the threaded area of the bar goes inside the hole in the steel plate. According to LRFD [LRFD, 2002] and ASD [ASD, 1999] the diameter of holes should be increased by 1/16-in. for fabrication purposes. If the diameter of the bar shoulder is set at 1 in., a thread with a ¾-in. diameter will leave an effective contact width between the flat portion of the shoulder and the steel plates equal to 3/32-in. which might not be sufficient to ensure proper contact between the bar and the plates in the compression transfer zone. The effective contact width is almost twice as much if 5/8-in. threads are used (Eq. 7.3). Therefore a 5/8 in. diameter along the threaded region was chosen as the optimal size.

Effective flat width = (Shoulder diameter – thread diameter -1/16")/2 <Eq. 7.3>

$$Effective\_flat\_width = \frac{\left(1in - \frac{5}{8}in - \frac{1}{16}in\right)}{2} = \frac{5}{32}in$$

Up until this point the changes introduced in the shape of the bar based on the preliminary HPCE test results and the FEA focused in improving the behavior of the bar when subjected to compression. Analyses show that the stress field in the bar is significantly different when the bar is subjected to tension (Fig. 7.13) .

Figure 7.13 shows that when the current bar configuration is subjected to axial tension the highest stress demand occur at two locations. The first location is at the 90 deg. transition between the shoulder and the threaded area labeled "stress

concentration a". The maximum stress demand at this point is 53 ksi. The second point where large stress demands take place is at the labeled "stress concentration b", with a magnitude of 60 ksi. The finite element model was subjected to a 40 ksi tensile stress applied at the ends of the bar. This stress is equivalent to applying a uniform stress of 50 ksi at the ½-in. diameter yield zone.

The enlarged shoulder was found to reduce the stress demand at the compression transfer area when the bar is subjected to compression. This enlarged area was also studied through finite element analysis to determine the compressive stress distribution, and how the compressive stress field could affect the performance of the fuse bars.

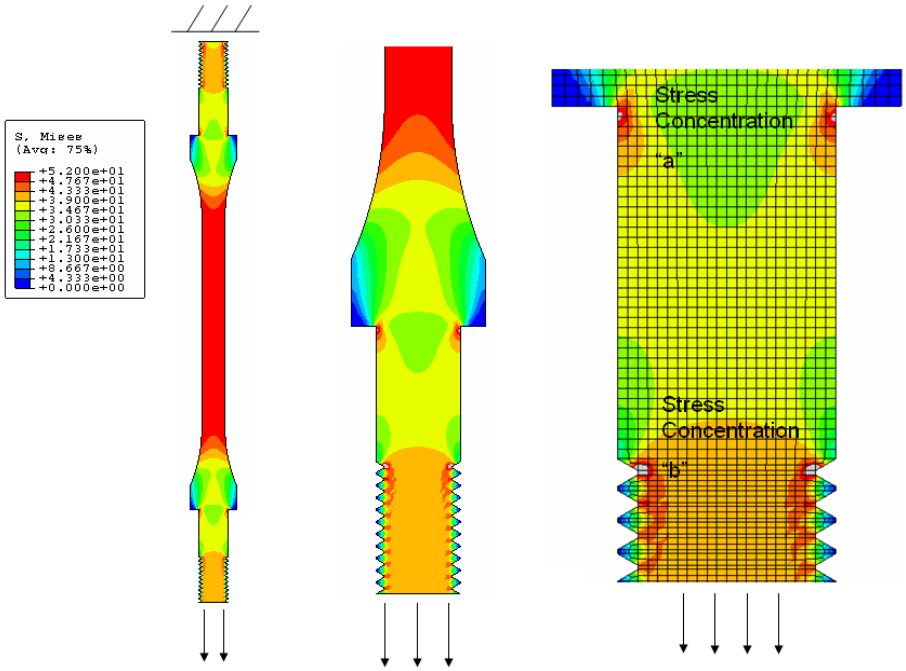

Fig. 7.13 -Von Mises Stresses under Axial Tensile Stress.

$$Kt(a) = \frac{\sigma_{FEM,\max um}(a)}{\sigma_{net}} = \frac{53ksi}{50ksi} = 1.06 \qquad \text{<Eq. 7.4>}$$

$$Kt(b) = \frac{\sigma_{FEM,\max imum}(b)}{\sigma_{net}} = \frac{60ksi}{50ksi} = 1.20 \qquad \text{<Eq. 7.5>}$$

The finite element model for the compression load case shows that when the current bar configuration is subjected to axial compressive stresses there is one location where the stress demand is significantly higher. This point is located at the 90 deg. transition between the 5/8-in. thread and the 1 in. shoulder. This region is shown in Fig. 7.14. The maximum stress was calculated to be 80 ksi, which is equal to the magnitude of the maximum stress obtained from the preliminary FEM shown in Fig. 7.8. A major improvement, however, was a significant reduction in the size of the area of high stress demand to a small localized zone. The finite element model was subjected to a compressive stress of 15.625 ksi applied at the 5/32-in. contact surface. This stress is equivalent to applying 50 ksi to the ½-in. diameter yield zone.

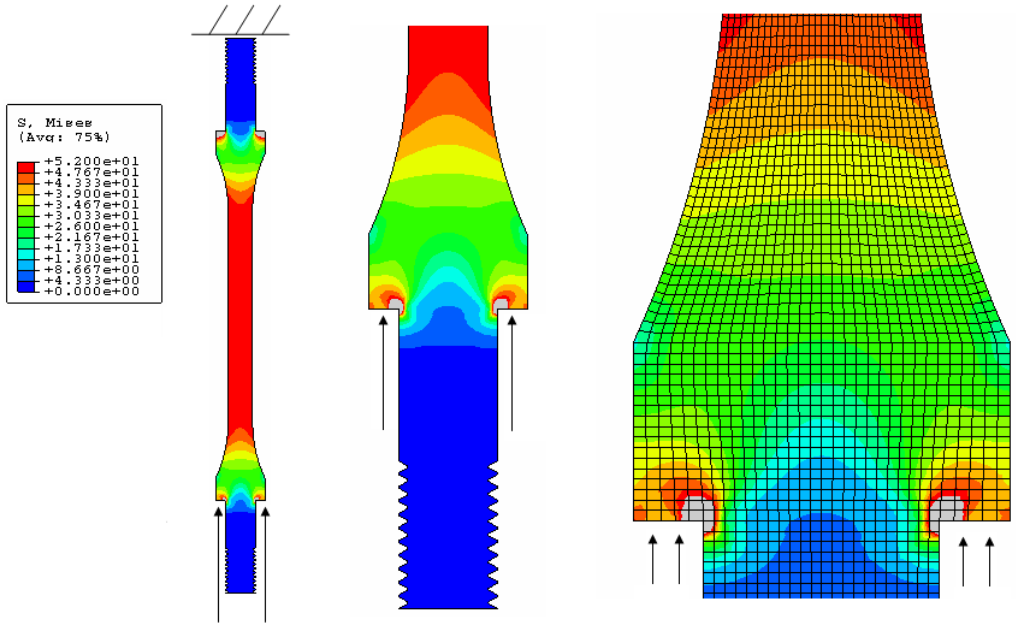

Fig. 7.14 - Von Mises Stress for Bar under Axial Compressive Stress.

$$Kt = \frac{\sigma_{FEM,\max imum}}{\sigma_{net}} = \frac{80ksi}{50ksi} = 1.60 \qquad \text{<Eq. 7.6>}$$

Different radiused configurations were analyzed in addition to the FEMs shown in Fig. 7.13 and Fig. 7.14 in an attempt to optimize the configuration of the bar in terms of reducing these stress demands. In total 8 different radiused relief configurations were modeled (Fig. 7.15 and Fig. 7.16).

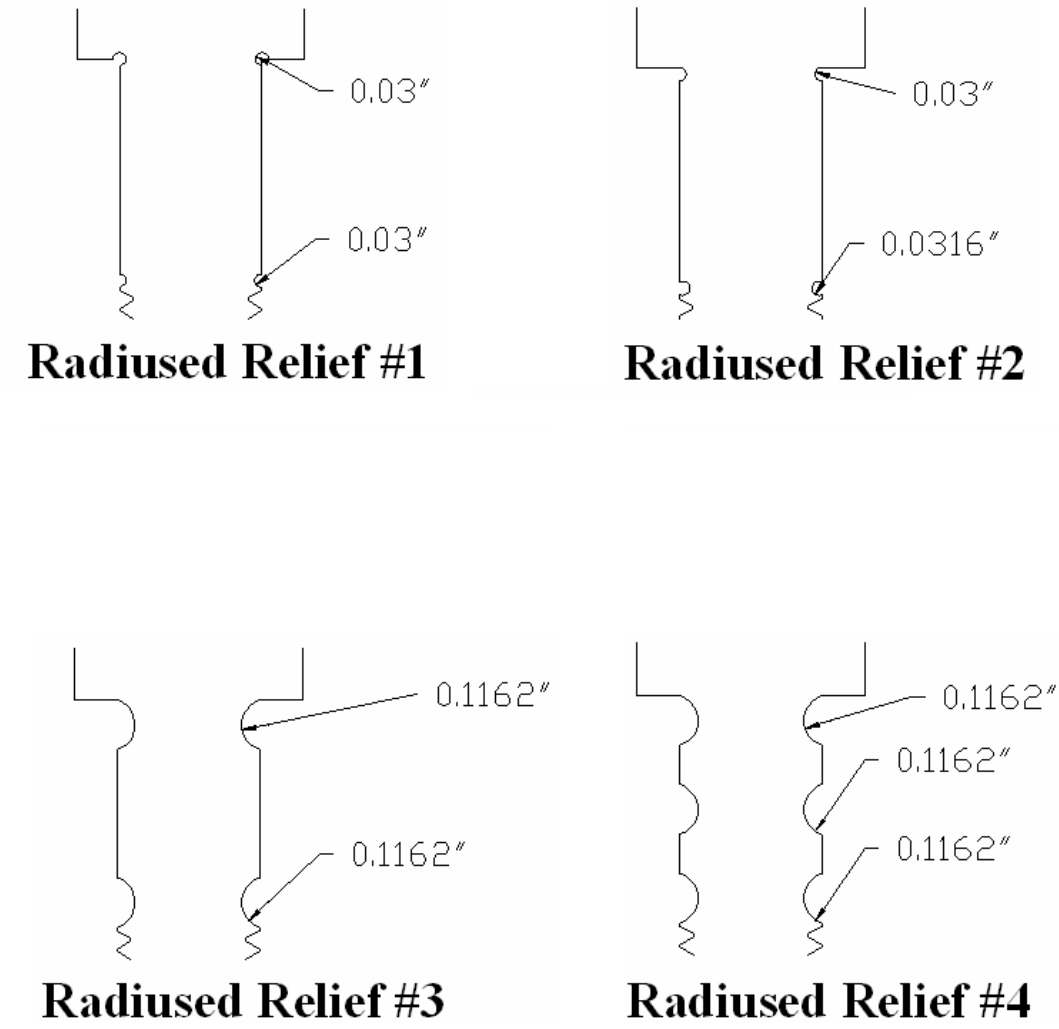

Fig. 7.15 - Radiused Relief Geometries 1 thru 4.

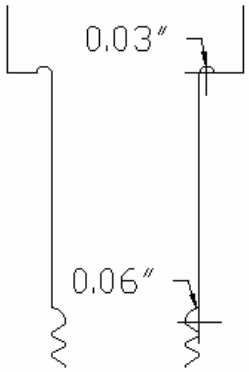

Radiused Relief #5

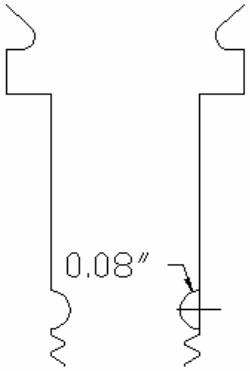

Radiused Relief #6

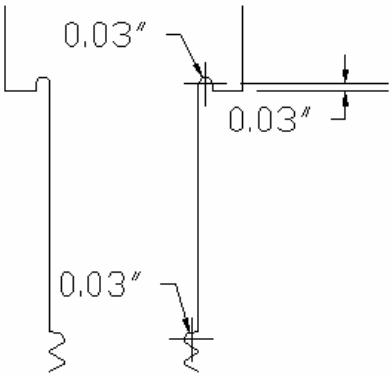

Radiused Relief #7

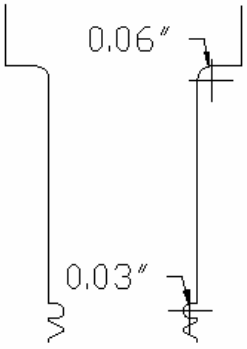

Radiused Relief #8

Fig. 7.16 - Radiused Relief Geometries 5 thru 8.

Of the different radiused relief geometries modeled only three showed improved stress fields. Radiused relief #6 was most effective in reducing the tensile stress concentration at point "a" located at the shoulder to thread transition, and geometry #3 was the most effective in reducing the compressive stress demand at the same location. Radiused relief #2 reduced the stress demand due to tension loads at point "b", as well as the stress demand due to compression loads. The stress concentration factors obtained from finite element analyses for the configurations with and without the radiused relief geometries are shown in Table 7.2. The finite element model results from all radiused relief geometries are included in the appendix.

Stress Concentration Study - (ksi)			
Radiused Relief	Tension		Compression
	Kt (a)	Kt (b)	Kt
none	1.06	1.2	1.6
1	1.36	1.2	2.1
2	1.42	1.16	1.54
3	1.64	1.32	1.46
4	1.6	1.26	-
5	1.16	1.26	2.2
6	0.98	1.36	1.9
7	1.16	1.22	2.2
8	1.1	1.24	1.9

Table 7.2 - Radiused Relief FEM Stress Concentration Results Summary.

$K_{t(a)}$ = stress concentration - shoulder

$K_{t(b)}$ = stress concentration – threads

$$K_t = \frac{\sigma_{max}}{\sigma_{net}} \qquad \text{<Eq. 7.7>}$$

Even though it was demonstrated that a radiused relief could reduce stress demands at the bar ends when subjected to both tensile and compressive stresses, it was determined that the improvement was likely to be cost-effective due to the fabrication cost.

The last bar configuration parameters were the shoulder depth and the radius of the circular transition between the 1-in. diameter shoulder and the ½-in. diameter reduced section. As mentioned before this transition was chosen to be circular to minimize stress demands that might compromise the performance of the bar when subjected to large inelastic deformations.

The radiused circular transition and the shoulder depth were computationally optimized using finite element analysis by defining different radiuses and depths as it is shown in Table 7.3. It was found that as the circular transition radius increased the stress demand at the point where the circular transition ends in the ½-in. diameter yield zone decreased for both tension and compression. Accordingly, the stress demand decreased with larger shoulder depth when the bar was loaded in both directions.

Specimen	r (in.)	d (in.)	Stress demand tension (ksi)	Stress demand compression (ksi)	Longitudinal elongation in tension (inches)
1	0.15	0.25	60.65	66.03	0.01358
2	0.25	0.25	57.51	58.26	0.01343
3	0.25	0.50	57.70	57.57	0.01287
4	1	0.25	52.74	52.75	0.01284
5	3	0	50.92	50.92	0.01272
6	3	0.25	50.86	50.84	0.01213
7	3	0.50	50.76	50.73	0.01150
8	5	0.25	50.50	50.59	0.01167

Table 7.3 - Summary of Stress Demands from Circular Transition FEM.

d = depth of the 1-in. diameter shoulder.

r = radius of the circular section where the 1-in. diameter shoulder transitions to the ½- in. diameter yield zone.

For a set bar length, as the circular radius and shoulder depth increase, the yield zone length shortens, decreasing the bar elongation capacity when subjected to large inelastic deformation in tension. This reduction in the bar displacement capacity

as a function of its yield zone length is considered negligible because the bar length can always be adjusted in the case of large circular transition radius or shoulder depth.

Under compression loads small changes in yield zone length due to variations in circular transition radius or shoulder depth do not have a significant effect on the buckling capacity of the bar. All 8 models with the different shoulder depths and circular transition radiuses are presented in the appendix.

It was decided to use a shoulder depth of 0.5-in. not only because it was the optimal depth in terms of stress demands, but also for ease of construction. Transitioning from the 1-in. diameter to the yield zone without a shoulder depth is more difficult to fabricate, and a 0.25-in. shoulder depth would also require more time to fabricate. In terms of the circular transition between the yield zone and the shoulder it was found that a circular transition radius of 3-in. was optimal because there were not significant reductions in stress demand using radiuses greater than 3-in., and also it was not desirable to reduce the length of the yield zone any further by using larger radiuses. In summary a 3-in. circular transition radius and a 0.5-in. shoulder depth were selected.

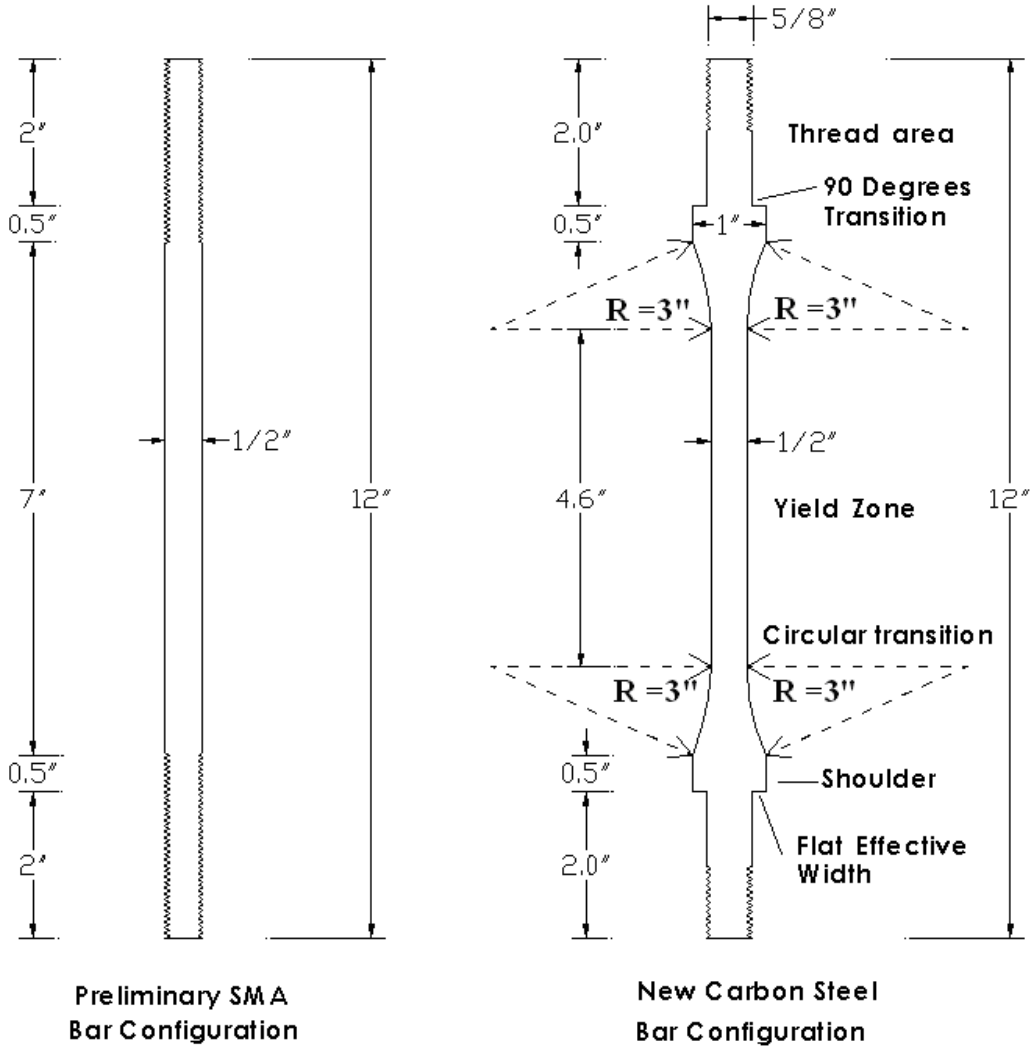

Fig. 7.17 - Plain Round ½-in. Diameter Bar and Optimized BCE New Bar Configuration.

The fuse bars described in Chapter 8 use this bar configuration for all specimens. The only variation between the three bar types is the length of the yield zone. Test specimens and the three bar types are further described in Chapter 8.

Based on the results from the finite element analyses it was found that compared with the plain round bars the stress demands were significantly reduced by the new bar shape, and that the stress demands at the first thread of the threaded tension nut area and at the 90 deg. transition between the shoulder and the threaded area were small enough to conclude that the new bar configuration will significantly improve the behavior of the brace composite element fuse.

7.4 Brace Composite Element Matrix Material

As used on the preliminary fuse study with shape memory alloy rods, urethane was selected as the matrix material due to its elastomeric properties. Optimal elastomeric materials for the fuse matrix should have a very low compression set, which is the degree to which materials do not fully recover their original shape after they have been subjected to compression stress over a long period of time. Urethane has a very low compression set, generally 30% or less, which is very beneficial to the overall performance of the BCE fuse as it is expected that a urethane matrix will perform appropriately under compression loads. A matrix made of an elastomeric material with a very low compression set was also very convenient because the matrix was intended to be re-used several times after bars embedded in the matrix failed.

Another property to consider when selecting the best-suited elastomeric material is the durometer, which indicates the hardness of the material, and is defined as the material resistance to permanent indentation. The durometer is an important

parameter because the urethane matrix must be capable of properly confining the bars. Even with the confinement provided by the carbon fiber reinforced polymer (which stiffens the matrix under compressive stresses) if the hardness of the matrix is not adequate the bars could buckle prematurely inside the matrix. Post-buckling deformations could cut into the matrix permanently damaging it. Unlike the urethane matrix used for the preliminary fuse tests, which was made with 70 durometer urethane, the urethane durometer selected for the full size BCE fuse specimens was a shore "A" 80 durometer castable urethane. The shore testing (durometer) on this type of urethane complies with ASTM D 2240 standards. Using castable urethane provided flexibility in terms of the matrix shape and also reduced fabrication costs because most of the cost of the urethane for the first study was associated with the fabrication of the molds to cast the desire shape, which made the fabrication of a limited amount of specimens particularly costly.

A second option for elastomeric material considered was Sorbothane. This material has good shock absorption, good memory, vibration isolation and vibration damping characteristics. While many materials exhibit one of these characteristics, Sorbothane combines all of them in a stable material with a long fatigue life. Although sorbothane absorbs considerable amounts of energy, which would be very beneficial for the fuse as an energy dissipation device, its shore "A" durometer is approximately 20, which was too low for the BCE fuse matrix applications.

A 94 durometer was also available on the market and it was actually used to cast one matrix. The drawback of using this higher durometer urethane is that

workable time is much less than that of 80 durometer urethane, making fabrication of the matrix more difficult as the liquid urethane cures too fast. This is very critical for large size matrices that require significant amount of liquid urethane. When the 94 durometer castable urethane matrix was fabricated it actually cured so fast that it hardened before the entire matrix was cast. After conversations with the manufacturer it was found that while the temperature of the castable mix increases its workability, it takes longer time to cure which allows for more time to pour the mix into the molds. The 80 durometer castable urethane was still selected over the 94 durometer urethane because even under a low temperature environment the 94 durometer castable urethane takes one third of the time it takes the 80 durometer to cure. To account for any uncertainties during fabrication it was decided that workable time was critical to the successful fabrication of the matrices.

Another advantage of the castable urethane material selected is that the size of the matrix can be increased or the matrix itself can be repaired if necessary by casting new urethane inside or around old matrices by using primers, which are available in the market. These primers create perfect bonding conditions between old urethane already cured and new urethane allowing for cold joints that will not affect the performance of the urethane matrices. These primers were successfully implemented to increase the size of a few urethane matrices and the primers also came in handy when a few urethane parts could not be finished with a single batch mix on a same day.

7.5 Brace Composite Element Matrix Shape

A matrix with cylindrical shape is ideal to accommodate the bars and also simplify its interaction with the fiber reinforced polymer layer. The matrix was intended to be re-used after the embedded bars had failed. Therefore, the shape of the matrix was chosen so that the bars would not be in contact with a urethane block, but instead the bars were embedded in individual urethane cores and then the bars embedded in these inner cores were placed into the main urethane matrix as shown in Fig. 7.18.

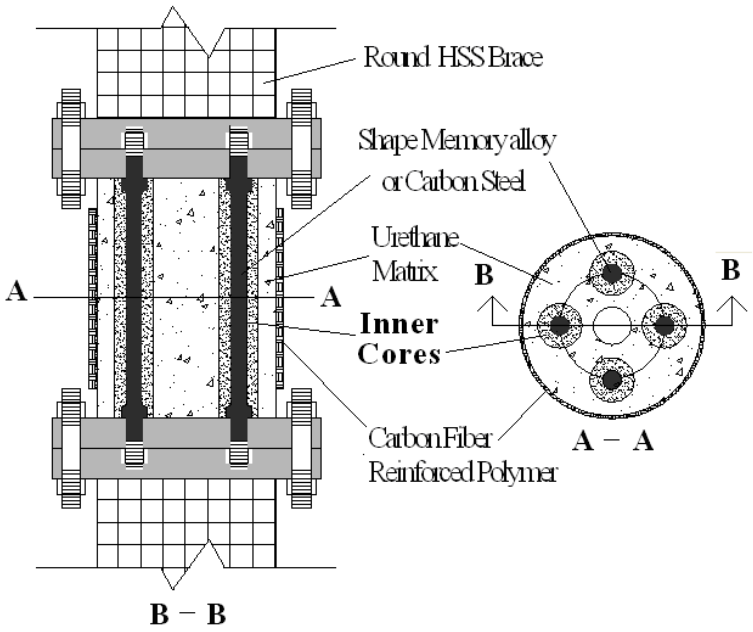

Fig. 7.18 – BCE Fuse Configuration with Inner Cores.

The purpose of the inner cores was to protect the main matrix block from any deterioration caused by the bars during repetitive post-buckling deformations. After

the fuse had failed the urethane block could be reused by replacing the old bars with their respective inner cores. Under tension the confining system is inactive and the load is carried entirely by the bars, therefore damage to the main matrix is not a concern.

A 5-in. diameter and 5-in. tall shore A 70 durometer urethane matrix was tested under monotonic compression to verify the hyperelastic properties of the material. The same cylindrical urethane matrix was heavily loaded in compression to confirm that this material was able to recover its original shape after repetitive compressive stresses. Results from applying compressive loads several times determined that the matrix performance was not altered by the repetitive high compressive stresses. Based on these experimental results an average stress-strain relationship was calculated resulting in modulus of elasticity for the unconfined block of 840 psi. These measured stress-strain values are shown in Table 7.4.

Nominal Stress (ksi)	Nominal Strain (in./in.)
0.00	0.00
170.75	0.05
341.50	0.10
512.25	0.15
683.00	0.20
853.75	0.25
1024.50	0.30
1195.25	0.35
1366.00	0.40

Table 7.4 - Stress-Strain Monotonic Compression Values for 70 Durometer Urethane Matrix.

A second matrix block made with the same material properties, also 5-in. tall, was tested. The second block had a smaller diameter equal to 2.75-in., and it was also subjected to monotonic compression several times. Experimental results were superimposed to those obtained from the 5-in. diameter matrix initially tested revealing a similar the same stress-strain relationship (Fig. 7.19).

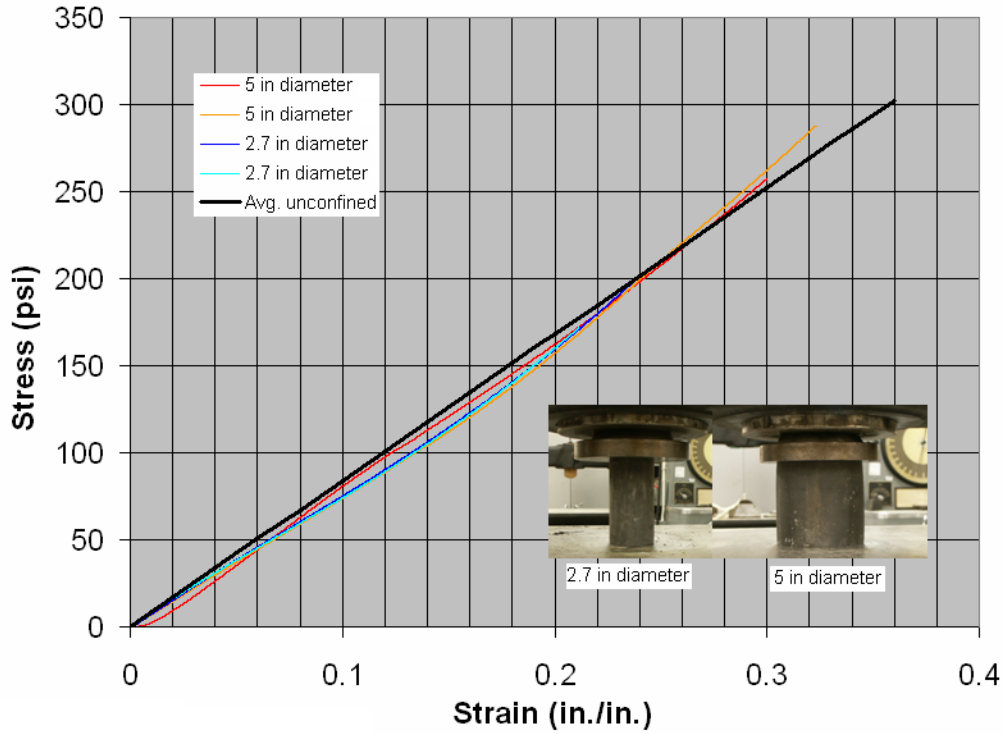

Fig. 7.19 - Monotonic Compression Tests for Unconfined Urethane Blocks.

These experimental results were modeled using finite element analysis in order to optimize the diameter of the urethane matrix. To simulate the urethane hyperelastic properties with a finite element model, material models that mathematically describe the behavior of rubber and elastomers were implemented. There were two mathematical models that are extensively used in the finite element analysis of rubber and elastomers:

a) Mooney-Rivlin model [Lobo, and Bethard, 2006].

b) Ogden model [Lobo, and Bethard, 2006].

The Mooney-Rivlin model [Lobo, and Bethard, 2006] is by far, the most common model used today because it presents many advantages in terms of being able to handle the different kinds of behaviors observed in rubbers. The Ogden model [Lobo, and Bethard, 2006] also has great versatility in fitting the complex behavior of rubber and elastomeric materials.

The choice between these models is often governed by the goodness of fit to the actual data. Results from FEA using both mathematical models were superimposed to the experimental data. Results are shown in Fig 7.20 and Fig. 7.21.

The Mooney-Rivlin mathematical model reproduced the experimental behavior of the matrices with great accuracy and simulated the actual experimental behavior of the urethane cylinders much better than the Ogden model. Therefore this mathematical model was adopted in all finite element analysis of the urethane matrix.

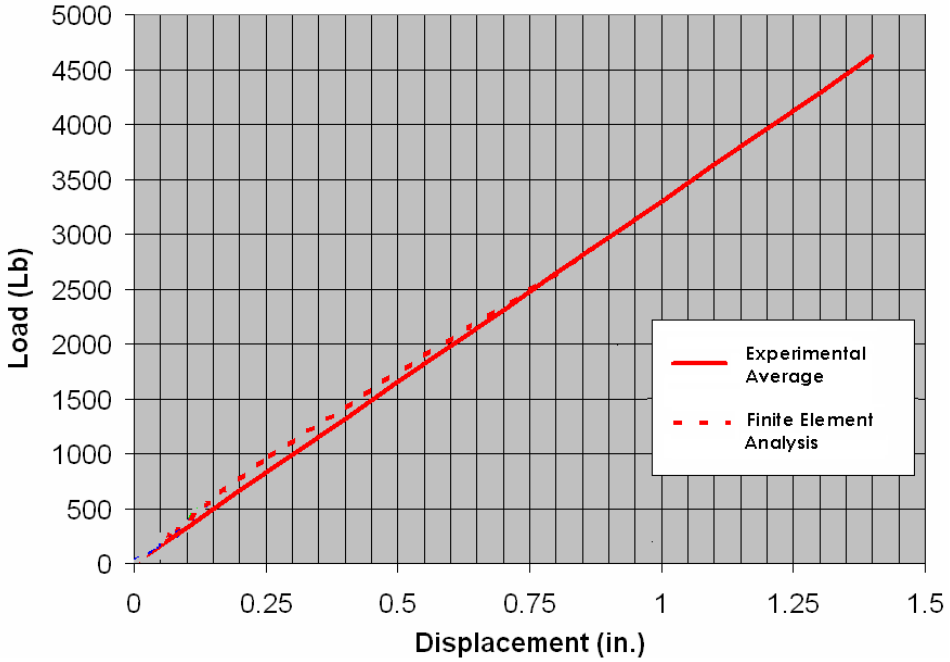

Fig. 7.20 - Mooney-Rivlin Model.

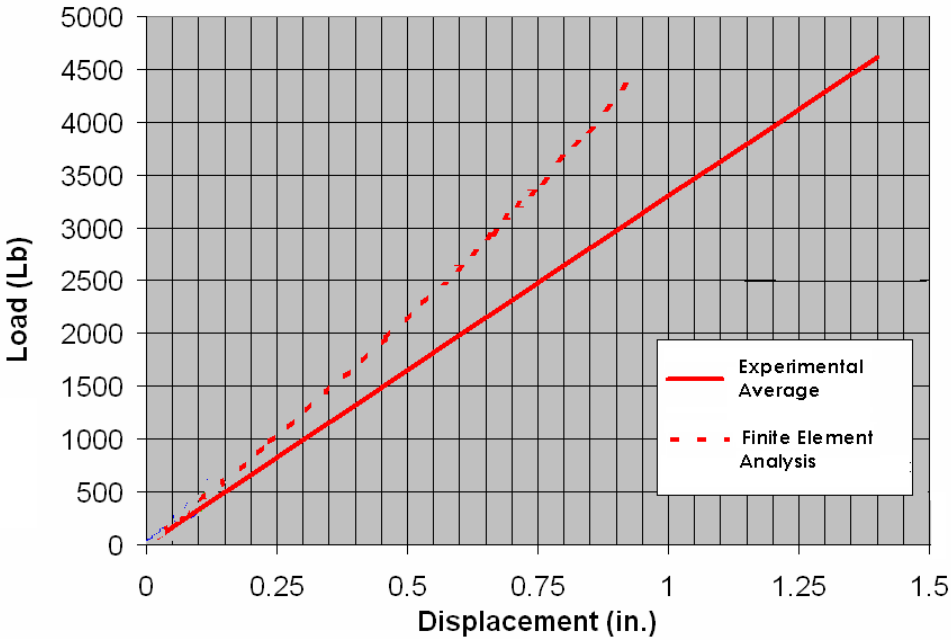

Fig. 7.21 - Ogden Model.

Because the urethane durometer used to experimentally investigate the behavior of the urethane matrix and optimize its performance was lower than the 80 durometer urethane selected for the BCE fuse, the modulus of elasticity was expected to be larger than that obtained from the 70 durometer cylinders. Even though this increment was not expected to improve the matrix stiffness significantly, a small urethane cylinder was fabricated and tested with the actual castable 80 durometer urethane used in the fuse. Results were use to determine its modulus of elasticity and to define the stress-strain relationship used in finite element models with the hyperlastic Mooney-Rivlin mathematical model for more accurate computational results. By increasing the urethane durometer from 70 to 80 durometer, the modulus of elasticity improved from 840.4 psi to 3415 psi. The experimental stress-strain relationship results are tabulated below.

Nominal Stress (ksi)	Nominal Strain (in./in.)
0.00	0.00
170.75	0.05
341.50	0.10
512.25	0.15
683.00	0.20
853.75	0.25
1024.50	0.30
1195.25	0.35

Table 7.5 - Stress-Strain Monotonic Compression Values for 80 Durometer Urethane Matrix.

These experimental and computational results presented above show that the height of the matrix relative to its diameter does not affect its compressive properties and that the matrix could be as short or as tall as the bars require. Additionally these results demonstrated that urethane was an appropriate elastomeric material with adequate compression set for use in the fuse.

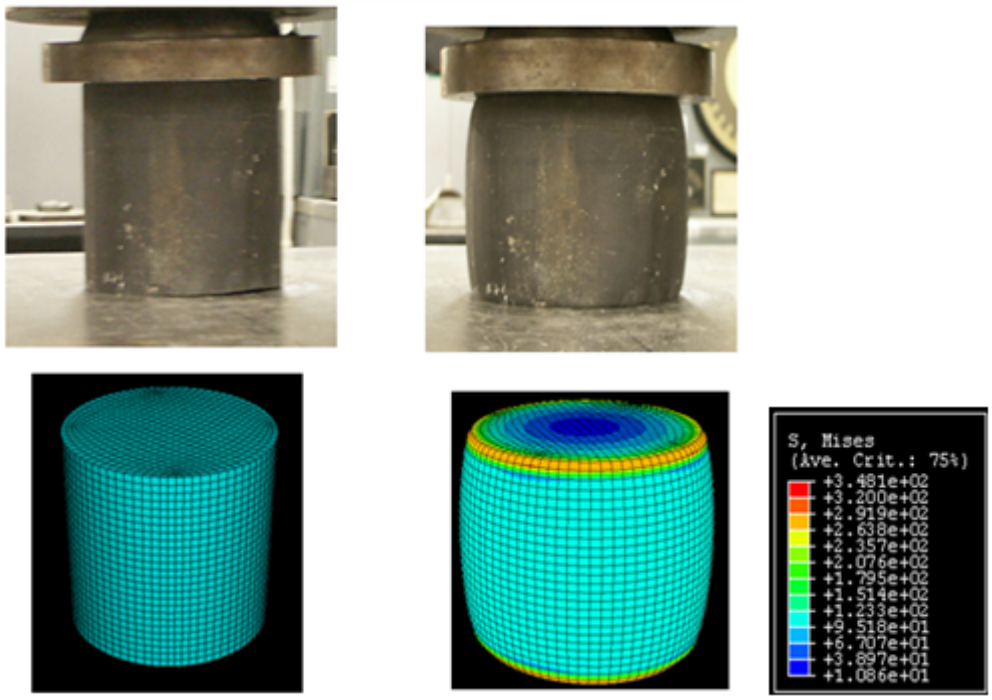

Fig. 7.22 - Experimental and Computational Undeformed and Deformed Shapes.

7.6 Brace Composite Element Carbon Fiber Reinforced Polymer Material

There were two fiber reinforced polymer (CFRP) systems considered: a) wet lay-up, and b) pre-preg (Pre-Impregnate). The wet lay-up system consists of dry unidirectional or multidirectional fiber sheets or fabrics that are impregnated on-site with a saturating resin. This saturating resin is used to provide a binding matrix for the fiber and also helps bond sheets to the surface of the element that is reinforced by it. Pre-preg or pre-impregnated fabrics, in this case with an epoxy resin at the shop, are much easier and cleaner to work with because they already have resin, but they have to be stored under special conditions such as temperatures below 32 F, and this

could increase fabrication costs. Storage was not difficult and due to fabrication simplicity and availability the pre-preg system was chosen over the wet lay-up.

The preliminary fuse with the SMA rods tested used a prepreg system produced by Cytec Engineered Material with a CYCOM 5276-1 toughened epoxy resin that has a service temperature range from -75 F to 260F, and a curing time of 2 hours under 350F in a vented vacuum bag at 20 psi.

A different pre-preg system was used for the full-scale BCE fuse specimens mainly because it was the system available at the time. The new system was a CYCOM 5215 toughened epoxy resin system which had higher fiber content compared to the pre-preg initially used and it also had higher tensile strength.

During the construction of the preliminary small fuses with the SMA rods, the CFRP wrapping sheets were applied directly around the cylindrical urethane matrix so that the fibers were oriented in the hoop direction. The matrix reinforced by the CFRP wrap was subsequently placed in the oven for two hours at 350 F to cure the CFRP wrap. After two hours it was found that even though the urethane matrix did not melt in the oven, the high temperatures affected the urethane, bubbles formed on the top of the material and the texture of the matrix changed too. Although matrix mechanical properties may have not changed, the concern was that the rod embedment holes inside the matrix could easily alter their shape due to the high temperatures making it difficult to insert the bars into the matrix. One alternative was to cure the CFRP with the rods embedded in the matrix, which would make the holes

retain their shape during curing of the CFRP at high temperatures. However, as the rod temperature increases, the urethane around the bars melts, damaging the material.

A feasible solution was to fabricate the CFRP wrap on a metal form, cure it, and then remove the metal form after curing. The CFRP wrap was placed around the urethane matrix by slowly pushing the wrap down until it reaches the desired location. The CYCOM 5276-1 pre-preg system was perfect for this construction method because the cured FRP was stiff enough to resist friction between the CFRP wrap and the urethane matrix as the wrap slid down the matrix surface. The CYCOM 5215 was not stiff enough to resist the friction with the urethane matrix, so this material had significant damage at the CFRP wrap edges. To prevent this type of damage the CFRP wrap was fabricated on a form with a slightly larger diameter than the outside diameter of the urethane matrix.

This alternative construction technique was experimentally studied by making CFRP wraps with an inside diameter approximately 1/8-in. larger than the diameter of the matrix with two confinement heights: 1.5-in. and 3-in. The urethane matrix used was the same 5-in. diameter and 5-in. tall shore “A” 70 durometer urethane matrix tested under monotonic compression to verify hyperelastic properties. The load-displacement relationship shown in Fig. 7.23 labels this alternative construction technique as method 2, and it shows that the matrix behaved as an un-confined system up to 1000 lb, when the matrix stiffness finally increased as it expanded in the transverse direction making contact with the CFRP wrap. The same matrix and same confinement heights were tested with CFRP wraps in full contact with the urethane

matrix at zero load and the test results are superimposed in Fig. 7.23 and labeled as method 1. For method 1 it did not take more than 250-lbs. to make the urethane matrix-CFRP wrap confining system active as compressive load was applied.

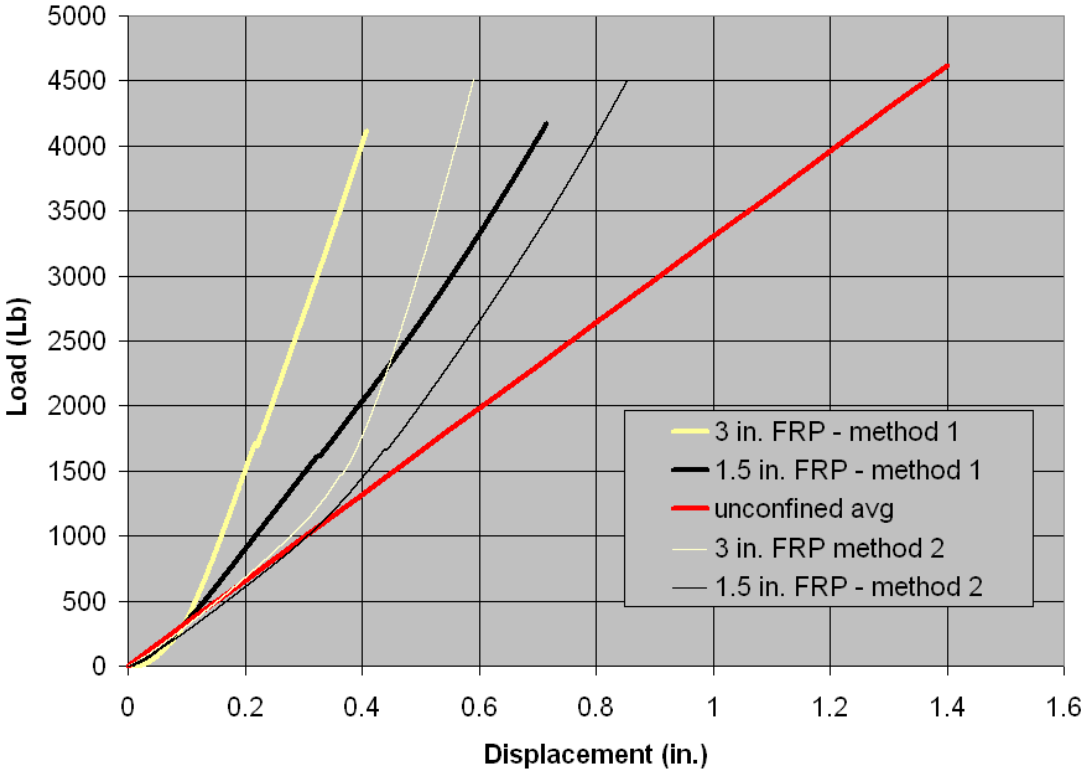

Fig. 7.23 - Confined Matrix Monotonic Compression Test Results, Construction Methods 1 and 2.

Without full contact between the matrix and the CFRP at zero compressive load, the bars are left partially unconfined up to a certain point during the compressive portion of the load cycles, until the fuse takes enough compressive load to make the urethane matrix expand in the transverse direction. Because the urethane

by itself does not provide sufficient stiffness to confine the bars, this second construction method could compromise the successful performance of the fuse. The fuse requires that the confinement system becomes active immediately after compressive loads are applied; therefore this second alternative construction technique was considered to be inadequate.

A new fabrication method had to be devised where the CFRP could be cured with the matrix at lower temperatures. The approach taken to develop this new fabrication method was to cure the CFRP at lower temperatures for a longer period of time. Small pieces of urethane were subjected to different temperatures below 350 F for 24 hours until it was found by visual inspection and touch that a temperature of 120F was an adequate temperature to cure the CFRP without altering properties of the urethane matrix. The question then remained of how long of a cure at 120F was necessary. Several CFRP coupons were fabricated and placed in the oven at 120F. Five CFRP test coupon were tested after one day and the CFRP tensile capacity showed that one day at 120F was not sufficient to develop an adequate tensile capacity of the CFRP. Five more test coupons were tested every day until it was found that by the sixth day the CFRP test coupons reached the desired tensile capacity. A urethane matrix 5-in. tall and with a 5-in. in diameter was tested under monotonic compression and then placed in the oven at 120 degrees F for six days. After curing the CFRP, the system was retested and it showed a similar stress-strain linear relationship as obtained before with the first construction method. Thus, this new fabrication procedure was to apply the CFRP sheets around the urethane matrix

to fabricate the wrap, and place the matrix with the CFRP wrap in the oven at 120F for six days to cure the CFRP. This new fabrication method neither complies with curing methods recommended by the composite material provider nor follows curing standards implemented by the composites industry but it experimentally proved to be an adequate curing method that provided satisfactory properties from the CFRP layer for the intended brace composite element application. It is likely that the CFRP was not really cured and did not exhibit typical stress-strain behavior. Again, the stiffness and strength achieved was adequate to contain the polyurethane matrix, and therefore adequate to task described herein.

Approximately 50 test coupons were fabricated and tested according to ASTM standards D3039/D3039M-00. These coupons were made from three different CFRP CYCOM 5215 batches and were cured at 120F during 6 days and then tested under monotonic tension. Of the test coupons tested 84% reached the desired tensile strengths. The other 16% of the test coupons did not perform well under tensile loads mainly due to poor grip between the coupons and the testing equipment, and were neglected. The linear relationship for a CYCOM 5215 system shown in Fig. 7.26 is the average of the 42 test coupons that performed well under tensile loads. Most of the test coupons failed between 90 ksi and 100 ksi. These results also showed that even though the CFRP layer strength obtained by implementing the 6 days 120 degrees F curing method was adequate for the brace composite element application, this strength and the CFRP layer stiffness was still low compare to the properties

given by the manufacturer [Cytec, 2003] for this composite material when cured by recommended methods.

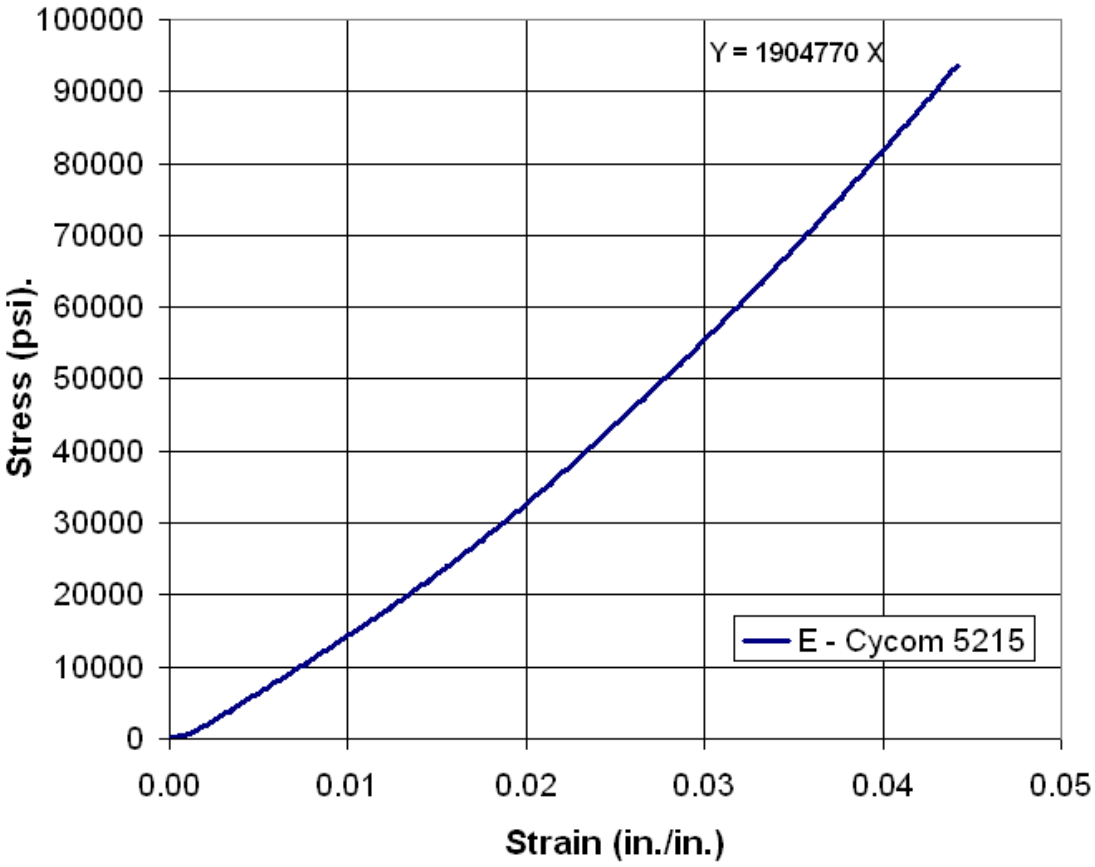

Fig. 7.24 - Average Pre-Preg FRP Systems Stress-Strain Relationship.

7.7 Carbon Fiber Reinforced Polymer Thickness and Height

The effectiveness of the confining system is determined by the height of the CFRP confining layer relative to the urethane matrix height. The effect of the CFRP confinement relative to the matrix height was experimentally determined by testing

the 5-in. tall and 5-in. diameter 70 durometer urethane matrix with a 1.5-in. confining layer over the 5-in. tall matrix. This corresponds to a confinement ratio of 30%. A second test was conducted with a 3-in. confining layer over the same 5-in. tall matrix, for a confinement ratio of 60%. The CFRP used was the CYCOM 5276-1 pre-preg system, and the confinement wrap was 0.08-in. thick. The experimental results were reproduced through finite element analysis using the Mooney-Rivlin mathematical hyperelastic model used on the analysis of the urethane matrix. Again the Mooney-Rivlin model matched the experimental results as it is shown in Figs 7.25 thru7.27.

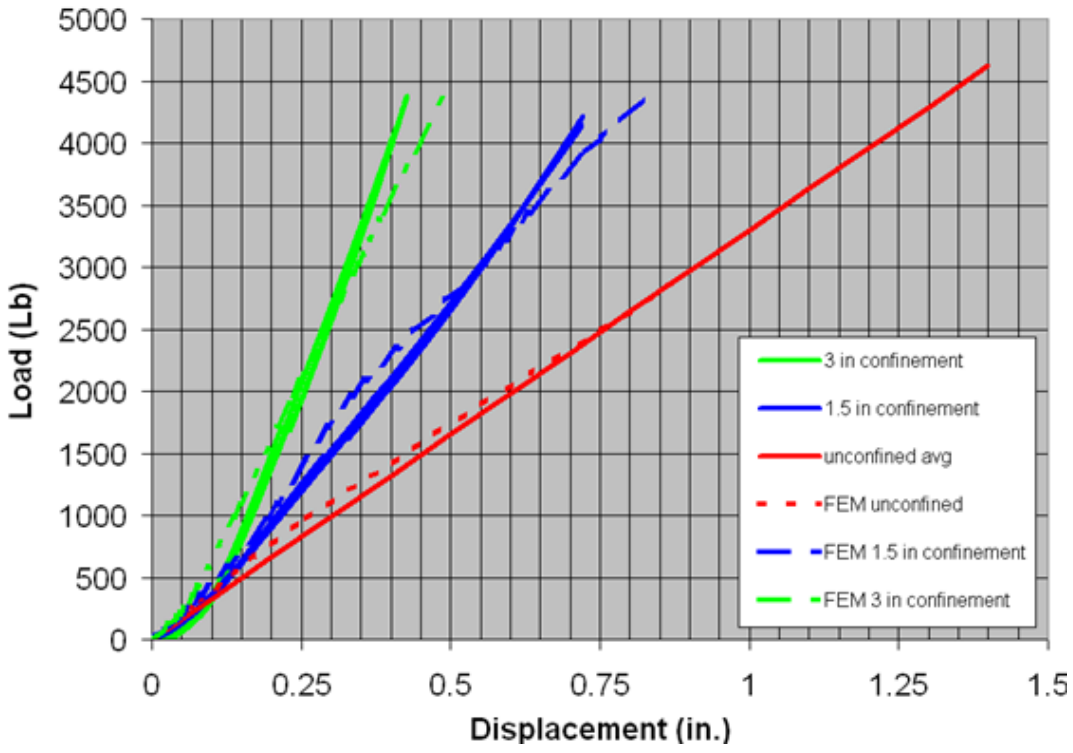

Fig. 7.25 – Confined Matrices Experimental and Computational Stress-Strain Relationships.

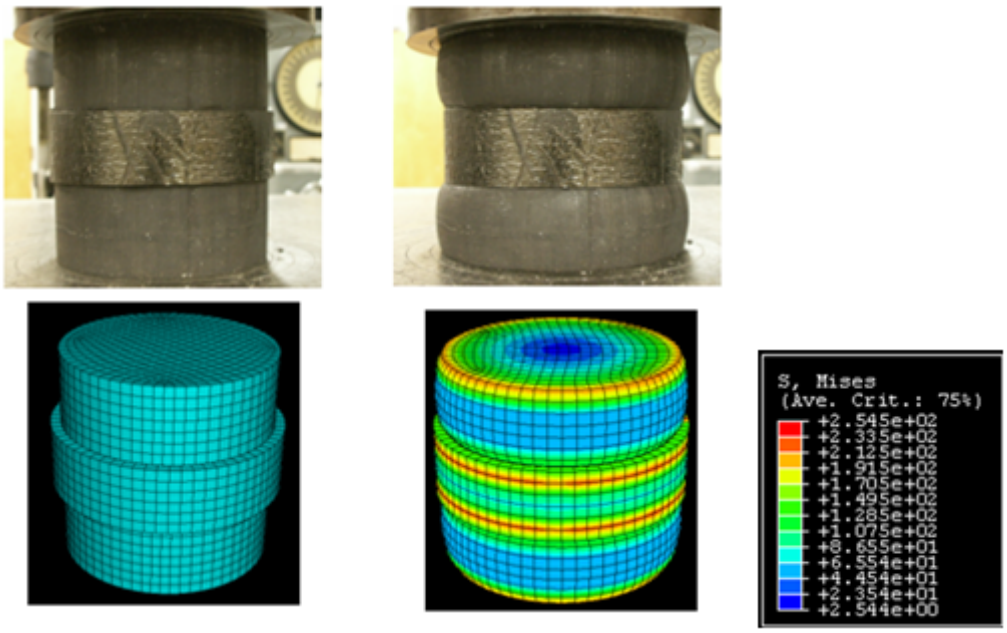

Fig. 7.26 – FEM Deformed and Undeformed Shapes, and Experimentally Observed Shape for 30% Confinement.

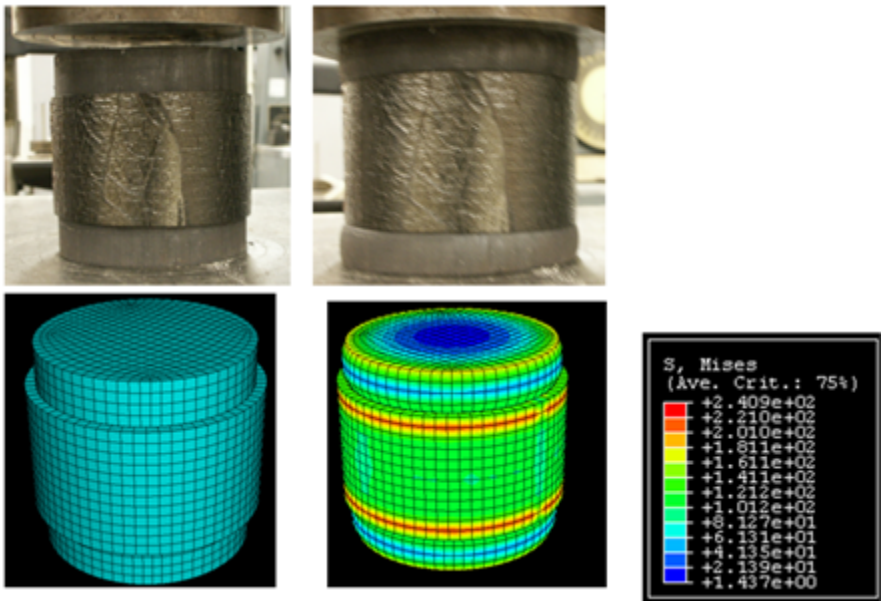

Fig. 7.27 - FEM Deformed and Undeformed Shapes, and Experimentally Observed Shape for 60% Confinement.

These experimental and computational results confirm that the stiffness of the urethane matrix/CFRP reinforcing wrap confining system is a function of the height of the confining layer relative to the urethane matrix. As the confinement ratio increases the effectiveness of the confining system improves.

Although it is recommended that the urethane matrix be almost completely confined by the CFRP wrap, 100% confinement is not desired due to: 1) the steel plates transferring the load from the bracing system to the fuse will make contact with the edges of the CFRP before the fuse is subjected to inelastic deformations and therefore will damage the CFRP wrap and increase the capacity in compression making it much higher than the capacity in tension, and 2) in order to make the confinement system active, the urethane matrix needs to be subjected to compressive loads so that it expands until it makes full contact with the CFRP wrap, which restrains the matrix from expanding further. As this happens the CFRP layer starts to deform which activates the entire confining system that restrains the lateral deformation of the bars. With a 100% confinement the load will be taken by the edges of the CFRP layer without the urethane matrix taking major compressive loads, resulting in an inadequate confining system because the stiffness of the urethane matrix does not increase.

For the above stated reasons a 100% confinement is not adequate because it would keep the fuse from its intended purpose as an energy dissipation device and as novel seismic connection system. A high confinement ratio is still recommended. Confinements in the range of 90%-98% of the matrix height should be provided

depending on the fuse size. The rationale for this recommendation is discussed in Chapter 8.

The effect of the CFRP wrap thickness on the confinement was also experimentally studied. The same 5-in. tall 5-in. diameter 70 durometer urethane matrix was tested with a 60% confinement made of CYCOM 5215 pre-preg CFRP. Two wraps were fabricated, one with a 0.08-in. thickness and a second with a 0.04-in. thickness. The same tests were repeated with the same materials and matrix height, but with a smaller 2.5-in. urethane matrix diameter. The CFRP wraps were fabricated on the urethane matrices and cured at 120 F during 6 days as recommended. Experimental results from these tests showed that the stiffness of the confining system did not improve significantly by increasing the thickness of the wrap, as the confinement height was maintained constant. As mentioned in the analysis of the urethane matrix diameter, the matrix did not have a major influence on the overall behavior of the confining system, but as the diameter decreases the load transfer to the CFRP layer increases.

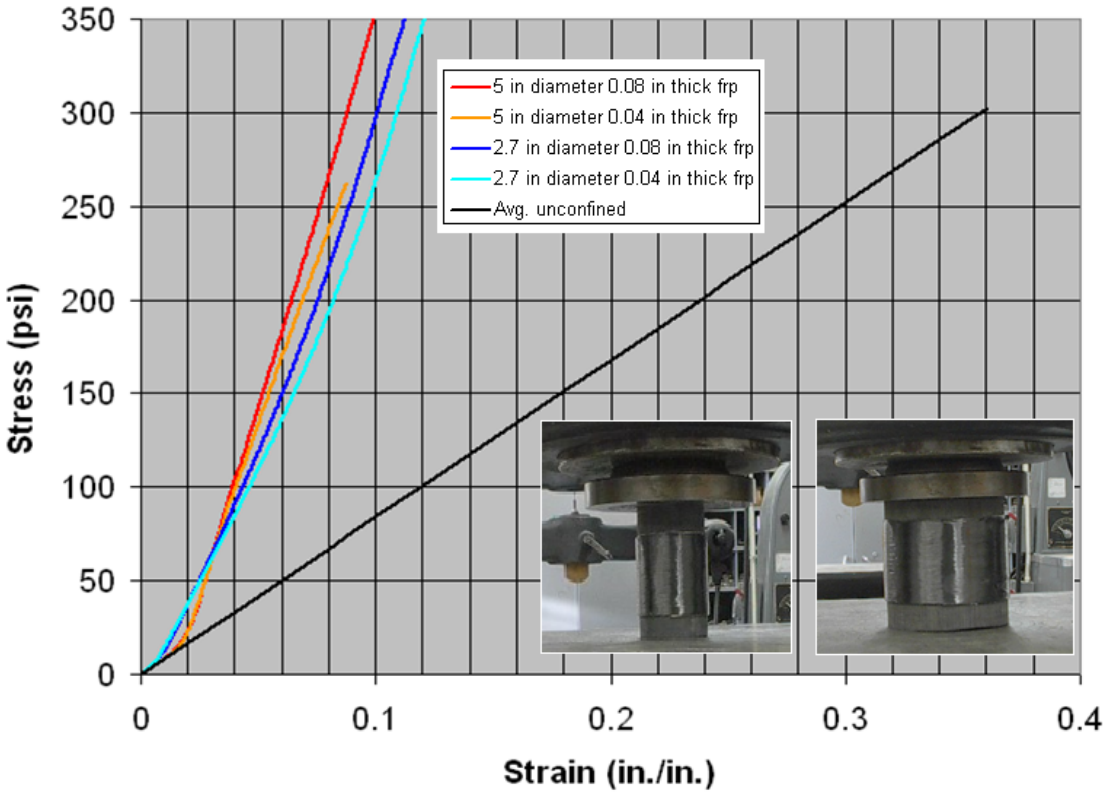

Fig. 7.28 - FRP Thickness Experimental Test Results.

The thickness of the CFRP layer is a function of the maximum axial load that is transferred through the urethane matrix to the wrap in the form of hoop stresses. Smaller urethane matrix diameters will require thicker CFRP wraps, but nevertheless the effectiveness of the CFRP layer on confining the urethane is mainly controlled by the confinement percentage with respect to the matrix height, and the only requirement in terms of CFRP thickness would be that the wrap should be thick enough to avoid failure of the CFRP.

7.8 Design Procedures

Design calculation for the BCE fuse presented in this section will be limited to the local capacities of the fuse. The interaction between the fuse elements and the bracing system were already described in Chapter 4 for the RXS fuse, and the BCE fuse interaction with the bracing system is intended to be similar if not exactly the same. Therefore only explicit calculations concerning the design of the BCE fuse are shown in the following pages. Design calculations are made for the following fuse size:

1-Bar Specimen	
Matrix Height	8 in.
Confinement	7.75/8 = 96.88%

Table 7.6 - 1-Bar BCE Fuse Dimensions.

7.8.1 Fuse Tensile Capacity

The BCE fuse system could be made with four or more bars depending on the bar diameter, tensile capacity required, and brace size. For the experimental matrix the 4-bar configuration was adopted, but the design calculations are based on a 1-bar BCE fuse specimen. The bar tensile capacity calculated using a procedure similar to that used with any steel shape:

$$Yielding\_capacity = 0.9 \cdot Ag \cdot Fy \qquad \text{<Eq. 7.8>}$$

$$Fracture\_capacity = 0.75 \cdot Ae \cdot Fu \qquad \text{<Eq. 7.9>}$$

The tensile force is fully taken by the bars because there is virtually no bonding between the bars and urethane matrix and because there is no confining effect on the matrix when loaded in tension and elasticity of the urethane is very low. Accordingly the tensile capacity is governed by:

- Bar yield strength.
- Bar diameter.
- Number of bars.

Four carbon steel ½-in. diameter bars with F_y = 36 ksi and F_u = 58 were selected for the fuse to comply with the loading range of the testing frame. Therefore the tensile capacity of a one bar fuse is:

$$Yielding\_capacity = 0.9 \cdot p \cdot \left(\frac{0.5}{2}\right)^2 in^2 \cdot 36ksi = 6.4kips \quad \text{<Eq. 7.8>}$$

$$Fracture\_capacity = 0.75 \cdot p \cdot \left(\frac{0.5}{2}\right)^2 in^2 \cdot 58ksi = 8.5kips \quad \text{<Eq. 7.9>}$$

The tensile capacity of the bar is not influenced by the bar length but rather by its cross section area. However, the bar length will determine the desired elongation before the fuse reaches its yield strength or the total fuse required elongation before it fractures.

7.8.2 Fuse Buckling Capacity

When loaded in compression and restrained from buckling by the urethane matrix/carbon-fiber-reinforced-polymer confining system the bars carry most of the axial load. As recommended above, the urethane matrix should not be fully confined by the CFRP since it is required that the matrix takes axial compression and expands to make contact with the CFRP layer, which makes the confining system active. Therefore there will always be an unconfined small portion of the bars, approximately 5% of their length.

The design of the fuse for buckling is based on the assumption that the buckling restraint system fully braces the bars against lateral buckling, and the strength of the bars in compression is controlled by the yield strength of the metal. Furthermore deformations beyond the yield point will take place without a significant reduction in strength.

Depending on the slenderness of the bars, the first, and in some instances higher buckling modes are expected to be eliminated by the confining system (Fig. 7.29). Deformations patterns of the bars are expected to be a second or higher buckling mode, depending on the effectiveness of the confining system.

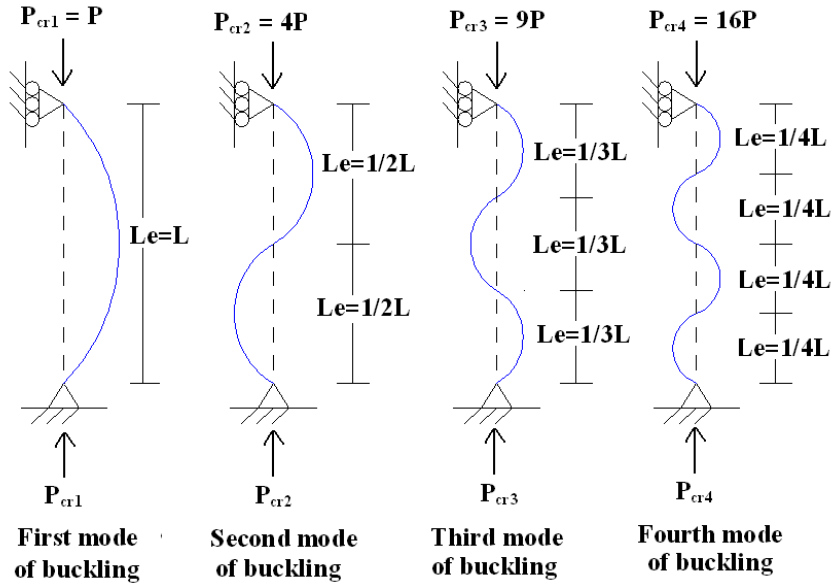

P_{cr} = Axial load at buckling.

L = element length.

L_e = equivalent element length.

Fig. 7.29 - First Four Modes of a Pin-Ended Column.

The AISC seismic provision [AISC, 2005], states that for slenderness ratios ***KL/r*** less than 25 the buckling capacity is equal to the yield strength.

$$KL/r < 25, \quad F_{cr} = F_y \qquad \text{<Eq. 7.10>}$$

K = effective length factor

L = element length

R = element radius of gyration

F_{cr} = critical buckling stress.

F_y = yield strength.

Accordingly, as an equivalent length factor ***K*Le*** decreases with higher buckling modes, the bar buckling capacity increases. For a moment restraint connection ***K*** is 0.5, and ***Le*** can be calculated as follows:

$$Le = L/n \qquad \text{<Eq. 7.11>}$$

n = buckling mode.

L = element length

The goal of the confining system is to restraint the bar from buckling so that the resulting buckling mode when the bar is subjected to repetitive inelastic deformations is high enough to maintain the equivalent length factor ***K*Le*** low.

Buckling Mode "n"	K*Le = KL/n
1	0.500 L
2	0.250 L
3	0.167L
4	0.125L
∞	0

Table 7.7 – Equivalent Length Factor vs. Buckling Mode.

7.8.3 Confining System Design

The CFRP wrap must be thick enough to avoid failure due to the pressure exerted by the radial stresses from the urethane matrix as it is restrained from expansion when subjected to compressive stresses. Since the thickness of the CFRP wrap depends on the hoop stress caused by the expansion of the urethane matrix, expansion and this stress decreases as the urethane matrix diameter decreases, the matrix diameter required is a function of the CFRP thickness and vice-versa. The smaller the matrix diameter the thicker the CFRP wrap needed.

As a general design criterion, it is recommended that a design approach should lean towards a thicker CFRP wrap and a smaller urethane matrix diameter. The urethane matrix should provide enough confinement, meaning that if the matrix diameter is too small, the urethane between bar inner cores will not be enough to avoid significant matrix deterioration after the bars and the inner cores fail. This will make the main urethane matrix unsuitable to be used again. For a one bar specimen a rule of thumb for determining the matrix dimensions is that the urethane matrix shall be composed of a urethane inner core diameter 1.5 times the diameter of the bar shoulder, and a main urethane matrix diameter at least 2 times the diameter of the inner core. This criterion is conservative enough to ensure that enough matrix material is provided to properly confine the bars.

For the given 1-in. shoulder diameter the diameter of the urethane inner core becomes:

$$1.5 \cdot 1 = 1.5in \qquad \text{<Eq. 7.12>}$$

and the diameter of the main urethane matrix becomes:

$$3 \cdot 1 = 3in \qquad \text{<Eq. 7.13>}$$

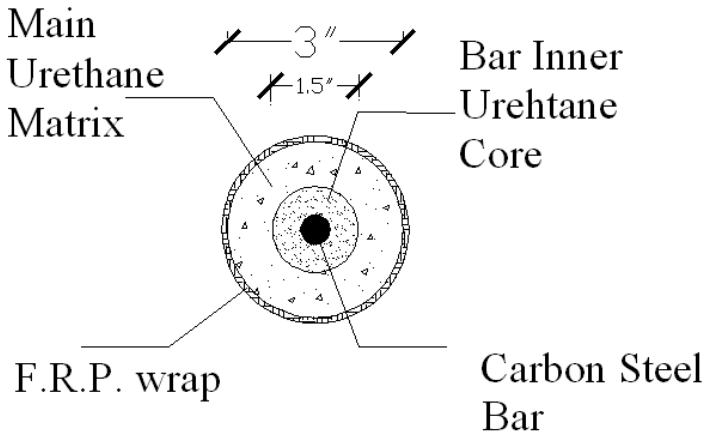

Fig. 7.30 – 1-Bar BCE Fuse Experimental Specimen Cross Section.

For a four bar specimen, which is the case of the second series, the inner core urethane diameter shall also be 1.5 times the bar shoulder diameter, but the main urethane matrix shall be at least 4 times the diameter of the inner core, that is at least 6 times the bar shoulder diameter. The spacing between the center of the fuse and the bar center should be at least equal to the inner core diameter.

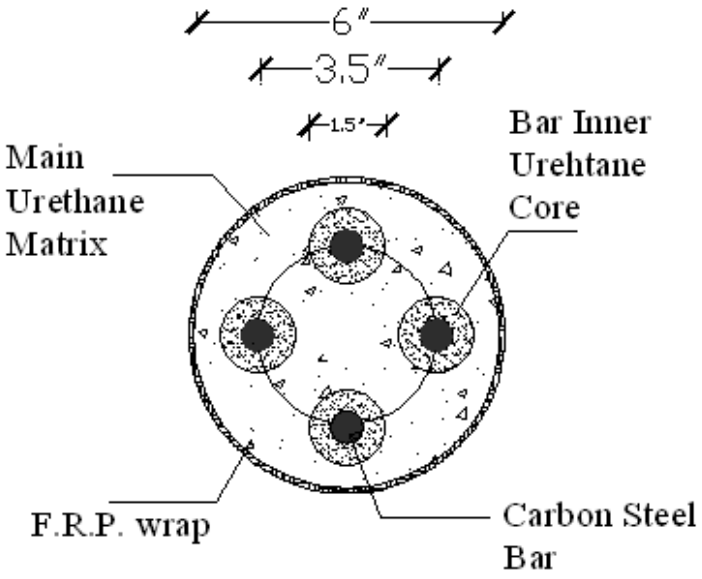

Fig. 7.31 - 4-Bar BCE Fuse Experimental Specimen Cross Section.

The thickness of the CFRP shall be designed so that when the fuse reaches its buckling capacity the CFRP elastic elongation does not go beyond 5% of its elongation at failure. By doing this it is certain that the CFRP elongation will be small enough to assume that the urethane matrix will be fully restrained against expansion once it makes contact with the CFRP wrap and also that the CFRP wrap will not fail since it will be subjected to a maximum of 5 % of its capacity.

It was found from CFRP test coupon results that the CFRP was able to resist stresses of up to 90-100ksi before failure. Because the CFRP showed a linear stress-strain relationship a hoop stress equal to 4605.5 psi for the given properties and a ¼-

in. thick CFRP wrap is approximately 5 % of the maximum 90 ksi stress before CFRP failure, which results in a 0.242% CFRP axial strain.

The highlighted row in Table 7.7 shows the calculated values for the 3-in. matrix diameter and the 0.25-in. thick CFRP wrap selected for the first specimen size. Other rows are shown for bigger urethane matrix diameters as a design reference.

thickness of the FRP wrap =				0.25	in				
r (in)	Area (in^2)	σ compression (psi)	ε longitudinal	ε trans	εr	εσ	Pressure (psi)	σ hoop (psi)	ε cfrp axial
6	28.274	223.878	0.066	0.020	0.020	0.020	95.948	2302.7	1.21E-03
5	19.635	322.384	0.094	0.028	0.028	0.028	138.165	2763.3	1.45E-03
4	12.566	503.725	0.148	0.044	0.044	0.044	215.882	3454.1	1.81E-03
3	7.069	895.512	0.262	0.079	0.079	0.079	383.791	4605.5	2.42E-03

Table 7.8 - CFRP Design Calculation Results.

E_{cfrp} = CFRP modulus of elasticity (cured without following recommended specifications)	1904 ksi
E_{um} = urethane matrix modulus of elasticity	3415 psi
P_{cr} = Critical buckling load	6330 Lbs
ν = Poisson's ratio	0.3
Matrix height	8-in.
r = main urethane matrix radius	3-in.
Area = cross section area of the main urethane matrix	7.07-in^2

Table 7.9 - CFRP Design Calculation Constants.

$\sigma_{compression}$ =6330 Lb / 7.07 in^2 = 895.5 psi <Eq. 7.14>

$\sigma_{compression}$ = axial compression stress apply to the unconfined matrix from the bracing system.

$\varepsilon_{longitudinal} = \sigma_{compression}/E_{um}$. <Eq. 7.15>

$\varepsilon_{longitudinal}$ = 895.5 psi / 3415 psi = 0.262 in./in.

$\varepsilon_{longitudinal}$ = unconfined matrix longitudinal elongation

$\varepsilon_{transverse} = \nu * \varepsilon_{longitudinal}$ <Eq. 7.16>

$\varepsilon_{transverse}$ = 0.3 * 0.262 in./in. = 0.079 in./in.

$\varepsilon_{transverse}$ = unconfined matrix transverse expansion

$\varepsilon_{rr} = \varepsilon_{transverse}$ = 0.079 in./in. <Eq. 7.17>

ε_{rr} = radial strain

$\varepsilon_{\sigma\sigma} = \varepsilon_{transverse}$ = 0.079 in./in. <Eq. 7.18>

$\varepsilon_{\sigma\sigma}$ = tangential strain

Pressure transferred from the urethane matrix to the FRP wrap as the urethane matrix is subjected to compressive stresses and tried to expand is:

$\sigma_{rr} = 1/(1- \nu_r * \nu_\sigma) * (E_r * \varepsilon_{rr} + \nu_r * E_\sigma * \varepsilon_{\sigma\sigma})$ <Eq. 7.19>

where:

Pressure = σ_{rr} <Eq. 7.20>

$\nu_r = \nu_\sigma = \nu_{urethane}$ <Eq. 7.21>

$E_r = E_\sigma = E_{um} = E_{urethane}$ <Eq. 7.22>

therefore the pressure equation becomes:

Pressure = $E_{urethane}$ / /(1- ν^2)*(ε_{rr} + ν * $\varepsilon_{\sigma\sigma}$) <Eq. 7.23>

Pressure = 3415 psi / (1-0.3^2)*(0.32 in./in. + 0.3 * 0.32 in./in.) = 383.791 psi

then:

σ_{hoop} = pressure * r/CFRP thickness <Eq. 7.24>

σ_{hoop} = 384 psi * 3 inch / o.25 inch = 4605.5 psi

σ_{hoop} = Hoop stress.

$\varepsilon_{cfrp} = \sigma_{hoop} / (E_{frp} * 1000)$ <Eq. 7.25>

ε_{cfrp} = 4608 psi /(1904ksi * 1000psi/ksi) = 2.42E-3 in./in.

ε_{cfrp} = Carbon fiber reinforced polymer axial strain.

8 BCE Fuse Experimental Program

The experimental program was intended to study the hysteretic behavior of axially loaded BCE fuse elements. The experimental matrix was divided into a proof of concept preliminary study and two testing series: a first series that examines the interaction between a single bar and the urethane matrix – carbon fiber reinforced polymer (CFRP) confining system, and a second series intended to experimentally verify the behavior of a full size four-bar BCE fuse.

The proof of concept portion of the experimental matrix consisted of a monotonic tension and a monotonic compression test. One bar without the confining system was subjected to monotonic tension. The tensile capacity of the fuse is provided by the metal bars because there is no effective mechanism to transfer tension to the urethane. The compressive capacity of the fuse is provided by the bar, but it is augmented by the confinement system, thus a confined bar was subjected to monotonic compression.

The effect of the following parameters was investigated during the two testing series: bar slenderness, fiber reinforced polymer confinement relative to polymer matrix height (confinement ratio), fuse connection end conditions, axial load eccentricity, and number of bars embedded in the polymer matrix. In total twenty-one specimens were tested under monotonic loads and cyclic loading.

8.1 Experimental Bar Configurations

The elongation capacity of the fuse is a function of the length of the bar yield zone. For this reason three bar configurations were selected for the experimental program, all with the same end details described in Chapter 7, but different yield zone lengths as listed in Table 8.1. The longest bar type was designated with the letter "A" and was 28-in. long with a yield zone length of 20.6-in. The mid size bar type was 20-in. long with a yield zone of 12.6-in. and was designated with the letter "B", and the shortest bar type was designated with the letter "C" and was 12-in. long with a yield zone of 4.6-in.

Bar Type	Length (in.)	Confining System Height (in.)	Yield Zone Length (in.)
A	28	24	20.6
B	20	16	12.6
C	12	8	4.6

Table 8.1 - Experimental Matrix Bar Types.

The bars ends consisted of a 2-in. long 5/8-in. diameter end followed by a 1-in. diameter ½-in. deep shoulder. The shoulder transitions to the ½-in. diameter yield zone through a 3-in. circular radius. Half of the 2-in. long 5/8-in. diameter end is threaded with 11 right hand threads per inch.

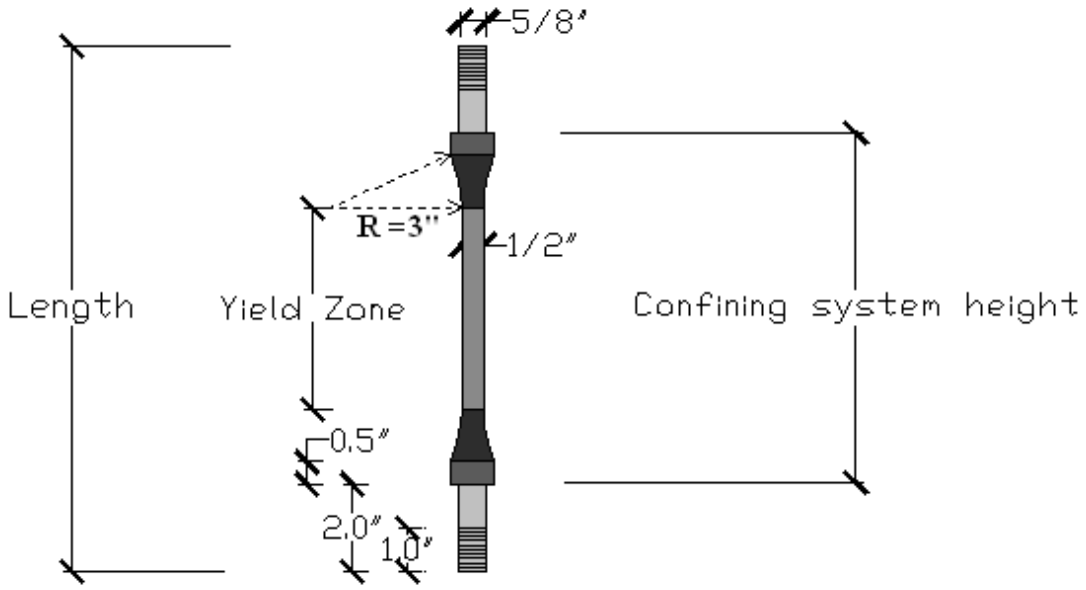

Fig. 8.1 - Generic Bar Configuration.

In total 48 bars were needed to fabricate the 21 test specimens: two bars for the proof of concept monotonic tests, ten 1-bar specimens for the first series, and nine 4-bar specimens for the second series. A total of 15 additional bars were ordered to account for testing uncertainties.

The bars were fabricated from plain round bars using a computer numerical center (CNC) machine with a 1/1000-in. tolerance.

8.2 Preliminary Proof of Concept

Among the three bar types, the mid-size yield zone bar type "B" was selected for the proof of concept study. The monotonic tension test specimen was made of a type B bar without the confining system, and the monotonic compression test

included the entire fuse configuration with the urethane matrix and CFRP reinforcing layer.

The bar ends had to be extended in order to anchor the monotonic tension test specimen in the test frame. The bar ends were extended using two 6-in. long stainless steel one-end threaded studs with a ¾-in.-10 thread size over a 1½-in. length. These studs were made of 75 ksi steel and were connected to the bar ends through a grade 2 steel hex reducing coupler. The coupler was 1½-in. long with a 5/8-in.-11x3/4-in.-10 thread size to fit both the bar ends and the studs (Fig. 8.2).

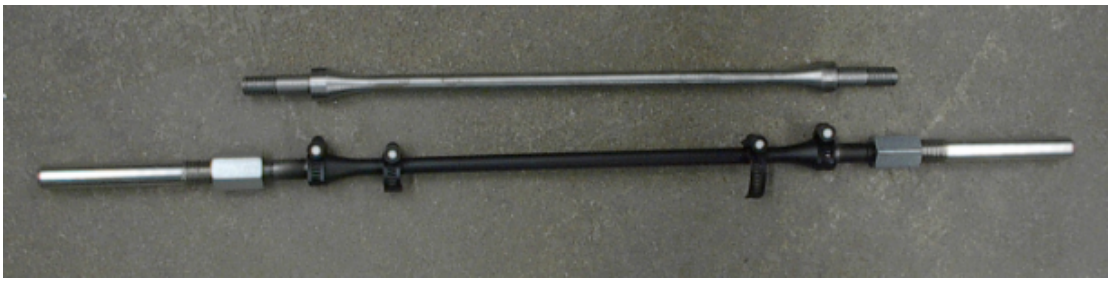

Fig. 8.2 - Monotonic Tension Test Specimen.

The monotonic compression test specimen required 4-in.x4-in. by 1-in. thick steel plates with a ¾-in. hole in the center to uniformly transfer compression load to the bar and the urethane matrix. A ¼-in. thick plate with a 1-¼-in. hole in the center was welded to the matrix side of the 1 inch thick plate so that the urethane matrix is pre-compressed and made full contact with the CFRP layer activating the confining system before the bar started taking compressive load. Additionally, ½-in. thick

slotted washers were used to make a tight fit between the testing equipment and the fuse.

The one end threaded studs were not necessarily required for this monotonic compression test because compression was transferred directly from the steel plates directly to the bar shoulder and urethane matrix simultaneously, but they were included to simulate real fuse fixed end conditions as the testing equipment grips fix the studs by hydraulic pressure (Fig. 8.3).

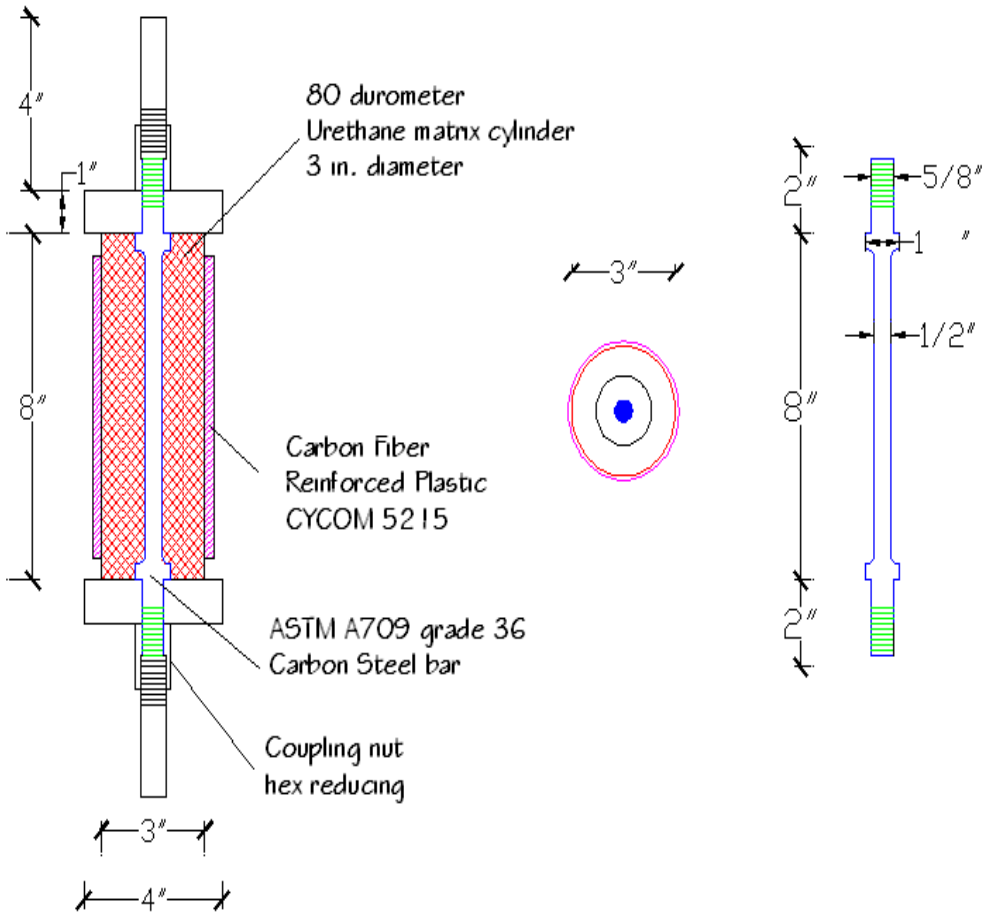

Fig. 8.3 - Monotonic Compression Test Specimen.

8.2.1 Monotonic Tension Test Results

The monotonic tension test loading sequence was to apply a tensile load, reach the specimen yield capacity, and then continue to load until the specimen began to neck down. The monotonic tension test was stopped before fracture to protect the extensometer used to measure the bar elongation.

The stress-strain relationship showed that the yield strength of the bar was not 36 ksi as assumed in Chapter 7, but 50 ksi instead. For the given bar configuration and the higher 50 ksi strength, the specimen strengths were still within the capacity of the testing equipment. The monotonic tension test showed that the bar had very ductile behavior as it was able to elongate 3-in., which corresponds to a strain of 25% over the length of the yield zone, before fracture.

Fig. 8.4 - Monotonic Tension Test Specimen Inelastic Deformation.

The stress-strain relationship obtained from the monotonic test (Fig. 8.5) is typical of the class of steel known as ductile or mild steel. The relationship was linear up to an upper yield point of 47.61 ksi and was followed by a flat region at the lower

yield point measured at 43.5 ksi. This portion of the relationship, known as the yield plateau, ended at approximately 12 times the yield strain, ε=0.00156-in./in. At this point is where the strain hardening area began. The specimen had an ultimate tensile strength F_u of 67.51 ksi. Fracture failure would have occurred after necking if the test had continued (Fig. 8.5).

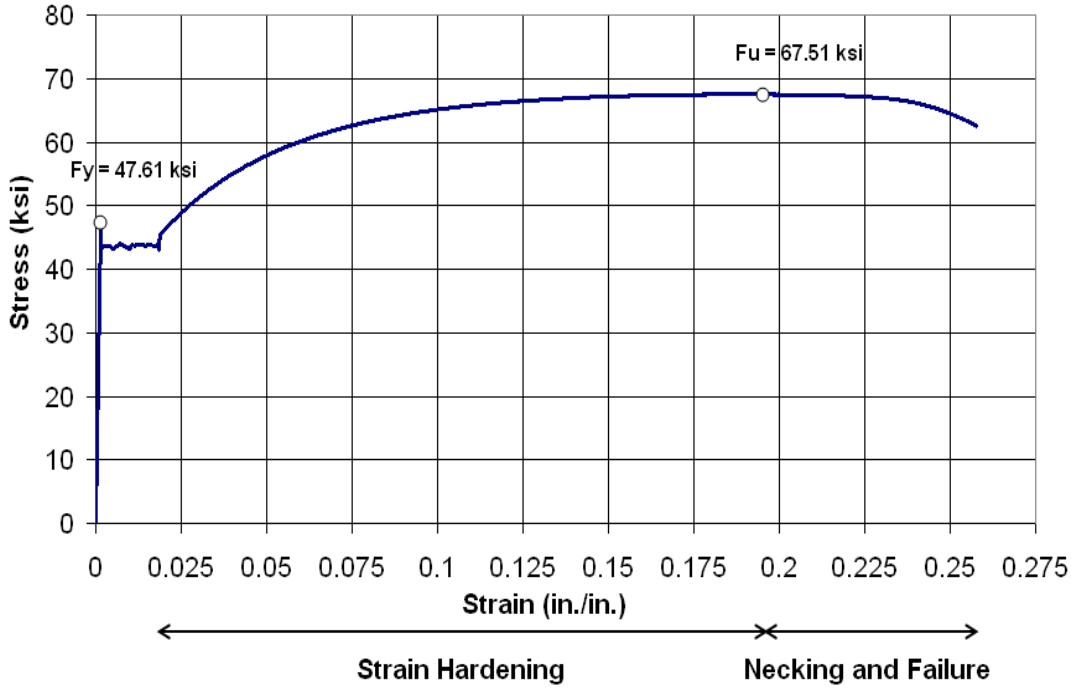

Fig. 8.5 - Stress vs. Strain Relationship for ASTM 709 36 Steel Bar.

The upper and lower yield points are usually treated as a single point, therefore the yield stress F_y was assumed to be 43.5 ksi. The stress-strain ratio or modulus of elasticity, denoted E, is usually 29,000 ksi for structural steel.

Measurements from the monotonic tension indicated that the bar steel was stiffer with a modulus elasticity of 32,900 ksi.

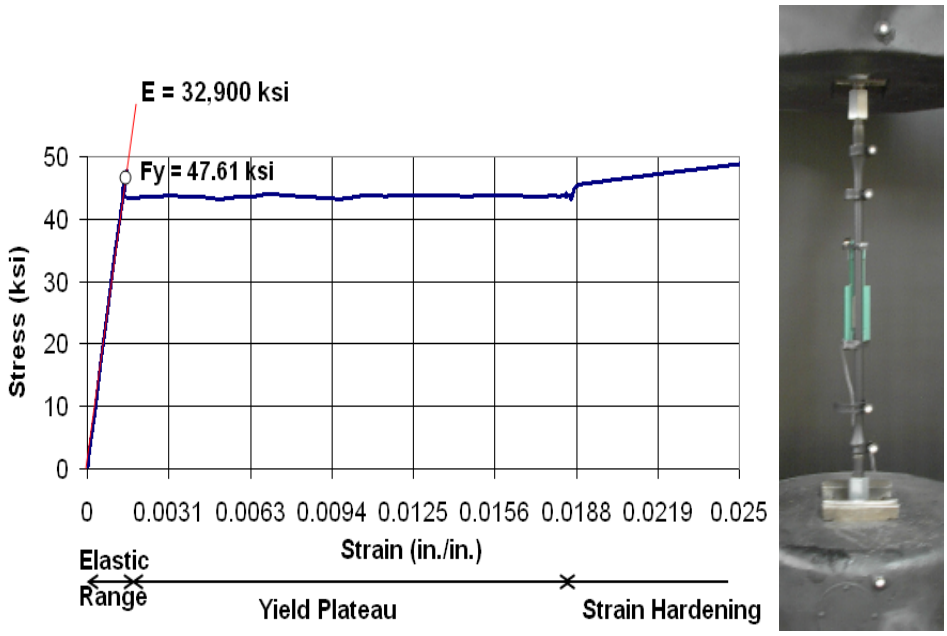

Fig. 8.6 - Bar Stress vs. Strain Relationship – Elastic Range and Yield Plateau Region Close Up.

8.2.2 Monotonic Compression Test Results

The loading sequence for the monotonic compression test consisted of applying axial concentric compressive load. After the buckling capacity was reached, loading continued until the edges of the CFRP layer made contact with the steel plate fixtures.

The fiber reinforced polymer was designed to restrain the expansion of the urethane matrix in the transverse direction as the axial compressive stress on the fuse increased. As mentioned in Chapter 7, the CFRP layer did not extend over the full

height of the urethane matrix because there was a portion of the matrix left unreinforced at top and bottom to allow for some axial deformation before the steel plates make contact with the CFRP layer. As this unreinforced portion of the matrix is smaller the fuse becomes stiffer in compression, but the edges of the CFRP layer make contact with the plates at smaller deformations. The monotonic compression loading sequence was also intended to study the contribution to the compressive capacity of the CFRP layer when its edges make contact with the steel plates, and also to determine how much deformation may be sustained before the CFRP layer is permanently damaged.

The monotonic compression specimen consisted of a full fuse made of a 20-in. long bar (type B) with a 12.4-in. yield zone length, a 3-in. diameter urethane matrix, and a ¼-in. thick CFRP layer providing 90% confinement over the total urethane matrix height (corresponding to a confinement ratio of 14.4-in./16-in). The CFRP fibers were initially oriented only in the hoop direction, but the CFRP layer failed as soon as the bar reached its calculated buckling capacity without the confinement.

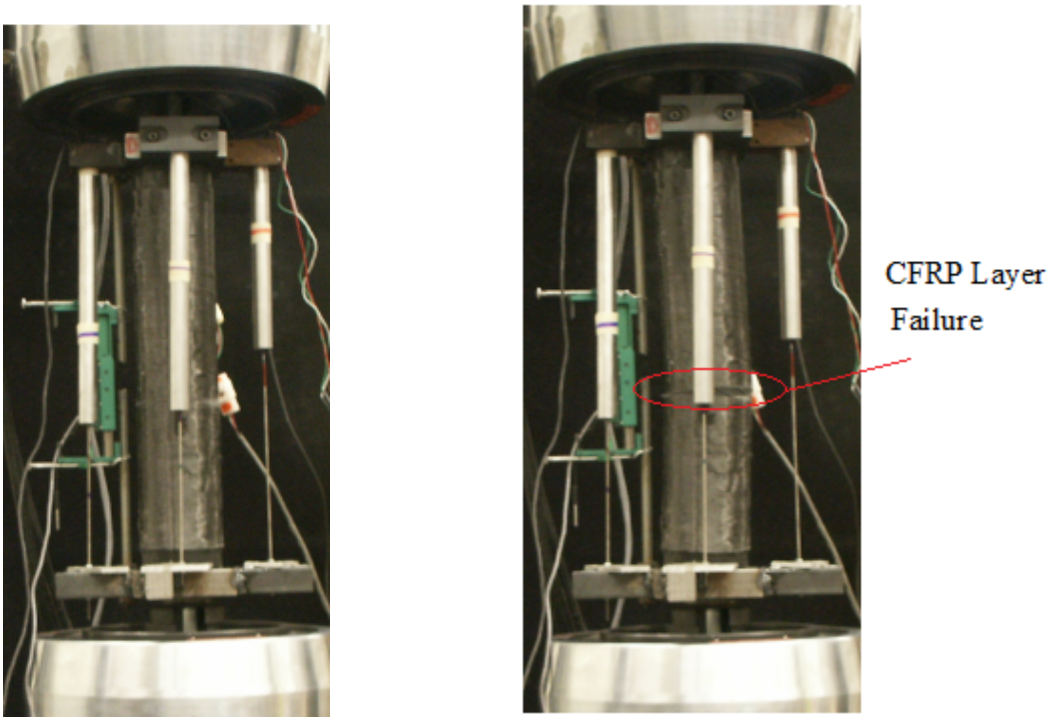

Test Set-Up. CFRP Layer Failure

Fig. 8.7 - Monotonic Compression Test Specimen.

After this initial monotonic compression test the carbon fiber reinforced polymer fabrication procedure was adjusted so that the same number of prepreg FRP sheets was applied around the urethane matrix to reach the desired ¼-in. thickness, but the orientation of the carbon fibers was varied. A third of the pre-preg CFRP sheets maintained the hoop fiber orientation, a third of the sheets were re-oriented 45 deg. clockwise with respect to the hoop direction, and the other third of the sheets were re-oriented 45 deg. counterclockwise with respect to the hoop direction. A second specimen with the same characteristics and the CFRP layer fibers oriented in

the three directions mentioned above was tested. Adding fibers at a 45 deg. angle in both directions proved to be a necessary adjustment to make the CFRP layer strong and stiff enough to provide proper confinement.

The stress-strain relationship obtained from the monotonic compression test exhibited six stages as follows (Fig. 8.8):

1) Linear elastic behavior up to fuse critical buckling capacity. The fuse compressive stiffness was at its maximum at this stage
2) Constant stress and increasing strain after critical buckling.
3) Compressive stiffness increment due to load transfer from the steel plates to the edges of the CFRP layer through the expanded unconfined portion of the urethane matrix.
4) A sharp increment in the slope of the stress-strain relationship due to direct contact between the CFRP layer and the steel plates after the CFRP edges cut through the expanded unconfined urethane matrix. The slope of the stress-strain curve was at its second maximum at this stage. At this stage the CFRP edges start making a significant contribution to the fuse compressive capacity.
5) Failure of either the top or bottom CFRP edge due to excessive compressive stress, followed by reduction in the slope of the stress-strain curve.
6) One last sharp increment in the slope of the stress-strain relationship before the fuse is fully crushed. This last increment was due to either the top or bottom fuse portion that failed on stage 5 taking more load before the opposite portion fails too and the fuse is completely crushed.

The fuse modulus of elasticity for each loading phase is:

Phase	Modulus of Elasticity, E (Ksi)
1	14,857
2	118
3	515
4	5,078
5	1,777
6	3,890

Table 8.2 - Modulus of Elasticity of each Loading Phase, Monotonic Compression Test.

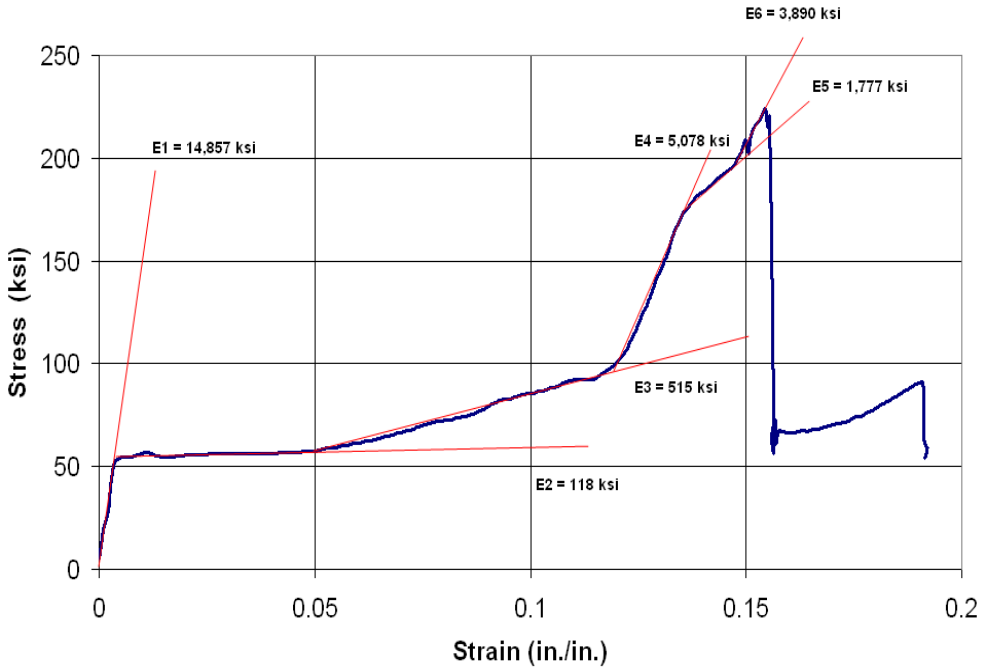

Fig. 8.8 - Monotonic Compression Test Stress-Strain Relationship.

As the specimen transitioned from one stage to another its compression capacity never decreased until the entire specimen was crushed at the end of stage 6, and even after the fuse collapsed the capacity simply went down to its initial critical buckling capacity. Also, the specimen was able to withstand severe buckling deformations before causing permanent damage to the urethane matrix or the CFRP layer. It was not until the buckling deformation reached a strain of 12% at the end of the third loading stage that the urethane matrix was cut by the edge of the CFRP layer, and until a strain of 13.5% one of the CFRP edges was severely damaged by contact with the steel plates.

As the confinement ratio varies the shape of the monotonic compression stress-strain relationship may change too. For example, for a CFRP confinement ratio greater than 90% it is expected that the yield plateau (stage 2) be reduced. In cases where the confinement ratio approaches 100% it is expected that the specimen would go from loading stage #1 (linear-elastic behavior) to the third loading stage without going through the second stage (yield plateau). If the confinement ratio is too close to a 100% it is possible that most of the load will be transferred directly to the CFRP due to contact with the plates before the fuse bars yield or buckle in compression. It is important to point out that even though those steel plates are merely experimental fixtures in a real brace system assembly the BCE fuse will require similar thick plates at top and bottom to have an adequate load transfer through the fuse.

The capacity of the fuse in compression during stage 2 was slightly higher than the yield strength of the yield zone (Fig. 8.9). This indicates that although there

was a reduction in the capacity of the bar in compression, the confining system compensated for that reduction in capacity so that the total capacity of the fuse was similar to the tensile strength of the bar. The capacity of the fuse in compression during stage 4 was three times higher than the ultimate strength of the yield zone (Fig. 8.9).

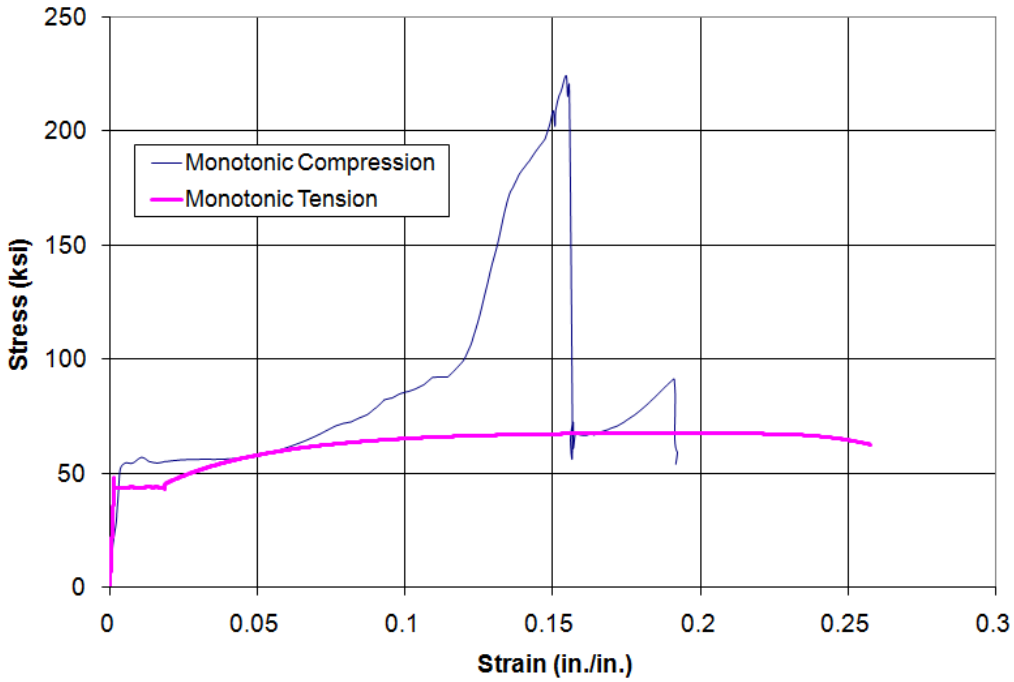

Fig. 8.9 - Superimposed Stress-Strain Curves, Monotonic Test Results.

Another important observation is that the fuse was able to maintain a stable yield plateau up to a deformation in compression of 5% (Fig. 8.10). This is more than half of the yield plateau maximum deformation in tension for the given fuse size. This yield plateau maximum deformation in compression is inversely proportional to the

confinement ratio. With higher confinement ratios the yield plateau deformation in compression decreases.

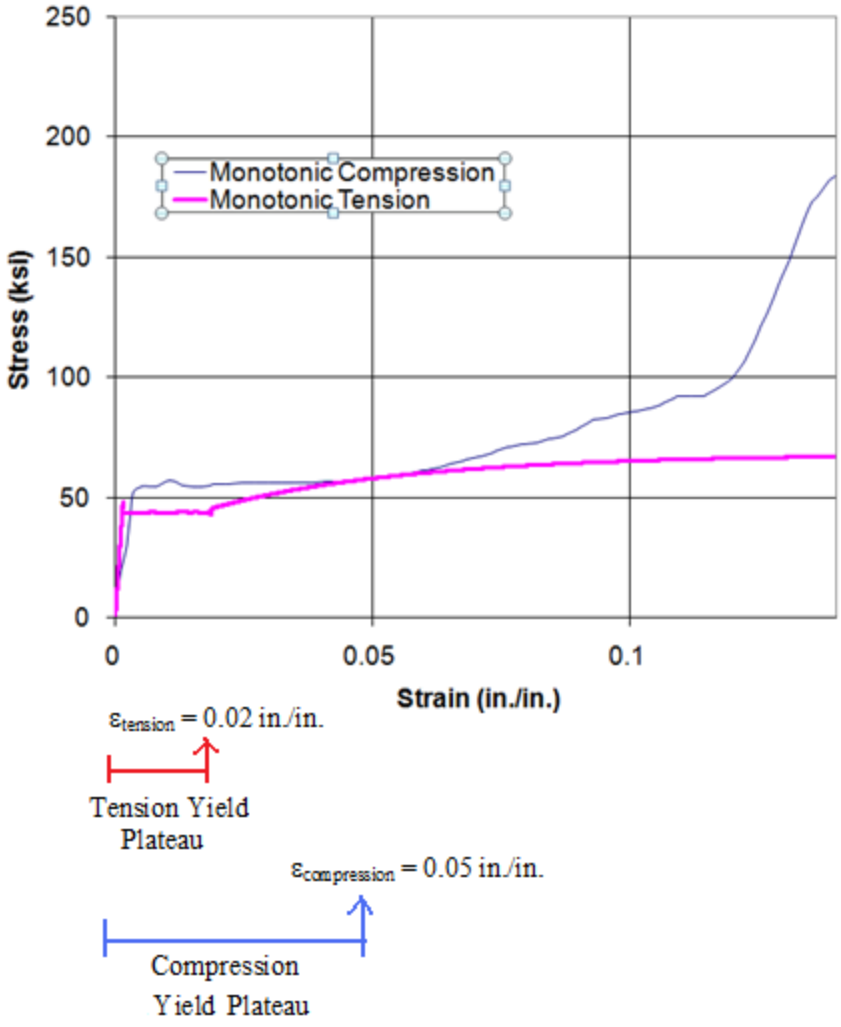

Fig. 8.10 - Superimposed Stress-Strain Curves, Monotonic Test Results, Zoom.

8.3 Series 1 - 1 Bar Specimens

The first series of the experimental matrix was intended to study the interaction between the bar and the confining system under cyclic loading. Specimens using the three different bar types were subjected to the same loading history used on the first RXS fuse test. The test-set up was the same used for the monotonic compression test. The end conditions, the test fixtures, the matrix diameter, and the configuration and thickness of the CFRP layer were the same used in the monotonic compression test. The load applied to all series 1 specimens was concentric.

The experimental matrix for the first series was made of 10 specimens with different confinement ratios, and bar types, as shown in Table 8.3.

Bar type	Confinement Ratio	CFRP Height to Matrix Height (in./in.)	# bars	Yield Zone Length (in.)	Urethane Matrix Diameter (in.)	CFRP Layer Thickness (in.)
A	98.7%	23.7/24	1	20.6	3	1/4
A	95.8%	23/24	1	20.6	3	1/4
B	97.7%	15.6/16	1	12.6	3	1/4
B	96.9%	15.5/16	1	12.6	3	1/4
B	93.8%	15/16	1	12.6	3	1/4
B	87.5%	14/16	1	12.6	3	1/4
C	96.9%	7.75/8	1	4.6	3	1/4
C	93.8%	7.5/8	1	4.6	3	1/4
C	87.5%	7/8	1	4.6	3	1/4
C	75.0%	6/8	1	4.6	3	1/4

Table 8.3 - Series 1 Experimental Program.

8.3.1 Series 1 - Bar Type A

Two 1-bars type A specimens were tested, both with a 24-in. tall urethane matrix but different confinement ratio. These two specimens with bars type A were actually the last two specimens tested of the first experimental series. The urethane matrix used was fabricated by adding 8-in. of fresh castable urethane mix to the cured 16-in. long matrix previously used to confine specimens with bars type B. Ideal bonding condition between the old and the new urethane were possible by using a

especial primer provided by the manufacturer. This primer was a perfect solution to avoid undesired cold joints. Specimens with type A bars had the longest yield zone, but also the highest effective slenderness ratio (Fig. 8.11).

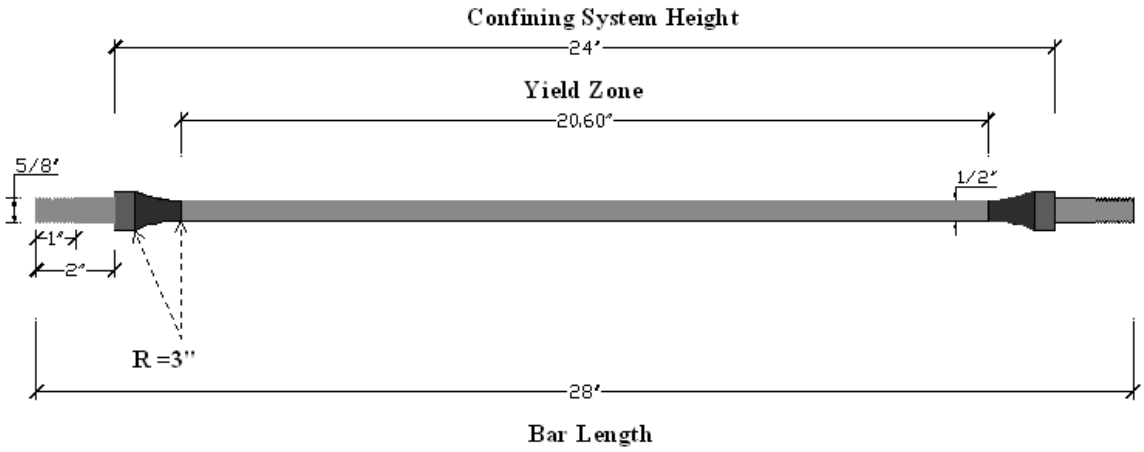

Fig. 8.11 – Bar Type A.

8.3.1.1 Specimen #1 – 1 Bar – Type A – 98.70% Confinement Ratio

Specimen #1 bar type A was subjected to 43 cycles and a maximum strain of 1.55% (Fig. 8.12). The test was stopped because the edge of the CFRP layer was taking axial stresses as it made contact with the steel plates due to fuse rotation under compression loads.

The buckling strength was measured to be 48.64 ksi, at a displacement amplitude of 0.0958-in. or a 0.5% strain over the length of the yield zone (Fig. 8.12). After buckling the maximum load in compression remained stable during the two

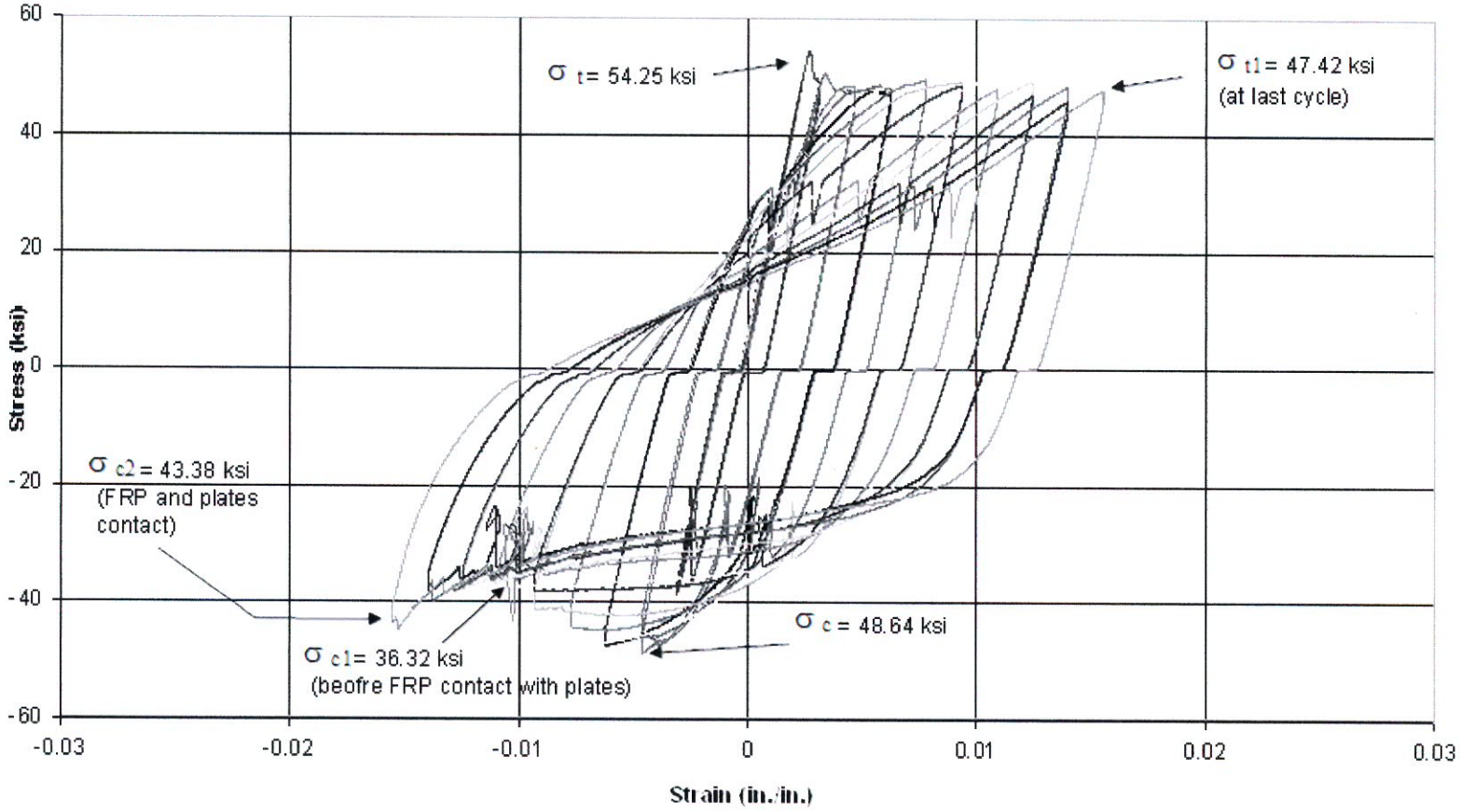

Fig. 8.12 - Specimen #1, 1 Bar Type "A", 98.70% Confinement Ratio.

subsequent cycles as it decreased down to just 47.4 ksi during load step 8 cycle 1 and 47.1 ksi during load step 9 cycle 1. After load step 9 the maximum load in compression decreased at a higher rate down to 94 ksi during load step 10 cycle 1, and further down during load steps 11 and 12. During cycle 1 of load step 13 the dges of the CFRP layer made contact with the steel plates. At this point the edges of the CFRP layer started to take compressive loads, increasing the stiffness of the fuse. The test was stopped at load step 14 cycle 1, overall cycle 43, with a displacement amplitude of 0.3193-in. over the 20.6-in. yield zone, for a average strain of 1.55%. The maximum load at this cycle increased again to 43.38ksi.

Under tension loads the fuse bar yielded during load step 6 cycle 1, at a yield stress F_y=54.25 ksi and a deformation of 0.0639-in. for an average strain over the yield zone of 0.31%. The fuse bar upper yield point was followed by a stable plateau at the lower yield point (48.06ksi).

8.3.1.2 Specimen #2 – 1 Bar – Type A – 95.83% Confinement Ratio

Specimen #2 used the same urethane matrix and CFRP confining layer used in specimen #1. This specimen was tested until the bar failed during the tension stage of load step 20, cycle 1, overall cycle 55. The bar was subjected to large inelastic buckling deformations until it failed by fatigue fracture under tension. The specimen was able to sustain inelastic deformations up to a maximum of 0.479-in. for an average strain of 2.33% over the 20.6-in. long yield zone (Fig. 8.13).

The bar reached its critical buckling capacity during load step 8, cycle 1, at an average stress of 48.12 ksi and a strain of 0.62%. After reaching its compressive capacity the capacity of the fuse in compression remained stable during the following two subsequent cycles, decreasing down to 47.73 ksi during load step 9, cycle 1, and 46.44 ksi during load step 10, cycle 2. At load step 11, cycle 1, there was a significant reduction in compressive capacity, as it went down to 41.93 ksi and it continued to decreased at a constant rate to a minimum of 30ksi during the last compression cycle, load step 19, cycle 2.

The fuse bar yielded during load step 6 cycle 1 at a yield stress $\boldsymbol{F_y}$=53.90 ksi and a deformation on 0.0639-in., corresponding to an average strain of 0.31% over the length of the yield zone. This is similar to the behavior of specimen 1. After the upper yield point was reached the bar maximum tensile stress during subsequent cycles at larger displacement amplitudes remained stable. It varied from 49.8 ksi at the lower yield point during load step 6 cycle 2, to 49.1 ksi during load step 14 cycle 1, corresponding to an average strain of 1.55% over the yield zone. After this load step the tensile stress at subsequent cycles started to decrease, and the minimum value recorded was 41.47 ksi during load step 19 cycle 1, overall cycle 54. This reduction in tensile capacity after load step 14 was caused by excessive buckling deformations. After the bar sustained large inelastic deformation under compression, the residual deformation had a significant effect on the maximum load reached in tension during the subsequent cycle.

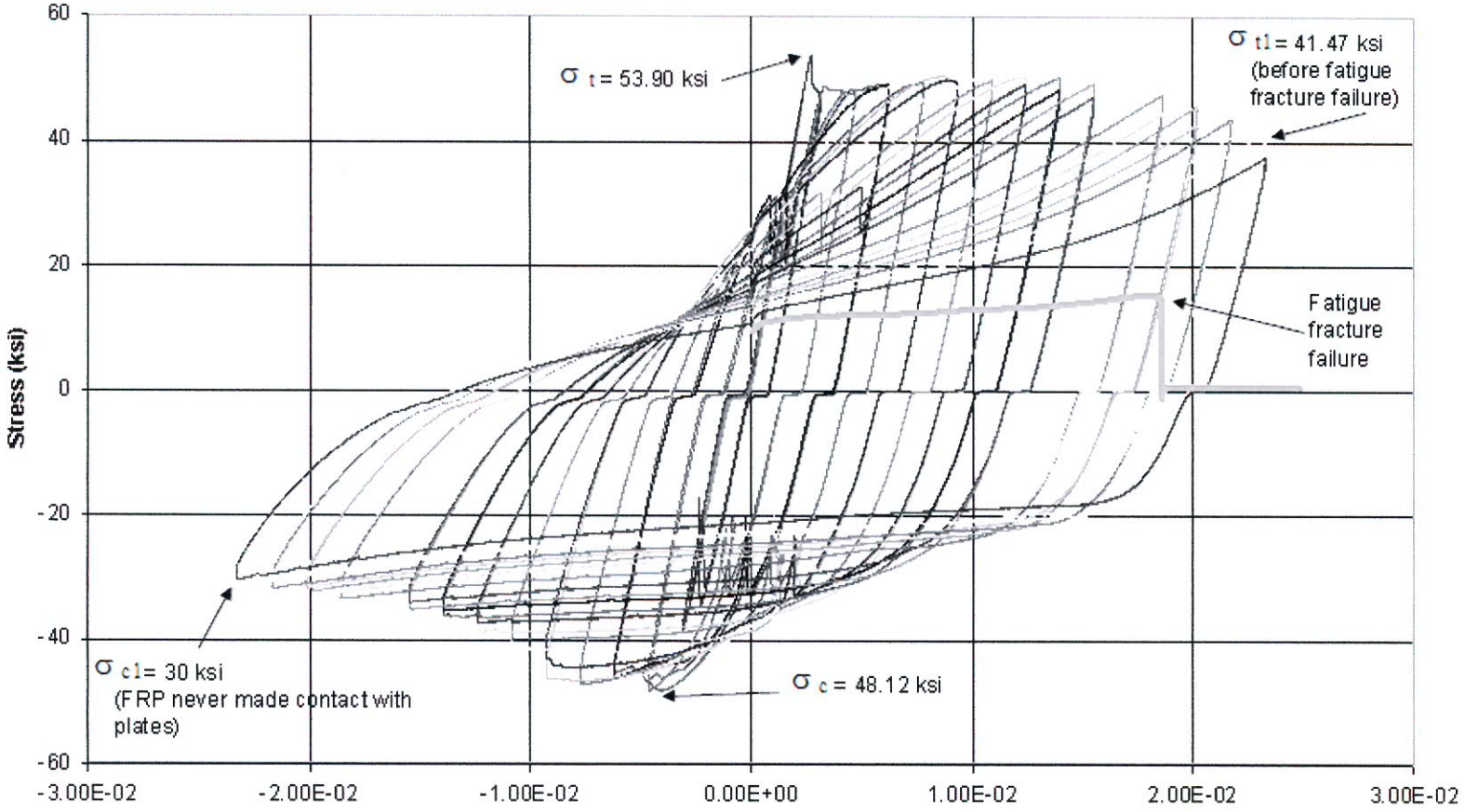

Fig. 8.13 - Specimen #2, 1 Bar Type "A", 95.83% Confinement Ratio.

8.3.2 Series 1 - Bar Type B

This portion of the first experimental matrix series included four specimens. All specimens had a single type B bar (Fig. 8.14), but different confinement ratios. In total six specimens were tested to complete this portion of the first series because two out of the 4 specimens had to be re-tested as they failed to produce the expected hysteretic response.

The first of these two specimens that had to be re-fabricated and tested again failed due to an error in fabrication of the bar urethane core. The durometer of the bar urethane core was measured after the test with a manual durometer gage and it was found that the core had a shore A 40 durometer instead of the desired 80 durometer. This low durometer of the core prevented the confining system from restraining the lateral motion of the bar, which practically allowed the bar to freely buckle within the radius of the core. Under large inelastic deformations the bar broke through the soft 40 durometer core. This low core durometer came from a mix batch that was prepared without following the recommended mix ratio between the resin and the curing agent. All cores and matrices made from this batch had to be discarded because they all turned out to be deficient, as indicated by a 40 shore A durometer.

A new specimen was re-assembled with the same testing fixtures, the same main 3 inch diameter urethane matrix, and CFRP layer, but adequate urethane core durometer and a new bar. During testing of this new specimen it was observed that after a few early cycles with low displacement amplitudes the fuse was not taking

tensile loads and the test was stopped. After further inspection of the loading equipment, fuse components, and testing fixtures it was found that one of the reducing couplers previously used on the first defective specimen with the low durometer core was severely damaged from excessive rotation, and the couplers were not transferring tensile loads.

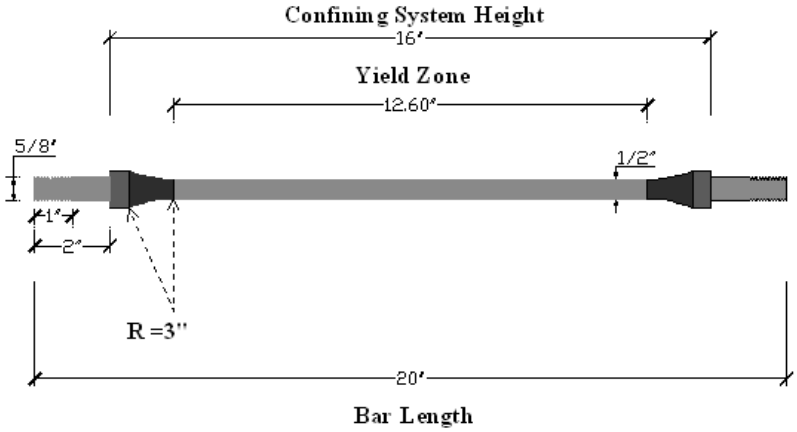

Fig. 8.14 - Bar Type B.

8.3.2.1 Specimen #3 – 1 Bar – Type B – 97.65% Confinement Ratio

Specimen #3, with a type B bar, was subjected to 41 cycles (Fig. 8.15). Loading history was stopped after load step 13, cycle 1. No further cycles were applied to avoid compromising the confining system as the rotation between the steel plates was significant during the last cycles and the confining system was to be used again on following specimens with smaller confinement ratios. Although the end

rotation was significant, the CFRP layer edge never made contact with the steel plates.

Of the four type B bar specimens of this first experimental series, specimen #3 had the highest confinement ratio. The fuse reached its buckling load during step 7, cycle 1, at 51.91 ksi (Fig. 8.15). After buckling, the maximum load in compression in subsequent cycles with larger displacement amplitudes remained stable as it only decreased to 49.12 ksi during the last step (step 13, cycle 1, overall cycle 41).

Under tensile stresses the fuse yielded during load step 7 cycle 1 (same cycle where it reached critical buckling) with an upper yield point of 54.01 ksi. After reaching $\boldsymbol{F_y}$ the bar reached a lower yield point of 48.93 ksi on the following load step, and during subsequent cycles the tensile stress continuously increased as the fuse was subjected to larger displacement amplitudes. The tensile stress gradually increased from the lower yield point up to 50.68 ksi during the last cycle at load step 13.

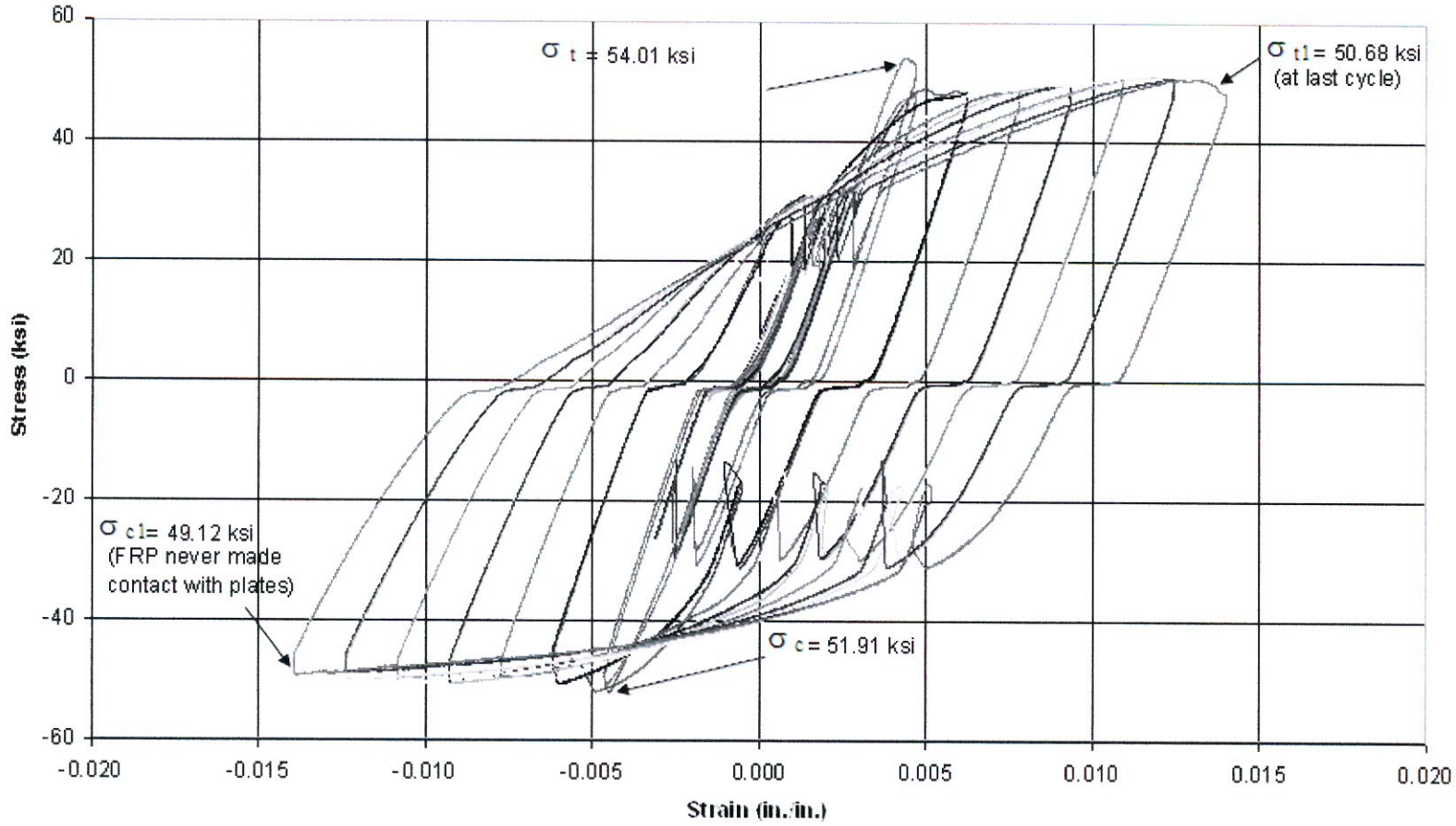

Fig. 8.15 - Specimen #3, 1 Bar Type "B", 97.65% Confinement Ratio.

8.3.2.2 Specimen #4 – 1 Bar – Type B – 96.87% Confinement

Specimen #4 with a type B bar, was subjected to 41 cycles (Fig. 8.16). The loading history was stopped after load step 13, cycle 1. Like it happened when testing other specimens no further cycles were applied to avoid compromising the confining system as the fuse rotation relative to the test fixture was significant during the last cycles, and the confining system was going to be used again on subsequent specimens with smaller confinement ratios. The edge of the CFRP layer made contact with one of the steel plates during the last cycle.

Of the four type B specimens of the first experimental series, specimen #4 had the second highest confinement ratio. The fuse reached its buckling load during load step 7, cycle 1, at a stress of 47.66 ksi. The maximum load in compression during subsequent cycles with larger displacement amplitudes remained stable, as it only decreased to 45.20 ksi during load step 12. The maximum compression load at load step 13, cycle 1, overall cycle 41, increased to 48.46 ksi due to contact between the edge of the CFRP layer and one of the steel plates.

Under tensile stresses the fuse started to yield during load step 6, cycle 1, at a stress of 50.54 ksi, reaching its lower yield point at 47.87 ksi during the next cycle with a larger displacement amplitude. During subsequent cycles the tensile stress increased as the fuse was subjected to larger displacement amplitudes, the maximum stress gradually increased from the lower yield point up to 52.94 ksi, during the last cycle at load step 13.

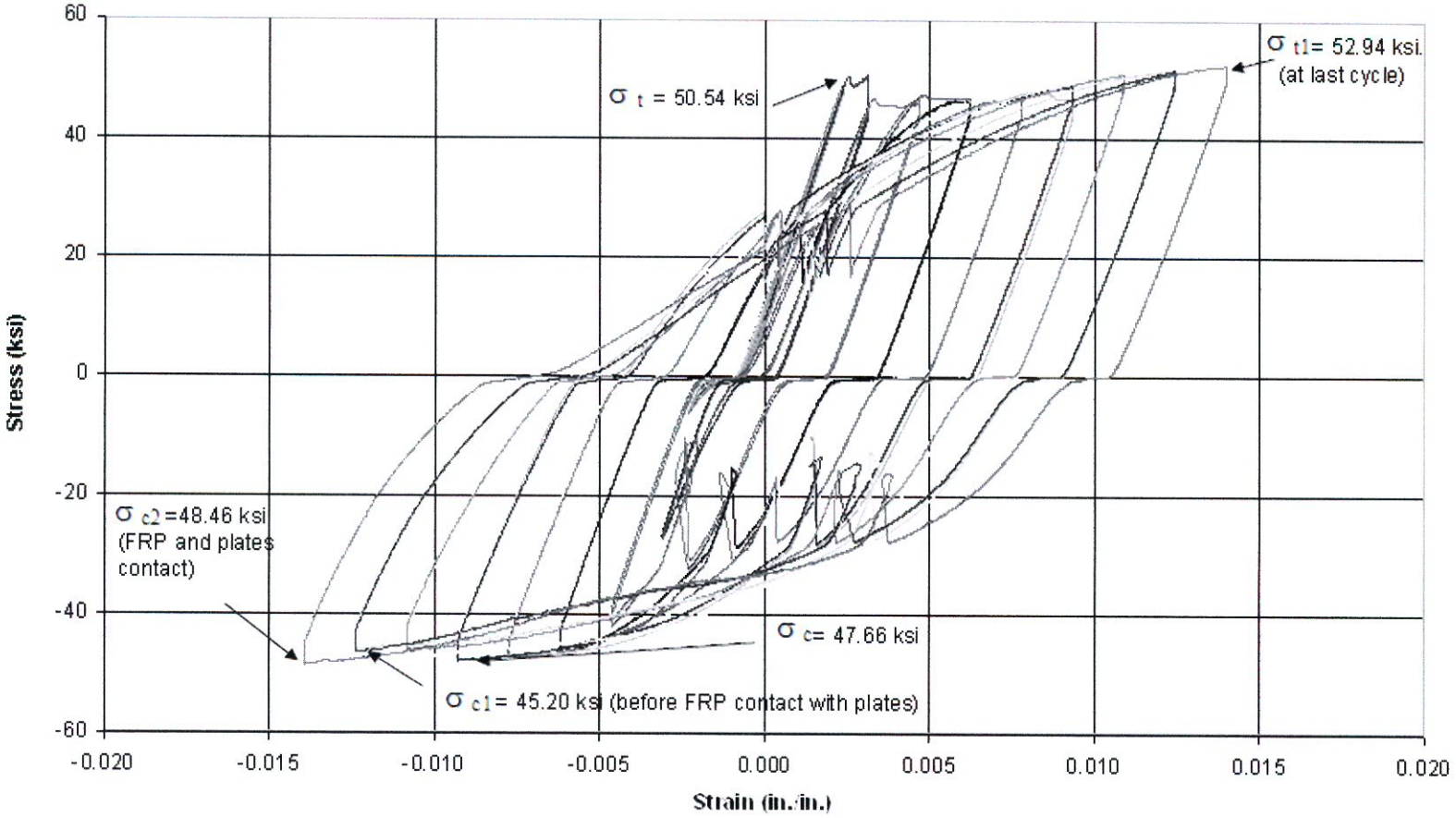

Fig. 8.16 - Specimen #4, 1 Bar Type "B", 96.87% Confinement Ratio.

8.3.2.3 Specimen #5 – 1 Bar – Type B – 93.75% Confinement Ratio

Specimen #5 with a type B bar, was also subjected to 41 cycles (Fig. 8.17). The loading history was stopped after load step 13, cycle 1. No further cycles were applied to avoid compromising the confining system because the rotation between the steel plates was very significant during the last cycles. Although the rotation was significant, the edge of the CFRP layer never made contact with any of the steel plates.

Of the four type B bar specimens of the first experimental series, specimen #5 had the third highest confinement ratio. The fuse reached its maximum compressive load during load step 10, cycle 1, at a stress of 49.47 ksi. During subsequent cycles with larger displacement amplitudes the maximum load in compression remained stable as it only decreased to a stress of 46.78 ksi during the last load step (step 13, cycle 1, overall cycle 41).

Under tensile stresses the fuse started to yield during load step 6, cycle 1, at a stress of 51.14 ksi. The maximum load in tension was recorded during load step 7, cycle 1, at an average stress of 53.71 ksi. The bar reached a maximum stress of 47.87 ksi during load step 8, cycle 1, and during subsequent cycles the maximum tensile stress continuously increased as the fuse was subjected to larger displacement amplitudes. The maximum stress that was recorded was 52.94 ksi, during the last cycle at load step 13.

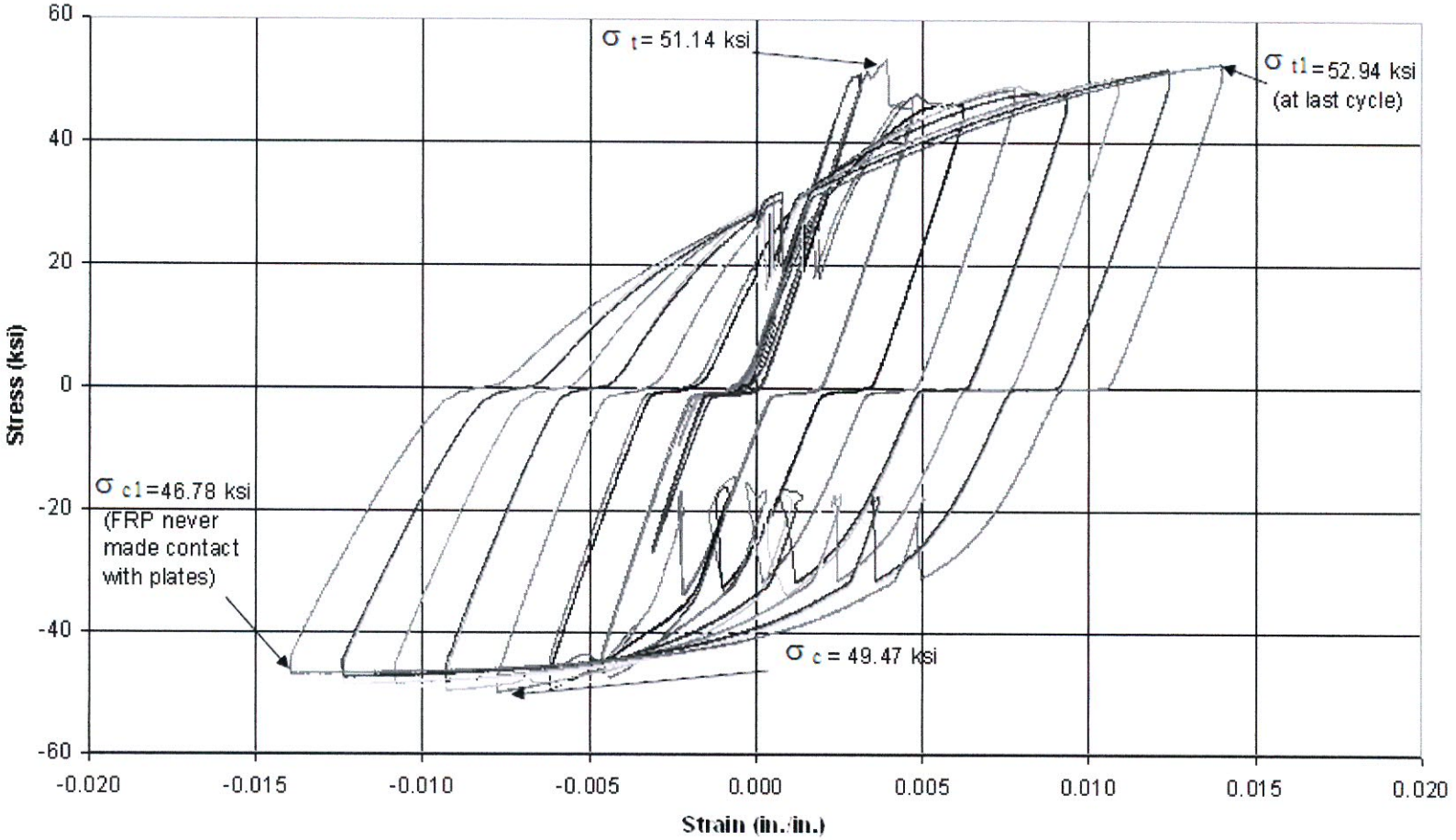

Fig. 8.17 - Specimen #5, 1 Bar Type "B", 93.75% Confinement Ratio.

8.3.2.4 Specimen #6– 1 Bar – Type B – 87.50% Confinement Ratio

Specimen #6 had a type B bar and was subjected to 41 cycles (Fig. 8.18). The loading history also stopped after load step 13, cycle 1. No further cycles were applied to avoid compromising the confining system. Although the fuse rotation was significant the edge of the CFRP layer never made direct contact with the steel plates.

Of the four type B bar specimens of the first experimental series, specimen #6 had the lowest confinement ratio. The fuse reached its maximum load in compression during load step 9, cycle 1, at an average stress of 48.87 ksi. During subsequent cycles with larger displacement amplitudes the maximum compression stress remained stable as it only decreased to 45.29 ksi during load step 11. At load step 12 the edge of the CFRP layer made contact with the unconfined portion of the urethane matrix and the maximum compressive stress increased in this cycle. During the last cycle, the maximum compressive stress increased once more to 46.83 ksi due to the contribution from the CFRP layer which took part of the stress from the steel plates through the bulging unconfined region of the urethane matrix.

Under tensile stresses the fuse started to yield during load step 6, cycle 1, at an average stress of 50.52 ksi. The maximum tensile stress was recorded during load step 7, cycle 1, and had a magnitude of 53.89 ksi. The bar reached a maximum stress of 46.66 ksi during the load step 8, cycle 1, and during subsequent cycles the tensile stress gradually increased as the fuse was subjected to larger displacement

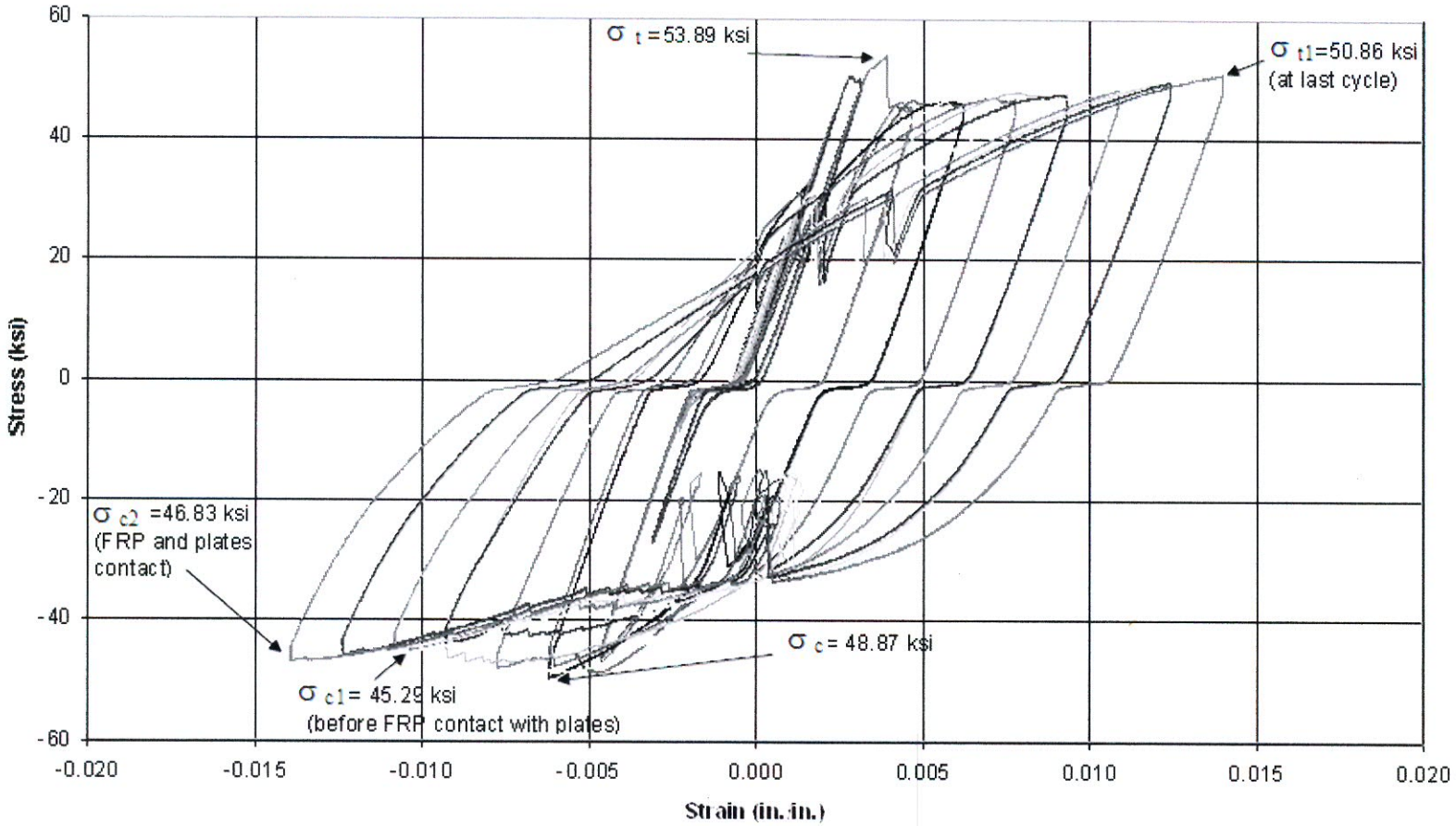

Fig. 8.18 - Specimen #6, 1 Bar Type "B", 87.50% Confinement Ratio.

amplitudes. The maximum tensile stress recorded during the last cycle, at load step 13, was 50.86 ksi.

8.3.3 Series 1 - Bar Type C

This third and last portion of the first experimental series included four specimens, all with one type C bar (Fig. 8.19), but different confinement ratios. The urethane matrices and CFRP confining layers used to assemble the specimens of this last series were made with those previously used in specimens with type B bars.

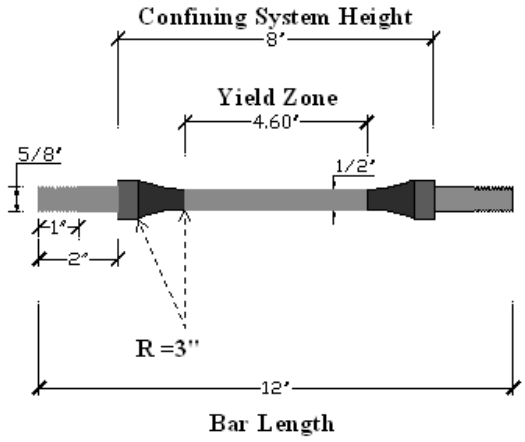

Fig. 8.19 - Bar Type C.

8.3.3.1 Specimen #7 – 1 Bar – Type C – 96.87% Confinement Ratio

Specimen #7, with one type C bar, was subjected to 77 cycles (Fig. 8.20). The test stopped after load step 26, cycle 1, due to excessive fuse rotation. The steel plates made contact with the CFRP layer at load step 18, with a displacement amplitude of 0.0998-in. Because neither the matrix nor the CFRP layer of this particular specimen were to be used on other specimens the test continued until the rotation and the

deterioration of the CFRP layer was so significant that the test had to be stopped in order to protect the loading equipment.

Of the four type C bar specimens of this first experimental matrix series, specimen #7 had the highest confinement ratio. The fuse reached its maximum load in compression during load step 11, cycle 1, at an average stress of 55.45 ksi. This was the highest compression stress reached by any specimen of the first experimental series. During subsequent cycles with larger displacement amplitudes the maximum stress remained stable and only decreased to 45.55 ksi during load step 18, cycle 1. After this load step the edges of the CFRP layer made contact with steel plates and the maximum compressive stress increased to 47.09 ksi indicating that the CFRP layer started taking axial compressive stresses directly from the plates. The maximum stress increased during subsequent cycles with larger displacement amplitudes, reaching a maximum of 55.23 ksi (almost equal to the peak stress in step 11) during load step 26, cycle 1, overall cycle 77. Although the test was stopped, all indications were that the fuse continued to take larger stress at larger displacement.

Under tensile stresses the fuse started to yield during load step 9, cycle 1, at a stress of 54.11 ksi. However, it was not until load step 11, cycle 2, when it reached the maximum stress of 60.28 ksi. The stress at load step 11 was followed by a lower maximum stress of 49.93 ksi during the subsequent displacement amplitude.

During subsequent cycles the maximum tensile stress gradually increased as the fuse was subjected to larger displacement amplitudes. The maximum stress increased to 54.04 ksi during the last cycle (load step 26, cycle 1, overall cycle 77).

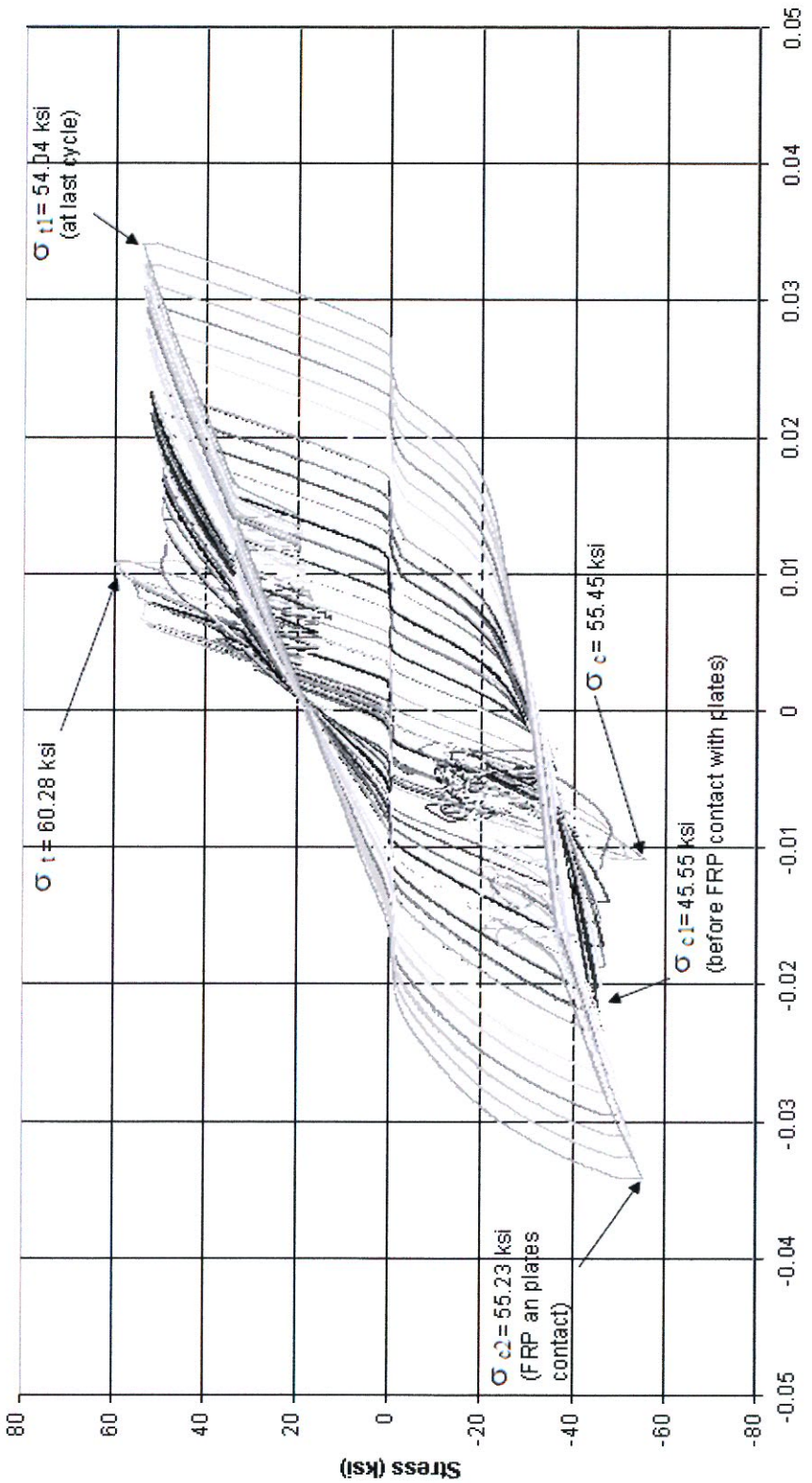

Fig. 8.20 - Specimen #7, 1 Bar Type "C", 96.88% Confinement Ratio.

8.3.3.2 Specimen #8 – 1 Bar – Type C – 93.75% Confinement Ratio

Specimen #8 with a type C bar was also subjected to 77 cycles (Fig. 8.21). The test was stopped after load step 26, cycle 1, due to excessive fuse rotation. The steel plates made contact with the edges of the CFRP layer at load step 22, with a displacement amplitude of 0.1283-in. and since severe deterioration of the matrix or the CFRP layer was not a concern the test continued until the CFRP layer deterioration became significant to protect the loading equipment.

Of the four type C bar specimens of this first experimental series, specimen 8 had the second highest confinement ratio. The fuse reached its maximum load in compression during load step 12, cycle 1, at a stress of 47.83 ksi. During subsequent cycles with larger displacement amplitudes, the maximum load remained stable as it only decreased to 41.69 ksi during load step 21, cycle 2. After this load step the edges of the CFRP layer made contact with the steel plates and the maximum load in compression increased to 42.28 ksi. During subsequent cycles the CFRP layer absorved part of the load directly from the plates. The maximum stress continuously increased during cycles with larger displacement amplitudes, reaching a maximum of 43.54 ksi during load step 26, cycle 1, overall cycle 77. The fuse could have taken higher compressive stresses if subjected to larger displacement amplitudes.

Under tensile stresses the fuse started to yield during load step 8, cycle 1, at a stress of 49.62 ksi. The maximum stress was reached during load step 10, cycle 1, and

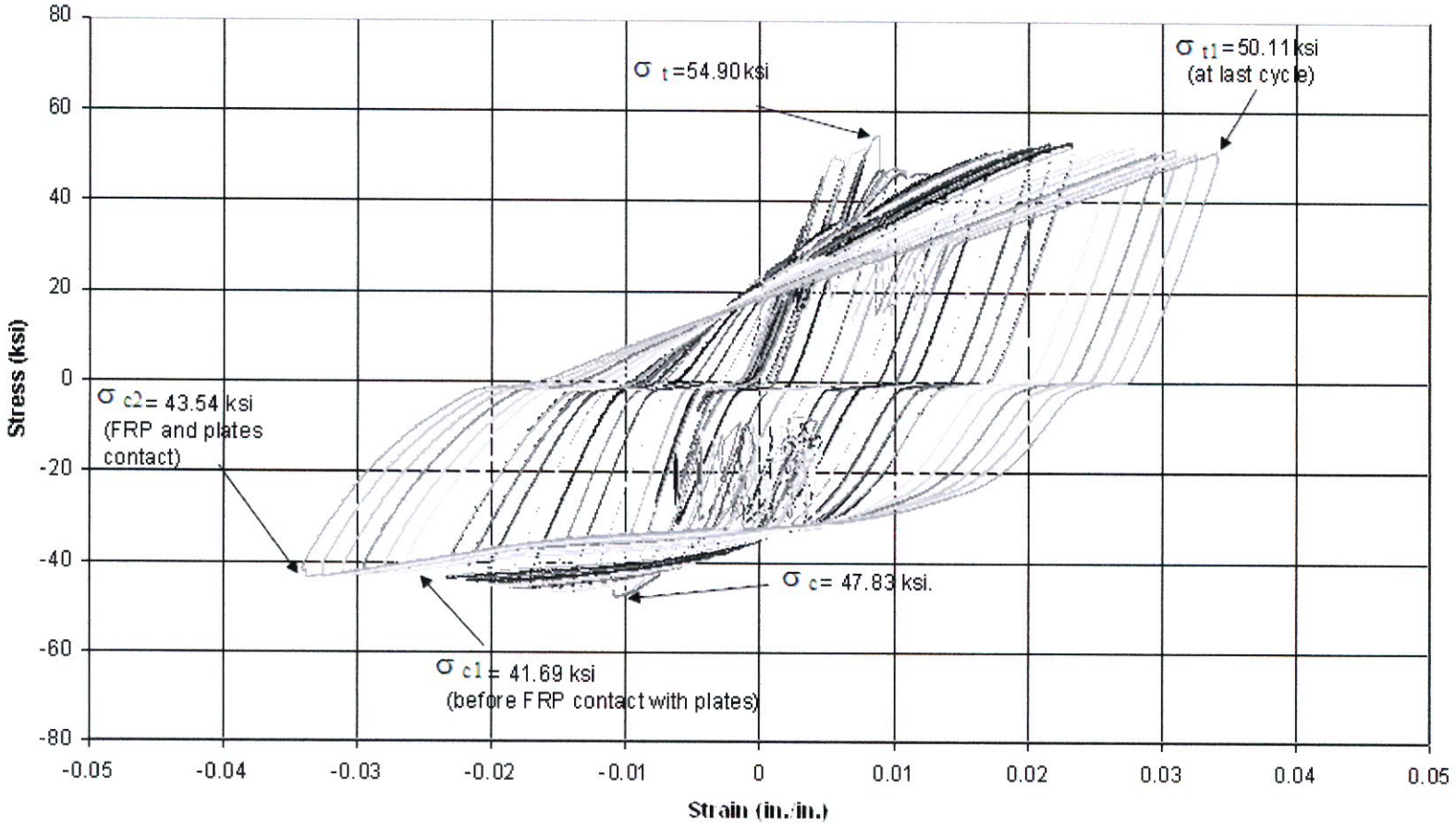

Fig. 8.21 - Specimen #8, 1 Bar Type "C", 93.75% Confinement Ratio.

it was measured to be 54.90 ksi. The maximum stress in the bar decreased to 47.03 ksi during load step 11, cycle 1. During subsequent cycles the maximum tensile stress continuously increased as the fuse was subjected to larger displacement amplitudes. The maximum stress at load step 19 reached 52.75 ksi, and then remained stable. The maximum stress was 50.11 ksi during the last cycle (load step 26, cycle 1, overall cycle 77).

8.3.3.3 Specimen #9 – 1 Bar – Type C – 87.50% Confinement Ratio

Specimen #9, with a type C bar, was also subjected to 77 cycles (Fig. 8.22). The test was stopped after load step 26, cycle 1, overall cycle 77, due to excessive fuse rotation. The steel plates never made contact with the CFRP layer.

Of the four type C bar specimens of the first experimental series, specimen #9 had the third highest confinement ratio. The fuse reached its maximum compressive stress of 53.30 ksi during load step 9, cycle 1. During subsequent cycles with larger displacement amplitudes the maximum compressive stress remained stable and it had decreased to 35.82 ksi during the last cycle (load step 26, cycle 1, overall cycle 77).

Under tensile stresses the fuse yielded during load step 11, cycle 1, at a stress of 47.45ksi. During subsequent cycles the tensile stress remained stable, increasing up to 49.69 ksi at load step 19, cycle 1, and then decreased to 46.91 ksi during the last cycle (load step 26, cycle 1, overall cycle 77).

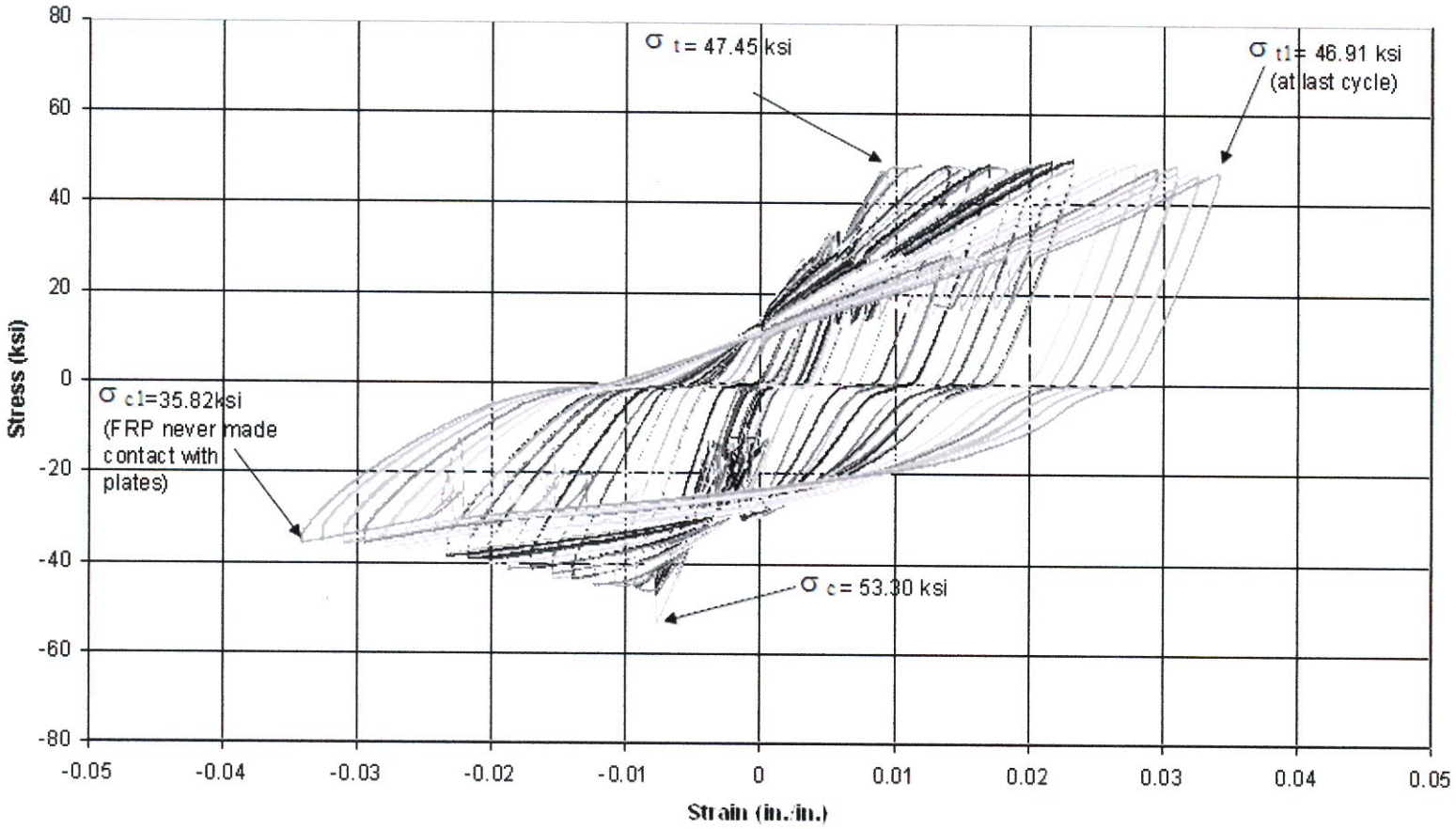

Fig. 8.22 - Specimen #9, 1 Bar Type "C", 87.5% Confinement Ratio.

8.3.3.4 Specimen #10 – 1 Bar – Type C – 75% Confinement Ratio

Specimen #10 with a type C bar, was also subjected to 77 following the same loading history (Fig. 8.23). The test was stopped after load step 26, cycle 1, overall cycle 77, due to excessive fuse rotation. The steel plates never made contact with the CFRP layer.

Of the four type C bar specimens of the first experimental series, specimen #10 had the lowest confinement ratio. The fuse reached its maximum compressive stress of 49.28 ksi during load step 10, cycle 1. During subsequent cycles with larger displacement amplitudes the maximum stress remained stable until load step 14, which had a maximum stress of 48.64 ksi. After step 14 the maximum stress in compression started to gradually decrease to a value of 34.86 ksi during the last cycle.

Under tensile stresses the fuse started to yield during load step 9, cycle 1, at a stress of 50.51 ksi. The maximum tensile stress was recorded during load step 10, cycle 1, with a value of 54.85 ksi. The maximum stress in the bar decreased to 47.46 ksi during load step 11, cycle 1. During subsequent cycles the maximum tensile stress continuously increased as the fuse was subjected to larger displacement amplitudes, up to a value of 52.60 ksi at load step 21, cycle 1. Then the maximum tensile stress at subsequent cycles with larger displacement amplitudes remained stable but progressively decreased to 45.89 ksi during the last cycle, at load step 26, cycle 1, overall cycle 77. This reduction in tensile capacity after load step 26 was caused by excessive buckling deformations.

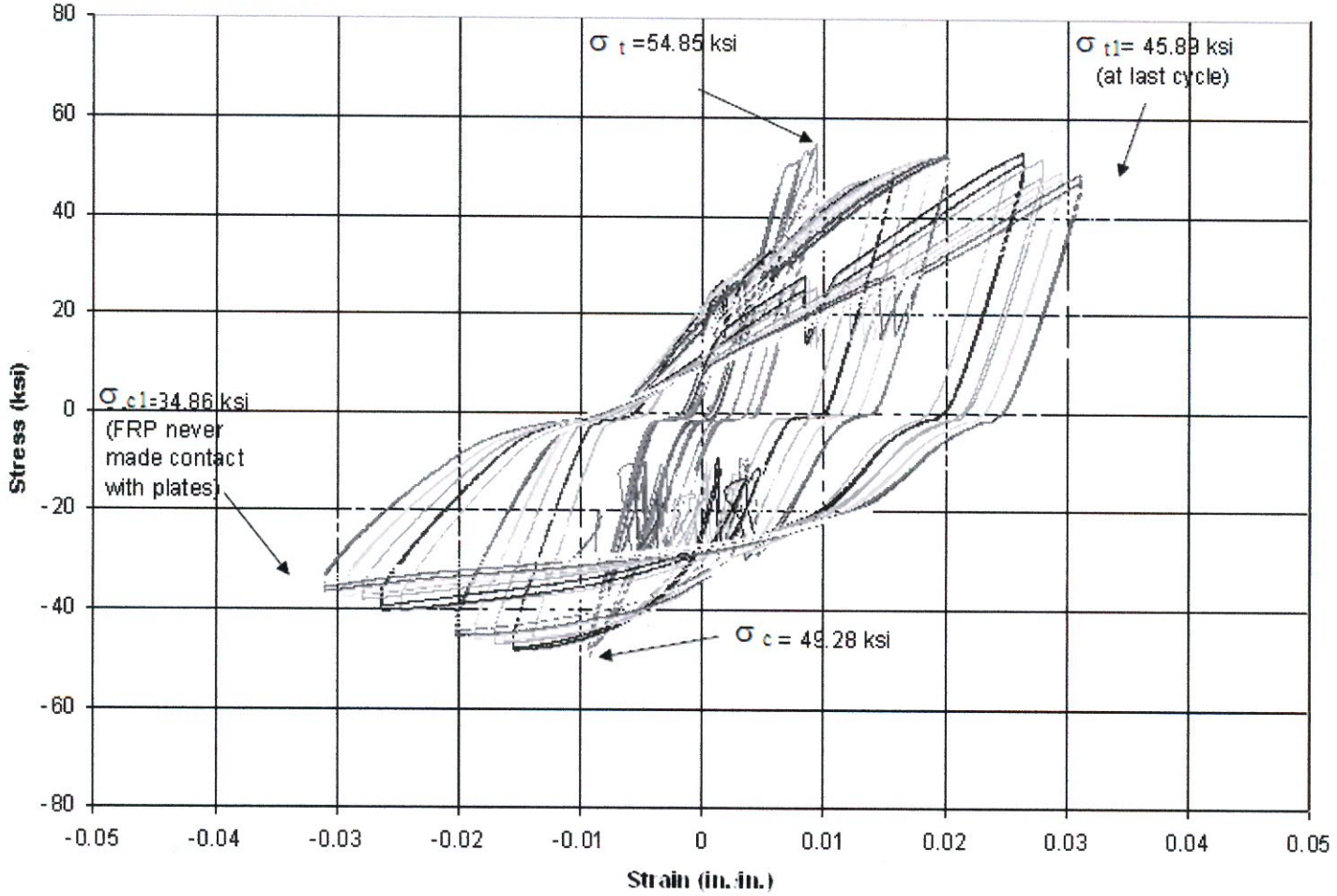

Fig. 8.23 - Specimen #10, 1 Bar Type "C", 75.00% Confinement Ratio.

8.3.4 Summary of Experimental Results for BCE Series 1

Under cyclic loading, the yield strength of single-bar fuse specimens was greater than that measured from the tensile test of the bar without confinement with the exception of specimen 9, with a type C bar, which had a yield strength equal to that of the monotonic tension test (F_y = 43.5 ksi). The tensile capacity of the fuse is provided by the bar as there is little bond between the bar and the urethane matrix, but the tensile strength of the bar improved with the urethane-matrix/CFRP confining system. There is bonding between the bar and the urethane core cast around the bar, but the inner core is tied to the urethane matrix only by friction. The small increment in tensile strength observed during cyclic loading was initially attributed to a difference in the calibration of the loading equipment because a different machine was used for the monotonic tension test.

Looking at the maximum stresses, in tension and compression, from all specimens tested during the experimental series (Table 8.4) one can see that there is no common pattern in terms of the small variations with respect to the confinement or even the fuse size (Fig. 8.24 and Fig. 8.25), since the maximum tensile stress decreases and increases as the confinement ratio and sizes varies.

Specimen	Bar type	Confinement Ratio (%)	Cycles	at Maximum Tensile Stress $\sigma_{t\ (tension)}$		at Maximum Compressive Stress σ_c (compression)	
				Strain amplitude (in./in.)	Stress (ksi)	Strain amplitude (in./in.)	Stress (ksi)
#1	A	98.70	54	0.00266	54.25	0.00399	48.64
#2	A	95.83	43	0.00266	53.90	0.00532	48.12
#3	B	97.66	41	0.00366	54.01	0.00366	51.91
#4	B	96.88	41	0.00244	50.54	0.00733	47.66
#5	B	93.75	41	0.00366	51.14	0.00733	49.47
#6	B	87.50	41	0.00366	53.89	0.00611	48.87
#7	C	96.88	77	0.006238	60.28	0.006238	55.45
#8	C	93.75	77	0.00535	54.90	0.007125	47.83
#9	C	87.50	77	0.00535	47.45	0.00535	53.30
#10	C	75.00	77	0.00535	54.85	0.00535	49.28

Table 8.4 – Experimental Series #1 Results Summary.

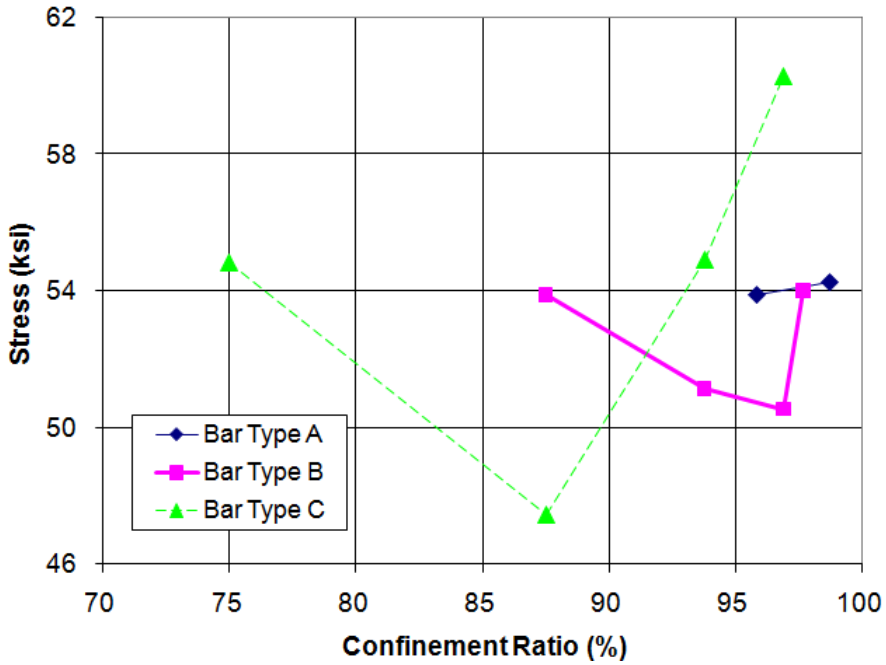

Fig. 8.24 - Maximum Tensile Stress "σt (tension)" vs. Confinement Ratio.

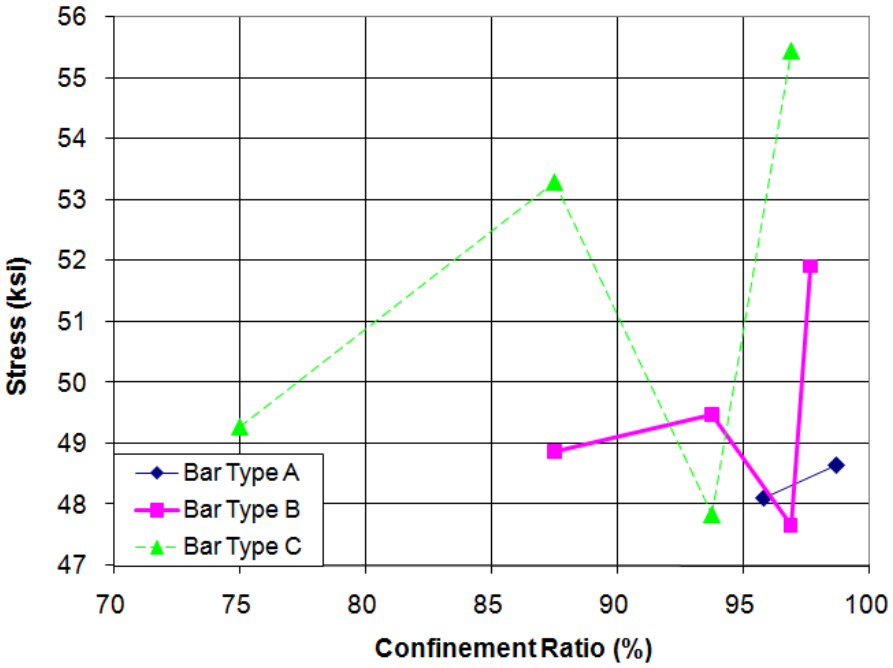

Fig. 8.25 - Maximum Compressive Stress "σc (compression)" vs. Confinement Ratio.

The maximum stress in compression was approximately 0.9 of the maximum stress in tension for most of the specimens. The maximum stress in tension was approximately 1.25 the yield stress and in compression it was approximately 1.15 of the yield stress (Table 8.5).

Specimen	Bar type	Confinement Ratio (%)	σ_t/F_y (F_y=43.5 ksi)	σ_c/F_y (F_y=43.5 ksi)	σ_t/σ_c
#1	A	98.70	1.25	1.12	1.12
#2	A	95.83	1.24	1.11	1.12
#3	B	97.66	1.24	1.19	1.04
#4	B	96.88	1.16	1.10	1.06
#5	B	93.75	1.18	1.14	1.03
#6	B	87.50	1.24	1.12	1.10
#7	C	96.88	1.39	1.27	1.09
#8	C	93.75	1.26	1.10	1.15
#9	C	87.50	1.09	1.23	0.89
#10	C	75.00	1.26	1.13	1.11

Table 8.5 - Single Bar BCE Fuse Stress Ratios.

Specimen	Bar type	Confinement ratio (%)	Tension	Compression	
			σ_{t1} (ksi)	σ_{c1} (ksi)	σ_{c2} (ksi)
#1	A	98.70	47.42 at last cycle	36.32 plates CFRP contact	43.38 last cycle
#2	A	95.83	41.47 before failure	30 no contact between CFRP and plates	-
#3	B	97.66	50.68 at last cycle	49.12 no contact between CFRP and plates	-
#4	B	96.88	52.94 at last cycle	45.2 plates CFRP contact	48.46 last cycle
#5	B	93.75	52.94 at last cycle	46.78 no contact between CFRP and plates	-
#6	B	87.50	50.86 at last cycle	45.29 plates CFRP contact	46.83 last cycle
#7	C	96.88	54.04 at last cycle	45.55 plates CFRP contact	55.23 last cycle
#8	C	93.75	50.11 at last cycle	41.69 plates CFRP contact	43.54 last cycle
#9	C	87.50	46.91 at last cycle	35.82 no contact between CFRP and plates	-
#10	C	75.00	45.89 at last cycle	34.86 no contact between CFRP and plates	-

Table 8.6 - Experimental Series #1 Results Summary, Stresses at Inelastic Deformations.

Only half of the single bar fuse specimens had the edge of the CFRP layer take compressive stress directly from the steel plates (Table 8.6). The compressive stress vs. the confinement ratios of those specimens was plotted and is shown in Fig. 8.26.

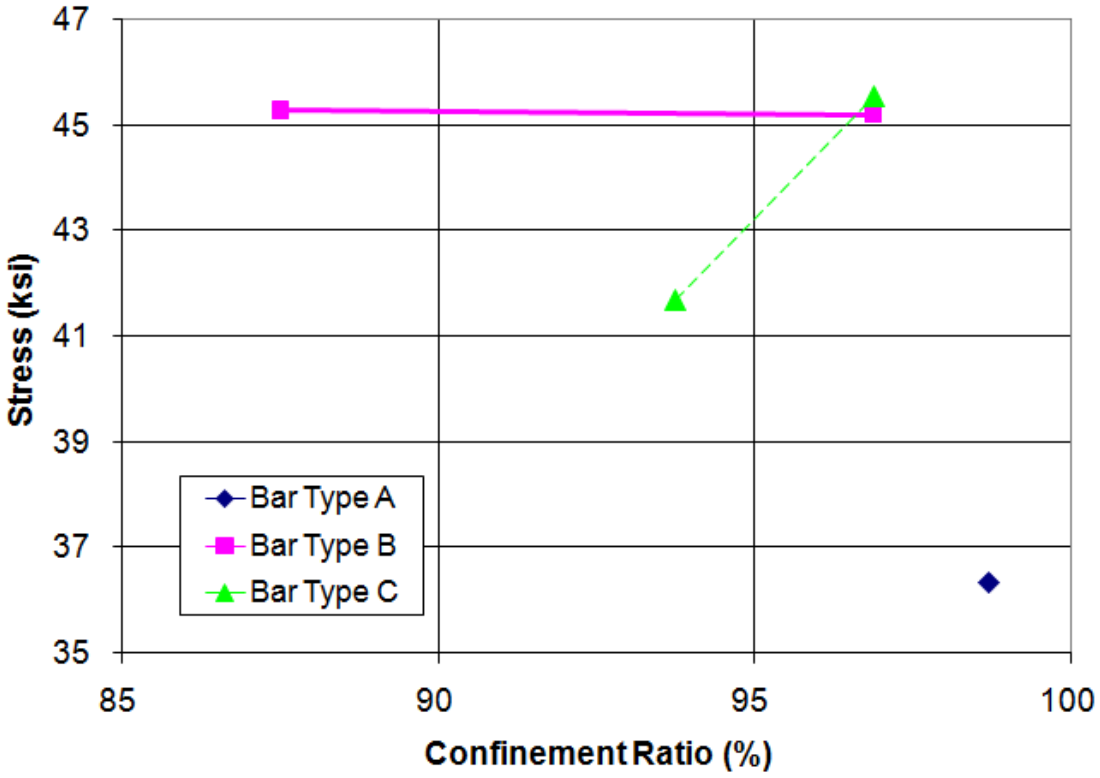

Fig. 8.26 - Maximum Compressive Stress before Contact Between CFRP Layer and Steel Plates.

The nominal buckling capacity of the bars without the confining system and assuming the length of the ½ diameter reduced section and fixed end conditions was calculated following the thirteenth edition of the AISC manual [AISC, 2005] as follows:

Bar Type	Yield Zone Length (in.)	Effective Length Factor "K"
A	20.6	0.65
B	12.6	0.65
C	4.6	0.65

Table 8.7 - Bar Nominal Capacity in Compression, Properties.

For a bar type A, the nominal capacity in compression can be calculated as follow:

$R = d/4 = 0.5/4 = 0.125\text{-in.}$ <Eq. 8.1>

$KL/r = 0.65*20.6\text{-in.}/0.125\text{-in.} = 107.12$ <Eq. 8.2>

$4.71*(E/F_y)^{0.5} = 123.814$ <Eq. 8.3>

From Eq. E3-2 of the AISC Manual, thirteenth edition:

$KL/r < 4.71*(E/F_y)^{0.5}.$ <Eq. 8.4>

Then:

$F_{cr} = 0.658^{(Fy/Fe)*}F_y$ <Eq. 8.5>

$$Fe = \pi^2 * E/(KL/r)^2 = 28.30 \text{ ksi} \quad \text{<Eq. 8.6>}$$

$$Fcr = 0.658^{(47.61ksi/28.3ksi)} * 47.61 \text{ ksi} = \boldsymbol{23.54 \text{ ksi}}$$

$$Ag = \pi * d^2/4 = \pi * 0.5\text{-in.}^2/4 = 0.19635 \text{ in}^2 \quad \text{<Eq. 8.7>}$$

$$Pn = Fcr * Ag = 23.54 \text{ ksi} * 0.19635 \text{ in}^2 = 4.62 \text{ kips} \quad \text{<Eq. 8.8>}$$

The nominal capacities of bars type B and C in compression were calculated following the same procedure illustrated above.

By comparing the nominal buckling capacity for the three unconfined bar types with experimentally measured values for the same bars embedded in the fuse it was found that the bars type A doubled their buckling capacity when embedded in the fuse, and bars type B and C improved their compressive capacities by 42% and 21% respectively (Table 8.8).

Bar Type	Fuse height (in.)	Length of ½-in. reduced section	Bar Nominal Capacity in Compression (ksi)	BCE Fuse Capacity in Compression (ksi)	Ratio of Fuse Experimental / Bar Nominal Stress
A	24	20.6	23.54	48.64	2.06
B	16	12.6	36.58	51.91	1.42
C	8	4.6	45.97	55.45	1.21

Table 8.8 – Fuse Capacity vs. Bar Capacity.

As stated in the literature review section, previous studies show that the compressive capacity of braces subjected to cyclic loads usually decreases to one third of the compressive capacity during post-buckling deformations. Looking at the experimental hysteretic loops obtained from all series 1 specimens it can be concluded that the confinement system had the effect of making the response in compression of the fuse similar to the response in tension. Furthermore, the compressive capacity of the fuse did not decrease considerably after it reached its buckling capacity, as it usually happens on bracing members, and instead maintained a stable post-buckling load as the displacement amplitudes of the cycles increased past the point of critical buckling. Even in specimens with very low confinement ratios, on the order of 75%, the capacity in compression did not decrease by more than 20% after buckling for strain demands on the order of 3.5%.

8.4 Series 2 – 4 Bar Specimens

The second series was intended to study the behavior of full-scale fuses with 4 bars (Fig.8.27) when subjected to cyclic loads. This experimental series was composed of three groups, one per bar type, and 3 specimens per group, for a total of nine full-scale specimens. Each group included: one specimen with a high confinement ratio subjected to concentric load, a second specimen with the same confinement ratio but with the load applied at an eccentricity of 1.5-in., and a third specimen with a lower CFRP confinement ratio subjected to concentric load.

The connection between the fuse and the brace is intended to be rigid so that it can resist any moment induced by eccentricity of the load or by rotation during large inelastic deformations when the fuse is subjected to concentric compression cycles. Unfortunately, a fixed end condition between the fuse and the testing frame implies that fuses will transfer significant moment stresses to the crossheads of the loading frame. Because the loading equipment was designed for axial load testing only, the moment transferred from the fuse had to be released in order to protect the loading equipment. For this reason test fixtures with a pin end condition were fabricated and used in the tests.

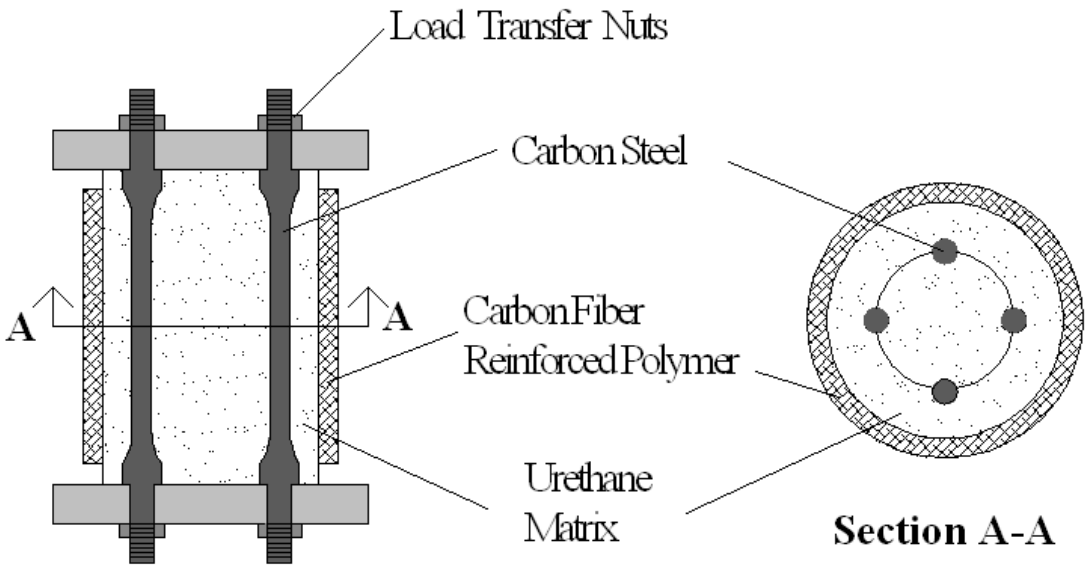

Fig. 8.27 - Series 2 Specimen Configuration.

The capacity of the fuse for dissipating energy under load reversals without major deterioration is significantly affected by the rotation of the end plates due to eccentricity of the axial load, and this rotation is significantly accentuated by the addition of pin end condition. The rotation of the end plates affected the experimental results of this second series in an unfavorable manner. It is expected that with rigid end connections the behavior of the fuse would improve with respect to that observed in the tests.

Considering that the fuse behavior/performance was extensively investigated through the first experimental series, the significance of this second series relies on how the specimen behavior changes from one case to the other. The tests were intended to provide information about the confinement ratio, bar type, and eccentricity of the load on the behavior of the fuse.

The same urethane matrix and CFRP layer was used to confine all 9 specimens of this second series. A 24.75-in. long confined matrix was fabricated and used to assemble the three full-scale 4-bar type A specimens. After the three specimens with type A bars were tested, the matrix with its respective CFRP confining layer was cut into a 16.5-in. long used matrix to assemble the second group of the full-scale 4-bar type B specimens. The last three full-scale 4-bar type C specimens were made by using the remaining 8.25-in. long segment from the original matrix block and by cutting the 16.5-in. long matrix in half.

Although the required matrix heights were 24-in., 16-in. and 8-in. respectively, for the three different bar types A, B, and C, the additional ¾-in. in

height for the type A specimen matrix, ½-in. for the type B and ¼-in. for the type C were necessary to pre-compress the urethane without applying axial compression to the bars, in order to activate the confining system at low axial loads.

Bar type	Confinement Ratio (%)	Confinement Ratio (in./in.)	Number of bars	Length of Yield Zone	Main Matrix Diameter	Thickness of CFRP Layer
A	**98.95**	**23.75/24**	**4**	**20.6**	**6 3/4**	**1/4**
A	**98.95**	**23.75/24**	**4**	**20.6**	**6 3/4**	**1/4**
A	**95.83**	**23/24**	**4**	**20.6**	**6 3/4**	**1/4**
B	**97.65**	**15.625/16**	**4**	**12.6**	**6 3/4**	**1/4**
B	**97.65**	**15.625/16**	**4**	**12.6**	**6 3/4**	**1/4**
B	**93.75**	**15/16**	**4**	**12.6**	**6 3/4**	**1/4**
C	**96.87**	**7.75/8**	**4**	**4.6**	**6 3/4**	**1/4**
C	**96.87**	**7.75/8**	**4**	**4.6**	**6 3/4**	**1/4**
C	**87.50**	**7/8**	**4**	**4.6**	**6 3/4**	**1/4**

Table 8.9 - Series 2 Experimental Program.

8.4.1 Series 2 - Bar type A

This first group of the second experimental series included three full-scale specimens with 4 type A bars. The first two specimens had the same urethane matrix and CFRP layer. Only the bars with their respective inner cores were replaced, and the text fixture was adjusted to apply concentric loads first and then to introduce an eccentricity of 1.5-in. with respect to the longitudinal axis. The third specimen was subjected to concentric loads with a lower confinement ratio.

8.4.1.1 Specimen #11 – 4 Bars – Type A – 98.95% Confinement Ratio - Concentric Load

Specimen 11, with 4 type A bars, was subjected to only 50 cycles because at that point the edges of the CFRP layer were taking significant compressive axial stress due to direct contact with the steel plates (Fig. 8.28).

The CFRP layer started to take axial compressive stresses during load step 17, cycle 1, before the fuse reached its maximum load in compression. This is the reason why the maximum compressive stress at the peak displacement of each step increased with displacement amplitude. The maximum compressive stress reached by the fuse before the CFRP layer made contact with the plates was 38.7 ksi, during load step 16, cycle 1, overall cycle 47. The maximum compressive stress reached by the specimen, including the contribution from the CFRP layer, was 43.87 ksi, achieved during the last cycle. All indications were that the specimen would have taken larger

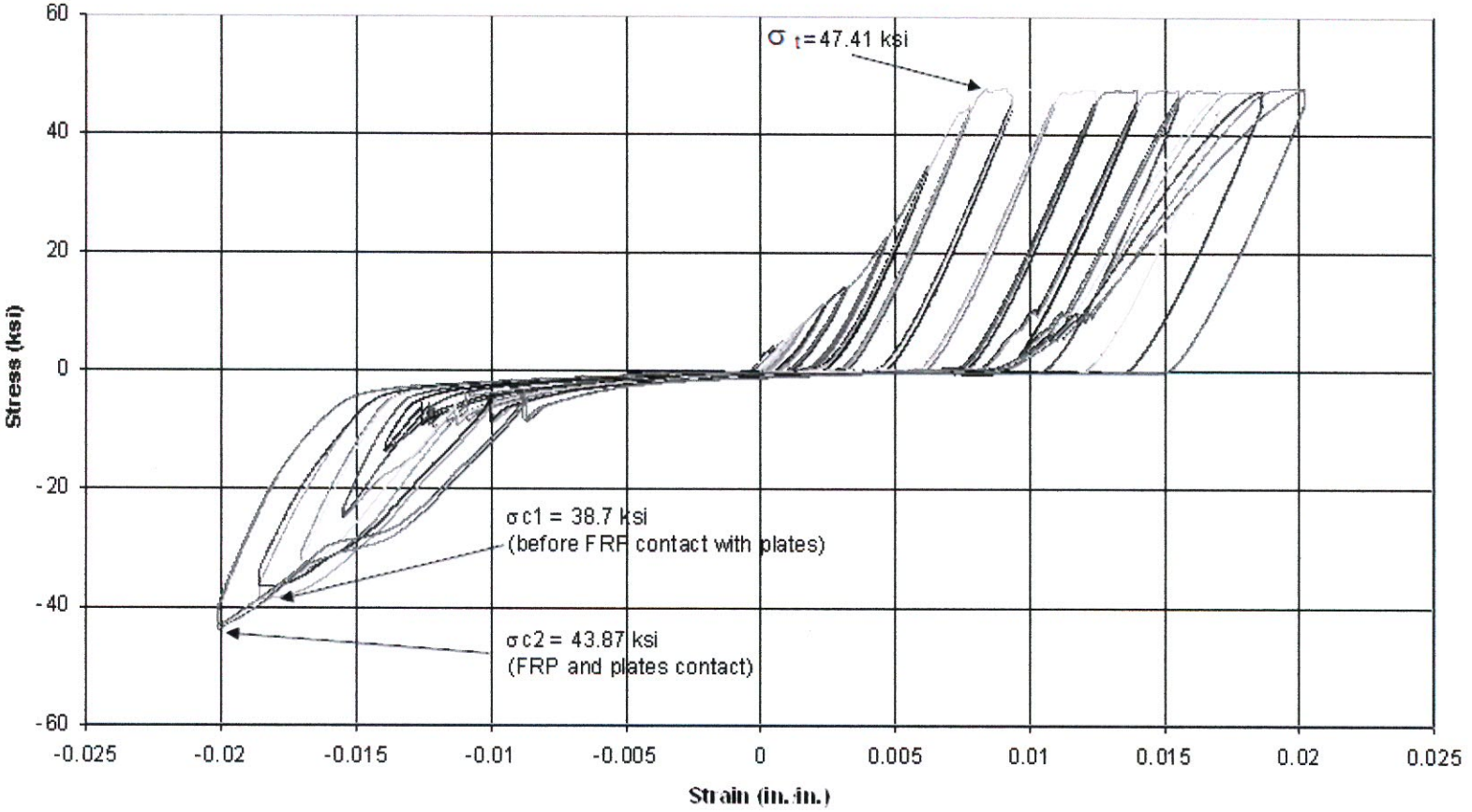

Fig. 8.28 - Specimen #11, 4 Bars Type "A", 98.95% Confinement Ratio, Concentric Load.

compressive stresses if more cycles with larger displacement amplitudes had been applied.

Under tension, the fuse yielded at a stress of 47.41 ksi during load step 10, cycle 1, and the maximum stress remained stable during subsequent cycles with larger displacement amplitudes. The "pinching effect observed in the curve (Fig. 8.28) is the result of small rigid displacement caused by a gap in the articulation at the ends of the specimen.

8.4.1.2 Specimen #12 – 4 bars – type A – 98.95% Confinement Ratio - Eccentric Load

Specimen 12 was the first of three full-scale 4 bar specimens subjected to eccentric cyclic loads. This specimen was an exact replica of the preceding specimen 11, with same confinement system, and it was subjected to 50 cycles as well. The only difference is the load was applied at an eccentricity of 1.5-in. with respect to the longitudinal axis of the fuse in between two of the four bars.

During the early stages of the cyclic test those two bars aligned with the point of load were taking almost the entire load, and were subjected to severe inelastic deformations in both tension and compression. The other two bars opposite to the point where the load was applied where hardly taking significant stresses. As the displacement amplitudes increased, these two bars started to make a more significant contribution to the fuse capacity in both tension and compression.

After the test the four bars with their respective inner urethane cores were removed from the urethane matrix, and it was observed that the two bars on the side of the eccentric axial load were severely deteriorated, while the other two bars on the other side opposite to the point of application of the load were almost straight with no major signs of deterioration.

The test was stopped when the edges of the CFRP layer started to make contact with the steel plates to protect both the urethane matrix and the CFRP layer. This happened at the end of load step 17, cycle 2, overall cycle 50. At this point significant fuse rotation was observed (Fig. 8.29).

The two bars aligned with the eccentric load point of application yielded during load step 7, cycle 1, overall cycle 29, at an average stress over the 4 bars of 24.67 ksi. The maximum tensile stress during subsequent cycles with larger displacement amplitudes gradually increased up to an average stress of 39.50 ksi, measured during the last load step. As the amplitude of the displacement at evey load step increased, the two bars located on the opposite side of the point of application of the load started to take tensile stresses, and the specimen almost reached the maximum tensile strength measured during testing of the preceding specimen 11.

During the first eight load steps the amplitude of the dispalcements was not sufficient to apply axial compressive load to the gap in the joints at the ends of the specimen. It was not until load step 9, cycle 1, overall cycle 33 that the specimen started to take compressive stresses. The bars of the fuse never reached buckling before the edges of the CFRP layer made contact with the steel plates, and the

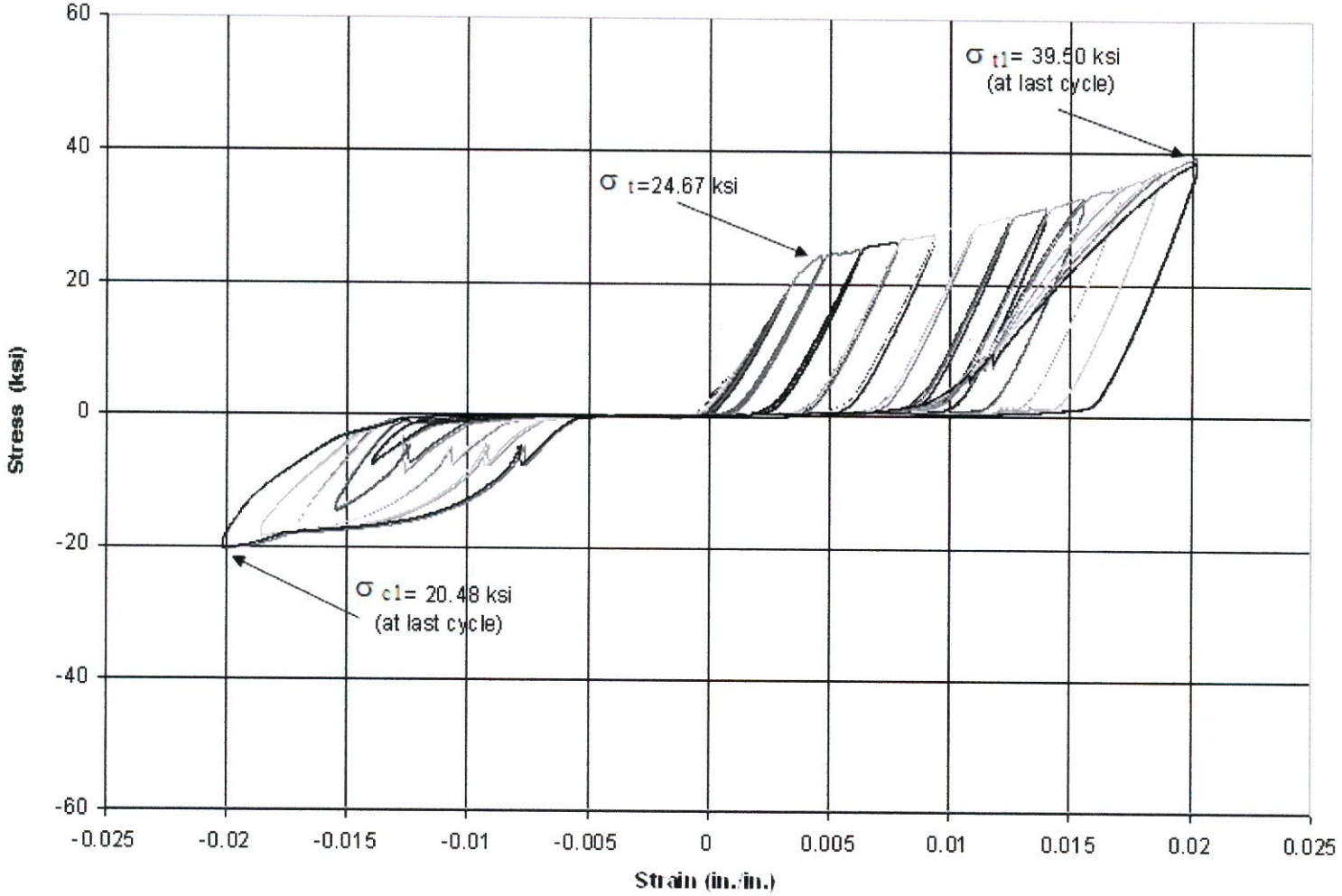

Fig. 8.29 - Specimen #12, 4 Bars Type "A", 98.95% Confinement Ratio, Eccentric Load.

capacity in compression progressively increased at larger displacement amplitudes. The fuse was able to reach an average maximum compressive stress of 20.48 ksi during the last load step (step17, cycle 2, overall cycle 50).

The specimen would have taken more stress in both directions if the fuse had been subjected to larger displacement amplitudes, but the test was stopped to preserve the integrity of the confining system.

8.4.1.3 Specimen #13 – 4 Bars – Type A – 97.92% Confinement Ratio – Concentric Load

Specimen 13 with 4 type A bars was subjected to only 47 cycles instead of 50 cycles because the steel plates were making contact with the CFRP layer. The test was stopped because the edges of the CFRP layer were being significantly damaged due to large rotation, and the urethane matrix inside holes was also at risk of sustaining significant damage.

The fuse yielded during load step 8, cycle 1, at an average stress of 46.16 ksi. The maximum tensile stress at subsequent cycles with larger displacement amplitudes remained stable. During the last cycle the maximum tensile stress reached a maximum up to 47.64 ksi (Fig. 8.30).

The specimen started to take compressive stresses during load step 11, cycle 37. This specimen never reached bukcling of the bars before the edges of the CFRP layer made contact with the steel plates. The maximum compressive stress, without contribution from the CFRP, was 30.35 ksi at load step 13, cycle 1, overall cycle 40.

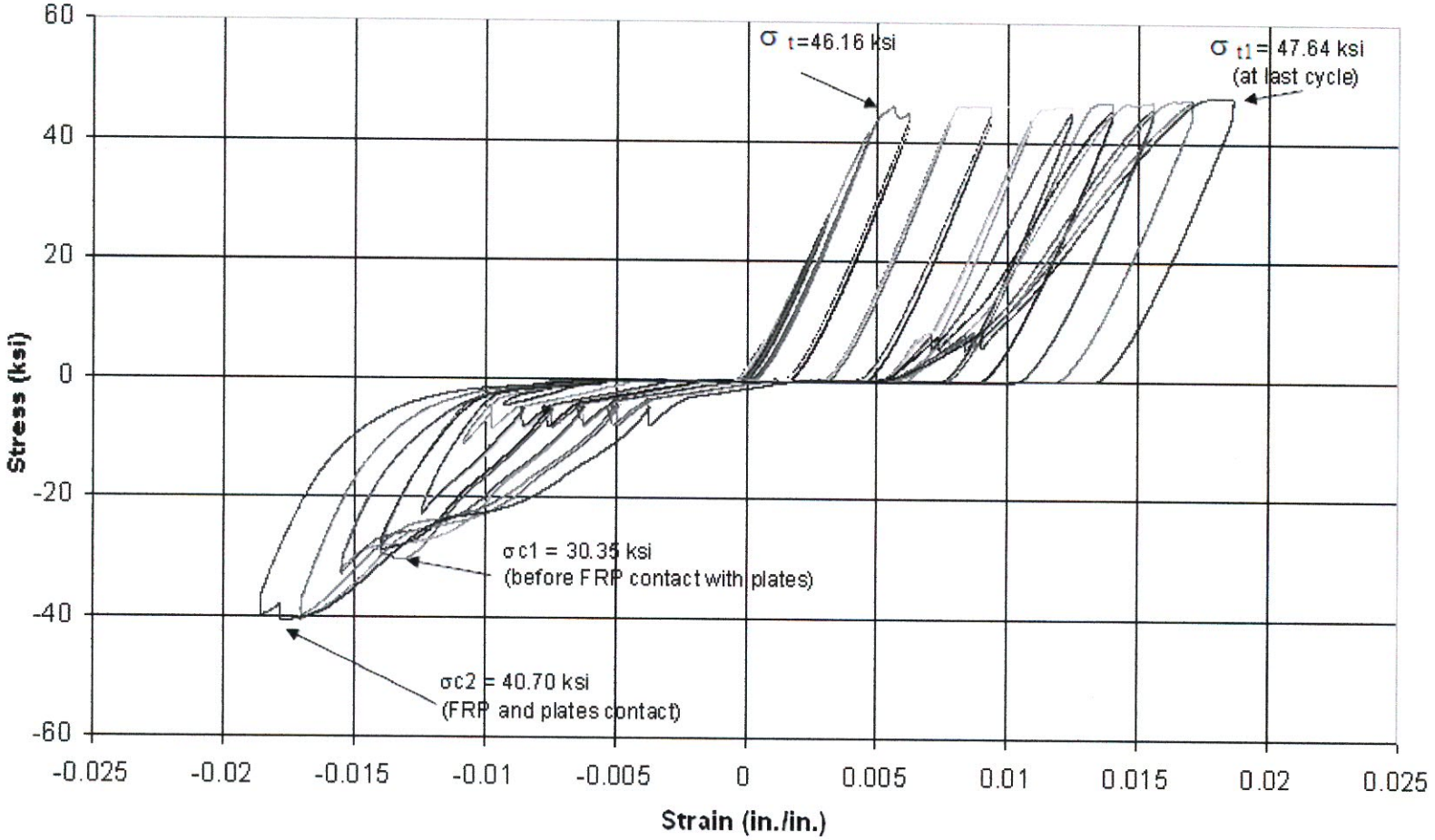

Fig. 8.30 - Specimen #13, 4 Bars Type "A", 97.92% Confinement Ratio, Concentric Load.

The maximum compressive stress was 40.7 ksi, measured during the last load step (step 16, cycle 1, overall cycle 47).

8.4.2 Series 2 - Bar type B

The second group of the second experimental series includes three full-scale specimens with 4 type B bars. Similar to the specimen selection with the type A bar, the first two specimens used exactly the same urethane matrix and CFRP layer. Only the bars with their respective inner cores were replaced, and the text fixture was adjusted to a different position so that the fuse was subjected to concentric loads first and then axial loads applied at an eccentricity of 1.5-in. from the longitudinal axis. The third specimen was subjected to concentric loads with a lower confinement ratio.

8.4.2.1 Specimen #14 – 4 Bars – Type B – 98.44% Confinement Ratio – Concentric Load

Specimen 14, with 4 type B bars, was subjected to 51 cycles. During load step 12 a very unusual loud sound came from the loading frame. At this point the test was interrupted to inspect the test fixtures and the fuse for possible failed parts. For safety reasons the hydraulic pump was turned off to prevent the specimen from being loaded while the inspection was taking place. It was observed during this thorough inspection that two tension nuts were loose and therefore two out of four bars were not taking loads under compression. The problem was corrected and since nothing else was found the test resumed at load step 12. After the hydraulic pump was turned

back on and the test resumed the fuse started to take compressive stresses. What happened with the two loose tension nuts is that it took additional displacement during the initial load steps to load the bars in compression as the plates were displacing without making contact with the bar shoulders.

Looking at the stress-strain hysteretic loops (Fig. 8.31) there is a discontinuity between load steps 11 and 13 due to the inspection, since the hydraulic pressure was released during load step 12.

The test stopped after load step 18, cycle 1, for the same reasons it was stopped during preceding tests (the CFRP layer was making contact with the steel plates).

The fuse reached buckling during load step 16, cycle 1, overall cycle 47, at an average stress of 51.23 ksi. The capacity in compression decreased a little to 49.88 ksi during the next load step (step 17), but then it increased to 53.53 ksi during load step 18 due to the contribution of the CFRP. At this point it was decided to stop the test in order to protect the confining system from severe deterioration.

Under tension the fuse initially started to take inelastic deformations during load step 8, cycle 1, overall cycle 31, at an average stress of 40.31 ksi. During subsequent cycles with larger displacement amplitudes the tensile stress increased to 46.91 ksi (during load step 11) before the inspection. After the test resumed the specimen was immediately subjected to tensile stresses during load step 13 but it was not until load step 16 when the fuse was subjected once more to inelastic deformations under tension loads, and the average stress increased to 45.25 ksi.

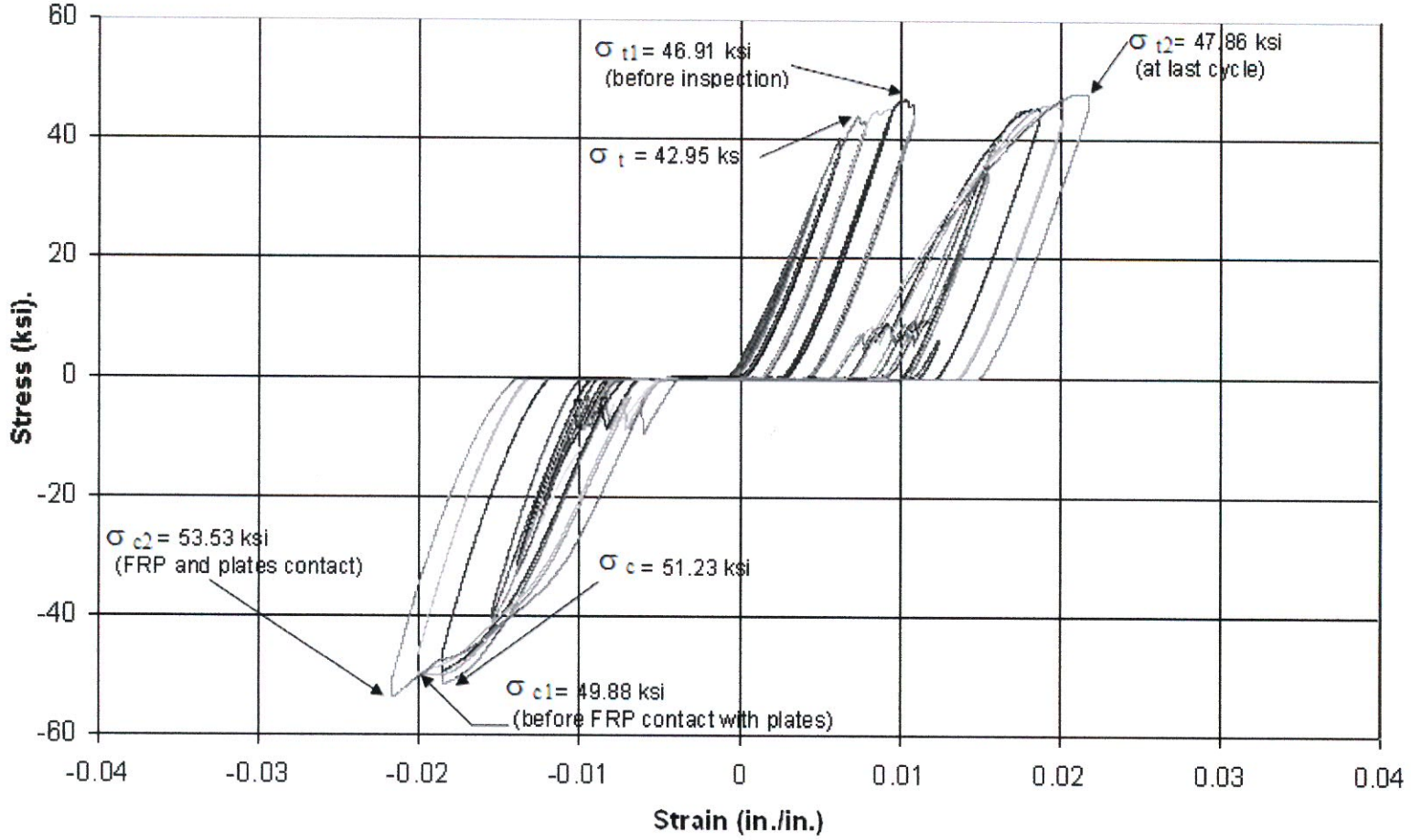

Fig. 8.31 - Specimen #14, 4 Bars Type "B", 98.44% Confinement Ratio, Concentric Load.

During the last load step (load step 18, cycle 1, overall cycle 51) the tensile stress reached a maximum of 47.86 ksi.

8.4.2.2 Specimen #15 – 4 Bars – Type B – 98.44% Confinement Ratio – Eccentric Load

Specimen 15 (Fig. 8.32) is the second of three full-scale – 4 bar specimens subjected to eccentric cyclic loads. This specimen was an exact replica of specimen 14, with the same confinement system. The only difference was that the axial load was applied eccentrically at 1.5-in. with respect to the centroid of the fuse in the middle of 2 of the four bars. During the test those two bars aligned with the point of load took almost the entire load and were subjected to severe inelastic deformations in both tension and compression, whereas the other two bars opposite to the point where the load was applied took a small fraction of the load. As the displacement amplitudes increased, these two bars started to make a gradually increasing contribution to the capacity of the fuse in both tension and compression. This specimen was subjected to a total 61 cycles.

After the test the four bars with their respective inner urethane cores were removed from the urethane matrix and it was observed that the two bars on the side of the eccentric axial load were severely deteriorated, whereas the other two bars on the other side opposite to the point of application of the load were almost straight with no major signs of deterioration.

The test was stopped to protect both the urethane matrix and the FRP wrap after load step 23, cycle 1, overall cycle 61, when significant rotation of the end plates was observed.

The two bars aligned with the eccentric load point of application yielded during load step 9, cycle 1, overall cycle 33, at an average stress of 24.04 ksi. The maximum tensile stress during subsequent cycles with larger displacement amplitudes continously increased at a constant rate up to an average stress of 39.50 ksi (during load step 20, cycle 1, overall cycle 55). During load step 21, cycle 1, overall cycle 57, the tensile stiffness of the fuse increased as the two bars opposite to the point of application of the load started to make a significant contribution to the tensile capacity of the fuse. At this load step the tensile stress increased to 36.49 ksi. During subsequent cycles with larger displacement amplitudes the tensile stress gradually increased at a higher rate up to a maximum of 42.77 ksi during the last load step (load step 23, cycle 1, overall cycle 61).

Under compression loads it was not until load step 12, cycle 1, overall cycle 41, that the fuse started to take compression. This is similar to the behavior of specimen 14. The urethane matrix was ½-in. larger than the bars to allow for pre-compression of the matrix during fuse assembly to make the confinement system active before the bar was subjected to compression loads. For this reason the fuse was displaced 0.1367-in. in compression before the bars sustained significant compressive stresses. The bars of the fuse reached buckling during load step 22, cycle 1, overall

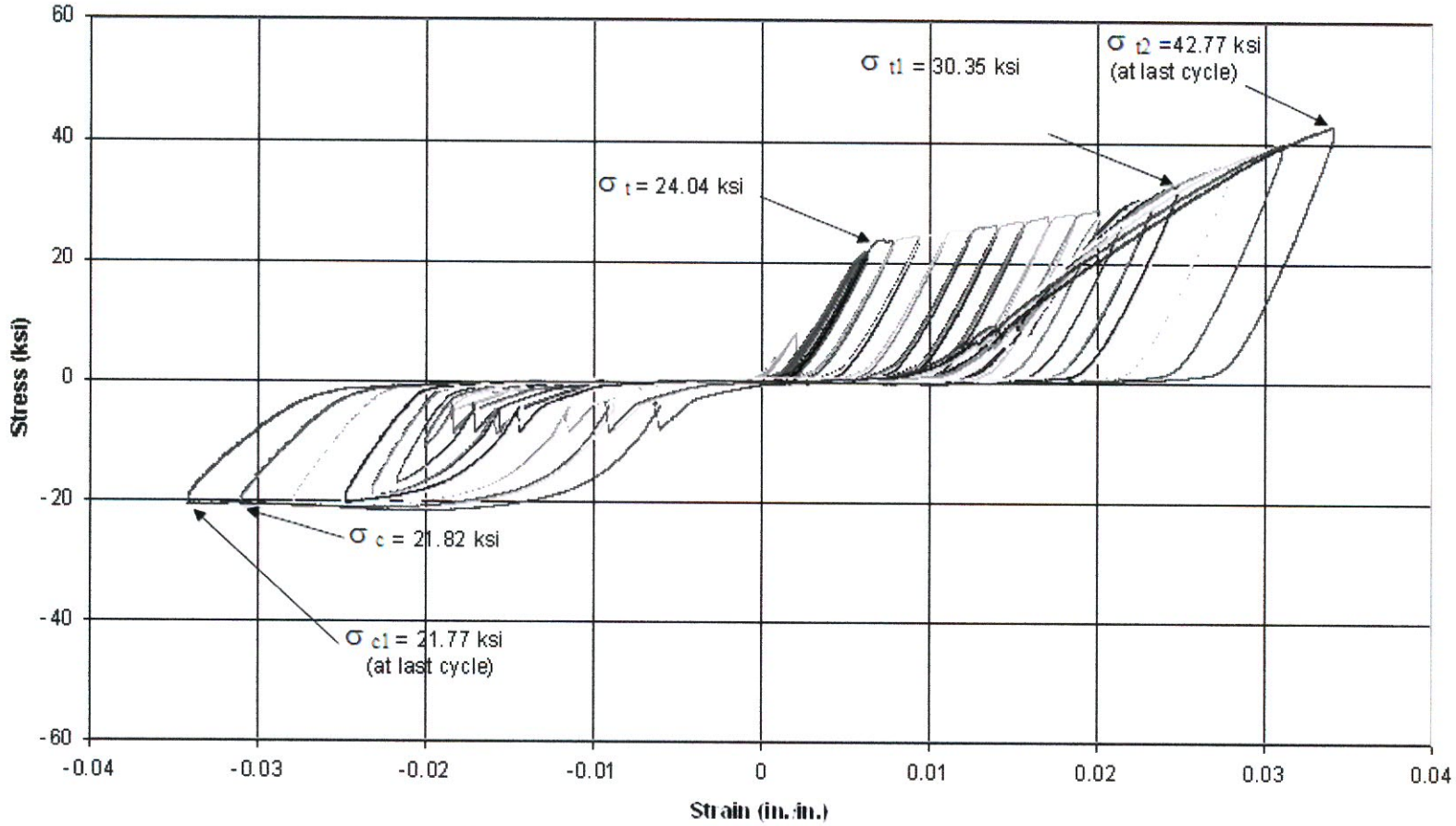

Fig. 8.32 - Specimen #15, 4 Bars Type "B", 98.44% Confinement Ratio, Eccentric Load.

cycle 59, at an average stress of 21.82 ksi. During the following load step, with a larger displacement amplitude, the average stress decreased to 21.77 ksi (Fig. 8.32).

The edges of the CFRP layer never made contact with the steel plates, but the test stopped anyways as significant fuse rotations raised concerns of excessive inelastic deformation of the bars under compression that could have damaged the urethane holes.

8.4.2.3 Specimen #16 – 4 Bars – Type B – 93.75% Confinement Ratio – Concentric Load

Specimen 16 with 4 type B bars was subjected to 61 cycles as well (Fig. 8.33). The test was stopped after load step 23, cycle 1, due to significant fuse rotation that caused the CFRP layer to take significant compressive stresses as it made contact with the steel plates at top and bottom of the fuse. In addition to concerns on the CFRP layer, the urethane matrix inside holes were at risk of sustaining significant damage as the bars were being subjected to large inelastic buckling deformation, which could cause the bars to cut through the inner core.

The fuse yielded in tension during load step 10, cycle 1, overall cycle 35, at an average stress of 48.77 ksi. The maximum tensile stress at subsequent cycles with larger displacement amplitudes remained stable and gradually increased without any major change. During the last load step (step 23, cycle 1, overall cycle 61) the maximum tensile stress was 52.64 ksi.

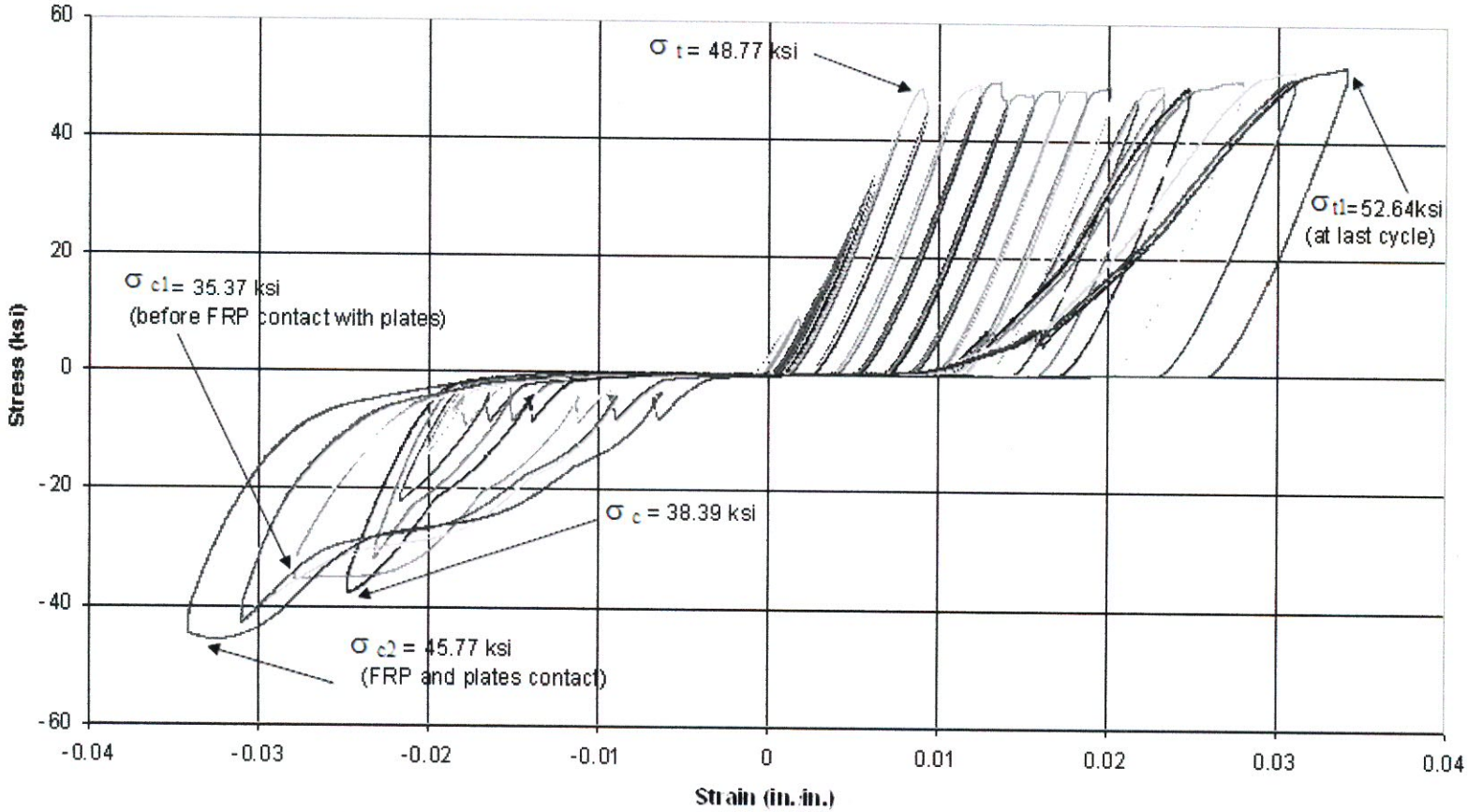

Fig. 8.33 - Specimen #16, 4 Bars Type "B", 93.75% Confinement Ratio, Concentric Load.

The specimen started to take compressive stresses during load step 12, cycle 1, overall cycle 39, and the bars buckled during load step 20, cycle 1, overall cycle 55, at an average stress of 38.39 ksi. After reaching buckling, the compressive stress at peak dispalcement amplitude during the following load step (step 21) decreased to 35.37 ksi. During load step 22 the CFRP layer made contact with the steel plates increasing the fuse compressive stiffness and reaching a maximum compressive stress at this load step of 41.49 ksi. During the last load step the fuse maximum stress increased to 45.77 ksi.

8.4.3 Series 2 - Bar type C

The last group of this second experimental series includes three full-scale specimens with 4 type C bars. Similar to the specimen selection with the type A and B bars, the first two specimens of this group used exactly the same urethane matrix and CFRP layer. Only the bars with their respective inner cores were replaced and the text fixture was adjusted to a different position to apply concentric loads first and then axial loads at a 1.5-in. eccentricity with respect to the centroidal axis of the fuse. The third specimen was subjected to concentric loads with a lower confinement ratio.

Because deterioration or failure of the urethane matrix or the CFRP layer was no longer a concern, all three specimens of this series were tested until failure or until testing equipment safety became a concern.

8.4.3.1 Specimen #17 – 4 Bars – Type C – 96.87% Confinement Ratio – Concentric Load

Specimen 17 with 4 type C bars was subjected to 66 cycles (Fig. 8.34). The test was stopped after load step 24, cycle 2, because the pins of the testing fixture used to released moment transfer from the fuse to the loading equipment started to fail. After the first pin fractured it was replaced twice by new pins but they both failed after the test resumed. The diameter and material of these pins was conservatively chosen to provide enough shear capacity to avoid this type of failure, but due to the nature of the testing fixture these pins were consistently subjected to small impact loads as the axial load changed from tension to compression.

Testing of specimen 17 was the most challenging of all. After the fuse seemed to have yielded the maximum tensile stress during subsequent cycle decreased with increasing displacement amplitude. It was not until load step 23 of this first full-scale specimen that the test was interrupted to perform a thorough inspection.

The inspection first focused on the threaded portion of one of the four bars because as the specimen was being assembled on the testing frame, it was noticed that one of the bars presented thread imperfections and several washers were required to make the nut properly tie the bar to the steel plates. During the inspection it was found that this tension nut was loose and it turned out that too many washers were used, keeping the nut from transferring a 100% of the tensile load as intended because the nut was not fully connected to the bar threads. For this reason, after the fuse

reached F_y, the tensile strength was basically provided by three bars acting at a 100% of their capacity, and a fourth bar partially taking tensile stress. A few washers were removed and the nut was properly tied to the bar before the test resumed and the fuse performed as expected under tensile stresses.

The CFRP layer made contact with the steel plates between load steps 21 and 22. The fuse never reached buckling of the bars as the compressive stress of every cycle increased at larger displacement amplitudes (Fig. 8.34). The fuse was able to reach an average compressive stress of 53.48 ksi before its stiffness increased due to the contribution from the CFRP layer. During the last cycle the fuse was able to sustain an average compressive stress of 68.96 ksi.

Under tension the fuse initially started to take inelastic deformations during load step 16, cycle 1, overall cycle 49, with an average tensile stress of 43.04 ksi. After the fuse bars yielded it started to behave erratically under tension during subsequent cycles due to the bar problem. After the problem was solved, the fuse started to performed as expected under tensile loads, and it was able to sustain a maximum tensile stress of 54.98 ksi during the last cycle at peak displacement amplitude.

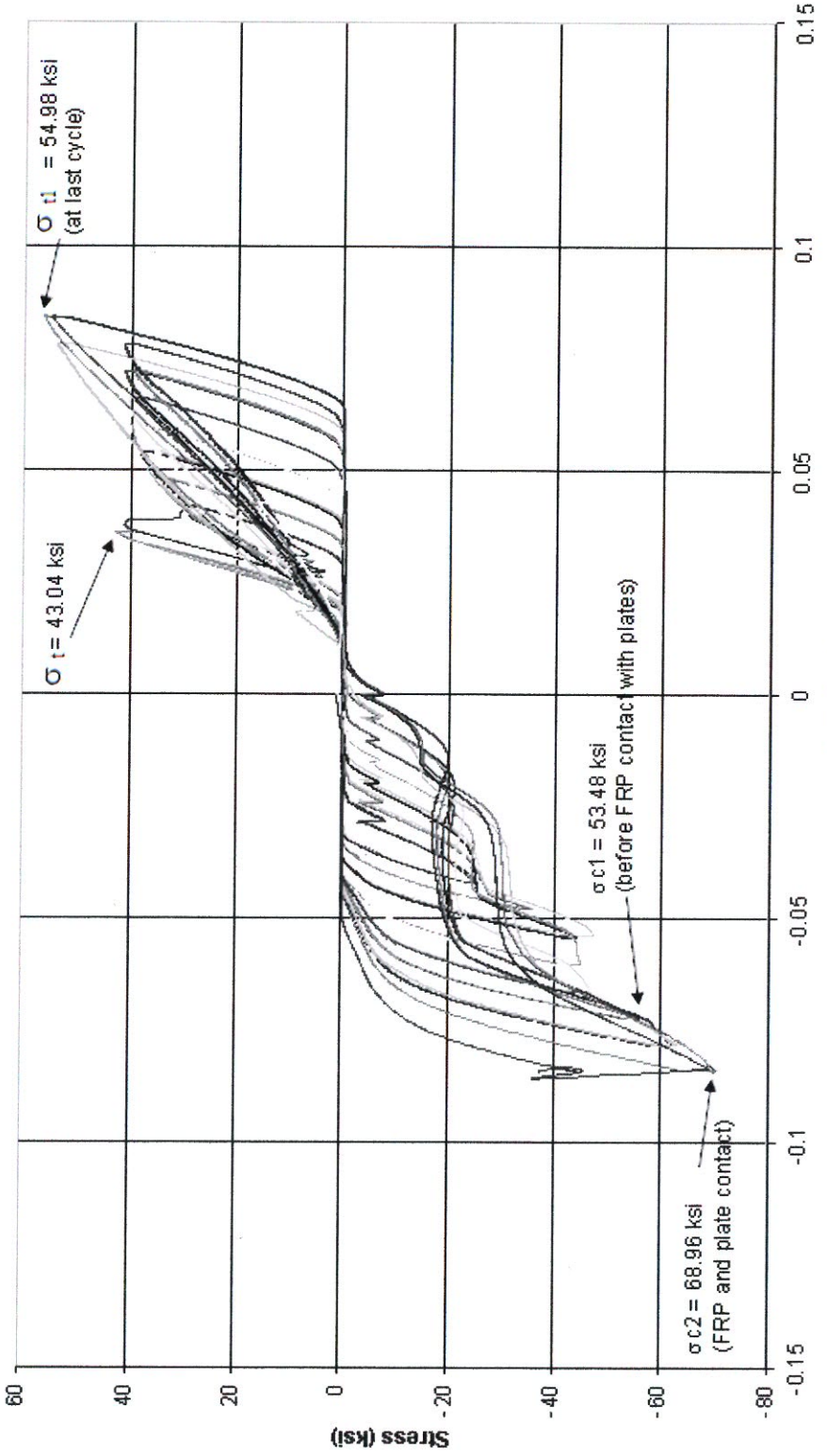

Fig. 8.34 - Specimen #17, 4 Bars Type "C", 96.87% Confinement Ratio, Concentric Load.

8.4.3.2 Specimen #18 – 4 Bars – Type C – 96.87% Confinement Ratio – Eccentric Load

Specimen 18 was the last full-scale 4 bar specimen subjected to eccentric cyclic loads and it was subjected to 66 cycles (Fig. 8.35). This specimen is a replica of specimen 17 with same confinement system. The only difference was the eccentric axial cyclic load which was applied at 1.5-in. with respect to the centroidal axis of the fuse. During the cyclic loading test the two bars aligned with the point of application of the load took almost the entire load, and were subjected to severe inelastic deformations in both tension and compression. Early in the test the other two bars, opposite to the point where the load was applied, were hardly damaged. As the displacement amplitude increased these two bars started to make a significant contribution to the fuse capacity in both tension and compression.

After the test, the four bars with their inner urethane cores were removed from the urethane matrix and the two bars on the side of the eccentric axial load were severely deteriorated, whereas the other two bars on the other side were almost straight with no major signs of deterioration.

The test was stopped after load step 24, cycle 2, due to excessive rotation and excessive contact between the CFRP layer and the steel plates (Fig. 8.35).

The two bars aligned with the point of application of the load yielded during load step 17, cycle 1, overall cycle 51, at an average stress of 21.65 ksi. The maximum tensile stress during subsequent cycles increased up to a maximum 34.72

ksi during the last load step (step 24, cycle 2, overall cycle 66). Even though the tensile stress increased at larger displacement amplitudes, the stiffness of the fuse decreased as the four bars were gradually taking the same load with larger displacement amplitudes.

The maximum compressive stress never decreased with respect to increasing displacement amplitude. The last displacement amplitude before the CFRP layer made contact with the plates was at load step 21, where the fuse reached a maximum average compressive stress of 31.98 ksi. The CFRP layer made contact with the steel plates during load step 22, cycle 1, overall cycle 61, and the fuse reached a maximum average compressive stress at the peak displacement amplitude of the last cycle (45.07 ksi) before the test was stopped.

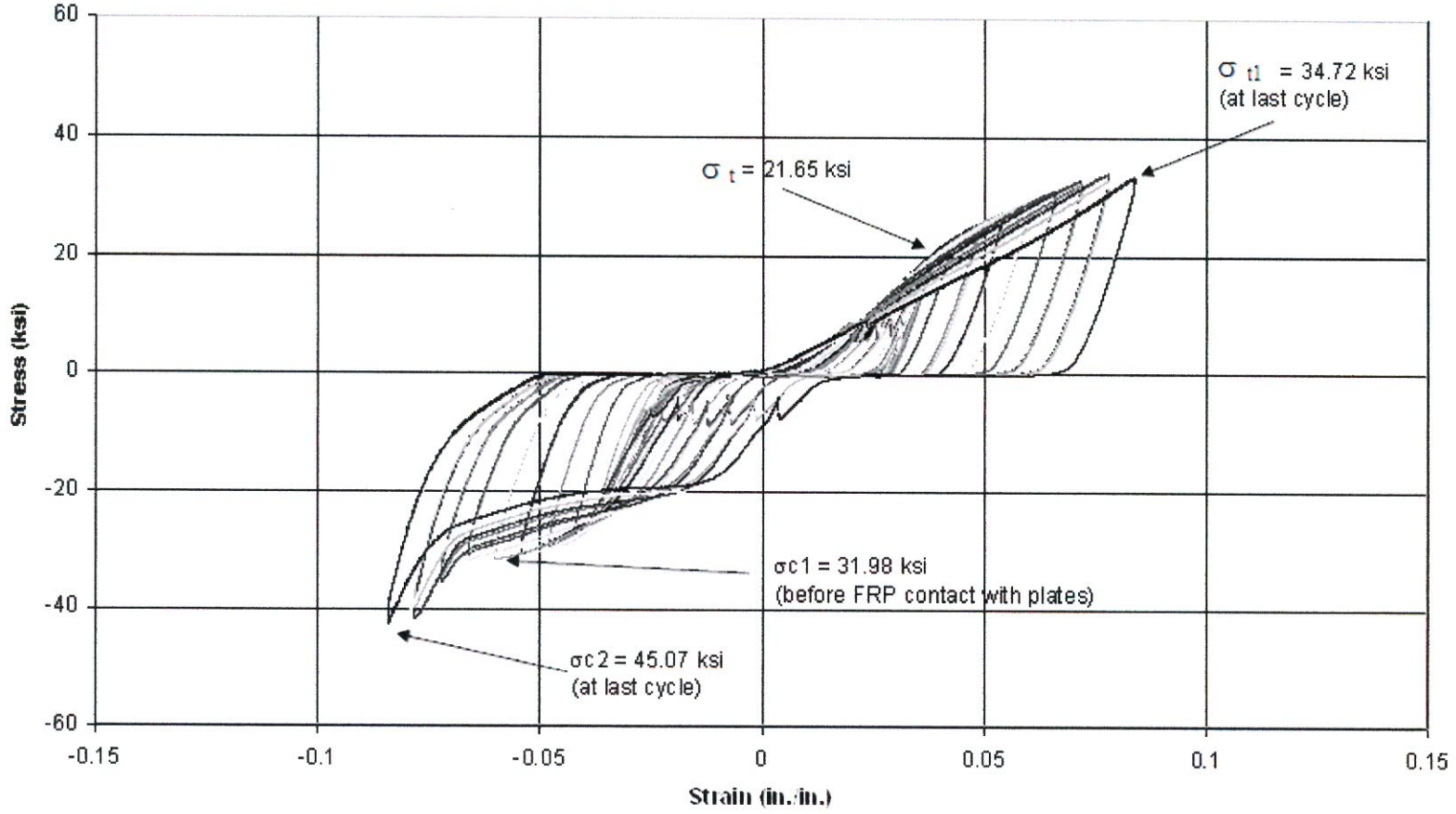

Fig. 8.35 - Specimen #18, 4 Bars Type "C", 96.87% Confinement Ratio, Eccentric Load.

8.4.3.3 Specimen #19 – 4 Bars – Type C – 91.41% Confinement Ratio – Concentric Load

Specimen 19, with 4 type C was subjected to 71 cycles (Fig. 8.36). This was the last specimen tested. The test was stopped after load step 27, cycle 1, because the pins of the test fixture started to fracture as they were not able to support more shear stress. After the first pin fracture, three more pins were used and all three failed as well.

The fuse yielded during load step 18, cycle 1, overall cycle 53, at an average stress of 48.67 ksi. The maximum tensile stress at subsequent cycles with larger displacement amplitudes gradually increased, and during the last load step (step 27, cycle 1, overall cycle 71) it increased up to 62.19 ksi at peak displacement amplitude (Fig. 8.36).

It appears that the bar bukcled during load step 19, cycle 1, overall cycle 55, at an average stress of 43.56 ksi, but the compressive stress never decreased sinigficantly with increasing displacement amplitude. The maximum compressive stress recorded was 43.43ksi after that the CFRP layer increased the stiffness of the fuse by making contact with the steel plates. During the last load step (step 27, cycle 1, overall cycle 71) the maximum average compressive stress was 64.64 ksi.

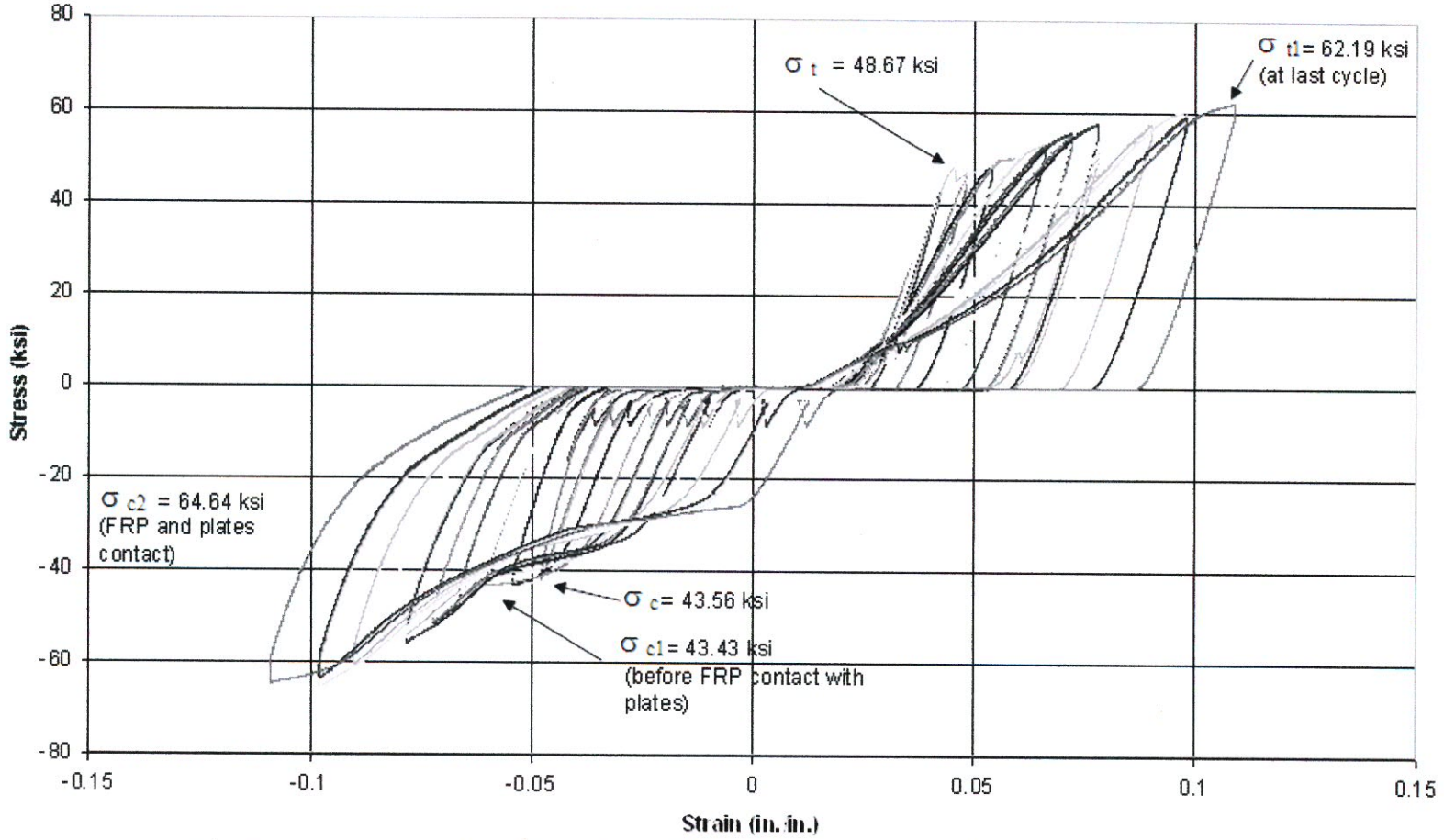

Fig. 8.36 - Specimen #19, 4 Bars Type "C", 91.41% Confinement Ratio, Concentric Load.

8.4.4 Series 2 Experimental Results Summary

Results obtained from the second series do not reflect the expected behavior of the fuse in a braced frame because the end conditions used during the tests are similar to a pinned condition instead of a more realistic fixed-end condition. These experimental results provided important information about the behavior of the fuse when subjected to concentric loads relative to its behavior when subjected to eccentric loads. The significance of this second series also relies on variations in the behavior of the fuses with respect to the confinement ratio and the fuse slenderness or yield zone capacity.

The yield strength of almost all these second series specimens subjected to axial concentric loads was equal to that obtained from the monotonic tension test on a bar without the confining system (Section 8.2.1), with the exceptions of specimens 14 and 17, where the yield strength was below the expected strength. This is attributed to difficulties presented during these tests. For specimen 14 there was an interruption of the test that was necessary at the time in order to inspect the specimen for safety reasons, as explained in Section 8.4.2.1. For specimen 17 there was a defect on a bar at the top threaded area that required special assembly methods as explained in Section 8.4.3.1.

One lesson learned from the first experimental series is that the magnitude of the pre-compressing force and how far the urethane matrix is pre-compressed affect the tensile and compressive capacities of the fuse. Different matrices were fabricated

from different castable urethane batches during fabrication of the first series specimens and the total height of some matrices were different as it was difficult to control or predict how much the urethane expanded as it cured. Unlike the first series where matrices were fabricated from different mix batches, for the second series only one urethane matrix was fabricated and then it was cut to obtain the shorter specimens. This allowed for more consistency in terms of matrix pre-compression force during specimen assembly on the test frame.

The matrix used in the type A 4-bar specimens, was 24.75-in. long instead of 24-in. After testing the first three type A 4-bar specimens the main matrix was cut in two pieces each, 16.5-in. long, instead of 16-in. For type C bars the matrix was 8.25-in.long. It was a difficult and tedious process to apply the same pre-compressive loads with the testing equipment. Due to the inconsistencies in matrix pre-compression during the first experimental series, and the testing difficulties with two specimens, 14 with type B bars and 17 with type C bars, the type A 4-bar specimens 11, 12, 13 are considered to be more reliable for the purposes of comparing the effects of eccentricity of the load and confinement ratio.

Between specimens 11 and 13, both subjected to concentric axial cyclic loads, the specimen with higher confinement ratio provided slightly larger yield strength. Specimen 12 was an exact replica of 11, but it was subjected to eccentric loads. Its average yield strength was half of that reached by specimen 11 under concentric loads, which indicates that the fuse tensile stress was concentrated on the two bars directly under the eccentric load instead of all 4 bars. Thus, the yield strength was that

of two bars. As the specimen was subjected to larger displacement amplitudes within the tensile inelastic range of response the two bars on the other side of the eccentric load started to take tensile stresses and the tensile capacity of the fuse gradually improved.

Under compression, none of the type A 4-bar specimens reached buckling of the metal bars before contact with the CFRP layer due to the fuse rotation. Even though the compressive capacity of specimen 12, subjected to eccentric loads, was almost half of that of its counterpart 11 under concentric loads. Load carried by the bars was still over the nominal buckling capacity without the confining system. Taking into account that the end conditions applied to the specimens were not representative of the real end conditions, and actually very detrimental to the fuse energy dissipation capabilities, the experimental results confirm that these fuse possibilities are very promising.

Between specimens 11 and 13, both subjected to concentric loads, the compressive capacity decreased as the confinement ratio decreased.

Specimen	Bar type	Confinement Ratio (%)	Cycles	Maximum Tensile Stress at yield σt (tension)		Maximum Compressive Stress at buckling σc (compression)	
				Strain amplitude (in./in.)	Stress (ksi)	Strain amplitude (in./in.)	Stress (ksi)
#11	A	98.96	50	0.00798	47.41	0.01597	38.7
#12	A	98.96	50 eccentric	0.00399	24.67	0.01597	18.28
#13	A	97.92	47	0.00532	46.16	0.01198	30.35
#14	B	98.44	51	0.00488	42.95	0.01465	49.88
#15	B	98.44	61 eccentric	0.00611	24.04	0.02441	21.82
#16	B	93.75	61	0.00733	48.77	0.01953	38.39
#17	C	96.87	66	0.0207	43.04	0.03795	53.48
#18	C	96.87	66 eccentric	0.02415	21.65	0.03795	31.98
#19	C	91.41	71	0.0276	48.67	0.03105	43.56

Table 8.10 - Experimental Series #2 Results Summary.

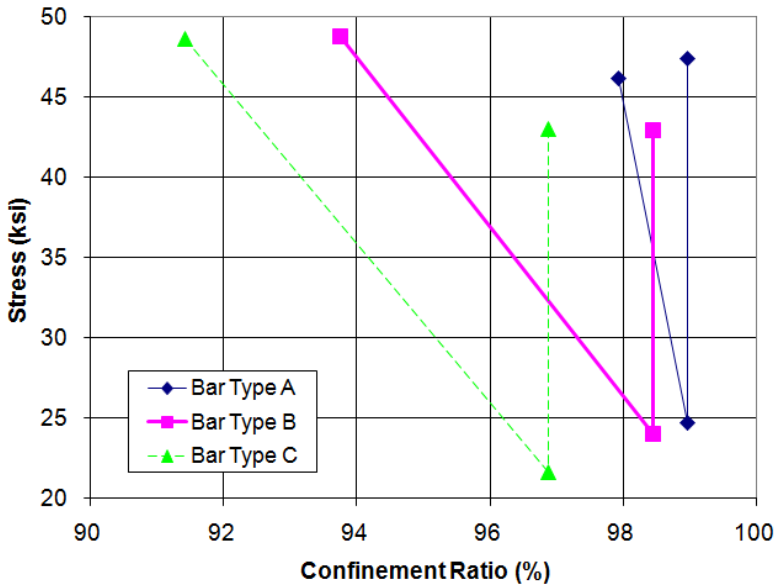

Fig. 8.37 - Maximum Tensile Stress "σ_t (Tension)" vs. Confinement Ratio

4-Bar BCE Fuse.

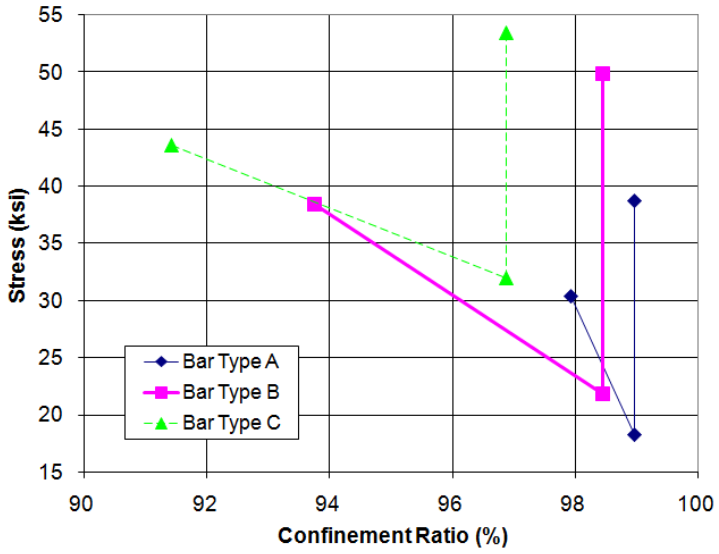

Fig. 8.38 - Maximum Compressive Stress "σ_c (Compression)" vs. Confinement Ratio

4-Bar BCE Fuse.

The maximum stress in compression was below the maximum stress in tension for most of the specimens with the exception of 14, 17, and 19. The maximum stress in tension was approximately equal or greater than the yield stress when the fuse was subjected to concentric loads and below the yield stress under eccentric loads. The maximum stress in compression was below the yield stress for most specimens with the exception of specimens 14, 17, and 19 (Table 8.11).

Specimen	Bar Type	Confinement Ratio (%)	$\sigma t / F_y$ (F_y=43.5 ksi)	$\sigma c / F_y$ (F_y=43.5 ksi)	σ_t/σ_c
#11	A	98.96	1.09	0.89	1.23
#12	A	98.96	0.57	0.42	1.35
#13	A	97.92	1.06	0.70	1.52
#14	B	98.44	0.99	1.15	0.86
#15	B	98.44	0.55	0.50	1.10
#16	B	93.75	1.12	0.88	1.27
#17	C	96.87	0.99	1.23	0.80
#18	C	96.87	0.50	0.74	0.68
#19	C	91.41	1.12	1.00	1.12

Table 8.11 - 4-Bar BCE Fuse Stress Ratios.

Specimen	Bar Type	Confinement ratio (%)	Tension		Compression	
			σ_{t1} (ksi)	σ_{t2} (ksi)	σ_{c1} (ksi)	σ_{c2} (ksi)
11	A	98.96	47.41 at last cycle	-	38.7 plates CFRP contact	43.87 at last cycle
12	A	98.96	39.5 at last cycle	-	20.48 at last cycle	-
13	A	97.92	47.64 at last cycle	-	30.35 plates CFRP contact	40.7 at last cycle
14	B	98.44	46.91 before inspection	47.86 at last cycle	49.88 plates CFRP contact	53.53 at last cycle
15	B	98.44	30.35 before stiffness increment	42.77 at last cycle	21.77 at last cycle	
16	B	93.75	52.64 at last cycle	-	35.37 plates CFRP contact	45.77 last cycle
17	C	96.87	54.98 at last cycle	-	53.48 plates CFRP contact	68.96 last cycle
18	C	96.87	34.72 at last cycle	-	31.98 plates CFRP contact	45.07 at last cycle
19	C	91.41	62.19 at last cycle	-	43.43 plates CFRP contact	64.64 at last cycle

Table 8.12 - Experimental Series #2 Results Summary, Stresses at Inelastic Deformations.

Almost all four bar fuse specimens had the edge of the CFRP layer take compressive stress directly from the steel plates (Table 8.12). The compressive stress vs. the confinement ratios of those specimens was plotted and is shown in Fig. 8.39.

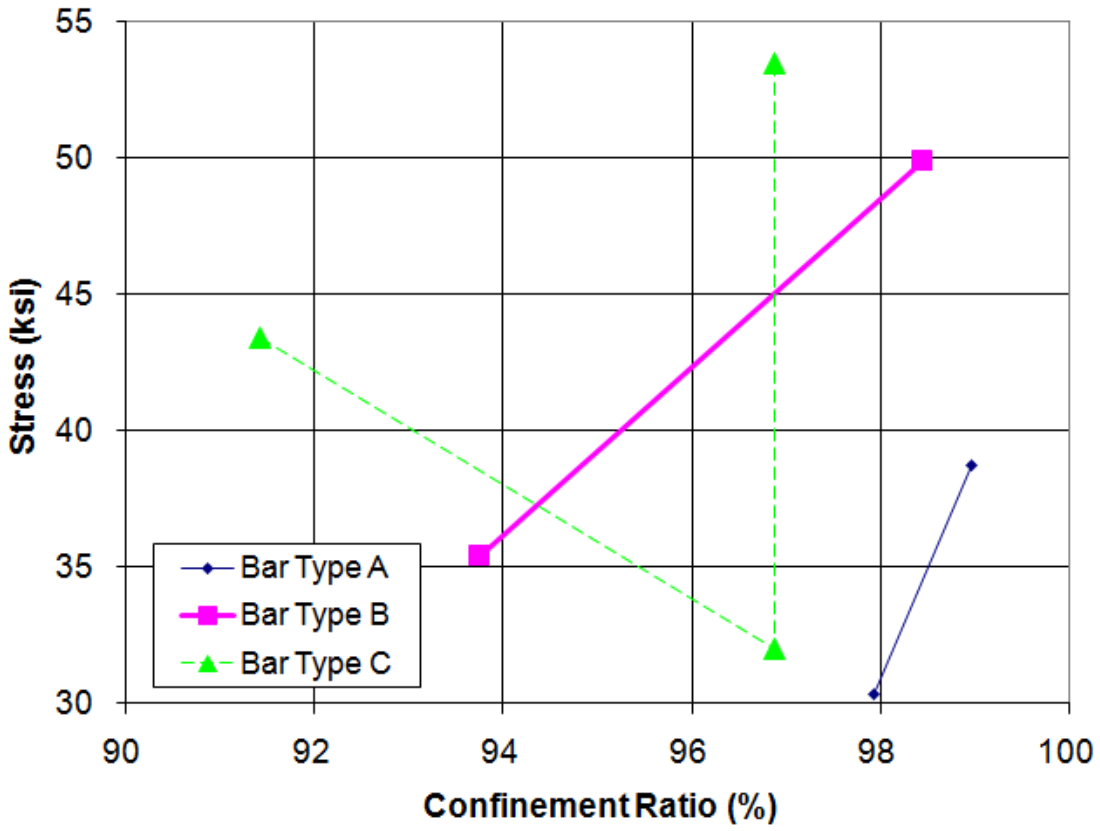

Fig. 8.39 - Maximum Compressive Stress before Contact between CFRP Layer and Steel Plates.

The nominal buckling capacity of the bars without the confining system and assuming the length of the ½-in. diameter reduced section and pin end conditions was calculated following the thirteenth edition of the AISC manual [AISC, 2005] as follows:

Bar Type	Yield Zone Length (in.)	Effective Length Factor "K"
A	20.6	1
B	12.6	1
C	4.6	1

Table 8.13 - Bar Nominal Capacity in Compression, Properties, Series #2.

For a bar type A, the nominal capacity in compression can be calculated as follow:

$R = d/4 = 0.5/4 = 0.125\text{-in.}$ <Eq. 8.1>

$KL/r = 1*20.6\text{-in.}/0.125\text{-in.} = 164.8$ ksi <Eq. 8.2>

$4.71*(E/F_y)^{0.5} = 123.814$ <Eq. 8.3>

From Eq. E3-2 of the AISC Manual, thirteenth edition:

$KL/r < 4.71*(E/F_y)^{0.5}.$ <Eq. 8.4>

Then:

$$Fcr = 0.658^{(Fy/Fe)*}F_y \quad \text{<Eq. 8.5>}$$

$$Fe = \pi^2*E/(KL/r)^2 = 11.96 \text{ ksi} \quad \text{<Eq. 8.6>}$$

$$Fcr = 10.49 \textbf{\textit{ksi}}$$

$$Ag = \pi*d^2/4 = \pi*0.5\text{-in.}^2/4 = 0.19635 \text{ in}^2 \quad \text{<Eq. 8.7>}$$

$$Pn = Fcr * Ag = 2.06 \text{ kips} \quad \text{<Eq. 8.8>}$$

The nominal capacities of bars type B and C in compression were calculated following the same procedure.

A comparison of bar nominal and fuse experimentally measured capacities showed that the fuse was able to improve the buckling capacity of the bars when subjected to both concentric and eccentric loads. Bars type A buckled at a compressive stress almost four times their nominal unconfined capacity, bars type B doubled their buckling capacity, and bars type C improved their compressive capacity by 22% when embedded in the fuse (Table 8.14).

Bar Type	Fuse height (in.)	Length of ½-in. reduced section (in.)	Bar Nominal Capacity in Compression (ksi)	BCE Fuse Capacity in Compression (ksi) Concentric load	Ratio of Fuse Experimental /Bar nominal Concentric load
A	24	20.6	10.49	38.70 no critical buckling	3.69
B	16	12.6	25.52	51.23	2.00
C	8	4.6	43.81	53.48 no critical buckling	1.22

Table 8.14 - Fuse Capacity vs. Bar Capacity, Series #2, Concentric Load.

Under eccentric loads the impact of the eccentricity on the fuse performance is investigated by assuming that the plates act as simply-supported beams with a point load applied at a distance e from the beam midspan (Fig. 8.40). According to this assumption the two bars on the side of the eccentric load take approximately 90% of the axial load.

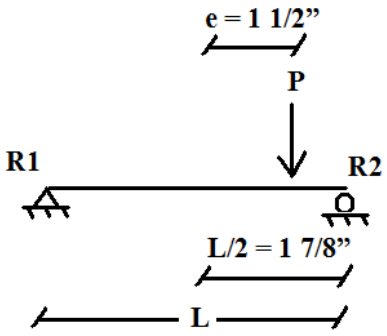

Fig. 8.40 - Simply Supported Beam with Eccentric Point Load.

From equilibrium of moments about support 1:

$$R2 = \frac{P \cdot \left[L - \left(\frac{L}{2} - e\right)\right]}{L} = P \cdot \frac{\left[2 \cdot 1\frac{7}{8} - \left(1\frac{7}{8} - 1.5\right)\right]}{\left(2 \cdot 1\frac{7}{8}\right)} = 0.9 \cdot P = 90\% \text{ of load P} \qquad \text{<Eq. 8.9>}$$

From equilibrium of vertical forces:

$$R1 = P - R2 = P - P \cdot 0.9 = 0.1 \cdot P = 10\% \text{ of load P} \qquad \text{<Eq. 8.10>}$$

If 90% of the total compressive stress is taken by the two bars on the fuse side where the eccentric load is applied, then the buckling capacity of each of these two bars becomes:

$$\sigma_{bar\ type} \cdot 0.9 = \frac{P_{total\ load\ per\ bar}}{Area_{2\ bars}} \qquad \text{<Eq. 8.11>}$$

$\sigma_{\text{bar type}}$ = fuse experimental maximum compressive stress under eccentric load.

solving Eq. 8.11 for P:

$$P_A = 19.8\ ksi \cdot 0.9 \cdot 2 \cdot \pi \cdot 0.25^2\ in^2 = 7.0\ kips$$

$$P_B = 22\ ksi \cdot 0.9 \cdot 2 \cdot \pi \cdot 0.25^2\ in^2 = 7.8\ kips$$

$$P_C = 31.4 ksi \cdot 0.9 \cdot 2 \cdot \pi \cdot 0.25^2\ in^2 = 11.1\ kips$$

Bars type A tripled their buckling capacity when embedded in the fuse, and bars type B and C improved their compressive nominal capacities by 56% and 29% respectively.

$$ratio = \frac{Bar\ buckling\ capacity\ embedded\ in\ fuse\ under\ eccentric\ load}{Bar\ nominal\ unconfined\ buckling\ capacity} \quad \text{<Eq. 8.12>}$$

$$ratio_{bar\ type\ A} = \frac{7\ kips}{2.1\ kips} = 3.33$$

$$ratio_{bar\ type\ B} = \frac{7.8\ kips}{5.0\ kips} = 1.56$$

$$ratio_{bar\ type\ C} = \frac{11.1\ kips}{8.6\ kips} = 1.29$$

The two bars type C on the side of the eccentricity were able to resists more compressive load than the bars type C embedded in a fuse with the same proportions under concentric loads. This can be attributed to the fact that approximately 90% of the compressive stress is concentrated on one side of the fuse increasing its compressive stiffness and therefore its ability to confine and improve the compressive capacity of the bars on that side of the fuse. But as the experimental results showed this is not the case for slender specimens with bars type A and B bars. For bars type B and C embedded in a fuse subjected to eccentric loads the buckling capacity of the bars on the side of the eccentricity improved but still remained below that of bars embedded in a fuse subjected to concentric loads.

Although the nominal buckling capacity of the two bars on the side of the eccentricity still improved when the bars were embedded in a fuse subjected to eccentric loads, the overall capacity of the fuse decrease by 14.5% with bars type B and 27% with bars type C (Table 8.15). In the case of the 4-bar fuse with bars type A the calculated nominal capacity of the unconfined bars increased by 74% when embedded in the fuse even when the fuse was subjected to eccentric loads. In other words, experimental results showed that as the bar slenderness increases there is a better stress distribution among the bars in the side of the eccentricity and the bars on the opposite side. As the fuse slenderness decreases the confining system becomes much stiffer on the side of the eccentricity improving the buckling capacity of the bars but at the same time the opposite side of the fuse confining system stiffness decreases significantly up to a point where it affects the overall buckling capacity of the fuse.

Bar Type	Fuse height (in.)	Length of ½-in. reduced section (in.)	Bar Nominal Capacity in Compression (ksi)	BCE Fuse Capacity in Compression (ksi) Eccentric load	Ratio of Fuse Experimental /Bar nominal Eccentric load
A	24	20.6	10.49	18.28 no critical buckling	1.74
B	16	12.6	25.52	21.82	0.86
C	8	4.6	43.81	31.98 no critical buckling	0.73

Table 8.15 - Fuse Capacity vs. Bar Capacity, Series #2, Eccentric Load.

9 BCE Fuse Computational Models

Experimental results from the BCE fuse were verified and further analyzed through finite element analysis. This chapter describes the results from the F.E. analysis and also includes a phenomenological model to represent the observed force-displacement relationship of the BCE fuse.

9.1 Computational Models – Finite Element Models (FEM's)

The behavior of the BCE fuse was extensively investigated by the experimental program described in Chapter 8. Specifically, the effects on behavior of variations in bar slenderness and confinement ratio were experimentally examined. Stress distribution through the brace composite element was investigated through finite element analysis (FEA) by modeling single-bar assemblies similar to those experimentally tested. The effect of eccentricities in the load on the performance of the fuse was also examined through FEA by modeling four bar BCE fuses. Different loading patterns were also investigated.

9.1.1 Single-Bar Finite Element Models (FEM's)

FEA was used to computationally demonstrate the effect of matrix diameter on fuse performance. A first control FEM consisted of a type "C" bar BCE fuse with a 3-in. diameter polyurethane matrix, 83% confinement ratio and a ¼-in. thick CFRP layer (Fig. 9.1). Hyperelastic properties of the polyurethane matrix were computationally modeled using the Mooney-Rivlin mathematical model and the stress-strain monotonic compression experimental data from the 80 durometer urethane matrix shown in table 7.4. Elastic properties were assumed for the bar and plates with a modulus of elasticity of 29,000 ksi typical for structural steel. The CFRP layer was modeled with elastic properties as well, but with a modulus of elasticity of 1904.77 ksi obtained as an average from FRP test coupons (Fig. 7.24). The CFRP layer was modeled as an isotropic material which did not have a significant impact in terms of the FEMs outcome given the fact that the CFRP layer was thick enough to constraint the matrix.

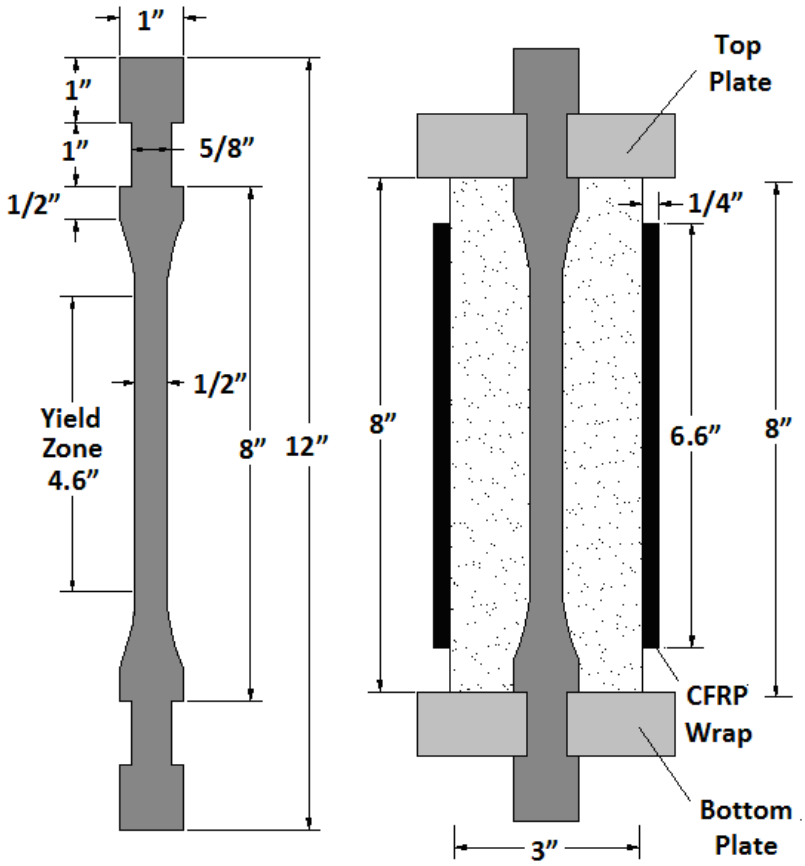

Fig. 9.1 - Single-Bar Fuse Finite Element Model Configuration.

Each of the BCE parts were individually modeled and then assembled by defining an interaction surface between parts. A tie constraint was used to define the surface interaction between the polyurethane matrix and the CFRP layer as well as the surface interaction between the polyurethane matrix and the 1-inch thick plates. The mesh of the single-bar computer model was constructed with two element controls, a hybrid formulation and a reduced integration, and an average strain

kinematic split element type, and it was refined as much as possible to obtain more accurate results.

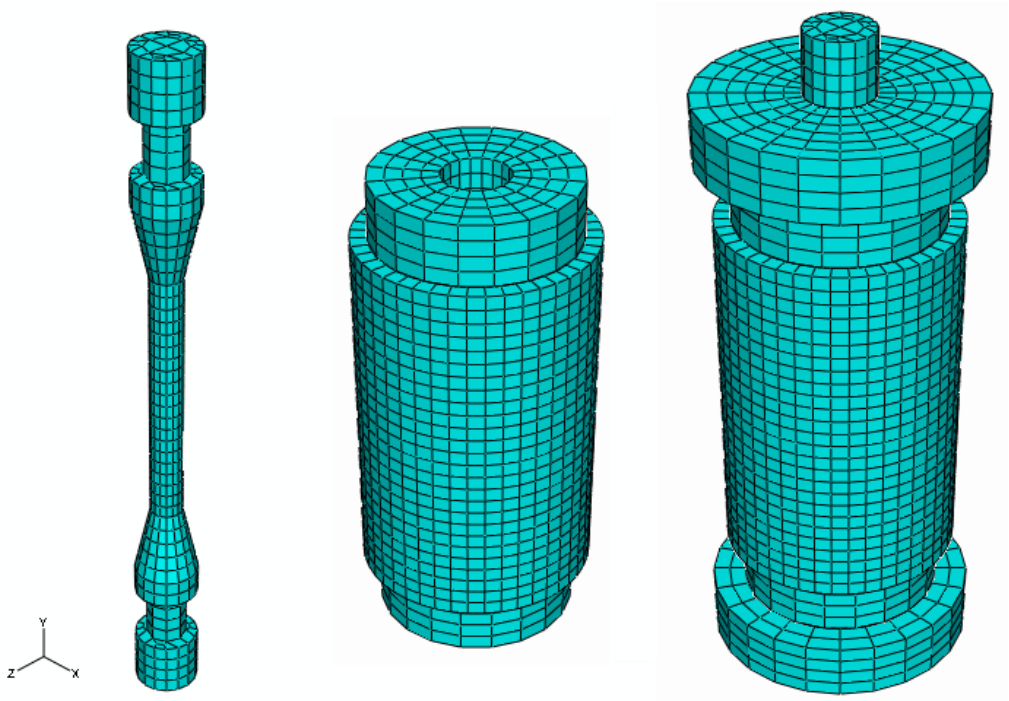

Fig. 9.2 - Single-Bar, Confining System, and Entire Single-Bar Fuse FEM Mesh.

A uniformly distributed load equivalent to applying a stress of 50 ksi to the bars was applied on the top plate (Fig. 9.3). Fixed boundary conditions were defined at the bottom of the lower plate. This uniform distributed load on the top plate was applied in both tension and then compression. This single-bar finite element model

simulated the load transfer as it was applied during the tests. The load is transferred from the plates through the bar shoulder and then to the yield zone.

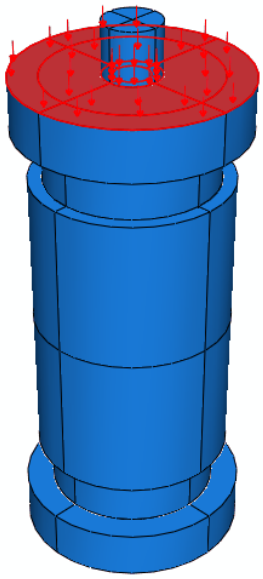

Fig. 9.3 - Single-Bar Fuse Uniform Compressive Stress Applied on the Top Plate.

The FEMs with a 3-in. diameter matrix were analyzed for a uniform stress of 50 ksi under tension and compression. Results from the FEM's showed significantly lower bar stresses for brace composite elements subjected to compression stresses. It is important to emphasize that the FEM results reflect an ideal condition where there is perfect contact between the CFRP layer and the urethane matrix. Also, this finite element analysis was based on elastic behavior and did not reflect the behavior of the fuse when the bars are subjected to inelastic deformations.

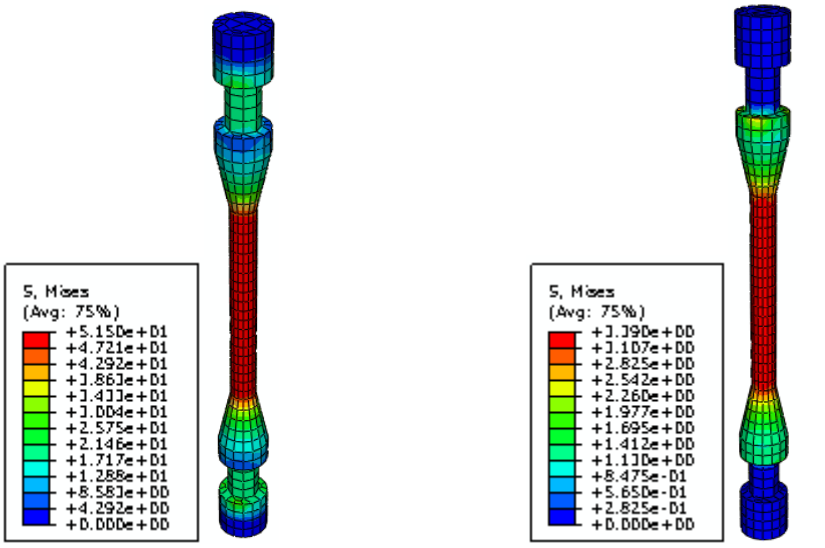

Bar under Tension Bar under Compression

Fig. 9.4 - 1-Bar FEM, Bar Von Mises Stress Distribution.

The FEM results showed that the 3-in. diameter CFRP layer sustained a maximum uniform stress of 2.067 ksi at the edges and a uniform stress of 0.689 ksi between the edges (Fig. 9.5).

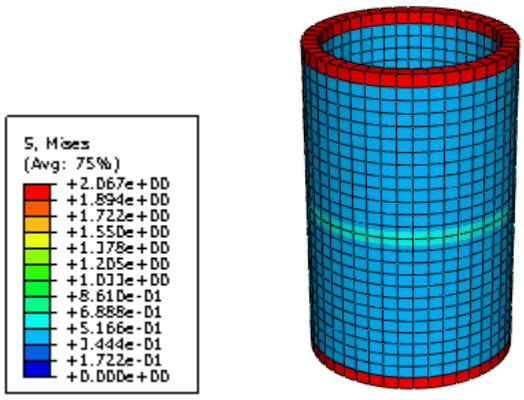

Fig. 9.5 - 1-Bar FEM, CFRP Layer Von Mises Stress Distribution.

The FEA results showed that the matrix was subjected to higher stresses at those areas on top and bottom where it was unconfined. The 3-in. diameter urethane matrix showed that these unconfined portions of the urethane matrix were subjected to a stress of 1.56 ksi (Fig. 9.6).

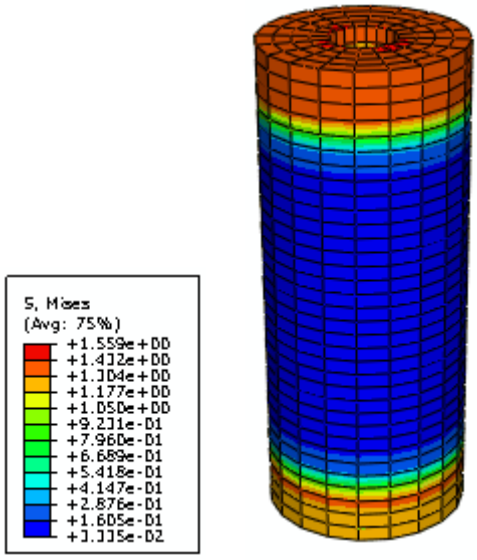

Fig. 9.6 - 1-Bar FEM, Polyurethane Matrix Von Mises Stress Distribution.

9.1.2 Four Bar Finite Element Models (FEM's)

This portion of the FEM study was focused on the load distribution between bars and the impact of axial load eccentricities on the performance of the BCE fuse when subjected to cyclic loads. Modeling the 4-bar BCE fuse through FEA was very challenging due to the complexity of the surface interaction between the different parts. Thus, it was necessary to simplify the model by modeling the bars and both plates together. A 6.75-in. diameter polyurethane matrix similar to that used on the 4-bar experimental program was modeled using the Mooney-Rivlin mathematical model and the stress-strain monotonic compression experimental data from the 80 durometer urethane matrix shown in table 7.4. Elastic properties were assumed for the bar-plate assembly with a modulus of elasticity of 29,000 ksi typical for structural steel. Similar to the 1-bar FEMs, the 4-bar FEM had an 83% confinement ratio and a ¼-in. thick CFRP layer. The CFRP layer was modeled with elastic properties as well, but with a modulus of elasticity of 1904.77 ksi obtained as an average from FRP test coupons (Fig. 7.24). The CFRP layer was modeled as an isotropic material.

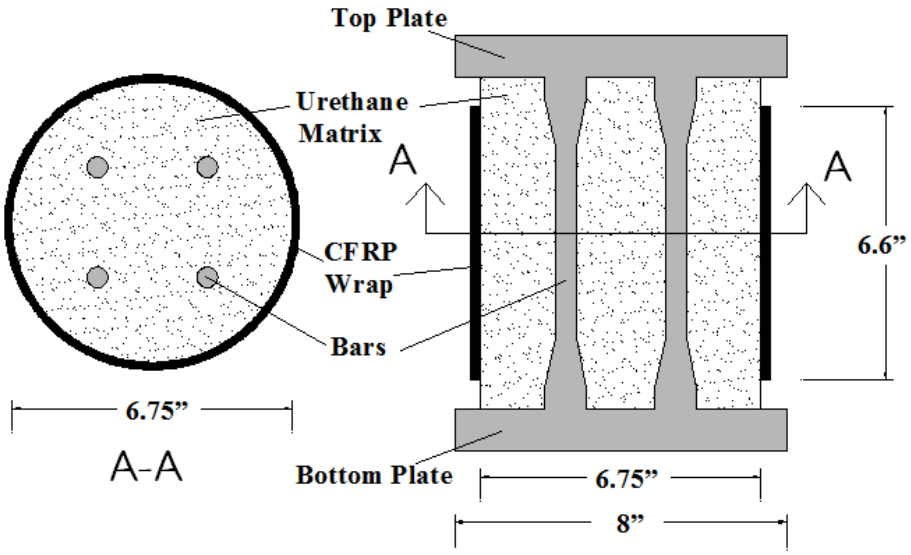

Fig. 9.7 - 4-Bar Fuse Finite Element Model Configuration.

The four bar specimens were modeled through FEA by defining each of the BCE fuse parts one by one: bars and plates were defined with a more refined mesh than that of the urethane matrix and the CFRP layer (Fig. 9.8).

Different approaches on how to apply the load to the FEM were attempted but one more time due to the complexity of the model, loads were applied directly on the top of each bar.

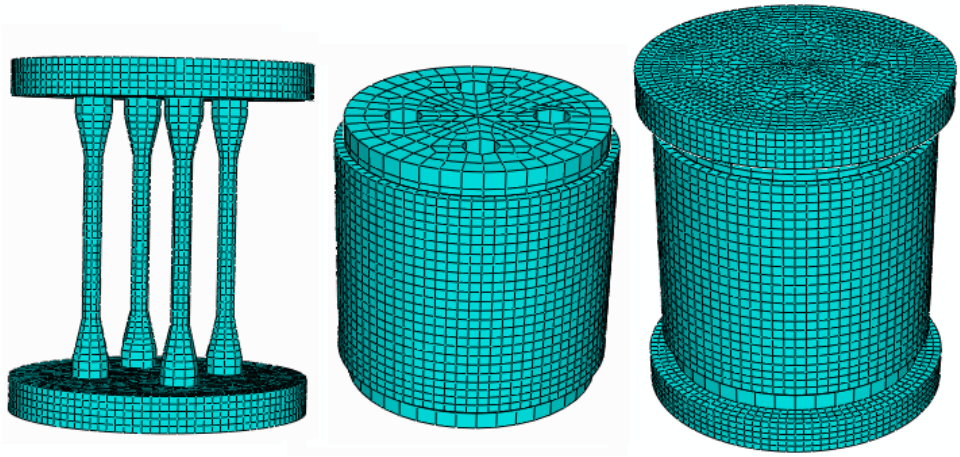

Fig. 9.8 - Bar, Confining System and Entire 1-Bar FEM Mesh.

9.1.2.1 Bar BCE Fuse under Concentric Loads

A first model was analyzed through FEA by applying a stress of 50 ksi over a ½-in. circular area at the top of each bar, simulating the case of a fuse subjected to pure concentric loads. In total a load of 39.27 kips was applied to the fuse.

For, $\sigma_{bar} = 50ksi$:

$$P_{total} = area/bar \cdot 4bars \cdot Fy = \pi \cdot 0.25^2 (in^2) * 50ksi = 39.27kips \qquad \text{<Eq. 9.1>}$$

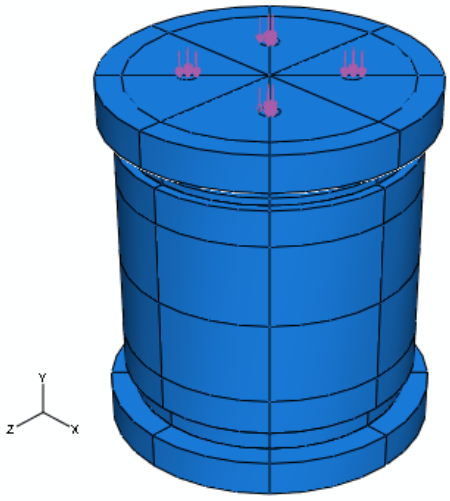

Fig. 9.9 - 4-Bar Fuse Concentric Compressive Stress Applied on Top Plate.

Under concentric loads, the bars were subjected to equal stresses. The CFRP layer was subjected to higher stress at top and bottom due to the deformation of the unconfined portion of the urethane matrix, which expanded freely when the fuse was under compressive loads. The analysis showed that the top region of the CFRP layer was subjected to higher stress than the bottom, but in reality a similar stress is expected at both top and bottom of the CFRP layer.

The Von Mises stress distribution shown on the right image of Fig. 9.10 included the transverse stress transferred from the urethane to the CFRP layer as the urethane matrix tried to expand under compressive loads and the axial stress due to the expansion of the matrix, which makes the plates interact directly with the CFRP layer edge by transferring axial stress through the expanded unconfined urethane

matrix. This is consistent with the behavior observed during the experimental program. The top of the CFRP layer was subjected to a maximum of 48 ksi, whereas the bottom was subjected to 48 ksi but over a smaller area (Fig. 9.10).

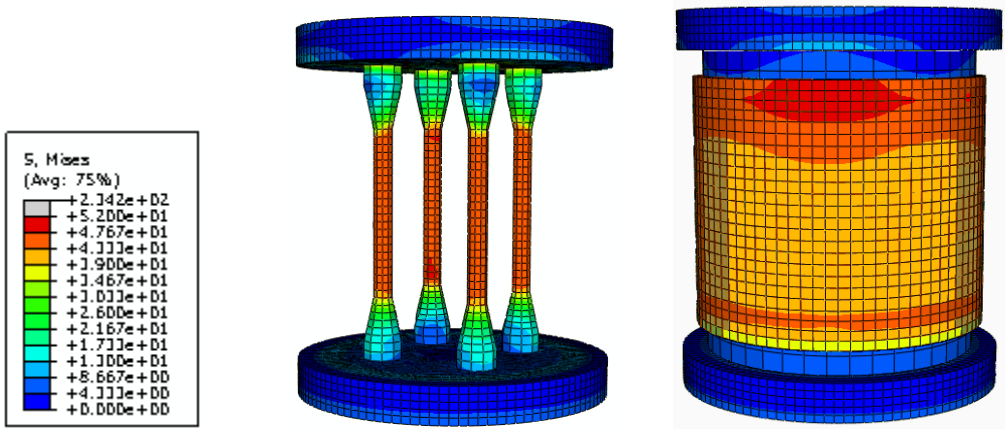

Fig. 9.10 - 4-Bar FEM, Bar Stress and CFRP Layer Von Mises Stress Distribution.

A transverse and longitudinal cut of the 4-bar FEM illustrates the stress distribution inside the fuse. The transverse cut on the left side of Fig. 9.11 shows the bars were subjected to a uniform stress of 50 ksi under concentric loads. At mid-height the urethane matrix was subjected to a uniform stress of 5 ksi and the CFRP layer was subjected to a uniform stress of 44 ksi. The longitudinal cut on the right side of Fig. 9.11 shows high stresses on the top plate directly above each bar. These stresses were due to the manner in which the load was applied and should be neglected because the load would be transferred uniformly throughout the plate to the bars when the fuse is assembled in a braced frame.

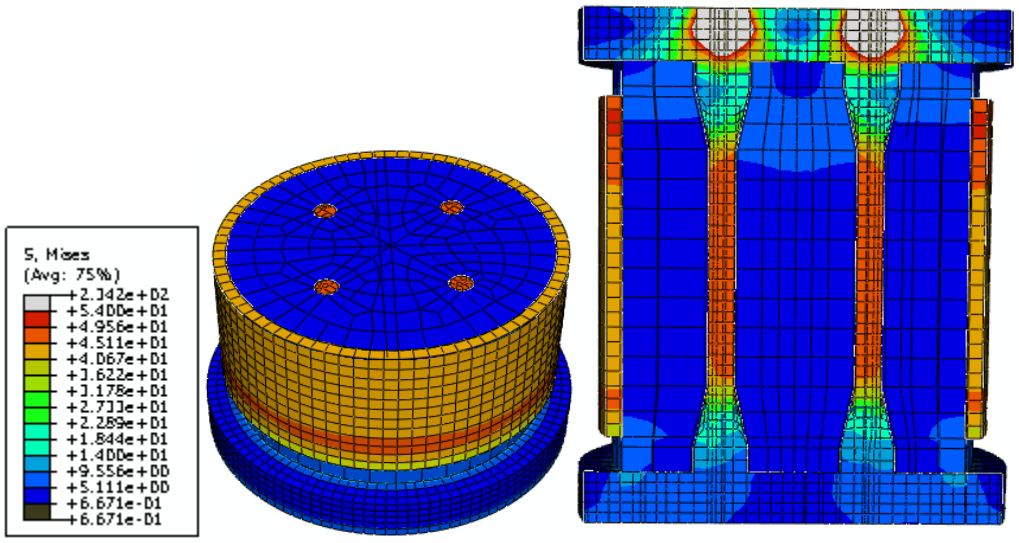

Fig. 9.11 - 4-Bar FEM, Von Mises Stress Distribution Transverse and Longitudinal Cut.

The Von Mises stress distribution of the CFRP is initially shown in Figs. 9.10 and 9.11, but both of these figures show the Von Mises stress distribution including both transverse and longitudinal stresses. Looking at the transverse stress distribution alone in Fig. 9.12 the FEM shows that from the 48 ksi Von Mises stress on the edge of the CFRP layer, 40 ksi alone came from transverse forces. In other words the expansion of the unconfined urethane matrix was more detrimental to the CFRP layer than the axial load transferred from the plate directly to the layer edge through the expanded unconfined matrix.

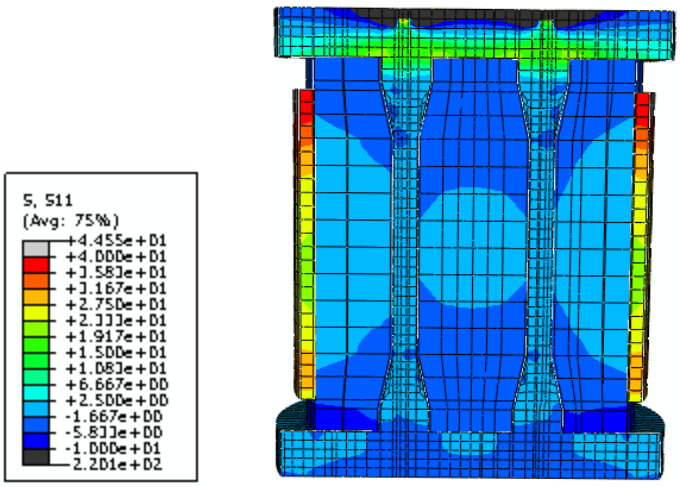

Fig. 9.12 - 4-Bar FEM, Transverse Stress Distribution (Longitudinal Cut).

Looking at the FEM displacement shown in Fig. 9.13, it can be seen both the matrix and the CFRP layer displace the same amount. This is a result of the type of surface interaction between the matrix surface and the CFRP layer used in the FEM. The FEM shows the bar displaced a little bit more than the matrix, but that was a consequence of the high stress concentration at a small area right on top of each bar. In reality as the plates transfer the load to the rest of the fuse the bars and urethane matrix should displace the same.

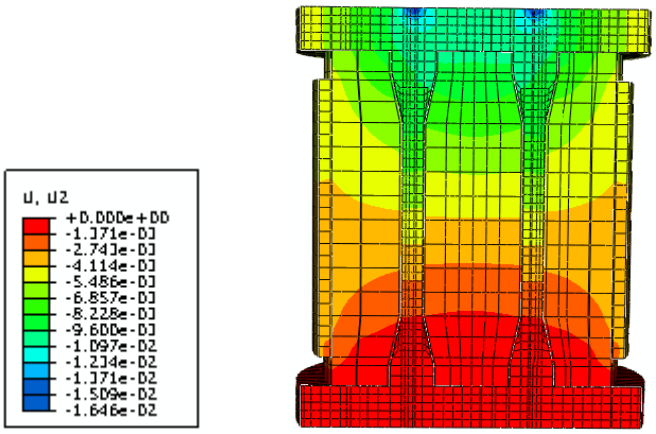

Fig. 9.13 - 4-Bar FEM, Longitudinal Displacement (Longitudinal Cut).

9.1.2.2 Bar BCE Fuse under Eccentric Loads and Moment

To study the stress distribution of the BCE fuse under eccentric loads and the impact of the eccentricities on the fuse performance, the load was gradually increased on one side of the fuse, and simultaneously decreased on the other side. Accordingly, a stress greater than 50 ksi was applied to two adjacent bars labeled as "σ1" (Fig. 9.14) and a stress smaller than 50 ksi was applied on the opposite two bars labeled "σ2".

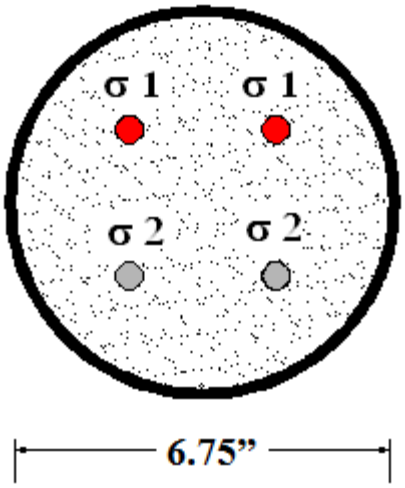

Fig. 9.14 - 4-Bar BCE Loading Pattern.

Following this approach to study the effect of axial eccentric loads BCE fuse a worst case scenario was applying the 39.27 kips between the two bars labeled “σ1” and leaving the two bars labeled “σ2” without load.

$$P_{total} = area/bar \cdot 4bars \cdot Fy = \pi \cdot 0.25^2 (in^2) * 50ksi = 39.27kips \quad \text{<Eq. 9.2>}$$

$$\sigma_1 = \frac{P/2}{area/bar} = \frac{39.27kips/2}{\pi \cdot 0.25^2 (in^2)} = 100ksi \quad \text{<Eq. 9.3>}$$

$$\sigma_2 = 0ksi \quad \text{<Eq. 9.4>}$$

The FEM results show that bars 1, with 100% of the load applied directly on top of them, sustained a 76 ksi stress each, which is 52% higher than 50 ksi. Bars 2 with zero load on top were still able to sustain a stress of 22 ksi each, which is 44% of 50 ksi .

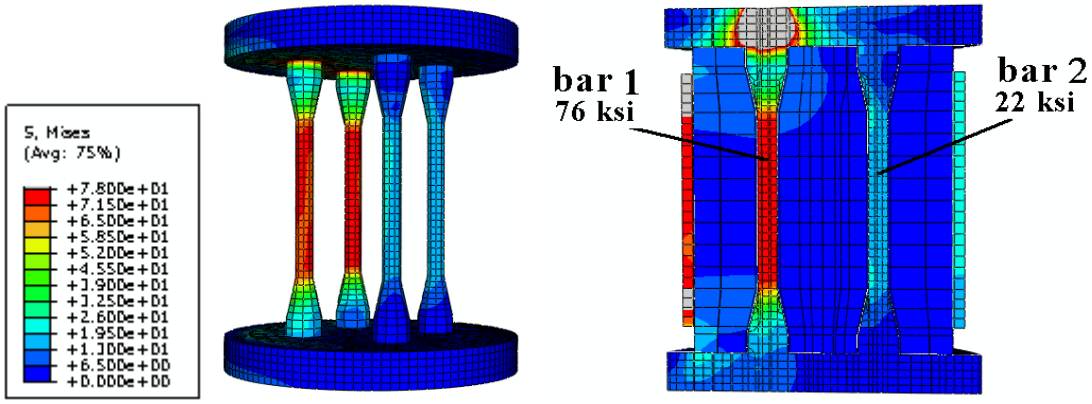

Fig. 9.15 - 4-Bar FEM – Bar Von Mises Stress Distribution.

The stress distribution in the CFRP layer for specimen A shows there was a higher stress demand on the side of the eccentric load. The Von Mises stress was 85 ksi on the top and bottom edges of the CFRP layer and the CFRP remained highly stressed in the mid region of the layer on the side of the eccentric load at 70 ksi. In other words the eccentricity of the load induced higher stresses on the edges of the CFRP layer, approximately 85/76= 10% higher than the stress in the overstressed bar. The stress in the mid region of the CFRP layer was approximately 92% of the stress in the overstressed bars.

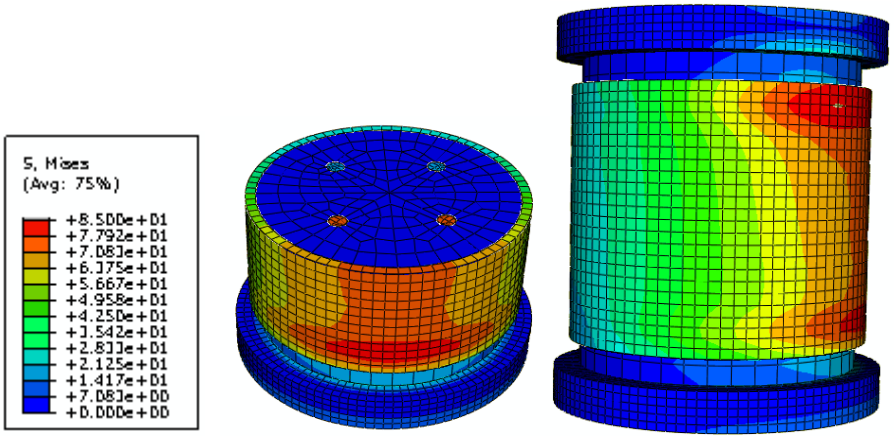

Fig. 9.16 - 4-Bar FEM, Eccentric Load Fuse Von Mises Stress Distribution.

An unbalanced loading condition occurs only in situations where the fuse is subjected to eccentric loads due to transfer of moments from the frame to the brace, but also fuse rotations caused by large post-buckling deformations. The nominal distance from the bars to the centroid of the fuse was 1-7/8 in., and the moment can be calculated as follows:

$$M = P \cdot e = (P2 - P1) \cdot 1.875" = {(\sigma_2 - \sigma_1)}/{1/(area/bar)} \cdot 1.875" \qquad \text{<Eq.9.5>}$$

$$M = {(76ksi - 22ksi)}/{1/(\pi \cdot 0.25^2)} \cdot 1.875" = 19.88kip - in$$

and the eccentricity due to the unbalanced load can be calculated as:

$$e = \frac{M}{P} = \frac{19.88kip - in}{39.27kips} = 0.51 - in \qquad \text{<Eq. 9.6>}$$

The same FEM analysis was repeated several times with a similar loading pattern gradually increasing the magnitude of the stress on two adjacent bars on one side of the fuse and gradually decreasing the stress on the opposite bars, as shown in Table 9.1. The first model labeled A corresponds to the worst case analyzed above. The stress distributions found from FEA for all specimens were similar, with only the magnitude of the stress along the bars changing between cases. A total of 9 cases were studied as shown in Table 9.1.

$$\text{Average load taken by the bars} = \left(\frac{10.85 + 6.81}{18}\right) = 0.981 = 98\% \text{ of } 50 \text{ ksi} \quad \text{<Eq. 9.7>}$$

Of the total compressive force, a fraction was carried by the urethane matrix and the remaining by the steel bar. An average distribution factor was found by adding the stress carried by bars one and two obtained from the nine analyses and dividing by the total number of bars. The resulting average stress carried by the bars was 98% of the stress applied, indicating that only 2% was carried by the matrix.

	Applied Stress		Bar stress				Eccentricity	Moment
	σ_1 (ksi)	σ_2 (ksi)	σ_{bar1} (ksi)	σ_{bar1}/50ksi	σ_{bar2} (ksi)	σ_{bar2}/50 ksi	E (in)	M (kip-in)
B	91.7	8.3	71	1.42	27	0.54	0.412499	16.19884
C	83.3	16.7	67	1.34	31	0.62	0.337499	13.25359
D	75	25	62	1.24	35	0.7	0.253124	9.940196
E	66.7	33.3	58	1.16	39	0.78	0.178125	6.994952
F	58.3	41.7	54	1.08	44	0.88	0.09375	3.681554
G	55.6	44.4	52.5	1.05	46	0.92	0.060937	2.39301
H	52.8	47.2	51.4	1.03	47.3	0.946	0.038437	1.509437
I	51.7	48.3	50.6	1.01	49	0.98	0.015	0.589049
				Σ= 10.85		**Σ = 6.81**		

Table 9.1 - 4-Bar FEM, Eccentricity Study Following Loading Pattern from Fig. 9.13.

Plotting the eccentricity as a function of the normalized stress in the bar (σ_{bar}/50 ksi) it was found that there was a linear relationship between the stress in the bars and the axial load eccentricity. As the eccentricity increased the stress on the bars designated 1 increased proportionally. Similarly, the stress on bars designated 2,

opposite to the point of application of the load, was inversely proportional to the eccentricity (Fig. 9.17).

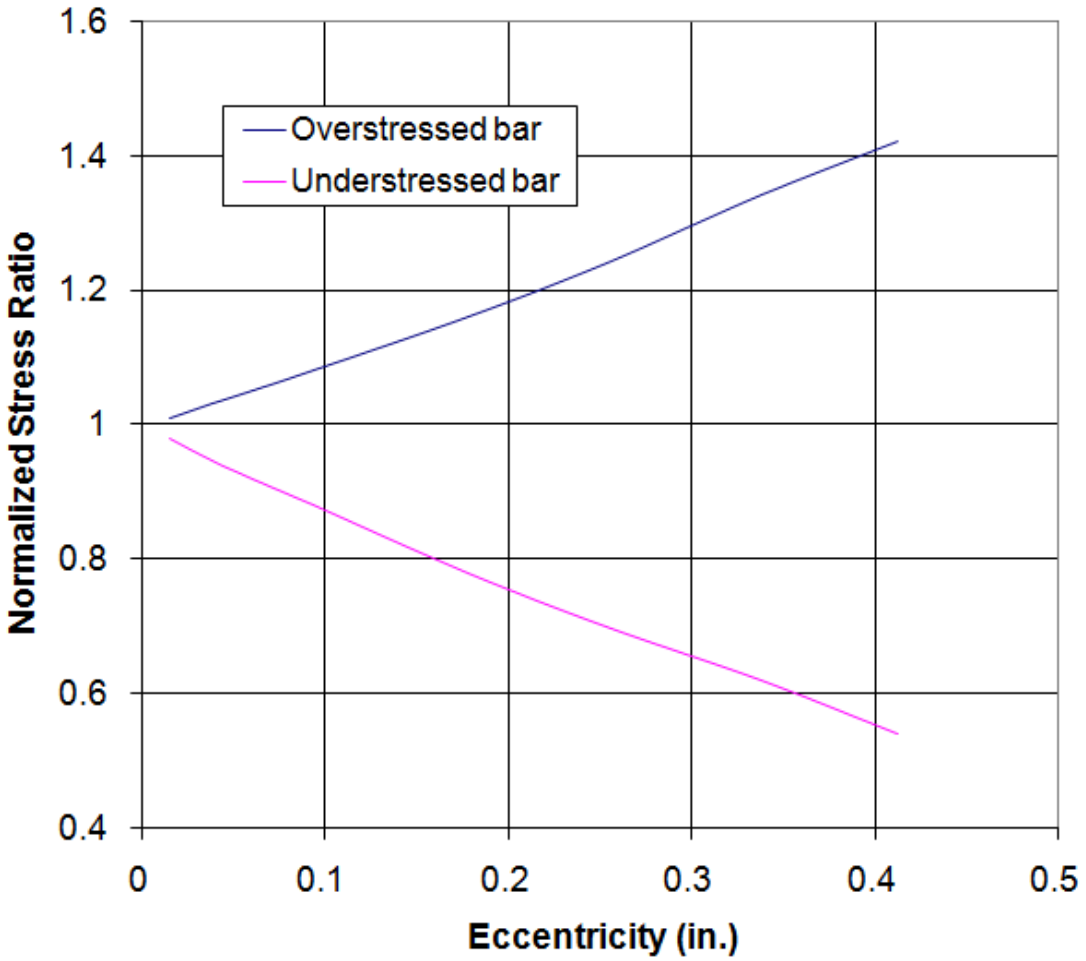

Fig. 9.17 - 4-Bar FEM, Eccentricity vs. Normalized Bar Stress.

The relationship between the bending moment and the normalized bar stress was also linear. This was to be expected due to the linear relationship between normalized bar stress and eccentricity. As the moment increased the normalized stress on bars designated 1 increased proportionally as well (Fig. 9.18).

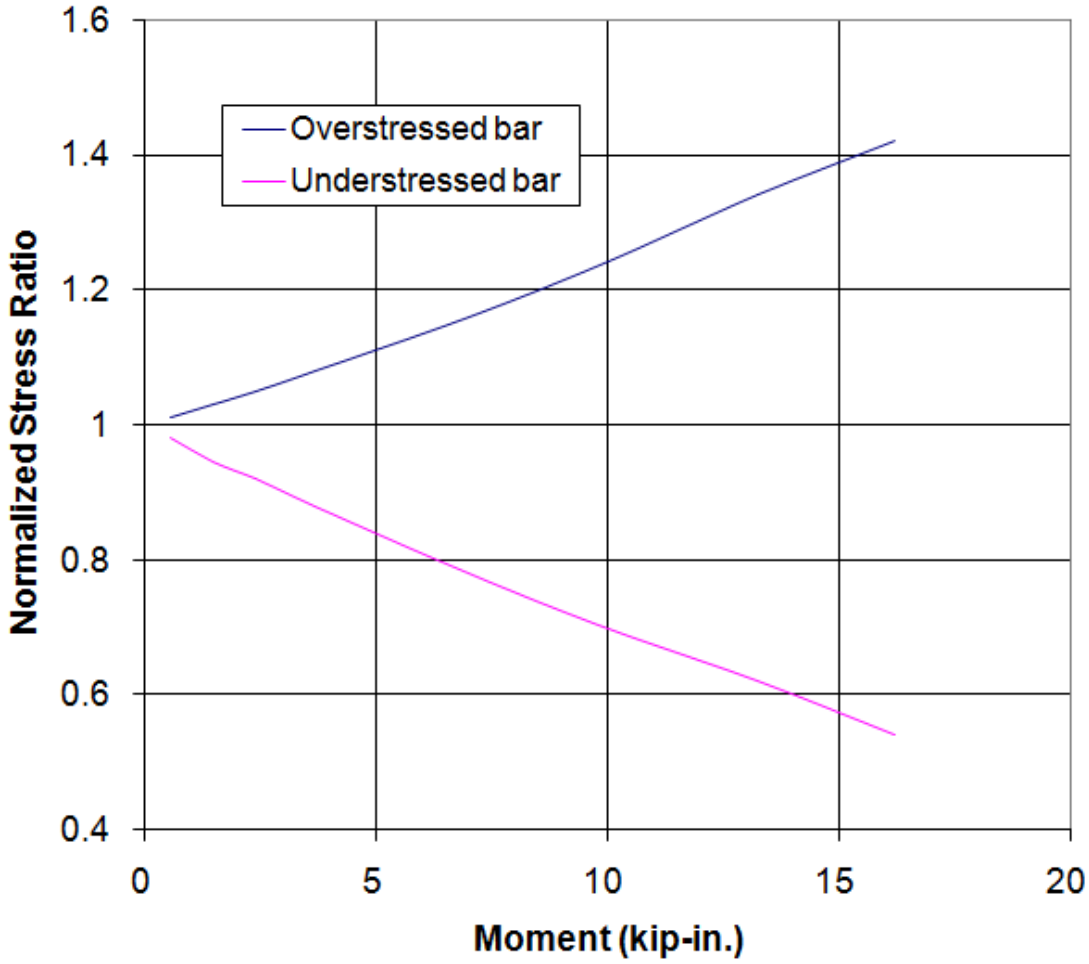

Fig. 9.18 - 4-Bar FEM, Moment vs. Normalized Bar Stress.

These results indicate that the simple model introduced at the end of Chapter 8 provided a good representation of the behavior of the fuse.

9.1.2.3 BCE Fuse – FEA with Additional Loading Patterns

Three additional load patterns were studied. First, the load is taken by two nonadjacent bars as shown in Fig. 9.19. For this case,

$$P_{total} = area/bar \cdot 4bars \cdot Fy = \pi \cdot 0.25^2 (in^2) * 50ksi = 39.27kips \quad \text{<Eq.9.8>}$$

$$\sigma_1 = \frac{P/2}{area/bar} = \frac{39.27kips/2}{\pi \cdot 0.25^2 (in^2)} = 100ksi \quad \text{<Eq. 9.9>}$$

$$\sigma_2 = 0ksi \quad \text{<Eq.9.10>}$$

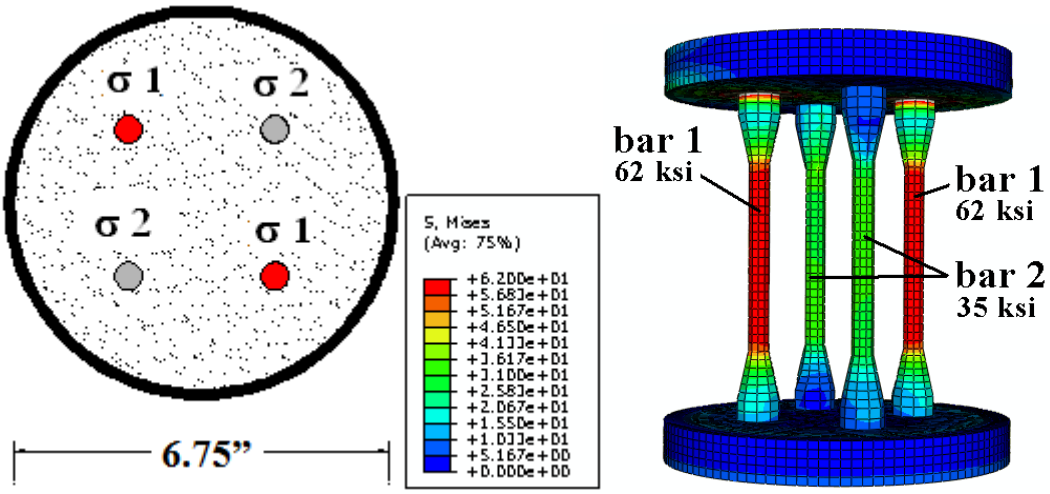

Fig. 9.19 - 4-Bar FEM, Von Mises Stress Distribution, Load Applied at 2 Nonadjacent Bars.

The FEM result shows that under this loading configuration the bars designated 1 were subjected to a stress of 62 ksi each and the bars designated 2

sustained a stress of 35ksi each. These results show that this loading pattern is not as detrimental in terms of unbalanced loads as the loading pattern with two adjacent bars out of the four with 100% of the load (Fig. 9.14). The total load taken by the bars under this loading pattern was still 98% of the total load applied.

This loading pattern would be expected to occur in a fuse at a short distance from the gusset plate connection, and the gusset plate aligned with the bars designated as 1. In an actual brace it is not expected that the entire load would be concentrated on the bars designated 1 because there would be imperfections in the alignment and out of plane forces.

The second load pattern analyzed consisted of applying the load on top of three bars (Fig. 9.20). For this case:

$$P_{total} = area/bar \cdot 4bars \cdot Fy = \pi \cdot 0.25^2 (in^2) * 50ksi = 39.27kips \qquad \text{<Eq. 9.11>}$$

$$\sigma_1 = \frac{P/3}{area/bar} = \frac{39.27kips/3}{\pi \cdot 0.25^2 (in^2)} = 66.67ksi \qquad \text{<Eq. 9.12>}$$

$$\sigma_2 = 0ksi \qquad \text{<Eq. 9.13>}$$

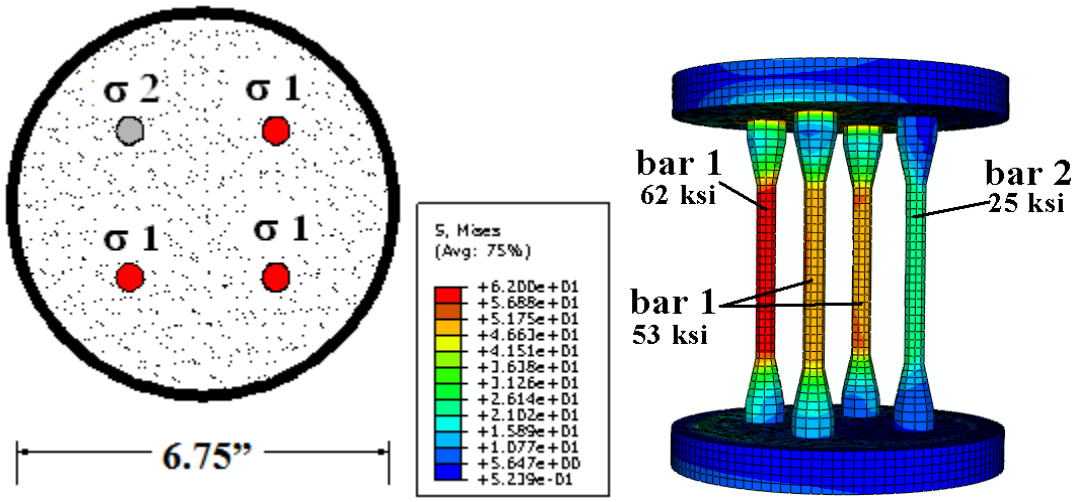

Fig. 9.20 - 4-Bar FEM, Von Mises Stress Distribution, Load Applied at 3 Bars.

The FEM results show that under this loading pattern the loaded bar furthest from the unloaded bar was subjected to a 62 ksi stress. The remaining two loaded bars sustained a stress of 53ksi each, with the bar designated 2 (unloaded bar) sustaining a 25 ksi stress. What was significant about this loading configuration was the ability of the fuse to redistribute stresses to the bars as the loading pattern changes.

The third and last additional load pattern was to apply the load on top of only one of the four bars (Fog. 9.21). For this case:

$$P_{total} = area/bar \cdot 4bars \cdot Fy = \pi \cdot 0.25^2 (in^2) * 50ksi = 39.27kips \qquad \text{<Eq. 9.14>}$$

$$\sigma_1 = \frac{P}{area/bar} = \frac{39.27kips}{\pi \cdot 0.25^2 (in^2)} = 200ksi \qquad \text{<Eq. 9.15>}$$

$$\sigma_2 = 0ksi \qquad \text{<Eq.9.16>}$$

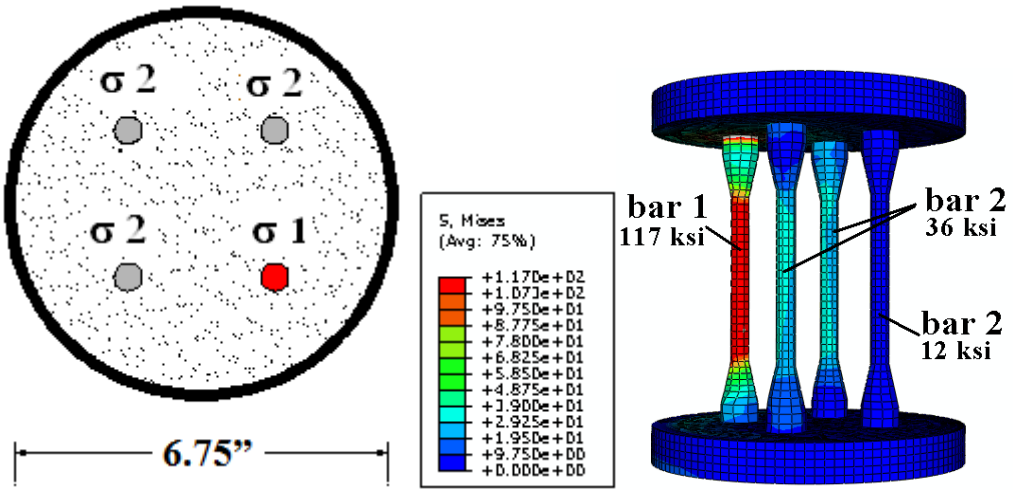

Fig. 9.21 - 4-Bar FEM, Von Mises Stress Distribution, Load Applied at 1 Bar.

The FEM results show that under this loading pattern the loaded bar was subjected to a stress of 117 ksi. The two unloaded bars adjacent to the loaded bar sustained a stress of 36 ksi each, while the unloaded bar furthest from the loaded bar sustained a stress of 12 ksi. This loading configuration confirmed the ability of the fuse to redistribute stresses. This load configuration, where the force is concentrated on top of one of the bars, is a much tougher loading pattern than those likely to take place on a braced frame.

9.2 Phenomenological Model

The phenomenological model proposed is intended to reproduce the observed axial force-axial displacement relationship of the fuse. Consequently, this model has only one degree of freedom (the axial deformation) and is applicable only to the concentric loading case. The hysteretic behavior obtained from the experimental study was simulated by linear segments that replicate the complex behavior of the BCE fuse.

This model represents the basic characteristics of the nonlinear behavior of the fuse. The main advantages of this model are:

1) This model represents the deterioration of nonlinear cyclic compression forces as function of the displacement amplitudes and the load instead of number of cycles.

2) It is capable of simulating the behavior of all specimens from the experimental series 1 and includes all the different stages of the behavior of the BCE fuse, both in tension and compression, for different confinement ratios and fuse proportions. The control points were selected to best fit the experimental results.

The shortcomings of this phenomenological model are:

1) Depending on the confinement ratio of the fuse and the fuse proportions, some stages of the model might not realistically represent the fuse hysteretic behavior.

2) Most of the control points are not well defined in terms of magnitude as they will vary depending on the confinement ratio and the fuse size.

The phenomenological model proposed is shown in Fig 9.22. A brief description of the different stages of this model is given below.

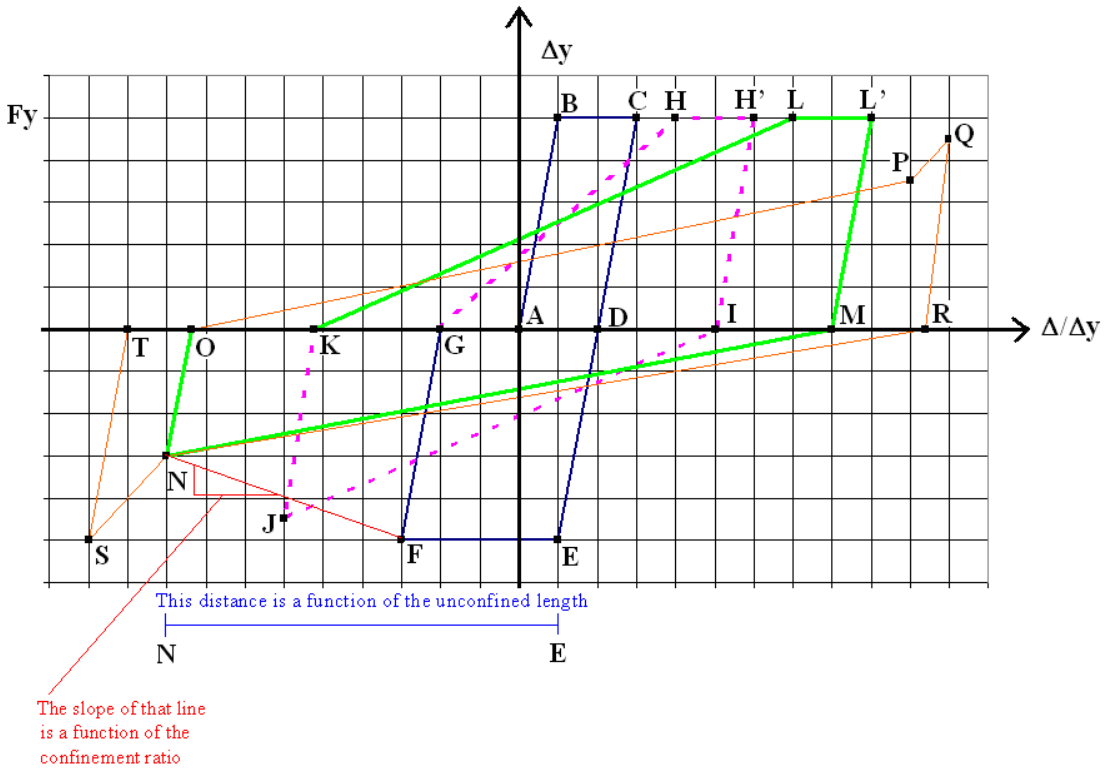

Fig. 9.22 - Phenomenological Model.

When the fuse is subjected to tension stresses first, it elongates elastically along line ***AB*** in Fig. 9.22 until it reaches its yield stress F_y. The initial elastic slope is equal to cross section area times the modulus of elasticity divided by the fuse length. Upper yield points are neglected to simplify the model. At displacements greater than

yield the fuse continues to elongate and the load does not increase. This constant stress region represents the first yield plateau along line ***BC***.

When the direction of the axial load reverses, the load-displacement relationship decreases at the same rate it increased elastically, following the elastic slope. This relationship remains as the load transitions from tension to compression at control point ***D***. The compression force increases from point ***D*** to point ***E*** up to the point where the fuse reaches its maximum/critical buckling stress $\boldsymbol{F_{cr}}$. At this maximum buckling stress $\boldsymbol{F_{cr}}$ the fuse continues to elongate from control point ***E*** to ***F***. This constant compression stress region can be designated as the buckling plateau.

When the direction of the axial load reverses one more time at point ***F***, the compression load decreases to zero following the elastic slope up to point ***G*** where the load transitions to tension, at this point the fuse starts taking tension once more but the slope or stress-strain relationship no longer follows the elastic slope as the fuse stiffness in tension decreases after the first buckling deformation. The specimen is loaded up to $\boldsymbol{F_y}$ at point ***C*** and then the fuse goes though the yield plateau once more from point ***H*** to point ***H'*** at a constant stress.

The direction of the load reverses again and the load decreases to zero going from point ***H'*** to point ***I*** following the elastic slope. When the fuse starts taking compression load once more the stiffness of the slope decreases and the load increases up to a maximum compressive stress at control point ***J*** approximately 10% smaller than its previous buckling capacity or buckling plateau along line *EF*.

The load reverses again decreasing to zero at point ***K*** following the elastic slope. At point ***K*** the fuse starts taking tensile stresses and it increases up to a maximum F_y at point ***L*** once more following a stress-strain relationship slope that shows tensile stiffness reduction. From point ***L*** to point ***L'*** the fuse reaches its yield plateau one more time and at point ***L'*** the load reverses down to zero at point ***M*** following the elastic slope.

As the fuse starts taking compression load again from point ***M*** up to point ***N*** not only the compressive stiffness of the fuse decreases but also the maximum compressive stress decreases by a significant amount which is a sign of significant post-buckling deformations. Point ***N*** represents the last stage at which the compressive capacity of the fuse is not affected by any contribution from the CFRP layer due to contact with the steel plate caused by rotation of the fuse during large post-buckling deformations or bulging of the unconfined portion of the urethane matrix.

At point ***N*** the load decreases down to zero following the elastic slope to point ***O***. At point ***O*** the fuse starts taking tension once more with a much more reduced stiffness up to a point ***P*** well below F_y and then at point ***P*** there is a small increment in tensile stiffness as the load increases up to a maximum tensile stress at control point ***Q*** which is still below F_y. This last increment in tensile stiffness represents the fuse strain hardening region where additional load is required to cause additional elongation.

At point ***Q*** the direction of the load reverses and the load decreases to zero at control point ***R*** following the elastic slope. Once the fuse starts taking compressive stresses at point ***R***, the compressive stiffness decreases once more and the compressive load increases up to point ***N*** right before the CFRP layer starts taking axial compression. After point ***N*** there is a significant increment in compressive stiffness due to the contribution from the CFRP layer to the compressive capacity and the load then increases up to point ***S***, which is greater than the critical buckling stress or buckling stress plateau.

The model presented does not account for Bauschinger effect. This can be adjusted rather easily by introducing mathematical terms to account for this effect in the loading segments of the load-deflection curves.

10 Conclusions and Recommendations

Results on this investigation of fused bracing systems showed that of the two systems studied (RXS, and BCE) the BCE fuse was a much better system with great potential as an energy dissipation device for building structures subjected to large dynamic loads such as occur in earthquakes.

The behavior of the RXS fuse system raised concerns about its applicability in seismic-resistant structures due to its susceptibility to damage under load reversals. Experimental results showed that the response of the RXS fuse to the loading history was rather poor mainly because of its limited energy dissipation capacity when subjected to axial eccentric load reversals. However, lessons learned from this first fuse configuration provided useful information about the detrimental effect of axial eccentricity on the response of braces to earthquakes and helped in the development of the second fuse configuration. One of the main lessons learned from the RXS fuse was that a normal bridge fabrication practice with smooth edge requirements would delay fracture failure and consequently improve the ductility of the RXS fuse.

The BCE fuse system exhibited great potential as an energy dissipation device. The biggest benefit of the composite fuse is its inherent toughness. The fact that the fuse bars can be easily replaced after large inelastic deformations is another significant advantage. Even though the fuse was subjected to large inelastic deformations, there was virtually no loss in strength in tension and compression, and

there was no meaningful overstrength in compression. The following are some concluding remarks and recommendation about the BCE fuse investigation results:

- Experimentally obtained hysteretic loops for all 1-bar BCE fuse specimens demonstrated that there was negligible difference between the behavior of the specimens in tension and compression, and that the capacity of the fuse in compression remained nearly constant after the bars of the fuse reached buckling. Even in specimens with very low confinement ratios the compressive capacity of the fuse at displacement amplitudes beyond critical buckling did not decrease by more than 30% at average strain demands on the bars exceding 3%.
- Experimental results from the full-scale 4-bar BCE fuse specimens showed that the efficiency of the system in compression decreased when the BCE fuse was subjected to eccentric axial loads. Damage to the BCE fuse was still very limited even at unit strains greater than 3%, indicating the fuse has remarkable toughness. The ability of the fuse to dissipate energy under large inelastic load reversals before fuse failure or major fuse deterioration was significantly affected by large end rotations caused by eccentric loads. This rotation was accentuated by the use of a pinned-end condition in the 4-bar full-scale test set-up. The 4-bar full-scale specimens were subjected to much tougher conditions than those likely to take place on a braced frame.

- Removing the bars at the end of the tests showed that the first buckling mode of the bars and, in some instances higher buckling modes, were effectively eliminated. The observed deformation patterns of the bars were indicative of higher buckling modes with increasing bar slenderness. Repetitive buckling deformations did not significantly deteriorate the bar or the inner core, and in all the experiments carried out, significant inelastic deformations took place without fracture of any of the bars.
- Carbon steel was selected as the bar material over shape memory alloys (SMA's) for the construction of the experimental BCE fuse specimens because this material is ductile, easy to machine, and does not cost as much as shape memory alloys. However, the ability of the BCE fuse to dissipate energy and its damage tolerance would be enhanced by using SMA instead of carbon steel as the bar material.
- SMA bars would be a feasible alternative for structures that require better performance under earthquake loads which would justify the added cost of using SMA bar. From a long term economic perspective, using shape memory alloy bars could also be a feasible option because a BCE fuse with SMA bars may be less susceptible to major repairs or even bar-inner core replacement after the system is subjected to a major seismic event.

- The effectiveness of the confining system was found to be strongly dependent on the height of the CFRP layer relative to the height of the urethane matrix, defined as the confinement ratio. The axial stiffness of the urethane matrix/CFRP confining layer system is directly proportional to the confinement ratio. It is recommended that the urethane matrix be almost completely confined by the CFRP layer but a 100% confinement is not recommended because the innermost steel plates will damage the CFRP layer after the fuse is subjected to compression cycles, and overstrength could compromise the intended purpose of the fuse of protecting the connection. Experimental results showed that the maximum force carried by the BCE fuses with confinement ratios less than 90% decreased at larger displacements after the bars had reached buckling. Therefore, depending on the drift capacity required, a high confinement ratio in the range of 90%-98% is recommended.
- One of the design criteria for the BCE fuse is that the CFRP layer should to be stiff enough to avoid significant elongation due to the pressure exerted by the urethane matrix when it is subjected to a compressive load. A recommended design goal uses the smallest urethane diameter possible and completes the design by providing CFRP layer with adequate thickness. FE analysis showed that the

stress of the CFRP layer was very low with respect to tensile strength, which resulted in adequate performance in the experimental program.

- By using low temperature curing resin systems and by properly curing the CFRP layer can result in materials with 5-10 times the stiffness described herein, which will allow thinner CFRP layers to be adequate.
- The CFRP layer effectiveness was found to be not only a function of the strength of the carbon fibers, but also of the orientation of the fibers. The CFRP fabricated with a third of the fibers oriented in the hoop direction, a third oriented 45 degrees clockwise with respect to the hoop direction and the other third oriented 45 degrees counterclockwise with respect to the hoop direction, showed much better performance than the CFRP layer with all the fibers oriented in the hoop direction. This is mainly due to the need for axial reinforcement to resist local bending at the CFRP layer termination due to free polyurethane expansion. The angular orientation can likely be localized near the free edges if the CFRP stiffness is high enough to prevent layer failure due to bar buckling.
- The urethane matrix should provide sufficient confinement to protect the integrity of the fuse in the case of a bar inner core failure. A recommendation for the proportioning of the urethane matrix for a fuse with one bar is that the urethane matrix shall have an inner core

diameter 1.5 times the diameter of the bar shoulder, and a urethane matrix diameter at least 2 times the diameter of the inner core. It was experimentally proved that this criterion was conservative and resulted in adequate confinement of the bars.

- An 80 durometer castable urethane proved to have sufficient hardness for the matrix. Although, in some instances the bar inner core was severely deteriorated due to large post-buckling deformations. For this reason a higher durometer bar inner core urethane is recommended. A configuration with greater number of bars with smaller diameter is preferable to one with less bars with larger diameters because the pressure exerted on the urethane core by the lateral deflection of the bars during post-buckling deformations would be less, and the urethane core would be more effective at confining the bar and protecting the matrix. Therefore, it is strongly recommended to use more than four bars in cases where the fuse size allows for enough space to accommodate an arrangement with a greater number of bars. A larger number of bars would also bring advantages in terms of redundancy; the effect of losing one bar on the performance of the fuse would be less.
- The ½-in. diameter reduced section or yield zone transitioning to a 1-in. diameter shoulder with a circular shape proved to be a suitable bar

configuration for the BCE. Although, for the bar dimensions used, a ¾-in. threaded diameter of the bar, instead of the 5/8-in. used, would have improved the ductility of the fuse in cases where the fuse sustained significant end rotations. For this reason, it is highly recommended to maximize the diameter of the threaded portion of the bar to reduce stress demands at the threads.

Suggestions for Further Research:

Additional tests with focus on the behavior of a braced frame with the BCE fuse are necessary to experimentally study the brace-BCE fuse interaction. An experimental matrix for this purpose should include two series: braces with one BCE fuse at the connection, and braces with one BCE fuse at each connection (bottom and top gusset plate).

Under large post-buckling deformations, the rotation at the brace mid-span is expected to be twice as much as the rotation at the connections. An additional BCE fuse with a high bending stiffness at brace midspan would reduce this rotation. For this reason a third series of experiments should focus on the response of the braced frame with BCE fuses not only located at the connections but also at mid-span of the bracing section. Another significant advantage of a BCE fuse located at brace midspan is that the brace slenderness ratio decreases by a factor of two and the compressive capacity of the brace increases.

It has been determined by other researchers that the cyclic behavior of braced frames is greatly influenced, among other factors, by the loading history [Tremblay, 2002]. For this reason, it is recommended to study the response of braced frames with the BCE fuse to different loading histories with unsymmetrical displacement amplitudes in tension and compression.

Even though the carbon constraint layer fabrication method proved to be an adequate curing method that provided satisfactory results for the intended brace composite element application, it is recommended to further improve the carbon constraint layer curing method in order to take advantage of CFRP properties when fully cured and reduce the required layer thickness.

A testing configuration such as the one shown in Chapter 5 (Fig. 5.26) with a diagonal brace is recommended. Other brace configurations could be used such as a chevron brace with a configuration similar to that used by Higashino (1996) (Chapter 3, section 3.6.2.1). Two BCE fuses at the top of the brace (Fig. 10.1) and two at the bottom (Fig. 10.1). BCE fuses at midspan of each brace could also be investigated with this brace configuration.

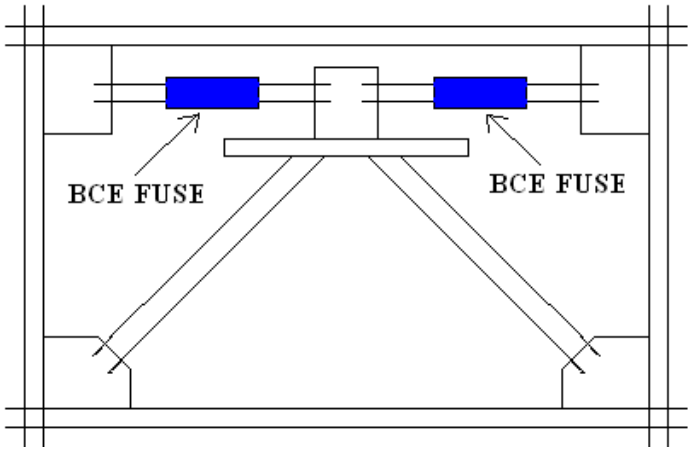

Fig. 10.1 - Schematic of Chevron Brace Configuration Testing Set-Up 1.

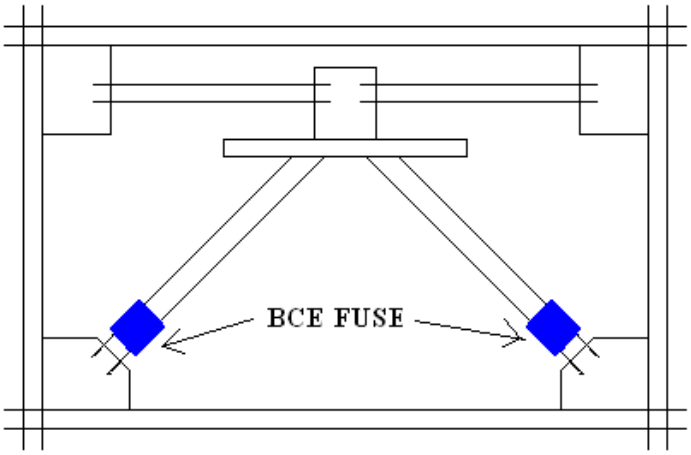

Fig. 10.2 - Schematic of Chevron Brace Configuration Testing Set-Up 2.

11 References

American Institute of Steel Construction, Inc. (AISC). (1999). Load and Resistance Factor Design Specification for Structural Steel Buildings. AISC, Chicago, IL, December 27.

American Institute of Steel Construction, Inc. (AISC). (1997). Hollow Structural Sections (HSS) Connections Manual, AISC, Chicago, IL.

American Institute of Steel Construction, Inc. (AISC) (1997), Seismic Provisions for Structural Steel Buildings, AISC, Chicago, IL.

American Institute of Steel Construction, Inc. (AISC) (2002), Seismic Provisions for Structural Steel Buildings, AISC, Chicago, IL.

American Society for Testing and Materials (ASTM). (2003). Annual Book of ASTM Standards, Metals Test Methods and Analytical Procedures. Section 3, Vol. 3.01, West Conshohocken, Pennsylvania.

Aristizabal-Ochoa, J. D. (1986). Disposable Knee-Bracing: Improvement in Seismic Design of Steel Frames. Journal of Structural Engineering, ASCE, vol. 123, page 11-18.

Aslani, F., and Goel, S. C. (1989). Experimental and analytical study of the inelastic behavior of double angle bracing members under cyclic loading. Report no. UMCE 89-5, Department of Civil Engineering, University of Michigan, Ann Arbor, Michigan.

Aslani, F., and Goel, S. C. (1991). An analytical criterion for buckling strength of built-up compression members. Engineering Journal, American Institute of Steel Construction, volume 28, number 4, pages 159-168.

Aslani, F., and Goel, S. C. (1991). Stitch Spacing and Local Buckling in Seismic-Resistant Double-Angle Braces. Journal of Structural Engineering, ASCE, vol. 117, pages 2442-2463.

Aslani, F., and Goel, S. C. (1992). Stitch Spacing and End Fixity in Seismic-Restraint Boxed Angles Braces. Journal of Structural Engineering, volume 118, number 10, pages 2872-2889.

Astaneh-Asl, A., and Goel, S. C. (1984). Cyclic In-plane Buckling of Double-Angle Bracing. Journal of Structural Engineering, ASCE, vol. 109, pages 2036-2055.

Astaneh-Asl, A., Goel, S. C., and Hanson, R. D. (1982). Cylic Behavior of Double Angle Bracing Members with End Gusset Plates. Report no. UMEE 82R7, Department of Civil Engineering, University of Michigan, Ann Arbor, Michigan.

Astaneh-Asl, A., Goel, S. C., and Hanson, R. D. (1985). Cyclic Out-of-Plane Buckling of Double-Angle Bracing. Journal of Structural Engineering, ASCE, vol. 111, page 1135-1153.

Astaneh-Asl, A., Goel, S. C., and Hanson, R. D. (1986). Earthquake-resistant design of double-angle bracings. Engineering Journal, American Institute of Steel Construction, volume 4, pages 133-147.

Balendra, T., Lim, E. L., and Liaw, C. Y. (1997). Large Scale Seismic Testing of Knee-Brace-Frame. Journal of Structural Engineering, ASCE, vol. 112, page 1544-1552.

Balendra, T., Sam, M., Liaw, Ch., and Lee, S. (1991). Preliminary studies into the behavior of knee braced frames subject to seismic loading. Engineering Structures, volume 13, number 1, pages 67-74.

Balendra, T., Sam, M., and Liaw, Ch. (1995). Earthquake-resistant steel frames with energy dissipating knee elements. Engineering Structures, volume 17, number 5, pages 334-343.

Ballio, G., and Perotti, F. (1985). Cyclic behavior of axially loaded members; numerical simulation and experimental verification. Journal of Constructional Steel Research 7, pages 3-41.

Barsom, J. M., and Rolfe, S. T. (1999). Fracture and Fatigue Control in Structures: Applications of Fracture Mechanics. Third Edition, ASTM, West Conshohocken, PA.

Beaulieu, D., and Picard, A. (1987). Design of diagonal cross bracings part 1: Theoretical study. Engineering Journal of the American Institute of Steel Construction, volume 24, number 3, pages 122-126.

Beaulieu, D., and Picard, A. (1988). Design of diagonal cross bracings part 2: Experimental study. Engineering Journal of the American Institute of Steel Construction, volume 25, number 4, pages 156-160.

Bertero, V., Uang, Ch., Llopiz, C. R., and Igarashi, K. (1989). Earthquake simulation testing of concentric braced dual system. Journal of Structural Engineering, ASCE, volume 115, number 8, pages 1877-1894.

Black, R. G., Wegner, W. A., and Popov, E. P. (1980). Inelastic Buckling of Steel Struts Under Cyclic Load Reversals. Report no. UBC/EERC-80/40, University of California, Berkeley, CA.

Blakeborough, A., Williams, M. S.,Clement, D., and Bourahla, N. (2002). Seismic behavior of knee braced frames. Proceedings of the institution of Civil Engineers: Structures and Buildings, volume 152, number 2, pages 147-155.

Brown, T., and Shaback, B. (2003). Behavior of square hollow structural steel braces with end connections under reversed cyclic axial loading. Canadian Journal of Civil Engineering, volume 30, number 4, pages 745-753.

Bruneau, M., Tremblay, R., Timler, P., and Filiatrault, A. (1995). Performance of steel structures during the 1994 Northridge earthquake. Canadian Journal of Civil Engineering, volume 22, number 2, pages 338-360.

Bruneau, M., Uang, Ch., and Whittaker, A. (1998). Ductile Design of Steel Structures. McGraw-Hill, New York.

Building Seismic Safety Council (BSSC). (1997). NEHRP Recommended Provisions for Seismic Regulations for New Buildings and Other Structures. Part 1 – Provisions, Washington, D.C.

Canadian Standard Association (CSA). (1994). CAN/CSA-S16.1-94, Limit States Design of Steel Structures. Canadian Standard Association, Rexdale, Ontario.

Chen, I., and Chen, W. (2000). Major design impact of 1997 LRFD steel seismic code revision in USA. Journal of Structural Engineering, volume 27, number 1, pages 1-16.

Chen, Ch., Chen, S, and Liuw, J. (2001). Application of low yield strength steel on controlled plastification ductile concentrically braced frames. Canadian Journal of Civil Engineering, volume 28, number 5, pages 823-836.

Cheng, J. J. R., and Grondin, G. Y. (1999). Recent Development in the Behavior of Cyclically Loaded Gusset Plate Connections. Proceedings North American Steel Construction Conference, Toronto, Canada, page 8.1-8-22.

Cheng, J. J. R., Kulak, G. L., and Khoo, H. (1998). Strength of slotted tubular tension members. Canadian Journal of Civil Engineering, volume 25, number 6, pages 982-991.

Cheng, J. J. R., and Kulak, G. L. (2000). Gusset plate connection to round HSS tension members. Engineering Journal, volume 37, number 4,pages 133-139.

Elghazouli, A. Y. (2003). Seismic design procedures for concentrically braced frames. Proceedings of the Institution of Civil Engineers: Structures and Buildings. volume 156, issue 4. Pages 381-394

Elsesser, E. (1986). A survey of seismic structural systems and design implications. ATC-17, Proceedings of a Seminar and Workshop on Base Isolation and Passive Energy Dissipation, San Francisco, CA, pages 51-62.

El-Tayem, A. A., and Goel, S. C. (1986). Effective Length Factor for the Design of X-bracing Systems. Engineering Journal, AISC, vol. 24, page 41-45.

El-Tayem, A. A., and Goel, S. C. (1986). Cyclic Load Behavior of Angle X-Bracing. Journal of Structural Engineering, vol. 112, Issue 11, pages 2528-2539.

Englekirk, R. (1994). Steel Structures: Controlling Behavior Through Design. Jhon Wiley & Sons, Inc., New York.

Estekanchi, H., Vafai, A., and Modif, M. (1995). Use of single diagonal bracing in improvement of the lateral response of tall buildings. The Structural Design of Tall Buildings, volume 4, number 2, pages 115-126.

Eurocode 8. (1998). Structures in Seismic Regions, Part 1.1: General Rules and Rules for Buildings. Commision of the European Communities, European Committee for Standardisation, ENV 1998-1-1.

FEMA. (1997). NEHRP recommended provisions for seismic regulations for new buildings Part 1-provisions. Federal Emergency Management Agency. Building Seismic Safety Council, Washington, D. C.

FEMA. (2000). State of the Art Report on Connection Performance. FEMA-355D, C, Federal Emergency Management Agency, Washington D. C.

Filiatrault, A., Stiemer, S., and Tremblay, R. (1991). Aspects of the seismic design of concentrically braced frames. 1991 Annual Conference of the Canadian Society for Civil Engineering. Vancouver, British Columbia.

FitzGerald, T. F., Anagnos, T., Goodson, M., and Zsutti, T. (1989). Slotted Bolted Connections in a Seismic Design of Concentrically Braced Connections. Earthquake Spectra, volume 5, pages 383-391.

Foutch, D. A., and Roeder, Ch. W. (1987). Performance of two full-scale buildings under seismic tests. Proceedings of the sessions at Structures Congress related to buildings, Orlando, FL, pages 68-83.

Gioncu, V., and Mazzolani, M. (2002). Ductility of Seismic Resistant Steel Structures. First Edition, Spon Press, New York.

Girard, C., Picard, A., and Fafard, M. (1995). Finite element modeling of the shear-lag effects in an HSS welded to a gusset plate. Canadian Journal of Civil Engineering, volume 22, number 4, pages 651-659.

Goel, S. C. (1993). Earthquake Resistance Design of Ductile Braced Steel Structures. Satability and Ductility of Steel Structures under Cyclic Loading, CRC press, pages 197-308.

Goel, S., Aslani, F., (1992), Stitch spacing and end fixity in seismic-resistant boxed angle braces, Journal of Structural Engineering, volume 118, number 10, pages 2872-2889.

Gregorian, C. E. and Popov, E. P. (1993). Slotted Bolted Connections for Energy Dissipation. Proceedings ATC 17-1 Seminar on Seismic Isolation, Passive Energy Dissipation, and Active Control, San Francisco, CA, pages 545-556.

Gugerli, H., and Goel S. C. (1982). Inelastic Cyclic Behavior of Steel Bracing Members. Report No. UMEE-82R1. The University of Michigan, Ann Arbor, Michigan.

Hanson, R., and Higginbotham, A. B. (1976). Axial hysteretic behavior of steel members. ASCE, Journal of the Structural Division, volume 102, number 7, pages 1365-1381.

Hassan, O. F., and Goel, S. C. (1991). Modeling of Bracing Members and Seismic Behavior of Concentrically Braced Steel Structures. Research Report No. UMCE 91-1, Department of Civil Engineering, University of Michigan, Ann Arbor, Michigan.

Henderson, J. E., and Packer, J. A. (1997). Hollow Structural Sections: Connections and Trusses. Canadian Institute of Steel Construction, Ontario, Canada.

Higginbotham, A. B. (1973). The Inelastic Cyclic Behavior of Axially-Loaded Steel Members. Report No.UMEE-73R1, Department of Civil Engineering, University of Michigan, Ann Arbor, Michigan.

Ikeda K. and Mahin S. A. (1984). Phenomenological modeling of steel braces under cyclic loading. Report no. UCB/EERC 84/09, Earthquake Research Center, University of California, Berkeley, CA.

Ikeda K. and Mahin S. A. (1984). A refined physical theory model for predicting the seismic behavior of braced steel frames. Report no. UCB/EERC 84/12, Earthquake Research Center, University of California, Berkeley, CA.

Ikeda K. and Mahin S. A. (1986). Cyclic response of steel braces. Journal of Structural Engineering, ASCE, 112, no. 2, 342-361.

Jain, A. K., Goel, S. C., and Hanson, R. (1978). Hysteresis behavior of bracing members and seismic response of braced frames with different proportions. Report No. UMEE-78R3. The University of Michigan, Ann Arbor, Michigan.

Jain, A. K., Goel, S. C., and Hanson, R. D. (1978). Inelastic Response of Restrained Steel Tubes. Journal of the Structural Division, ASCE, vol. 104, pages 897-910.

Jain, A. K., Goel, S. C., and Hanson, R. D. (1980). Hysteretic Cycles of Axially Loaded Steel Members. Journal of the Structural Division, ASCE, vol. 106, page 1777-1795.

Jain, A. K., Redwood, R. G., and Lu, F. (1993). Seismic response of concentrically braced dual steel frames. Canadian Journal of Civil Engineering, volume 20, number 4, pages 672-687.

Kahn, L. F., and Hanson, R. D. (1976). Inelastic Cycles of Axially Loaded Steel Members. Journal of the Structural Division, ASCE, vol. 102, pages 947-959.

Kathib I. F., Mahin, S. A. (1987). Dynamic inelastic behavior of chevron braced steel frames. Fifth Canadian Conference on Earthquake Engineering, Balkema, Rotterdam, pages 211-220

Kathib I. F., and Mahin, S. A. (1987). Methods for improving the seismic response of concentrically braced frames. Dynamics of Structures, Proceedings of the Sessions at Structures Congress, Orlando, FL, USA, pages 101-116.

Kathib I. F., Mahin, S. A., and Pister, K.S. (1988). Seismic behavior of concentrically braced frames. Report no. UCB/EERC-88/01. Earthquake Engineering Research Center, University of California, Berkeley, CA.

Kim, H. I., and Goel, S. C. (1992). Seismic evaluation and upgrading of braced frame structures for potential local failures. Report no. UMCEE 92-24, Department of Civil Engineering, University of Michigan, Ann Arbor, Michigan.

Kim, H. I., and Goel, S. C. (1996). Upgrading of Braced Frames for Potential Local Failure. Journal of Structural Engineering, May 1996, pages 470-475.

Korol, R. M. (1996). Shear lag in slotted HSS tension members. Canadian Journal of Civil Engineering, volume 23, number 6, pages 1350-1354.

Krawinkler, H., and Osteraas, J. (1990). Seismic design based on strength of structures. Proceedings of the US National Conference on Earthquake Engineering, volume 2, pages 955-963.

Lee, S., and Goel S. C. (1987). Seismic behavior of hollow and concrete-filled square tubular bracing members. Report no. UMCE 87-11, Department of Civil Engineering, University of Michigan, Ann Arbor, Michigan.

Leowardi, L. S., Walpole, W. R. (1996). Performance of steel brace members. Research Report no. 96-03, Christchurch, New Zealand: Department of Civil Engineering, University of Canterbury.

Liu, Z., and Goel, S. C. (1987). Investigation of concrete-filled steel tubes under cyclic bending and buckling. Report no. UMCE 87-3, Department of Civil Engineering, University of Michigan, Ann Arbor, Michigan.

Malley, J. (2003). Update on the AISC seismic provisions. American Institute of Steel Construction, electronic publications, pages 133-138.

Martinelli, L., Perotti, F., and Bozzi, A. (2000). Seismic Design and Response of a 14-Story Concentrically Braced Steel Building. Proceedings STESSA 2000 Conference, Montreal, Canada, pages 327-334.

Medhekar, M. S., and Kennedy, D. J. L. (1997). Seismic evaluation of steel buildings with concentrically braced frames. Structural Engineering Report 219, Department of Civil Engineering, The university of Alberta, Edmonton, Alberta, Canada.

Medhekar, M. S., and Kennedy, D. J. L. (1997). An assessment of the effect of brace overstrength on the seismic response of a single-storey steel building. Canadian Journal of Civil Engineering, volume 24, number 5, pages 692-704.

Medhekar, M. S., and Kennedy, D. J. L. (1999). Seismic response of two-storey buildings with concentrically braced steel frames. Canadian Journal of Civil Engineering, volume 26, number 4, pages 497-509.

Medhekar, M. S., and Kennedy, D. J. L. (1999). Seismic evaluation of single-story steel buildings. Canadian Journal of Civil Engineering, volume 26, number 4, pages 379-394.

Medhekar, M. S., and Kennedy, D. J. L. (1999). Proposed strategy for seismic design of steel buildings. Canadian Journal of Civil Engineering, volume 26, number 5, pages 564-571.

Medhekar, M. S., and Kennedy, D. J. L. (2000). Displacement-based seismic design of buildings – Theory. Engineering Structures, volume 22, number 3, pages 201-209.

Medhekar, M. S., and Kennedy, D. J. L. (2000). Displacement-based seismic design of buildings – application. Engineering Structures, volume 22, number 3, pages 210-221.

Naeim, F. (1989). The Seismic Design Handbook. Structural Engineeging Series, Van Nostrand Reinhold, New York.

Nakashima, M., and Wakabayashi, M. (1992). Analysis and design of steel braces and braced frames in buildings structures. Stability and ductility of steel structures under cyclic loading, pages 309-321.

National Building Code of Canada, NBCC. (1995). National Research Council of Canada, Ottawa, Ontario.

Nordenson, G. J. P. (1984). Notes on the seismic design of steel concentrically braced frames. Proceedings of the 8th World Conference on Earthquake Engineering, San Francisco, CA. volume 5, pages 395-402.

Perotti, F., and Scarlassara, P. (1991). Concentrically Braced Steel Frames under Seismic Actions: Non-linear Behavior and Design Coefficients. Earthquake Engineering and Structural Dynamics, vol. 20, pages 409-427.

Plumier, A. (1997). The Dogbone: Back to the Future. Engineering Journal, volume 34, number 2, pages 61-67.

Popov, E. P., and Black, R. G. (1981). Steel Struts under Severe Cyclic Loadings. Journal of the Structural Engineering Division, ASCE, Vol. 107, pages 1857-1881.

Popov, E. P. (1979). Inelastic Behavior of Steel Braces Under Cyclic Loading, Proceedings, Second U.S. National Conference on Earthquake Engineering, Standford University, Stanford, CA, pages 923-932

Popov E. P., and Maison B. F. (1980). Cyclic response prediction for braced steel frames. Journal of Structural Engineering, ASCE, volume 106, pages 1401-1416.

Popov, E. (1986). On California Structural Steel Seismic Design. Earthquake spectra the professional journal of the earthquake engineering, volume 2, number 4, pages 703-727.

Plumier, A., (1997), The dogbone: back to the future, Engineering Journal, vol.34, number 2, pages 61-67.

Prathuangsit, D. (1976). Inelastic Hysteresis Behavior of Axially Loaded Steel Members with Rotational End Restraints. Ph.D. Thesis, Department of Civil Engineering, University of Michigan, Ann Arbor, Michigan.

Prathuangsit, D., Goel, S. C., and Hanson, R. D. (1978). Axial Hysteresis Behavior with end Restraints. Journal of the Structural Division, ASCE, vol. 104, pages 883-895.

Rahgozar, M.A., and Humar, J.L. (1998). Accounting for overstrength in seismic design of steel structures. Canadian Journal of Civil Engiineering, volume 25, number 1, pages 1-15.

Rai, D. C., and Goel, S. C. (1997). Seismic evaluation and upgrading of existing steel concentric braced structures. Research Report UMCEE 97-03, Department of Civil Engineering, University of Michigan, Ann Arbor, Michigan.

Redwood, R. G., and Channagiri, V. S. (1991). Earthquake Resistant Design of Concentrically Braced Steel Frames. Canadian Journal of Civil Engineering, vol. 18, pages 839-850.

Redwood, R. G., Lu, F., Bouchard, G., and Paultre, P. (1991). Seismic Response of Concentrically Braced Steel Frames. Canadian Journal of Civil Engineering, vol. 18, pages 1062-1077.

Redwood, R. G., and Jain, A. K. (1992). Code provisions for seismic design of concentrically braced steel frames. Canadian Journal of Civil Engineering, volume 19, pages 1025-1031.

Remennikov, A., and Walpole W. (1995). Incremental model for predicting the inelastic hysteretic behavior of steel bracing members. Research Report no. 95-6. Department of Civil Engineering, University of Canterbury, Christchurch, New Zeland.

Remennikov, A., and Walpole, W. (1996). Modelling the inleastic cyclic behavior of a bracing member for work-hardening material. International Journal of Solids and Structures, volume 34, number 27, pages 3491-3515.

Remennikov, A., and Walpole, W. (1997). Analytical Prediction of Seismic Behavior for Concentrically-Braced Steel Systems. Earthquake Engineering and Structural Dynamics, vol. 26, pages 859-874.

Remennikov, A., and Walpole W. (1998). Note on compression strength reduction factor for a buckled strut in seismic-resisting braced system. Engineering Structures, volume 20, number 8, pages 779-782.

Rezai, M., Prion, H., Tremblay, R., Bouatay, N., and Timler, P. (1999). Seismic Performance of Brace Fuse Elements for Concentrically Steel Braced Frames. Proceedings STESSA 2000 Conference, Montreal, Canada, pages 39-46.

Roeder, C. W. (1989). Seismic behavior of concentrically braced frame. ASCE Journal of Structural Engineering, volume 115, number 8, pages 1837-1856.

SAC. (1994). Analytical and Field Investigations of Buildings affected by the Northridge earthquake of January 1994. SAC 9504 Part 1 & 2, SAC Joint Venture, Sacramento, CA.

SAC. (1997). Protocol for fabrication, inspection, testing and documentation of beam-column connection tests and other experimental specimens. Report No. SAC/BD-97/02, SAC Joint Venture, Sacramento, CA.

Salmon, Charles G., and Johnson, John E. (1996). Steel Structures: Design and Behavior, Emphasizing Load and Resistance Factor Design. Fourth Edition, Harper Collins, Inc., New York.

Sabelli, R., and Hohbach, D. (1999). Design of cross-braced frames for predictable buckling behavior. ASCE Journal of Structural Engineering, volume 125, number 2, pages 163-168.

Segui, W. T. (2003). LRFD Steel Design. Third Edition. Brooks/Cole-Thomson Learning, Pacific Grove, CA.

Shing, P., Bursi, O., and Vannan, T. (1994). Pseudodynamic test of a concentrically braced frame using substructuring techniques. Journal of Constructional Steel Research, volume 29, number 1-3, pages 121-148.

Singh, P. (1977). Seismic behavior of braces and braced steel frames. Ph.D. Thesis, University of Michigan, Ann Arbor, Michigan.

Tang, X. and Goel, S. C. (1989). Brace fracture and analysis of Phase-I structure. Journal of Structural Engineering, ASCE, 15, no. 8, 1960-1976.

Tang, X., and Goel, S. C. (1987). Seismic analysis and design considerations of braced steel structures. Report No. UMCE 87-4. Department of Civil Engineering, University of Michigan, Ann Arbor, Michigan.

Tremblay, R., Prion, H. G. L., Stiemer, S., and Filiatrault, A. (1991). Proceedings of the Annual Technical Session of the Structural Stability Research Council, pages 291–302.

Tremblay, R., and Stiemer, S. F. (1993). Energy Dissipation Through Friction Bolted Connections in Concentrically Braced Steel Frames, Proceedings ATC 17-1 Seminar on Seismic Isolation, Passive Energy Dissipation, and Active Control, San Francisco, CA., pages 557-568.

Tremblay R., Archambault, M., and Filiatrault, A. (1995). Seismic behavior of ductile concentrically steel x-bracings. Proceedings 7th Canadian conference on earthquake engineering, Montreal, Canada, pages 549-556.

Tremblay, R., and Filiatrault, A. (1996). Seismic Impact Loading in Inelastic Tension-Only Concentrically Braced Steel Frames: Myth or Reality?. Earthquake Engineering and Structural Dynamics, vol. 25, pages 1373-1389.

Tremblay, R., Bruneau, M., Nakashima, M., Prion, H. G. L., Filiatrault, A., and DeVall, R. (1996). Seismic Design of Steel Buildings: Lessons From the 1995 Hyogo-ken Nanbu Earthquake. Canadian Journal of Civil Engineering, vol. 23, pages 727-756.

Tremblay, R., and Filiatrault, A. (1997). Tension-Only Bracing: A viable Earthquake-Resistant System for Low-rise Steel Buildings? Proceedings SDSS 1997, 5th Intern, Colloquium on Stability and Ductility of Steel Structures, Nagoya, Japan, vol. 2, pages 1163-1170.

Tremblay, R., Filiatrault, A. (1998). Design of tension-only concentrically braced steel frames for seismic induced impact loading. Engineering Structures, volume 20, number 12, pages 1087-1096

Tremblay, R. (2000). Influence of Brace Slenderness on the Seismic Response of Concentrically Braced Steel Frames. Proceedings STESSA 2000 Conference, Montreal, Canada, pages 527-524.

Tremblay, R. (2001). Seismic Behavior and Design of Concentrically Braced Steel Frames. Engineering Journal, vol. 38. issue 3, pages 148-166.

Tremblay, R. (2002). Inelastic seismic response of steel bracing members. Journal of constructional steel research, volume 28, number 5-8, pages 665-701.

Tremblay, R., Tirca, L. (2003). Behavior and design of multi-storey zipper concentrically braced steel frames for mitigation of soft-storey response. STESSA 2003, Proceedings of the Conference on Behavior of Steel Structures in Seismic Areas, pages 471-477.

Wakabayashi, M., Nakamura, T., and Yoshida, N. (1977). Experimental Studies on the Elastic-Plastic Behavior of Braced Frames under Repeated Horizontal Loading. Bulletin, Disaster Prevention Research Institute, Kyoto University, vol. 27, no. 251, pages 121-154.

Walpole, W. R. (1985). Concentrically Braced Frames. Bulletin of the New Zealand National Society for Earthquake Engineering, volume 18, number 4, pages 351-354.

Xu, P., and Goel, S. C. (1990). Experimental and analytical study of the inelastic behavior of full-scale double angle channel bracing members under cyclic loading,

Report no. UNCE 90-1, Department of Civil Engineering, University of Michigan, Ann Arbor, Michigan.

Yamanouchi, Y., Midorikawa, M., Nishiyama, I., and Watabe, M. (1989). Seismic behavior of full scale concentrically braced steel building structure. Journal of structural engineering, volume 115, pages 1917-1929.

Yam, M. C. H., and Cheng, J. J. R. (2002). Behavior and design of gusset plate connections in compression. Journal of Constructional Steel Research, volume 58, number 5-8, pages 1143-1159.

Yanev, P, Gillengerten, J. D., and Hamburger, R. O. (1991). Performance of Steel Buildings in Past Earthquakes. American Iron and Steel Institute (AISI) and EQE Engineering, Inc.

12 Appendix

APPENDIX A – RXS, Design Procedures

General design procedures for braces with the RXS fuse system are presented. Calculations are shown for a brace sized for its global buckling capacity. All calculations were developed for a round HSS 6.625x0.500 A500 Grade B steel, which was the size chosen to experimentally reproduce local behavior at the laboratory. The design calculations comply with the third edition of the AISC LRFD Manual of Steel Construction and the 2002 AISC Seismic Provision. These two provisions were updated in 2005 after this study was completed, and only a few changes concern the design procedure of the fuse. Those changes between the two provisions are discussed. Braces sized for their local buckling capacity can also be designed with the same procedure presented by changing a few variables as it is described in this section.

A.1 Round HSS Test Specimen Selection

Among pre-selected sections chosen as economically feasible from an availability point of view that also complied with width-thickness requirements (Table A1), HSS 6.625x0.25 was selected because the calculated failure load of this section was within the verified loading range of the testing equipment.

HSS Diameter x thickness	Weight (Lb/ft)	D/t	Fy (ksi)	Limiting D/t	Width-thickness check (D/t < Limiting D/t)
6.625 x 0.250	***17.020***	***28.40***	***42***	***30.95***	***OK***
6.625 x 0.280	18.970	25.40	42	30.95	OK
6.625 x 0.280	18.970	25.38	35	37.14	OK
6.625 x 0.312	21.040	22.80	42	30.95	OK
6.625 x 0.375	25.030	19.00	42	30.95	OK
8.625 x 0.322	28.550	28.70	42	30.95	OK
8.625 x 0.322	28.550	28.75	35	37.14	OK
8.625 x 0.375	33.040	24.70	42	30.95	OK
10.750 x 0.365	40.480	31.71	35	37.14	OK
10.750 x 0.500	49.560	36.53	35	37.14	OK
12.750 x 0.375	54.740	23.10	42	30.95	OK
12.750 x 0.500	65.420	27.40	42	30.95	OK
14.000 x 0.500	72.090	30.10	42	30.95	OK

Table A1 - Pre-Selected HSS Sizes.

A.2 RXS Test Specimen Design Calculation Spreadsheet

In general, design calculations for round hollow structural braces with the RXS fuse should follow the same procedure presented in this section. All calculations comply with the following provisions: AISC LRFD third edition Design Manual [AISC, LRFD, 2001], AISC May 21, 2002 "Seismic Provisions for Structural Steel Buildings" [AISC, 2002], and the "Hollow Structural Sections Manual" [AISC, 1997].

Design calculations were developed using a Microsoft Excel spreadsheet that was divided into two worksheets: a list of section worksheet, and a second design worksheet that includes all calculations for the chosen HSS size. This second worksheet is broken into 5 parts: Part I: "Input Data" contains most of the design input parameters. Main design calculations are located in: Part II: "Global Capacities", Part III: "End Connection Design", and Part IV: "Local Capacities". Part V includes a summary of the fuse design that presents some informative ratios from design calculation results.

A.2.1 List of Sections Worksheet

This worksheet contains user input data for all pre-selected HSS sizes. This input data is related to the RXS fuse design parameters, section properties, and

assumptions made for brace connection design such as gusset plate properties, and weld characteristics. Although more hollow structural sections (HSS) comply with the seismic design provision requirements for width/thickness ratios, the sections included in table A2 are only those economical choices from availability point of view in the Kansas City area. Design calculations are only presented for the chosen HSS 6.625x0.25, but main design parameters are included for all pre-selected sizes in this table for an area reduction coefficient ***f*** of 0.5 (50%) and 3 oval cutouts as a design reference.

Standard Sections that meet D/t criteria

Sections represent economical choices from availability point of view

ϕ1 =	0.9	number of holes =	3	K global =	1
ϕ2 =	0.75	"f" provided =	0.5	K local =	0.65
ϕ3 =	0.85				
E =	29000	ksi			

Outside diameter (in)	Nominal thickness (in)	Design thickness (in)	Gross area (in^2)	Fy (ksi)	Fu (ksi)	Ry	Length (ft)	Hole Aspect ratio (HAR)	Length Aspect ratio (LAR)	Weld size	FEXX
6.625	0.250	0.233	4.68	42	58	1.3	22	3	2.50	3/16	70
6.625	0.280	0.261	5.22	42	58	1.3	28	3	3.00	3/16	70
6.625	0.280	0.261	5.22	***35***	***60***	***1.4***	28	3	2.50	3/16	70
6.625	0.312	0.291	5.79	42	58	1.3	28	3	2.00	4/16	70
6.625	0.375	0.349	6.88	42	58	1.3	28	3	2.00	4/16	70
8.625	0.322	0.300	7.85	42	58	1.3	30	3	2.00	4/16	70
8.625	0.322	0.300	7.85	***35***	***60***	***1.4***	32	3	2.00	4/16	70
8.625	0.375	0.349	9.07	42	58	1.3	29	3	2.50	4/16	70
10.75	0.365	0.339	11.09	***35***	***60***	***1.4***	39	3	2.00	4/16	70
10.75	0.500	0.465	15.00	42	58	1.3	36	3	2.50	5/16	70
12.75	0.500	0.465	17.90	42	58	1.3	42	3	2.50	5/16	70
14	0.500	0.465	19.80	42	58	1.3	47	3	2.50	5/16	70

Gusset plate		
t =	0.75	in
Fy =	36	ksi

red font indicates user input

Table A2 - List of Sections Worksheet.

ϕ_1 = resistance factor for yielding.

ϕ_2 = resistance factor for fracture.

ϕ_3 = resistance factor for compression.

E = steel modulus of elasticity.

f = area reduction coefficient.

K = effective length factor for compression members.

R_y = ratio of the expected yield stress to the specified minimum yield stress.

FEXX = tensile strength of the weld metal.

A.2.2 Design Calculation Worksheet

The calculation worksheet presented in this section was used to select the round HSS size for the experimental program. A round HSS 6.625X 0.250 A500 Grade B steel (first size, Table A1 and A2) was selected.

A.2.2.1 Part I: Input Data

General input parameters such as material properties, member properties, weld size, number of oval cutouts, and design constants such as resistance factors for tension strength, width thickness requirement, and limiting slenderness ratio KL/r are listed in Part I of the spreadsheet, shown in Fig. A1.

As braces, round HSS should have an outside diameter to wall thickness ratio that complies with seismic provisions for special concentrically braced frames. The limiting width thickness ratio is determined by the following expression [AISC, 2002, 13.2d]:

$$\frac{D}{t} < 0.044\frac{E}{Fy} \qquad \text{<Eq. A1>}$$

The slenderness ratio of braces is considered to be the most important parameter having a dominant influence on the seismic behavior of steel braces [Jain, Goel and Hanson 1978; Popov and Black 1981; Remennikov, Walpole, 1997]. As a second condition in part I, the brace length shall not exceed the limiting slenderness ratio KL/r calculated as [AISC, 2002, 13.2a]:

$$\frac{KL}{r} < 5.87\sqrt{\frac{E}{Fy}} \qquad \text{<Eq. A2>}$$

The maximum brace length allowed was calculated based on the limiting KL/r, and the radius of gyration of the HSS size (which was actually calculated in part II). Other input entries were located in other parts of this worksheet for better arrangement.

The latest 2005 seismic provision requires that bracing members shall have:

$$\frac{KL}{r} < 4\sqrt{\frac{E}{Fy}} \qquad \text{<Eq. A3>}$$

which is a more conservative approach as the limiting brace length was reduced by the 2005 seismic design provision. This latest edition of the seismic provision also

has exceptions as it allows an effective slenderness ratio up to 200 for braces when the available strength of the column is at least equal to the maximum load transferred to the column considering R_y, as appropriate, times the nominal strengths of the connecting brace elements.

The column design is out of the scope of the work in hand and the effective slenderness ratio requirement from the preceding 2002 seismic provision is assumed to be adequate for this design example since this parameter is a function of the brace length provided of 22.5 ft and this variable can be adjusted if necessary by user input.

Part I											
HSS	6.625	x	0.25	Ry =	1.3						
Fy =	42	ksi		Length =	22.5	ft				ϕ1=	0.9
Fu =	58	ksi		FEXX =	70		t gusset=	0.75	in	ϕ2=	0.75
E =	29000	ksi		weld size(ww)=	3/16	in	Fy gusset=	36	ksi	ϕ3=	0.85
Outside diameter "do" (in)	Wall thickness "t" (in)	Gross area "Ag" (in^2)	Number of holes "n"			Limiting width thickness ratio	Width Thickness ratio D/t	Meets width thickness ratio requirement *"check"*	Limiting KL/r	Maximum brace length (ft)	HSS length meets KL/r requirement *"check"*
6.625	0.233	4.68	3			30.38	28.43	*OK*	154	29.08	*OK*
red font indicates user input from list of sections (input) worksheet											
blue italic font indicates user output											

Fig. A1 - Design Calculation Worksheet Part I: Input Data.

Width/Thickness ratio check <Eq. A1>:

$$\frac{D}{t}\text{limit} = 0.044\left(\frac{E}{Fy}\right) = 0.044\left(\frac{29000ksi}{42ksi}\right) = 30.38$$

$$\frac{D}{t} = \frac{do}{t} = \frac{6.625in}{0.233in} = 28.43$$

$$\frac{D}{t}\ \text{limit} < \frac{D}{t} \qquad \therefore \text{OK}$$

Effective slenderness ratio check <Eq. A2>:

$$\frac{KL}{r}\ \text{limit} = 5.87\sqrt{\frac{E}{Fy}} = 5.87\sqrt{\frac{29000ksi}{42ksi}} = 154.3$$

$$\text{Max. brace length} = \frac{KL}{r}\text{lim}it \times \frac{radius\_of\_gyration}{12} = 154.3\frac{2.26in}{12in/ft} = 29.08ft$$

(radius of gyration is calculated in part II)

Given brace length = 22.5 ft < 29.08 ft $\qquad \therefore$ OK

A.2.2.2 Part II: Global Capacities

Overall brace capacities are calculated in the second portion of the design worksheet, shown in Fig. A2. Global strength calculations are based on the entire length and cross-sectional area of the HSS size. Two major outputs, global design compressive strength and global design tensile strength are calculated here. Because the compressive strength of a brace is bounded by the effective length factor ***k***, part II includes one input parameter, the global effective length factor $\boldsymbol{K_{global}}$. It was decided to use a hinged-end condition for the selection of $\boldsymbol{K_{global}}$, according to AISC LRFD third edition Design Manual [AISC, LRFD, 2001], instead of a fixed-end condition, because such condition may underestimate the global compressive strength of the member, even though a fixed-end condition would be a better representation of the actual end-condition provided by a gusset plate [Kim, Goel 1992]. The purpose of

these calculations was not to proportion the gusset plate. By assuming that the gusset plate capacity does not control the design, a conservative approach was to use a hinged-end condition.

Part II

GLOBAL CAPACITY

Mid diameter "dm" (in)	Inside diameter "di" (in)	Outside radius "ro" (in)	Mid circumference (in)	Moment of Inertia Global "I" (in^4)	Radius of gyration Global (in)	K factor Global	K*L/r Global	λ Global	Critical Buckling Stress "Fcr" (ksi)	Global design compressive strength (Kips)	Global design tensile strength (Kips)
6.392	6.159	3.313	20.08	23.93	2.26	1	119	1.45	17.50	*69.60*	*176.9*

red font indicates user input from list of sections (input) worksheet

blue italic font indicates user output

Fig. A2 - Design Calculation Worksheet Part II: Global Capacities.

Mid-circumference = $mid\_diameter \cdot \pi = 6.392 \cdot \pi = 20.08in$

Moment of Inertia = $\frac{\pi}{4}\left(\left(\frac{outside\_diameter}{2}\right)^4 - \left(\frac{inside\_diameter}{2}\right)^4\right)$

Moment of Inertia = $\frac{\pi}{4}\left(\left(\frac{6.625}{2}\right)^4 - \left(\frac{6.159}{2}\right)^4\right) = 23.93in^4$

Radius of Gyration = $\sqrt{\frac{moment\_of\_inertia}{gross\_area}}$

Radius of Gyration = $\sqrt{\frac{23.93in^4}{4.68^2}} = 2.26in$

K = 1 (pin end condition)

$$\frac{KL}{r}global = \frac{(1 \cdot 22.5ft \cdot 12in/ft)}{2.26in} = 119$$

$$\lambda_{global} = \frac{KL}{(r * \pi)}\sqrt{\frac{Fy}{E}} = \frac{119}{\pi}\sqrt{\frac{42ksi}{29000ksi}} = 1.45 < 1.5$$

$$\lambda < 1.5 \therefore Fcr = 0.658^{\lambda^2} \cdot Fy = 0.658^{1.45^2} \cdot 42ksi = 17.5ksi$$

Global design buckling capacity =

$= \phi 3 \cdot Fcr \cdot Ag = 0.85 \cdot 17.5ksi \cdot 4.68^2 = 69.6kips$

Global design tensile capacity = $\phi 1 \cdot Fy \cdot Ag = 0.9 \cdot 42ksi \cdot 4.68^2 = 176.9kips$

A.2.2.3 Part III: End Connection Design

The minimum area reduction coefficient depends on the factored connection capacity, for this reason Part III, shown in Fig. A3, includes the gusset plate to HSS connection design. The connection design method implemented is based on the design examples for slotted HSS/gusset plate connection for both axial tension and axial compression from the AISC Hollow Structural Sections Connection Manual.

The minimum area reduction coefficient was calculated based on the lower bound expression from Chapter 4 - section 4.3.1 once the capacity of the end connection was determined. If the minimum required area reduction coefficient from Chapter 4 - equation 4.8 becomes zero or a negative number reinforcement of the brace at the connection is not required since actually the factored connection capacity

would be less than the nominal axial tensile strength of the bracing member determined by $R_y*F_y*A_g$, where R_y is the ratio of the expected yield stress to the specified minimum yield stress..

The behavior of the end connection is not the purpose of this project, thus, assumptions were made so that weld capacity, bolting to gusset, or buckling capacity of gusset do not control connection capacity. Part III includes three major outputs: the connection capacity, connection demand with respect to AISC Seismic Provisions [AISC, 2002], and the minimum area reduction coefficient, which is a function of the two preceding outputs.

The actual provided reduction coefficient f, greater than or equal to the calculated minimum area reduction coefficient is specified as input by the user at the end of Part III. Since actual material yield strength, F_y, and ultimate strength, F_u, may be, and indeed usually are, substantially higher than the minimum values specified for A500 grade B steel, the effect of expected variations between minimum specified ASTM material properties, and actual F_y and F_u, was analyzed to select an adequate area reduction coefficient that would not represent a major impact on design calculations as the actual lower bound of the area reduction coefficient could be expected to increase due to higher material properties values. This lower bound could also decrease due to larger actual material properties if the test coupon R_y becomes smaller than the ratio of the expected yield strength to the minimum specified yield strength R_y specified by AISC Seismic Provisions for concentrically braced frames

[AISC, 2002], but that case is rather harmless to the system since it actually allows a wider range of area reduction coefficients and would not be considered.

Part III

END CONNECTION DESIGN

Assume that bolting to gusset or buckling capacity of gusset doesn't control.
Make weld strong enough, so that, weld capacity doesn't control connection capacity

Net area "Anec" (in^2)	Length Aspect Ratio "LAR"	length of weld to HSS	Length of weld to HSS provided "Lw" (in)	X bar	U	shear strength at welds "Vnaw" (Kips)	effective area of weld throat "Aw"	t1	Factored weld strength "WS" (kips)
4.27225	2.5	16.5625	17	2.109	0.876	*359.342*	6.01	0.430	*189.2993*
Fy * Ag "yield_ec" (kips)	**shear lag fracture in HSS "Vnsl" (Kips)**	**governing end connection tensile capacity "Tc_end_conn"**	**Controlling Connection Capacity (kips)**	**Weld strength "check"**	**demand on connection**	**Minimum Required area reduction coefficient "f_min"**	**Area reduction coefficient provided "f"**	**Maximum Required area reduction coefficient "f_max"**	**Provided reduction coefficient "check"**
176.904	162.8	*162.790*	*162.790*	*OK*	255.528	*0.363*	0.5113	*0.667*	*OK*

red font indicates user input from list of sections (input) worksheet
blue italic font indicates user output

Fig. A3 - Design Calculation Worksheet Part III: End Connection Design.

The lower bound of the area reduction coefficient f is calculated using Chapter 4 - equation 4.8. The equation includes the factored brace connection capacity and the factored brace yield capacity, which are as follows.

$$\text{Net Area} = Ag - 2\left(\left(gusset\_thickness + \frac{1}{8}\right)HSS\_wall\_thickness\right)$$

$$\text{Net Area} = 4.68in - 2\left(\left(0.75in + \frac{1}{8}\right)0.233in\right) = 4.27in^2$$

The controlling connection capacity is the weaker between three connection limit states:

(a) Shear strength at the weld "Vnaw" is equal to $\phi 0.6Fy \cdot 4Lw \cdot t$

where:

ϕ = resistance factor for yielding, 0.9.

L_w = Length of weld to HSS provided (as a rule of thumb should be equal to or greater than the HSS depth).

LAR = The Length Aspect Ratio is not a design parameter as it does not affect the length of the weld required but rather a ratio that was initially intended for comparison with other sizes as can be seen in table 4.3 above.

Length of the weld to HSS = $LAR \cdot outside\_diameter = 2.3 \cdot 6.625 = 16.5625in$

L_w should be greater than 16.5625in $\therefore$ Lw = 17in.

t= wall thickness of the HSS = 0.233in.

$V_{naw} = 0.9 \cdot 0.6 \cdot 42ksi \cdot 4 \cdot 17in \cdot 0.233in = 359.342kips$

(b) Factored weld strength "WS" is calculated as follows:

If the thickness of the gusset plate is greater than $t1 = 1.18 \cdot fexx \cdot \frac{ww}{Fygusset}$

$WS = \phi 2 \cdot 0.6 \cdot fexx \cdot Aw$

Otherwise

$$WS = \phi 2 \cdot 0.6 \cdot fexx \cdot Aw \cdot \frac{tgusset}{1.18} \cdot fexx \cdot \frac{ww}{Fygusset}$$

where

F_{exx} = weld metal tensile strength = 70 ksi

A_w = effective area of weld throat = $4 \cdot 0.707 \cdot \left(ww - \frac{1}{16} \right) \cdot Lw$

ww = fillet weld size = $\frac{3}{16} in$

$$Aw = 4 \cdot 0.707 \left(\frac{3}{16} - \frac{1}{16} \right) 17 = 6.01 in^2$$

$$t1 = 1.18 \cdot 70 ksi \frac{3/16 in}{36 ksi} = 0.43 in$$

since the thickness of the guseet plate is greater than t_1 then:

$$WS = \phi 2 \cdot 0.6 \cdot fexx \cdot Aw = 0.75 \cdot 0.6 \cdot 70 ksi \cdot 6.01 in^2 = 189.3 kips$$

(c) The governing end connection tensile capacity between the brace yield capacity and

the shear lag fracture of the over-slot HSS section required for erection of the knife-plate type of connections

Factored brace Connection capacity = smaller of $\left(0.9 \cdot Fy \cdot Ag, 0.75 \cdot Fu \cdot Anet \cdot U\right)$

where

F_y = yield strength of the HSS = 42 ksi

F_u = ultimate strength of the HSS = 58 ksi

A_{net} = net area of the over-slot = $4.27225 in^2$

U = connection shear lag coefficient = $1 - \frac{X}{Lw}$

$$X = \frac{outside\_diameter}{\pi} = \frac{6.625}{\pi} = 2.109$$

$$U = 1 - \frac{2.109}{17} = 0.876$$

$$0.9Fy \cdot Ag = 0.9 \cdot 42ksi \cdot 4.68in^2 = 176.904kips$$

$$0.75 \cdot 58ksi \cdot 4.27225in^2 \cdot 0.876 = 162.8kips$$

Factored brace connection capacity = 162.8 kips

The governing tensile capacity of the connection, limit state (c) controls as shown in Fig. 4.11 and is equal to 162.79 kips.

The demand on the connection is given by the factored brace yield capacity calculated by multiplying $Ry \cdot Ag \cdot Fy = 1.3 \cdot 4.68in^2 \cdot 42ksi = 255.528kips$

where

R_y = Ratio of the Expected Yield Strength to the minimum specified yield strength $\boldsymbol{F_y}$

A_g = HSS gross area

F_y = yield strength of the HSS

Therefore, the lower bound of the area reduction coefficient is, using equation 4.8:

f_{min}= 1 – factored brace connection capacity = 1 – 162.79 kips = 0.363 <Eq. 4.8>

factored brace yield capacity 255.528 kips

As can be seen in Fig. A3, this minimum area reduction coefficient of 0.363 was set as the starting point to study variations between expected specified values in $\boldsymbol{F_y}$ and $\boldsymbol{F_u}$. The effect of these variations were studied by increasing the material yield strength, $\boldsymbol{F_y}$, and ultimate strength, $\boldsymbol{F_u}$, calculating the respective connection capacity

and connection demand for the given mechanical properties and finally calculating the area reduction coefficient using equation 4.8. It was found that if F_u is held constant, f_{min} increases as F_y increases and for F_y held constant, f decreases as F_u increases. Since the yield strength F_y is expected to have a significant increment compared to F_u, and since there is no major design impact if f decreases due to F_u increments because a lower limit value is being studied, attention focuses on the effect of F_y on f. Three variation patterns were considered:

F_y increases, F_u remains constant (continuous line Fig. A4).

F_y increases twice the amount of F_u increments (dotted line Fig. A4).

F_y and F_u increase the same amount (dashed line Fig. A4)

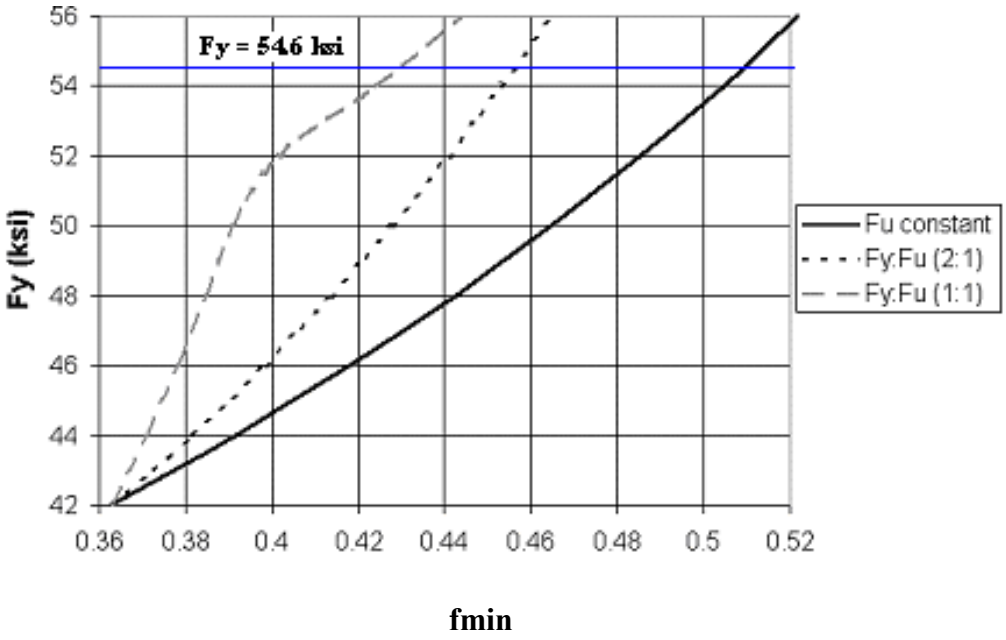

Fig. A4 - Fy vs. fmin on HSS 6.625x0.25.

Looking at Fig. A4 it can be seen that as the increment margin between F_y and F_u increases, the area reduction coefficient f increases. The case where F_u is held constant as F_y increases is not realistic because as the actual F_y increases with respect to the minimum specified, the actual F_u also increases with respect to its minimum specified. But the increment margin between F_y and F_u is not known until test coupons are tested, and therefore this case is included in Fig. A4 as a theoretical referential worst-case scenario. Higher increments of F_y with respect to F_u are not included, because as mentioned before, the area reduction coefficient tends to decrease with F_u increments.

Based on the Ratio of the Expected Yield Strength to the minimum specified yield strength R_y equal to 1.3, and the specified minimum yield strength equal to 42 ksi, the expected yield strength is anticipated to be around 54.6 ksi. For F_y equal to 54.6 ksi, from Fig. 4.11 the minimum area reduction coefficient could be anywhere between 43 percent and a theoretical referential worst-case scenario of approximately 51 percent.

Therefore, in order to provide enough allowance for the minimum area reduction coefficient to increase beyond the initial calculated 36 percent without having a major impact on design calculations, and taking into account specimen fabrication simplicity a conservative and optimal solution was to use a provided area reduction coefficient of 50 percent instead of using f_{min}. For the targeted 50 percent area reduction coefficient f, the resulting cutout width was 3 ½" (rounded up for

fabricability from calculated width of 3.42 inches) giving a final provided area reduction coefficient ***f*** of 51.13 percent.

The upper limit of the area reduction coefficient ***f*** is given by Chapter 4 - equation 4.9, and it is equal to 60.7%, therefore the area reduction coefficient selected complies with the upper and lower limit requirements for the first design philosophy.

$$f_{max} = 1 - \frac{\text{Global buckling capacity of brace}}{\text{Global tensile capacity of brace}} = 1 - \frac{69.60 \text{ kips}}{176.9 \text{ kips}} = 0.607 \quad \text{<Eq. 4.9>}$$

As mentioned before, this RXS fuse study was completed by the time the 2005 AISC seismic provision was published. Even though the updated seismic provision includes a few changes that are related to the design of the RXS fuse element, these changes do not affect the design procedure described in this section. Furthermore, it was found that the area reduction coefficient selected still complies with those changes from the updated provision.

As mentioned in Chapter 2 the 2005 AISC seismic provision increased the Ratio of the Expected Yield Strength to the minimum specified yield strength $\boldsymbol{R_y}$ for HSS ASTM A500, A501 from 1.3 (as used in the design spreadsheet calculations) to 1.4. This increment represents a more conservative approach that confirms the significance of the difference between the expected yield strength and the specified yield strength for concentrically braced frame connections. Spreadsheet calculations were checked using the updated $\boldsymbol{R_y}$ ratio, and by increasing this ratio from 1.3 to 1.4, only the lower bound of the area reduction coefficient increased from 0.363 to 0.408,

and since the area coefficient provided is 0.5113, it still complies with the area reduction coefficient lower bound.

One last update related to the RXS fuse design is the addition of the ratio of the expected ultimate strength to the minimum specified ultimate strength $\boldsymbol{F_u}$. Like $\boldsymbol{R_y}$, values for $\boldsymbol{R_t}$ also depend on member type [AISC, 2005, table I-6-1], and for HSS ASTM A500 (Grade B or C), and A501 $\boldsymbol{R_t}$ is 1.3. The addition of this ratio adds another equation to the design procedure that does not affect the spreadsheet calculations since it rather confirms if reinforcement of the brace at the connection is required or not. From Chapter 2, equation 2.2:

$$Ae = Ry \cdot \frac{Ag}{(0.75 \cdot Rt \cdot Fu)} \qquad \text{<Eq. 2.2>}$$

$$Ae = \frac{1.4 \cdot 42ksi \cdot 4.68in^2}{0.75 \cdot 1.3 \cdot 58ksi} = 4.87in^2$$

Since $Ae = 4.87in^2 > Ag = 4.68in^2$

$\therefore$ Connection requires local reinforcement of the brace section.

where:

R_t = Ratio of the expected ultimate strength to the minimum specified ultimate strength $\boldsymbol{F_u}$.

R_y = Ratio of the expected yield strength to the minimum specified yield strength $\boldsymbol{F_y}$ Values for $\boldsymbol{R_y}$ depend on member type [AISC, 2002, table I-6-1].

F_y = Brace specified minimum yield stress.

F_u = Brace specified minimum ultimate stress.

A_g = Brace gross area, in^2

A_e = Brace effective area, in^2 calculated from equation 2.2.

A.2.2.4 Part IV: Local Capacities

RXS local capacities are calculated in Part IV, Fig. A7, based on the provided reduction coefficient ***f*** from Part III. The reduced section is defined by a number of identical oval cutouts; hence, all calculations are based on the capacity of a set of three identical arms. Calculations were developed for a single arm with an arc cross-sectional area, and the total local capacity was estimated as the product of the number of oval cutouts and the calculated capacity of a single arm. The geometry of the arc cross sectional area is shown at the very beginning of Part IV. The local capacity calculation part of the spreadsheet includes two inputs: hole aspect ratio ***HAR***, and the RXS arm local effective length factor $\boldsymbol{K_{local}}$. It was decided to use a fixed-end condition for the selection of $\boldsymbol{K_{local}}$, according to LRFD [LRFD, 1999], because such condition represents the end constraint provided by the non-reduced section of the system. Part IV includes two outputs: local design compressive strength and local design tensile strength (Fig. A7).

For three oval cutouts, once the value of the area reduction coefficient ***f*** was set in part III, the value of the ***HAR*** parameter should be now properly selected to define the length of the oval shaped cutout following the first strength design criteria. The desire RXS fuse ***HAR***, based on the first design approach, is selected close

enough, but also above the buckling limit state threshold, that is a ratio of nominal local to global buckling capacity equal to 1. Based on spreadsheet calculations presented in this section (Fig. A7), the ratio of nominal local to global buckling capacity vs. ***HAR*** curve for different HSS sizes can be seen in Fig. A5. For a given global brace length, as the ***HAR*** increases, the local buckling capacity decreases and the buckling capacity ratio decreases

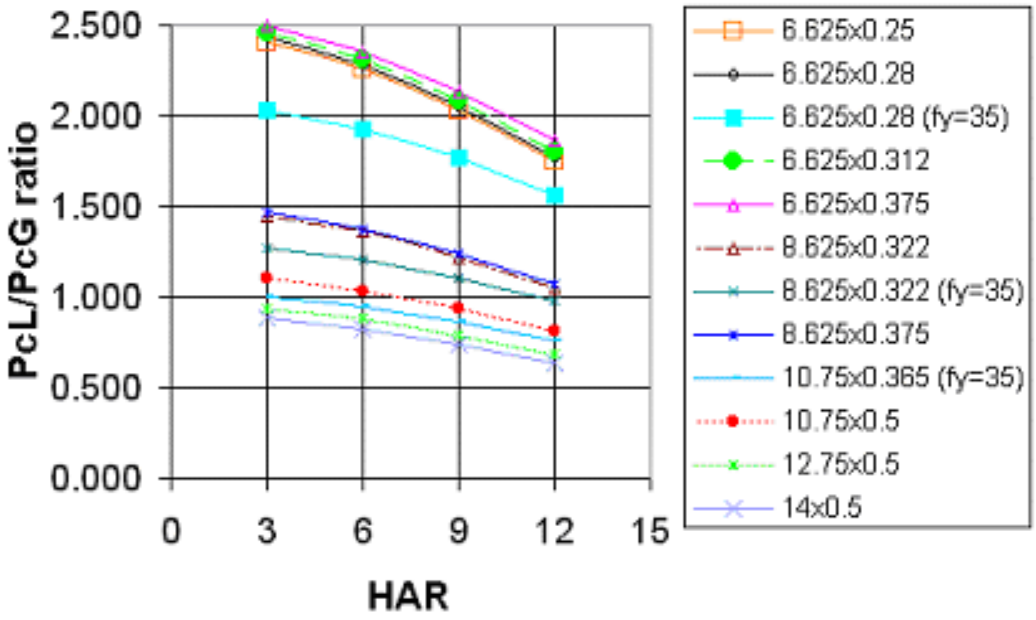

Fig. A5 - Hole Aspect Ratios vs. Buckling Capacity Ratios.

The relationship between ***HAR*** and buckling capacity ratio for an HSS 6.625X0.25 can be seen in Fig. A6. ***HAR*** values with ratios of nominal local to global buckling capacity below the split threshold are to be discarded so that the design complies with the first strength approach, and for this case, any ***HAR*** value smaller

than 3 will be adequate. Thus a ***HAR*** of 3 is selected for this fuse example design calculation.

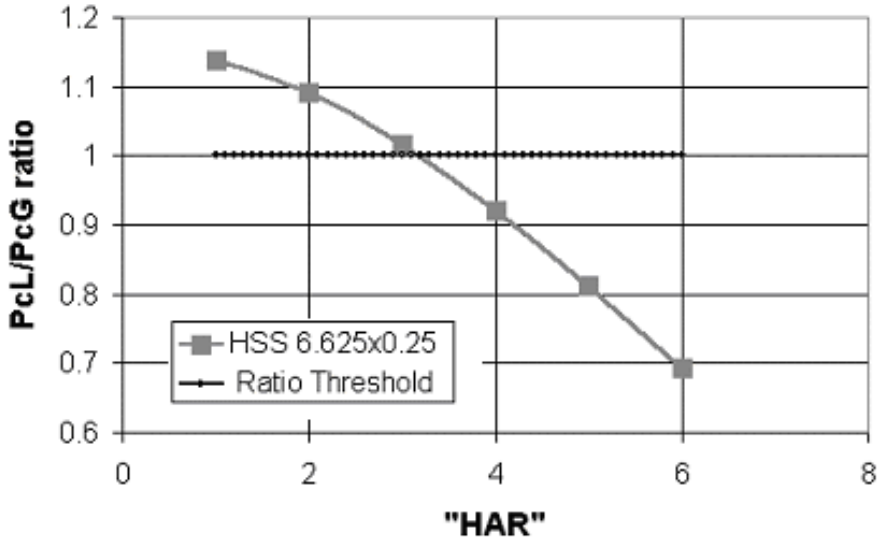

Fig. A6 - Hole Aspect Ratio vs. Buckling Capacity Ratio HSS 6.625X0.25.

To comply with the second compression strength design method (Chapter 4), a larger ***HAR*** shall be selected so that the buckling capacity ratio remains close but under the buckling limit state threshold (Fig. A6), therefore to comply with the second compression design method, a ***HAR*** of 4 or greater than 4 will be adequate.

As shown in Fig. A7 the hole diameter is calculated by dividing the circumference removed of 10.04 inches due to the area reduction coefficient of 51.13 percent by the number of oval cutouts, which was set at 3 cutouts. The cutout length, which governs the buckling capacity of the fuse, is then the result of multiplying the

HAR of 3 by the hole diameter equal to 3.42 inches, this results in a cutout length of 10.27 inches, which for fabrication purposes was rounded down to a 10 inches long cutout length. For a 10 inches long cutout and the three arms cross sectional area equals to 2.29 in2, the design capacity of the fuse is 71.3 kips which is less than the 69.6 kips global buckling capacity and therefore complies with the first compression design method requirements. The fuse tensile capacity is the second output of Part IV and it resulted to be 88.5 kips because local tensile capacity based on yielding of the reduced section controls over local tensile capacity based on fracture of the reduced section as shown at the end of Part IV, Fig. A7.

Part IV

LOCAL CAPACITY				*Local capacities are based on "f provided"*						
single arc length (in)	Mid circumference removed (in)	Hole diameter (in)	Net area "An" (in^2)	single arc gross area (in^2)	Arc Half angle alpha "rad" (radians)	Arc Moment of Inertia Minor axis (in^4)	Arc Moment of inertia Major axis (in^4)	Arc Radius of gyration minor axis "rminor" (in)	Arc Radius of gyration major axis "major" (in)	Hole Aspect ratio "HAR"
3.271	10.27	3.42	2.29	0.762372	0.5118	0.01460	7.61646	0.1383965	3.16077	**3**
Hole length	Hole length provided	K factor Local	K"L/r Local	Lambda Local	Critical Buckling Stress Local "Fcr" (ksi)	Local design compressive strength (Kips)	Local design compressive strength *"check"*	Local tensile capacity based on yielding (reduced section) "Lty"	Local tensile capacity based on fracture (reduced section) "Ltf"	governing design Local tensile capacity (Kips)
10.267	10	**0.65**	46.97	0.568937	36.68	***71.36***	***OK***	86.45	99.49	***86.5***

red font indicates user input from list of sections (input) worksheet

blue italic font indicates user output

Fig. A7 - Design Calculation Worksheet Part IV: Local Capacities.

Single Arc Length (in.) = $(1-f)\frac{Mid\_circumference}{n} = (1-0.5113)\frac{20.08in}{3} =$

Single Arc Length (in.) = 3.271

Mid Circumference Removed (in.) = $Mid\_circumference \cdot f = 20.08in \cdot 0.5113 =$

Mid Circumference Removed (in.) = 10.27 in

Hole Diameter (in.) = $\frac{Mid\_circumference\_removed}{n} = \frac{10.27in}{3} = 3.42$ in

Net Area "A_n" $(in^2) = Ag(1-f) = 4.68in^2(1-0.5113) = 2.29$ in^2

Single Arc Gross Area $(in^2) = \frac{An}{n} = \frac{2.29in^2}{3} = 0.76237$ in^2

Say: arc length = alpha*r

r = arc radius

alpha = arc angle

Mid_circumference = 2 * 3.1416 * r

then,

Arc Half Angle Alpha "rad" (radians) =

$= \frac{arc\_length}{Mid\_circumference} \cdot \pi = \frac{3.271in}{20.08in} \cdot 3.142 = 0.5118$ rad

Arc Moment of Inertia Minor Axis $(in^4) =$

$= ro^3 \cdot t \cdot \left(\left(\frac{1-3\cdot t}{(2\cdot ro)} + \frac{t^2}{(ro^2)} - \frac{t^3}{(4\cdot ro^3)}\right)\cdot \right.$ .....

$$\ldots\ldots \cdot \left(rad + SIN(rad) \cdot COS(rad) - 2\left(SIN(rad)\right) \cdot \frac{SIN(rad)}{rad} + t^2 \cdot SIN(rad) \right) \cdot \ldots\ldots$$

$$\ldots\ldots \cdot \frac{SIN(rad)}{\left(3 \cdot ro^2 \cdot rad \cdot \left(2 - \frac{t}{ro} \right) \right)} \cdot \left(\frac{1 - \frac{t}{ro} + t^2}{\left(6 \cdot r^2\right)} \right) = 0.01460 \text{ in}^4$$

where:

r_o=outside radius

t = wall thickness

rad = arc half angle alpha radius

Arc Moment of Inertia Major Axis $\left(in^4\right)$ =

$$= \; ro^3 \cdot t \cdot \left(\frac{1 - 3 \cdot t}{(2 \cdot ro)} + \frac{t^2}{ro^2} - \frac{t^3}{\left(4 \cdot ro^3\right)} \right) = 7.61646 \text{ in}^4$$

Radius of Gyration Minor Axis “minor” (in) =

$$= \sqrt{\frac{I\_arc\_\min or}{Ag\_arc}} = \sqrt{\frac{0.01460}{0.76237}} = 0.138396476 \text{ in}$$

Radius of Gyration Major Axis (in) = $\sqrt{\frac{I\_arc\_major}{Ag\_arc}} = \sqrt{\frac{7.61646}{0.76237}} =$

= 3.16077067 in

Hole Aspect Ratio (HAR) = 3 (User Input)

Hole Length = $HAR \cdot Hole\_diameter = 3 \cdot 3.42in = 10.2674461$ in

Hole Length Provided = 10

K Factor Local = 0.65 (Ideal fixed and conditioned)

As mentioned before the updated version of the AISC Manual of Steel Construction, published in spring 2006, increased the resistance factor for compression members from 0.85 to 0.9. By using the updated resistance factor both the global buckling and local buckling capacities increased but by the same approximately 5%, and therefore the difference between the two buckling capacities does not vary and does not affect the RXS fuse design procedure presented whether the first or second design philosophy is used.

A.2.2.5 Part V: Ratios

The purpose of Part V, Fig. A8, is to summarize some significant outputs from the RXS fuse design calculations, such as: minimum required area reduction coefficient, provided area reduction coefficient, the upper bound of the area reduction coefficient, and some ratios between global and local capacities at the end of Part V.

If the provided area reduction coefficient is between the lower and the upper limits, Part V provides a message confirming that the design complies with the first design philosophy. On the other hand, if the provided area reduction coefficient is greater than the upper limit, the message indicates that the design follows the second

design philosophy. The ratio of local buckling to global buckling capacity also shows whether the system was designed based on the first design philosophy or the second design philosophy. If this ratio is greater than 1 then a message is provided confirming that the first design philosophy was implemented; otherwise if it is less than 1 the message confirms that the second design philosophy was used.

Because large discrepancies between the brace tensile and compressive strengths impose significance disadvantages on the use of concentrically braced frame systems for low-rise buildings in particular [Rezai, Prion, and Timler 1999], Part V also includes two ratios between the governing tensile and compressive capacities of the system. First the ratio of local tensile to global buckling capacity is shown. If the brace member with the RXS is proportioned for its global buckling capacity this ratio will be greater than 1. For a brace member with the RXS proportioned for its local buckling capacity this ratio could become less than one in theory but it seems very unpractical to have such a short brace with a global buckling capacity higher than the fuse tensile capacity. The second ratio between governing tensile and compressive capacities is the local tensile to local buckling capacity. This ratio is either one or greater than one because the local compressive capacity is similar to the local tension capacity but always smaller even for the case of maximum local buckling capacity using circular cutouts instead of oval cutouts.

The resistance factor for compression members was recently increased by the updated version of the AISC Manual of Steel Construction. This increment in the compression resistance factor increases both local and global buckling capacities and

consequently the ratios between the governing tensile and compressive capacities of the system get closer to one, which is rather favorable to the system since the discrepancy between governing tension and compression capacities becomes smaller.

Finally the ratio of nominal global tensile to local tensile capacity, which is proportional to the cross sectional area reduced, is shown. This ratio will always be greater than 1 since reducing the cross sectional area at the fuse makes the fuse tensile capacity smaller than the brace tension capacity and basically shows for this particular design that the nominal tensile capacity is approximately twice the nominal local tensile capacity due to the 51.13 percent area reduction.

Part V											
To ensure that local tensile yields before connection overstress, the end section of the HSS must be reduced at least											*36.3%*
of its gross area.											
First design philosophy maximum area reduction coefficient =						*60.7%*					
Provided area reduction coefficien		*51.13%*		*OK*							
36.3%	<	51.13%	<	60.7%	∴	**Design complies with first design philosophy**					
					=	1.02	> 1	∴	**First design philosophy**		
Local tension capacity/Global compression capacity =						1.24	∴	PtL is	24%	larger than	of PcG
Local tension capacity/Local compression capacity =						1.21	∴	PtL is	21%	larger than	of PcL
Global tension capacity/Local tension capacity =						2.05	∴	PtG is	105%	larger than	of PtL
red font indicates user input from list of sections (input) worksheet											
blue italic font indicates user output											

Fig. A8 - Design Calculation Worksheet Part V: Ratios.

APPENDIX B – RXS Tests

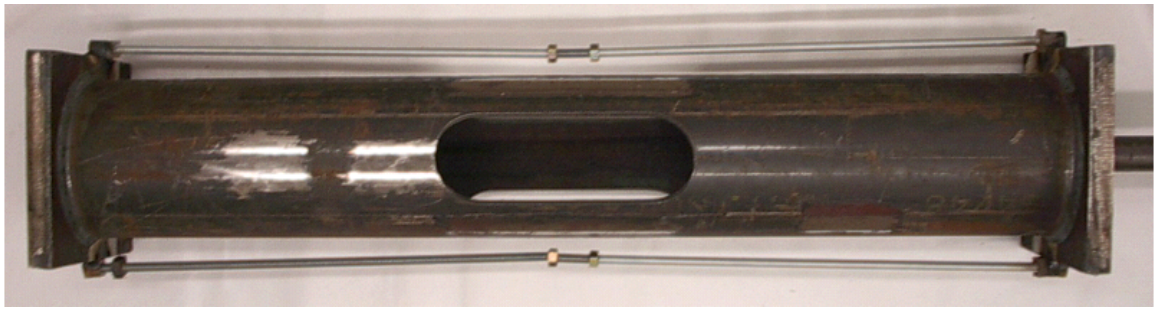

Fig. B1 -Typical Test specimen.

Fig. B.1 shows the monotonic test specimen fabricated by Butler Heavy Structures. Threaded bars were welded at end plated at The University of Kansas facilities to properly place the extensometers.

Fig. B2 - Test Specimen Reduced Area.

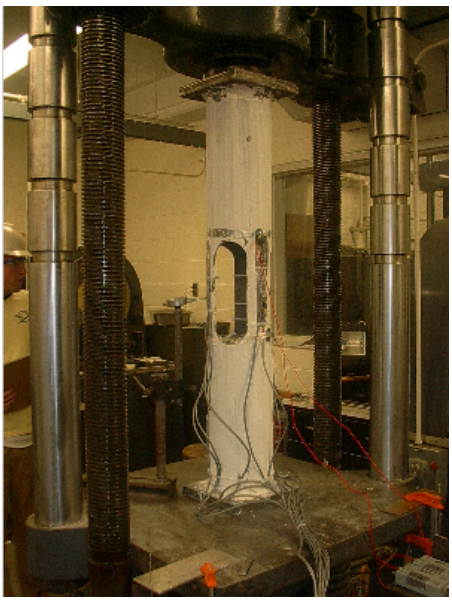

Fig. B3 - Monotonic Compression, Test Set Up.

Fig. B3 shows the monotonic compression test specimen as it was set up on the Baldwin Universal Testing Machine before starting the compression test. Bondable strain gages were adhered to the outer surface of the test specimen along the three arms and at specific areas along the non-reduced section of the specimen. Two LVDTs were located between the machine loading table and a support fixed to the ground to measure linear displacement. Dial gages were placed perpendicular to the longitudinal axis of the arms to measure the RXS lateral buckling deflection.

Fig. B4 - Monotonic Compression, Test Specimen after Failure.

During monotonic compression test major buckling deformations were observed after the critical buckling load was reached. As the arms at the RXS buckled, the lateral deflection along the longitudinal axis increased towards the outside direction of test specimen as shown in Fig. B5.

Fig. B5 - Monotonic Compression, RXS After Buckling Failure.

Fig. B6 - Monotonic Tension, Test Set Up.

Fig. B6 shows the monotonic tension test specimen as it was set up on the Baldwin Universal Testing Machine before starting the tension test. Like the monotonic compression test bondable strain gages were adhered to the outer surface of the test specimen along the three arms and at specific areas along the non-reduced section of the specimen. But unlike the monotonic compression test, an extensometer was used instead of LVDTs to measure linear displacement.

Fig. B7 - Monotonic Tension, Test Specimen after Fracture Failure.

Even though some yield deformation was detected by the instrumentation used to measure linear displacement during the monotonic tension test, no major deformation was visually detected during the entire test until fracture failure occurred.

Fig. B8 - Monotonic Tension, RXS after Fracture Failure.

Fracture failure occurred at arm #3, exactly at the location of strain gage 11.

Fig. B9 - Monotonic Tension, Fracture Failure Close View from Outside.

Fracture failure occurred where the semicircular cut transitions to the straight longitudinal cut, as shown in Fig. B9.

Fig. B10 - Monotonic Tension, Fracture Failure Close View from Inside.

The edge fracture would have been bigger, increasing until the arm had been broken in two pieces, if the loading machine had continued loading.

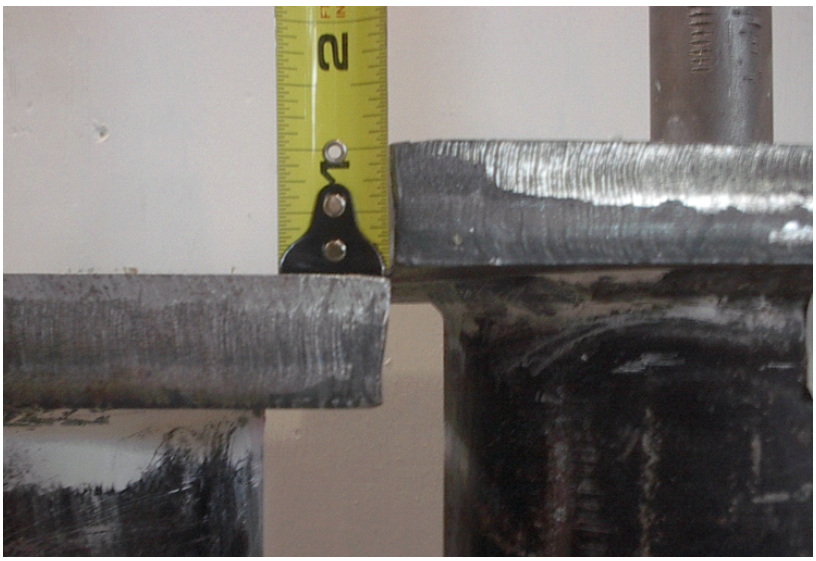

Fig. B11 - Relative Axial Displacement between Specimens.

Post-test hand measurements, as well as axial displacement calculated from stress-strain curves obtained from monotonic tension and compression tests, showed that under tensile loads the tension monotonic test specimen elongated a maximum of 5/8 in. before it failed by fracture, and the compression monotonic test specimen shortened 3/8 in. under compression loads. As shown in Fig. B11, as expected, the

relative axial displacement between the two specimens tested was measured and resulted to be 1 inch.

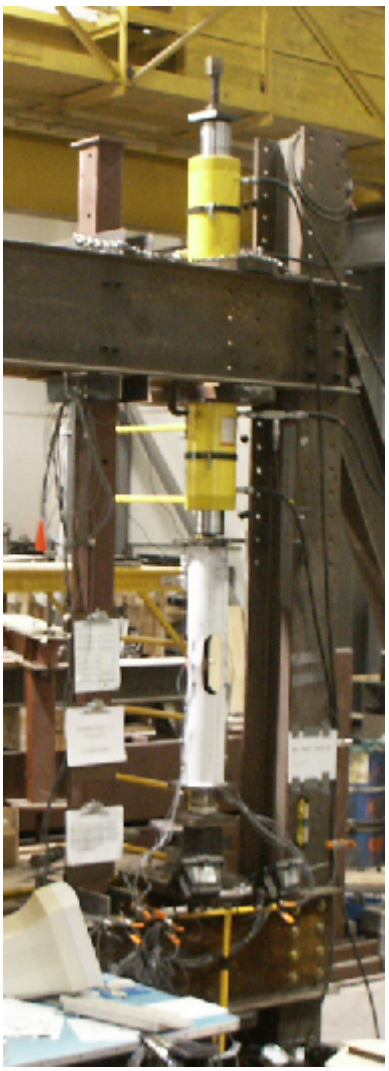

Fig. B12 - Cyclic load, Test Set Up.

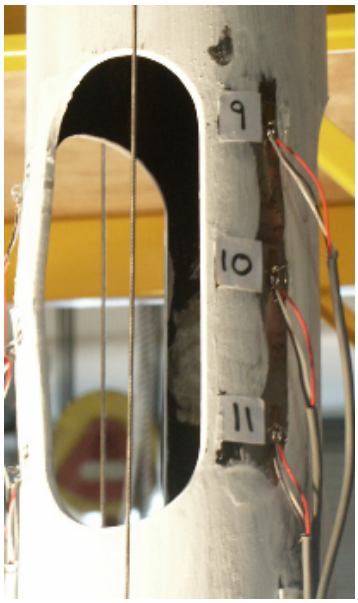

Fig. B13 - Cyclic loading, Initial Buckling Deformation.

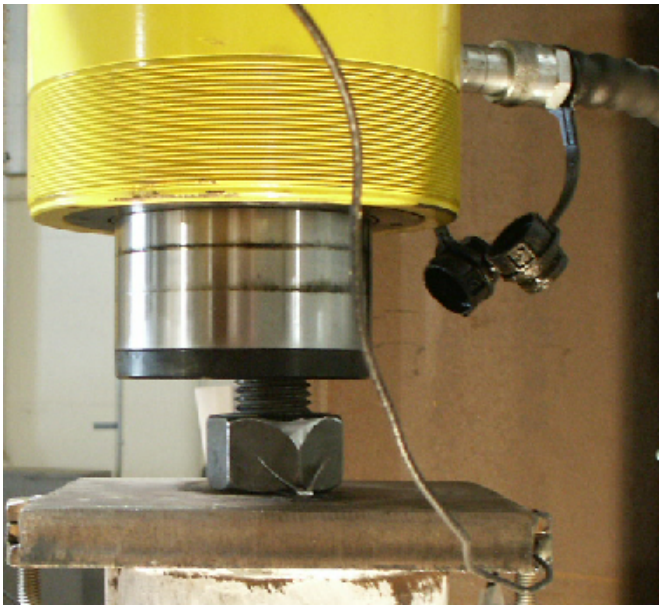

Fig. B14 -Cyclic loading, Initial Eccentricity on Axial Load.

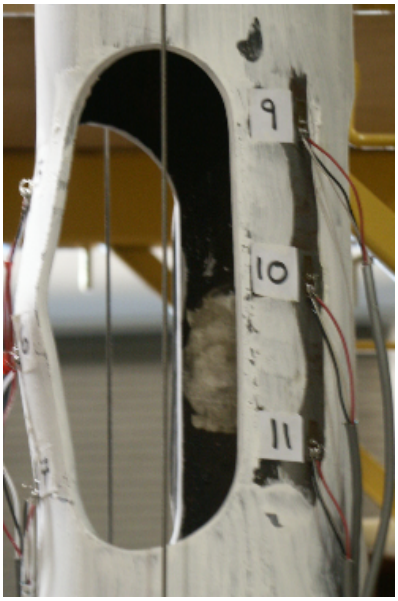

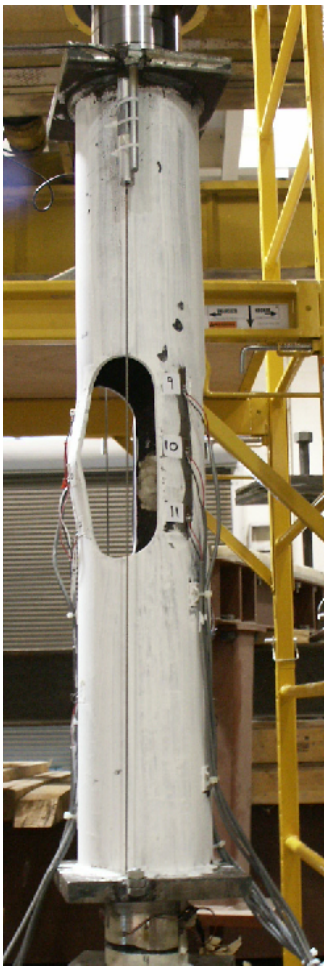

Fig. B15 - Cyclic loading, Buckling Deformation at Last Cycle of Load Step #4.

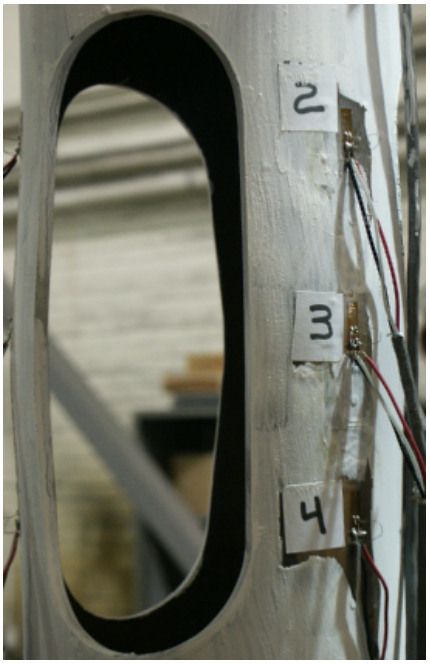

Early signs of
buckling deformations
at other two arms
during load step #6

Arm that initially buckled
at load step #6

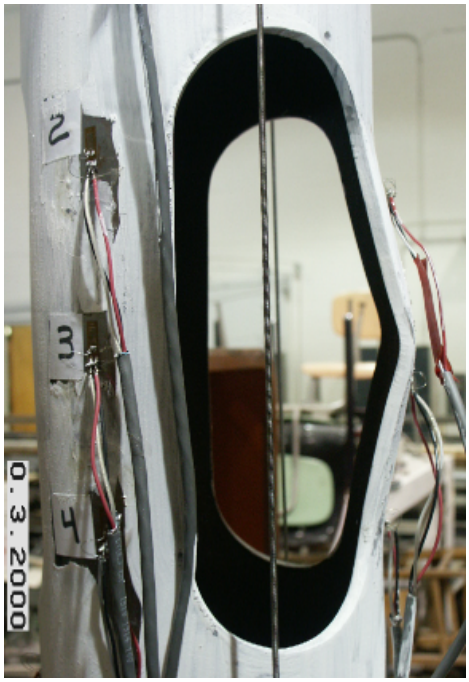

Fig. B16 - Cyclic Loading, Load Step # 6.

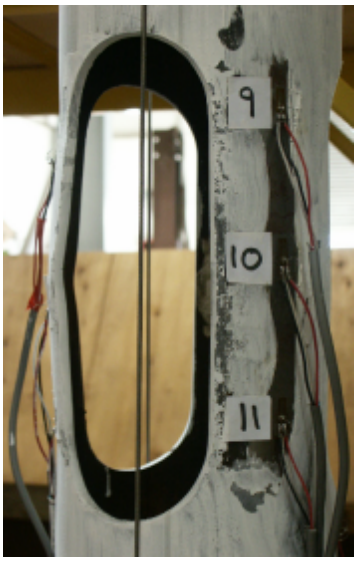

Peak deformation
under tension loads
last cycle
load step #8

Peak deformation
under compression loads
last cycle
load step #8

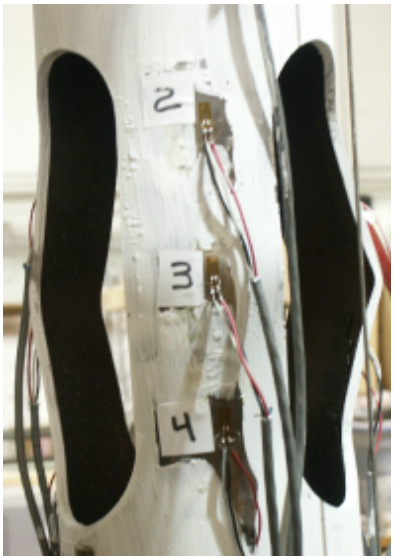

Fig. B17 - Cyclic Loading, Load Step # 8.

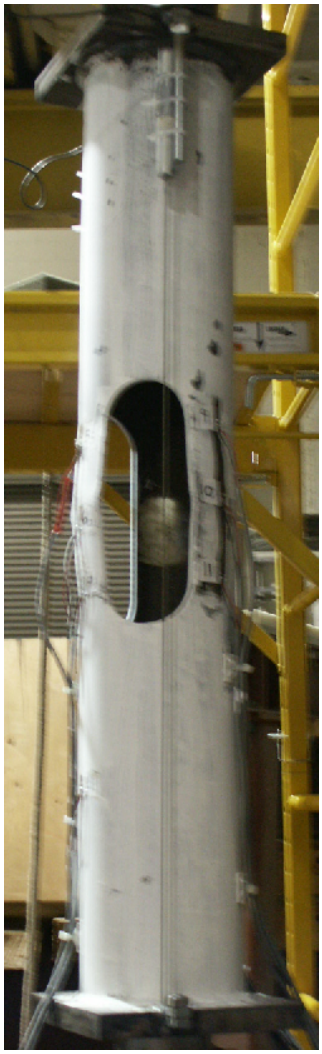

Peak deformation

under tension

last cycle

load step #9

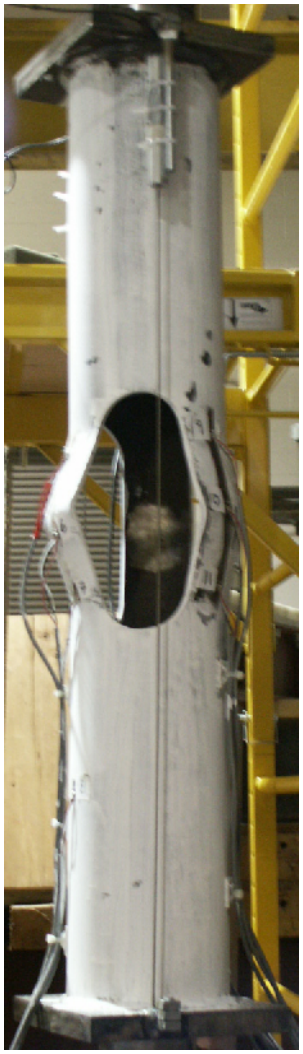

Peak deformation

under compression

last cycle

load step #9

Fig. B18 - Cyclic Loading, Load step # 9.

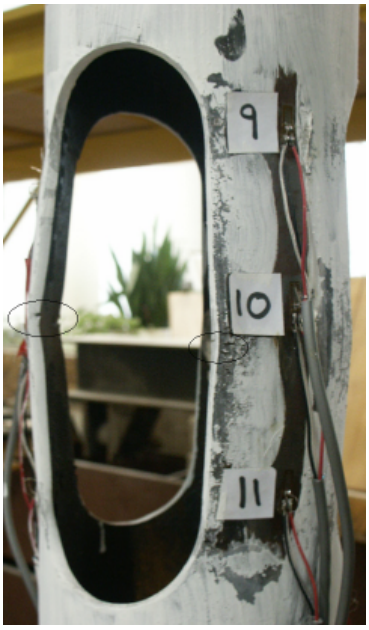

Failure occurred
at first cycle of
load step #12
fifty-first cycle overall

Steel was severely
deteriorated by the
beginning of
load step #12

Fig. B19 - Cyclic Loading, Load Step # 12, Fatigue Failure.

APPENDIX C – BCE Bar Configuration, FEM's

Bar Configuration Type	r (in.)	d (in.)	stress concentration tension (ksi)	stress concentration compression (ksi)	longitudinal elongation (inches)
1	0.15	0.25	60.65	65.63	0.01358
2	0.25	0.25	57.51	58.26	0.01343
3	0.25	0.50	57.70	57.57	0.01287
4	1	0.25	52.74	52.75	0.01284
5	3	0	50.92	50.92	0.01272
6	3	0.25	50.86	50.84	0.01213
7	3	0.50	50.76	50.73	0.01150
8	5	0.25	50.50	50.59	0.01167

d = depth of the shoulder

r = radius of the circular section where the 1 in. diameter shoulder transitions to the 0.5 in. diameter yield zone.

Table C1 - Summary of Results, Bar Configuration.

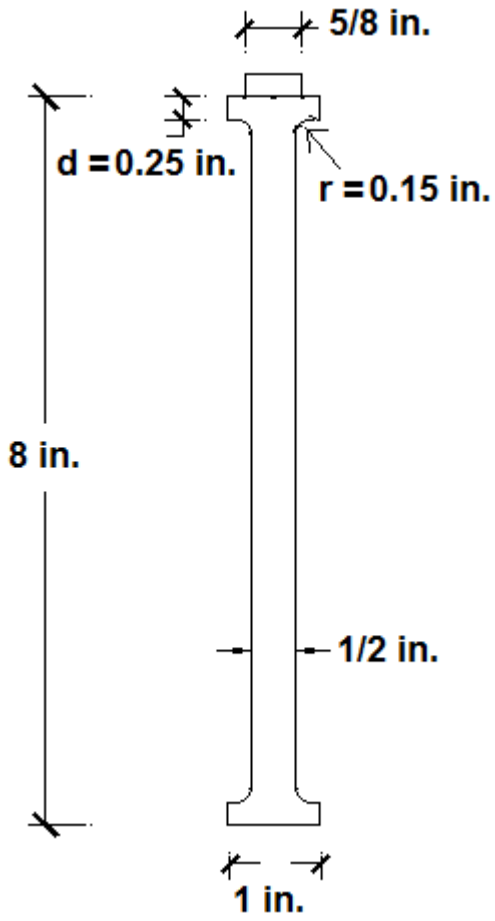

d $_{\text{(shoulder depth)}}$ = 0.15 in.

r $_{\text{(circular transition radius)}}$ = 0.25 in.

Fig. C1 - Bar Configuration Type #1, Geometry.

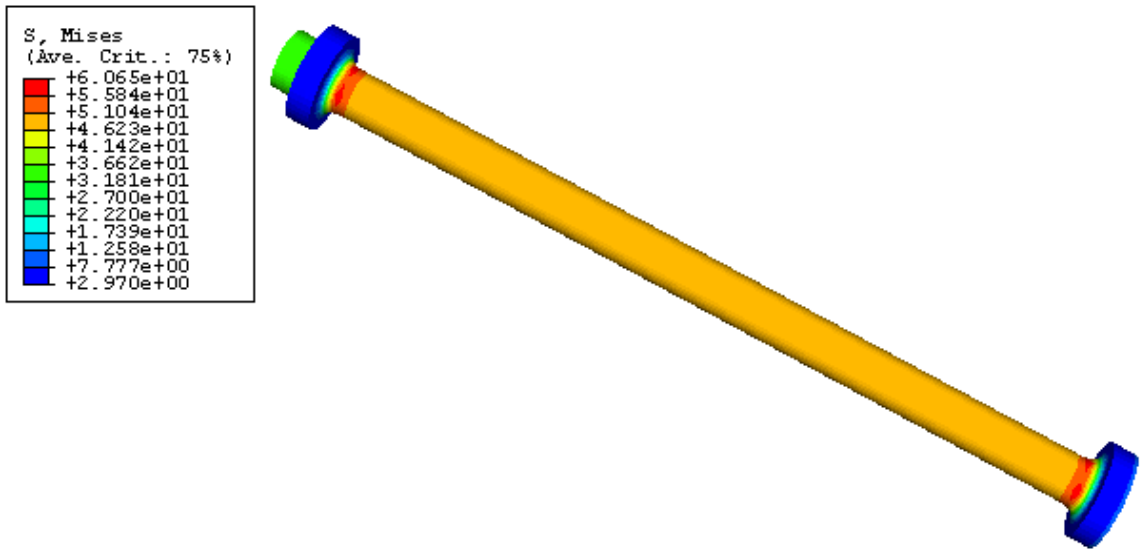

$d_{\text{(shoulder depth)}} = 0.15$ in.

$r_{\text{(circular transition radius)}} = 0.25$ in.

Fig. C2 - Bar Configuration Type 1, Von Mises Stress, Tension Load.

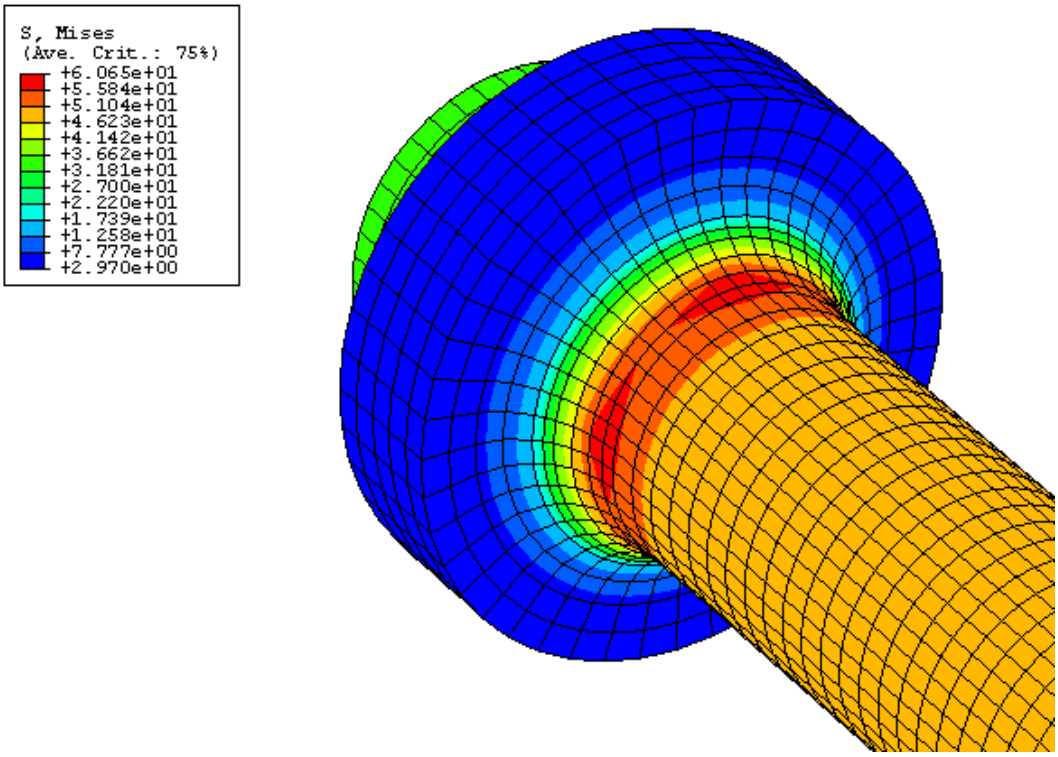

$d_{\text{(shoulder depth)}} = 0.15$ in.

$r_{\text{(circular transition radius)}} = 0.25$ in.

Fig. C3 - Bar Configuration Type 1, Von Mises Stress, Tension Load, Zoom.

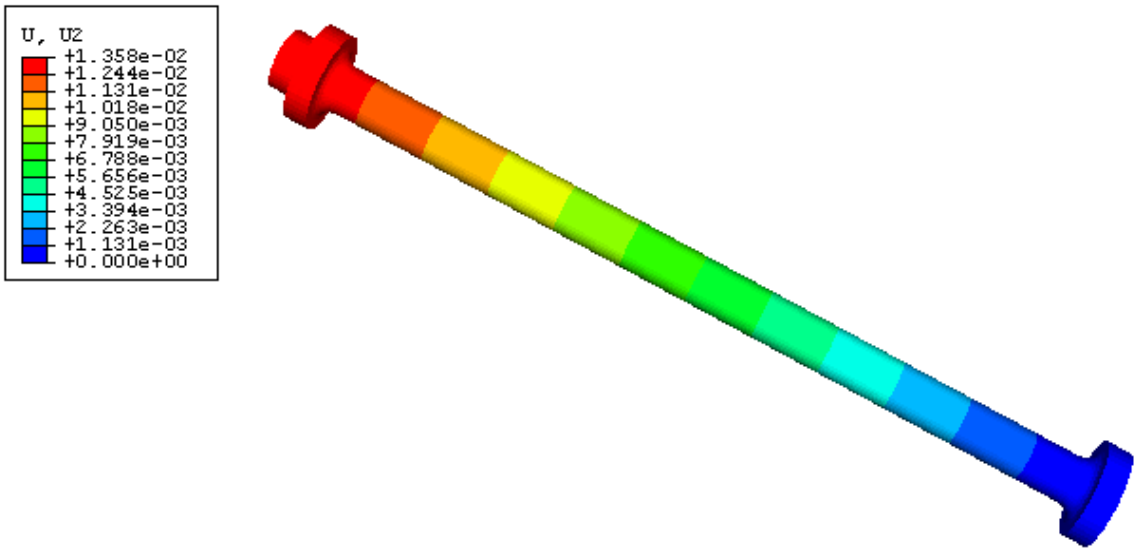

$d_{\text{(shoulder depth)}} = 0.15$ in.

$r_{\text{(circular transition radius)}} = 0.25$ in.

Fig. C4 - Bar Configuration Type 1, Displacement, Tension Load.

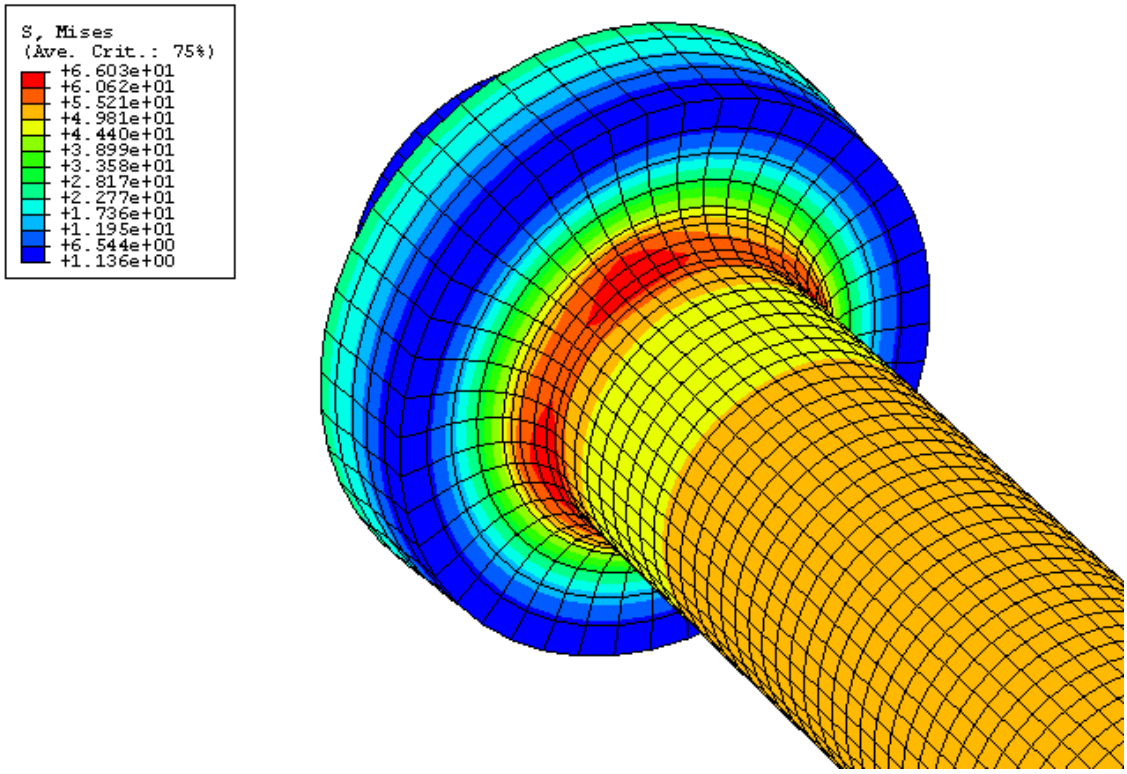

$d_{\text{(shoulder depth)}} = 0.15$ in.

$r_{\text{(circular transition radius)}} = 0.25$ in.

Fig. C5 - Bar Configuration Type 1, Von Mises Stress, Compression Load, Zoom.

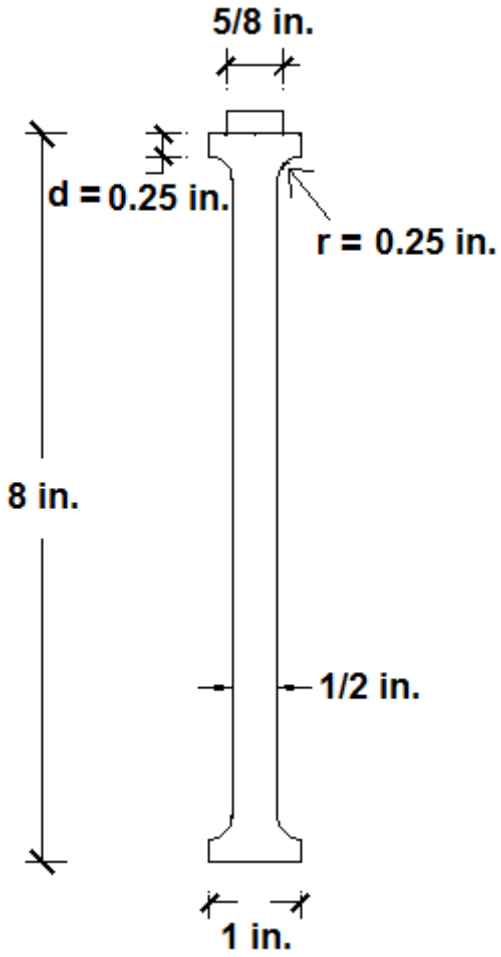

$d_{(\text{shoulder depth})} = 0.25$ in.

$r_{(\text{circular transition radius})} = 0.25$ in.

Fig. C6 - Bar Configuration Type #2, Geometry.

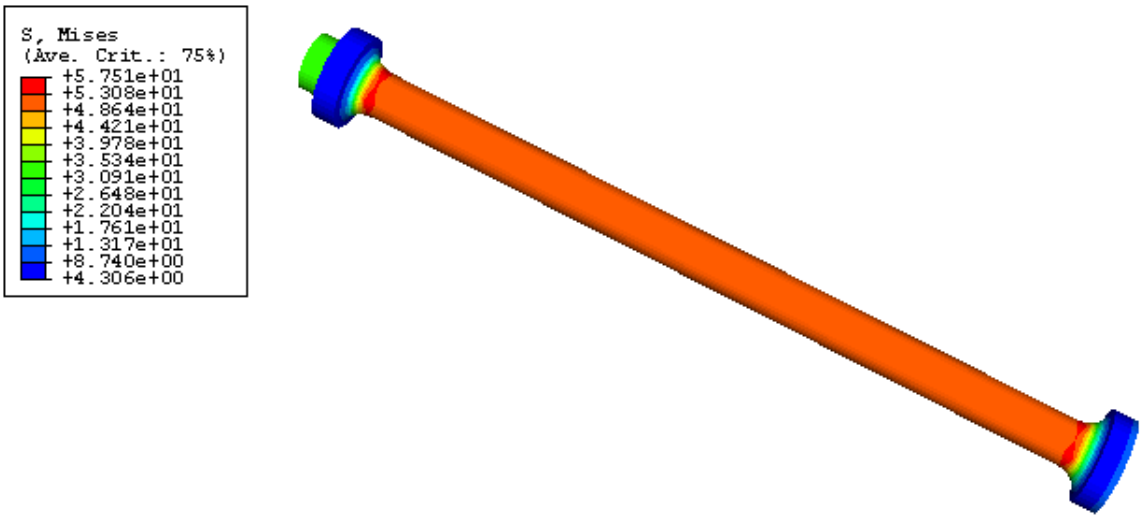

$d_{\text{(shoulder depth)}} = 0.25$ in.

$r_{\text{(circular transition radius)}} = 0.25$ in.

Fig. C7 - Bar Configuration Type 2, Von Mises Stress, Tension Load.

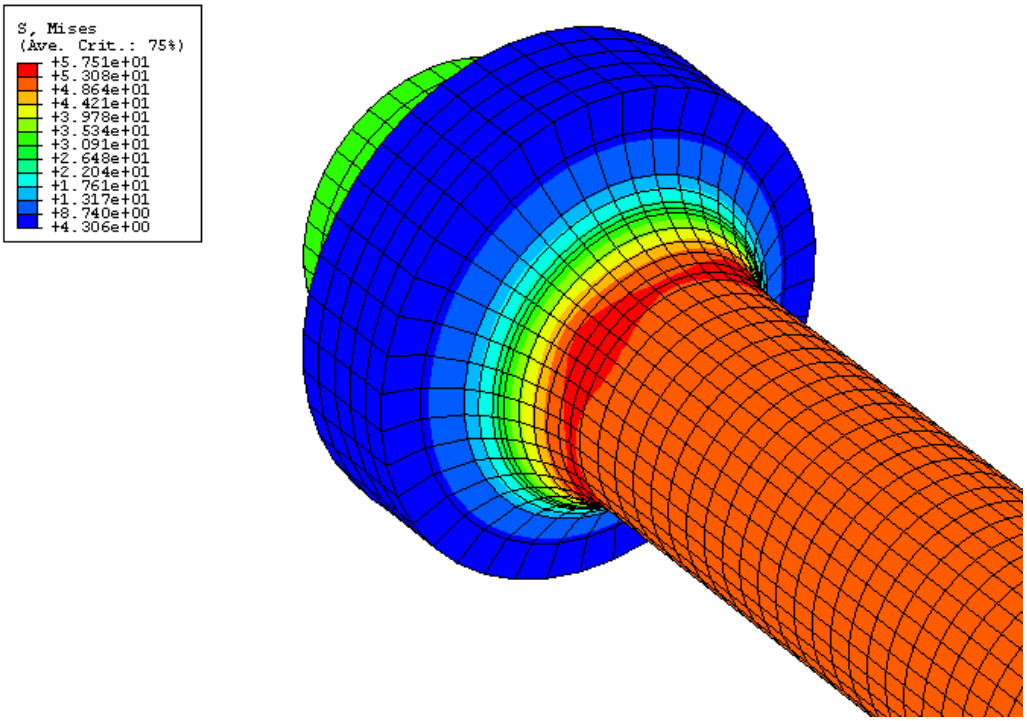

$d_{\text{(shoulder depth)}} = 0.25$ in.

$r_{\text{(circular transition radius)}} = 0.25$ in.

Fig. C8 - Bar Configuration Type 2, Von Mises Stress, Tension Load, Zoom.

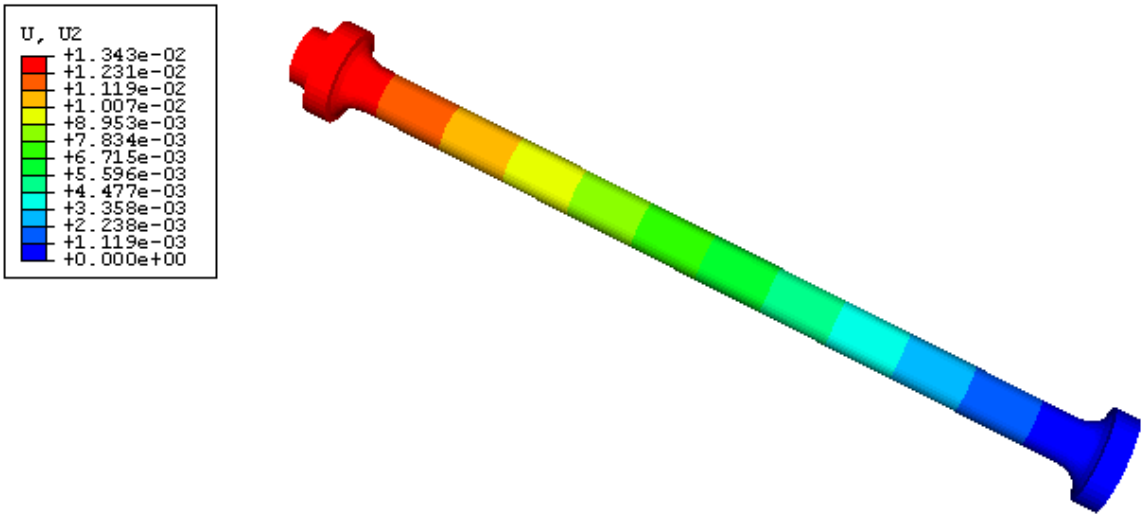

$d_{\text{(shoulder depth)}} = 0.25$ in.

$r_{\text{(circular transition radius)}} = 0.25$ in.

Fig. C9 - Bar Configuration Type 2, Displacement, Tension Load.

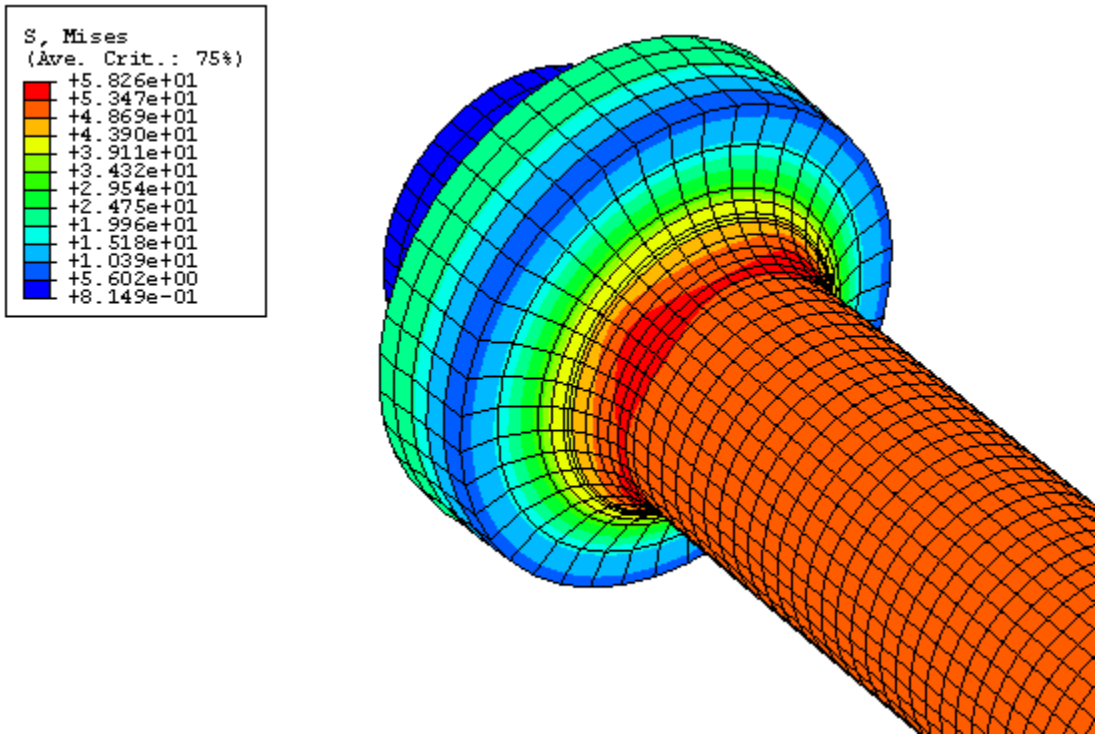

$d_{\text{(shoulder depth)}} = 0.25$ in.

$r_{\text{(circular transition radius)}} = 0.25$ in.

Fig. C10 - Bar Configuration Type 2, Von Mises Stress, Compression Load, Zoom.

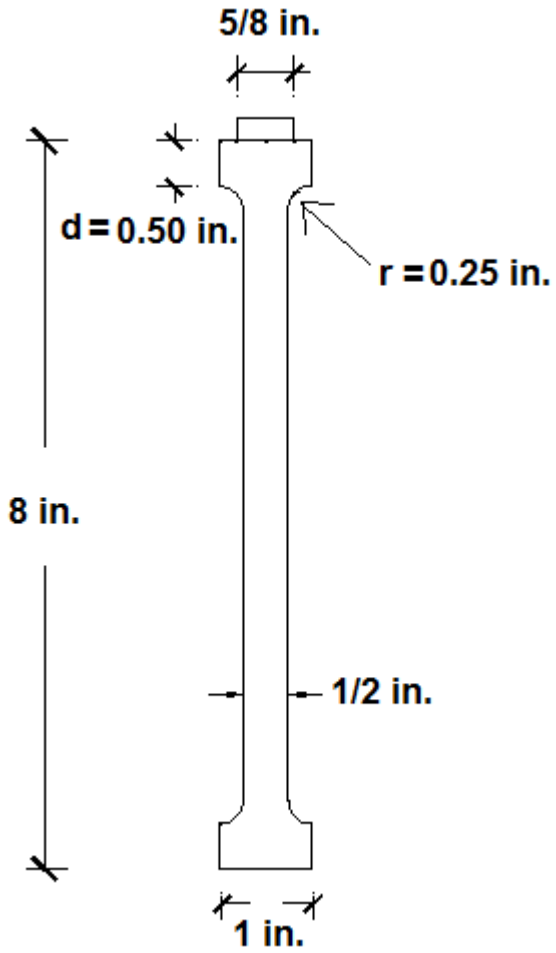

d $_{\text{(shoulder depth)}}$ = 0.50 in.

r $_{\text{(circular transition radius)}}$ = 0.25 in.

Fig. C11 - Bar Configuration Type #3, Geometry.

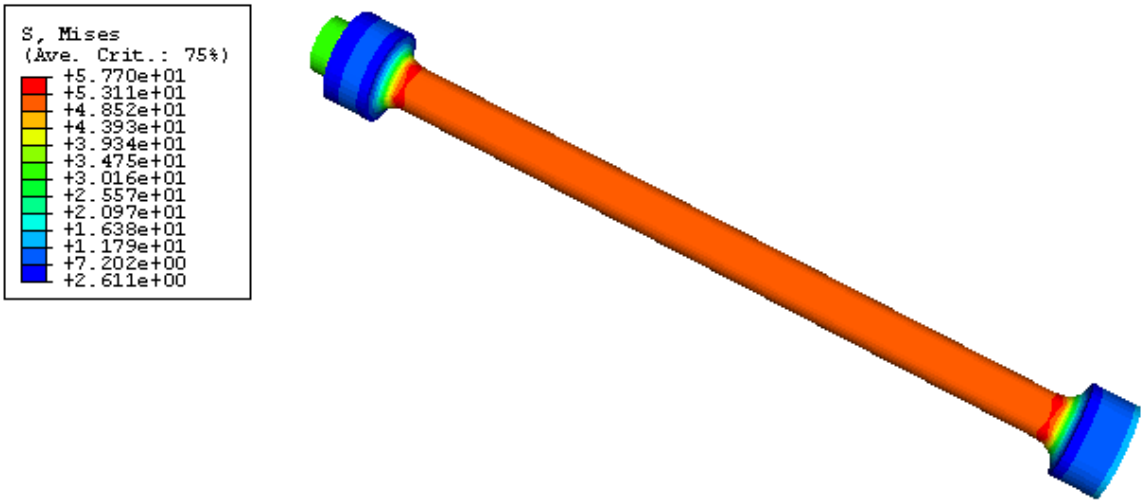

$d_{\text{(shoulder depth)}} = 0.50$ in.

$r_{\text{(circular transition radius)}} = 0.25$ in.

Fig. C12 - Bar Configuration Type 3, Von Mises Stress, Tension Load.

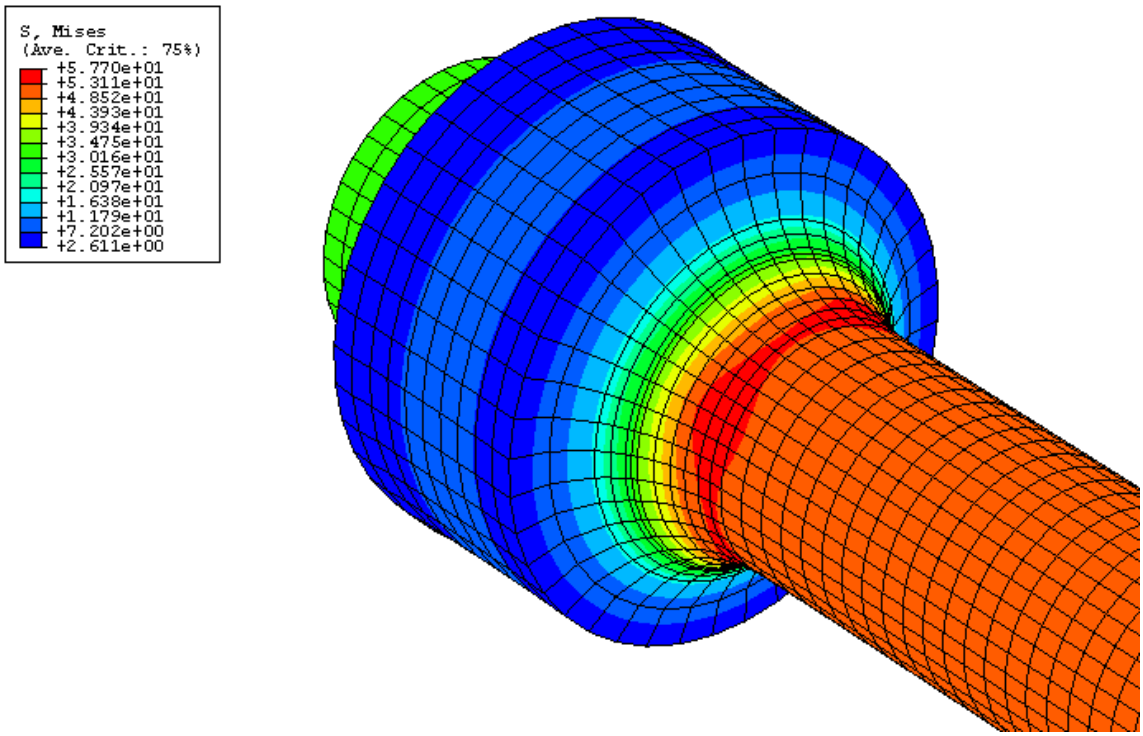

$d_{\text{(shoulder depth)}} = 0.50$ in.

$r_{\text{(circular transition radius)}} = 0.25$ in.

Fig. C13 - Bar Configuration Type 3, Von Mises Stress, Tension Load, Zoom.

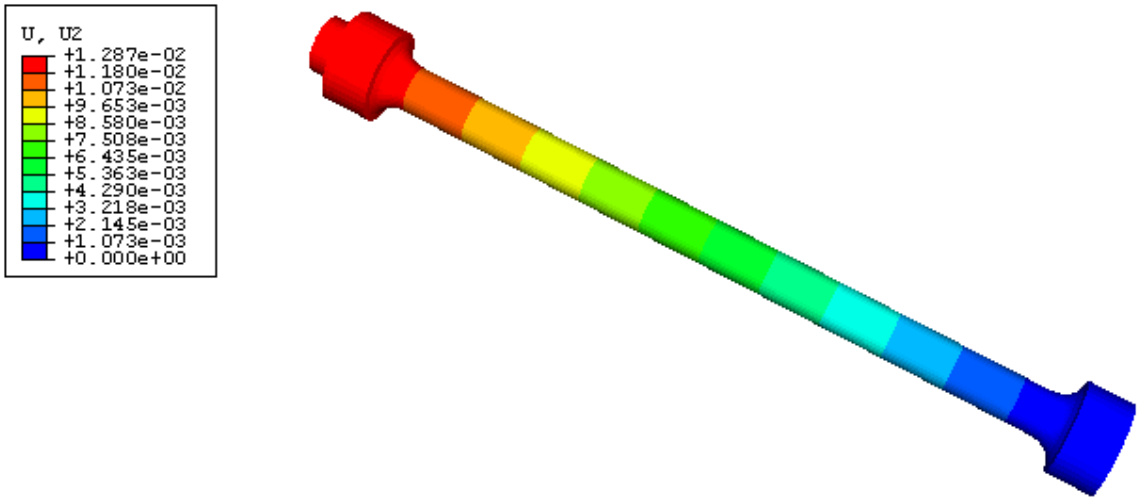

$d_{\text{(shoulder depth)}} = 0.50$ in.

$r_{\text{(circular transition radius)}} = 0.25$ in.

Fig. C14 - Bar Configuration Type 3, Displacement, Tension Load.

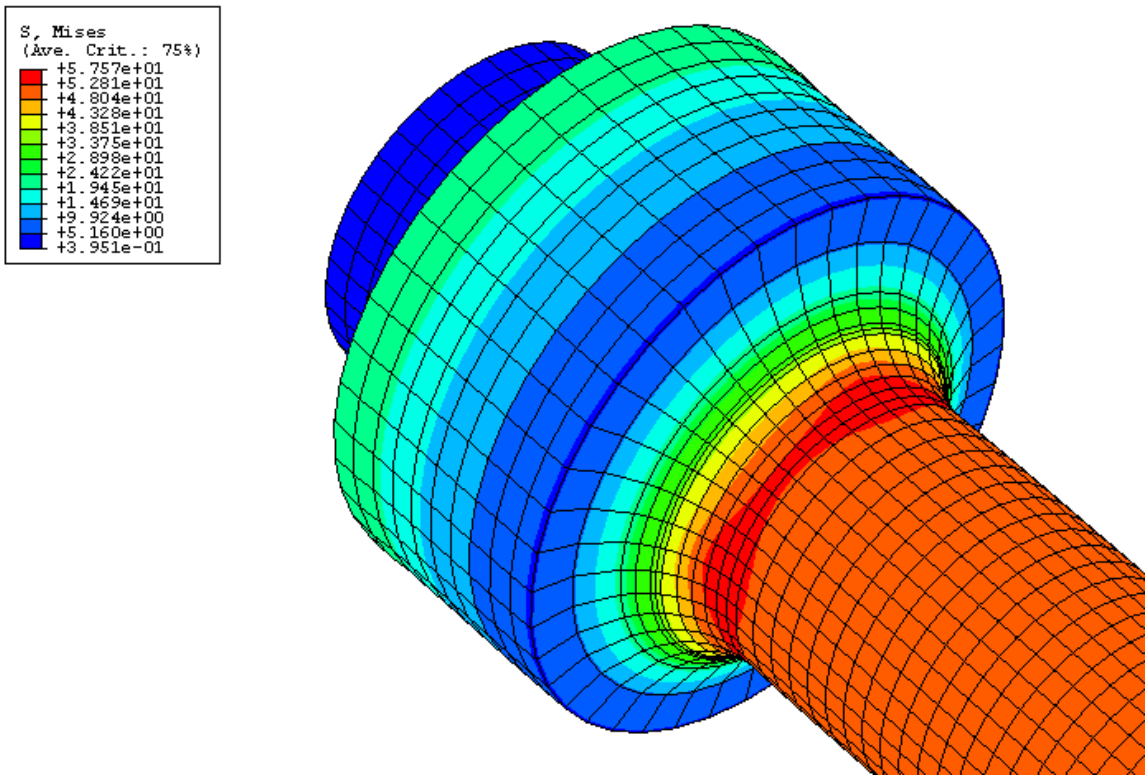

$d_{\text{(shoulder depth)}} = 0.50$ in.

$r_{\text{(circular transition radius)}} = 0.25$ in.

Fig. C15 - Bar Configuration Type 3, Von Mises Stress, Compression Load, Zoom.

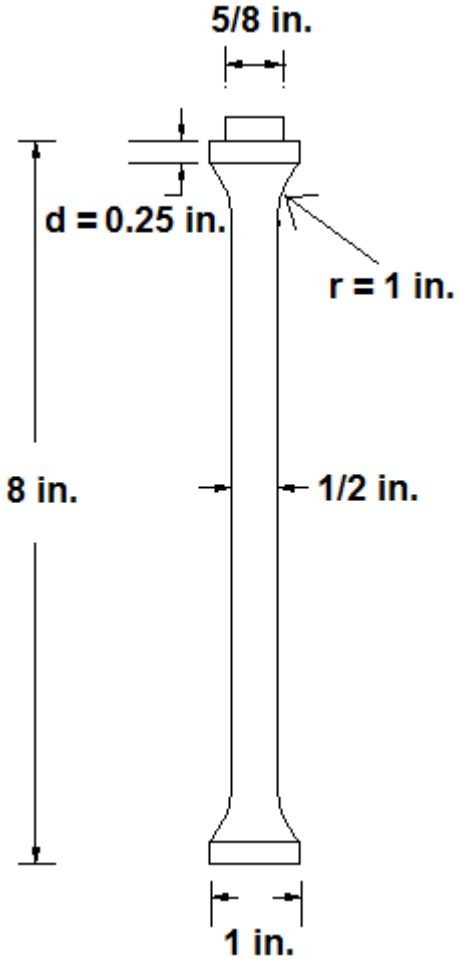

$d_{(\text{shoulder depth})} = 0.25$ in.

$r_{(\text{circular transition radius})} = 1$ in.

Fig. C16 - Bar Configuration Type #4, Geometry.

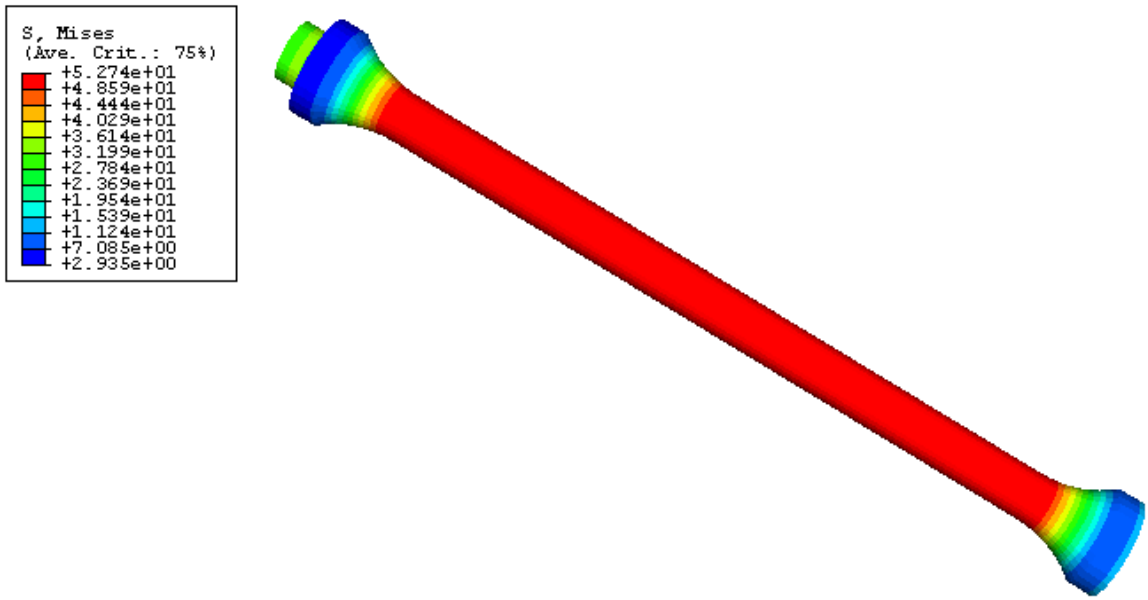

$d_{\text{(shoulder depth)}} = 0.25$ in.

$r_{\text{(circular transition radius)}} = 1$ in.

Fig. C17 - Bar Configuration Type 4, Von Mises Stress, Tension Load.

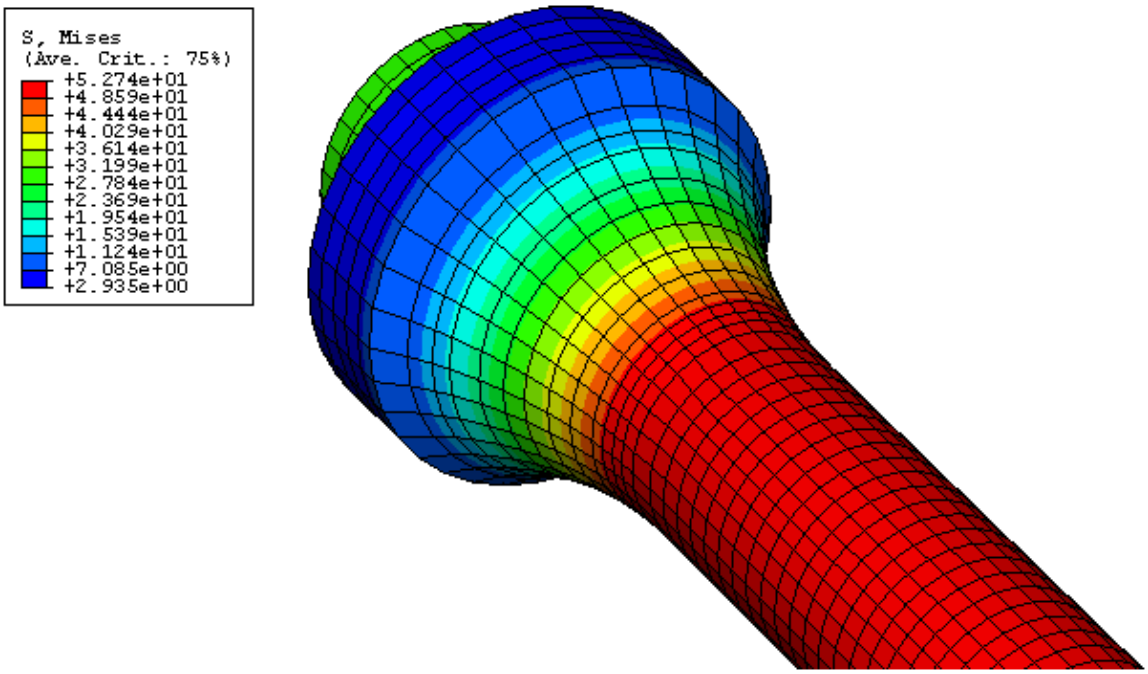

$d_{\text{(shoulder depth)}} = 0.25$ in.

$r_{\text{(circular transition radius)}} = 1$ in.

Fig. C18 - Bar Configuration Type 4, Von Mises Stress, Tension Load, Zoom.

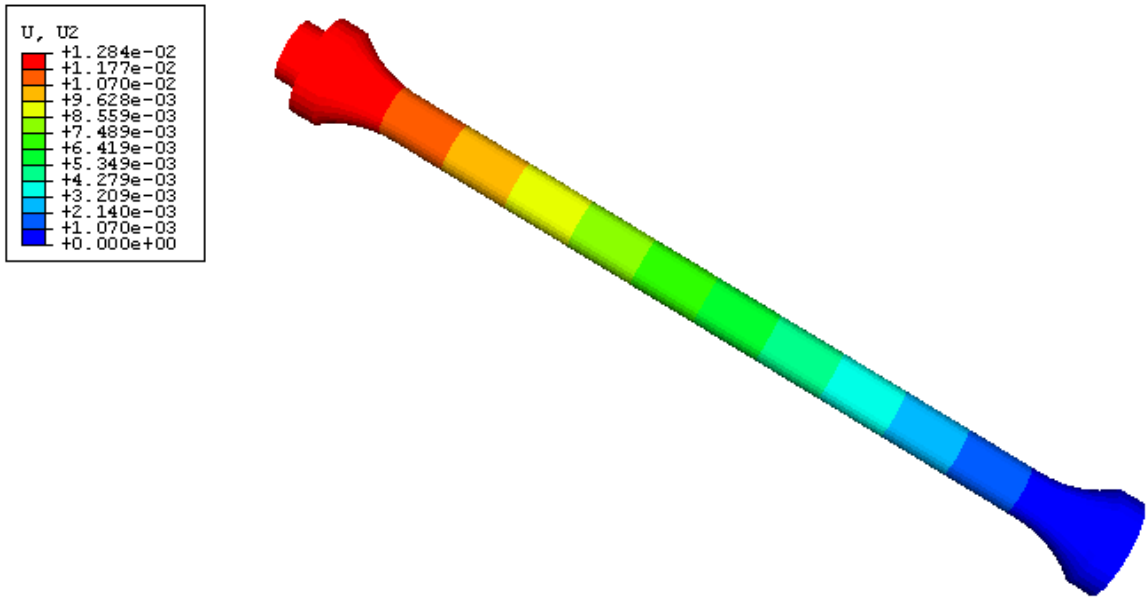

$d_{\text{(shoulder depth)}} = 0.25$ in.

$r_{\text{(circular transition radius)}} = 1$ in.

Fig. C19 - Bar Configuration Type 4, Displacement, Tension Load.

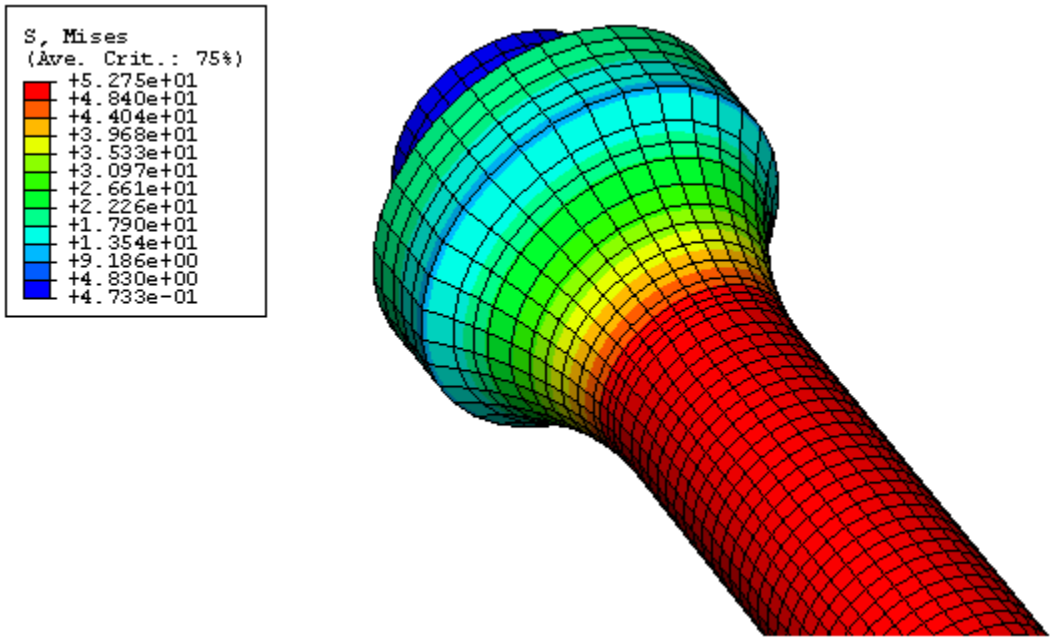

$d_{\text{(shoulder depth)}} = 0.25$ in.

$r_{\text{(circular transition radius)}} = 1$ in.

Fig. C20 - Bar Configuration Type 4, Von Mises Stress, Compression Load, Zoom.

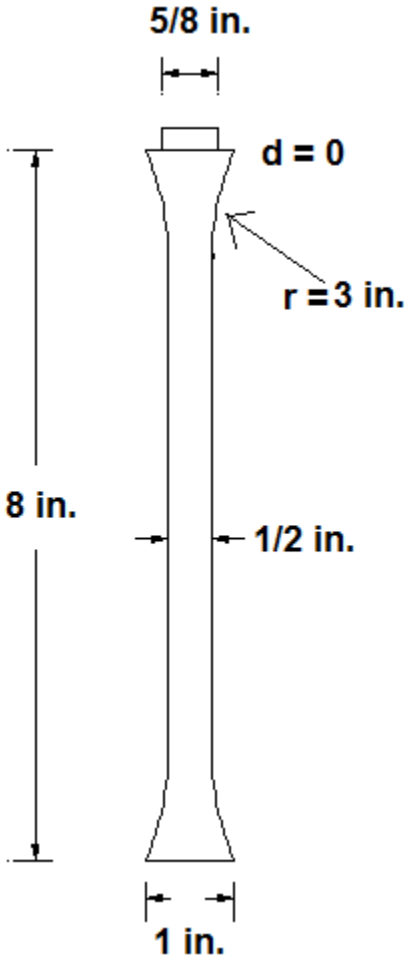

$d_{(\text{shoulder depth})} = 0$

$r_{(\text{circular transition radius})} = 3$ in.

Fig. C21 - Bar Configuration Type #5, Geometry.

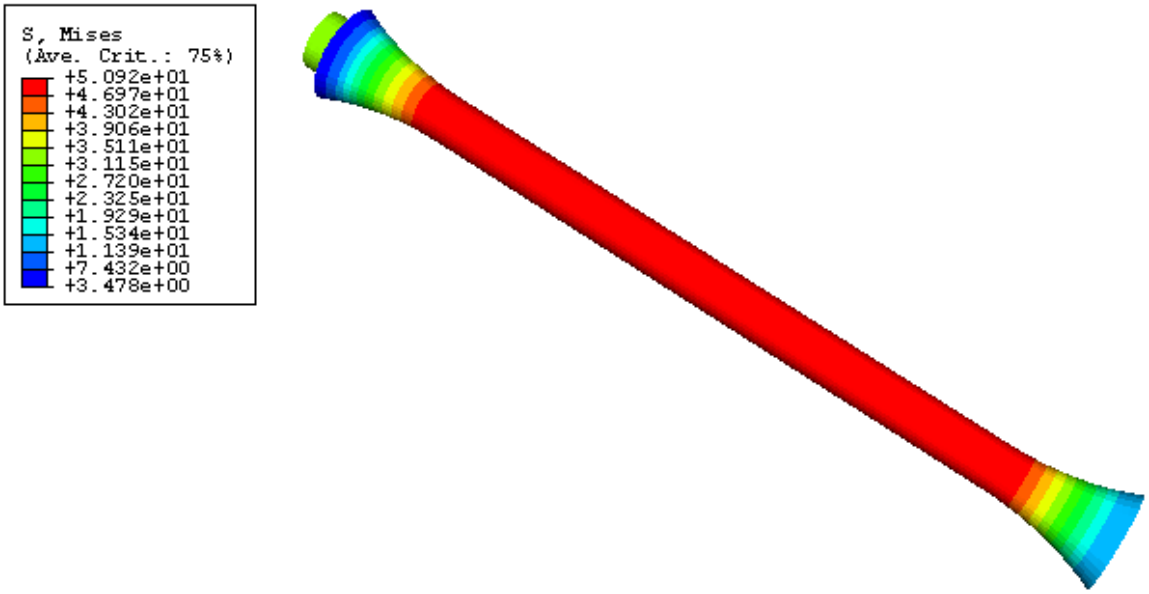

$d_{\text{(shoulder depth)}} = 0$

$r_{\text{(circular transition radius)}} = 3$ in.

Fig. C22 - Bar Configuration Type 5, Von Mises Stress, Tension Load.

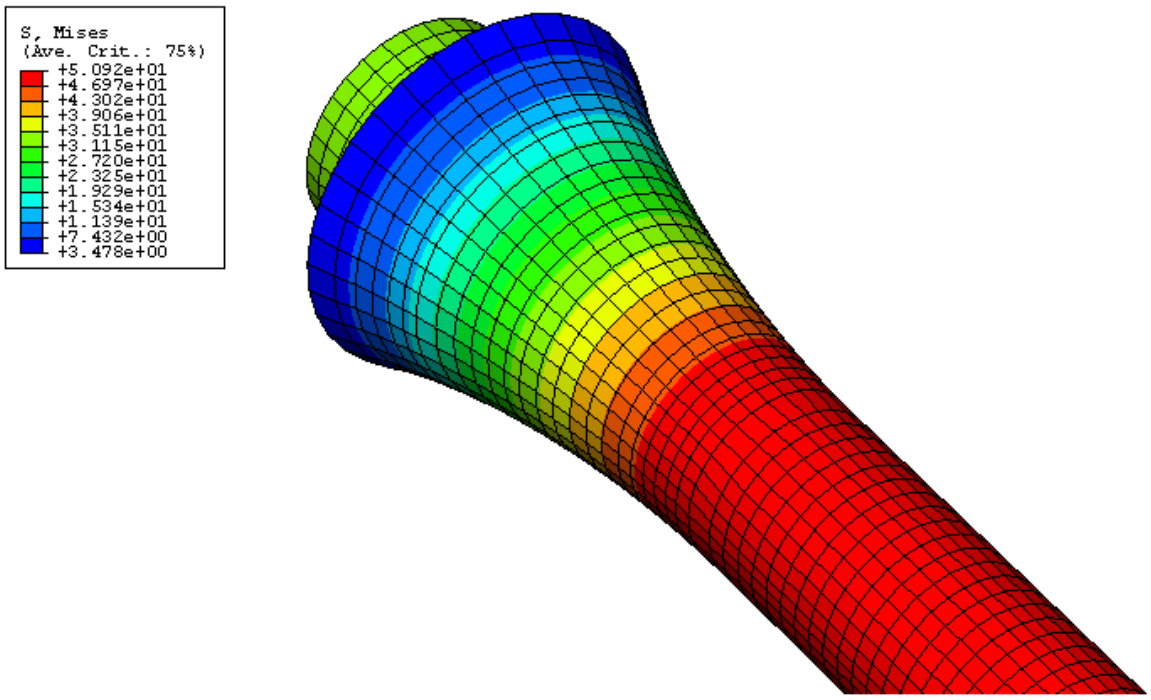

$d_{\text{(shoulder depth)}} = 0$

$r_{\text{(circular transition radius)}} = 3$ in.

Fig. C23 - Bar Configuration Type 5, Von Mises Stress, Tension Load, Zoom.

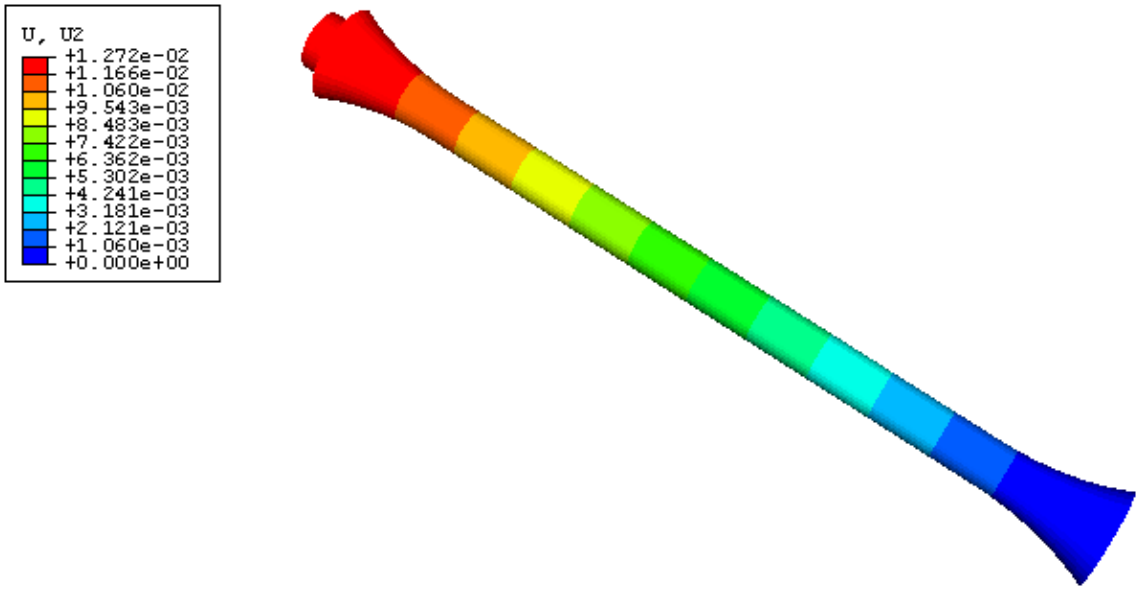

$d_{\text{(shoulder depth)}} = 0$

$r_{\text{(circular transition radius)}} = 3$ in.

Fig. C24 - Bar Configuration Type 5, Displacement, Tension Load.

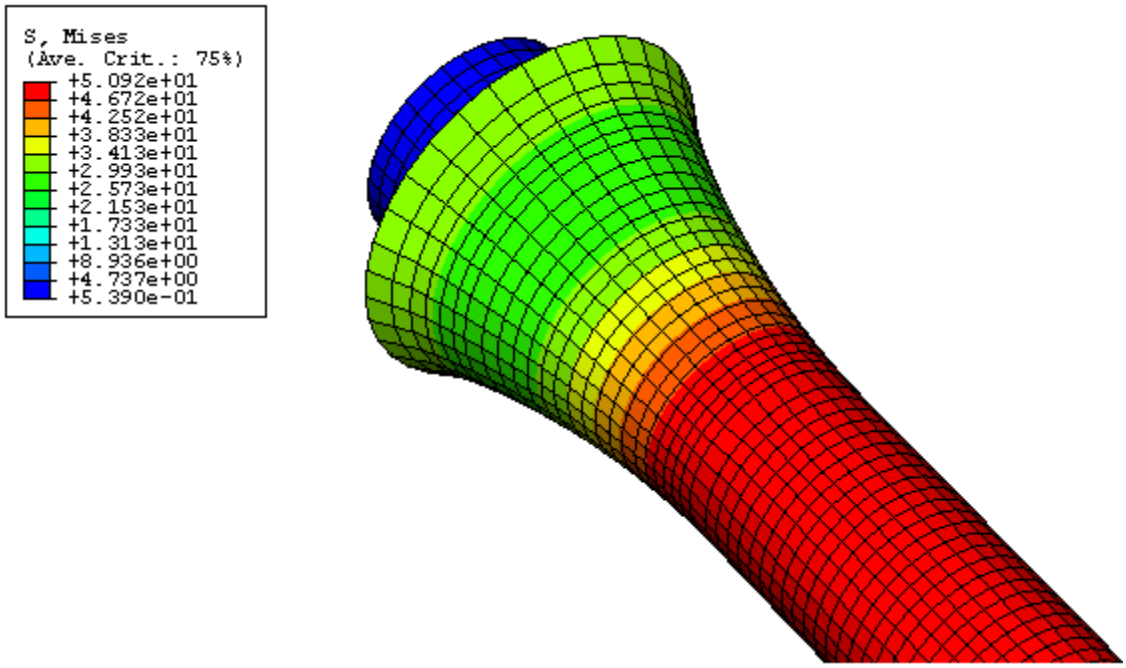

$d_{\text{(shoulder depth)}} = 0$

$r_{\text{(circular transition radius)}} = 3$ in.

Fig. C25 - Bar Configuration Type 5, Von Mises Stress, Compression Load, Zoom.

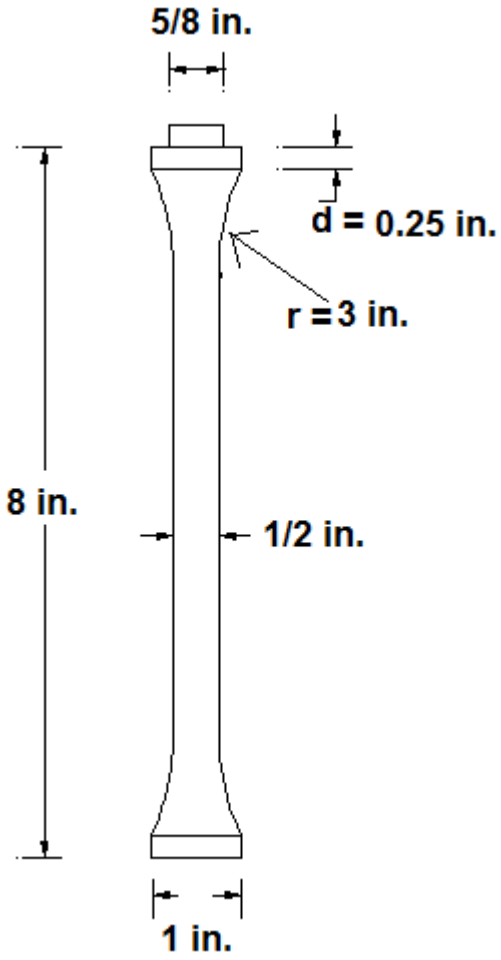

$d_{(\text{shoulder depth})} = 0.25$ in.

$r_{(\text{circular transition radius})} = 3$ in.

Fig. C26 - Bar Configuration Type #6, Geometry.

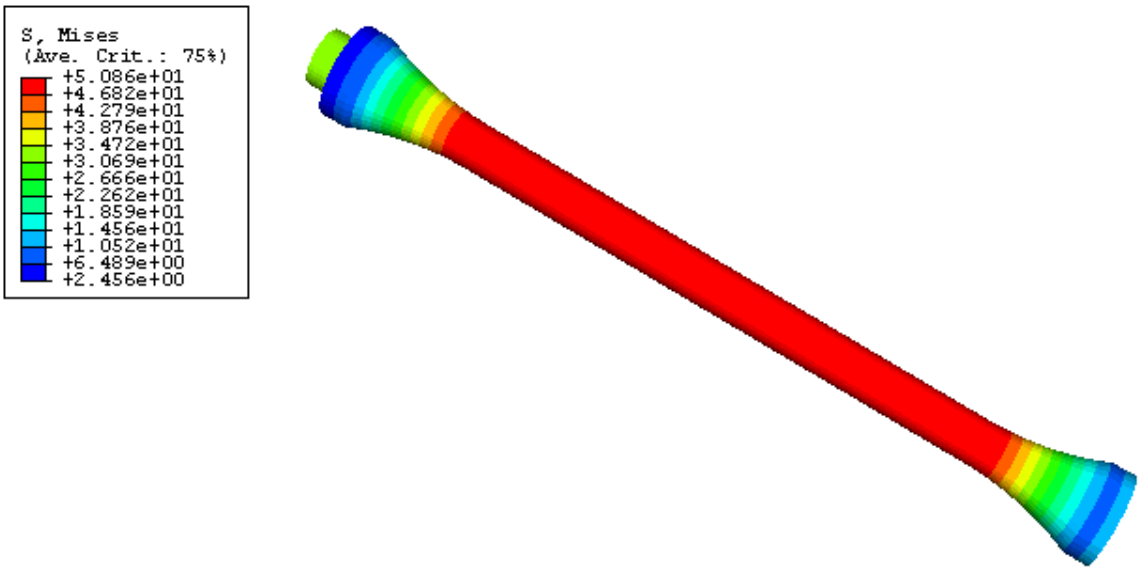

$d_{\text{(shoulder depth)}} = 0.25$ in.

$r_{\text{(circular transition radius)}} = 3$ in.

Fig. C27 - Bar Configuration Type 6, Von Mises Stress, Tension Load.

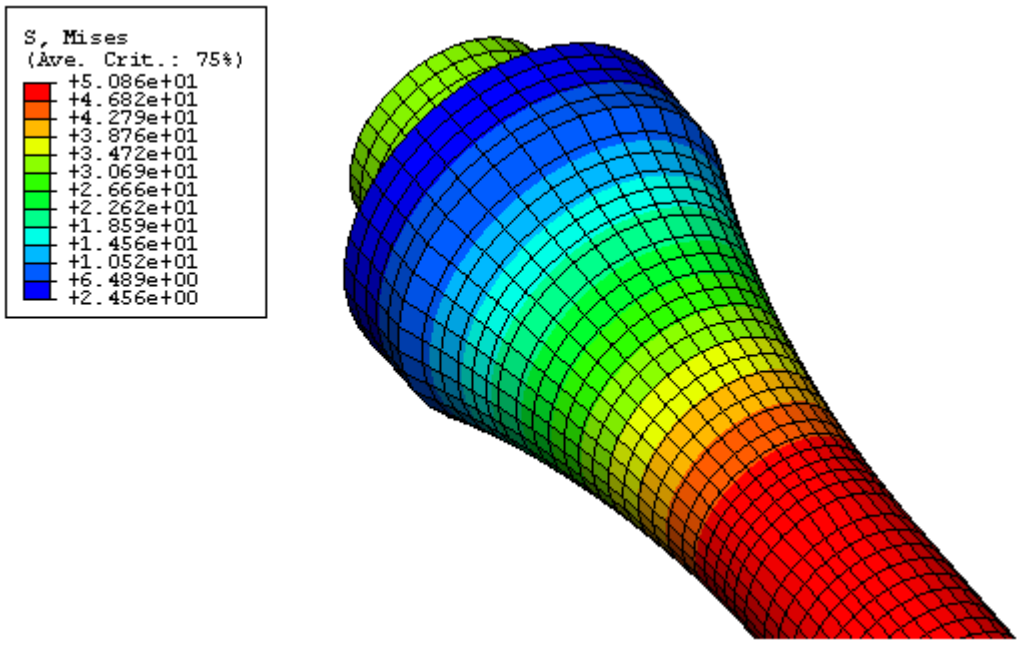

$d_{\text{(shoulder depth)}} = 0.25$ in.

$r_{\text{(circular transition radius)}} = 3$ in.

Fig. C28 - Bar Configuration Type 6, Von Mises Stress, Tension Load, Zoom.

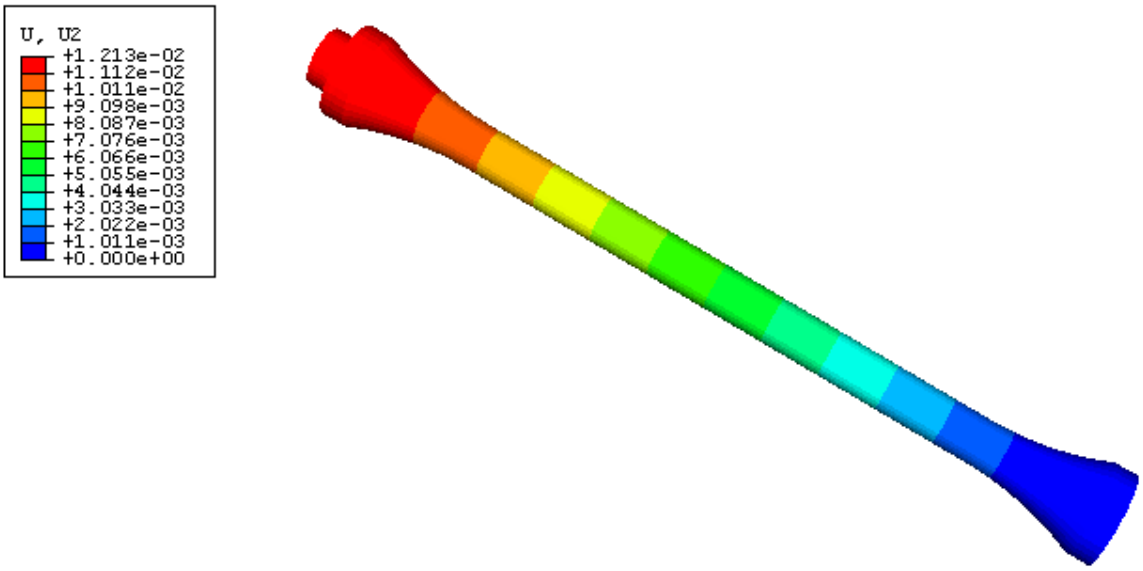

$d_{\text{(shoulder depth)}} = 0.25$ in.

$r_{\text{(circular transition radius)}} = 3$ in.

Fig. C29 - Bar Configuration Type 6, Displacement, Tension Load.

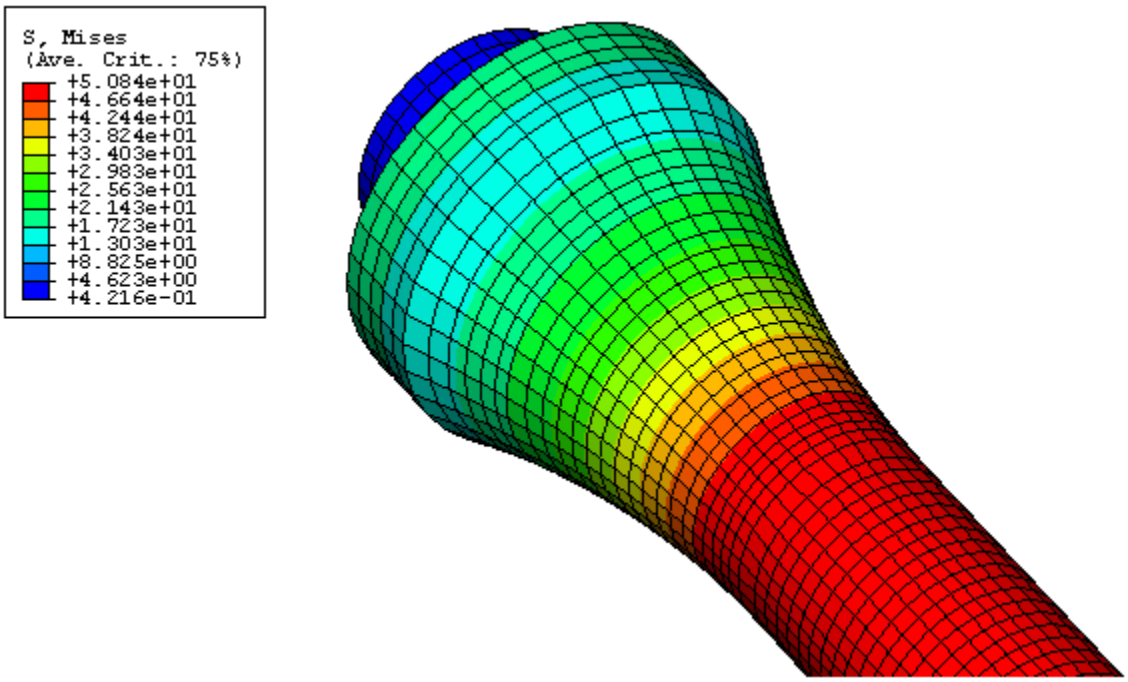

$d_{\text{(shoulder depth)}} = 0.25$ in.

$r_{\text{(circular transition radius)}} = 3$ in.

Fig. C30 - Bar Configuration Type 6, Von Mises Stress, Compression Load, Zoom.

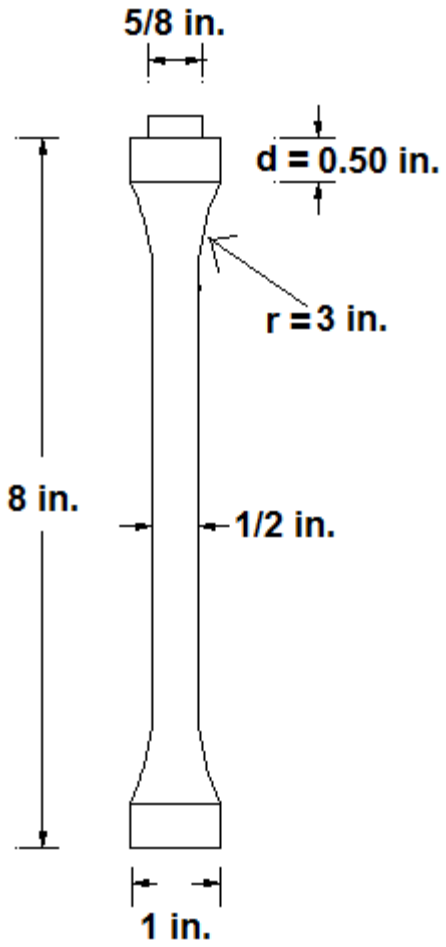

$d_{(\text{shoulder depth})} = 0.50$ in.

$r_{(\text{circular transition radius})} = 3$ in.

Fig. C31 - Bar Configuration Type #7, Geometry.

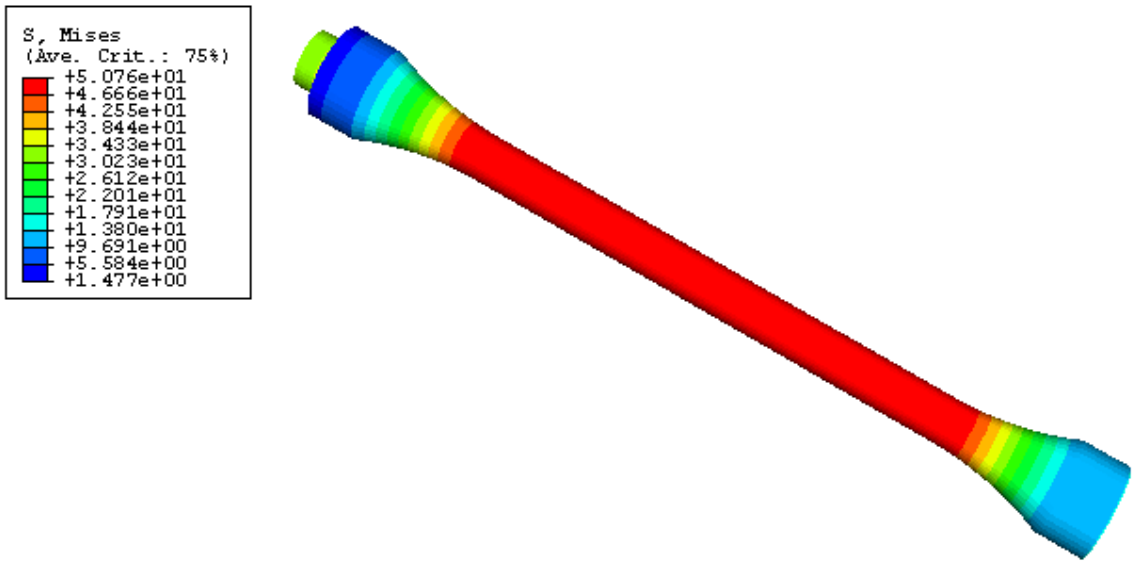

$d_{\text{(shoulder depth)}} = 0.50$ in.

$r_{\text{(circular transition radius)}} = 3$ in.

Fig. C32 - Bar Configuration Type 7, Von Mises Stress, Tension Load.

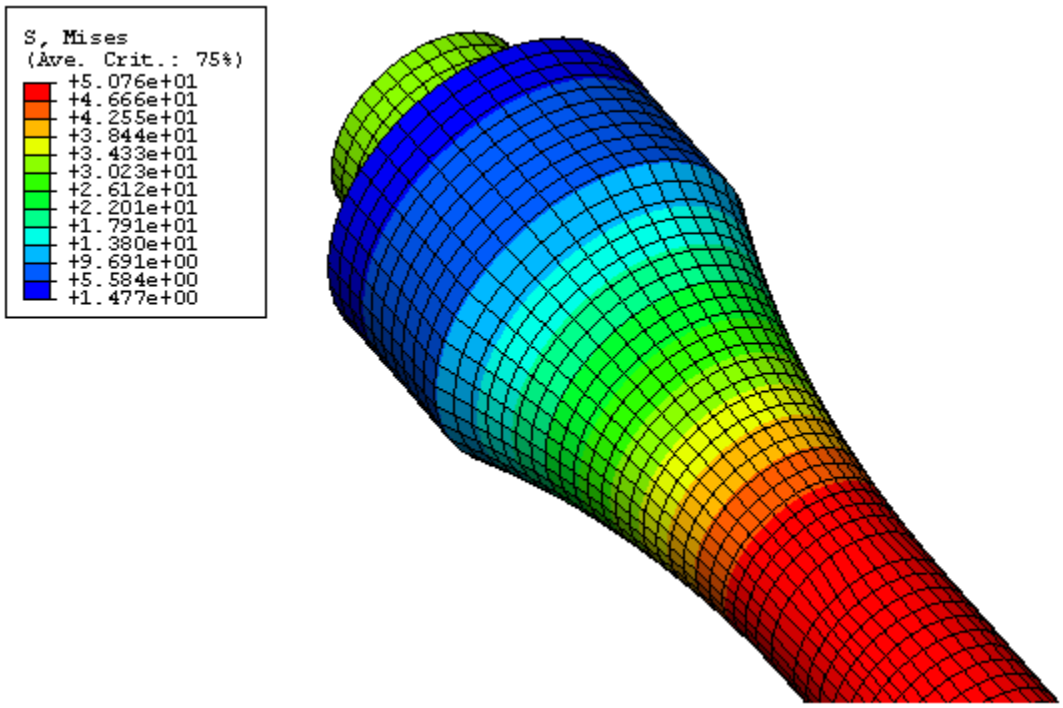

$d_{\text{(shoulder depth)}} = 0.50$ in.

$r_{\text{(circular transition radius)}} = 3$ in.

Fig. C33 - Bar Configuration Type 7, Von Mises Stress, Tension Load, Zoom.

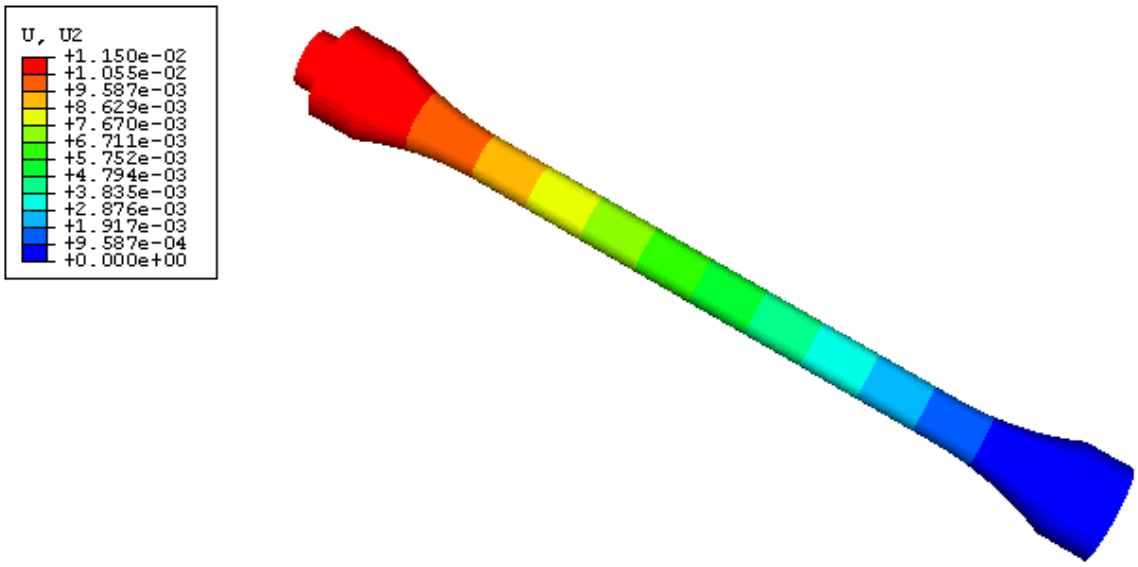

$d_{\text{(shoulder depth)}} = 0.50$ in.

$r_{\text{(circular transition radius)}} = 3$ in.

Fig. C34 - Bar Configuration Type 7, Displacement, Tension Load.

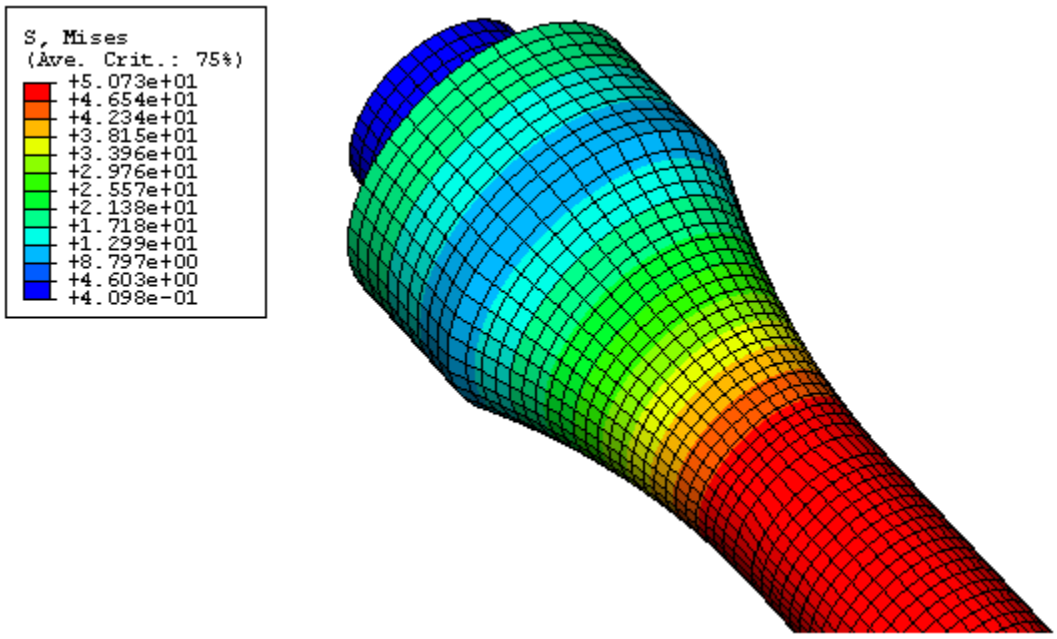

$d_{\text{(shoulder depth)}} = 0.50$ in.

$r_{\text{(circular transition radius)}} = 3$ in.

Fig. C35 - Bar Configuration Type 7, Von Mises Stress, Compression Load, Zoom.

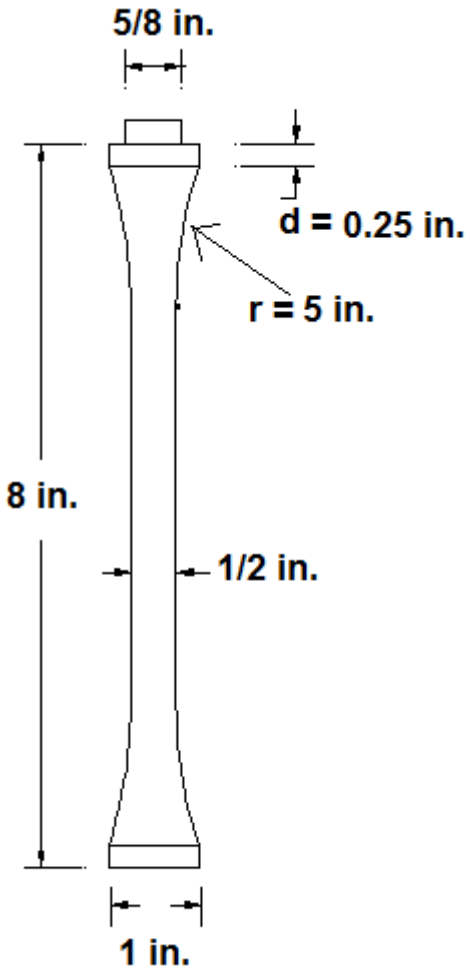

$d_{(\text{shoulder depth})} = 0.25$ in.

$r_{(\text{circular transition radius})} = 5$ in.

Fig. C36 - Bar Configuration Type #8, Geometry.

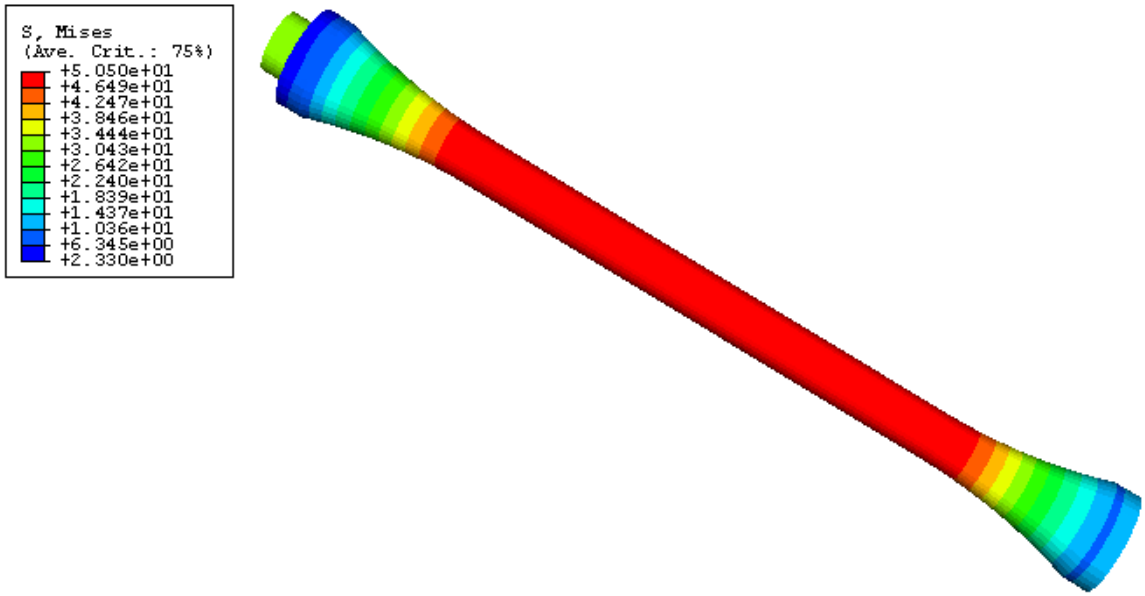

$d_{\text{(shoulder depth)}} = 0.25$ in.

$r_{\text{(circular transition radius)}} = 5$ in.

Fig. C37 - Bar Configuration Type 8, Von Mises Stress, Tension Load.

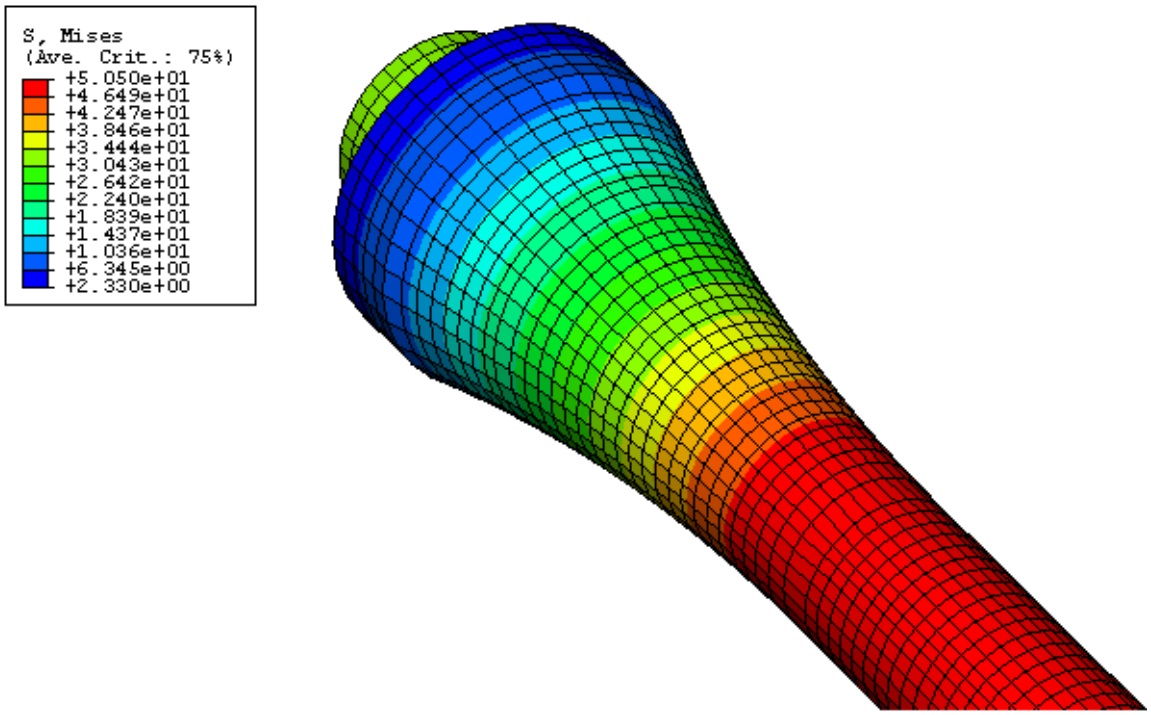

$d_{\text{(shoulder depth)}} = 0.25$ in.

$r_{\text{(circular transition radius)}} = 5$ in.

Fig. C38 - Bar Configuration Type 8, Von Mises Stress, Tension Load, Zoom.

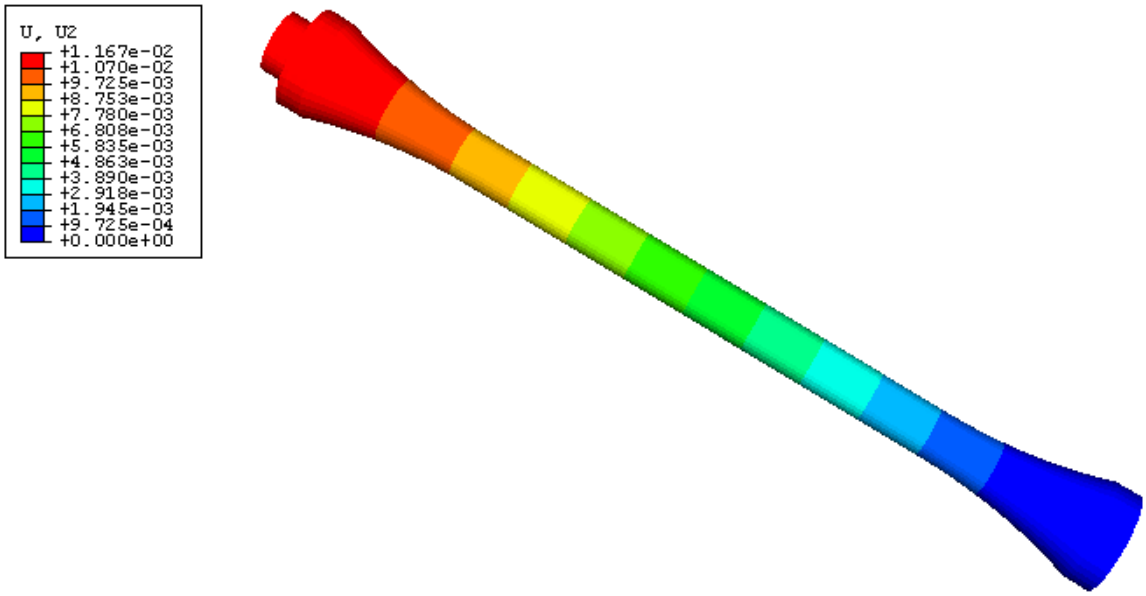

$d_{\text{(shoulder depth)}} = 0.25$ in.

$r_{\text{(circular transition radius)}} = 5$ in.

Fig. C39 - Bar Configuration Type 8, Displacement, Tension Load.

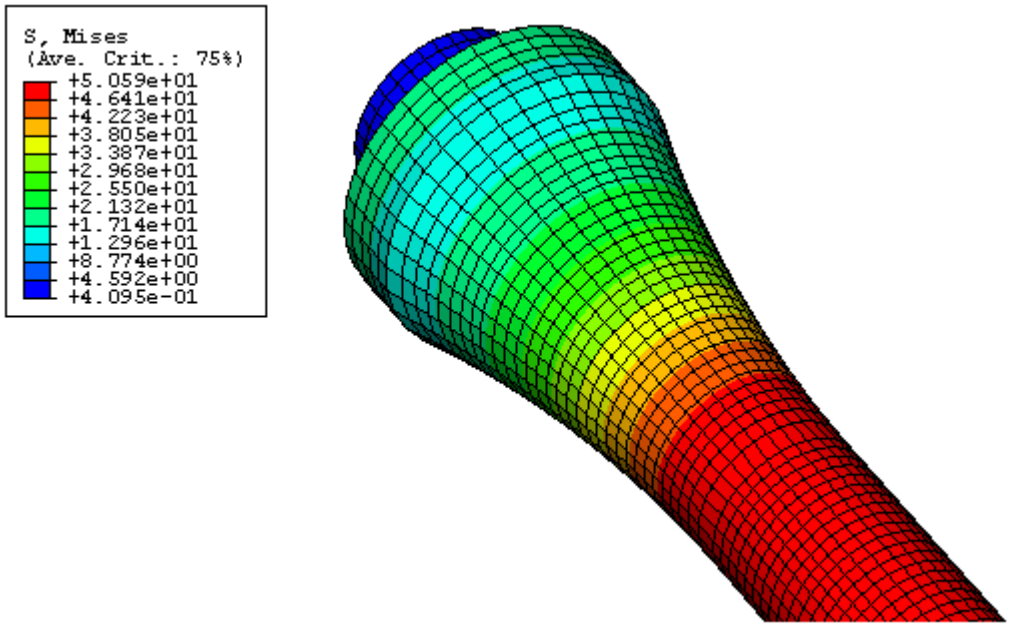

$d_{\text{(shoulder depth)}} = 0.25$ in.

$r_{\text{(circular transition radius)}} = 5$ in.

Fig. C40 - Bar Configuration Type 8, Von Mises Stress, Compression Load, Zoom.

APPENDIX D – BCE Bar Stress Concentration Radiused Relief

Stress Concentration Study - (ksi)			
Radiused Relief	Tension		Compression
	Kt (a)	Kt (b)	Kt
none	**1.06**	**1.2**	**1.6**
1	**1.36**	**1.2**	**2.1**
2	**1.42**	**1.16**	**1.54**
3	**1.64**	**1.32**	**1.46**
4	**1.6**	**1.26**	**-**
5	**1.16**	**1.26**	**2.2**
6	**0.98**	**1.36**	**1.9**
7	**1.16**	**1.22**	**2.2**
8	**1.1**	**1.24**	**1.9**

$K_{t(a)}$ = Stress Concentration, Tension Load – Shoulder.

$K_{t(b)}$ = Stress Concentration, Tension Load – Threads.

$$K(t) = \frac{\sigma \text{ max}}{\sigma \text{ net}}$$

Table D1 - Summary of Results, Stress Concentration Radiused Relief Study.

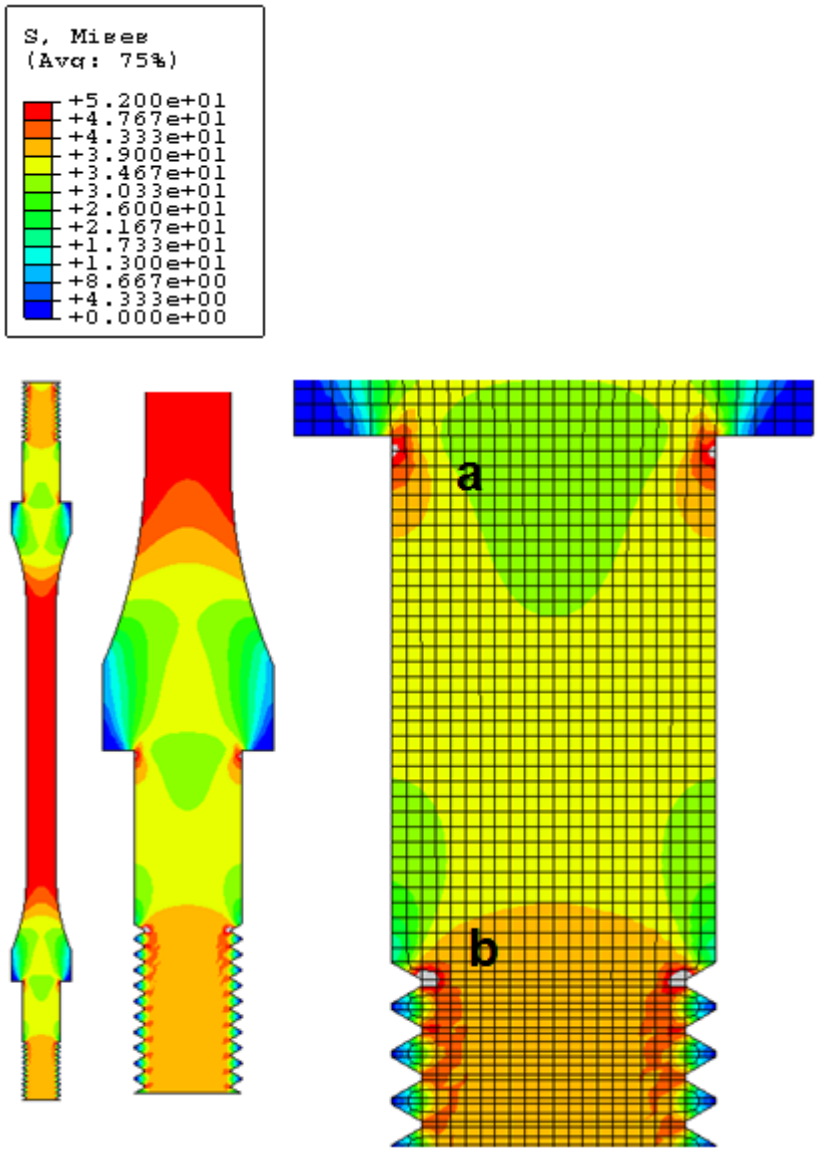

Kt(a) = 53ksi/50ksi = 1.06

Kt(b) = 60ksi/50ksi = 1.2

Fig. D1 - Bar Von Mises Stress, Tension Load.

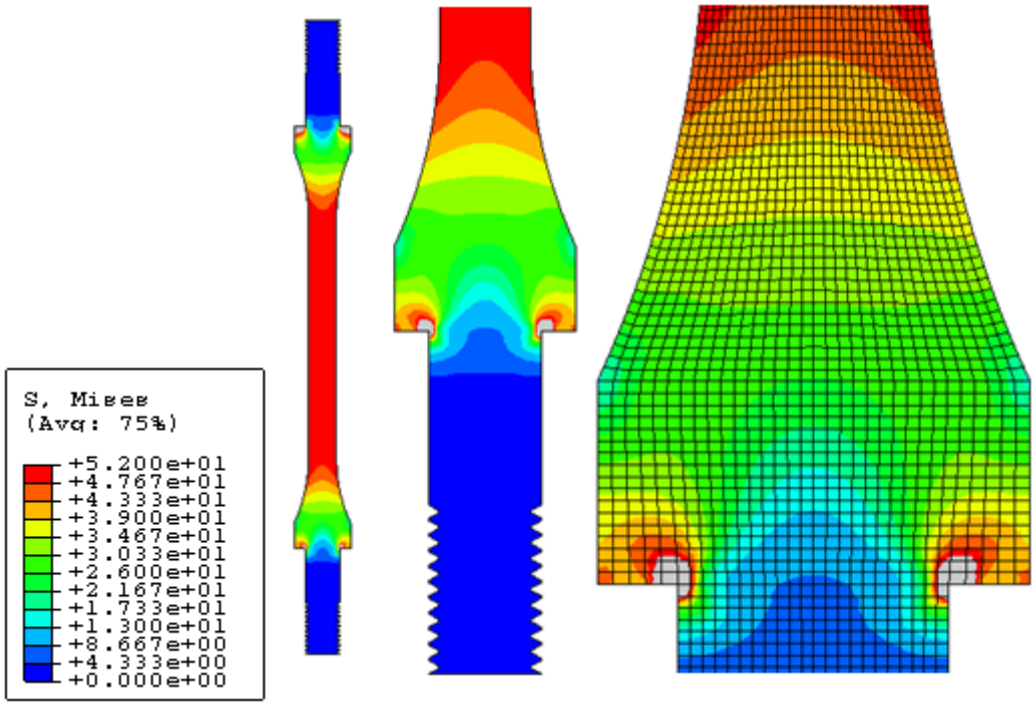

Kt = 80ksi/50ksi = 1.6

Fig. D2 - Bar Von Mises Stress, Compression Load.

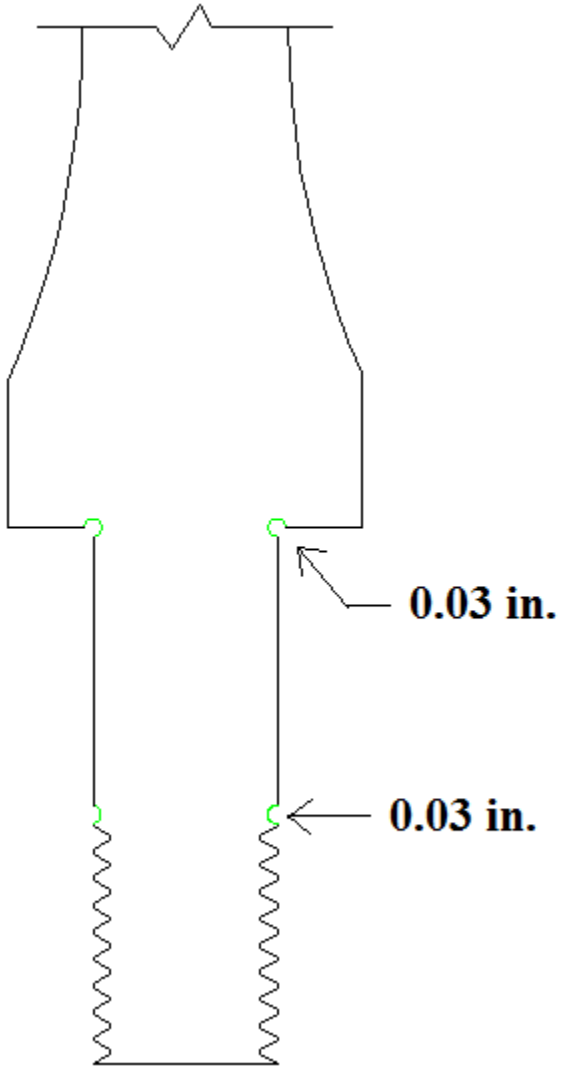

Fig. D3 - Stress Concentration Radiused Relief #1, Geometry.

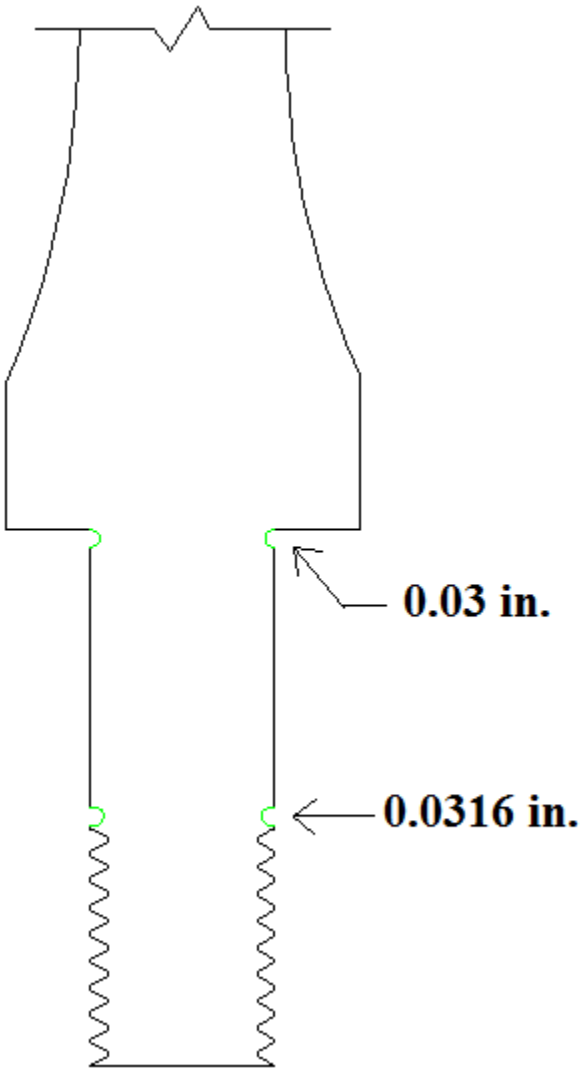

Fig. D4 - Stress Concentration Radiused Relief #2, Geometry.

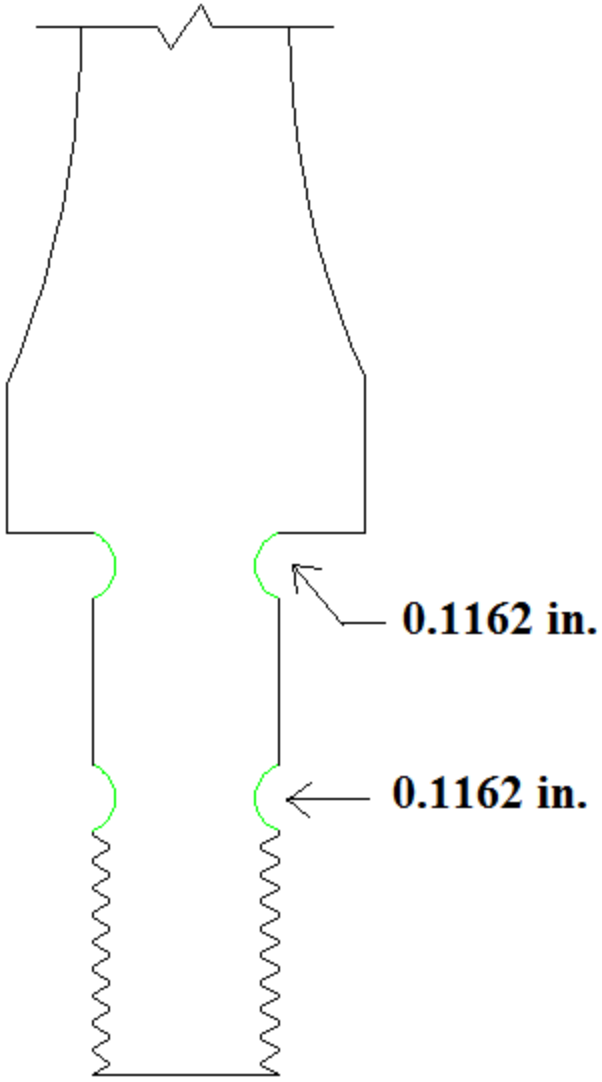

Fig. D5 - Stress Concentration Radiused Relief #3, Geometry.

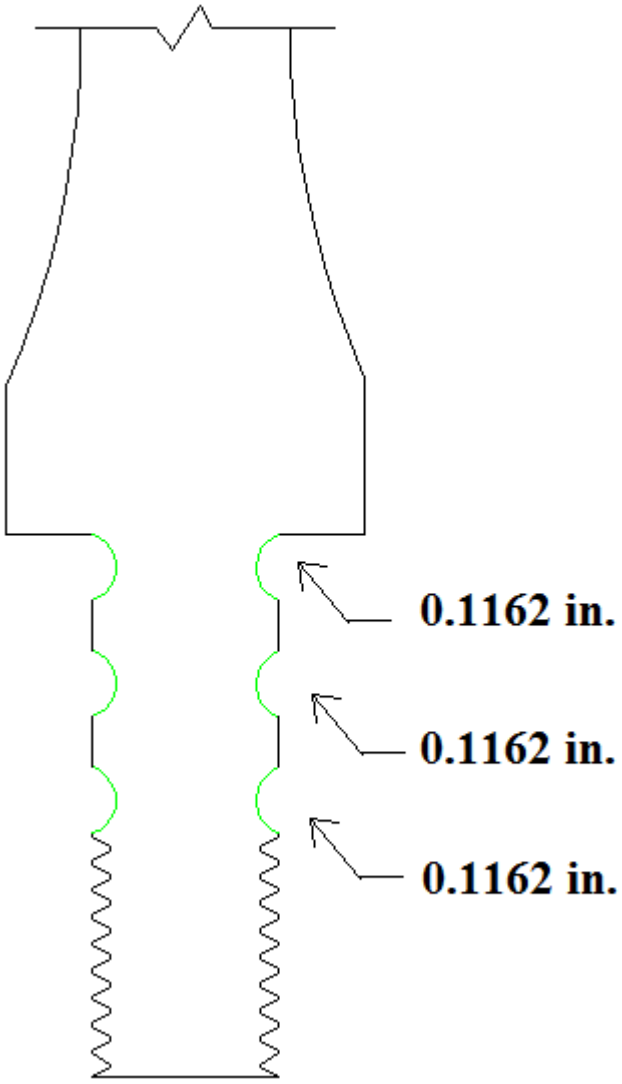

Fig. D6 - Stress Concentration Radiused Relief #4, Geometry.

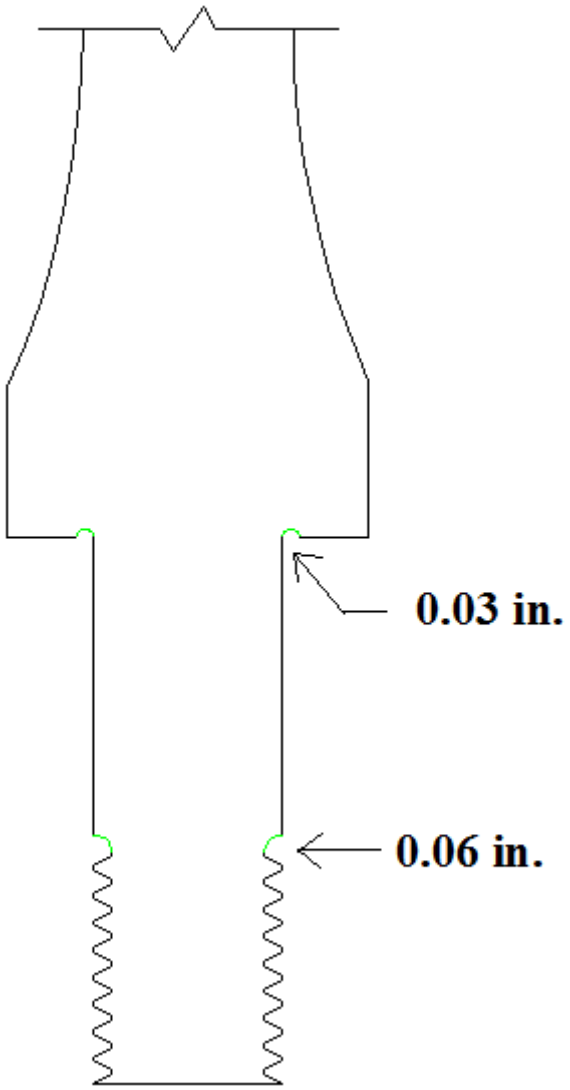

Fig. D7 - Stress Concentration Radiused Relief #5, Geometry.

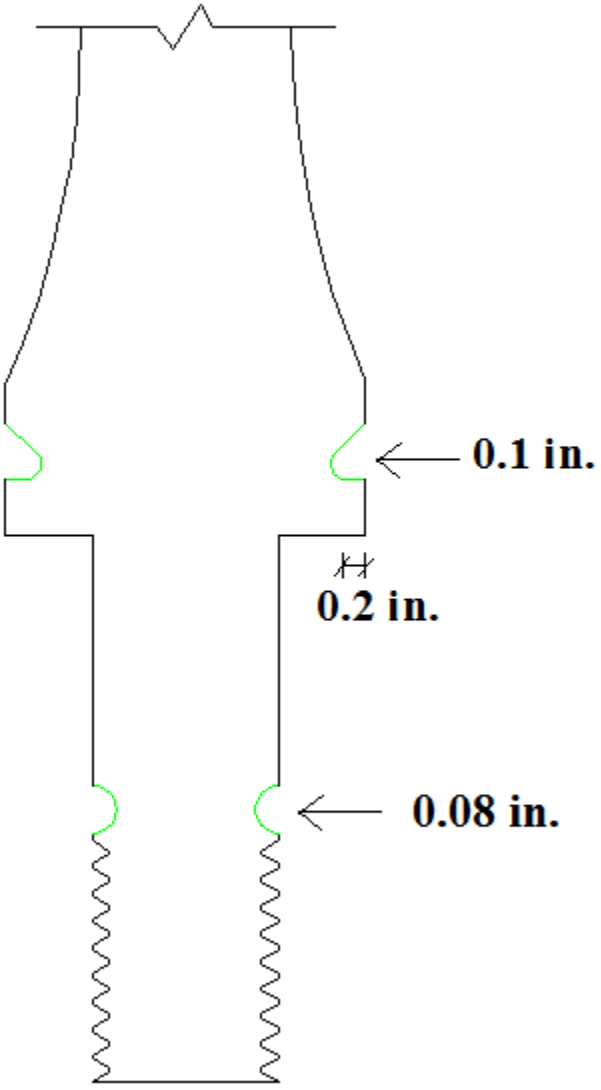

Fig. D8 - Stress Concentration Radiused Relief #6, Geometry.

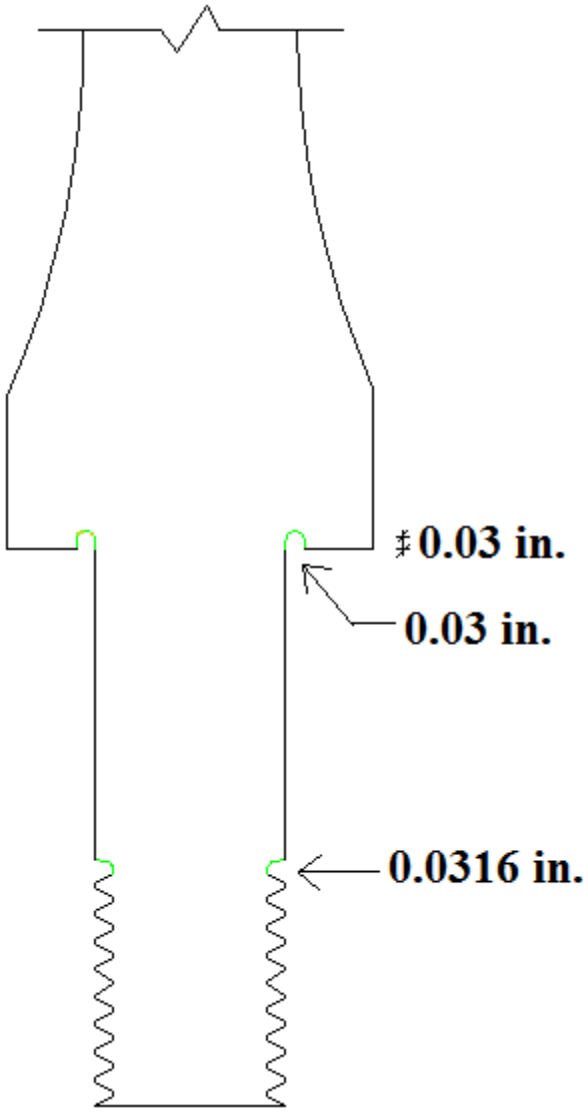

Fig. D9 - Stress Concentration Radiused Relief #7, Geometry.

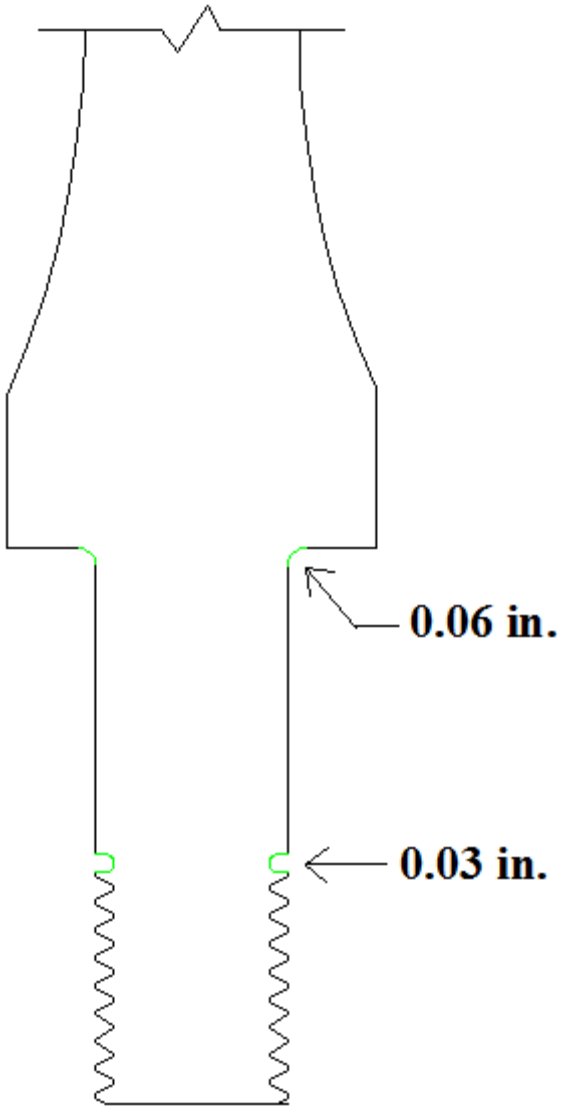

Fig. D10 - Stress Concentration Radiused Relief #8, Geometry.

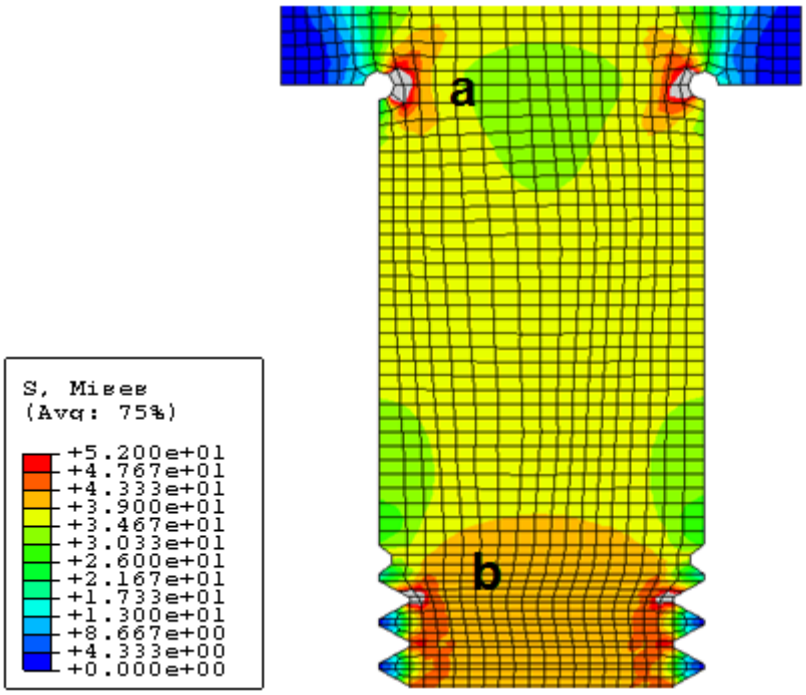

Kt(a) = 68ksi/50ksi = 1.36

Kt(b) = 60ksi/50ksi = 1.2

Fig. D11 - FEM Radiused Relief #1, Tension Load, Von Mises Stress.

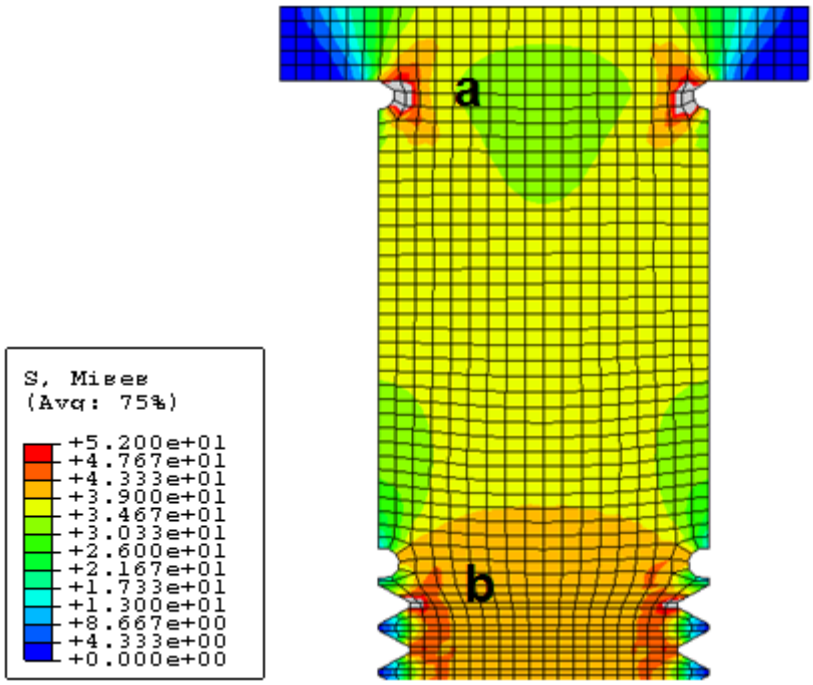

Kt(a) = 71ksi/50ksi = 1.42

Kt(b) = 58ksi/50ksi = 1.16

Fig. D12 - FEM Radiused Relief #2, Tension Load, Von Mises Stress.

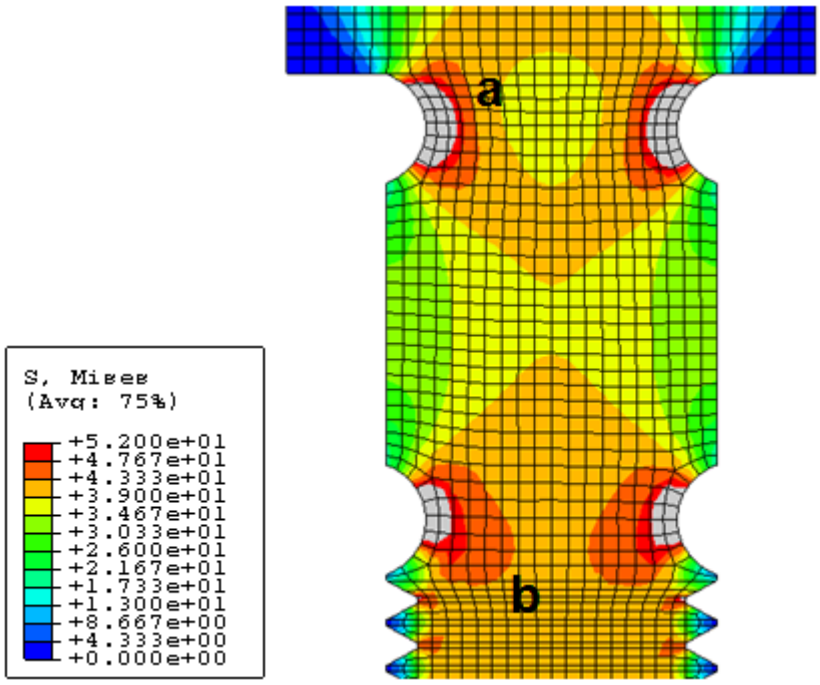

Kt(a) = 82ksi/50ksi = 1.64

Kt(b) = 66ksi/50ksi = 1.32

Fig. D13 - FEM Radiused Relief #3, Tension Load, Von Mises Stress.

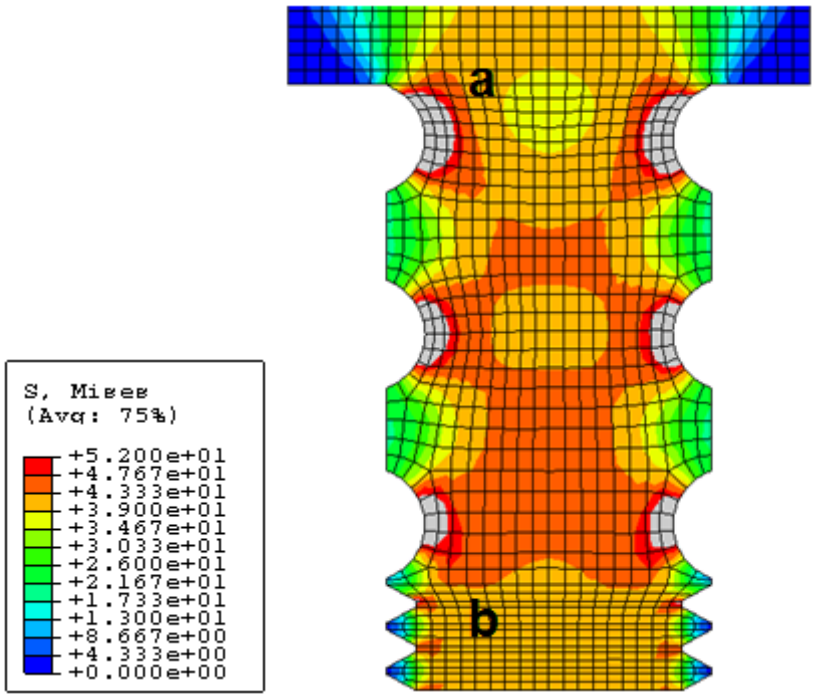

Kt(a) = 80ksi/50ksi = 1.6

Kt(b) = 63ksi/50ksi = 1.26

Fig. D14 - FEM Radiused Relief #4, Tension Load, Von Mises Stress.

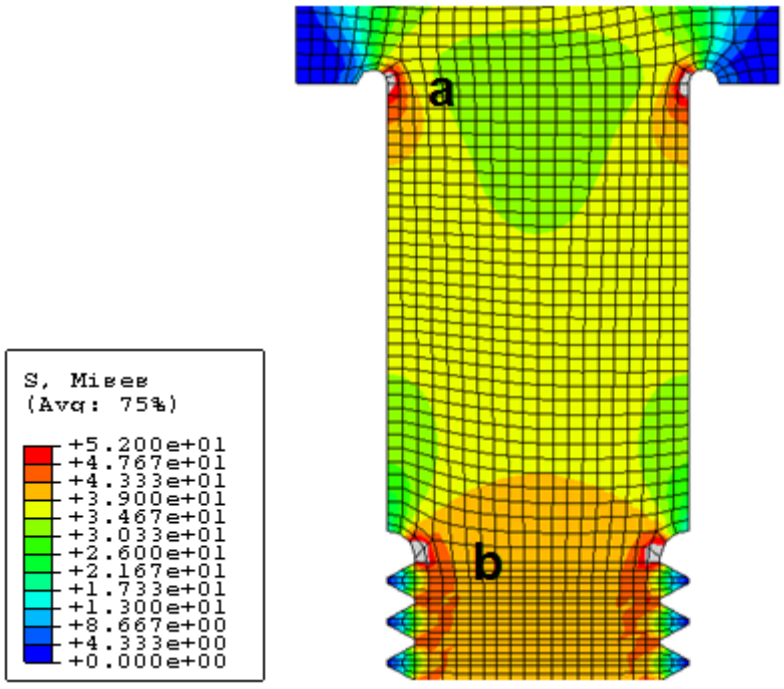

Kt(a) = 58ksi/50ksi = 1.16

Kt(b) = 63ksi/50ksi = 1.26

Fig. D15 - FEM Radiused Relief #5, Tension Load, Von Mises Stress.

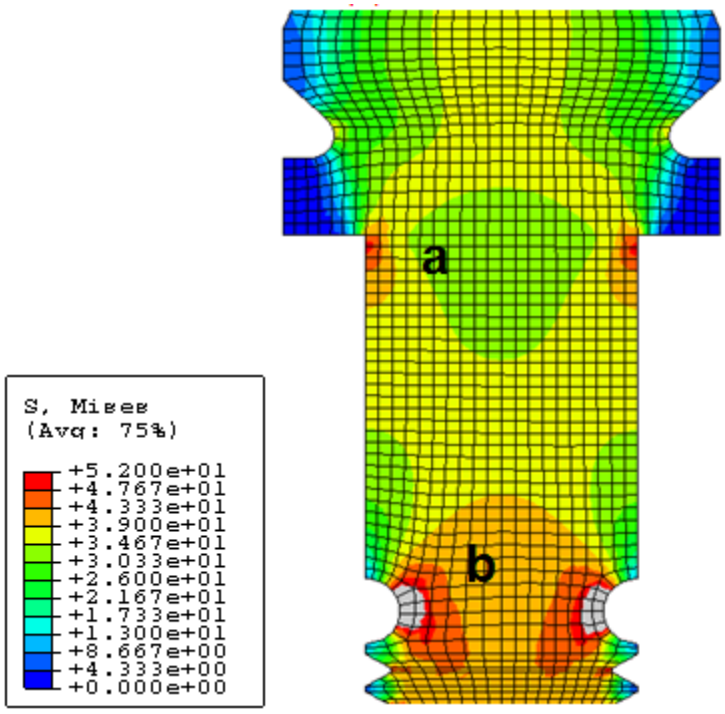

Kt(a) = 49ksi/50ksi = 0.98

Kt(b) = 68ksi/50ksi = 1.36

Fig. D16 - FEM Radiused Relief #6, Tension Load, Von Mises Stress.

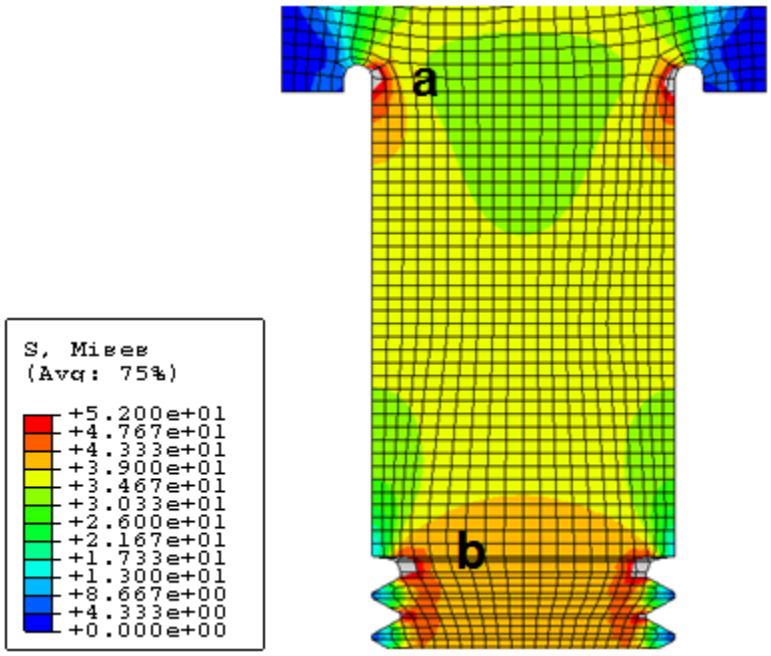

Kt(a) = 58ksi/50ksi = 1.16

Kt(b) = 61ksi/50ksi = 1.22

Fig. D17 - FEM Radiused Relief #7, Tension Load, Von Mises Stress.

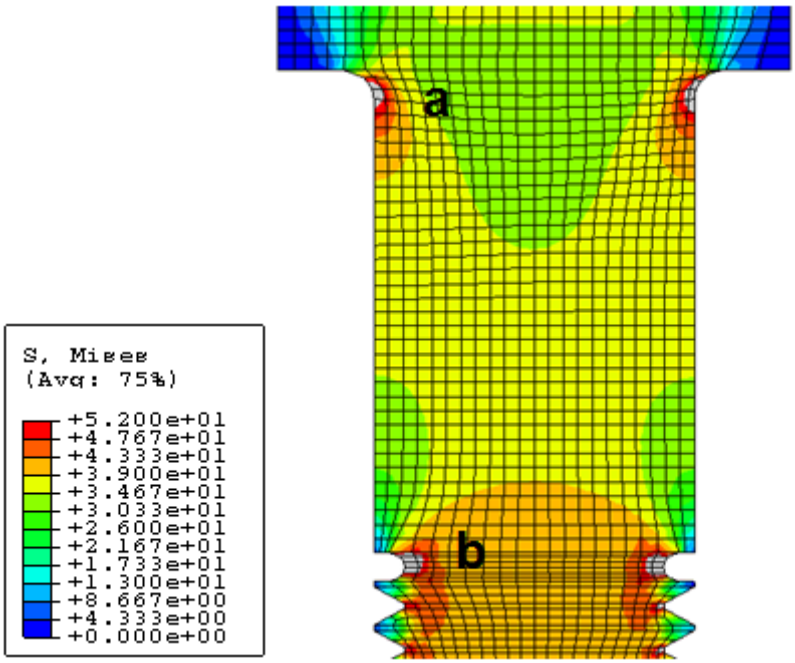

Kt(a) = 55ksi/50ksi = 1.1

Kt(b) = 62ksi/50ksi =1.24

Fig. D18 - FEM Radiused Relief #8, Tension Load, Von Mises Stress.

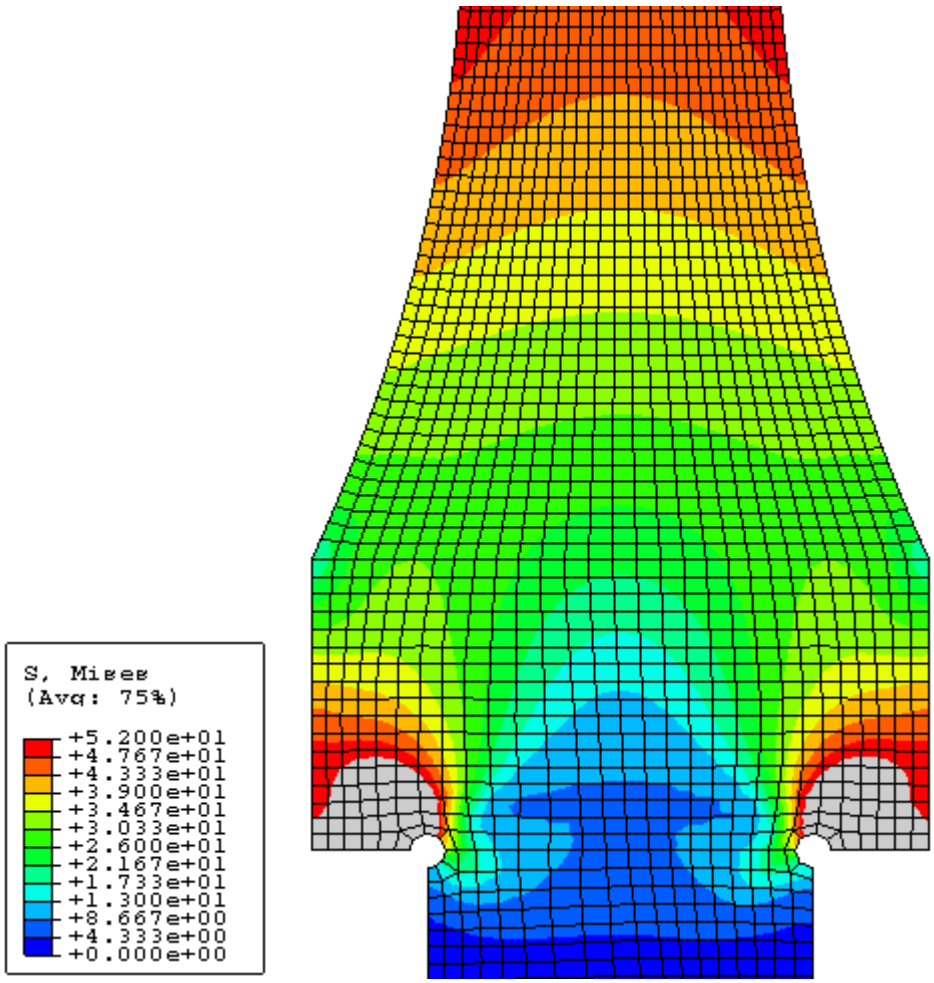

Kt = 105ksi/50ksi = 2.1

Fig. D19 - FEM Radiused Relief #1, Compression Load, Von Mises Stress.

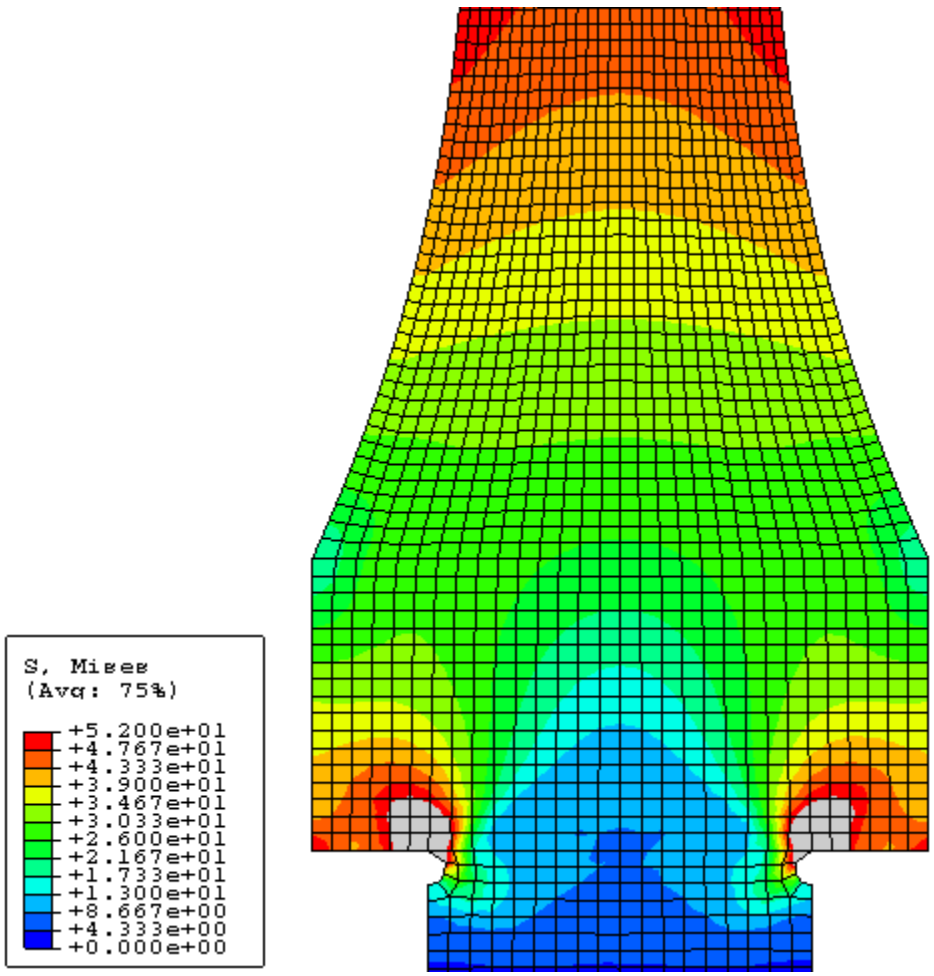

Kt = 77ksi/50ksi = 1.54

Fig. D20 - FEM Radiused Relief #2, Compression Load, Von Mises Stress.

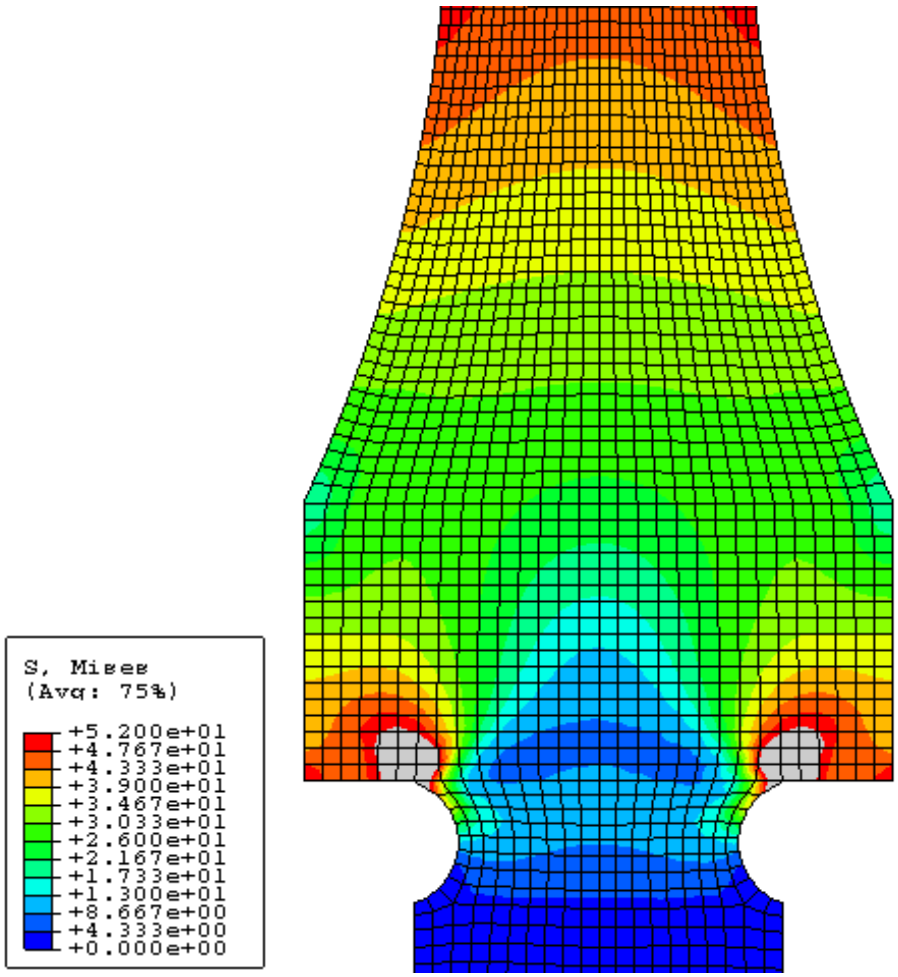

Kt = 73ksi/50ksi = 1.46

Fig. D21 - FEM Radiused Relief #3, Compression Load, Von Mises Stress.

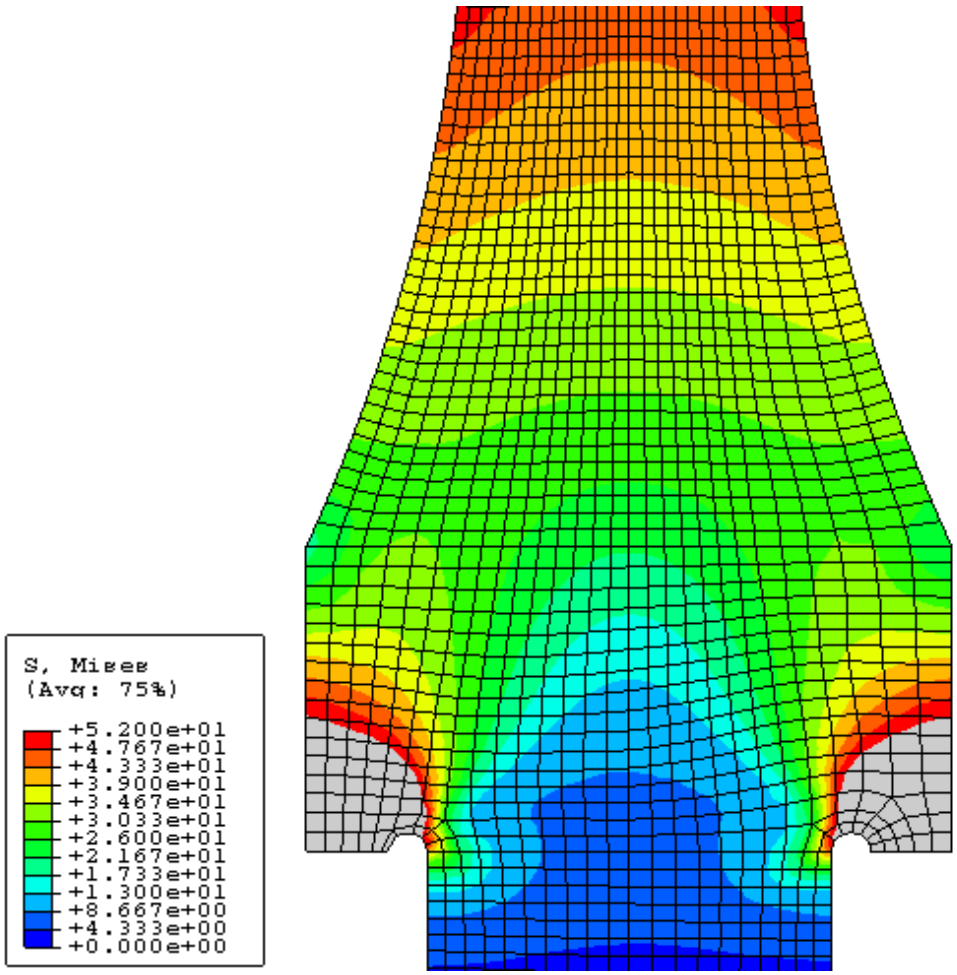

Kt = 110ksi/50ksi = 2.2

Fig. D22 - FEM Radiused Relief #5, Compression Load, Von Mises Stress.

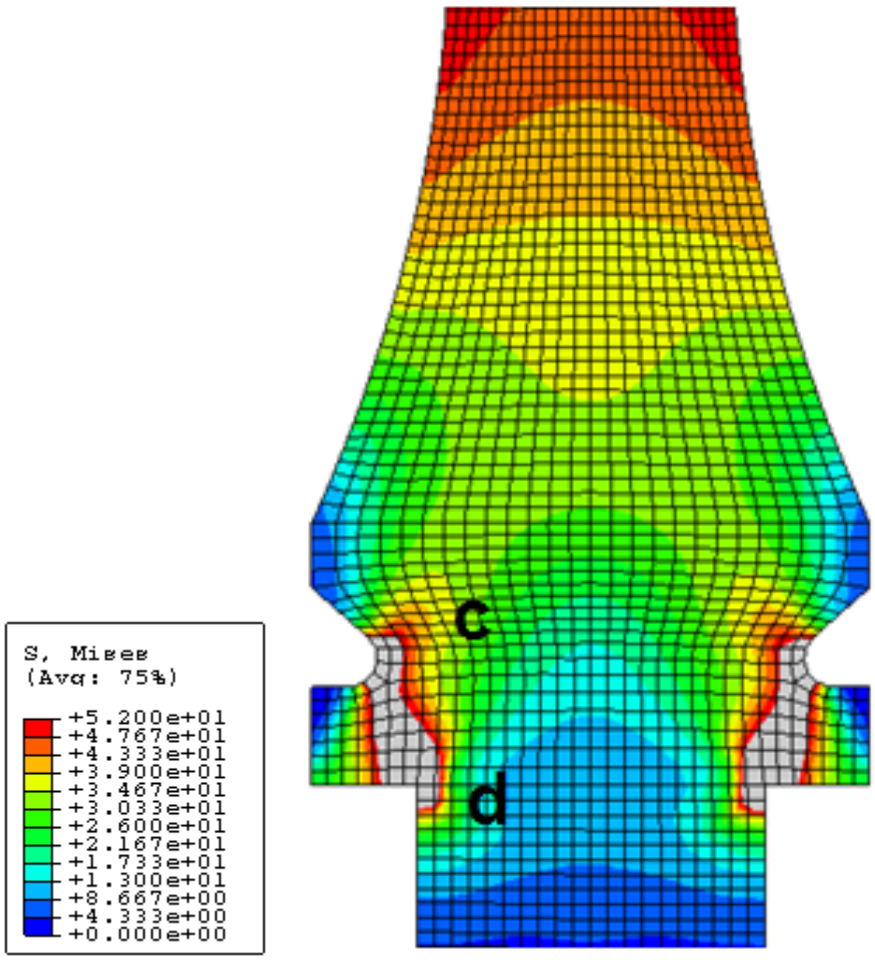

Kt(c) = 79ksi/50ksi = 1.58

Kt(d) = 95ksi/50ksi = 1.9

Fig. D23 - FEM Radiused Relief #6, Compression Load, Von Mises Stress.

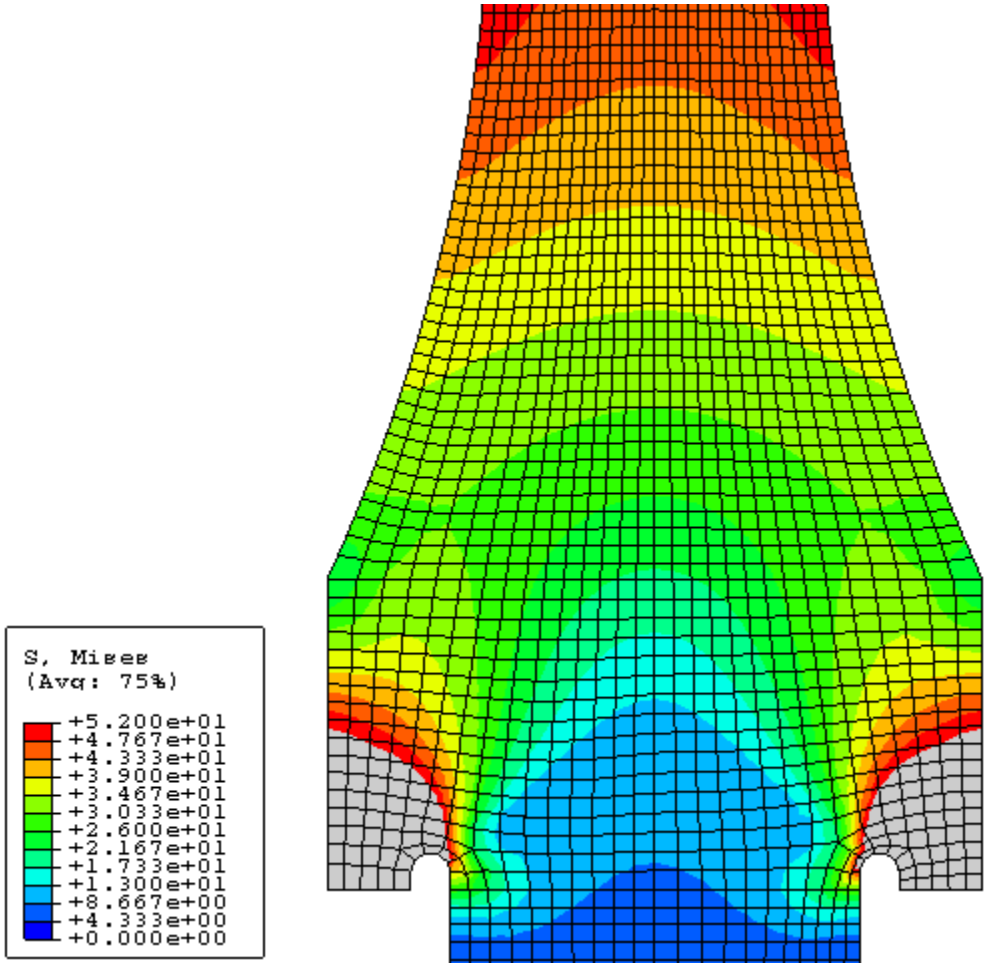

Kt = 110ksi/50ksi = 2.2

Fig. D24 - FEM Radiused Relief #7, Compression Load, Von Mises Stress.

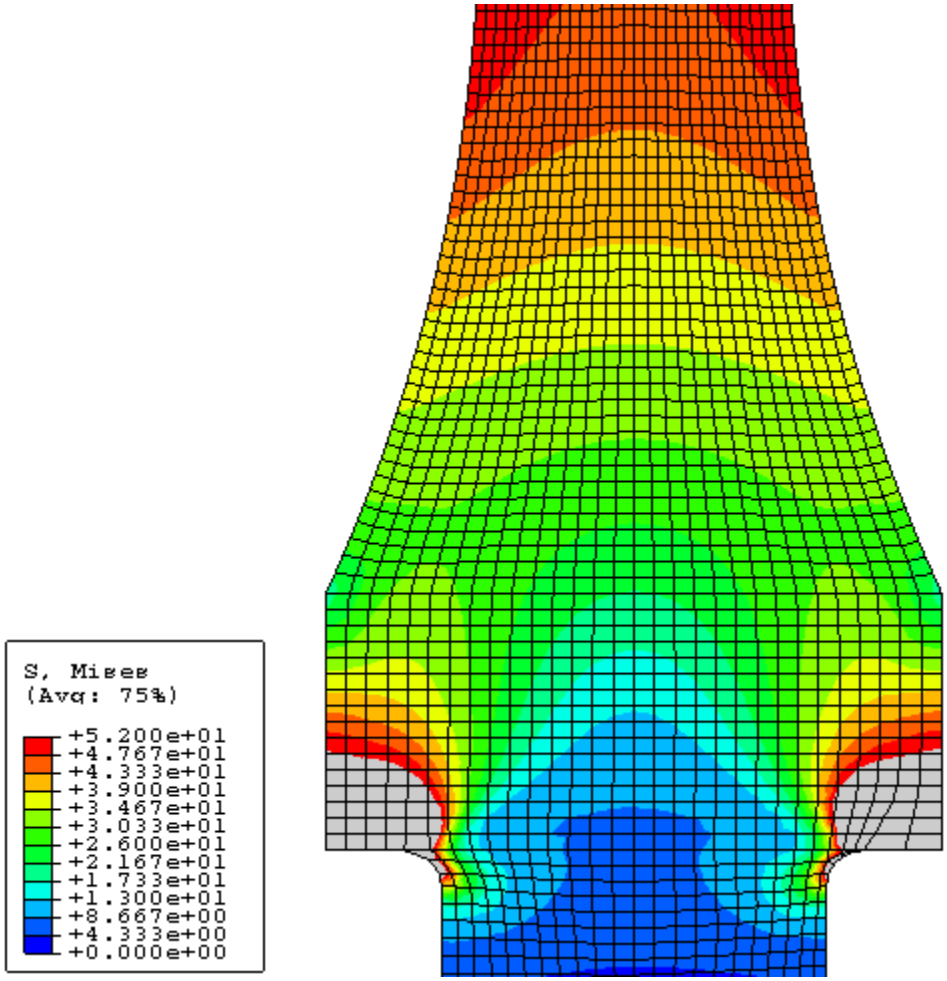

Kt = 95 ksi/50ksi = 1.9

Fig. D25 - FEM Radiused Relief #8, Compression Load, Von Mises Stress.

APPENDIX E – BCE, Polyurethane Matrix and Inner Core Fabrication

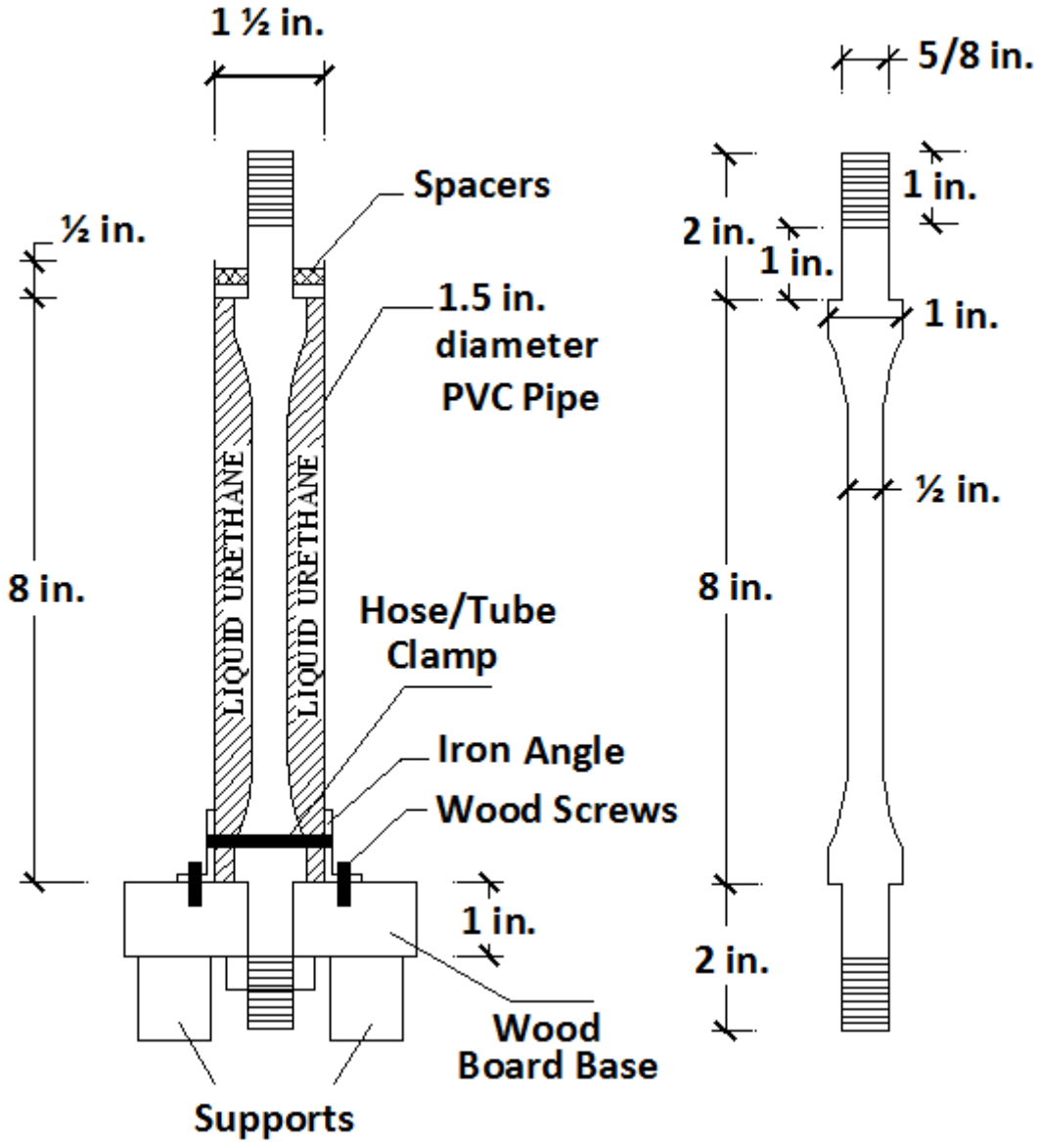

Fig. E1 - Inner Core, Bar Type C, Fabrication Set-Up, Sketch.

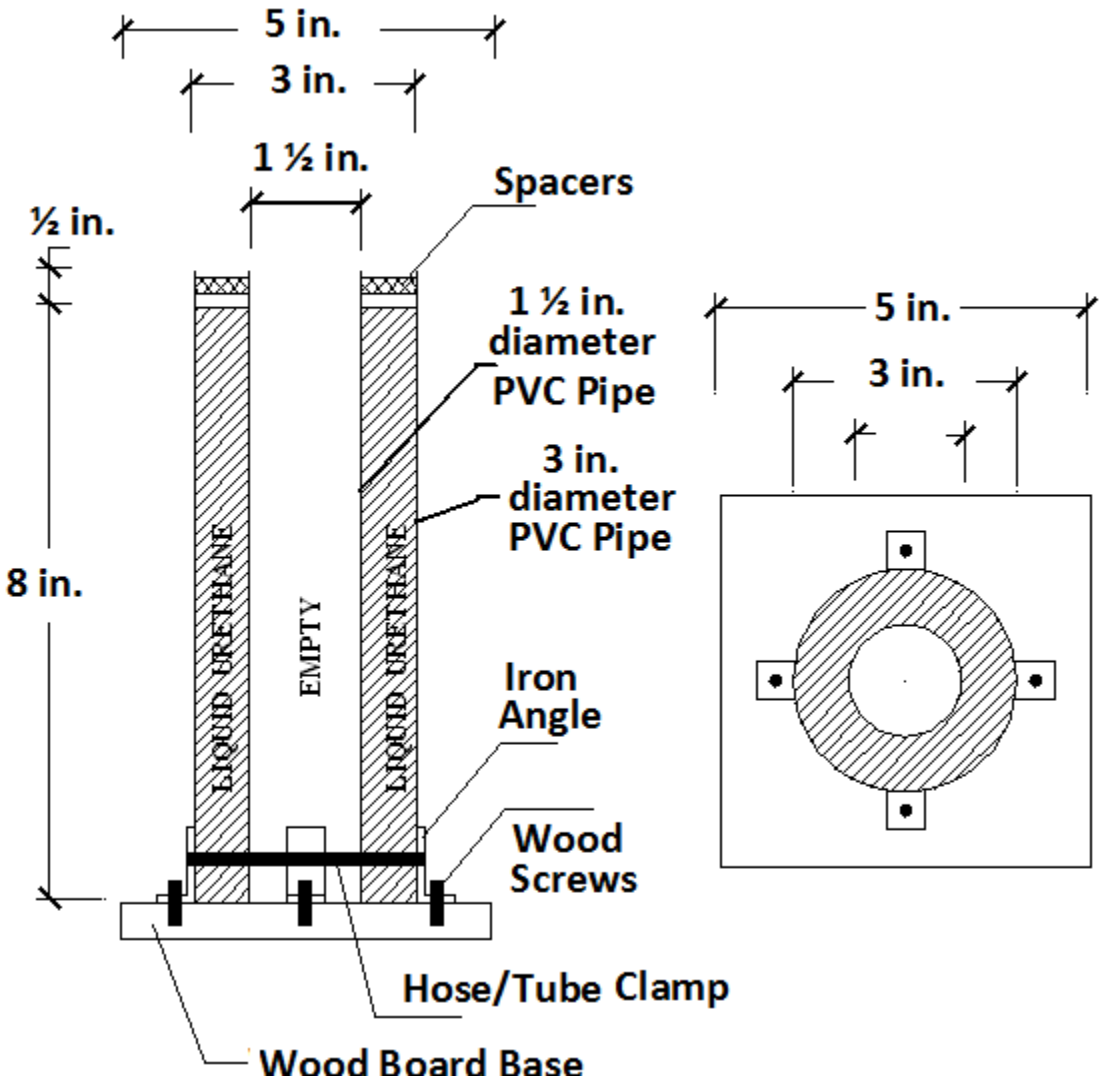

Fig. E2 - One-Bar Matrix, Bar Type C, Fabrication Set-Up, Sketch.

Fig. E3 - Inner Core, Bar type C, Fabrication Set-Up.

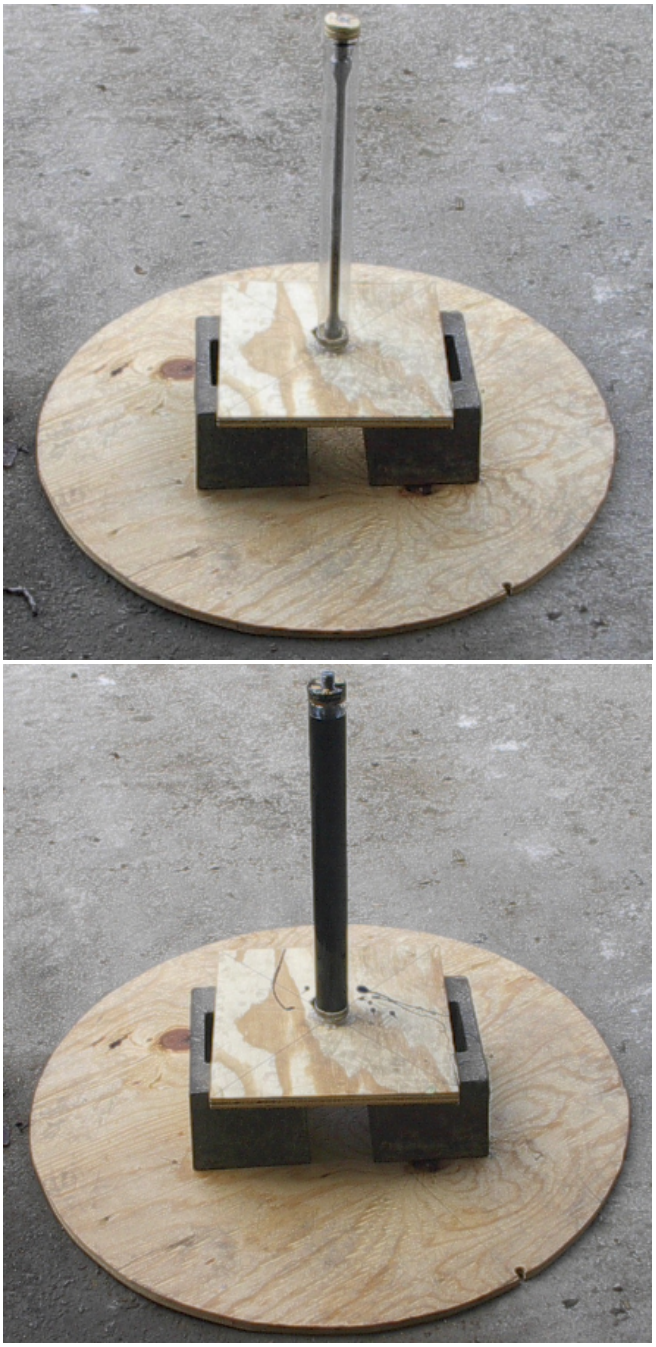

Fig. E4 - Inner Core, Bar Type B, Fabrication, before and after Pouring Castable Urethane.

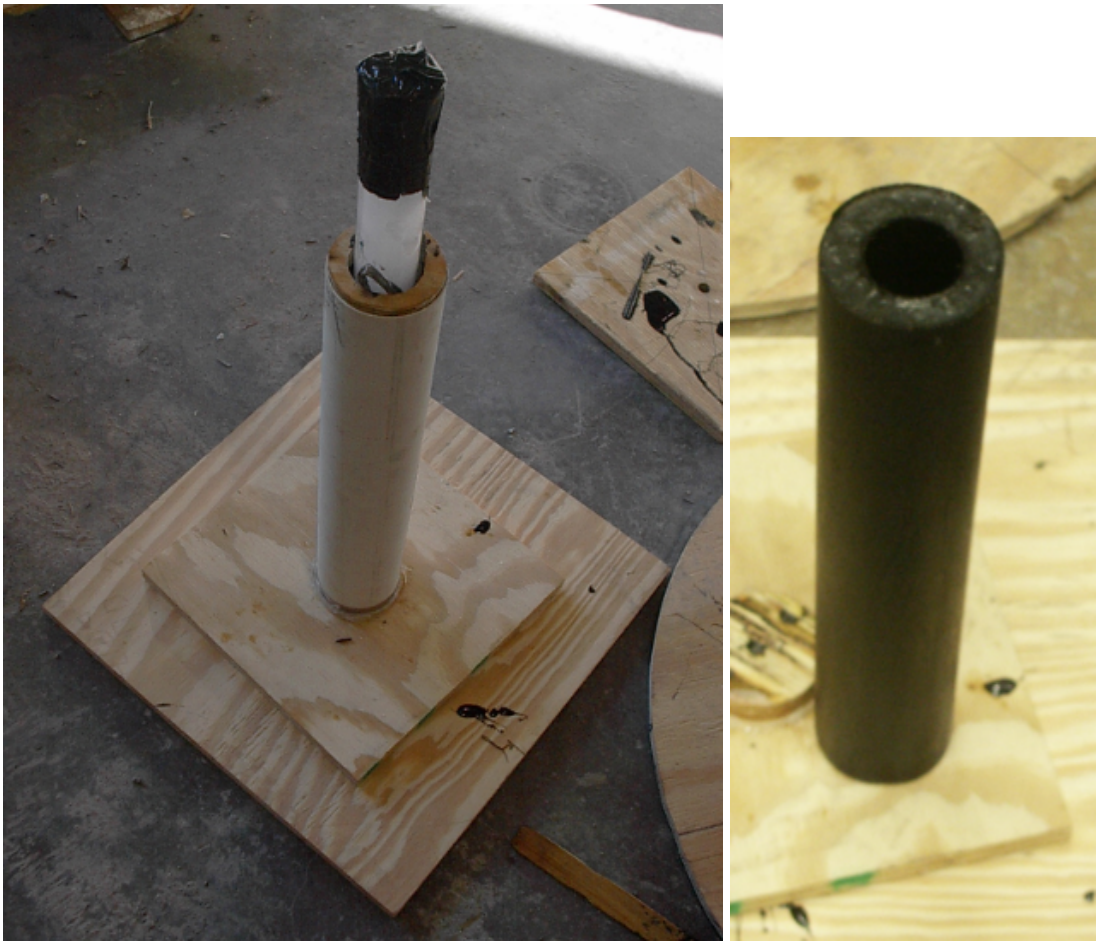

Fig. E5 - 1-Bar Matrix, Bar Type B, Fabrication.

Fig. E6 - 4-Bar Matrix, Bar Type A, Fabrication Set-Up.

Fig. E7 - 4-Bar Matrix, Bar Type A, Fabrication.

Fig. E8 - Bar Type B with Inner Core and 1-bar Matrix.

APPENDIX F – BCE, FRP-Matrix Confinement System

Fig. F1 - FRP Layer Curing in the Oven, Bar Type B.

Fig. F2 - FRP-Matrix Confining System, 1-Bar and 4-Bar Systems, Bar Type C.

Fig. F3 - 1-Bar FRP matrix Confining System, Bar Type C with Inner Core, and without Inner Core.

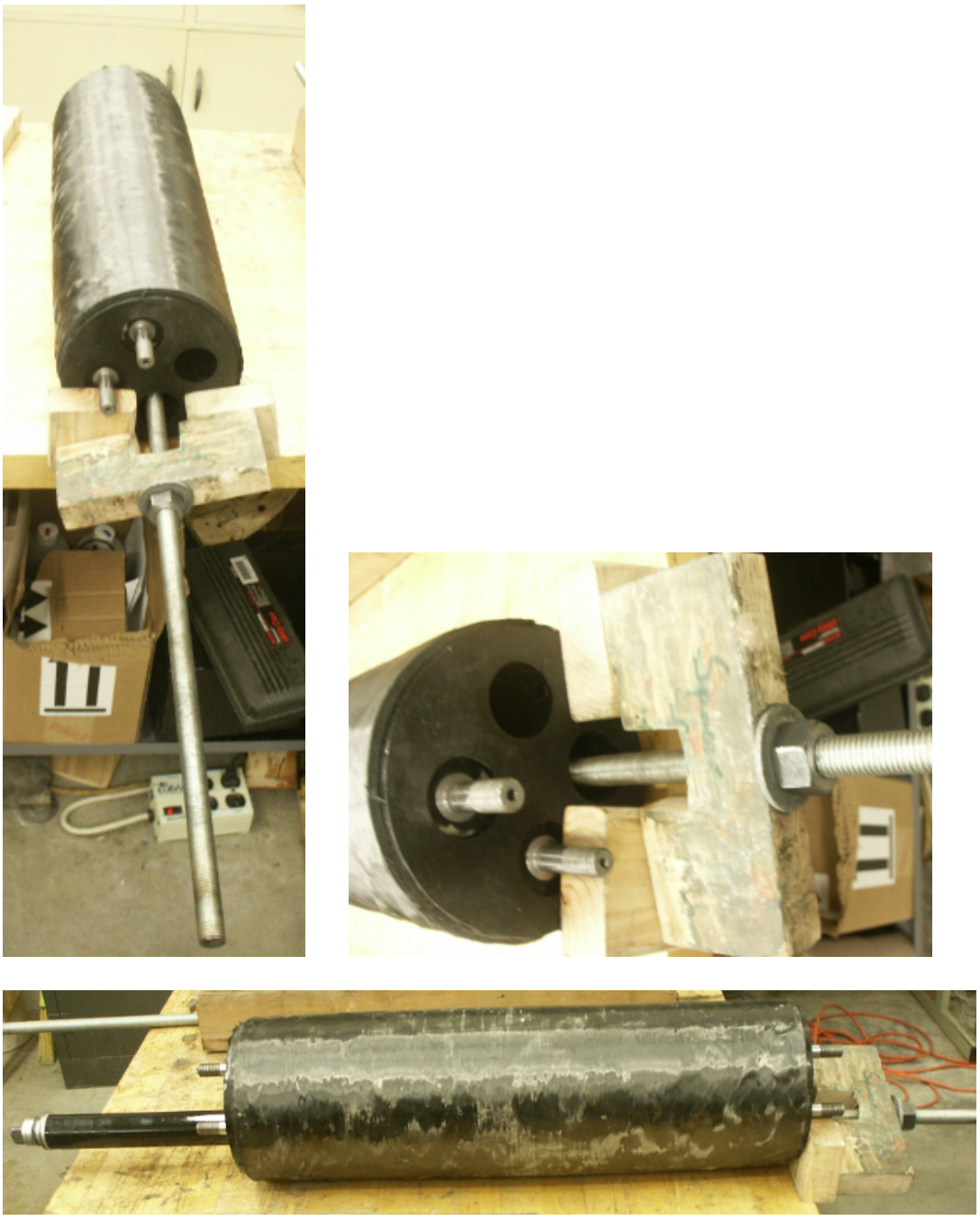

Fig. F4 - 4-Bar Fuse Assembly before Test, Bar Type A.

APPENDIX G – BCE, Loading History

Load Step	Displacement amplitude	Cycles
1	**0.0120”**	**6**
2	**0.0160”**	**6**
3	**0.0239”**	**6**
4	**0.0319”**	**4**
5	**0.0479”**	**4**
6	**0.0639”**	**2**
7	**0.0958”**	**2**
8	**0.1277”**	**2**
9	**0.1597”**	**2**
10	**0.1916”**	**2**
11	**0.2235”**	**2**
12	**0.2554”**	**2**
13	**0.2874”**	**2**
14	**0.3193”**	**1**

43 cycles total

Table G1 - Loading History, 1-Bar BCE Fuse, Bar Type A, Specimen #1, 98.70% Confinement Ratio.

Load Step	Displacement amplitude	Cycles
1	0.0120”	6
2	0.0160”	6
3	0.0239”	6
4	0.0319”	4
5	0.0479”	4
6	0.0639”	2
7	0.0958”	2
8	0.1277”	2
9	0.1597”	2
10	0.1916”	2
11	0.2235”	2
12	0.2554”	2
13	0.2874”	2
14	0.3193”	2
15	0.3512”	2
16	0.3832”	2
17	0.4151”	2
18	0.4470”	2
19	0.4790”	2

54 cycles total

Table G2 - Loading History, 1-Bar BCE Fuse, Bar Type A, Specimen #2, 95.83% Confinement Ratio.

Load Step	Displacement amplitude	Cycles
1	**0.0073”**	**6**
2	**0.0098”**	**6**
3	**0.0146”**	**6**
4	**0.0195”**	**4**
5	**0.0293”**	**4**
6	**0.0391”**	**2**
7	**0.0586”**	**2**
8	**0.0781”**	**2**
9	**0.0977”**	**2**
10	**0.1172”**	**2**
11	**0.1367”**	**2**
12	**0.1562”**	**2**
13	**0.1758”**	**1**

41 cycles total

Specimen	#3	#4	#5	#6
Confinement Ratio	97.66%	96.88%	93.75%	87.50%

Table G3 - Loading History, 1-Bar BCE Fuse, Bar Type B.

Load Step	Displacement amplitude	Cycles
1	**0.0027”**	**6**
2	**0.0036”**	**6**
3	**0.0053”**	**6**
4	**0.0071”**	**4**
5	**0.0107”**	**4**
6	**0.0143”**	**4**
7	**0.0214”**	**4**
8	**0.0285”**	**4**
9	**0.0357”**	**4**
10	**0.0428”**	**4**
11	**0.0499”**	**2**
12	**0.0570”**	**2**
13	**0.0642”**	**2**
14	**0.0713”**	**2**
15	**0.0784”**	**2**
16	**0.0856”**	**2**
17	**0.0927”**	**2**
18	**0.0998”**	**2**
19	**0.1070”**	**2**
20	**0.1141”**	**2**
21	**0.1212”**	**2**
22	**0.1283”**	**2**
23	**0.1355”**	**2**
24	**0.1426”**	**2**
25	**0.1497”**	**2**
26	**0.1569”**	**1**

77 cycles total

Specimen	#7	#8	#9	#10
Confinement Ratio	96.88%	93.75%	87.50%	75.00%

Table G4 - Loading History, 1-Bar BCE Fuse, Bar Type C.

Load Step	Displacement amplitude	Cycles
1	**0.0120”**	**6**
2	**0.0160”**	**6**
3	**0.0239”**	**6**
4	**0.0319”**	**4**
5	**0.0479”**	**4**
6	**0.0639”**	**2**
7	**0.0958”**	**2**
8	**0.1277”**	**2**
9	**0.1597”**	**2**
10	**0.1916”**	**2**
11	**0.2235”**	**2**
12	**0.2554”**	**2**
13	**0.2874”**	**2**
14	**0.3193”**	**2**
15	**0.3512”**	**2**
16	**0.3832”**	**2**
17	**0.4151”**	**2**

50 cycles total

Specimen	#11	#12
Load	Concentric	Eccentric

Table G5 - Loading History, 4-Bar BCE Fuse, Bar Type A, 98.96% Confinement.

Load Step	Displacement amplitude	Cycles
1	**0.0120”**	**6**
2	**0.0160”**	**6**
3	**0.0239”**	**6**
4	**0.0319”**	**4**
5	**0.0479”**	**4**
6	**0.0639”**	**2**
7	**0.0958”**	**2**
8	**0.1277”**	**2**
9	**0.1597”**	**2**
10	**0.1916”**	**2**
11	**0.2235”**	**2**
12	**0.2554”**	**2**
13	**0.2874”**	**2**
14	**0.3193”**	**2**
15	**0.3512”**	**2**
16	**0.3832”**	**1**

47 cycles total

Table G6 - Loading History, 4-Bar BCE Fuse, Bar Type A, Specimen #13,

Concentric Load, 97.92% Confinement Ratio.

Load Step	Displacement amplitude	Cycles
1	0.0073”	6
2	0.0098”	6
3	0.0146”	6
4	0.0195”	4
5	0.0293”	4
6	0.0391”	2
7	0.0586”	2
8	0.0781”	2
9	0.0977”	2
10	0.1172”	2
11	0.1367”	2
12	0.1562”	2
13	0.1758”	2
14	0.1953”	2
15	0.2148”	2
16	0.2344”	2
17	0.2539”	2
18	0.2734”	1

51 cycles total

Table G7 - Loading History, 4-Bar BCE Fuse, Bar Type B, Specimen #14,

Concentric Load, 98.44% Confinement Ratio.

Load Step	Displacement amplitude	Cycles
1	**0.0073”**	**6**
2	**0.0098”**	**6**
3	**0.0146”**	**6**
4	**0.0195”**	**4**
5	**0.0293”**	**4**
6	**0.0391”**	**2**
7	**0.0586”**	**2**
8	**0.0781”**	**2**
9	**0.0977”**	**2**
10	**0.1172”**	**2**
11	**0.1367”**	**2**
12	**0.1562”**	**2**
13	**0.1758”**	**2**
14	**0.1953”**	**2**
15	**0.2148”**	**2**
16	**0.2344”**	**2**
17	**0.2539”**	**2**
18	**0.2734”**	**2**
19	**0.2930”**	**2**
20	**0.3125”**	**2**
21	**0.3515”**	**2**
22	**0.3906”**	**2**
23	**0.4297”**	**1**

61 cycles total

Specimen	#15	#16
Confinement Ratio	98.44%	93.75%
Load	Eccentric	Concentric

Table G8 - Loading History, 4-Bar BCE Fuse, Bar Type B.

Load Step	Displacement amplitude	Cycles
1	**0.0052”**	**6**
2	**0.0069”**	**6**
3	**0.0104”**	**6**
4	**0.0138”**	**4**
5	**0.0207”**	**4**
6	**0.0276”**	**4**
7	**0.0414”**	**2**
8	**0.0552”**	**2**
9	**0.0690”**	**2**
10	**0.0828”**	**2**
11	**0.0966”**	**2**
12	**0.1104”**	**2**
13	**0.1242”**	**2**
14	**0.1380”**	**2**
15	**0.1518”**	**2**
16	**0.1656”**	**2**
17	**0.1932”**	**2**
18	**0.2208”**	**2**
19	**0.2484”**	**2**
20	**0.2760”**	**2**
21	**0.3036”**	**2**
22	**0.3312”**	**2**
23	**0.3588”**	**2**
24	**0.3864”**	**2**

66 cycles total

Specimen	#17	#18
Load	Concentric	Eccentric

Table G9 - Loading History, 4-Bar BCE Fuse, Bar Type C, 96.87% Confinement.

Load Step	Displacement amplitude	Cycles
1	0.0052”	6
2	0.0069”	6
3	0.0104”	6
4	0.0138”	4
5	0.0207”	4
6	0.0276”	4
7	0.0414”	2
8	0.0552”	2
9	0.0690”	2
10	0.0828”	2
11	0.0966”	2
12	0.1104”	2
13	0.1242”	2
14	0.1380”	2
15	0.1518”	2
16	0.1656”	2
17	0.1932”	2
18	0.2208”	2
19	0.2484”	2
20	0.2760”	2
21	0.3036”	2
22	0.3312”	2
23	0.3588”	2
24	0.3864”	2
25	0.4140”	2
26	0.4500”	2
27	0.5000”	1

71 cycles total

Table G10 - Loading History, 4-Bar BCE Fuse, Bar Type C, Specimen #19,

Concentric Load, 91.41% Confinement Ratio.

APPENDIX H – BCE, Specimens During Tests

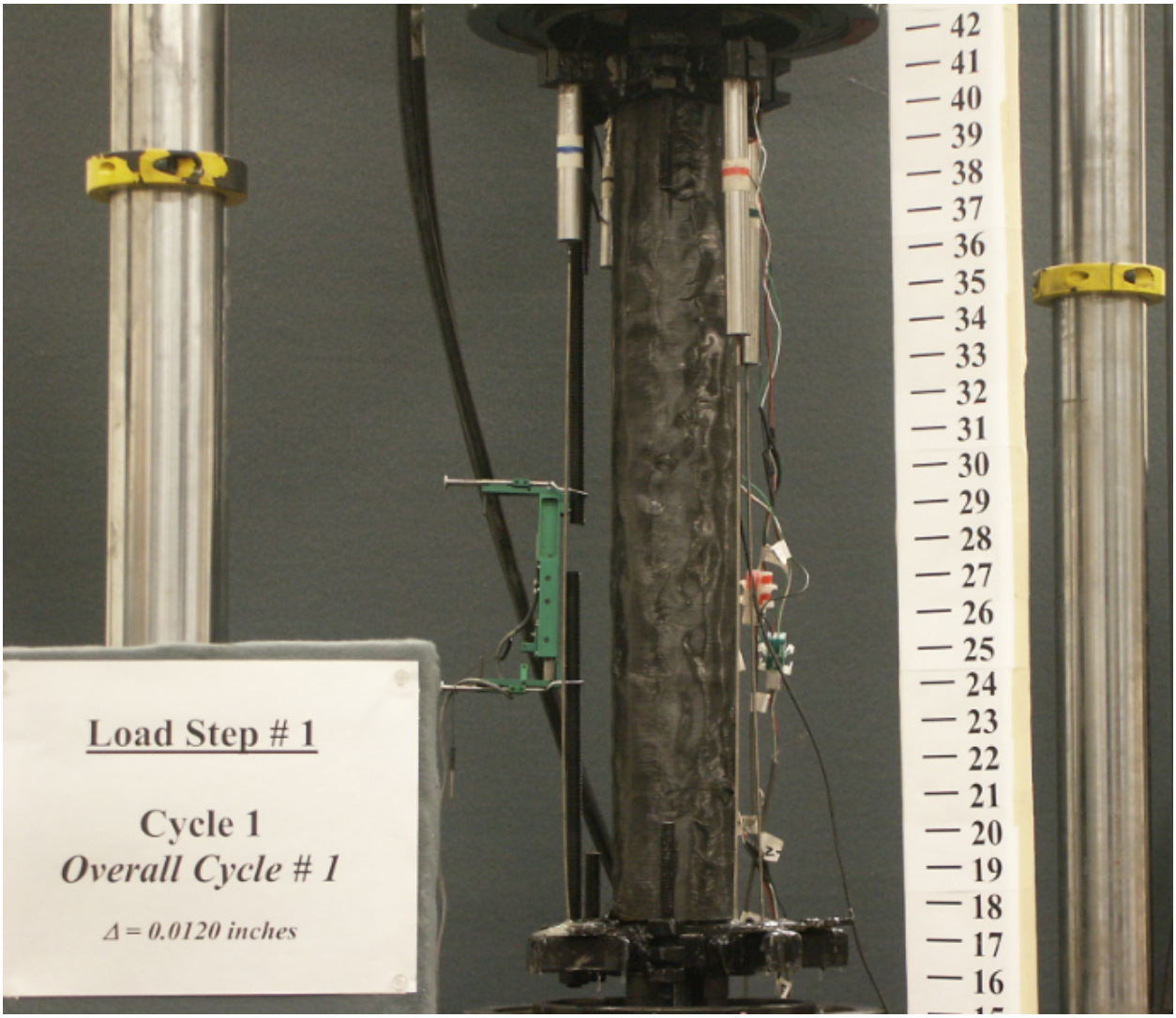

Fig. H1 - 1-Bar Fuse, Bar Type A, Confinement Ratio 98.70%, Specimen #1, First Cycle.

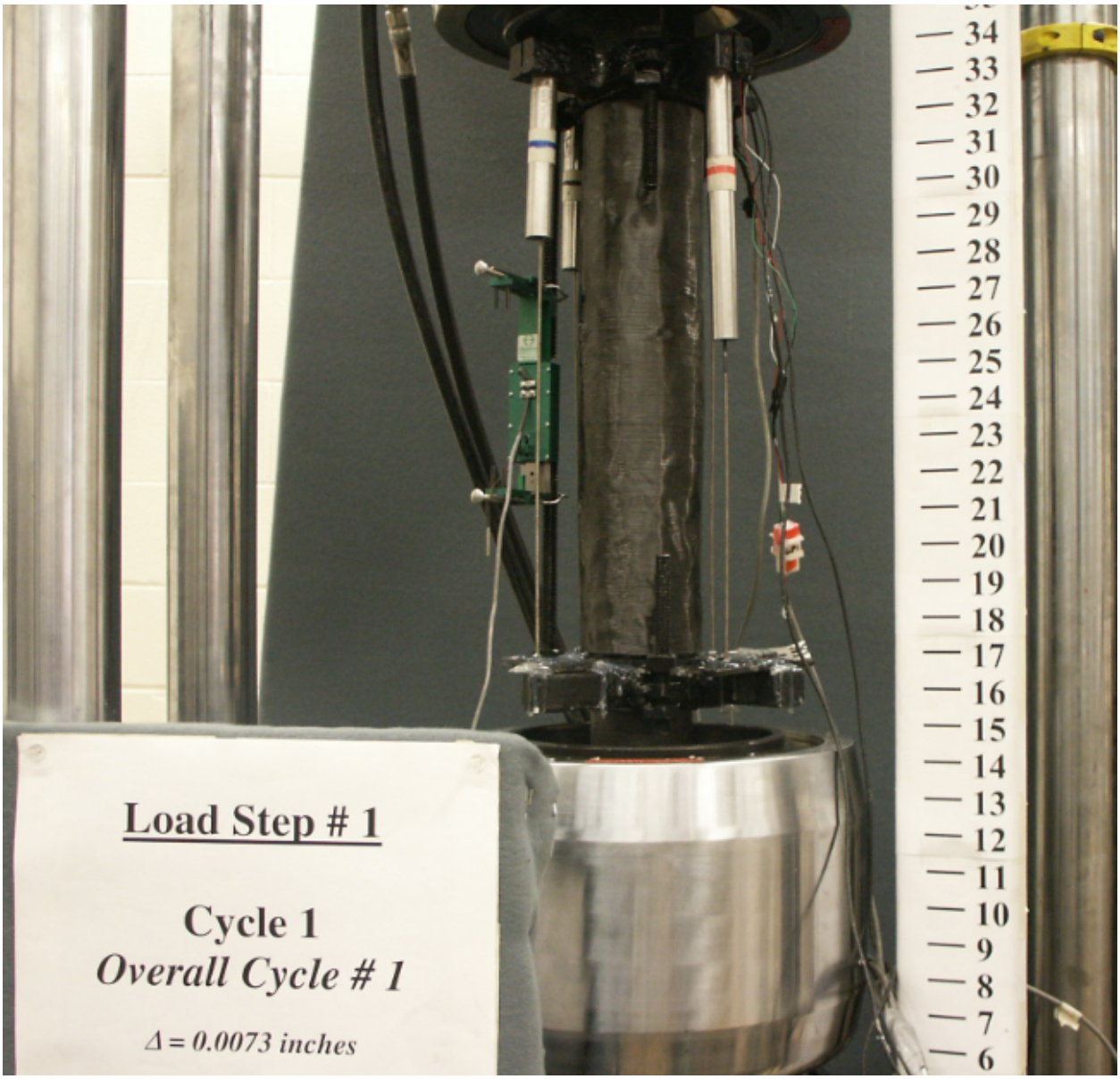

Fig. H2 - 1-Bar Fuse, Bar Type B, Confinement Ratio 97.66%, Specimen #3, First Cycle.

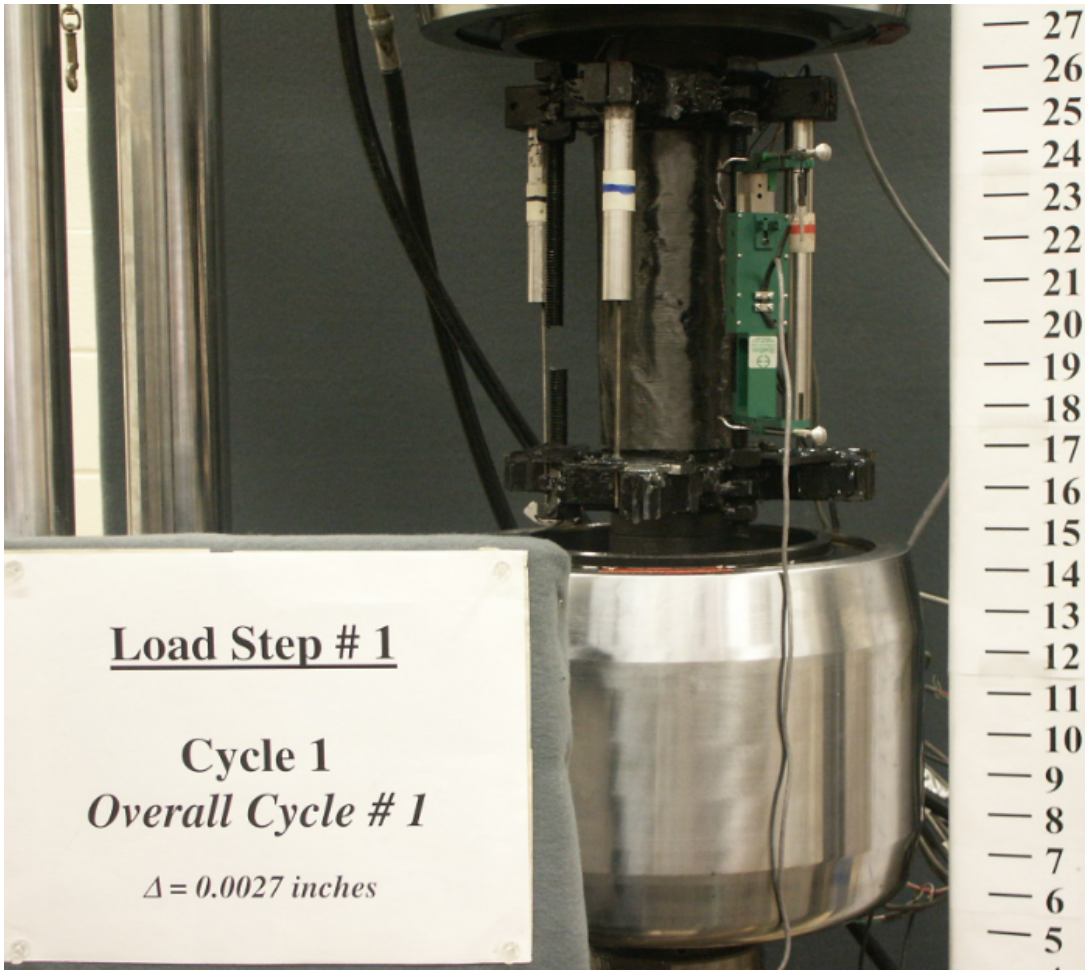

Fig. H3 - 1-Bar Fuse, Bar Type C, Confinement Ratio 97.88%, Specimen #12, First Cycle.

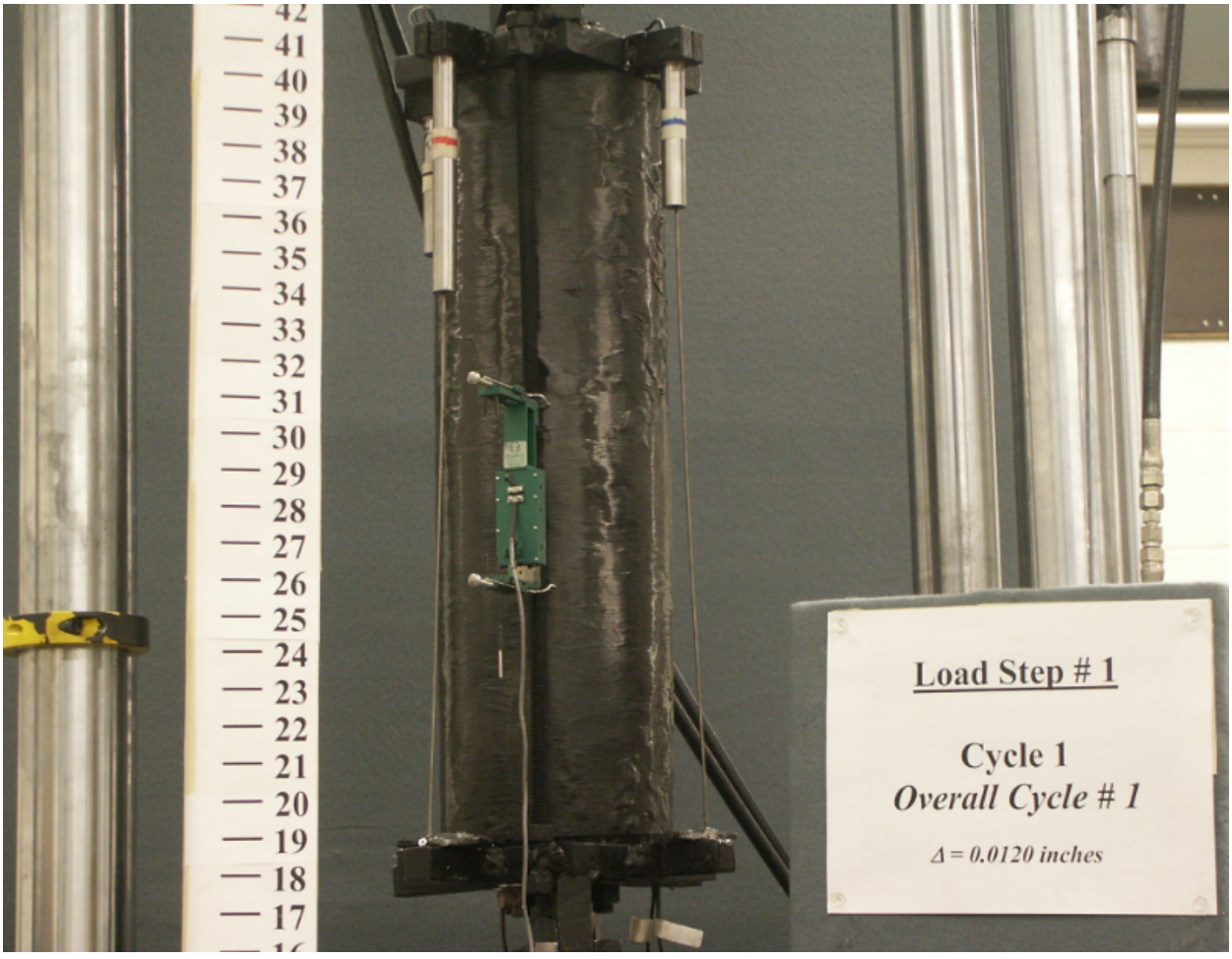

Fig. H4 - 4-Bar Fuse, Bar Type A, Confinement Ratio 98.96%, Specimen #11, First Cycle, Concentric Load.

Fig. H5 - 4-Bar Fuse, Bar Type A, Confinement Ratio 98.96%, Specimen #11, Tension Cycle #50, Concentric Load.

Fig. H6 - 4-Bar Fuse, Bar Type A, Confinement Ratio 98.96%, Specimen #11, Compression Cycle #50, Concentric Load.

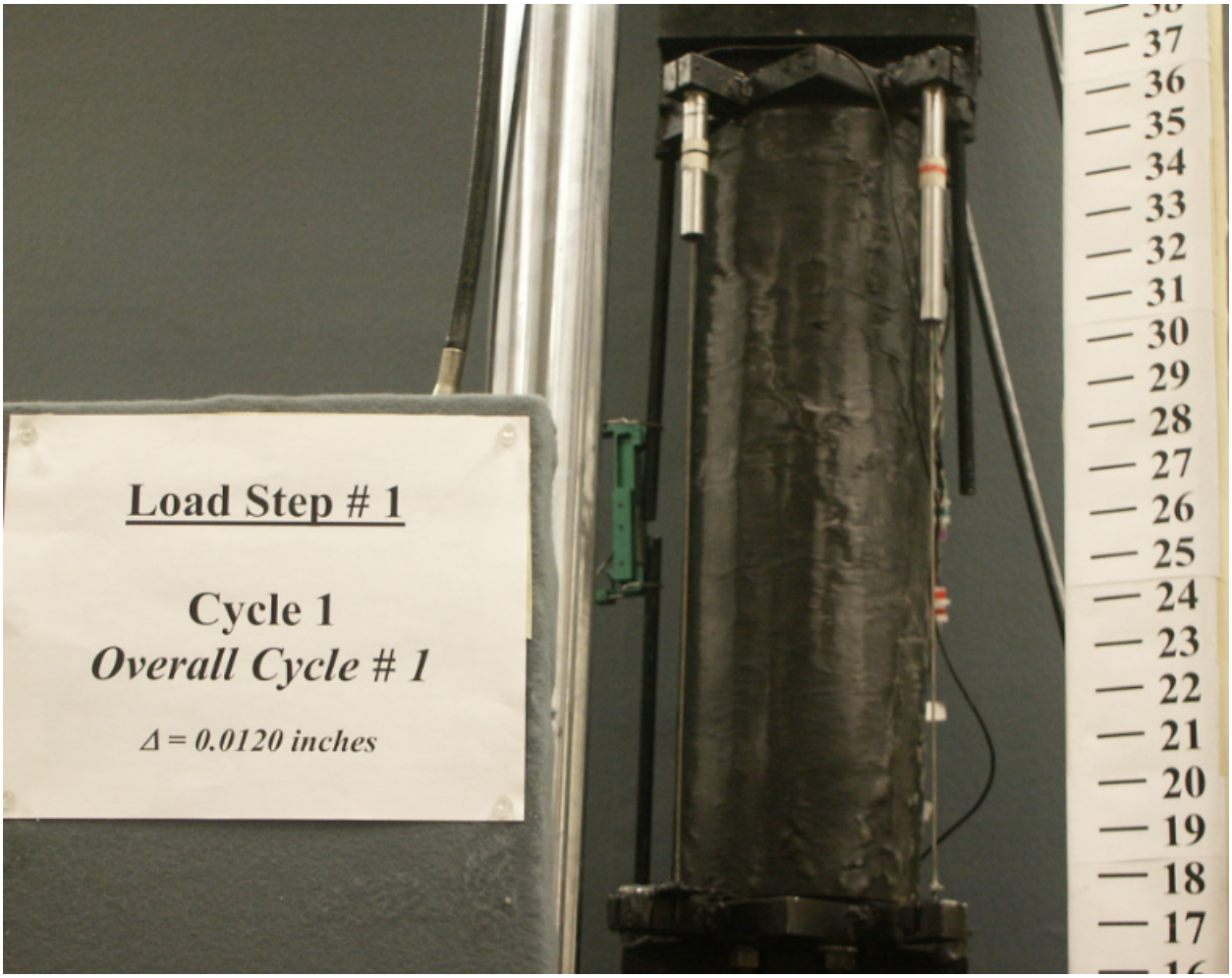

Fig. H7 - 4-Bar Fuse, Bar Type A, Confinement Ratio 98.96%, Specimen #12, First Cycle, Eccentric Load.

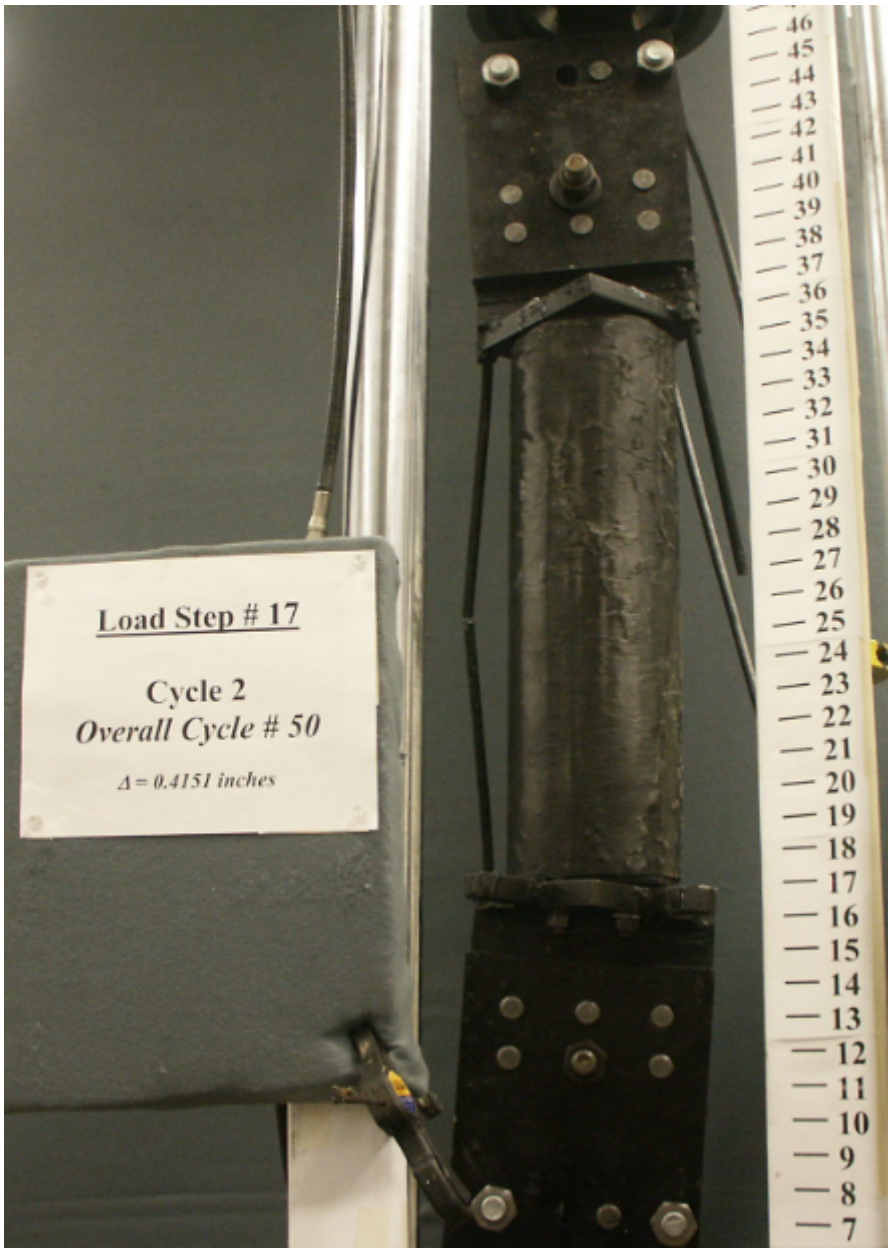

Fig. H8 - 4-Bar Fuse, Bar Type A, Confinement Ratio 98.96%, Specimen #12, Tension Cycle #50, Eccentric Load.

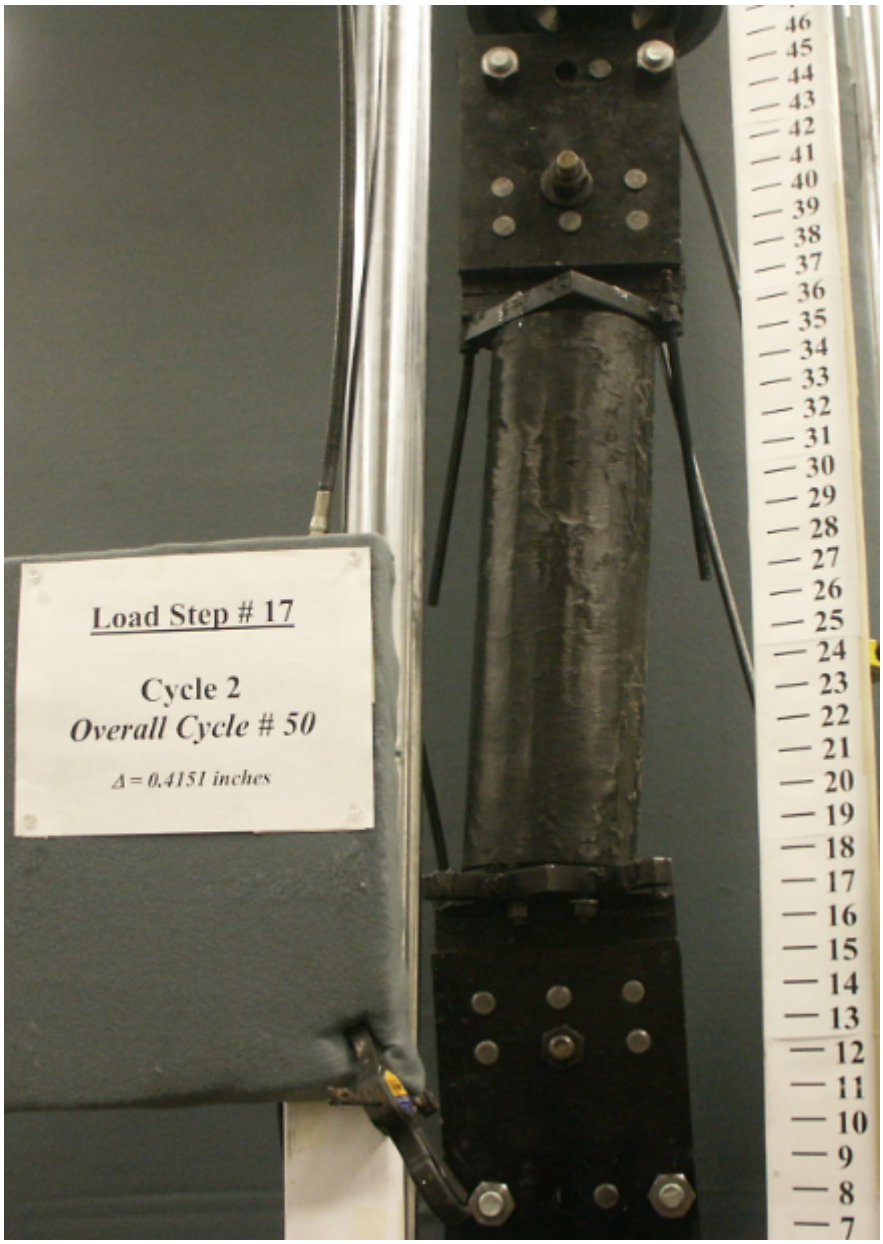

Fig. H9 - 4-Bar Fuse, Bar Type A, Confinement Ratio 98.96%, Specimen #12, Compression Cycle #50, Eccentric Load.

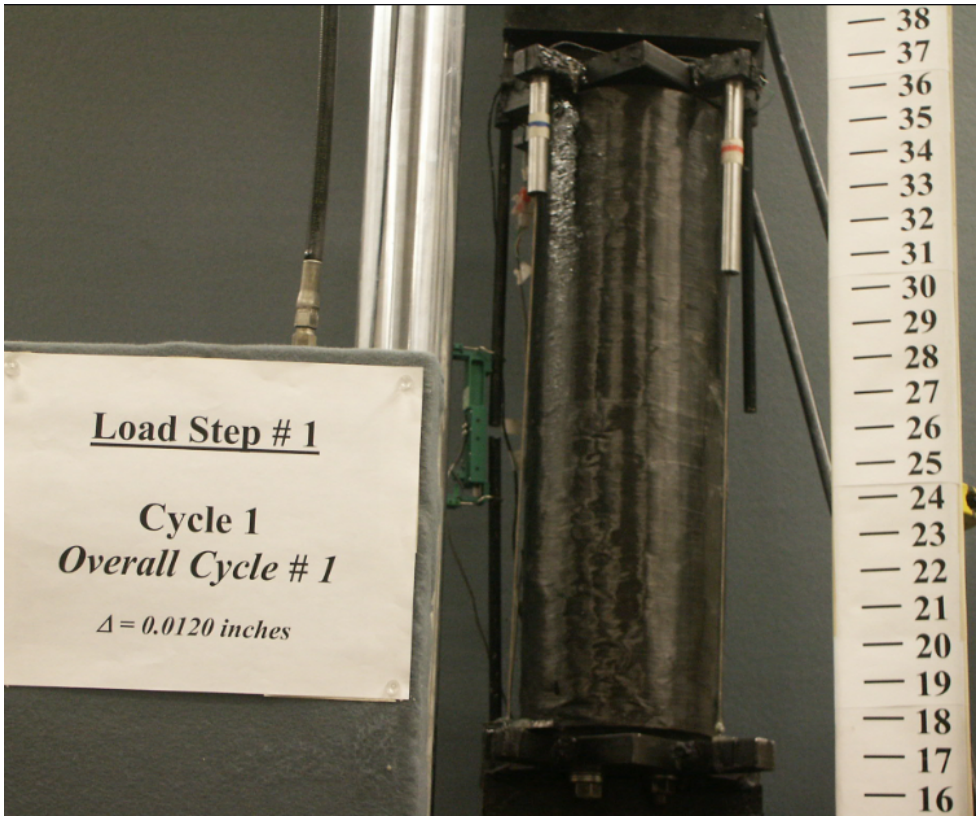

Fig. H10 - 4-Bar Fuse, Bar Type A, Confinement Ratio 97.92%, Specimen #13, First Cycle, Concentric Load.

\

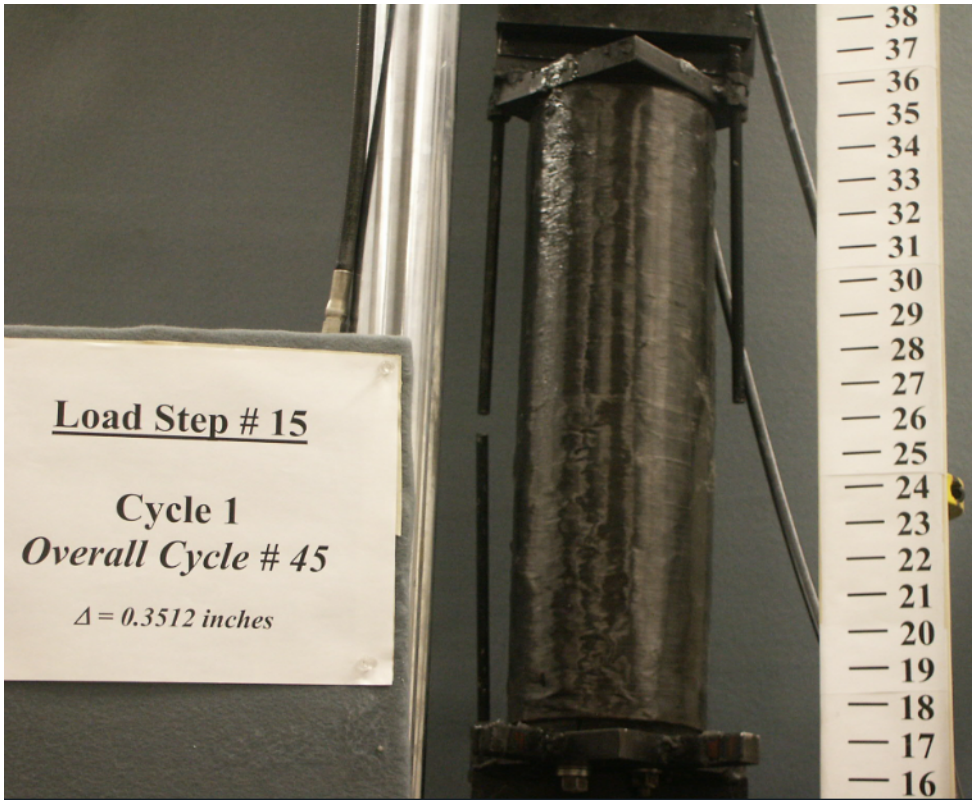

Fig. H11 - 4-Bar Fuse, Bar Type A, Confinement Ratio 97.92%, Specimen #13, Tension Cycle #45, Concentric Load.

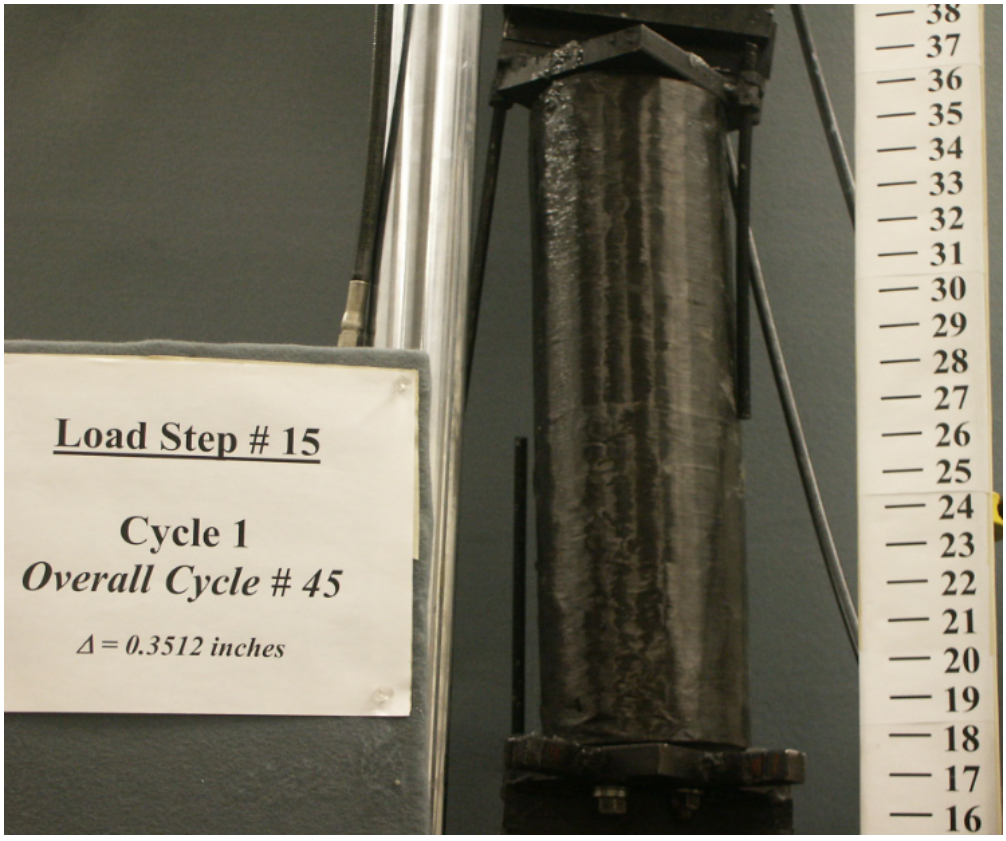

Fig. H12 - 4-Bar Fuse, Bar Type A, Confinement Ratio 97.92%, Specimen #13, Compression Cycle #45, Concentric Load.

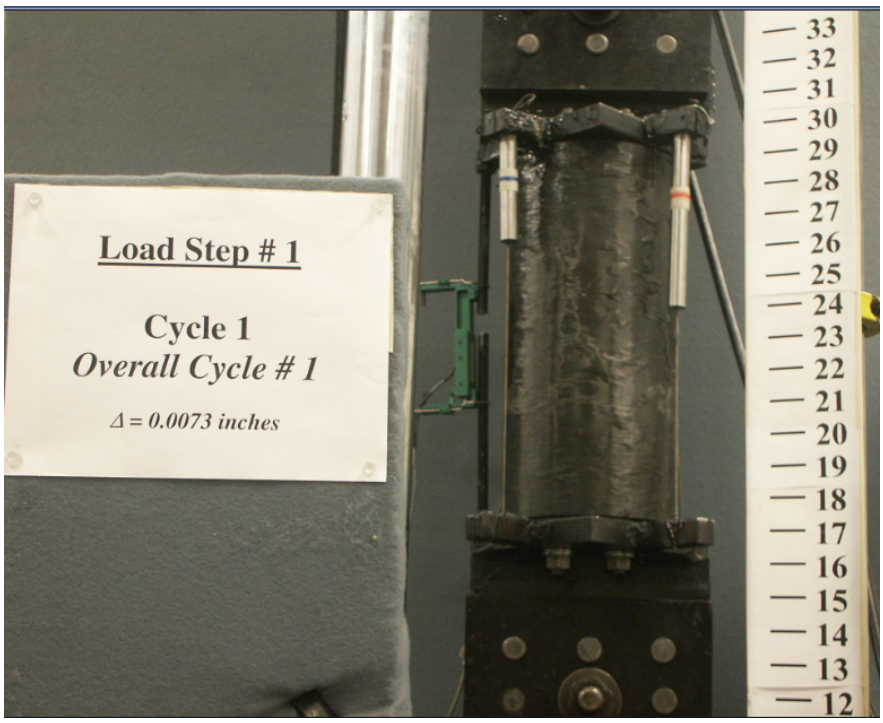

Fig. H13 - 4-Bar Fuse, Bar Type B, Confinement Ratio 98.44%, Specimen #14, First Cycle, Concentric Load.

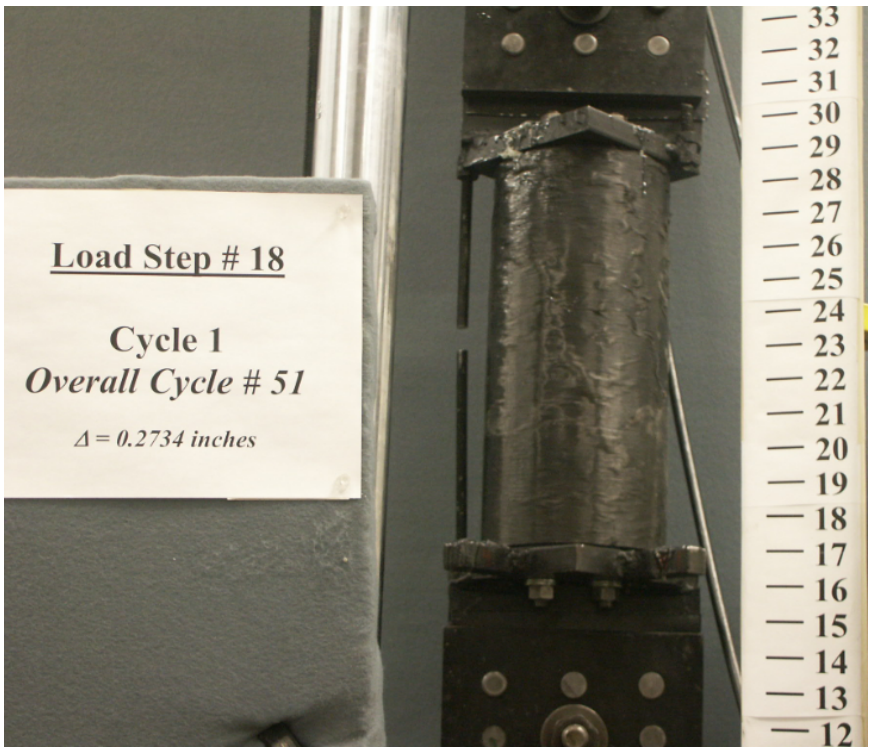

Fig. H14 - 4-Bar Fuse, Bar Type B, Confinement Ratio 98.44%, Specimen #14, Tension Cycle #51, Concentric Load.

Fig. H15 - 4-Bar Fuse, Bar Type B, Confinement Ratio 98.44%, Specimen #14, Compression Cycle #51, Concentric Load.

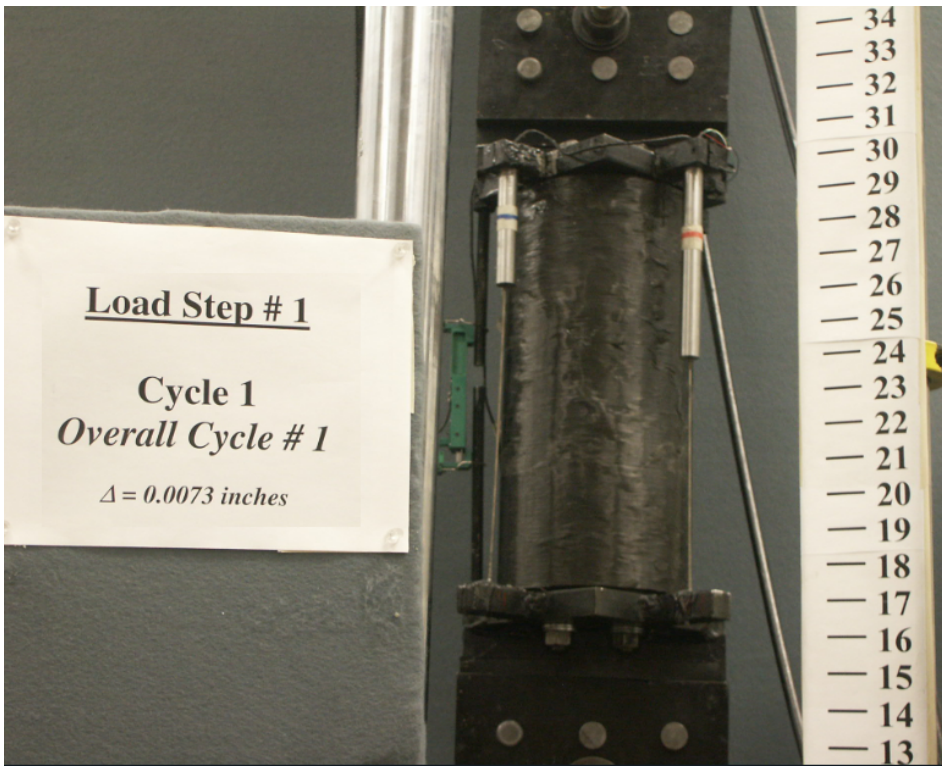

Fig. H16 - 4-Bar Fuse, Bar Type B, Confinement Ratio 98.44%, Specimen #15, First Cycle, Eccentric Load.

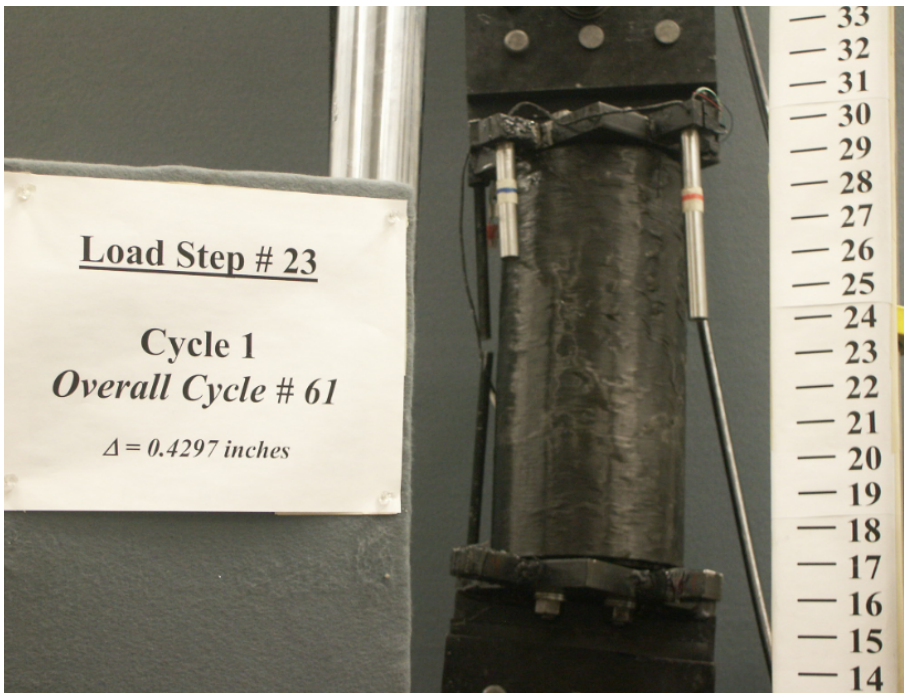

Fig. H17 - 4-Bar Fuse, Bar Type B, Confinement Ratio 98.44%, Specimen #15, Tension Cycle #61, Eccentric Load.

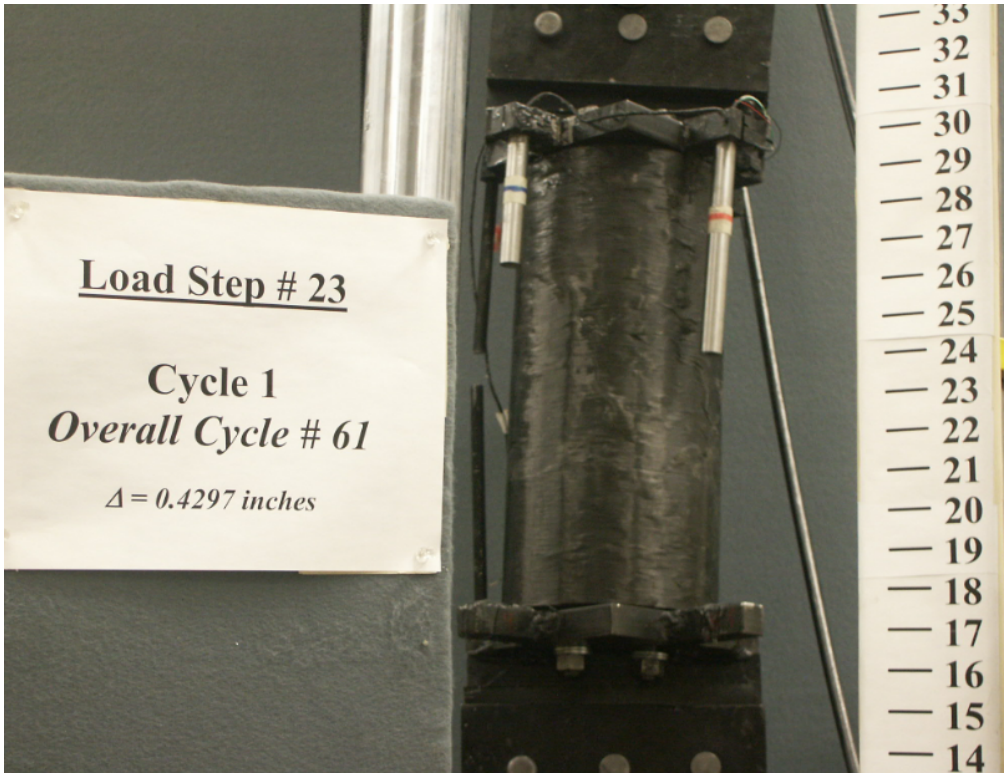

Fig. H18 - 4-Bar Fuse, Bar Type B, Confinement Ratio 98.44%, Specimen #15, Compression Cycle #61, Eccentric Load.

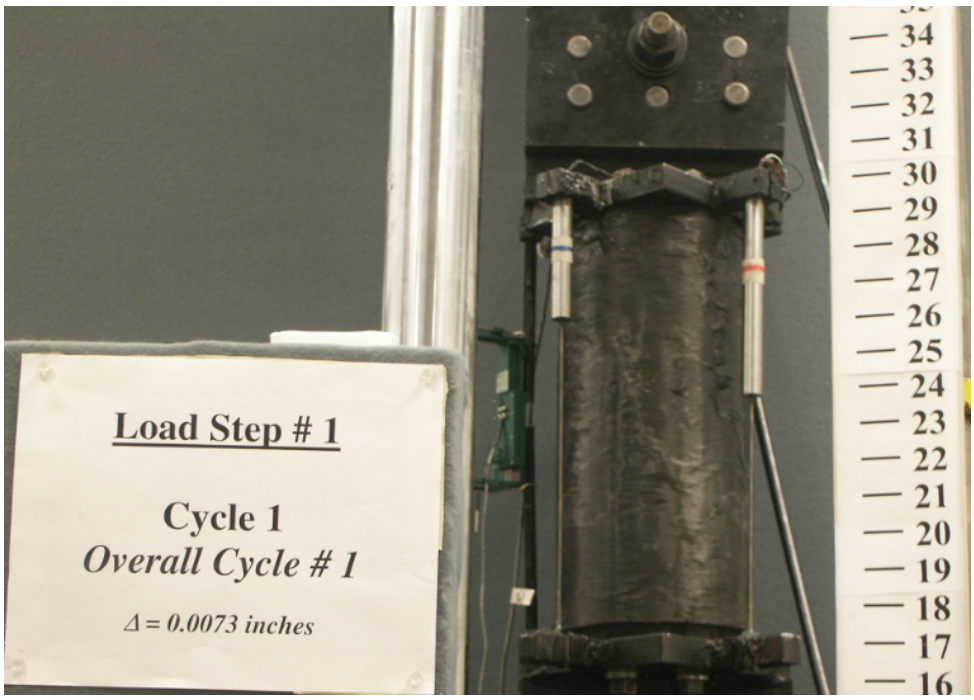

Fig. H19 - 4-Bar Fuse, Bar Type B, Confinement Ratio 93.75%, Specimen #16, First Cycle, Concentric Load.

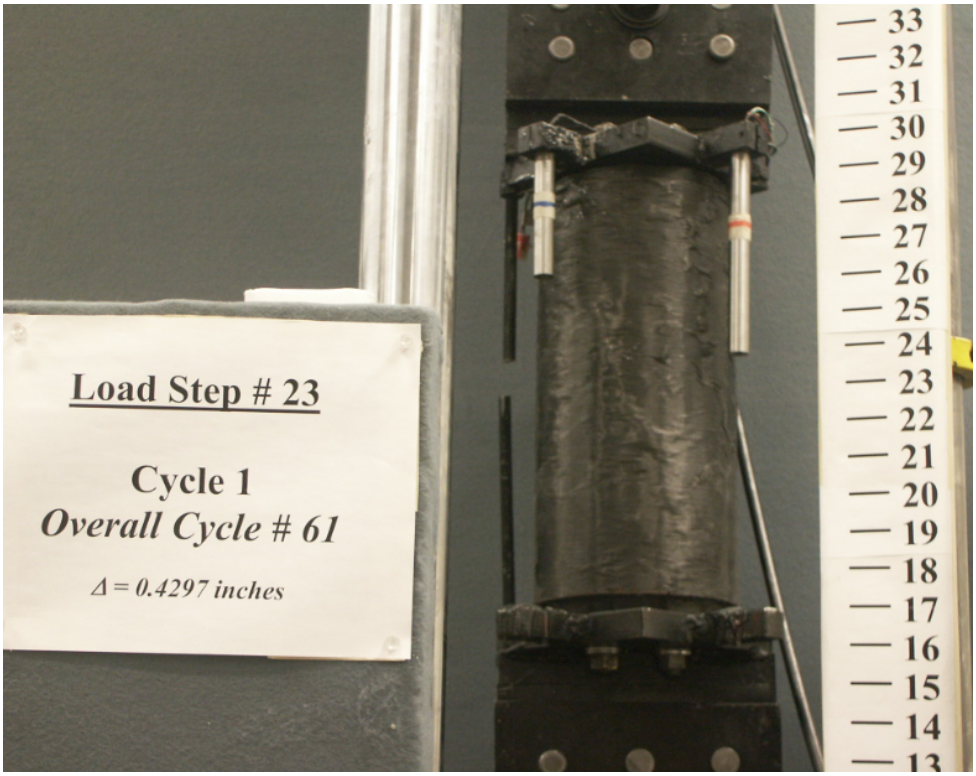

Fig. H20 - 4-Bar Fuse, Bar Type B, Confinement Ratio 93.75%, Specimen #16, Tension Cycle #61, Concentric Load.

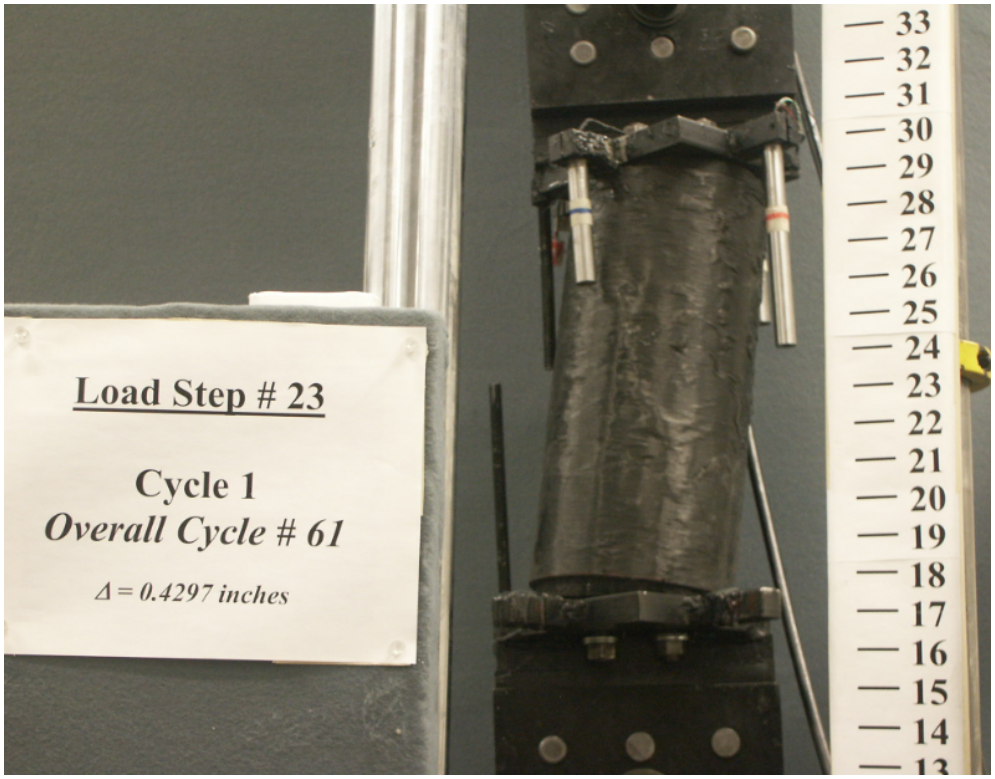

Fig. H21 - 4-Bar Fuse, Bar Type B, Confinement Ratio 93.75%, Specimen #16, Compression Cycle #61, Concentric Load.

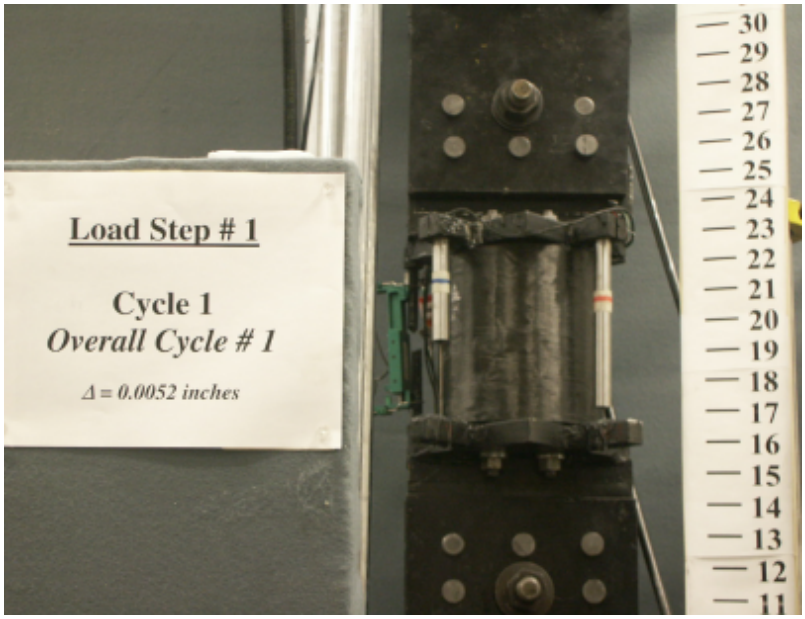

Fig. H22 - 4-Bar Fuse, Bar Type C, Confinement Ratio 96.87%, Specimen #17, First Cycle, Concentric Load.

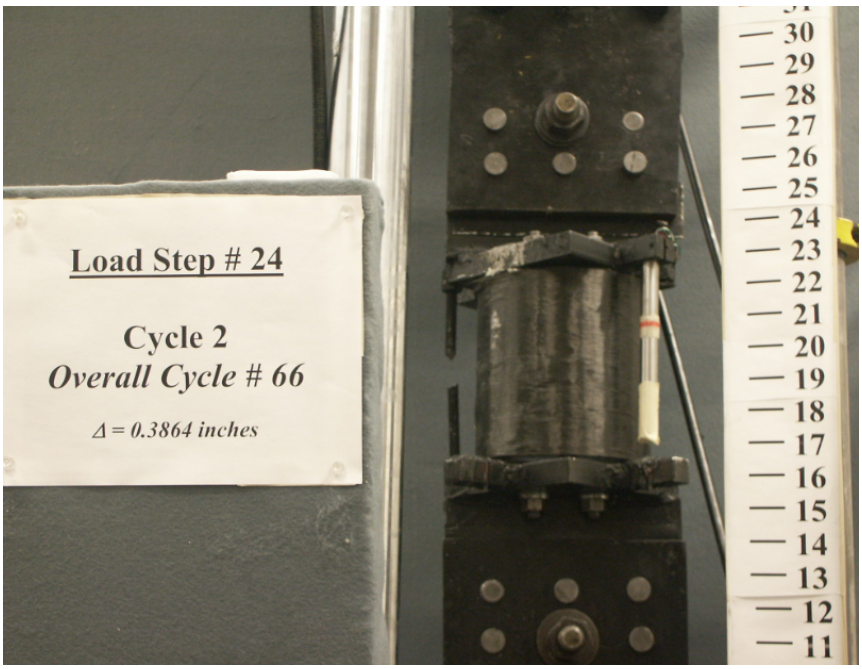

Fig. H23 - 4-Bar Fuse, Bar Type C, Confinement Ratio 96.87%, Specimen #17, Tension Cycle #66, Concentric Load.

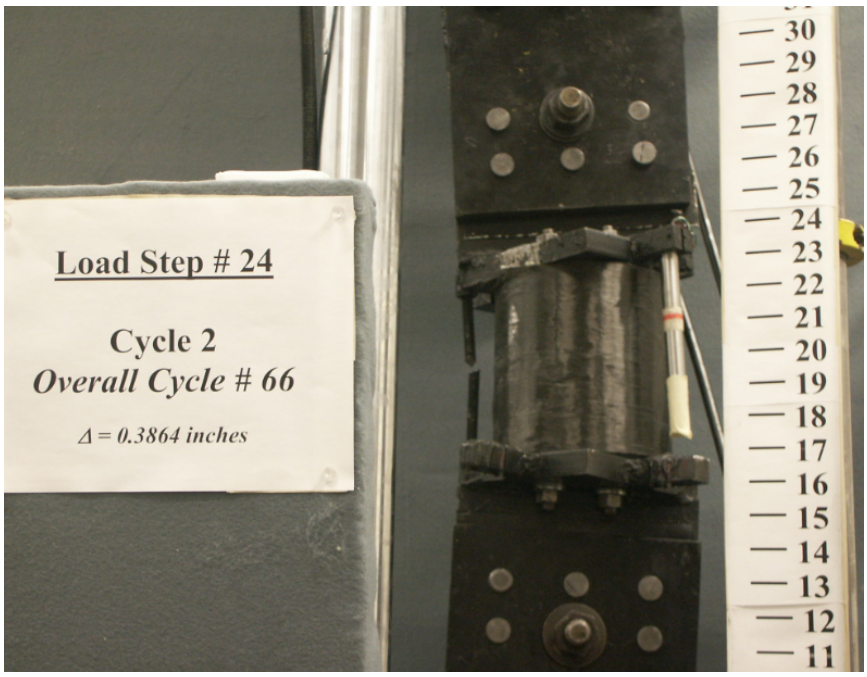

Fig. H24 - 4-Bar Fuse, Bar Type C, Confinement Ratio 96.87%, Specimen #17, Compression Cycle #66, Concentric Load.

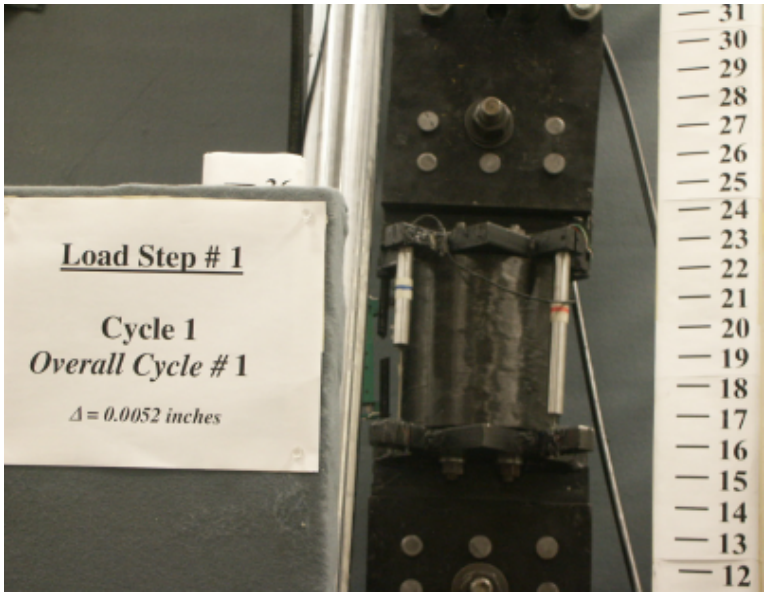

Fig. H25 - 4-Bar Fuse, Bar Type C, Confinement Ratio 96.87%, Specimen #18, First Cycle, Eccentric Load.

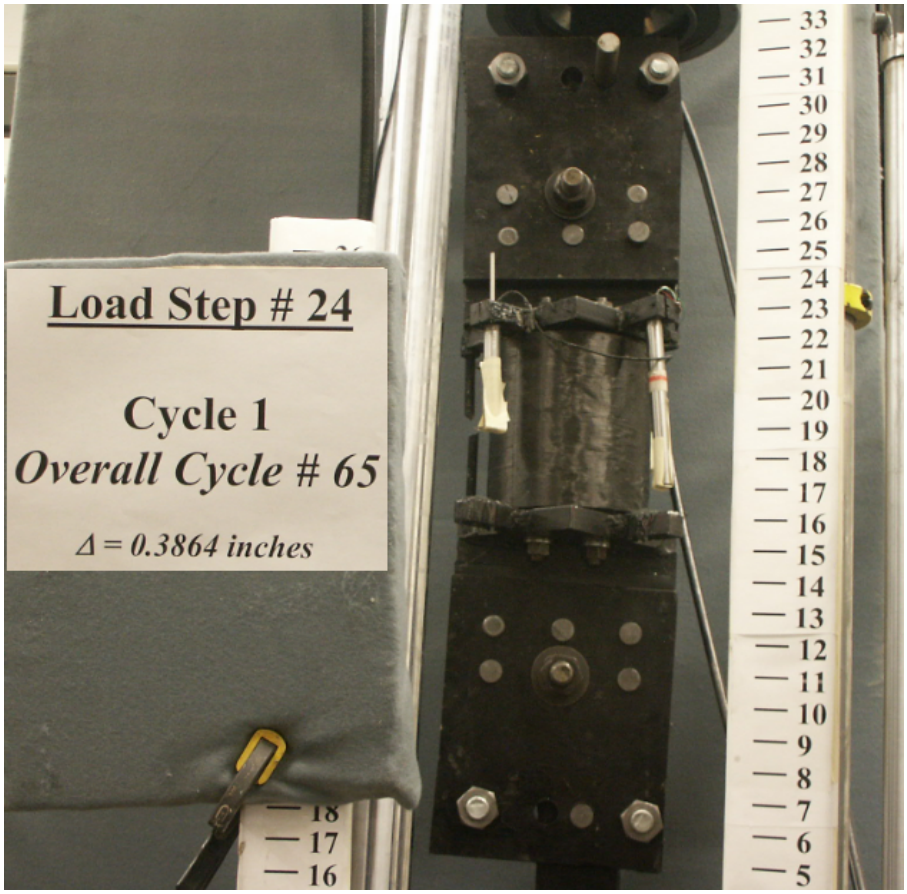

Fig. H26- 4-Bar Fuse, Bar Type C, Confinement Ratio 96.87%, Specimen #18, Tension Cycle #65, Eccentric Load.

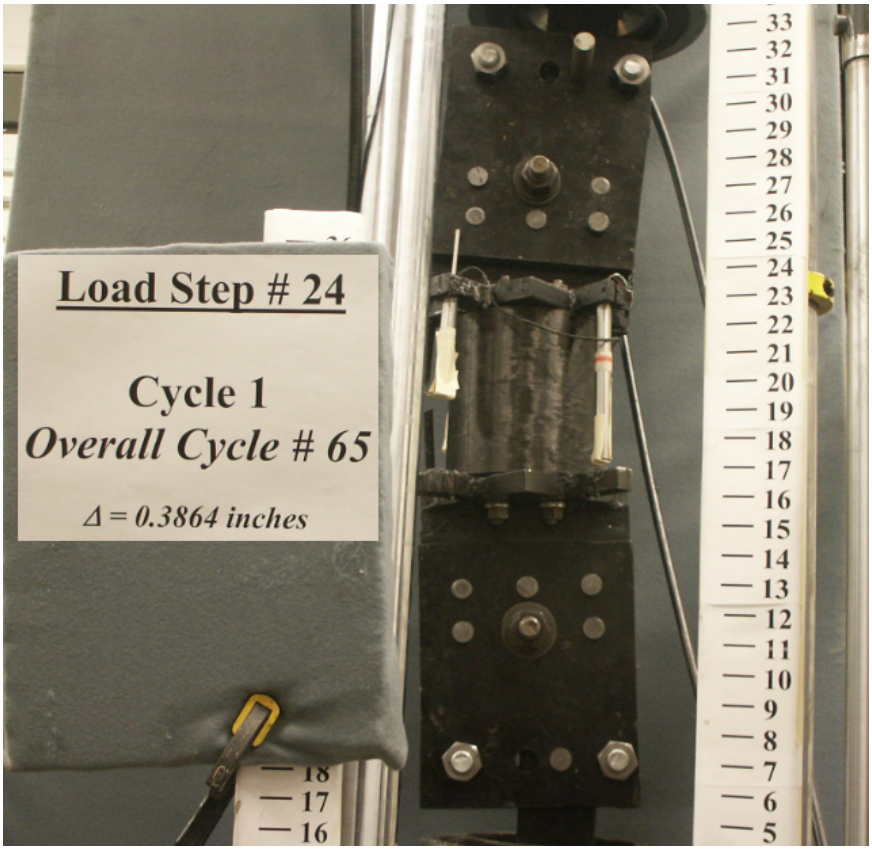

Fig. H27 - 4-Bar Fuse, Bar Type C, Confinement Ratio 96.87%, Specimen #18, Compression Cycle #65, Eccentric Load.

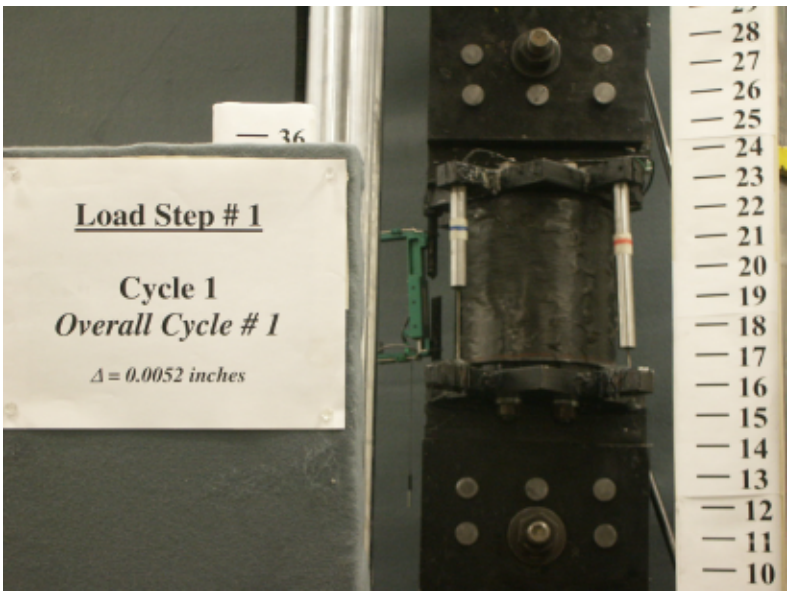

Fig. H28 - 4-Bar Fuse, Bar Type C, Confinement Ratio 91.41%, Specimen #19, First Cycle, Concentric Load.

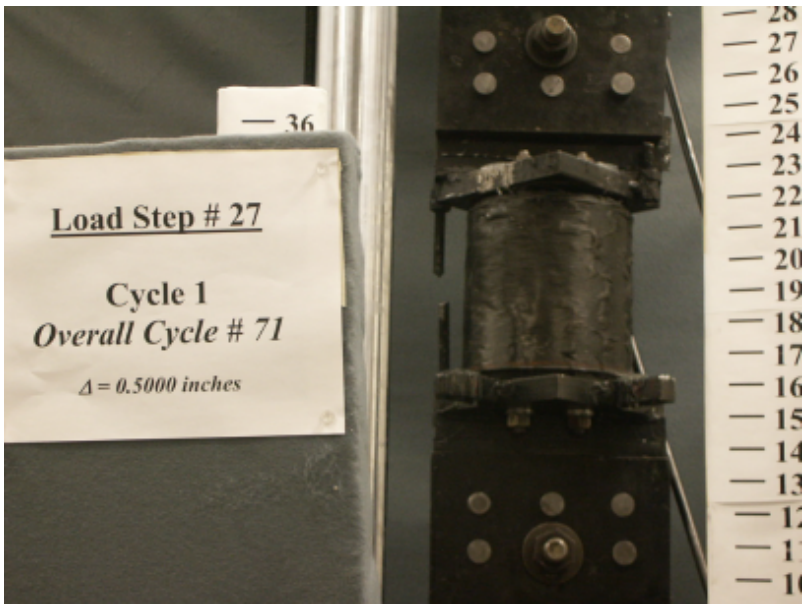

Fig. H29 - 4-Bar Fuse, Bar Type C, Confinement Ratio 91.41%, Specimen #19, Tension Cycle #71, Concentric Load.

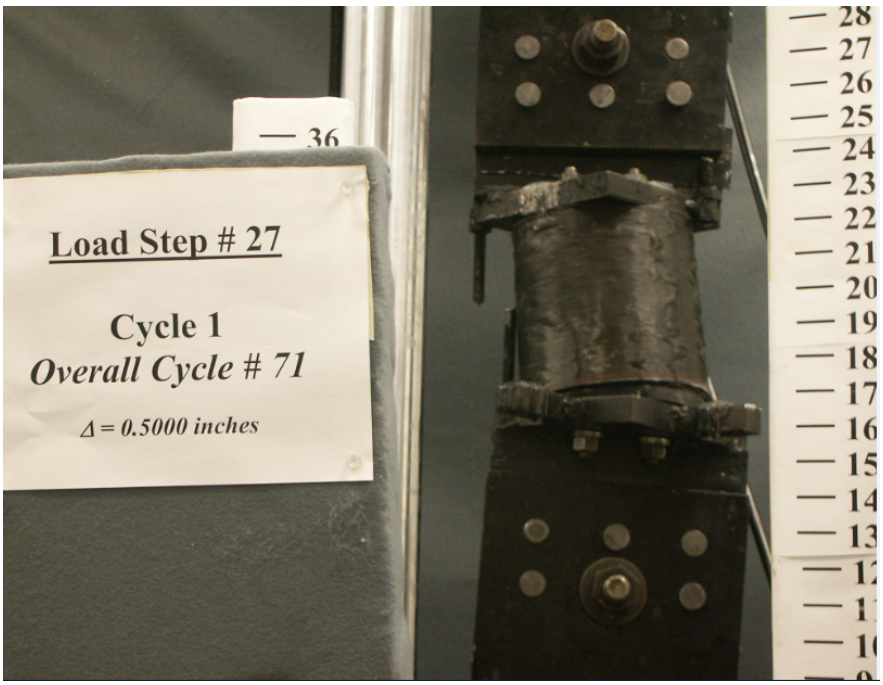

Fig. H30 - 4-Bar Fuse, Bar Type C, Confinement Ratio 91.41%, Specimen #19, Compression Cycle #71, Concentric Load.

APPENDIX I – BCE, Specimens After Tests

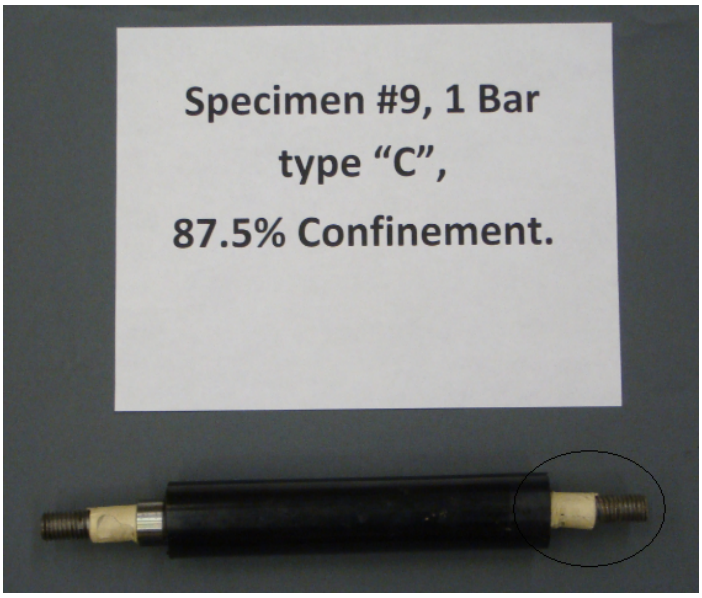

Fig. I1 - 1-Bar Type C, 87.50% Confinement Ratio, Specimen #9.

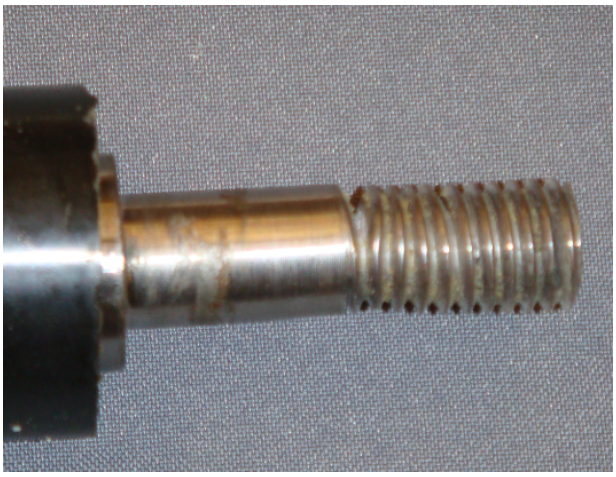

Fig. I2 - 1-Bar Type C, 87.50% Confinement Ratio, Specimen #9, Zoom.

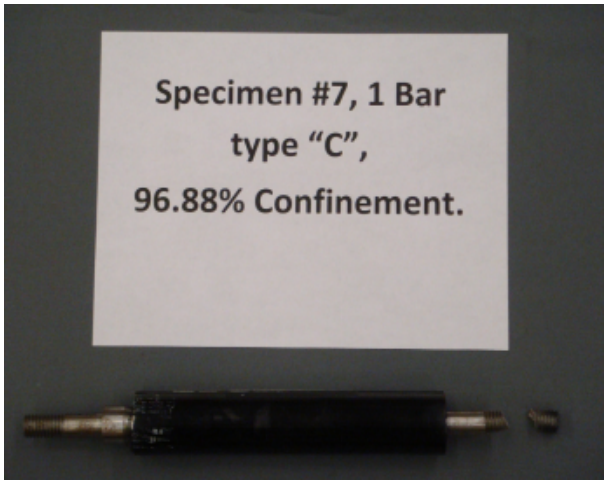

Fig. I3 - 1-Bar Type C, 96.88% Confinement Ratio, Specimen #7.

Fig. I4 - 1-Bar Type B, 96.87% Confinement Ratio, Specimen #4.

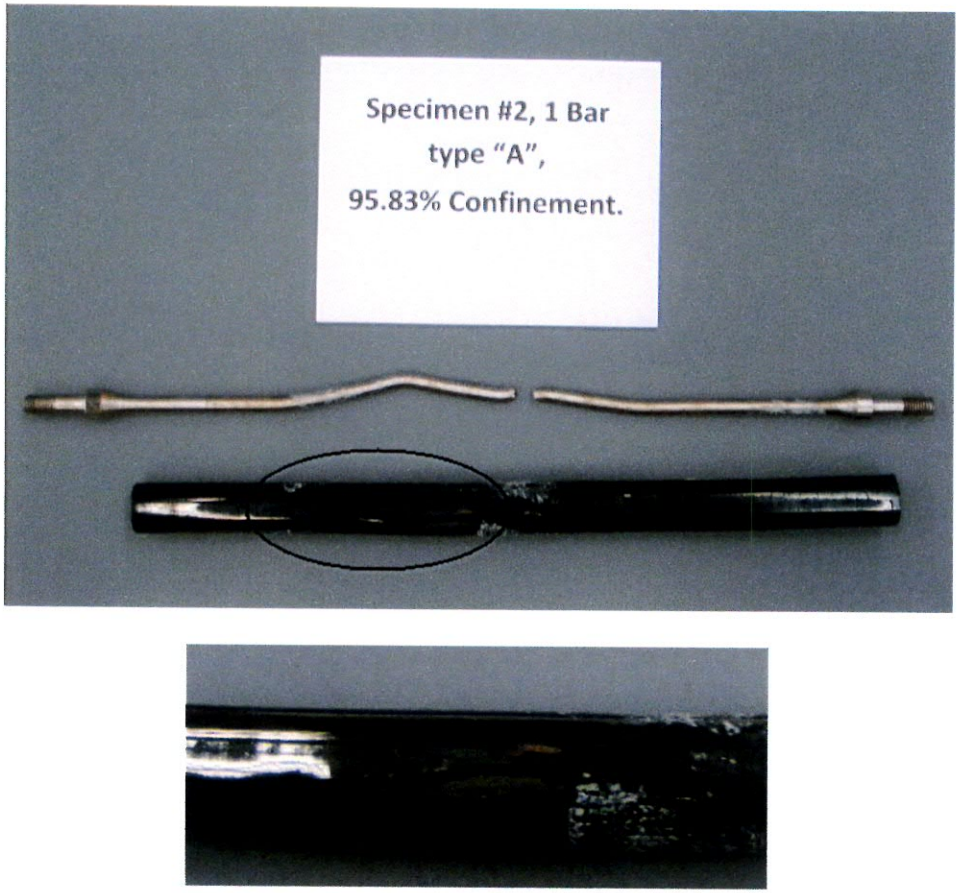

Fig. I5 - 1-Bar Type A, 95.83% Confinement Ratio, Specimen #2.

Fig. I6 - 1-Bar Type A, 98.70% Confinement Ratio, Specimen #1.

Fig. I7 - 4-Bar Type C, 96.87% Confinement Ratio, Eccentric Load, Specimen #18.

Fig. I8 - 4-Bar Type B, 98.44% Confinement Ratio, Eccentric Load, Specimen #15.

Fig. I9 - 4-Bar Type A, 98.95% Confinement Ratio, Eccentric Load, Specimen #12.

Fig. I10 - 4-Bar Type C, 91.41% Confinement Ratio, Concentric Load, Specimen #19.

Fig. I11 - 4-Bar Type C, 96.87% Confinement Ratio, Concentric Load, Specimen #17.

APPENDIX J – BCE, FRP - Matrix Confinement System Monotonic Compression Test

Fig. J1 - FRP-Matrix Confinement System, 60% Confinement Ratio, Monotonic Compression Test.

Fig. J2 - FRP-Matrix Confinement System, 60% Confinement Ratio, Monotonic Compression Test at 0.1 in./in.

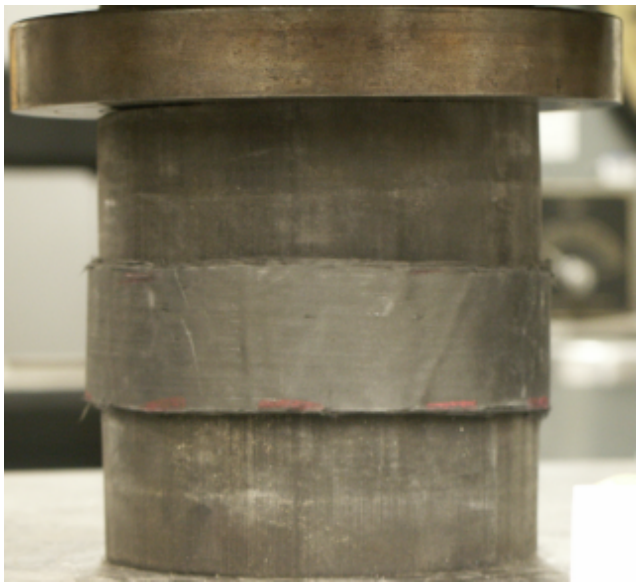

Fig. J3 - FRP-Matrix Confinement System, 30% Confinement Ratio, Monotonic Compression Test.

Fig. J4 - FRP-Matrix Confinement System, 30% Confinement Ratio, Monotonic Compression Test at 0.4 in./in.

APPENDIX K – 2-D FEM Eccentric Load

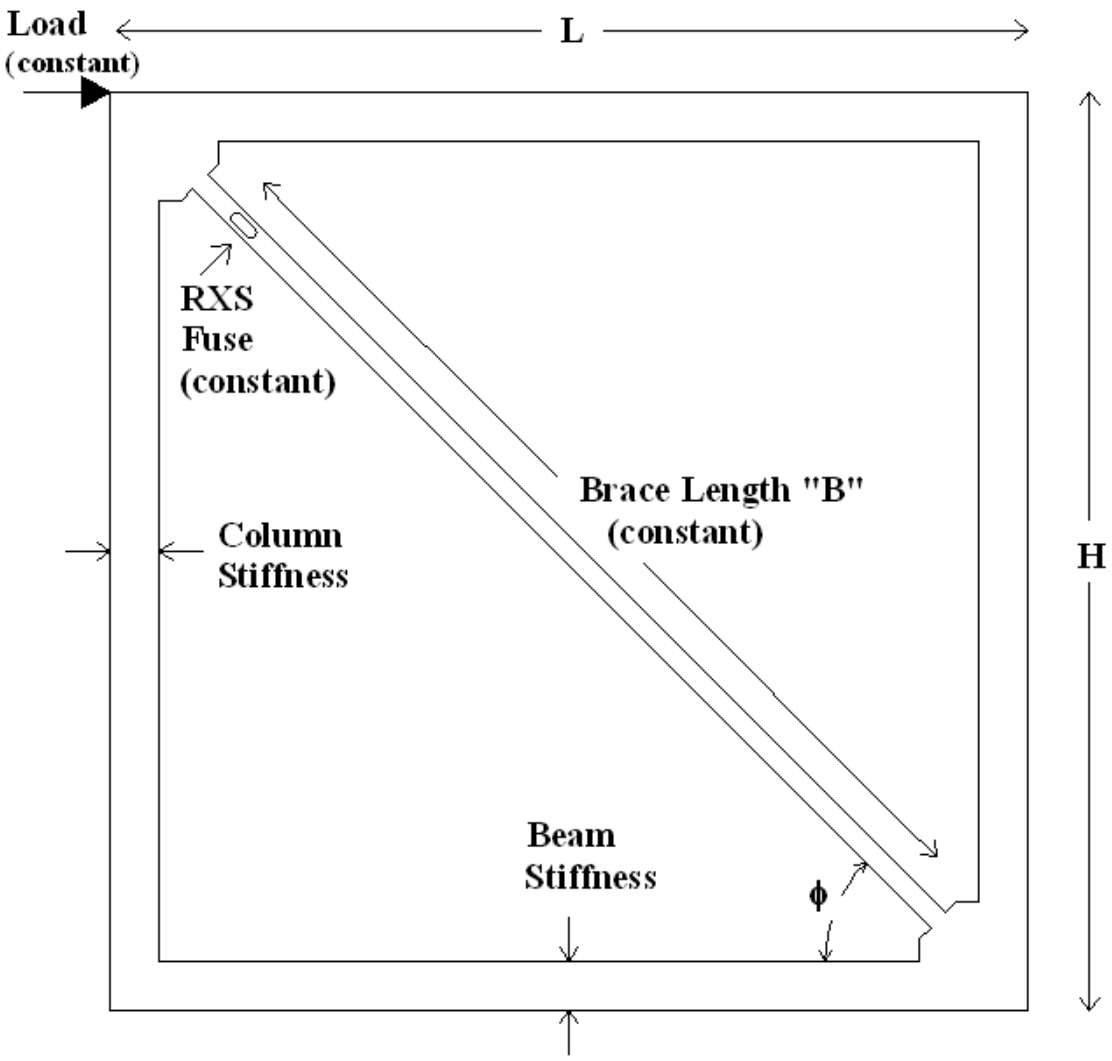

Fig. K1 - Braced Frame Model Setup.

Frame	Beam/Column Length Ratio	Beam/Column Stiffness		Brace Angle "ϕ"	P Lateral Load (Kips)
		Beam-depth/Column-depth	Ratio	(degrees)	
A	H/L = 1	2"/16"	***0.13***	45	100.00
B	H/L = 1	4"/16"	***0.25***	45	100.00
C	H/L = 1	6"/16"	***0.38***	45	100.00
D	H/L = 1	8"/16"	***0.50***	45	100.00
E	H/L = 1	10"/16"	***0.63***	45	100.00
F	H/L = 1	12"/16"	***0.75***	45	100.00
G	H/L = 1	14"/16"	***0.88***	45	100.00
H	H/L = 1	16"/16"	***1.00***	45	100.00
I	H/L = 1	16"/14"	***1.14***	45	100.00
J	H/L = 1	16"/12"	***1.33***	45	100.00
K	H/L = 1	16"/10"	***1.60***	45	100.00
L	H/L = 1	16"/8"	***2.00***	45	100.00
M	H/L = 1	16"/6"	***2.67***	45	100.00
N	H/L = 1	16"/5"	***3.20***	45	100.00
O	H/L = 1	16"/4"	***4.00***	45	100.00
P	H/L = 1	16"/2"	***8.00***	45	100.00

Table K1 - Beam/Column Stiffness Ratio Frame Properties.

Frame	Beam/Column Length Ratio	Beam/Column Stiffness Ratio		Brace Angle "ϕ"	P Lateral Load (Kips)
		Beam-depth/Column-depth	Ratio	(degrees)	
Q	1 < H/L	16"/16"	1.00	***55***	100.00
R	1 < H/L	16"/16"	1.00	***50***	100.00
H	H/L = 1	16"/16"	1.00	***45***	100.00
S	1 > H/L	16"/16"	1.00	***40***	100.00
T	1 > H/L	16"/16"	1.00	***35***	100.00
U	1 > H/L	16"/16"	1.00	***30***	100.00
V	1 > H/L	16"/16"	1.00	***25***	100.00

Table K2 - Bracing Angle “ϕ” Frame Properties.

FRAME A

Beam/Column Length Ratio = H/L = 1

Beam-depth/Column-depth = 2”/16”

Brace Angle “ϕ” = 45˚

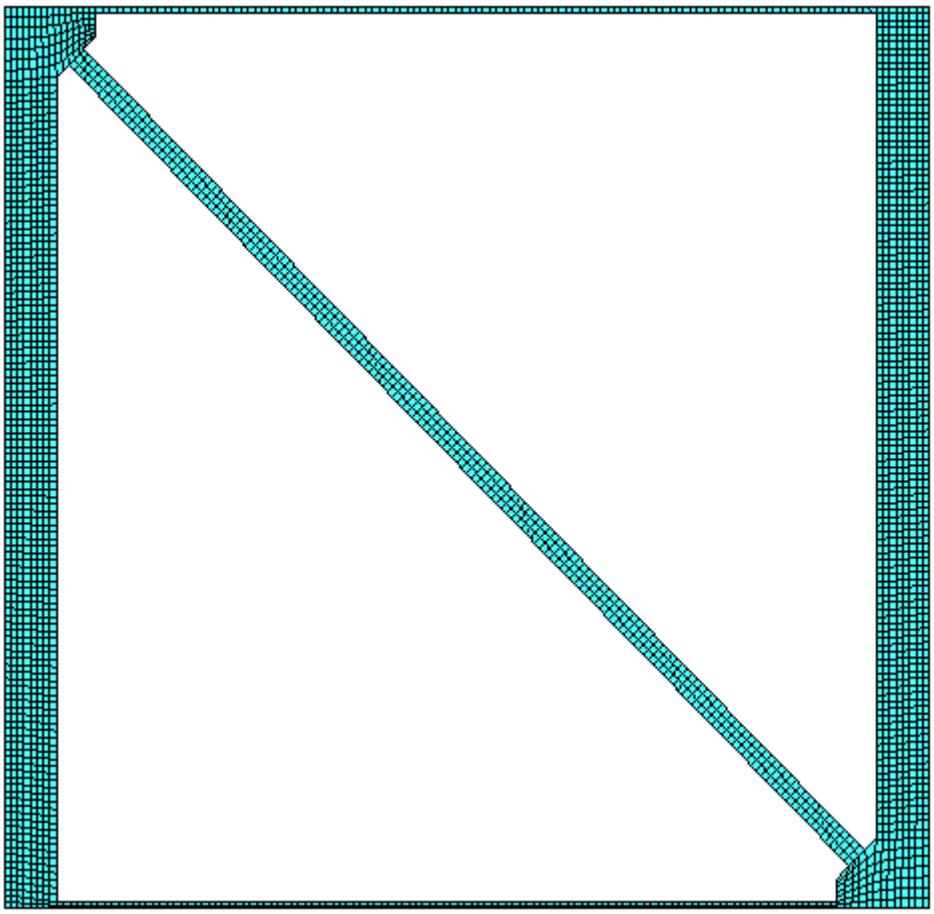

Fig. K2 - FEM Mesh – Frame “A” without RXS Fuse.

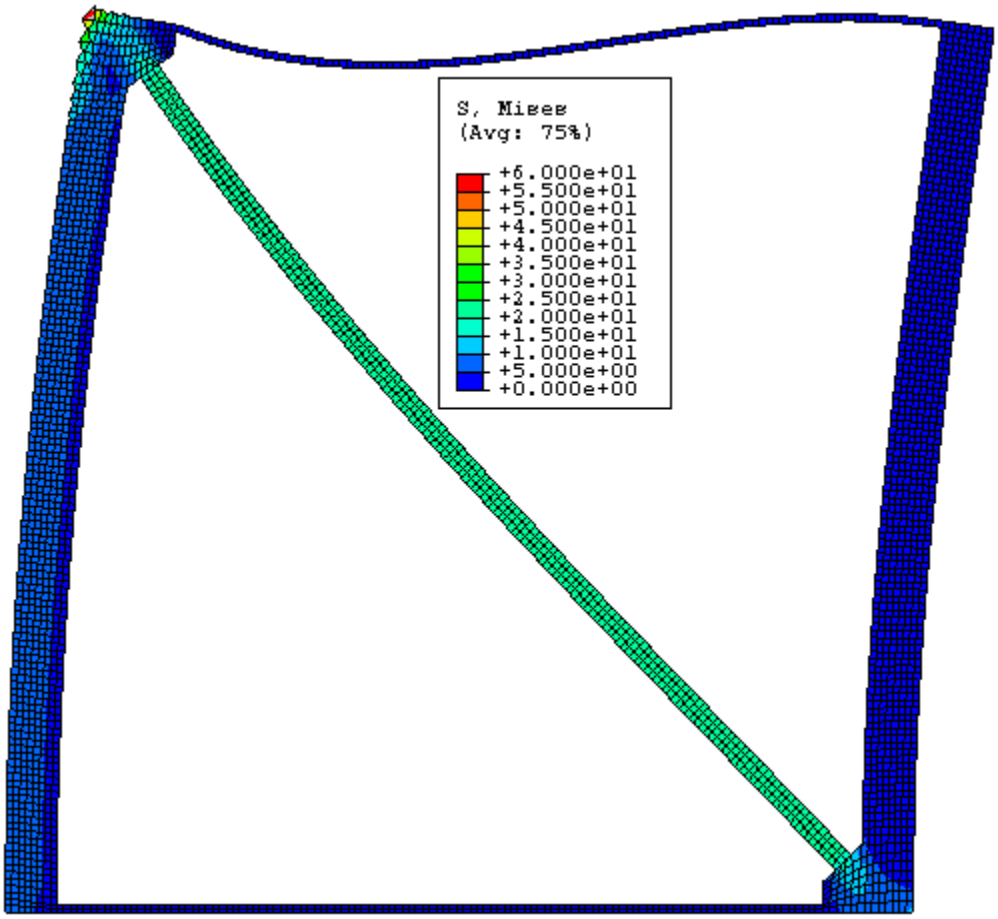

Fig. K3 - Von Mises Stress – Frame “A” without RXS Fuse.

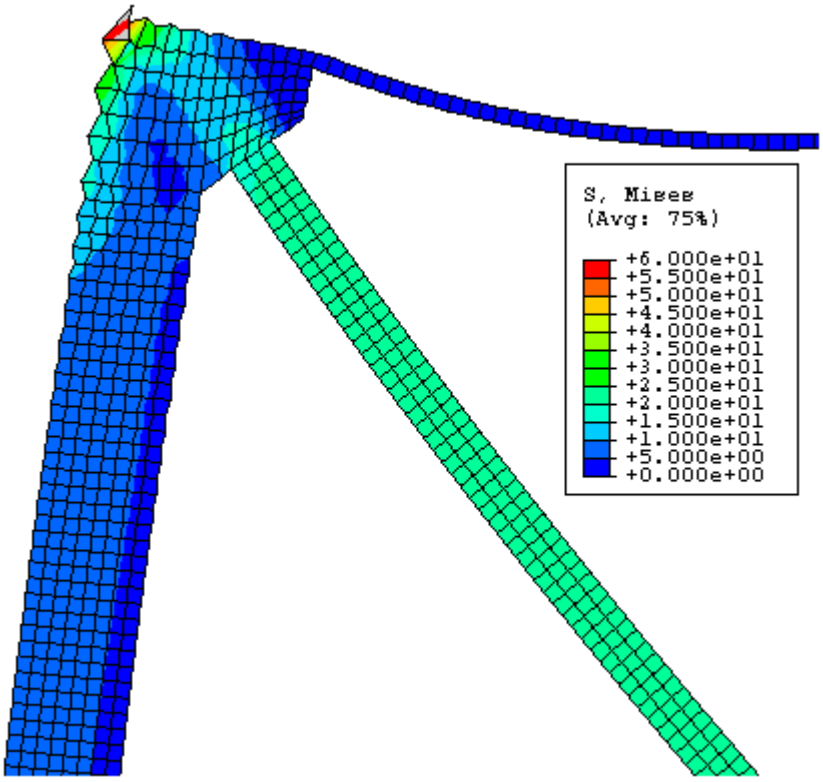

Fig. K4 - Von Mises Stress – Frame “A” without RXS Fuse – Zoom.

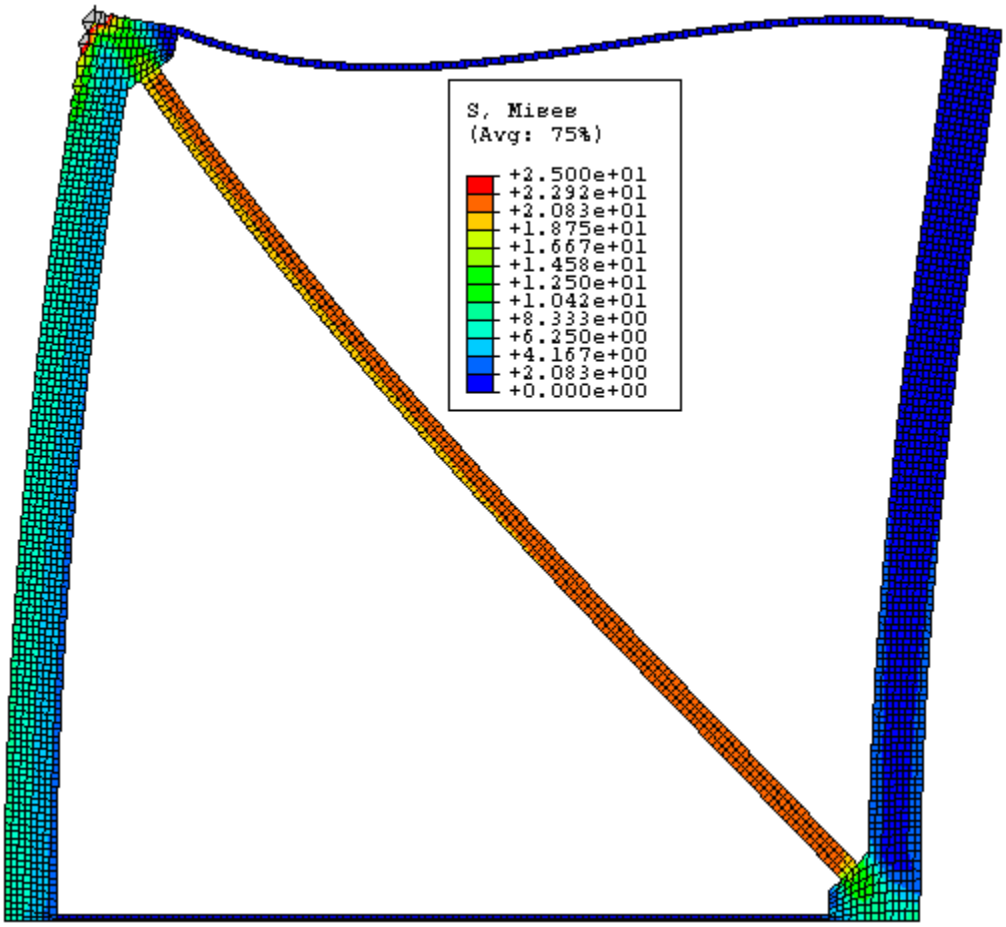

Fig. K5 - Von Mises Stress – Frame “A” without RXS Fuse – Stress Scale #2.

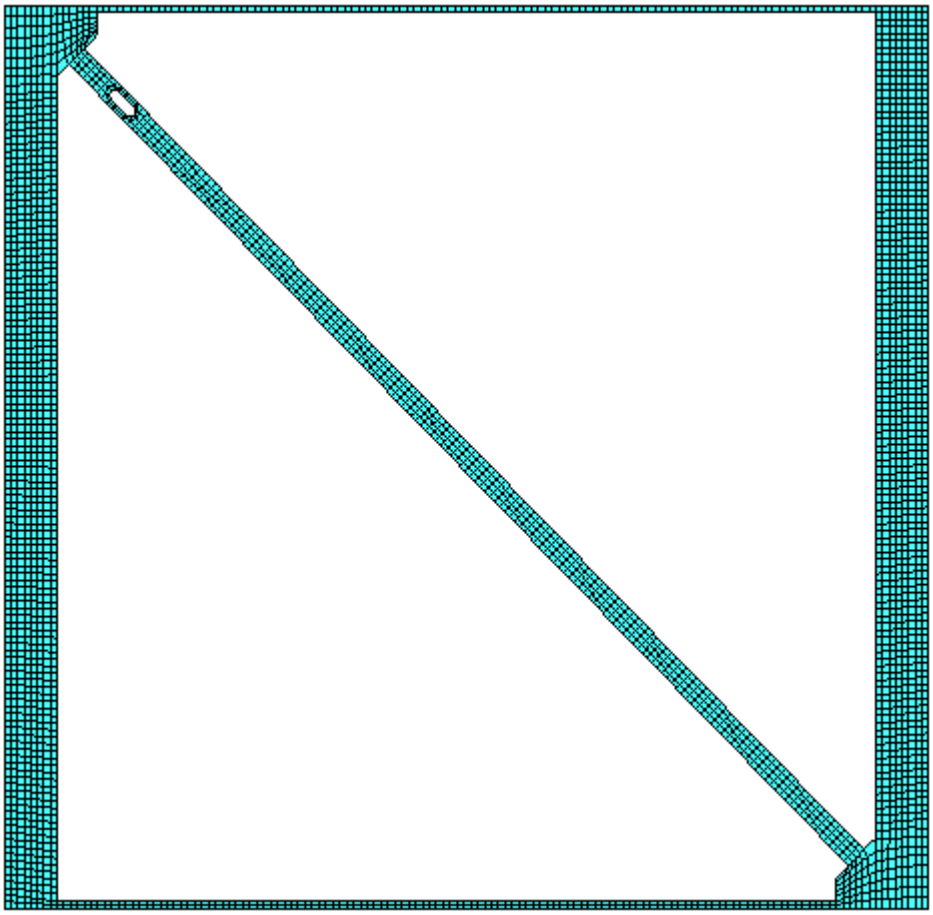

Fig. K6 - FEM Mesh – Frame “A” with RXS Fuse.

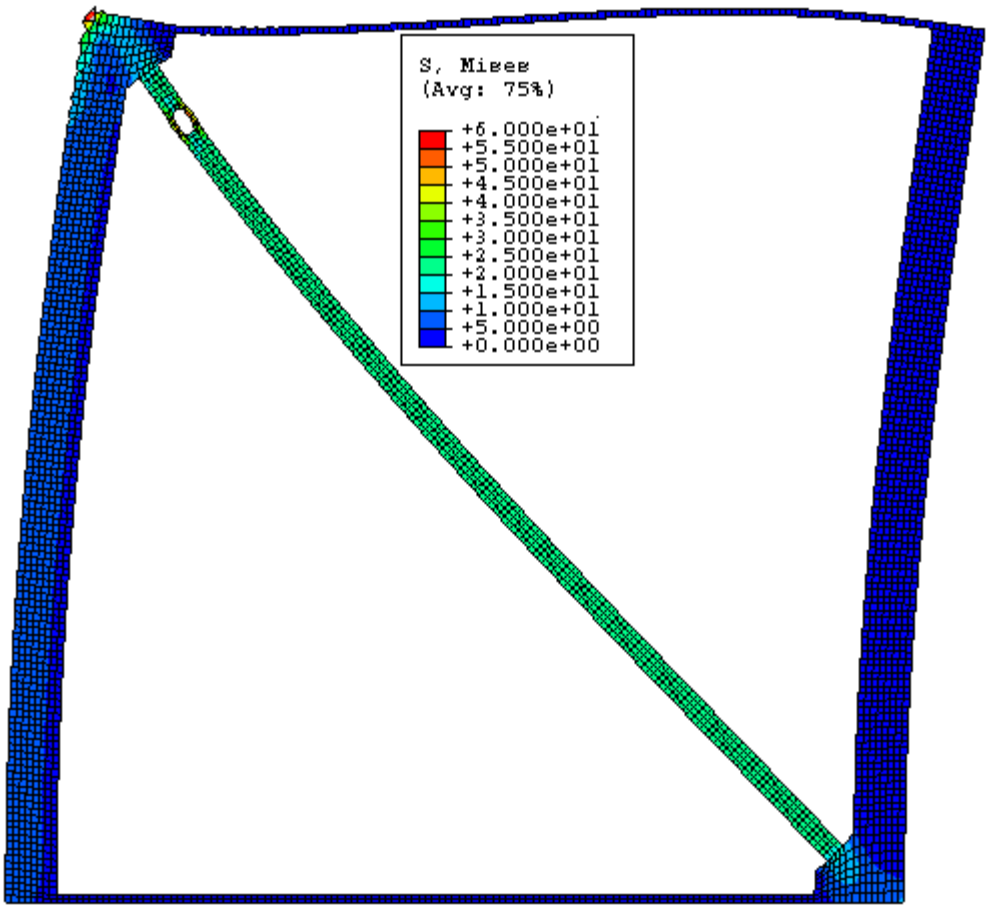

Fig. K7 - Von Mises Stress – Frame “A” with RXS Fuse.

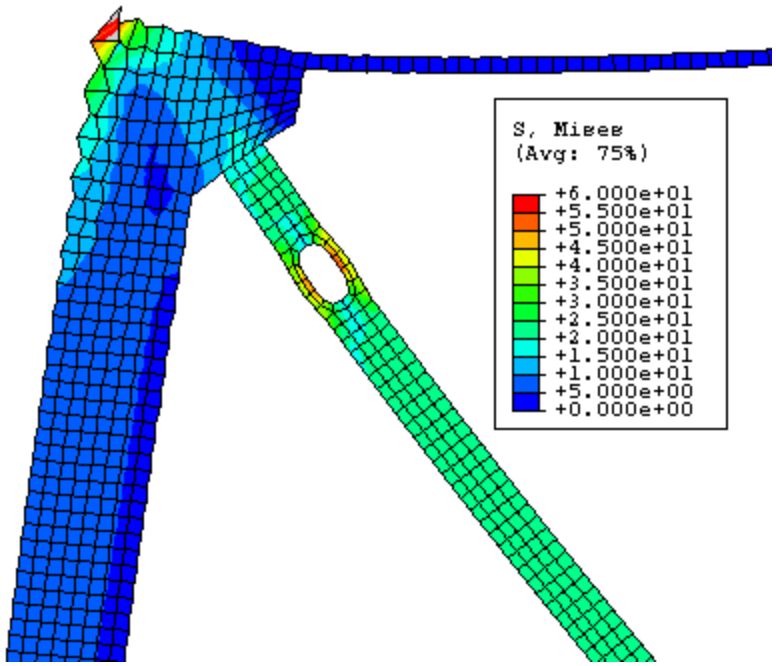

Fig. K8 - Von Mises Stress – Frame "A" with RXS Fuse – Zoom #1.

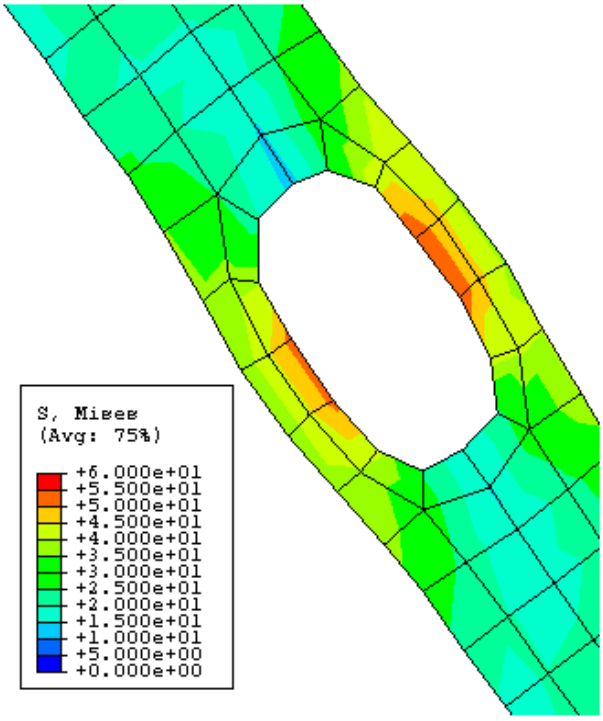

Fig. K9 - Von Mises Stress – Frame "A" with RXS Fuse – Zoom #2.

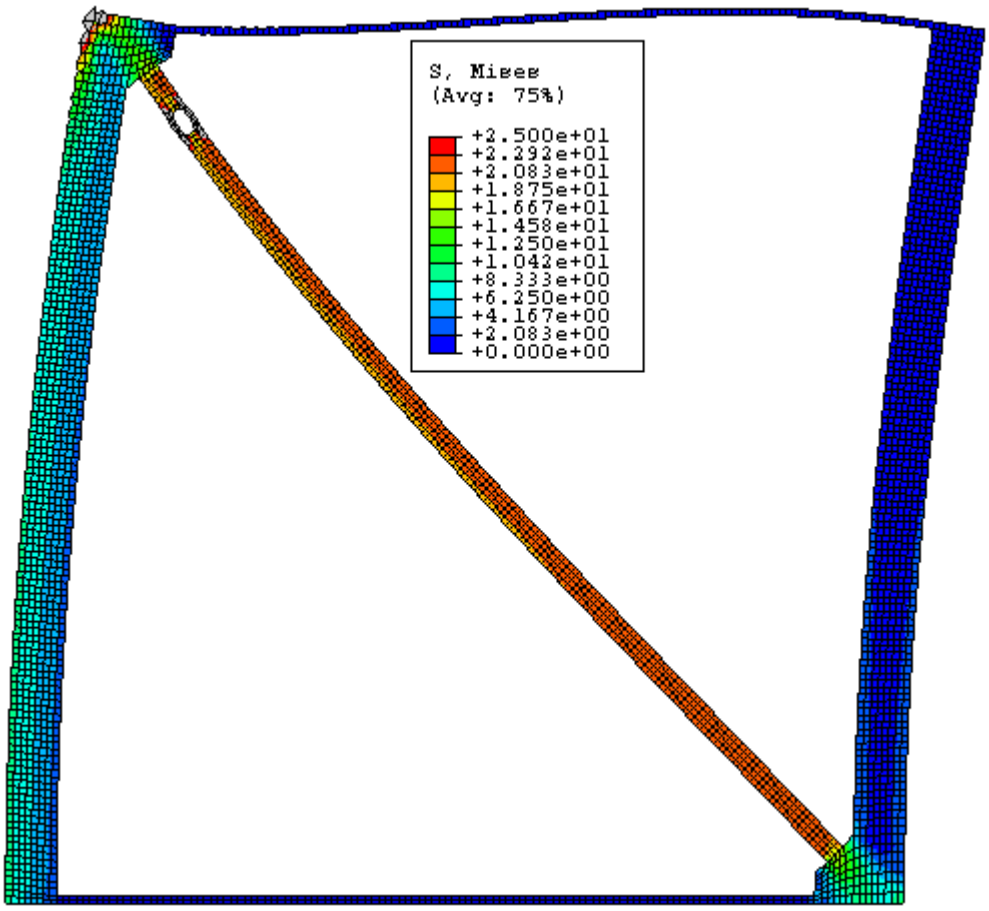

Fig. K10 - Von Mises Stress – Frame “A” with RXS Fuse – Stress Scale #2.

FRAME B

Beam/Column Length Ratio = H/L = 1

Beam-depth/Column-depth = 4”/16”

Brace Angle “ϕ” = 45˚

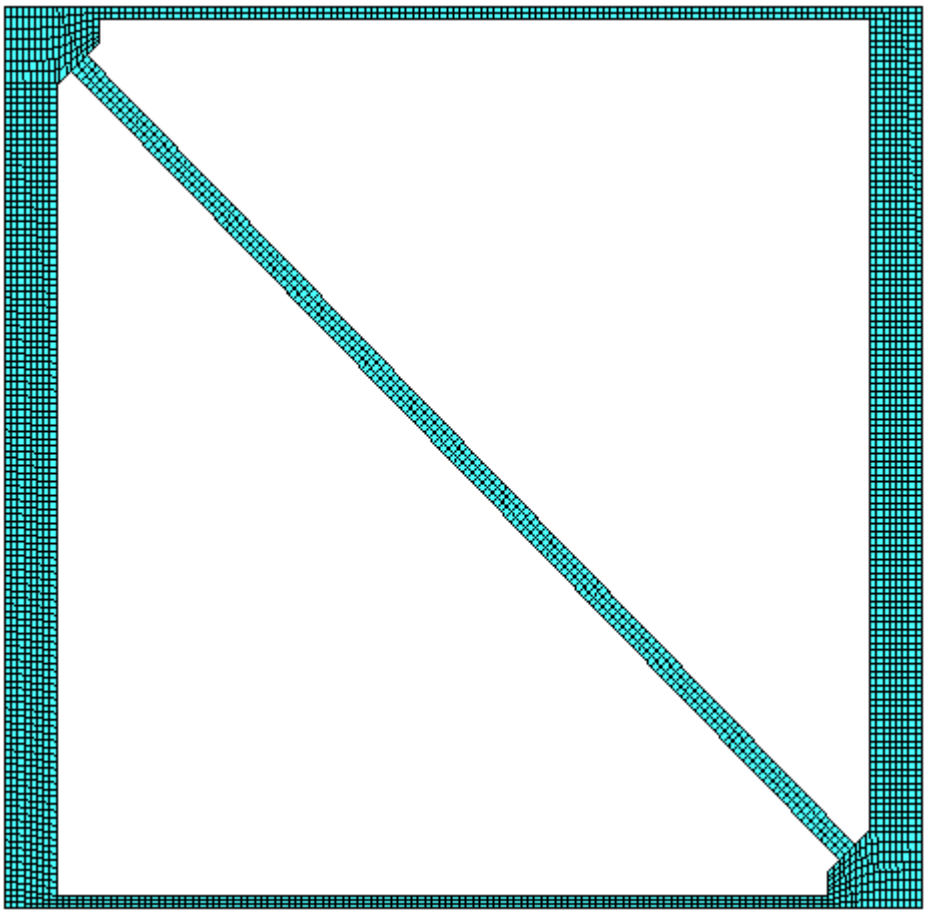

Fig. K11 - FEM Mesh – Frame “B” without RXS Fuse.

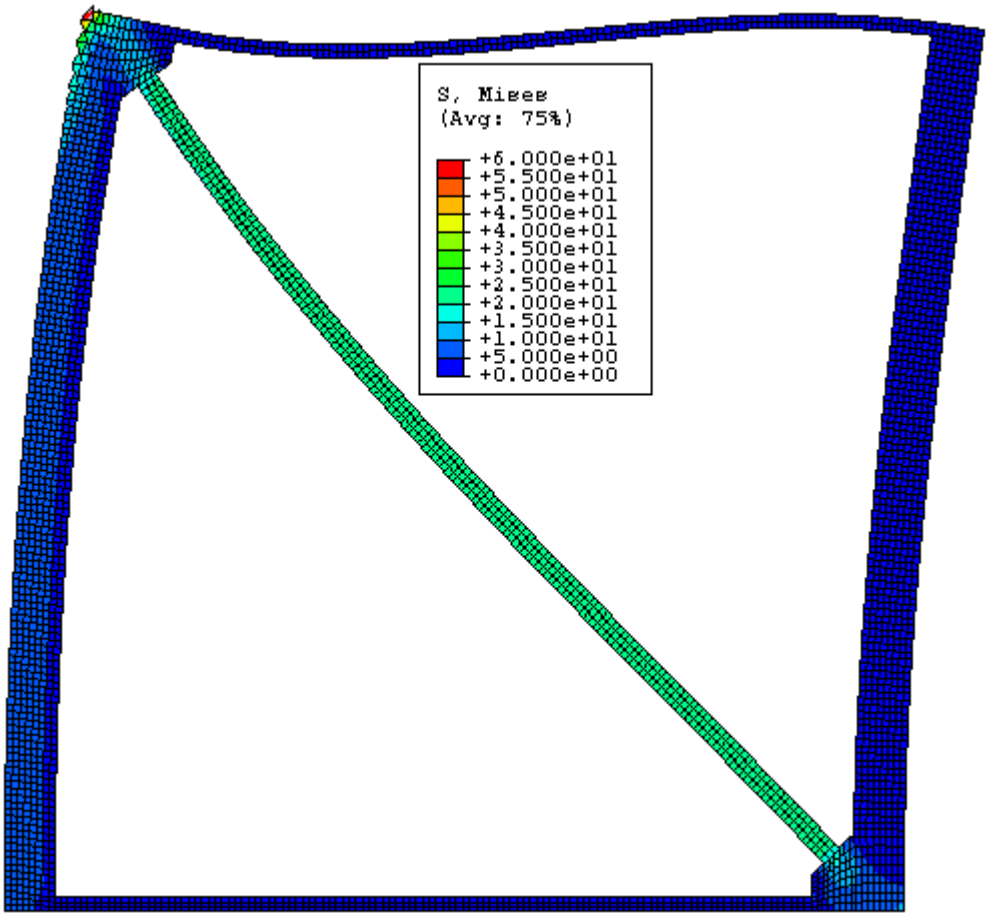

Fig. K.12 - Von Mises Stress – Frame “B” without RXS Fuse.

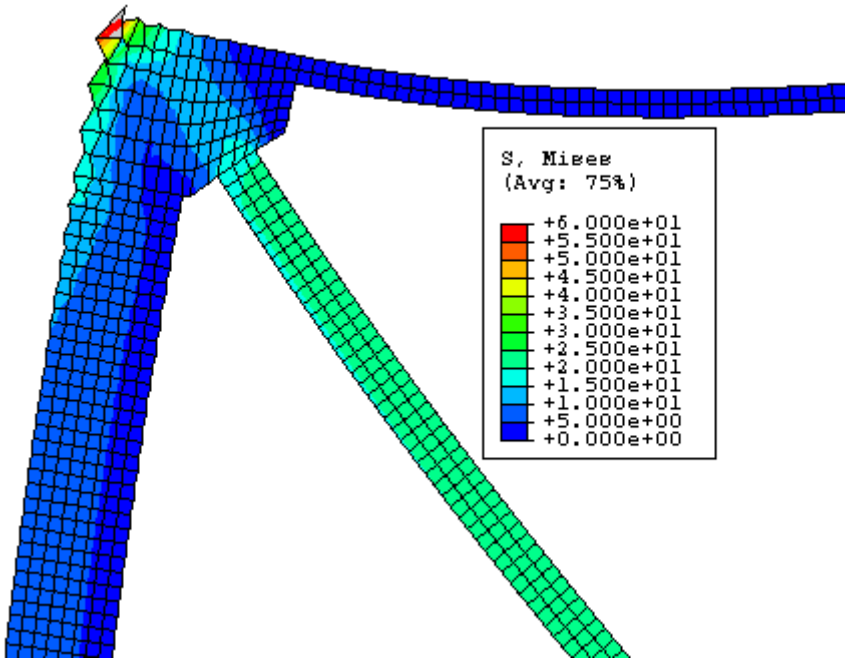

Fig. K.13 - Von Mises Stress – Frame “B” without RXS Fuse – Zoom.

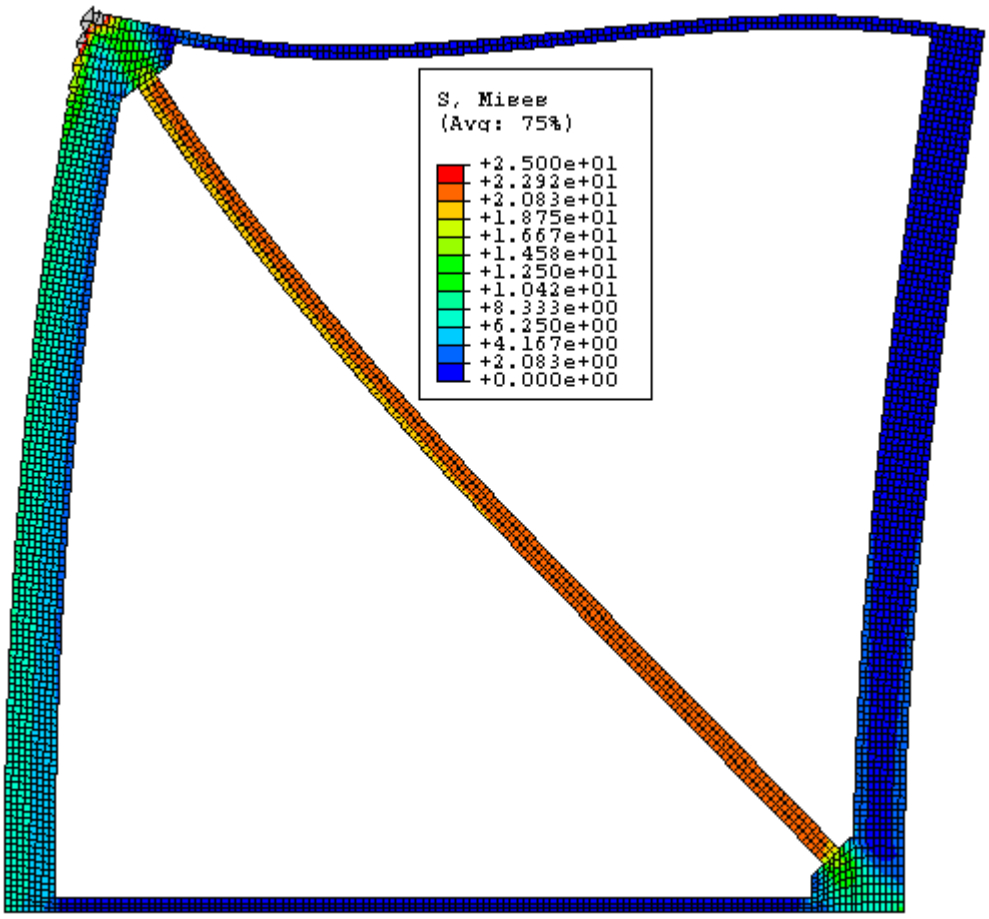

Fig. K.14 - Von Mises Stress – Frame “B” without RXS Fuse – Stress Scale #2.

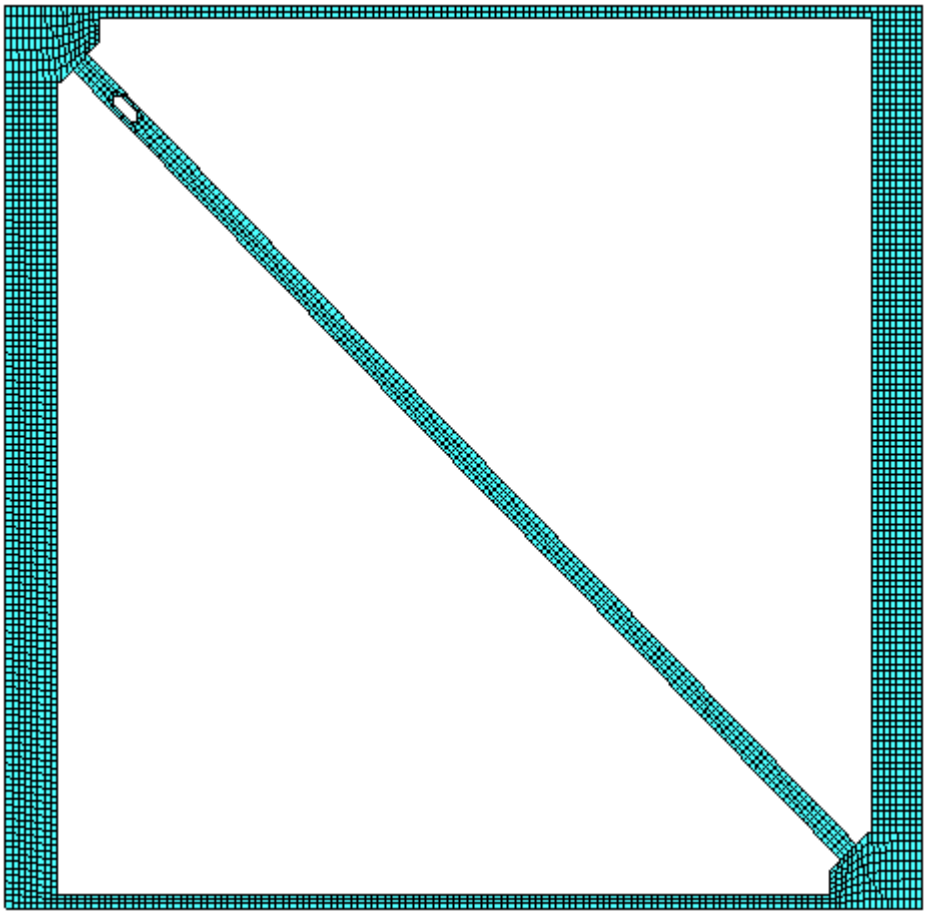

Fig. K15 - FEM Mesh – Frame “B” with RXS Fuse.

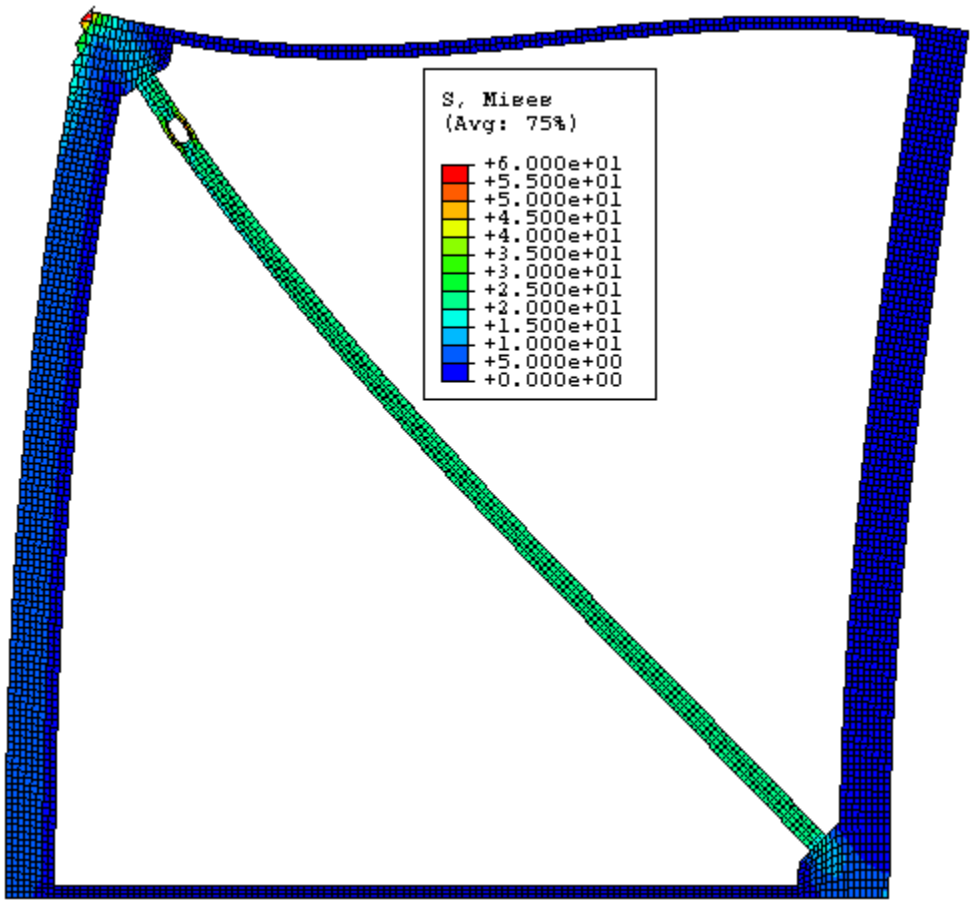

Fig. K16 - Von Mises Stress – Frame “B” with RXS Fuse.

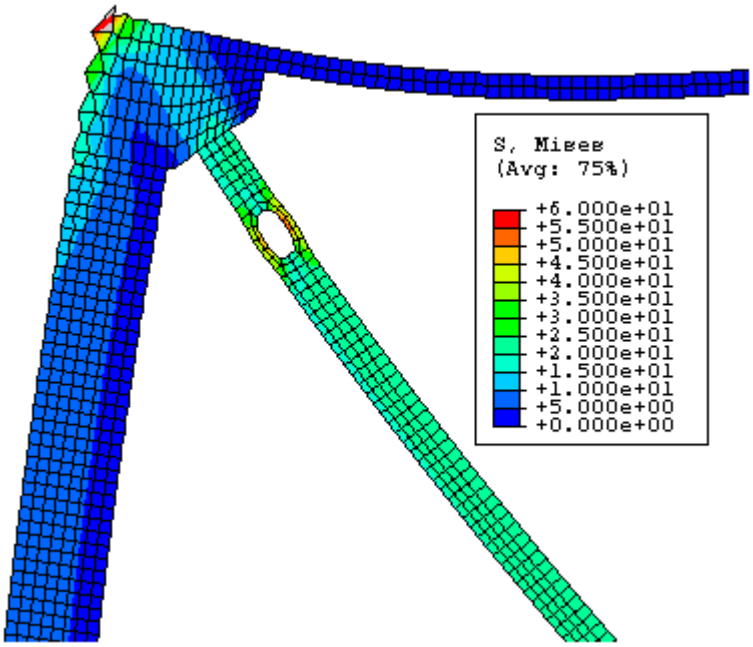

Fig. K17 - Von Mises Stress – Frame “B” with RXS Fuse – Zoom #1.

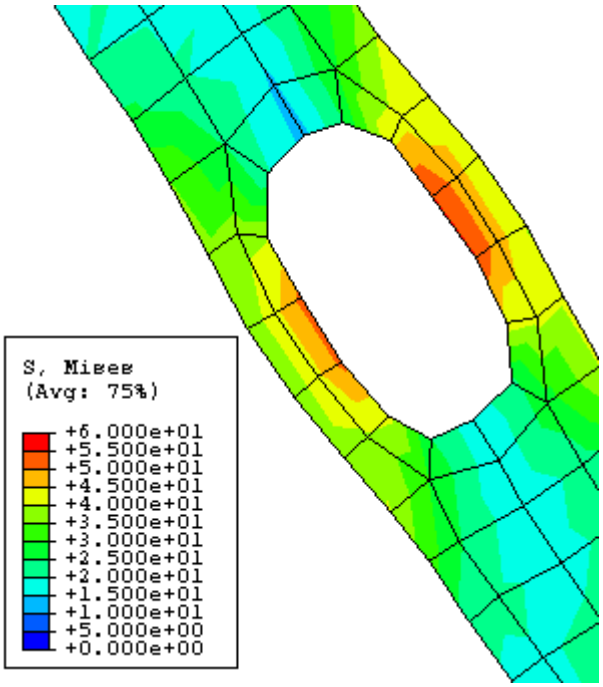

Fig. K18 - Von Mises Stress – Frame “B” with RXS Fuse – Zoom #2.

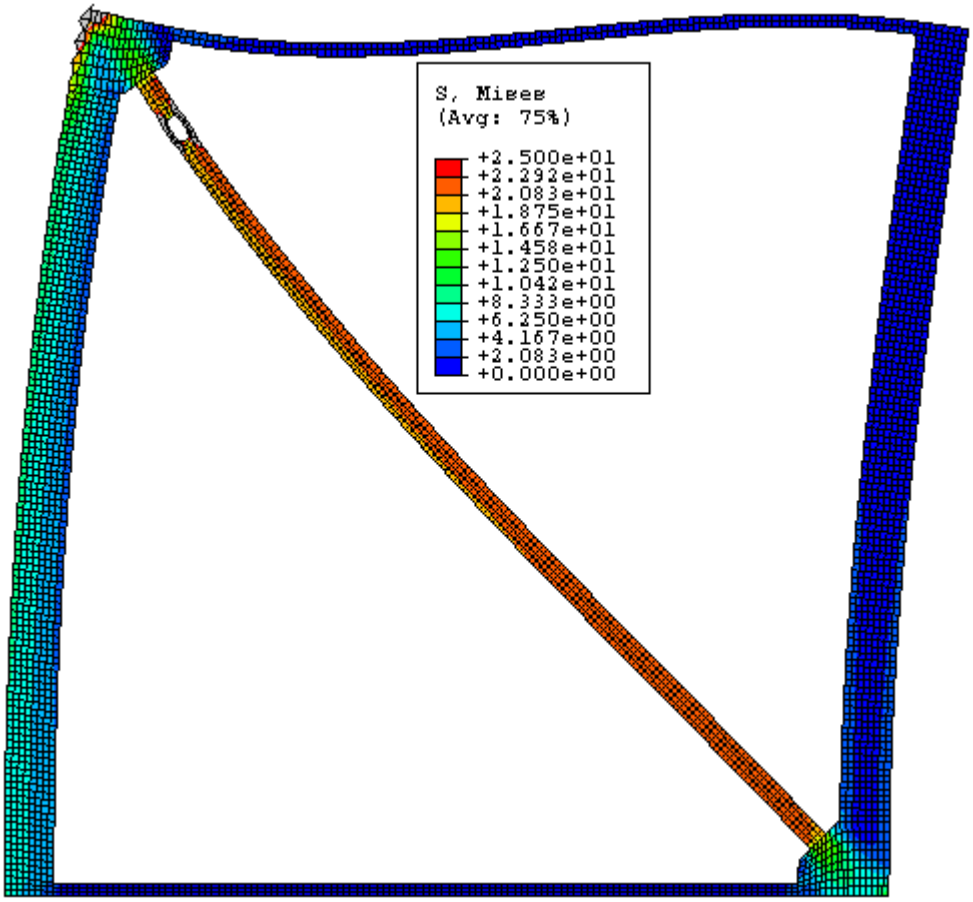

Fig. K19 - Von Mises Stress – Frame “B” with RXS Fuse – Stress Scale #2.

FRAME C

Beam/Column Length Ratio = H/L = 1

Beam-depth/Column-depth =6”/16”

Brace Angle “ϕ” = 45˚

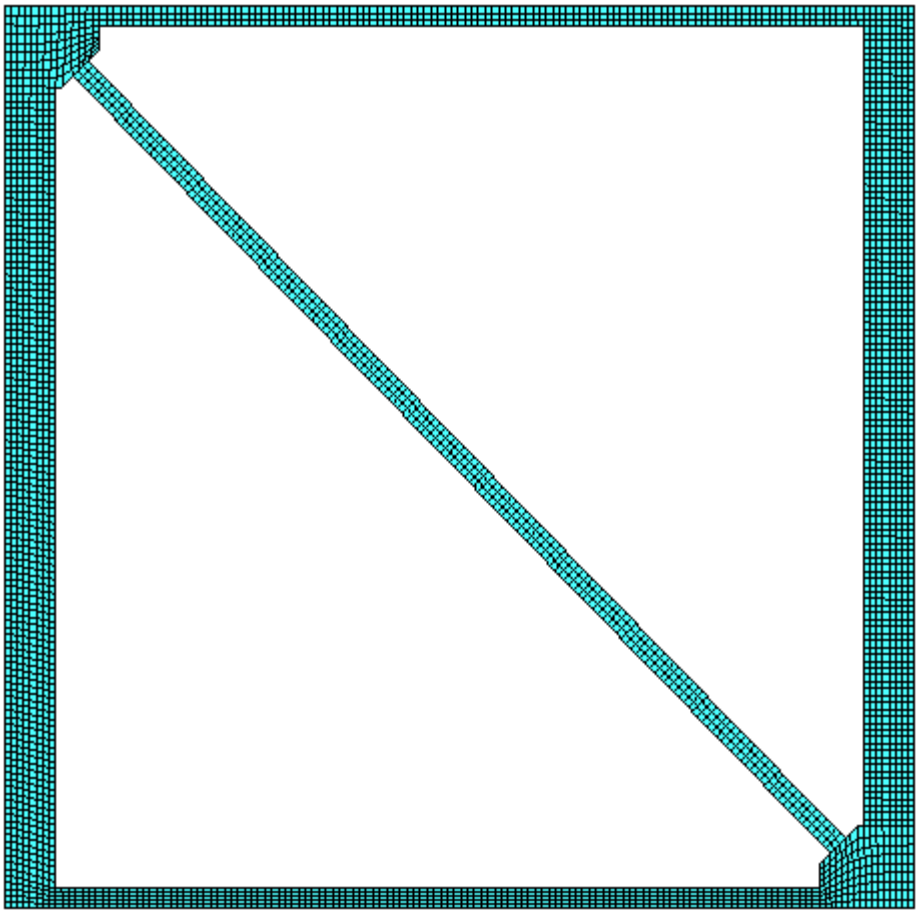

Fig. K20 - FEM Mesh – Frame “C” without RXS Fuse.

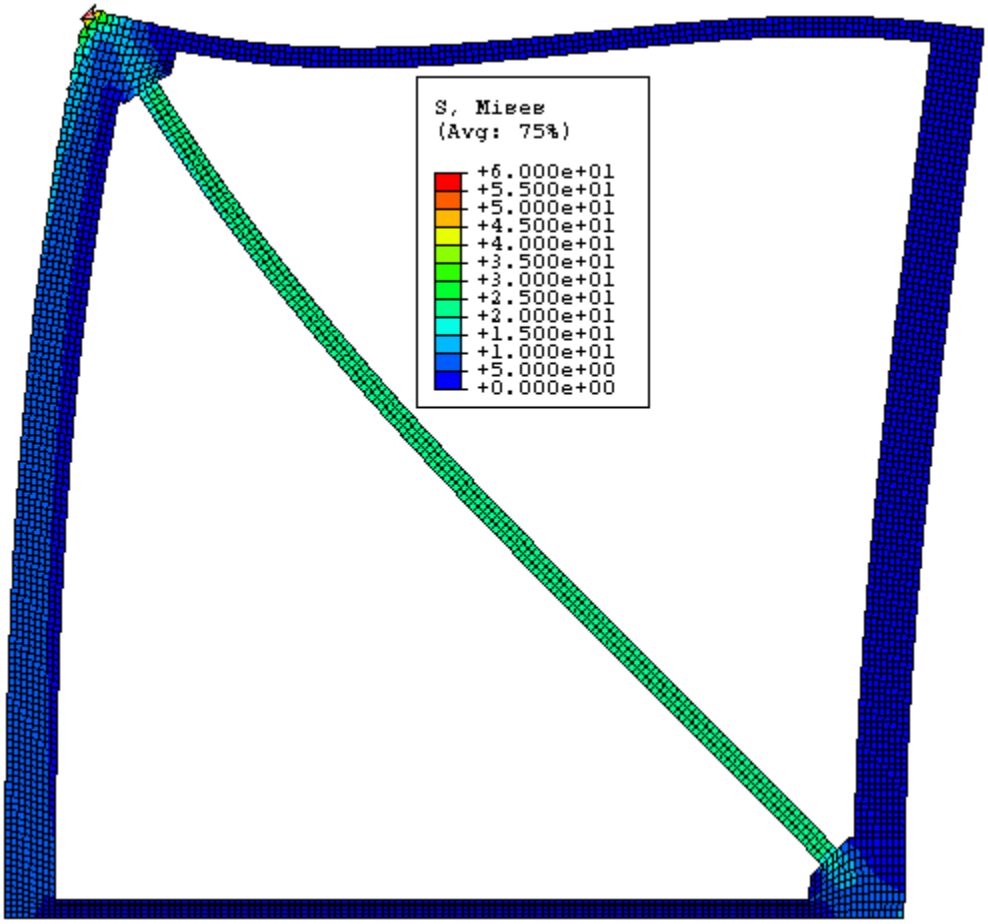

Fig. K21 - Von Mises Stress – Frame “C” without RXS Fuse.

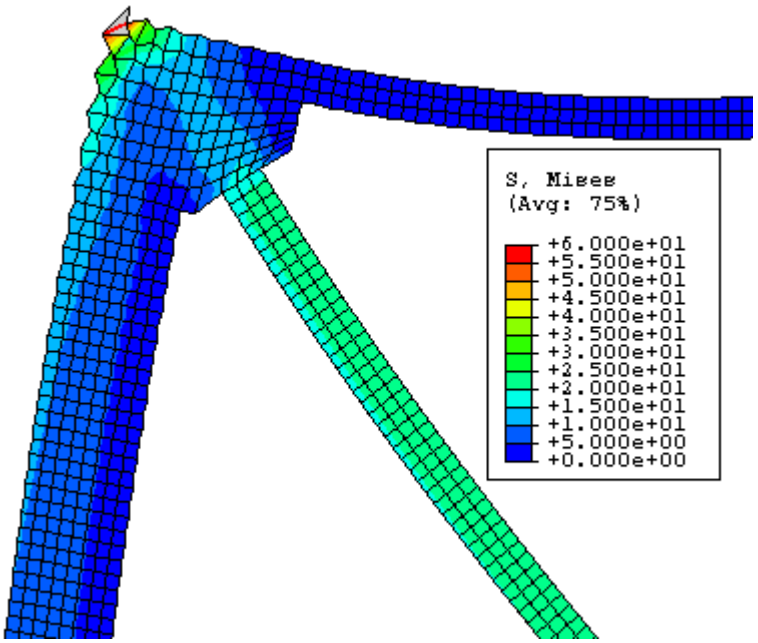

Fig. K22 - Von Mises Stress – Frame “C” without RXS Fuse – Zoom.

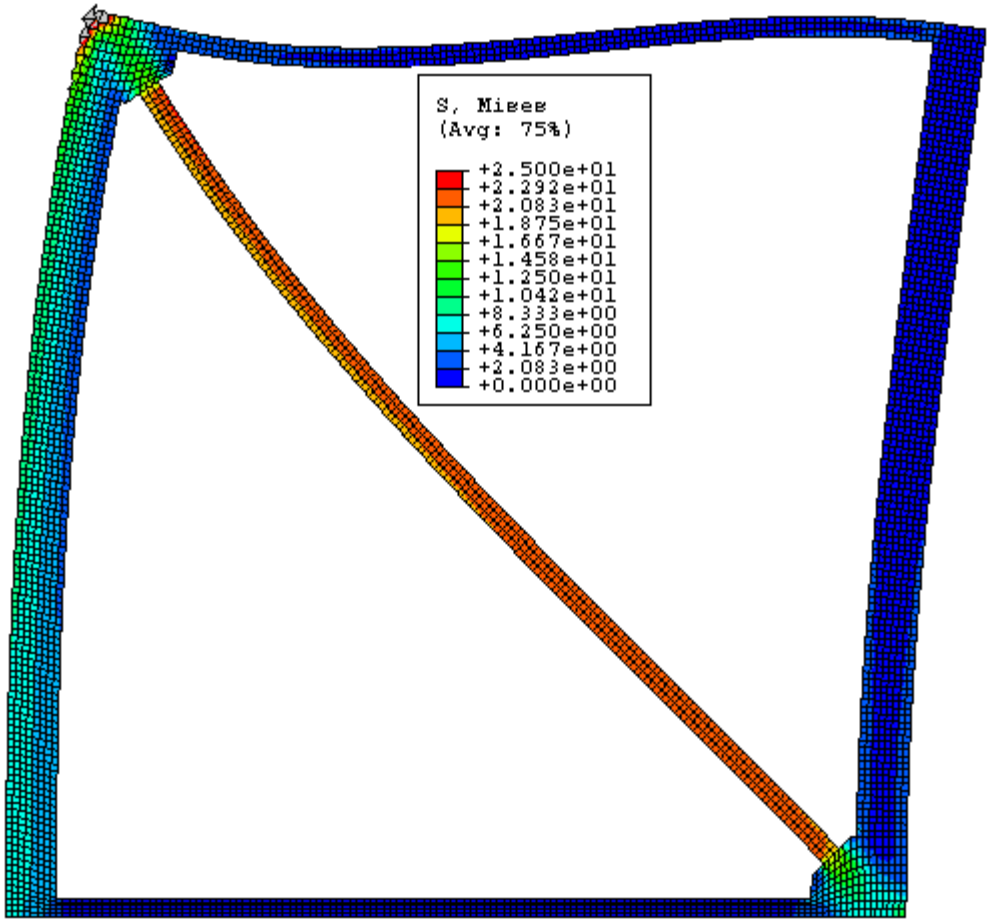

Fig. K23 - Von Mises Stress – Frame “C” without RXS Fuse – Stress Scale #2.

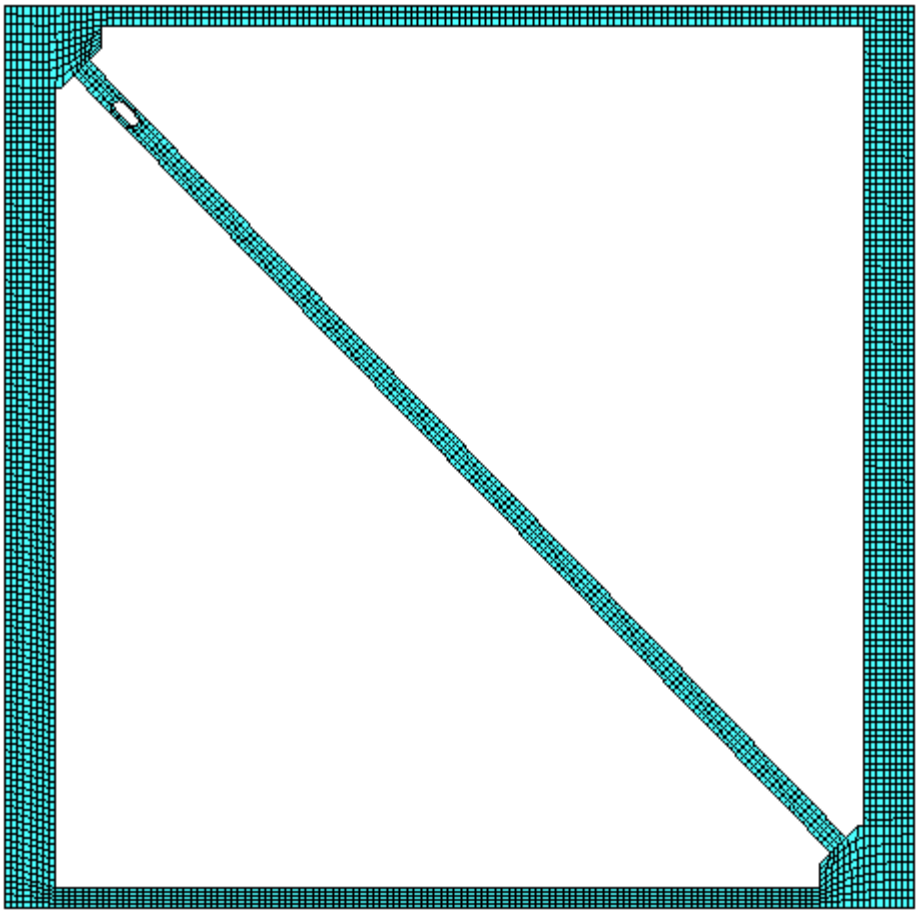

Fig. K24 - FEM Mesh – Frame “C” with RXS Fuse.

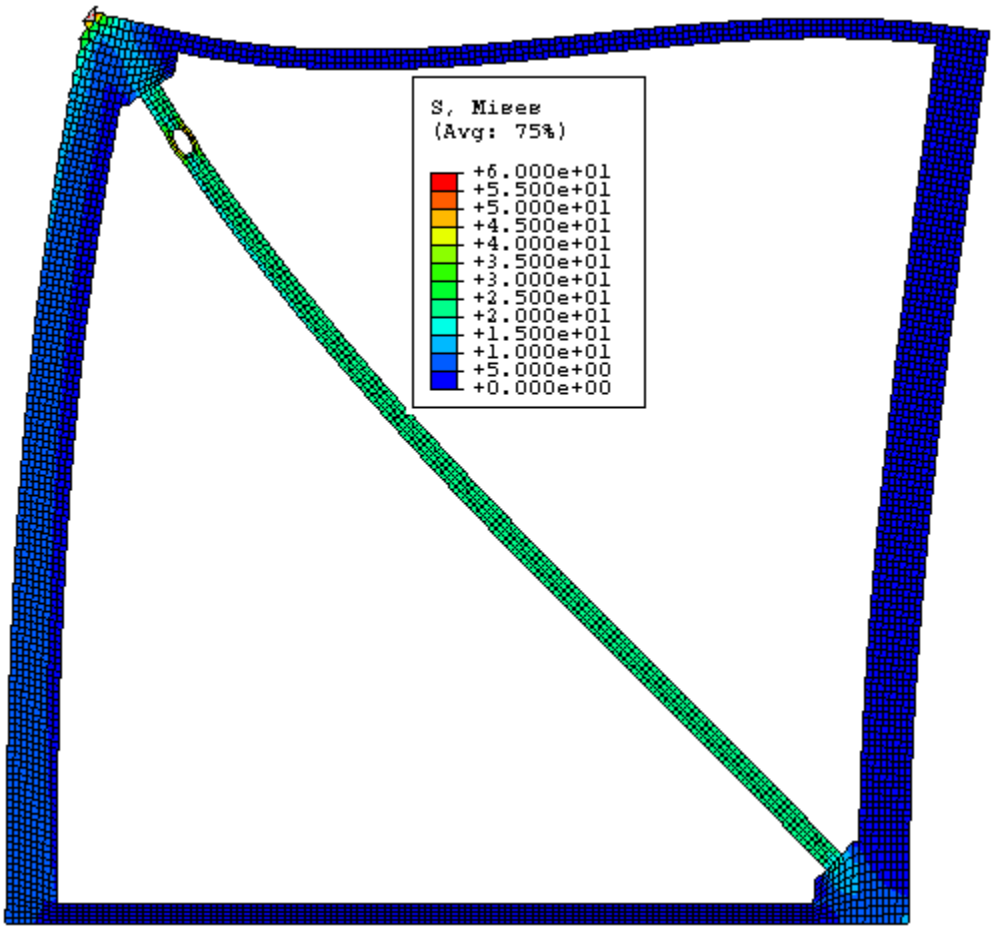

Fig. K25 - Von Mises Stress – Frame “C” with RXS Fuse.

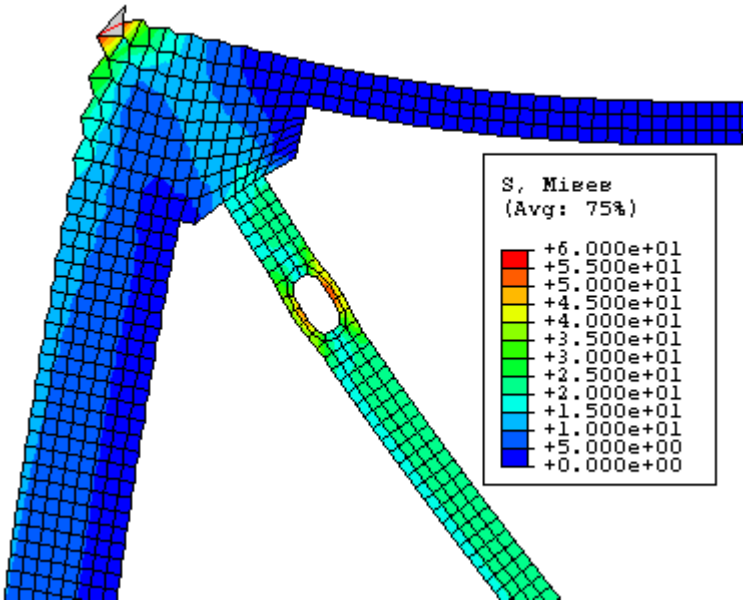

Fig. K26 - Von Mises Stress – Frame “C” with RXS Fuse – Zoom #1.

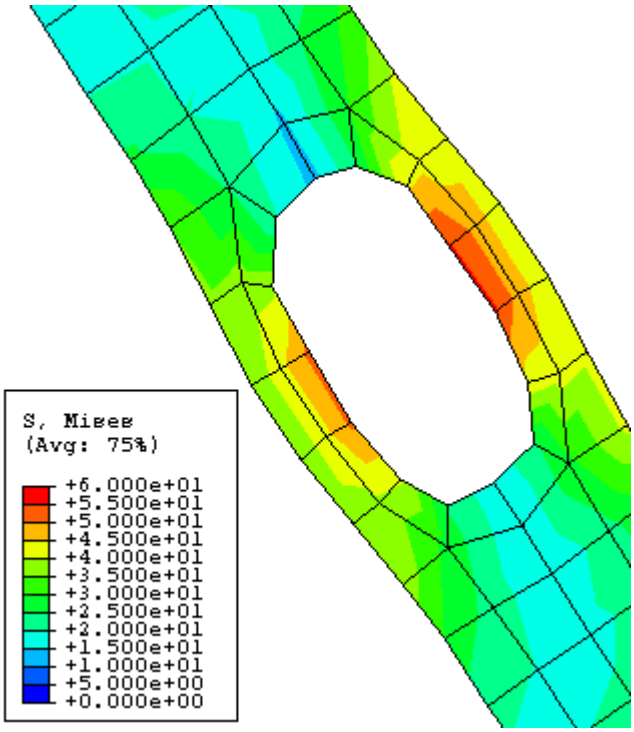

Fig. K27 - Von Mises Stress – Frame “C” with RXS Fuse – Zoom #2.

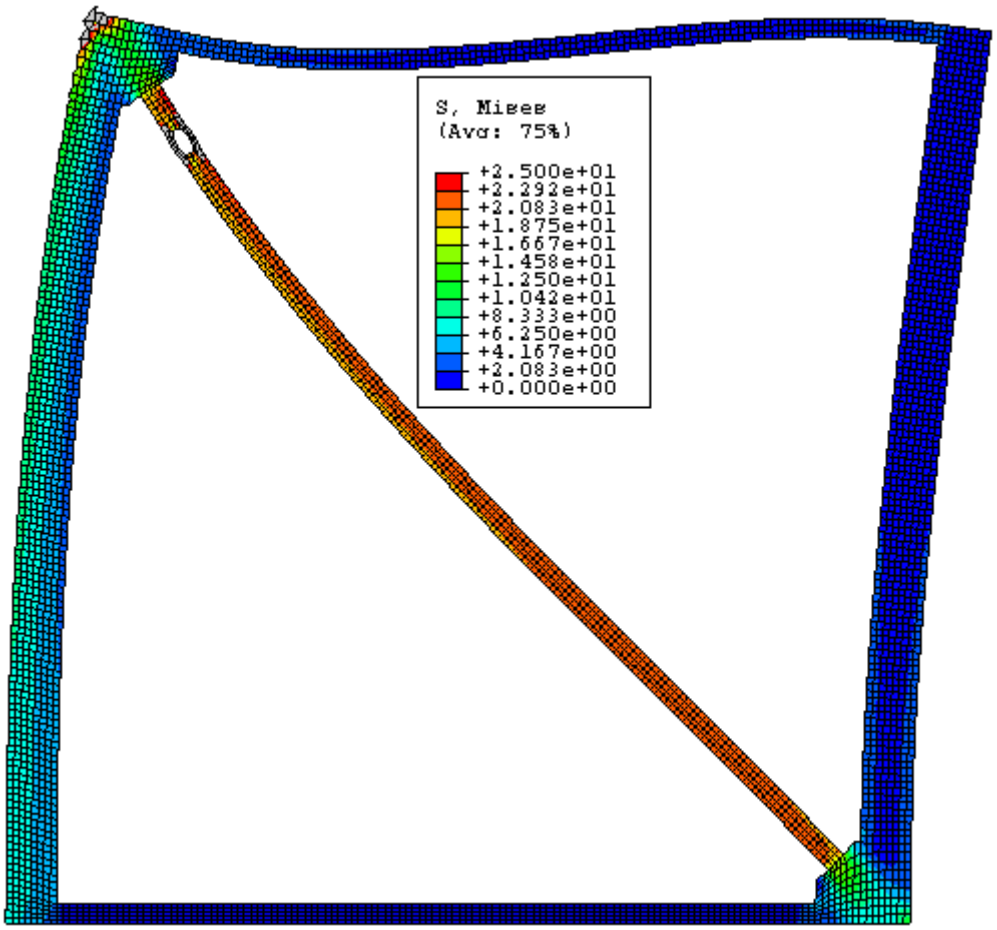

Fig. K28 - Von Mises Stress – Frame “C” with RXS Fuse – Stress Scale #2.

FRAME D

Beam/Column Length Ratio = H/L = 1

Beam-depth/Column-depth = 8”/16”

Brace Angle “ϕ” = 45˚

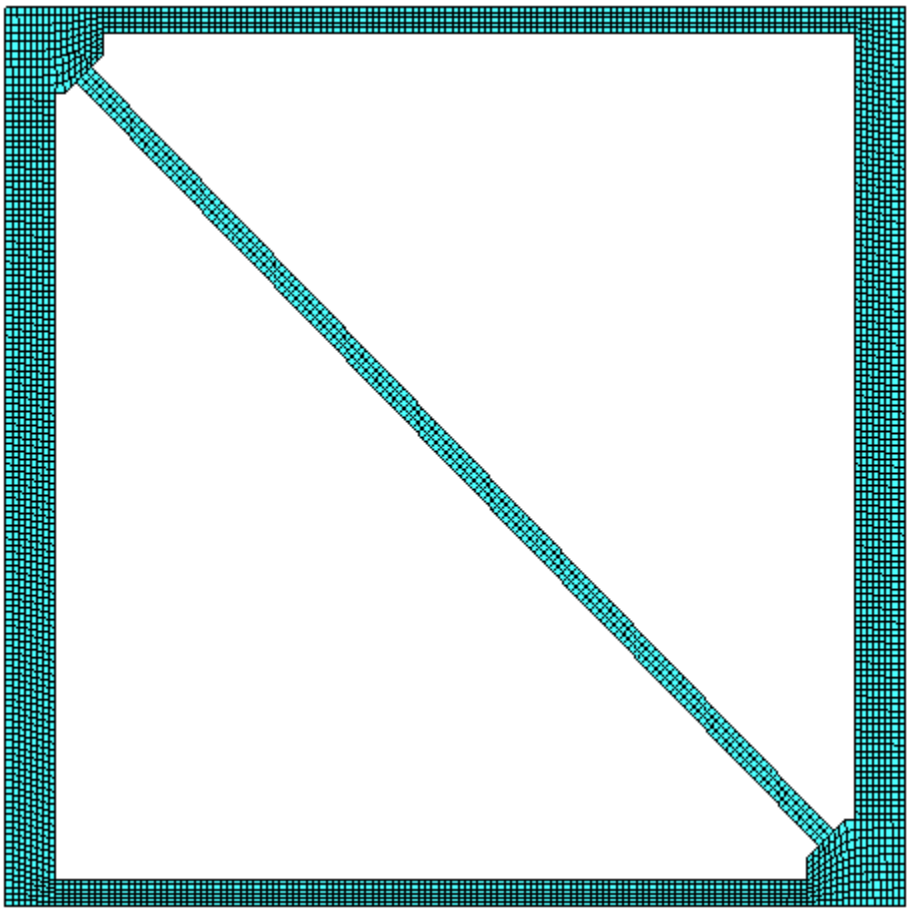

Fig. K29 - FEM Mesh – Frame “D” without RXS Fuse.

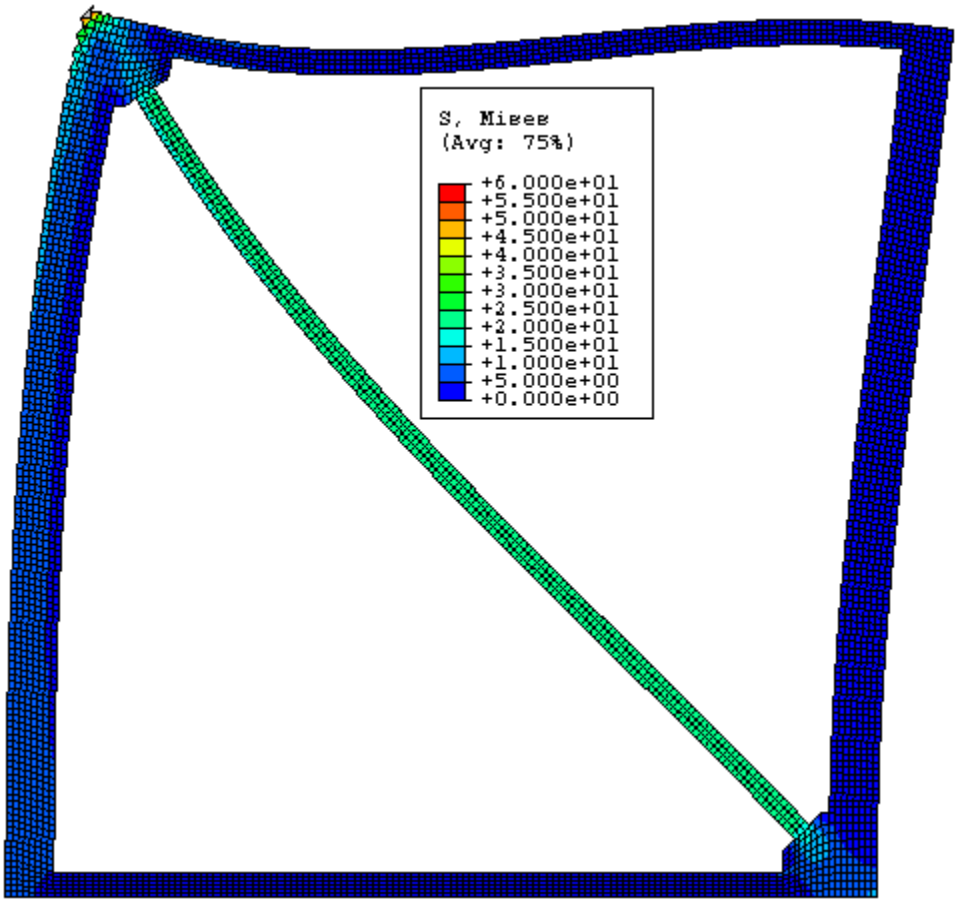

Fig. K30 - Von Mises Stress – Frame “D” without RXS Fuse.

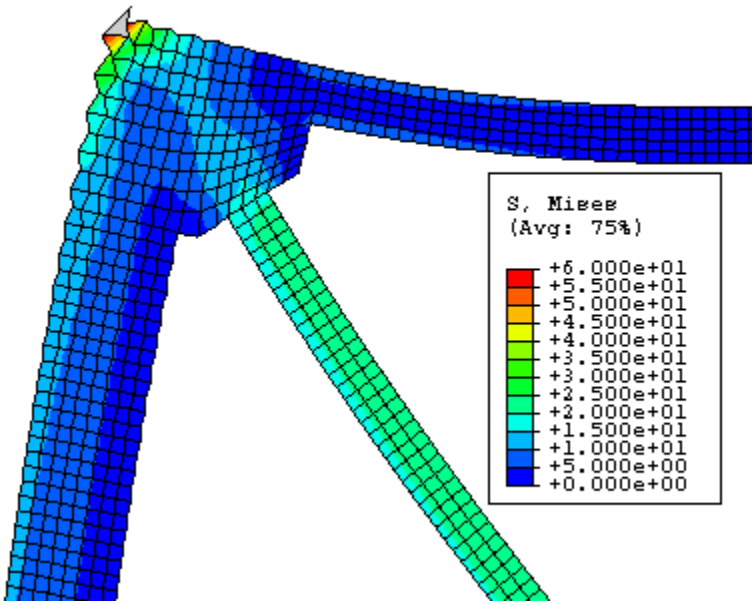

Fig. K31 - Von Mises Stress – Frame “D” without RXS Fuse – Zoom.

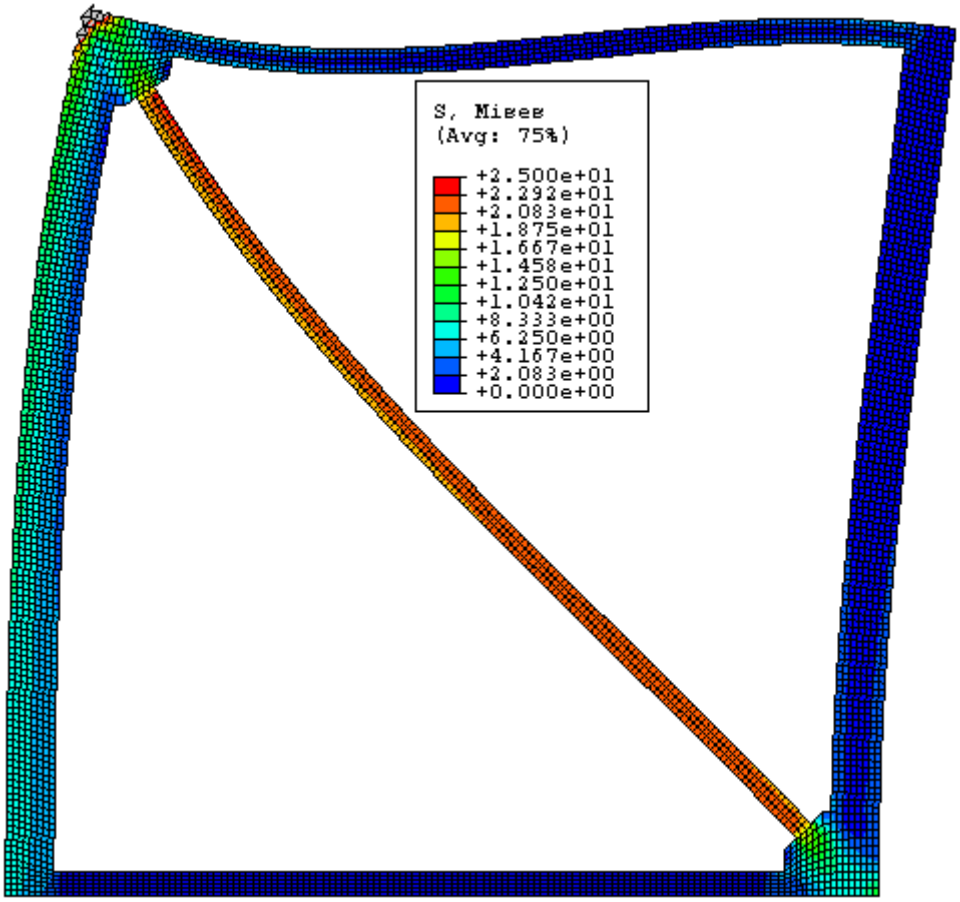

Fig. K32 - Von Mises Stress – Frame “D” without RXS Fuse – Stress Scale #2.

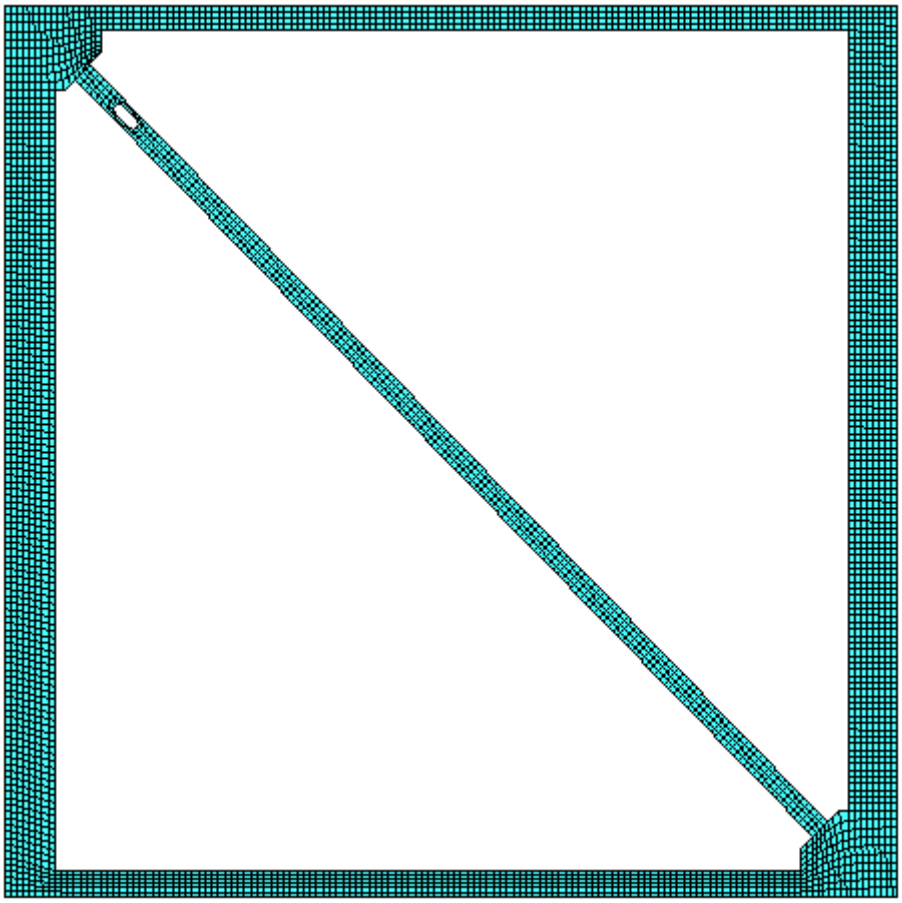

Fig. K33 - FEM Mesh – Frame “D” with RXS Fuse.

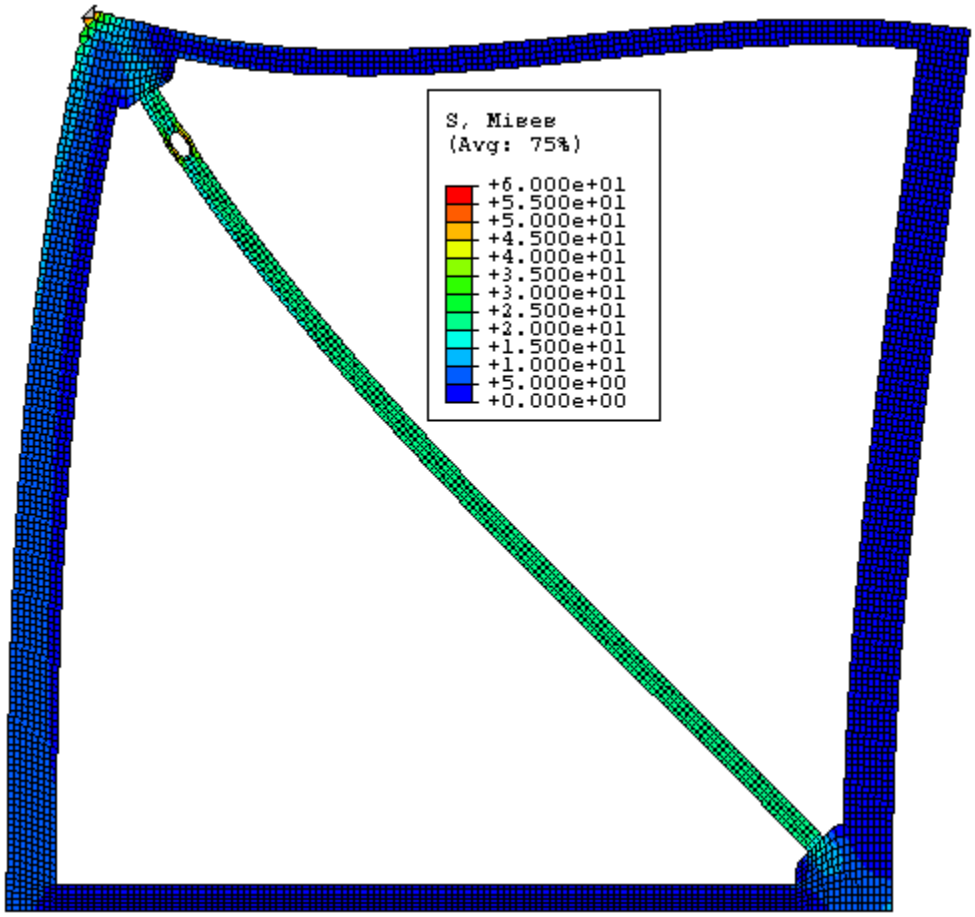

Fig. K34 - Von Mises Stress – Frame “D” with RXS Fuse.

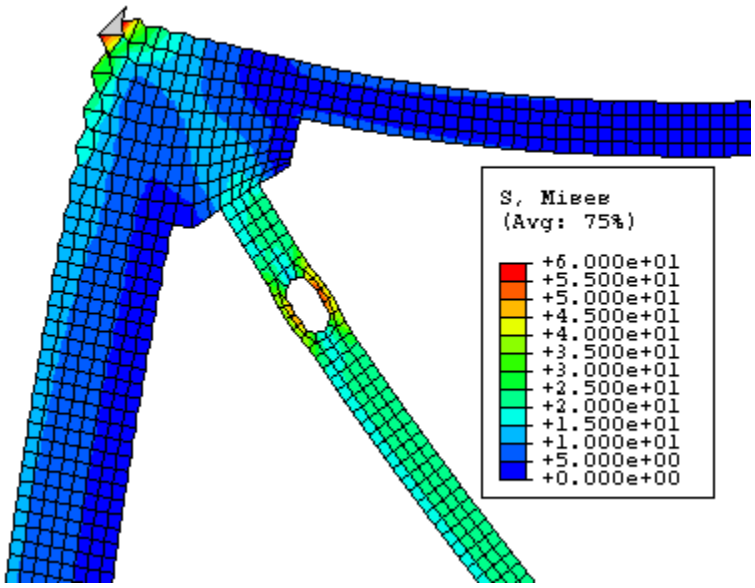

Fig. K35 - Von Mises Stress – Frame “D” with RXS Fuse – Zoom #1.

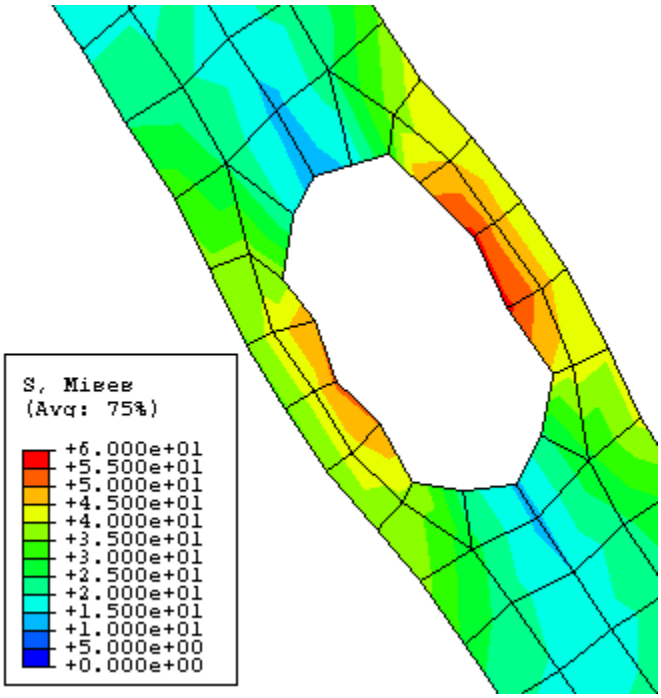

Fig. K36 - Von Mises Stress – Frame “D” with RXS Fuse – Zoom #2.

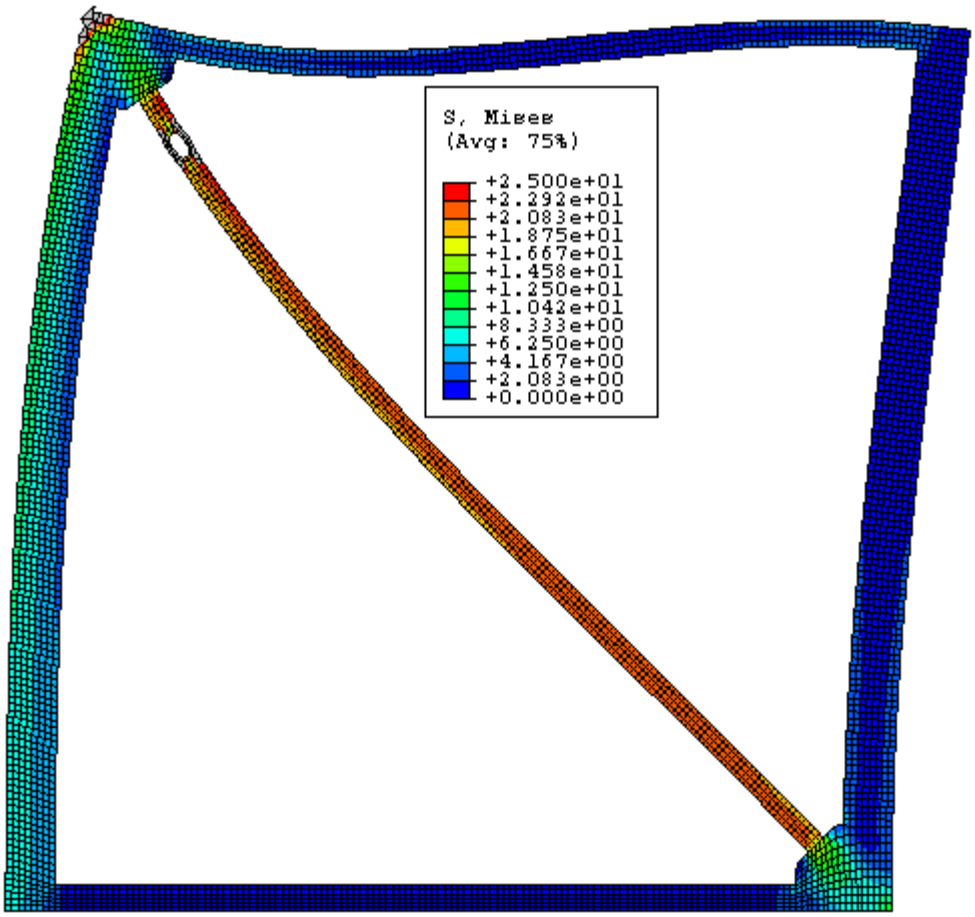

Fig. K37 - Von Mises Stress – Frame “D” with RXS Fuse – Stress Scale #2.

FRAME E

Beam/Column Length Ratio = H/L = 1

Beam-depth/Column-depth = 10”/16”

Brace Angle “ϕ” = 45˚

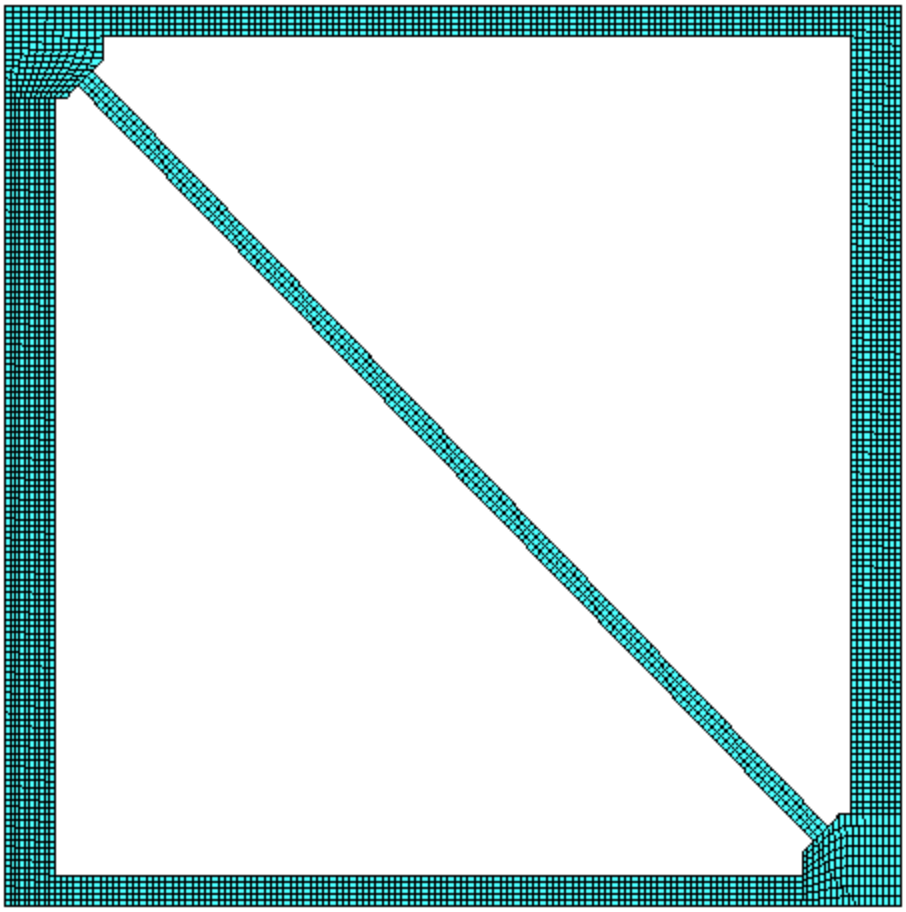

Fig. K38 - FEM Mesh – Frame “D” without RXS Fuse.

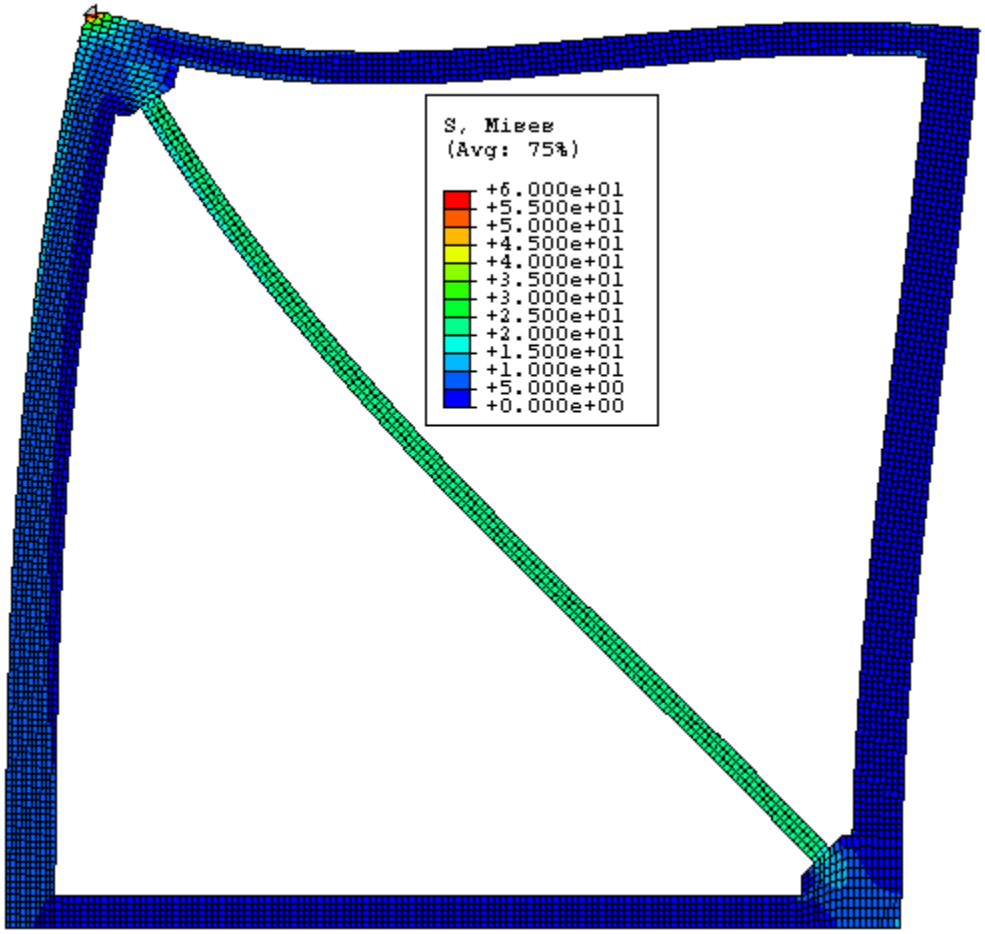

Fig. K39 - Von Mises Stress – Frame “E” without RXS Fuse.

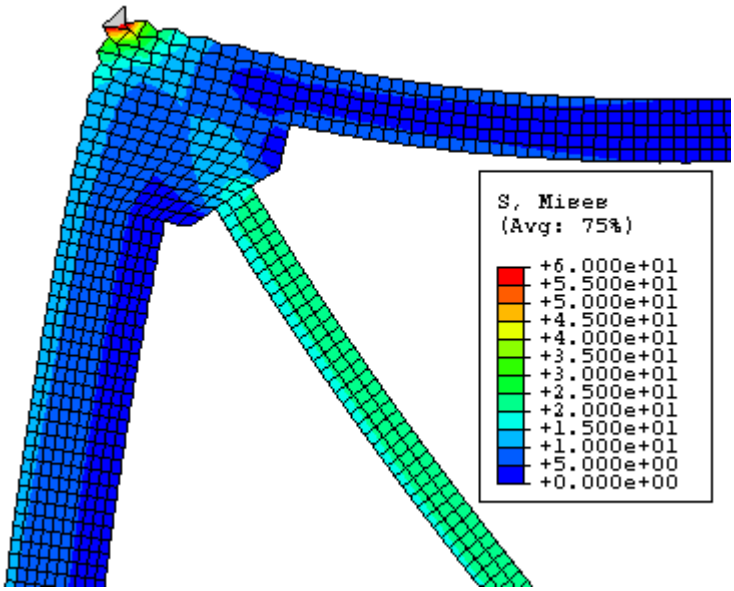

Fig. K40 - Von Mises Stress – Frame “E” without RXS Fuse – Zoom.

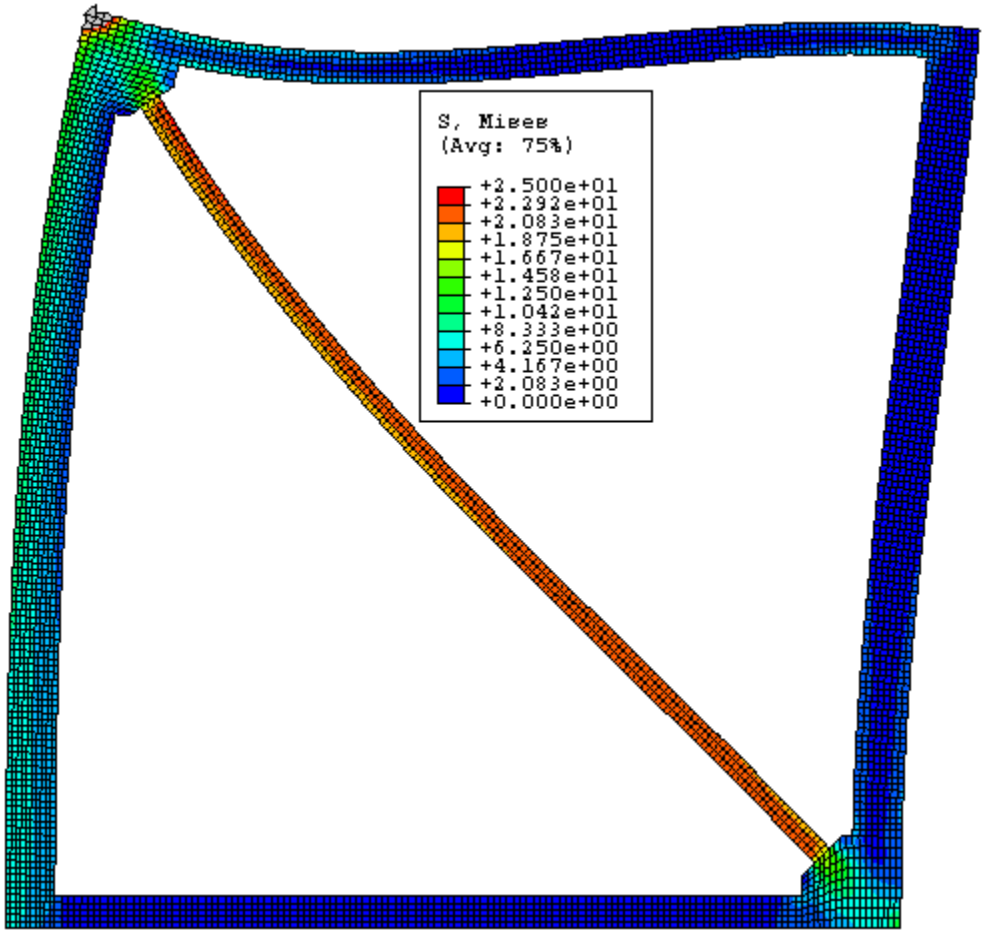

Fig. K41 - Von Mises Stress – Frame “E” without RXS Fuse – Stress Scale #2.

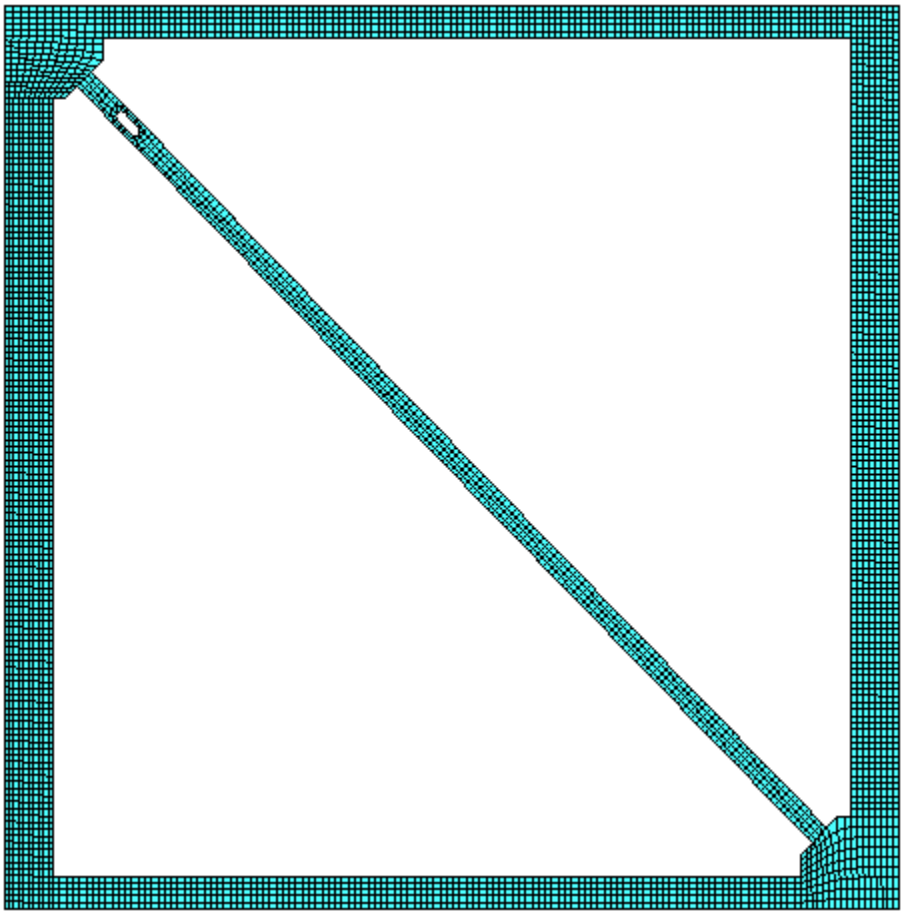

Fig. K42 - FEM Mesh – Frame “E” with RXS Fuse.

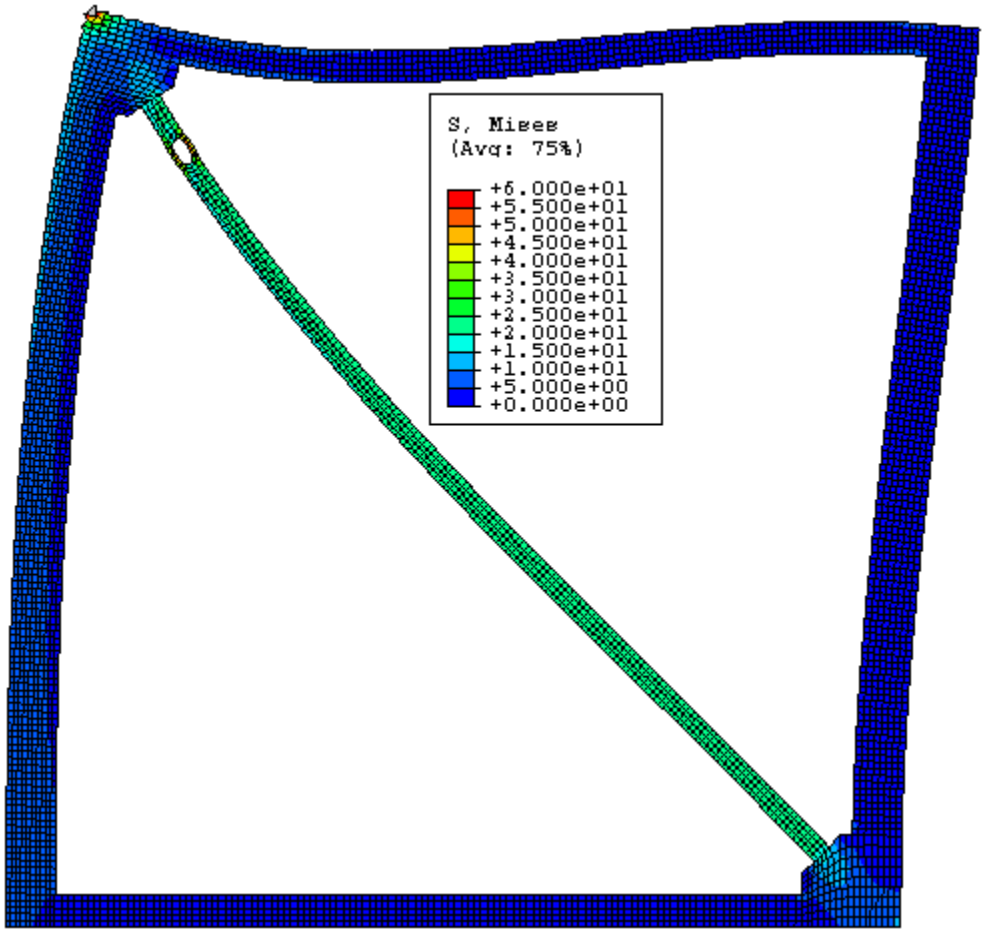

Fig. K43 - Von Mises Stress – Frame “E” with RXS Fuse.

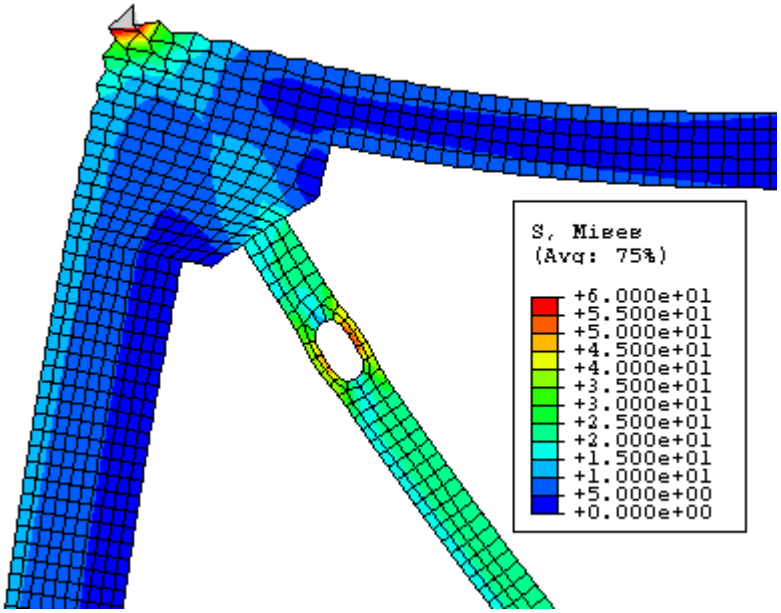

Fig. K44 - Von Mises Stress – Frame “E” with RXS Fuse – Zoom #1.

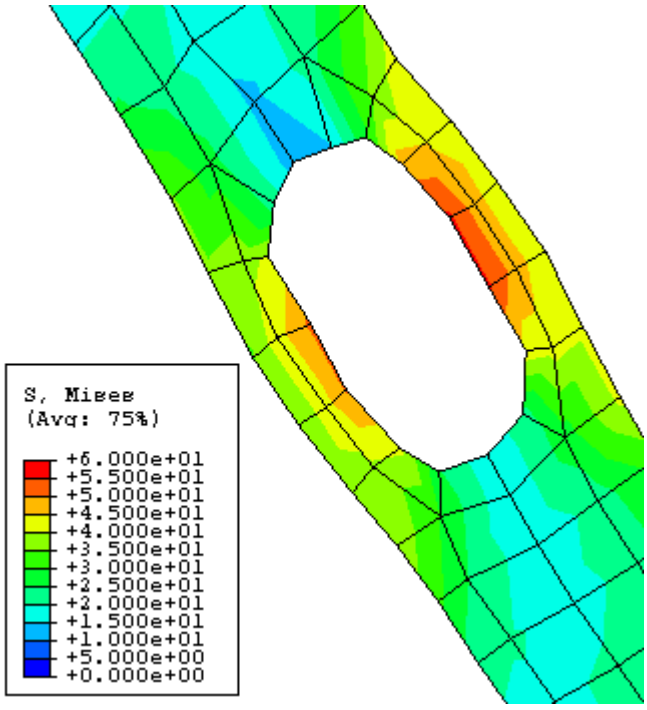

Fig. K45 - Von Mises Stress – Frame “E” with RXS Fuse – Zoom #2.

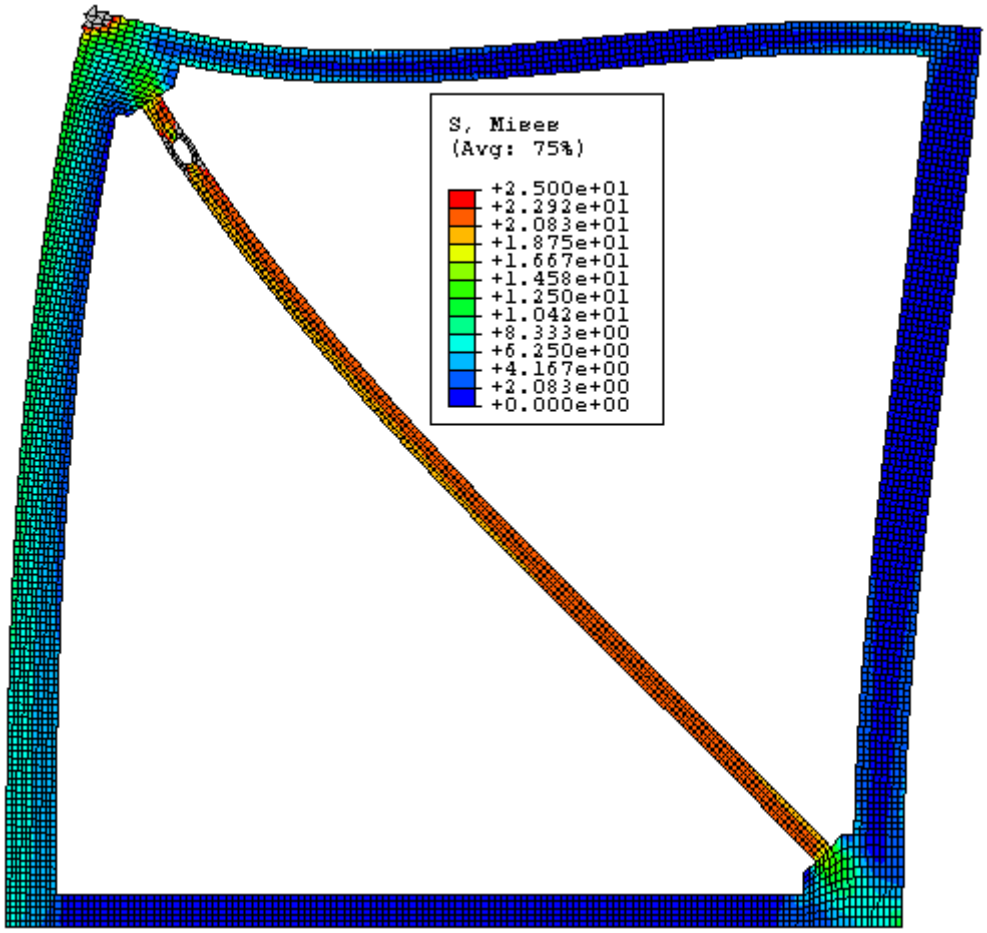

Fig. K46 - Von Mises Stress – Frame “E” with RXS Fuse – Stress Scale #2.

FRAME F

Beam/Column Length Ratio = H/L = 1

Beam-depth/Column-depth = 12”/16”

Brace Angle “ϕ” = 45˚

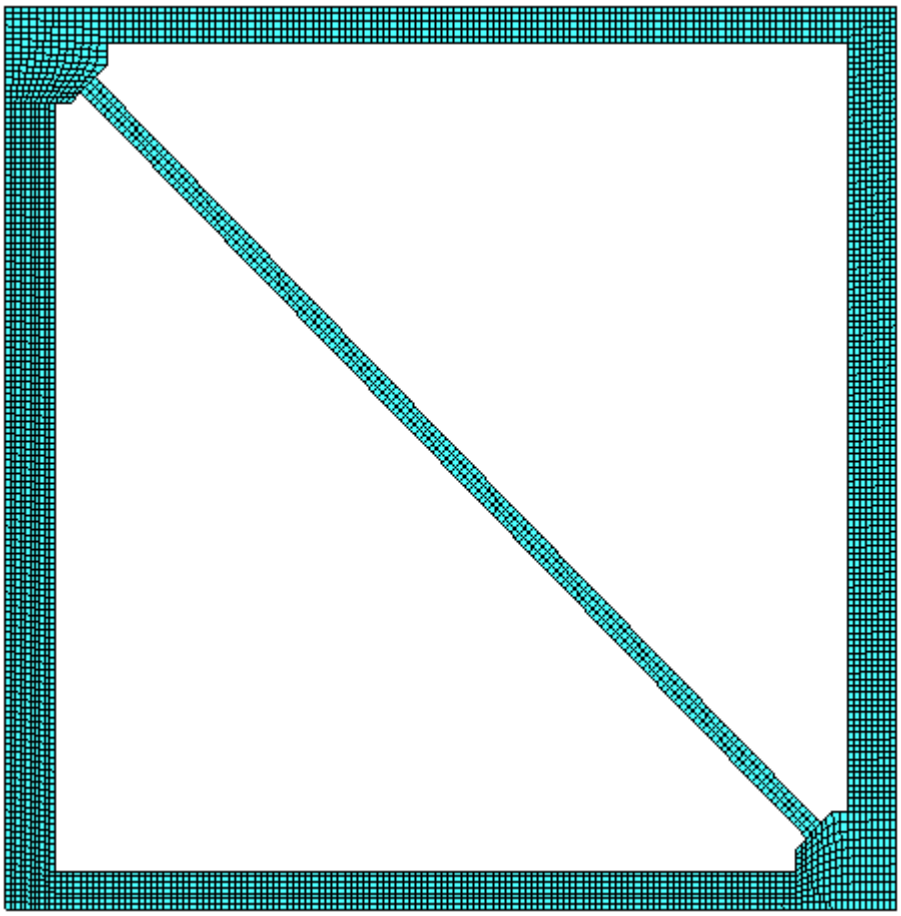

Fig. K47 - FEM Mesh – Frame “F” without RXS Fuse.

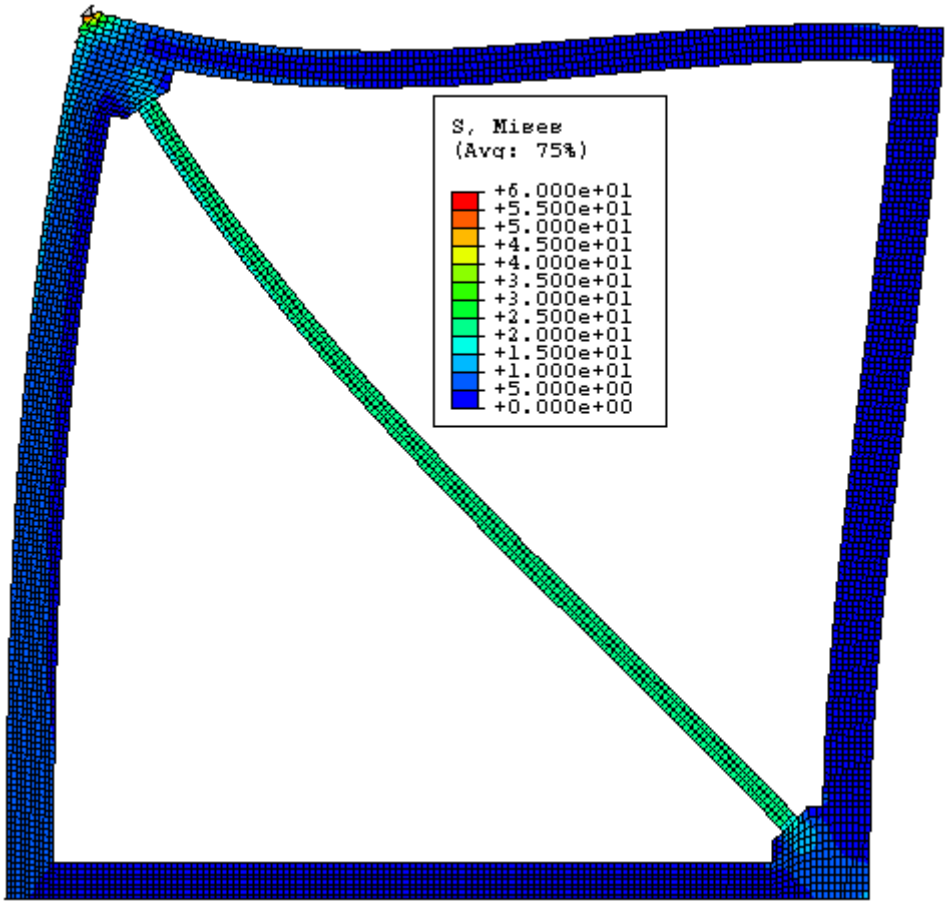

Fig. K48 - Von Mises Stress – Frame “F” without RXS Fuse.

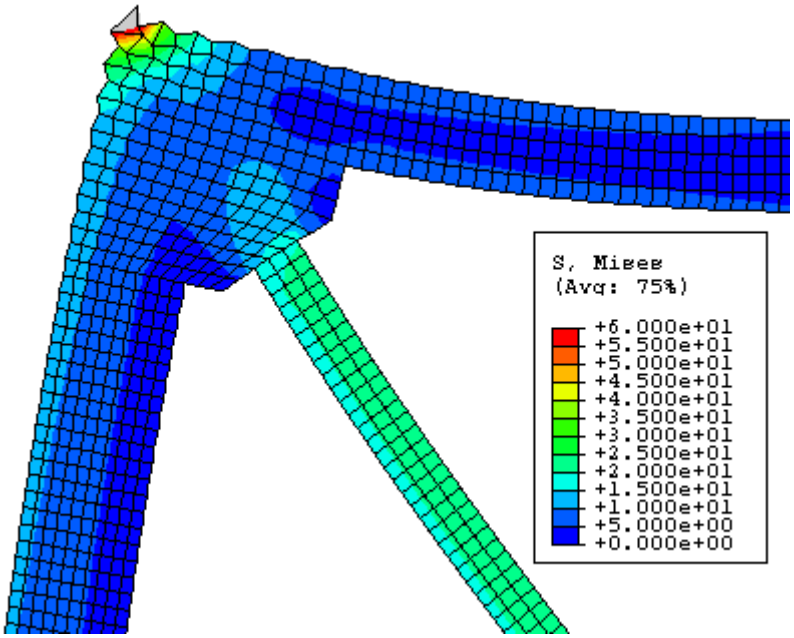

Fig. K49 - Von Mises Stress – Frame “F” without RXS Fuse – Zoom.

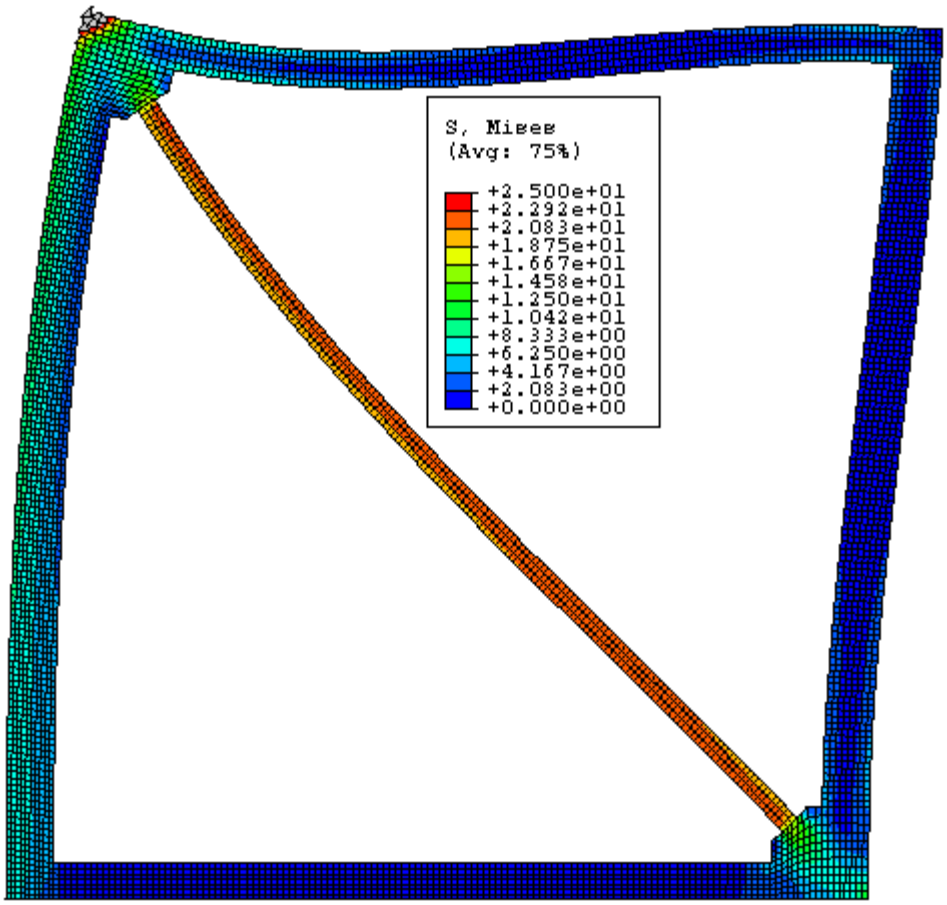

Fig. K50 - Von Mises Stress – Frame “F” without RXS Fuse – Stress Scale #2.

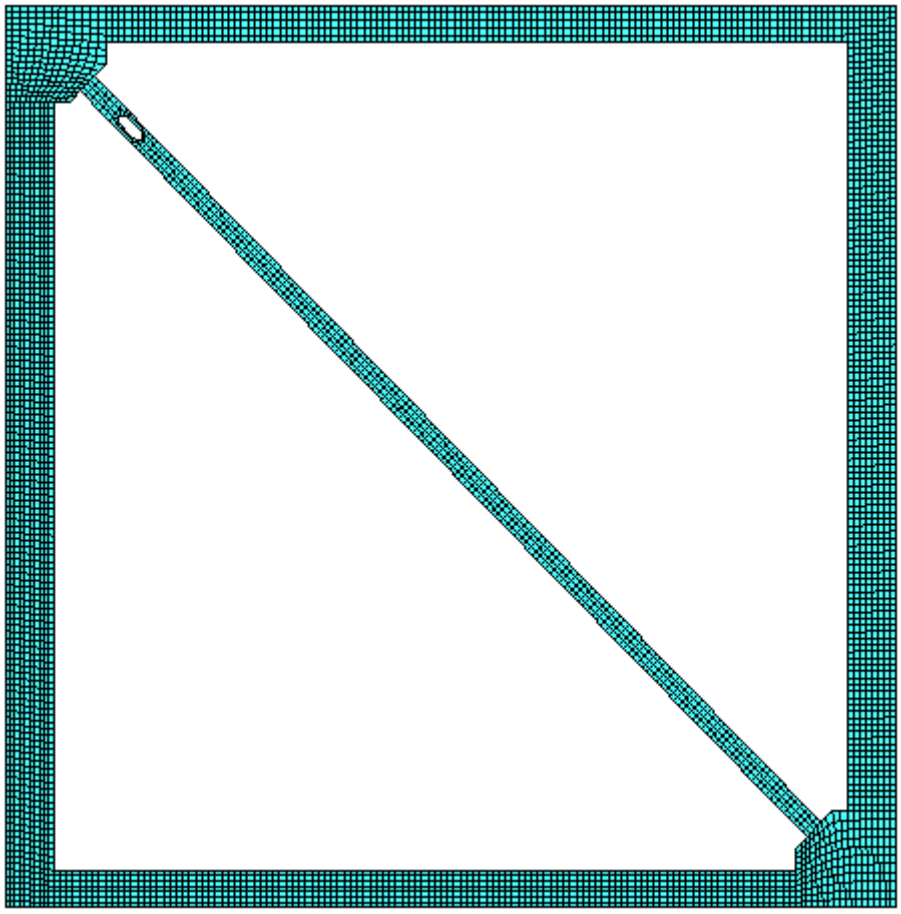

Fig. K51 - FEM Mesh – Frame “F” with RXS Fuse.

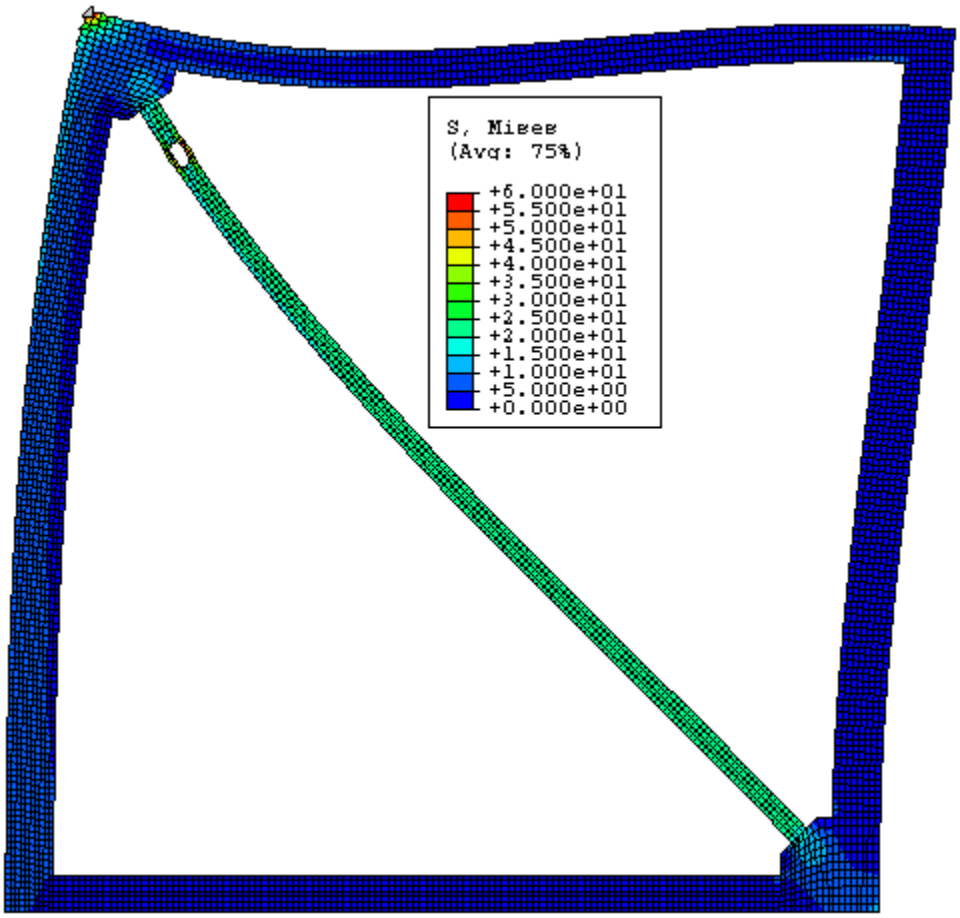

Fig. K52 - Von Mises Stress – Frame “F” with RXS Fuse.

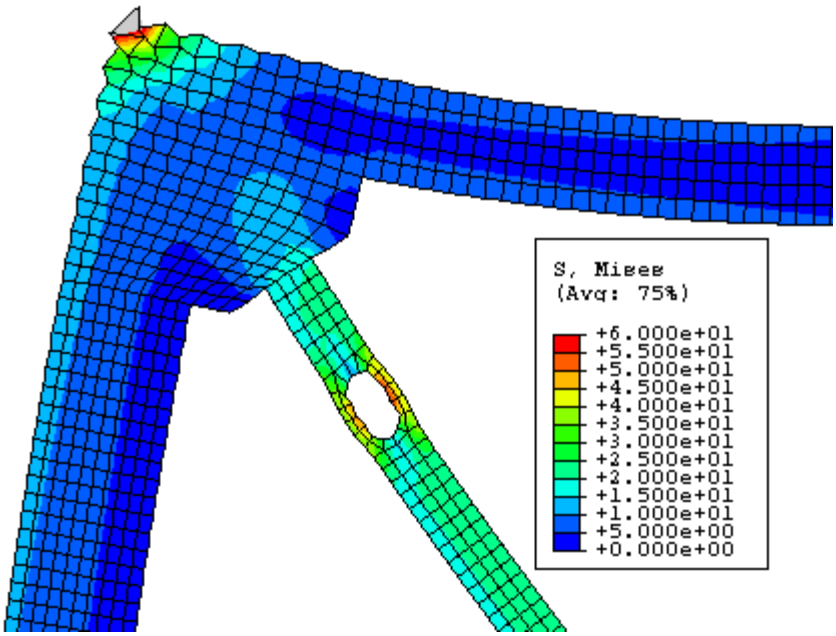

Fig. K53 - Von Mises Stress – Frame “F” with RXS Fuse – Zoom #1.

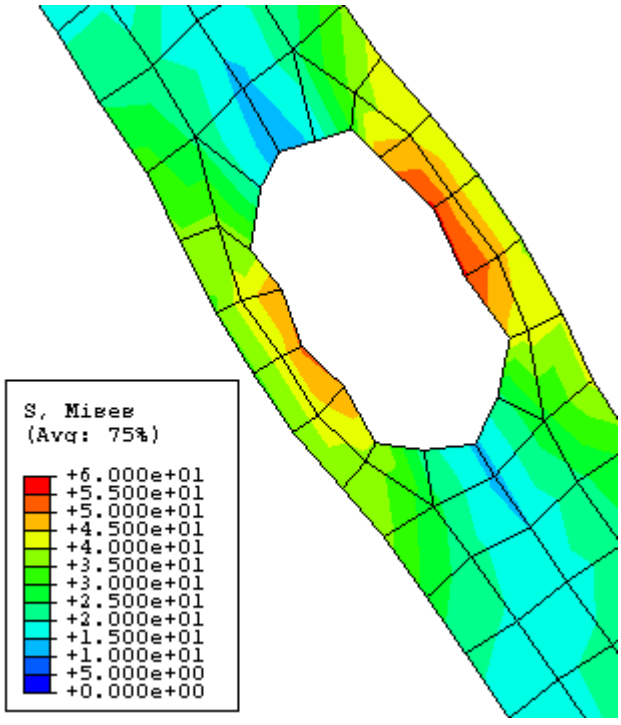

Fig. K54 - Von Mises Stress – Frame “F” with RXS Fuse – Zoom #2.

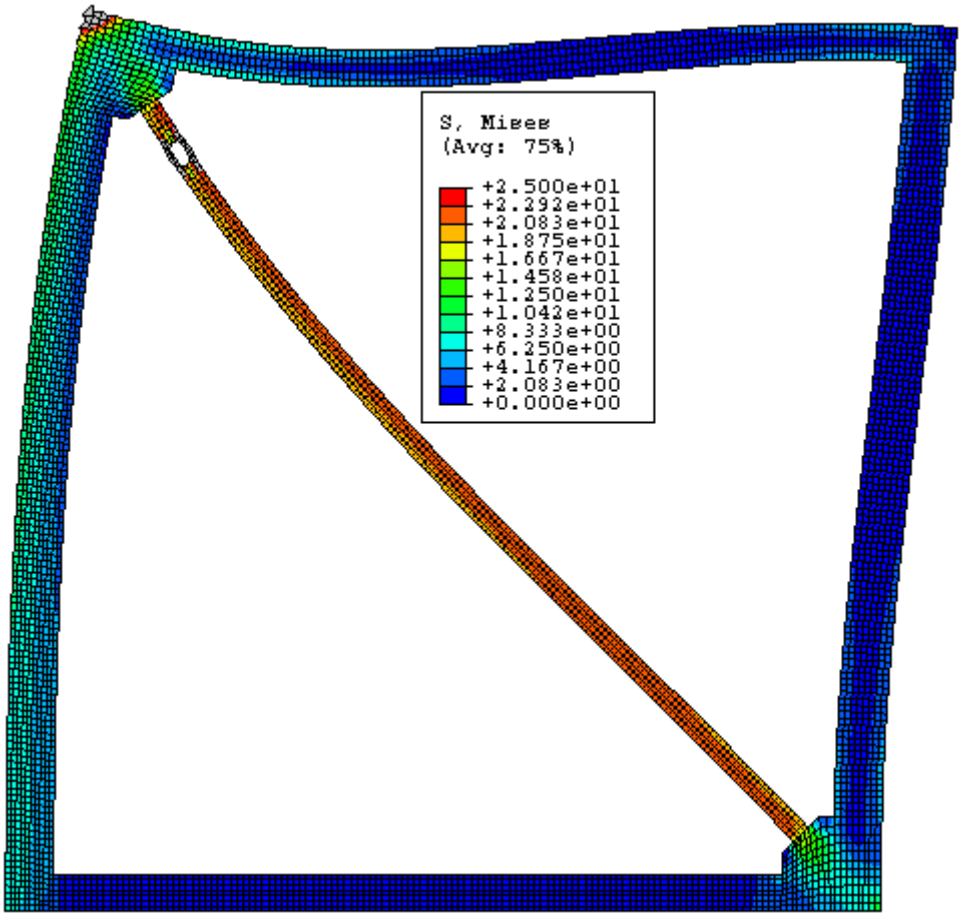

Fig. K55 - Von Mises Stress – Frame “F” with RXS Fuse – Stress Scale #2.

FRAME G

Beam/Column Length Ratio = H/L = 1

Beam-depth/Column-depth = 14”/16”

Brace Angle “ϕ” = 45˚

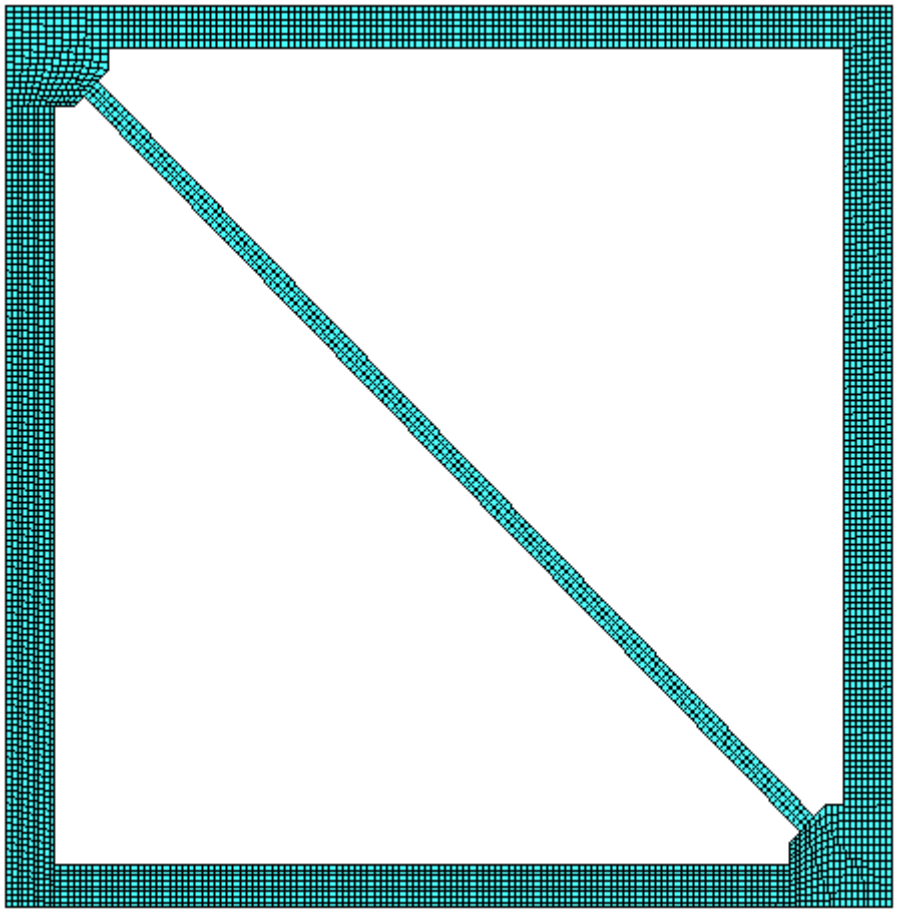

Fig. K56 - FEM Mesh – Frame “G” without RXS Fuse.

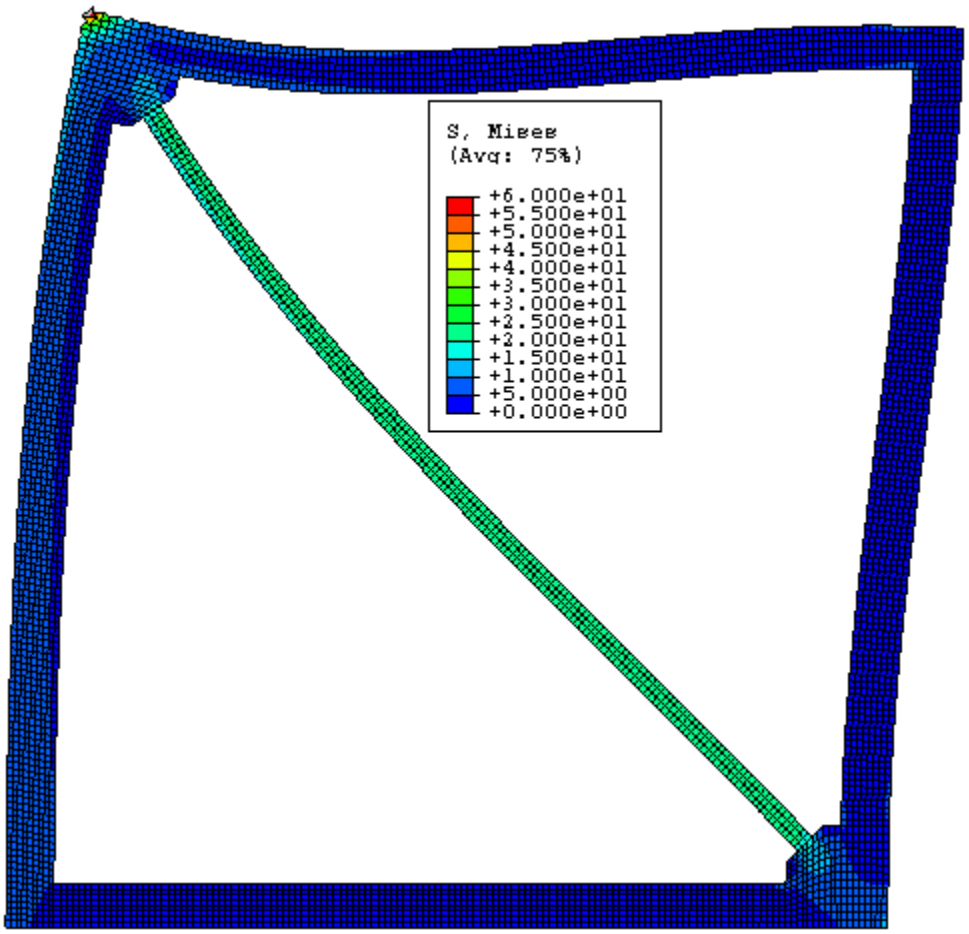

Fig. K57 - Von Mises Stress – Frame “G” without RXS Fuse.

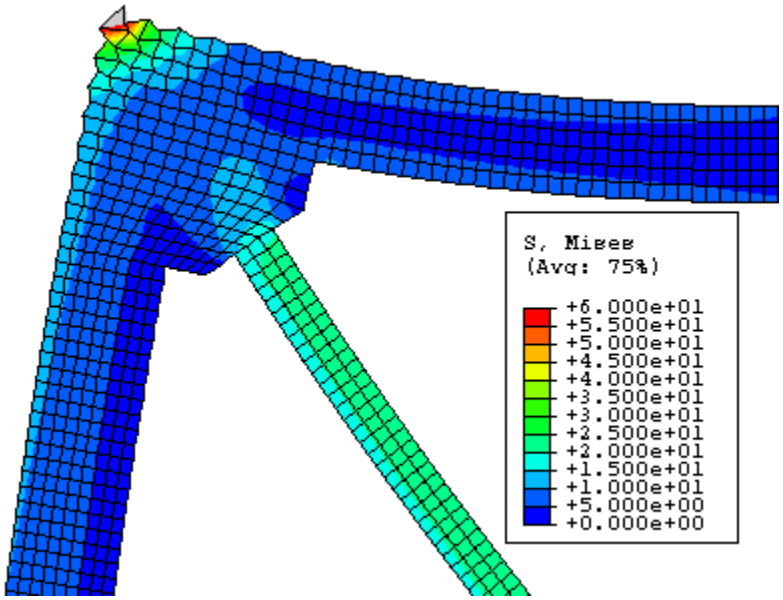

Fig. K58 - Von Mises Stress – Frame “G” without RXS Fuse – Zoom.

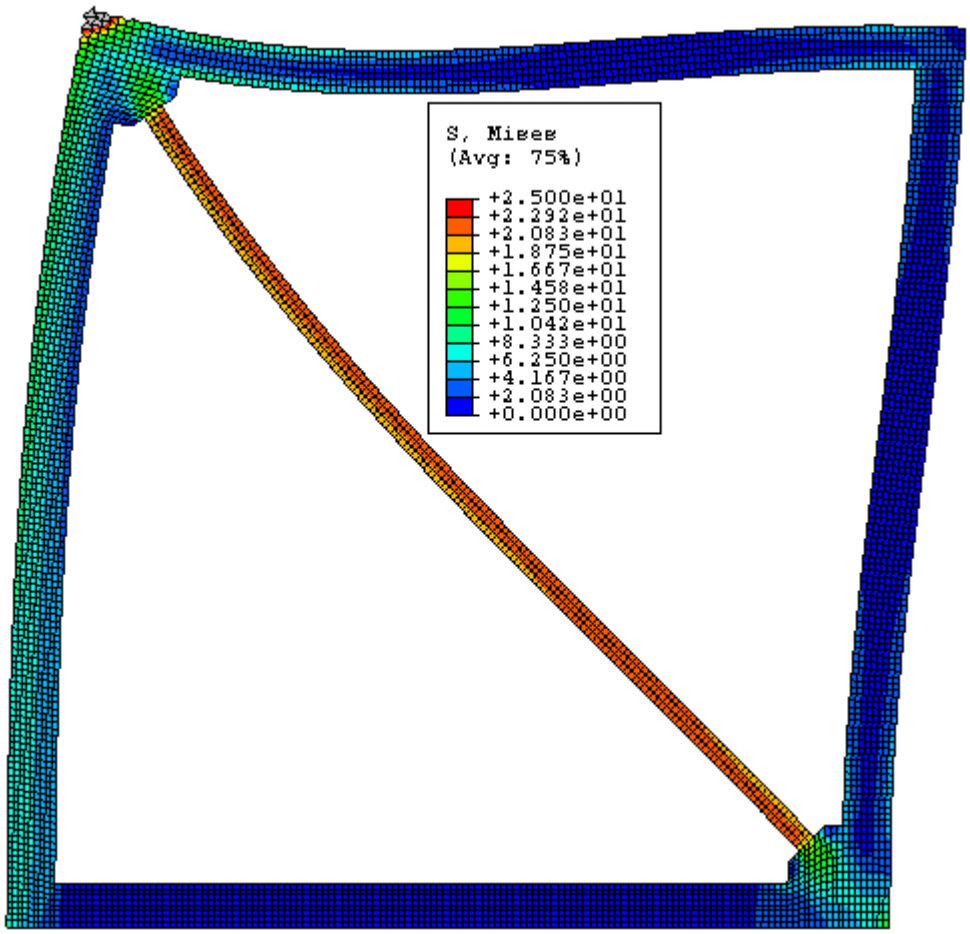

Fig. K59 - Von Mises Stress – Frame “G” without RXS Fuse – Stress Scale #2.

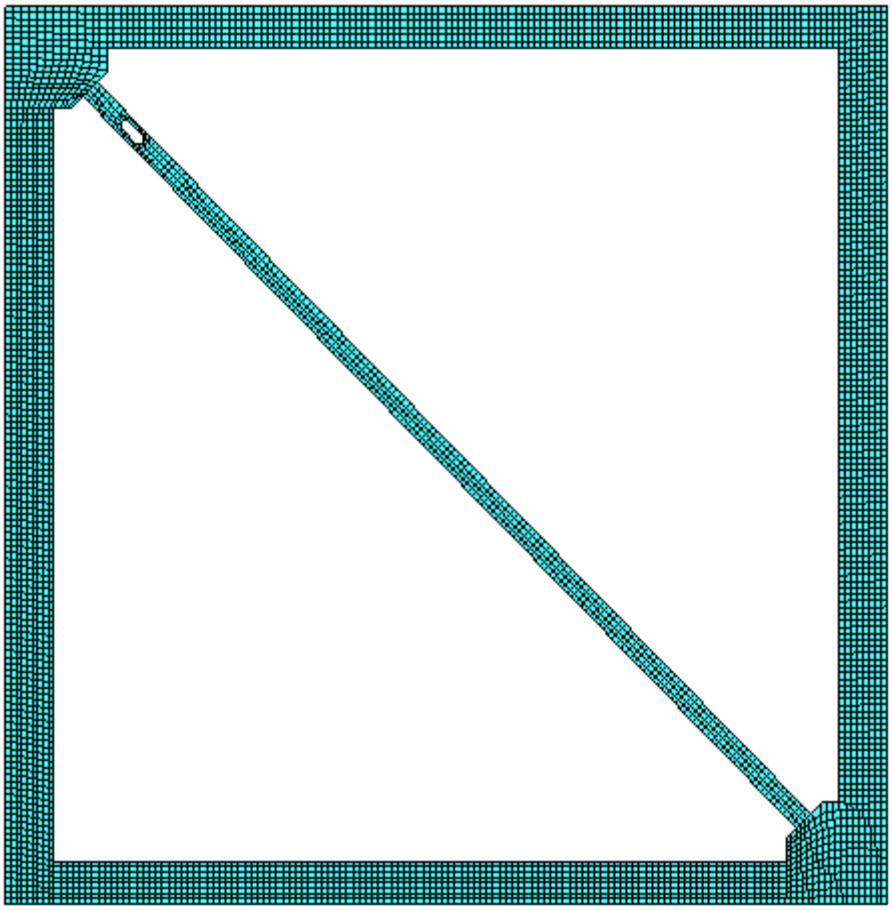

Fig. K60 - FEM Mesh – Frame “G” with RXS Fuse.

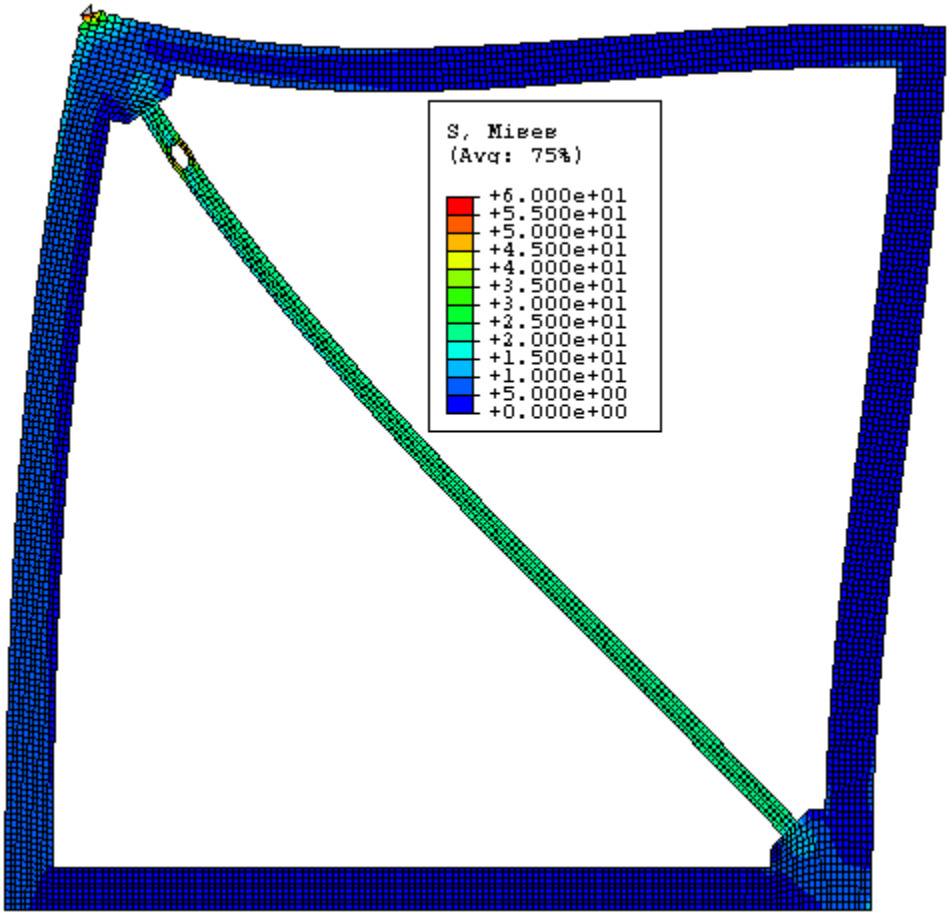

Fig. K61 - Von Mises Stress – Frame “G” with RXS Fuse.

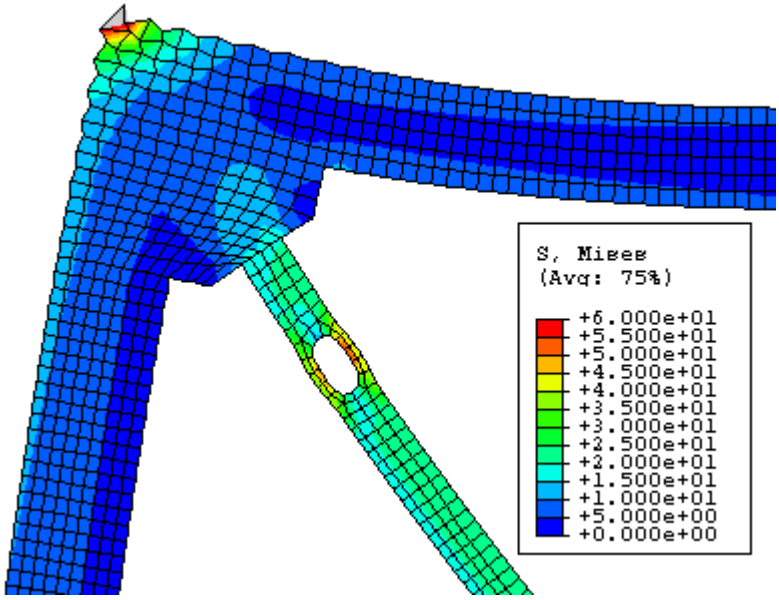

Fig. K62 - Von Mises Stress – Frame "G" with RXS Fuse – Zoom #1.

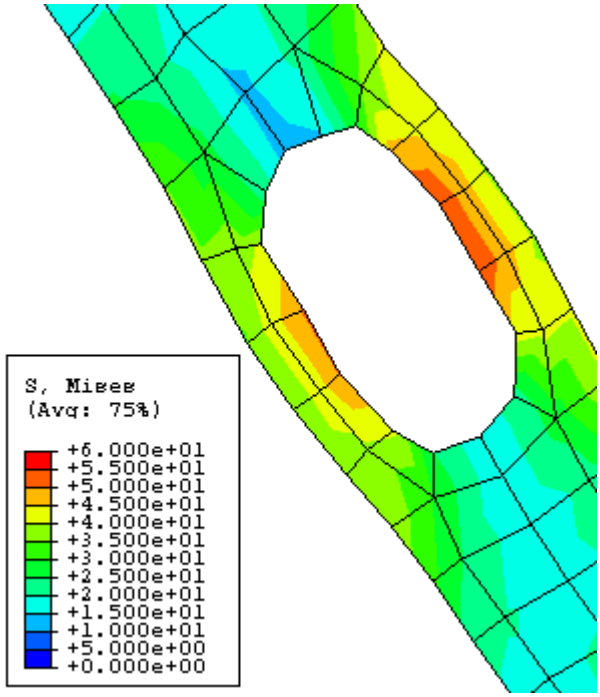

Fig. K63 - Von Mises Stress – Frame "G" with RXS Fuse – Zoom #2.

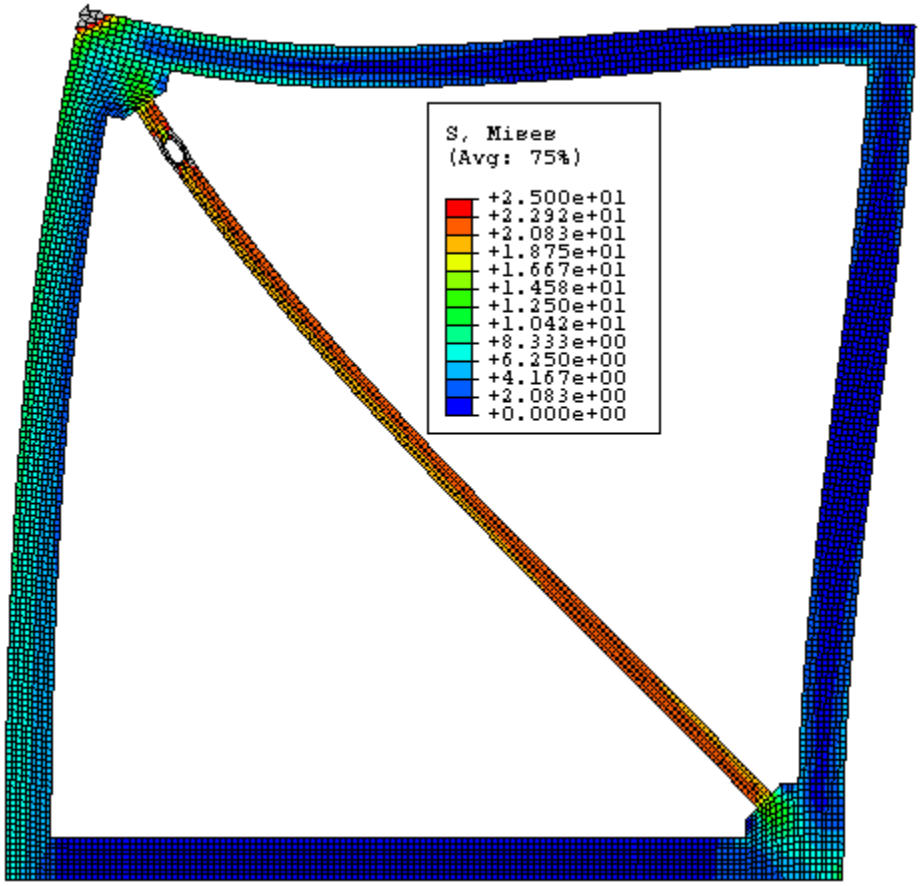

Fig. K64 - Von Mises Stress – Frame “G” with RXS Fuse – Stress Scale #2.

CONTROL FRAME H

Beam/Column Length Ratio = H/L = 1

Beam-depth/Column-depth = 16”/16”

Brace Angle “ϕ” = 45˚

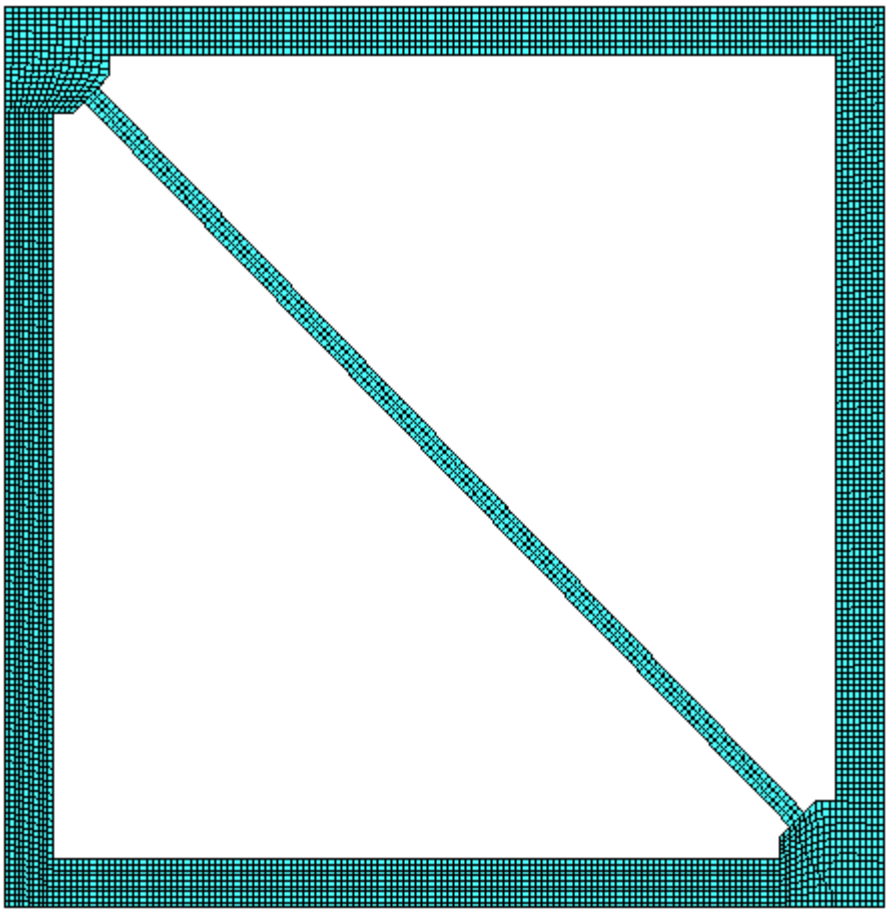

Fig. K65 - FEM Mesh – Frame “H” without RXS Fuse.

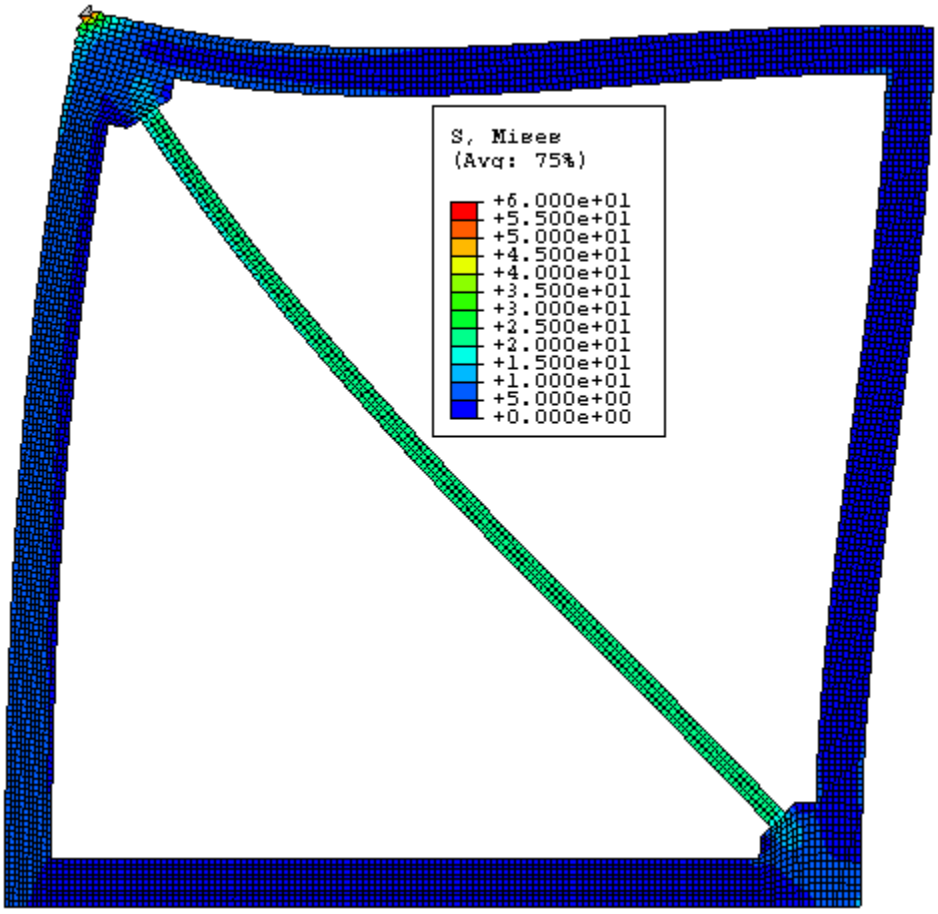

Fig. K66 - Von Mises Stress – Frame “H” without RXS Fuse.

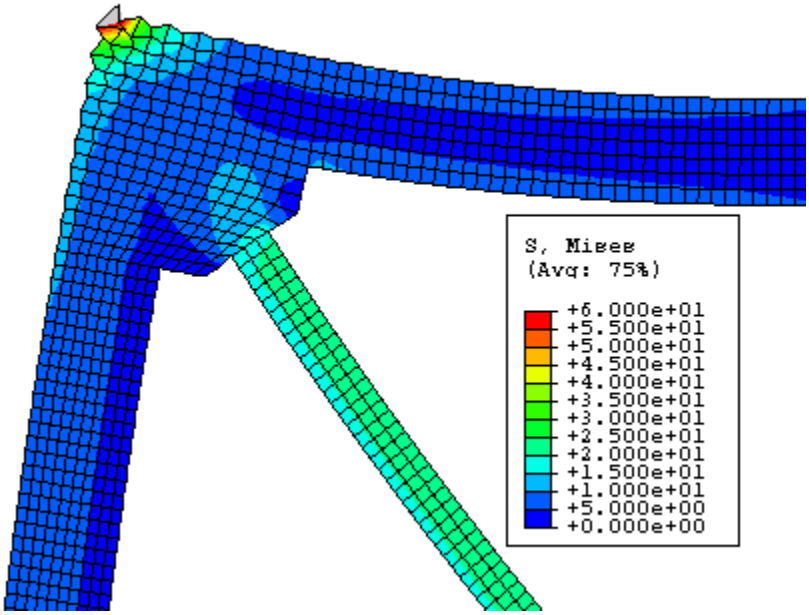

Fig. K67 - Von Mises Stress – Frame “H” without RXS Fuse – Zoom.

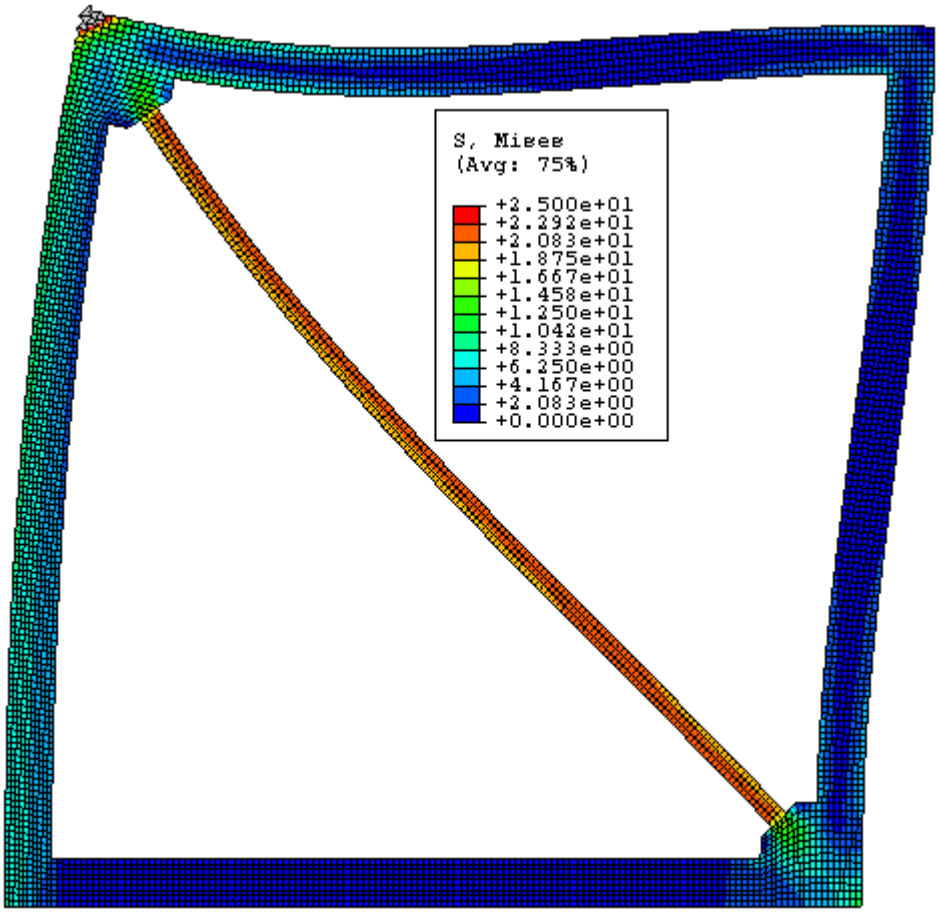

Fig. K68 - Von Mises Stress – Frame “H” without RXS Fuse – Stress Scale #2.

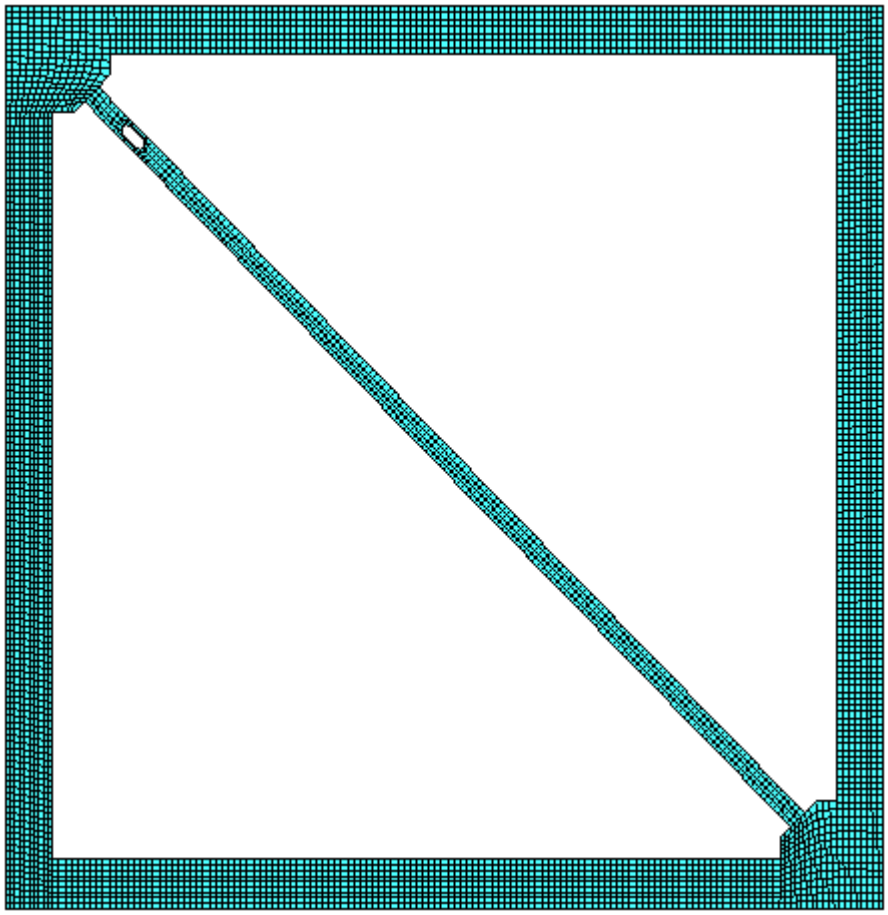

Fig. K69 - FEM Mesh – Frame “H” with RXS Fuse.

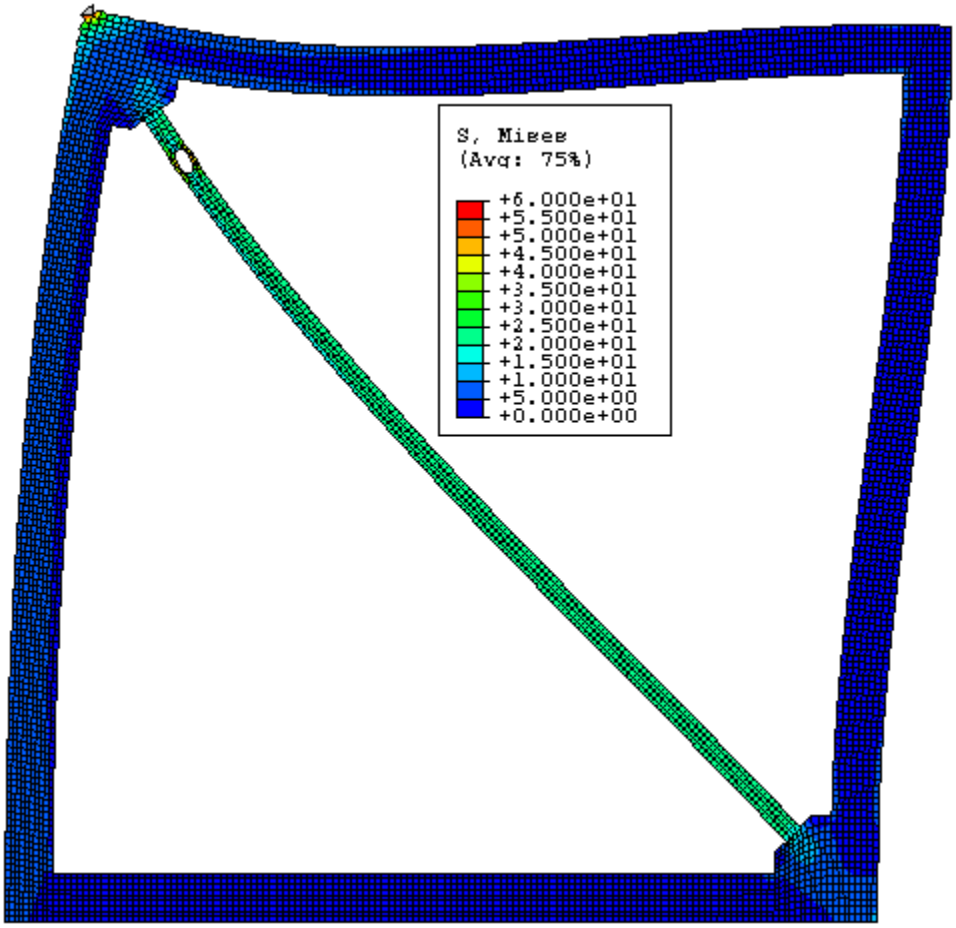

Fig. K70 - Von Mises Stress – Frame “H” with RXS Fuse.

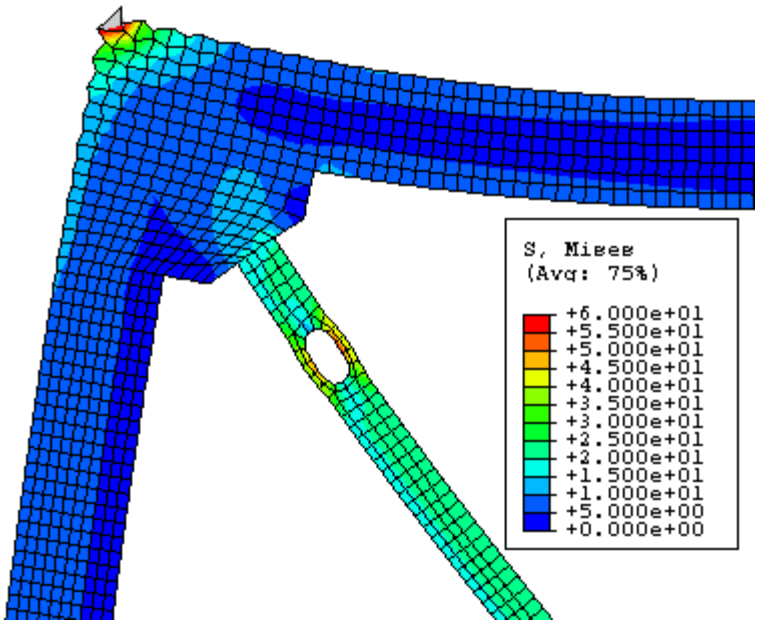

Fig. K71 - Von Mises Stress – Frame "H" with RXS Fuse – Zoom #1.

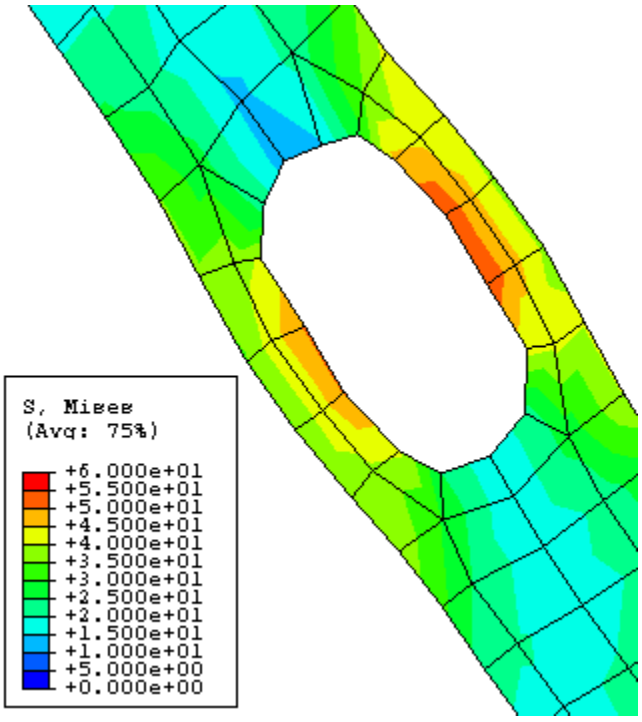

Fig. K72 - Von Mises Stress – Frame "H" with RXS Fuse – Zoom #2.

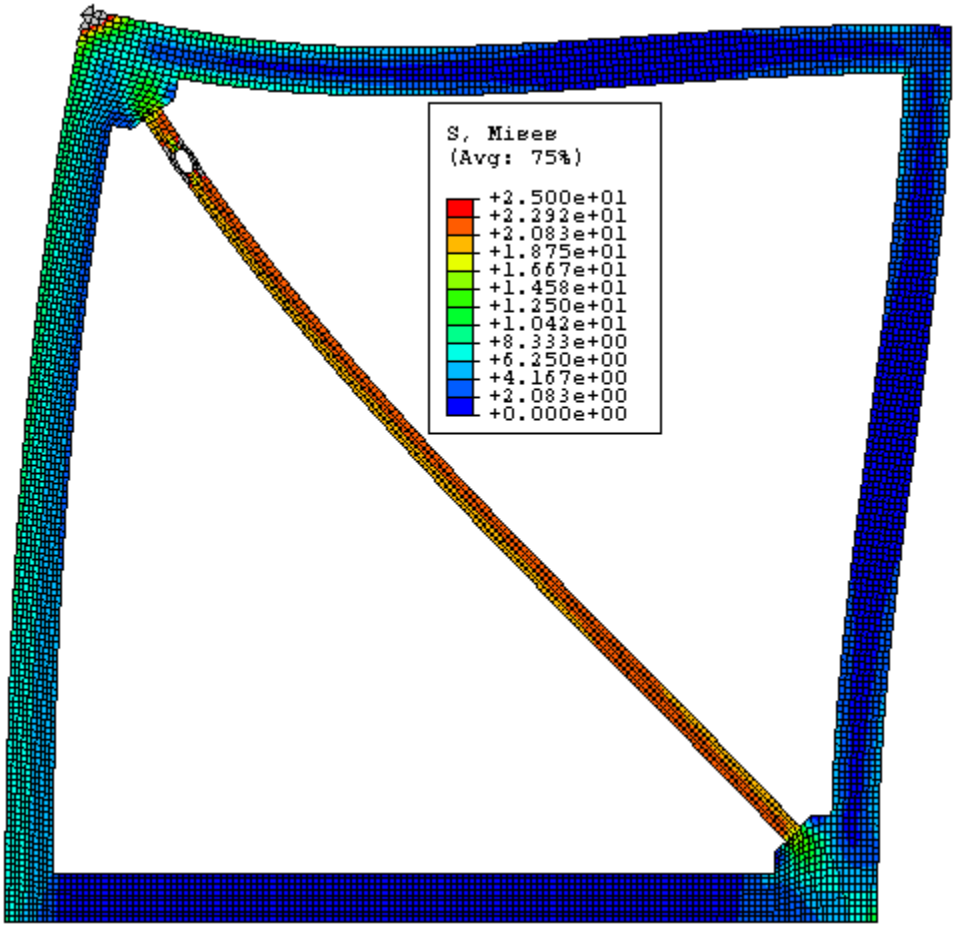

Fig. K73 - Von Mises Stress – Frame “H” with RXS Fuse – Stress Scale #2.

FRAME I

Beam/Column Length Ratio = H/L = 1

Beam-depth/Column-depth = 16”/14”

Brace Angle “ϕ” = 45˚

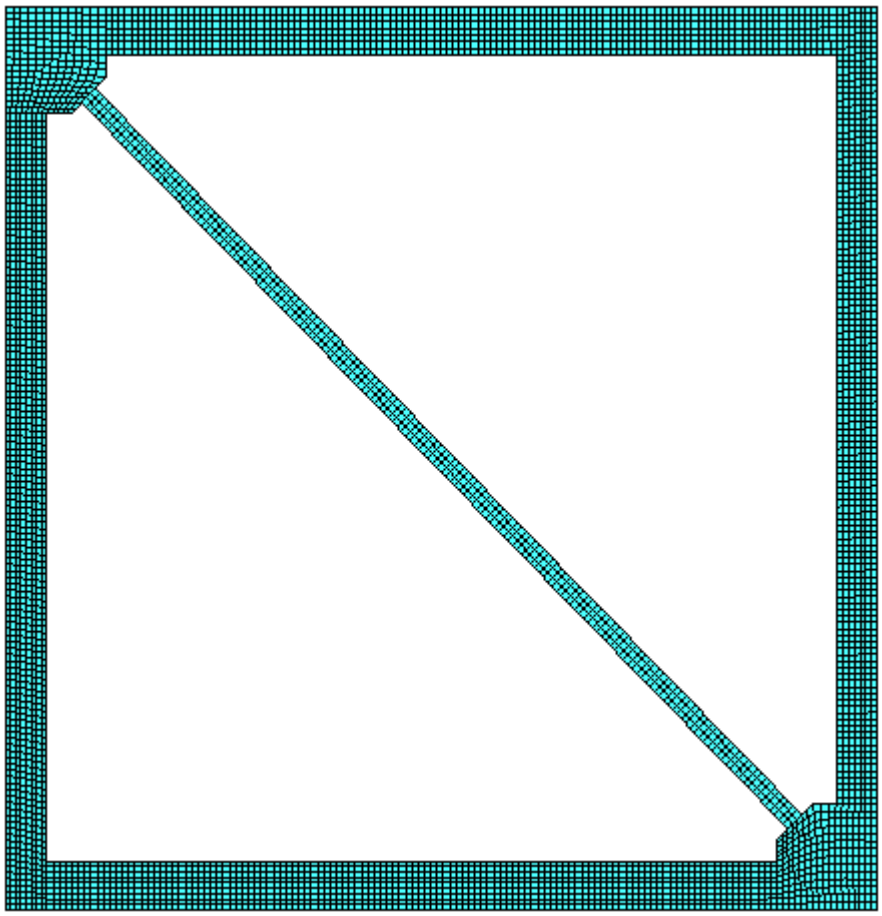

Fig. K74 - FEM Mesh – Frame “I” with RXS Fuse.

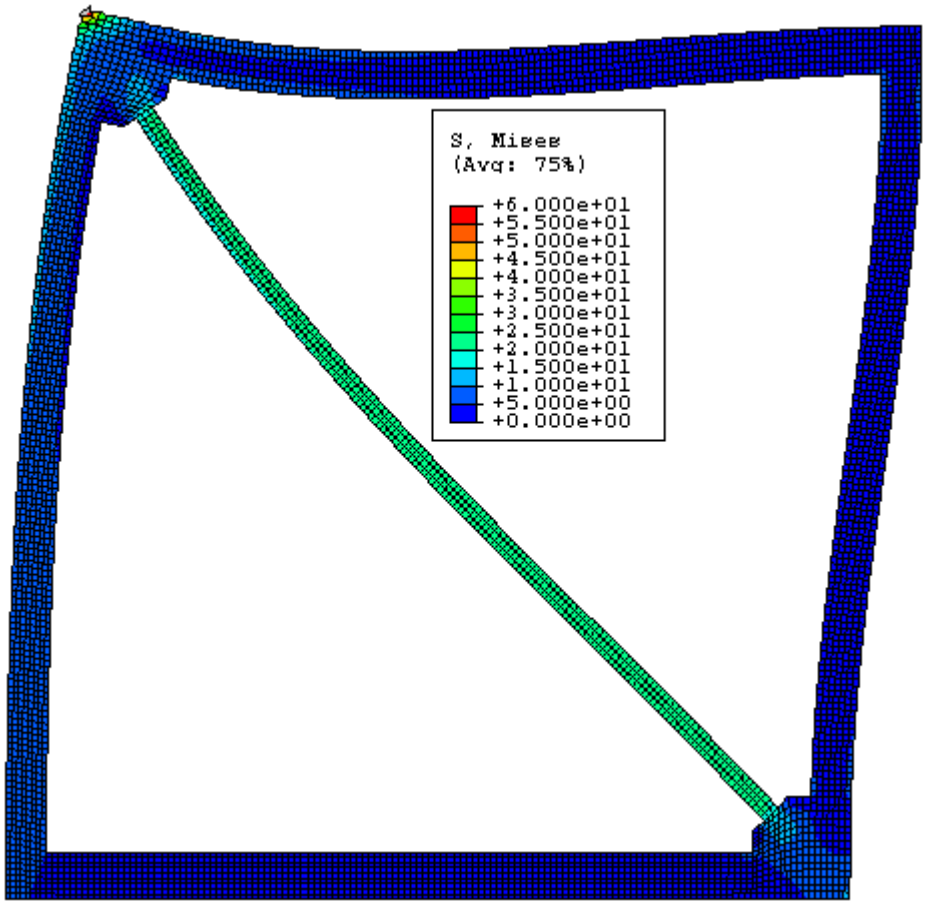

Fig. K75 - Von Mises Stress – Frame “I” without RXS Fuse.

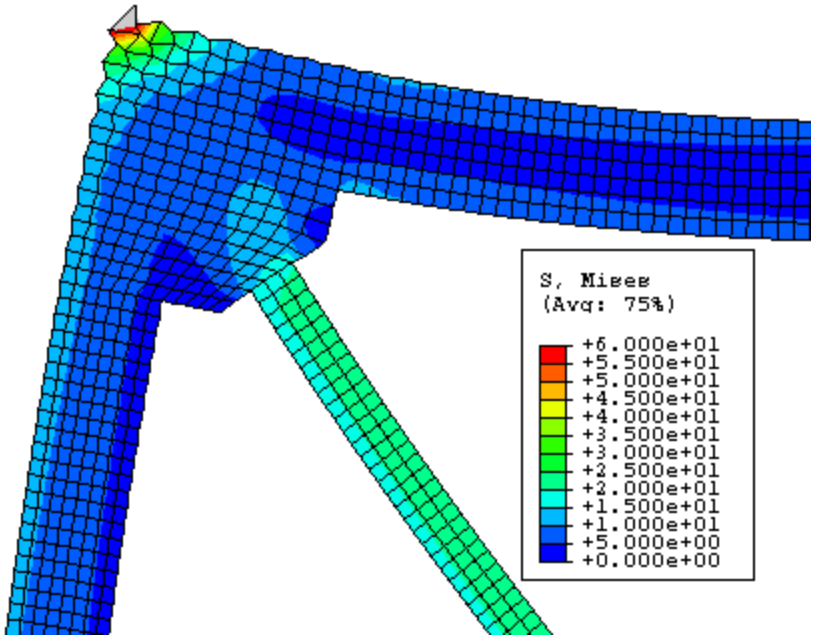

Fig. K76 - Von Mises Stress – Frame “I” without RXS Fuse – Zoom.

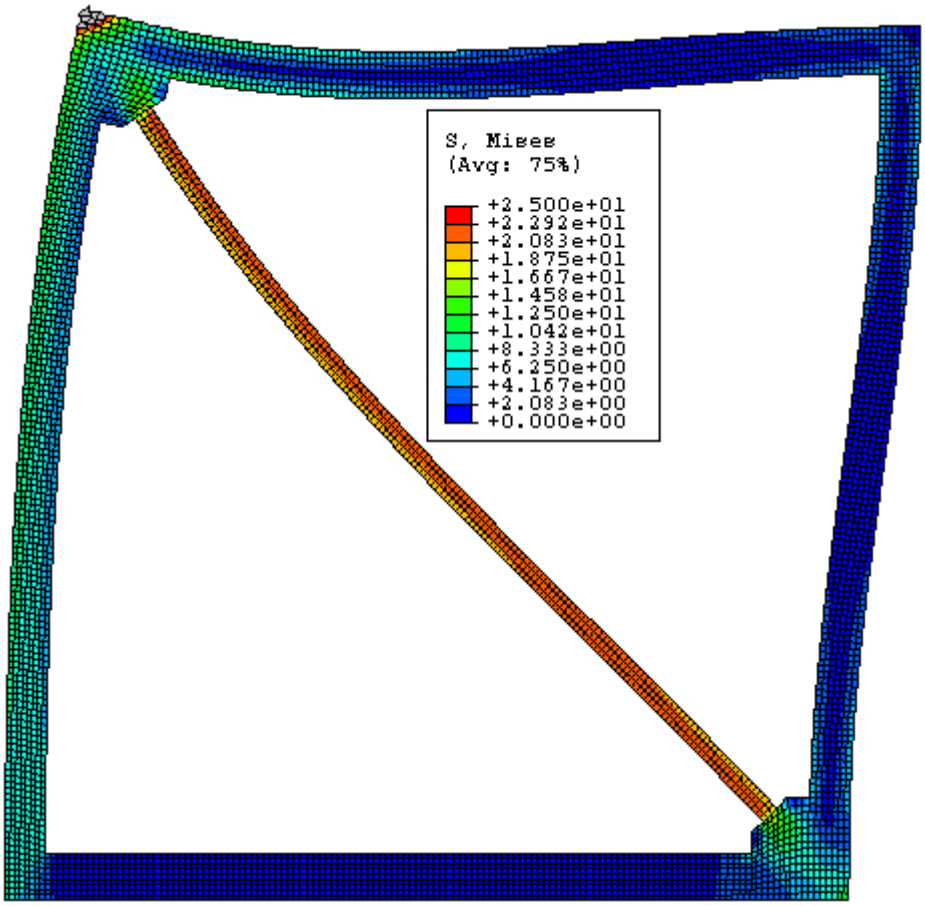

Fig. K77 - Von Mises Stress – Frame “I” without RXS Fuse – Stress Scale #2.

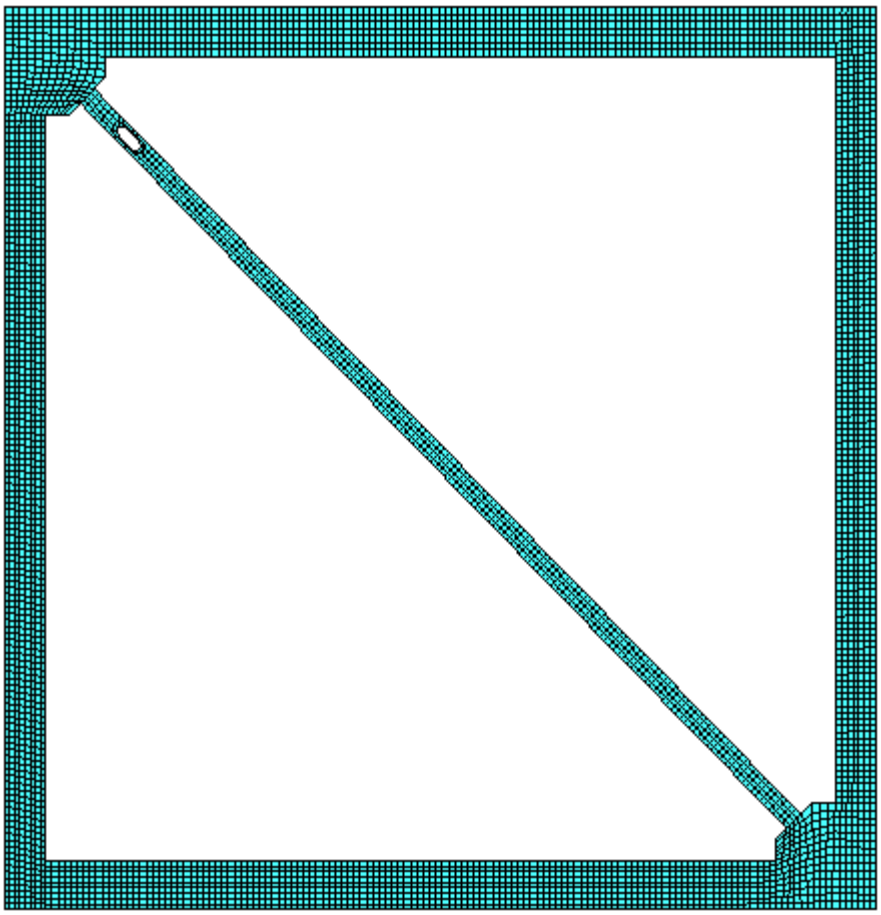

Fig. K78 - FEM Mesh – Frame “I” with RXS Fuse.

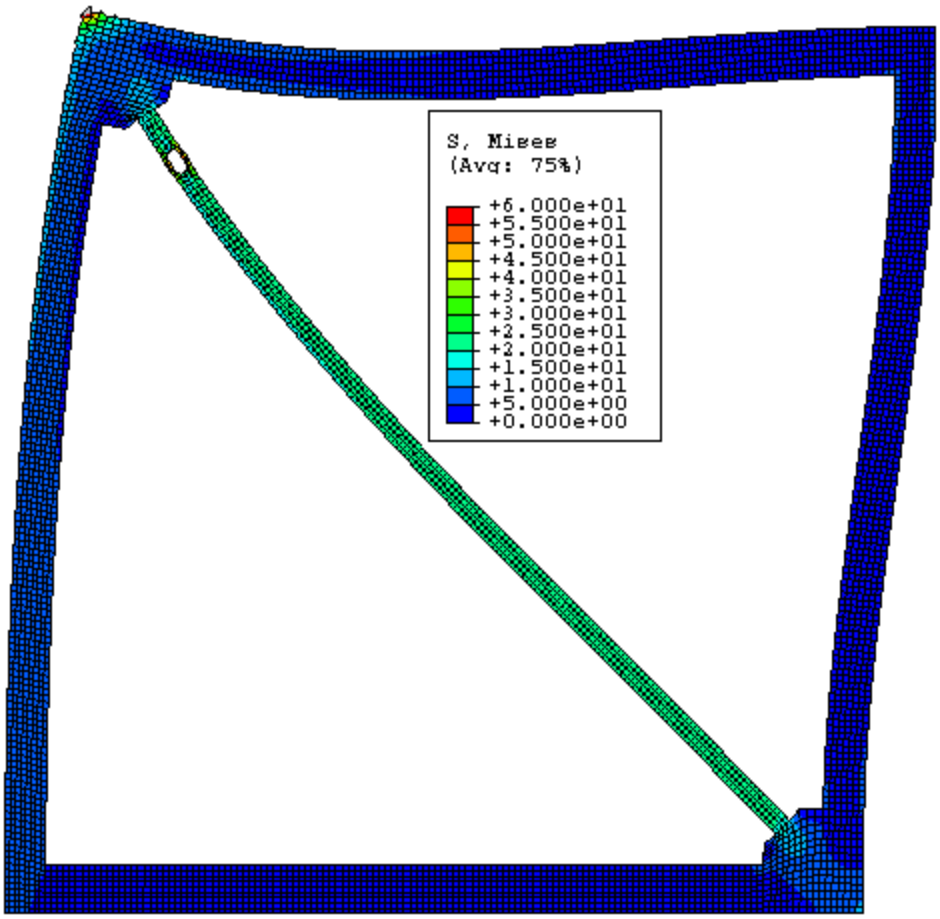

Fig. K79 - Von Mises Stress – Frame “I” with RXS Fuse.

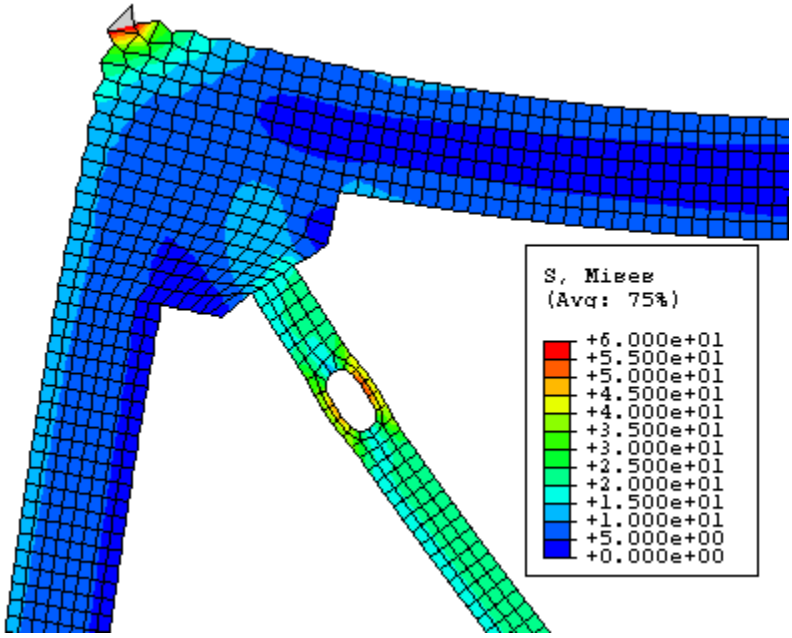

Fig. K80 - Von Mises Stress – Frame “I” with RXS Fuse – Zoom #1.

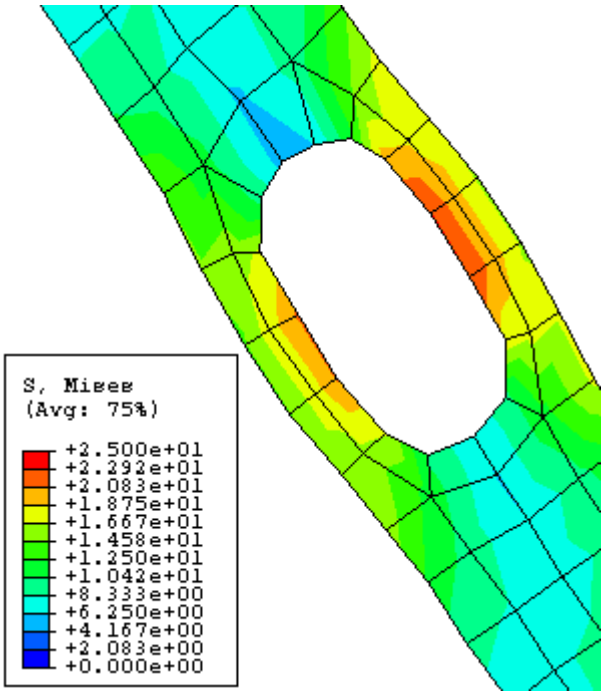

Fig. K81 - Von Mises Stress – Frame “I” with RXS Fuse – Zoom #2.

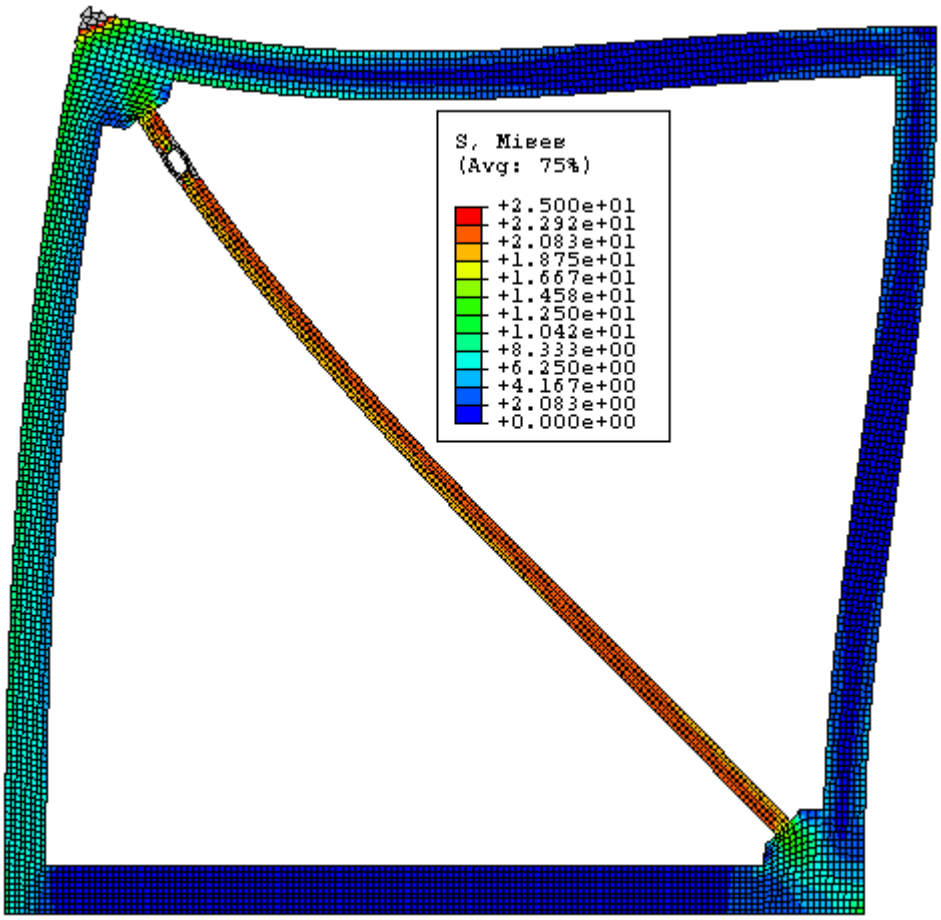

Fig. K82 - Von Mises Stress – Frame “I” with RXS Fuse – Stress Scale #2.

FRAME J

Beam/Column Length Ratio = H/L = 1

Beam-depth/Column-depth = 16”/12”

Brace Angle “ϕ” = 45˚

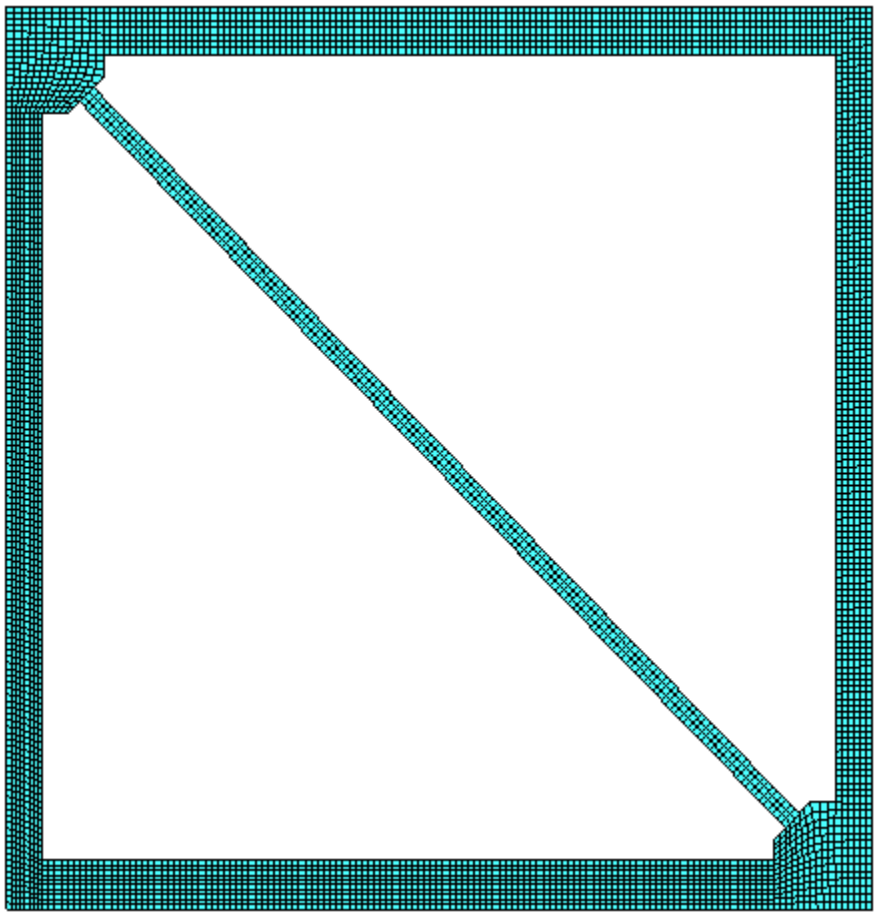

Fig. K83 - FEM Mesh – Frame “J” without RXS Fuse.

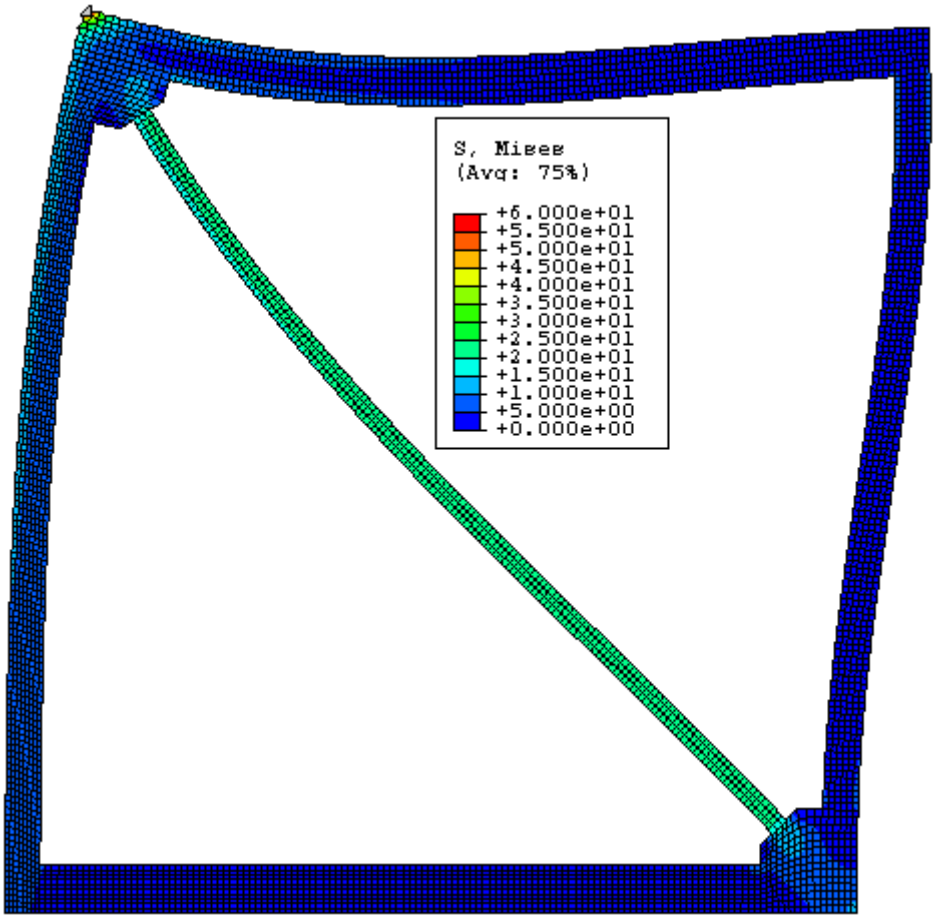

Fig. K84 - Von Mises Stress – Frame “J” without RXS Fuse.

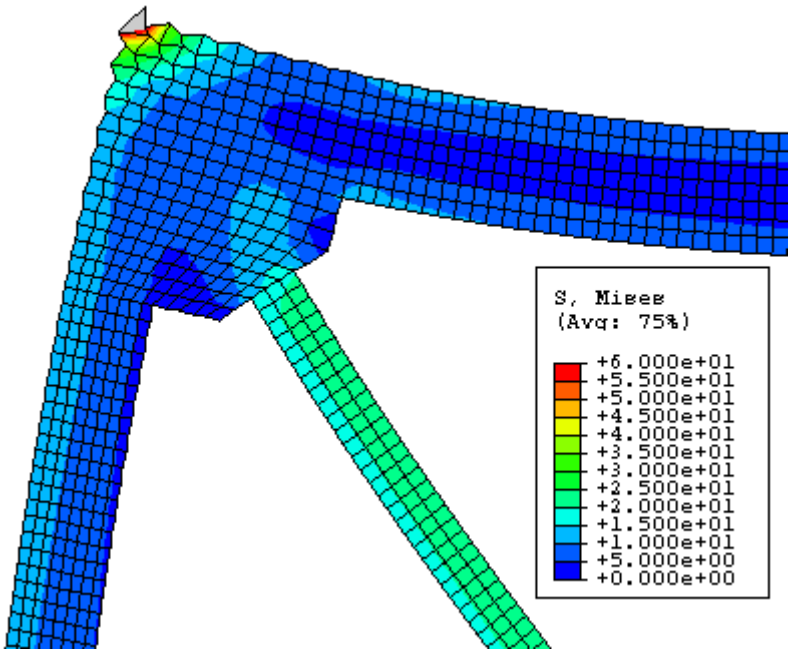

Fig. K85 - Von Mises Stress – Frame “J” without RXS Fuse – Zoom.

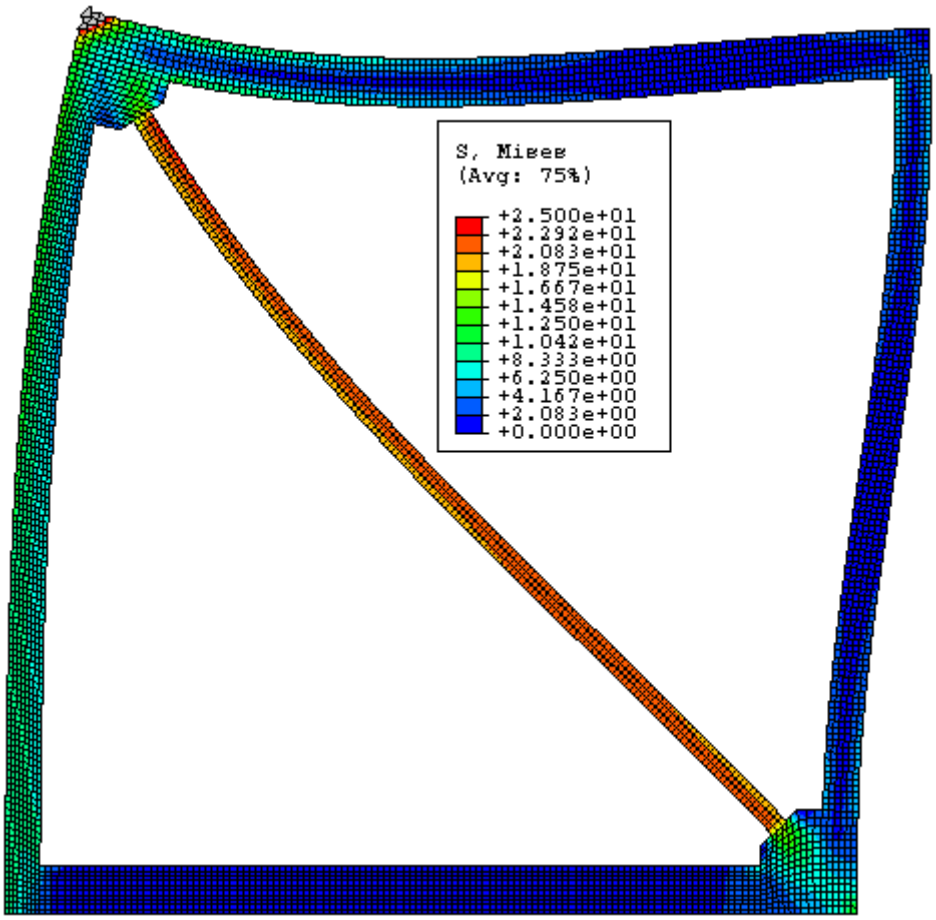

Fig. K86 - Von Mises Stress – Frame “J” without RXS Fuse – Stress Scale #2.

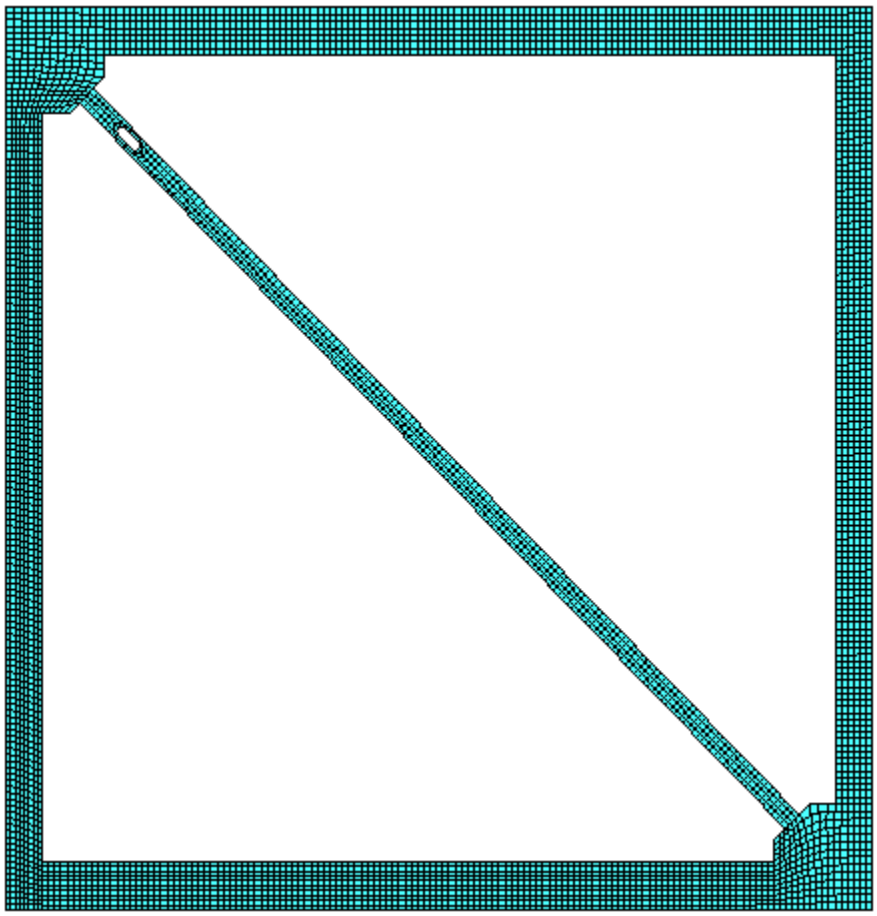

Fig. K87 - FEM Mesh – Frame “J” with RXS Fuse.

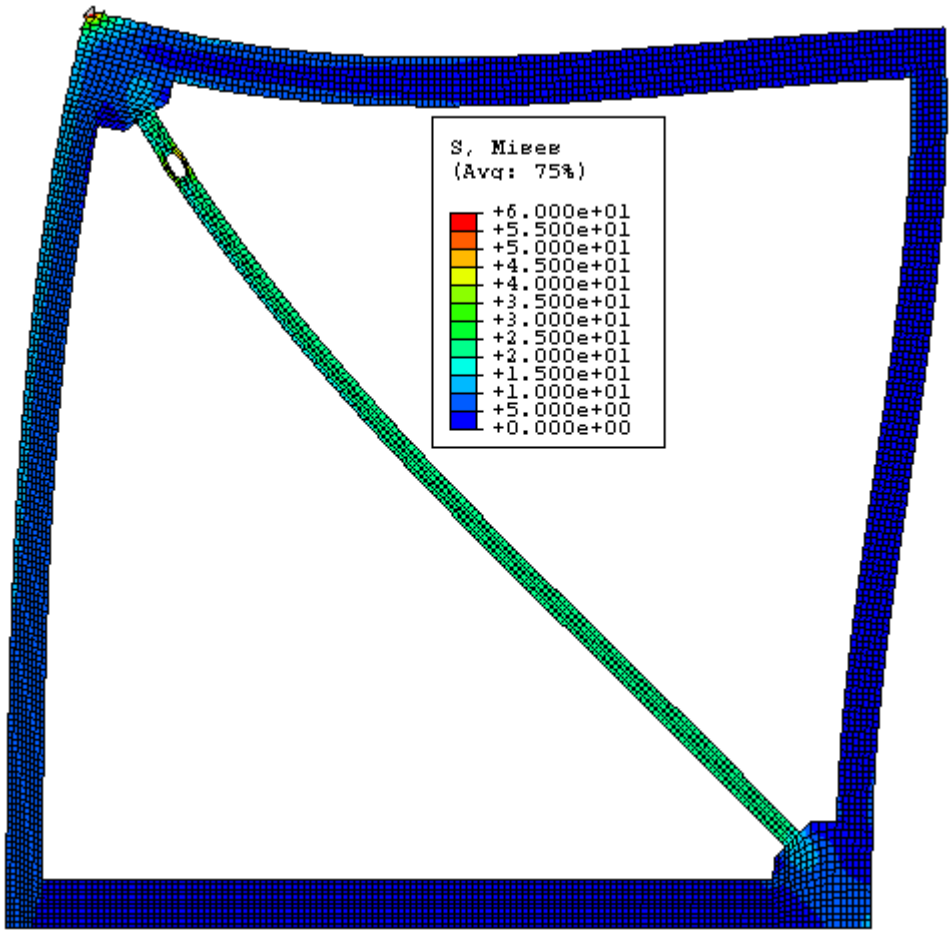

Fig. K88 - Von Mises Stress – Frame “J” with RXS Fuse.

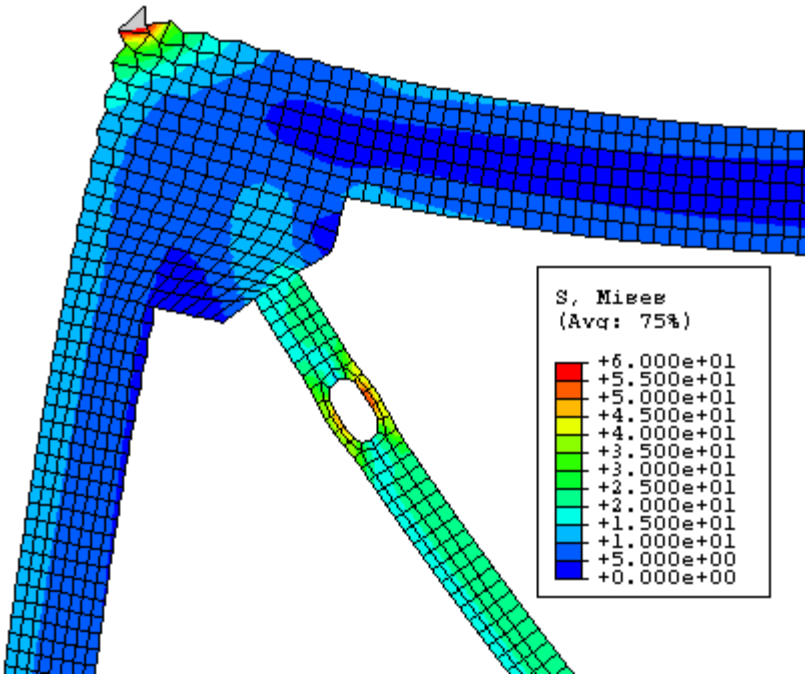

Fig. K89 - Von Mises Stress – Frame “J” with RXS Fuse – Zoom #1.

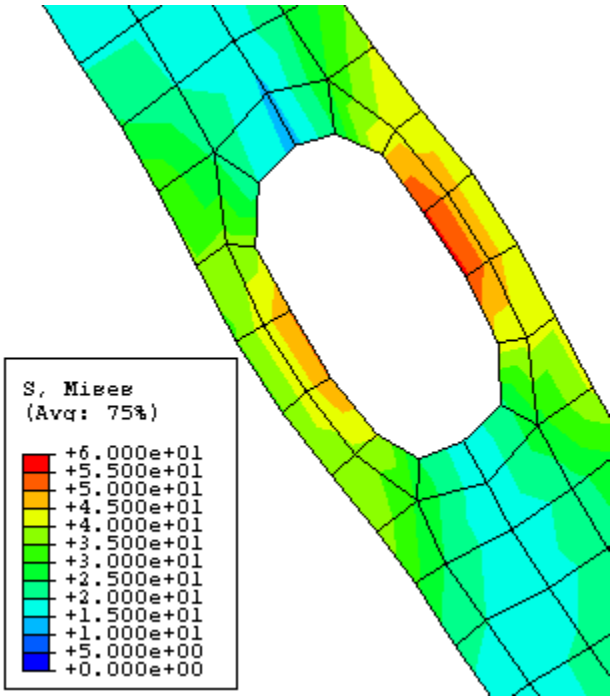

Fig. K90 - Von Mises Stress – Frame “J” with RXS Fuse – Zoom #2.

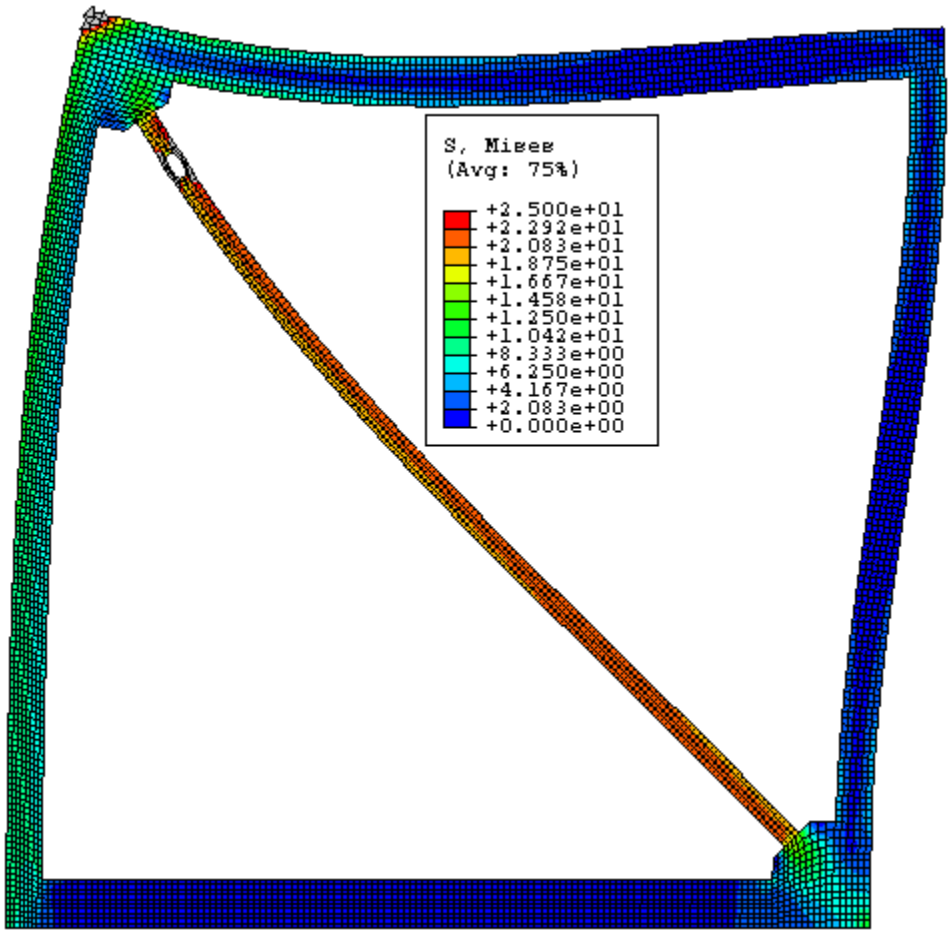

Fig. K91 - Von Mises Stress – Frame “J” with RXS Fuse – Stress Scale #2.

FRAME K

Beam/Column Length Ratio = H/L = 1

Beam-depth/Column-depth = 16”/10”

Brace Angle “ϕ” = 45˚

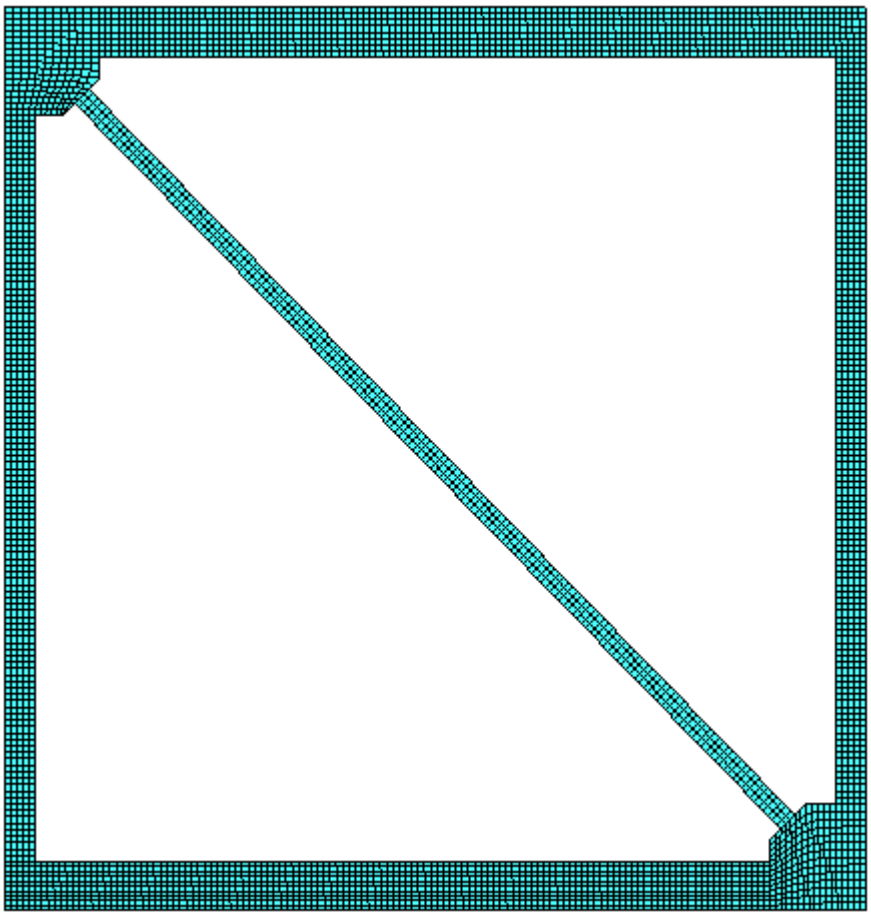

Fig. K92 - FEM Mesh – Frame “K” without RXS Fuse.

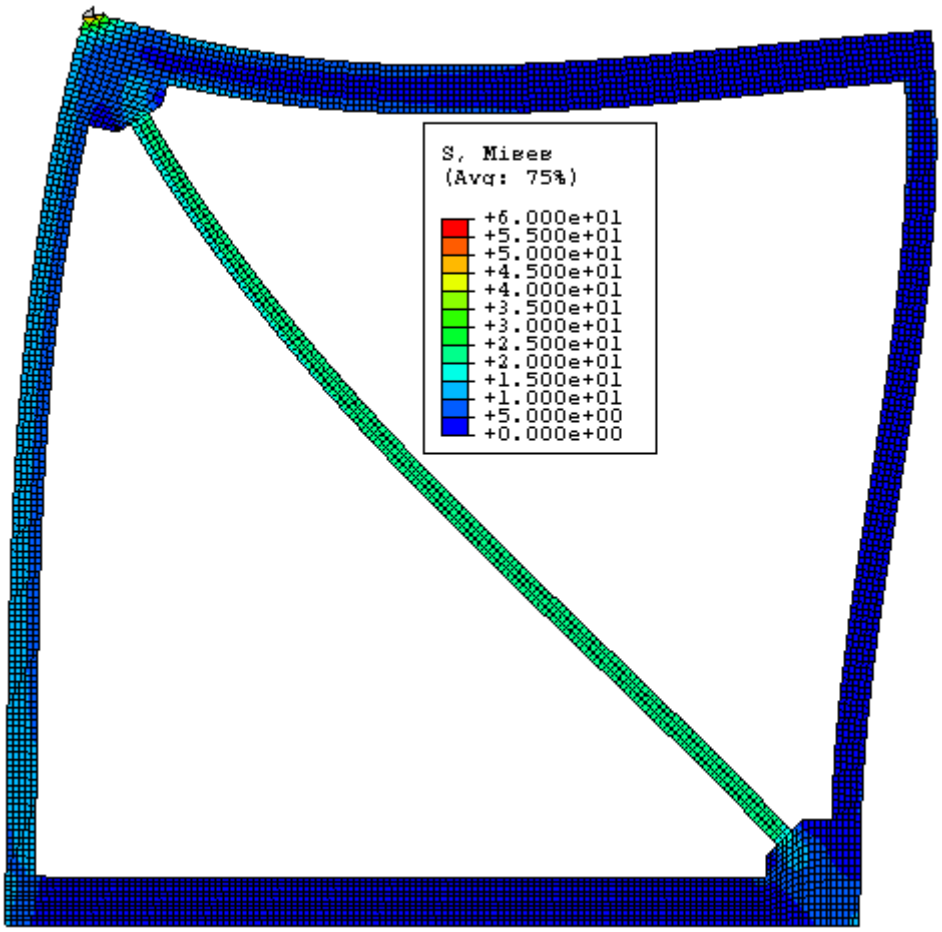

Fig. K93 - Von Mises Stress – Frame “K” without RXS Fuse.

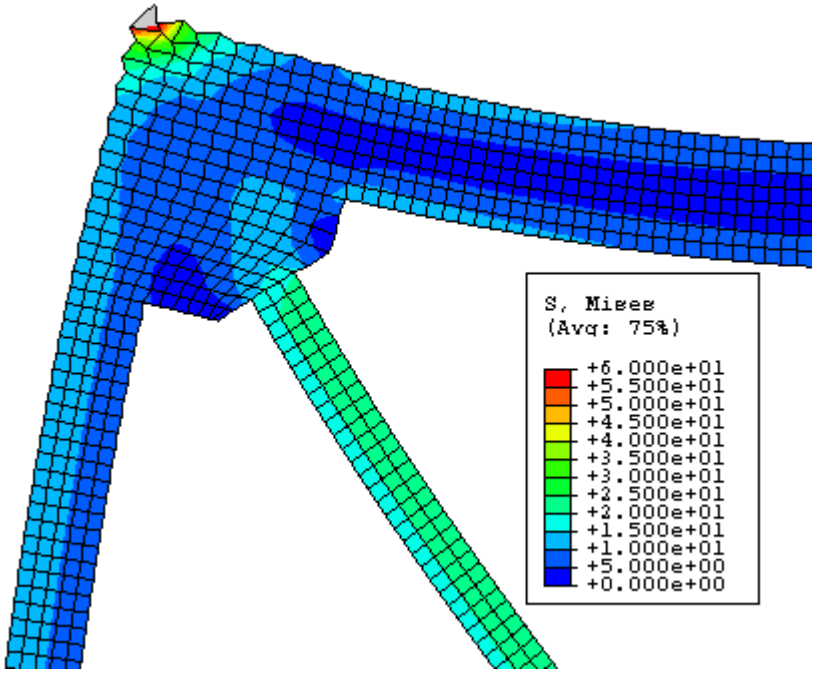

Fig. K94 - Von Mises Stress – Frame “K” without RXS Fuse – Zoom.

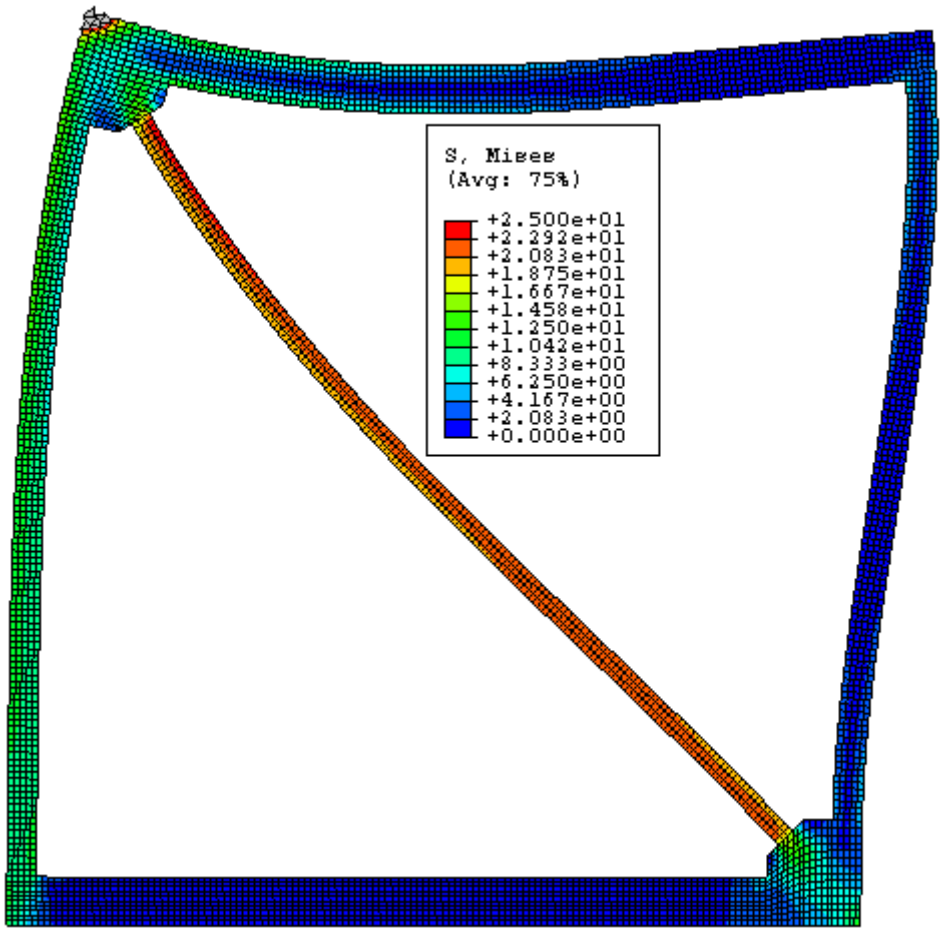

Fig. K95 - Von Mises Stress – Frame “K” without RXS Fuse – Stress Scale #2.

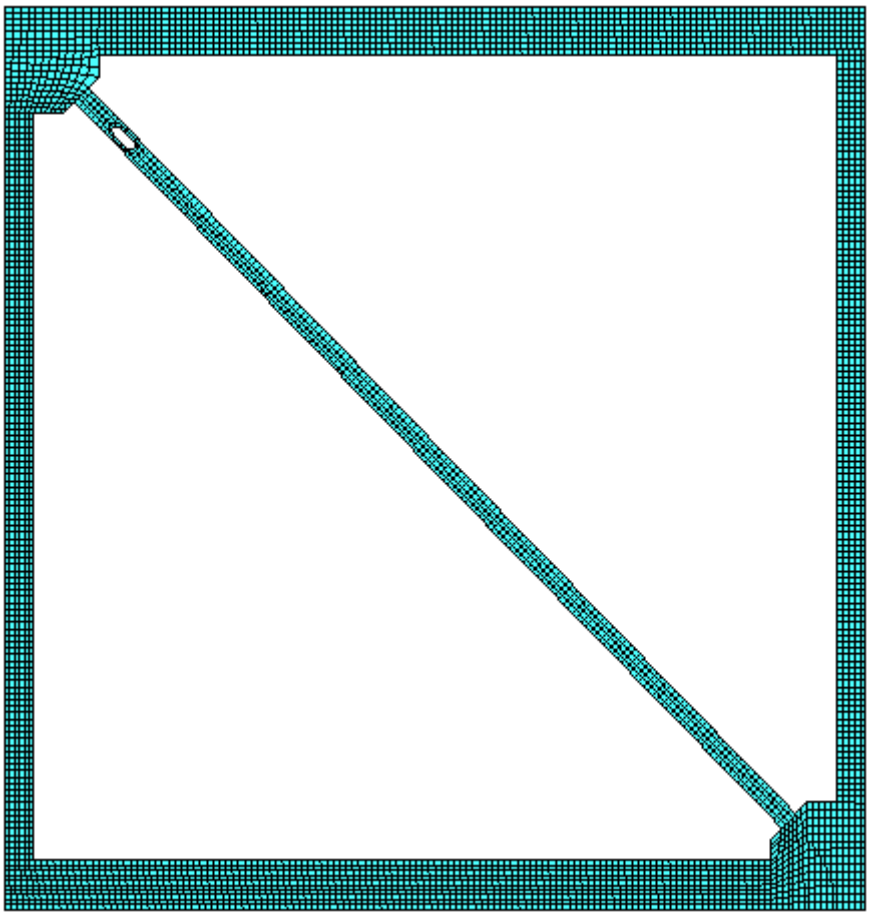

Fig. K96 - FEM Mesh – Frame “K” with RXS Fuse.

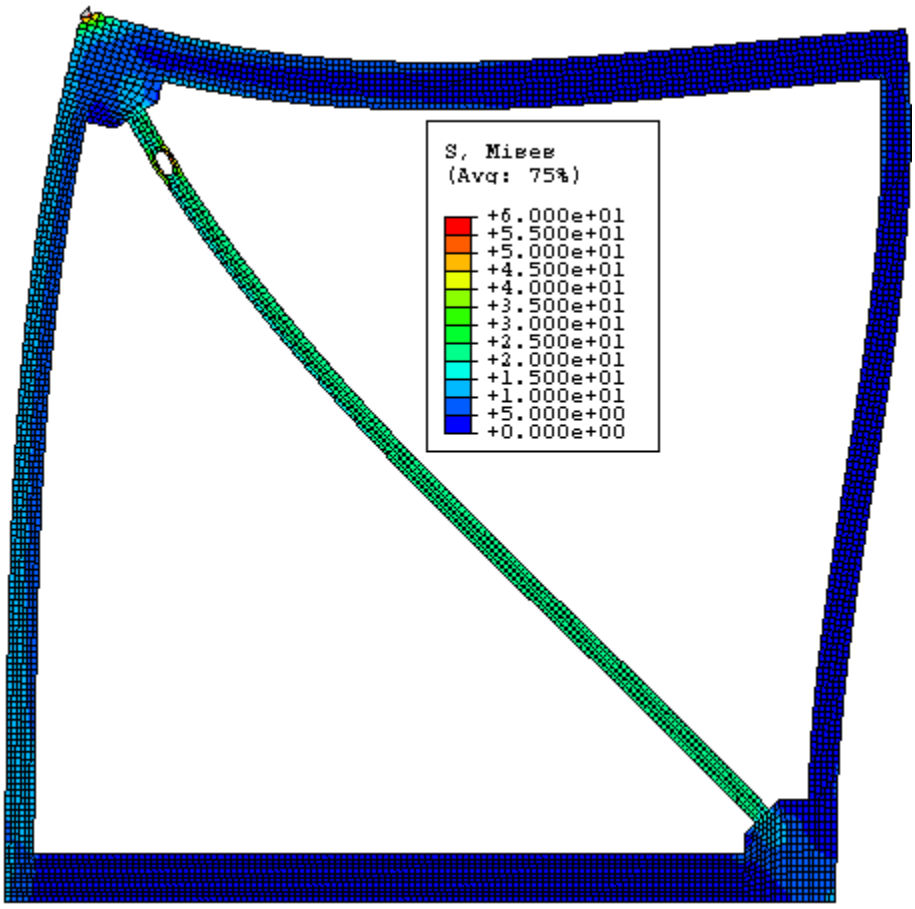

Fig. K97 - Von Mises Stress – Frame “K” with RXS Fuse.

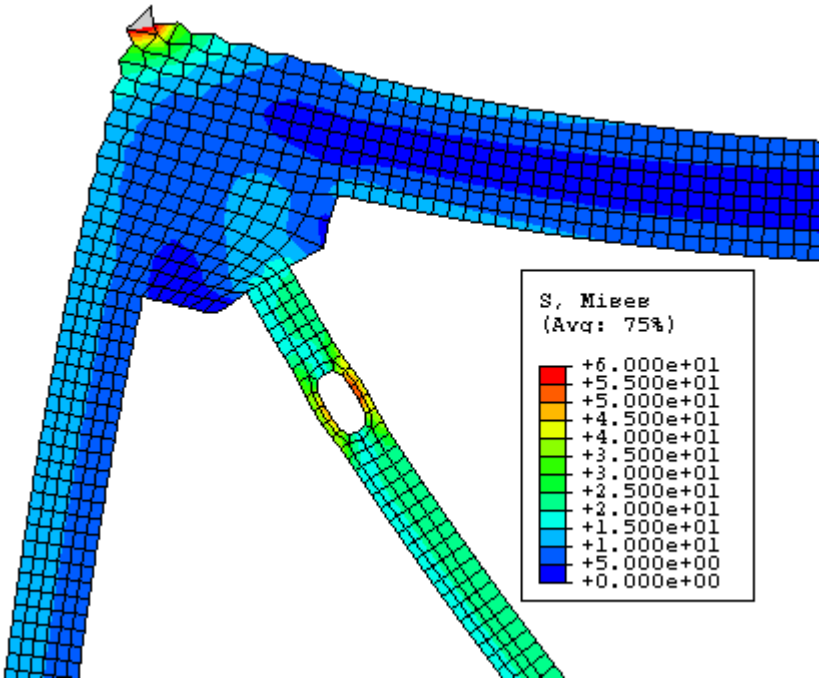

Fig. K98 - Von Mises Stress – Frame “K” with RXS Fuse – Zoom #1.

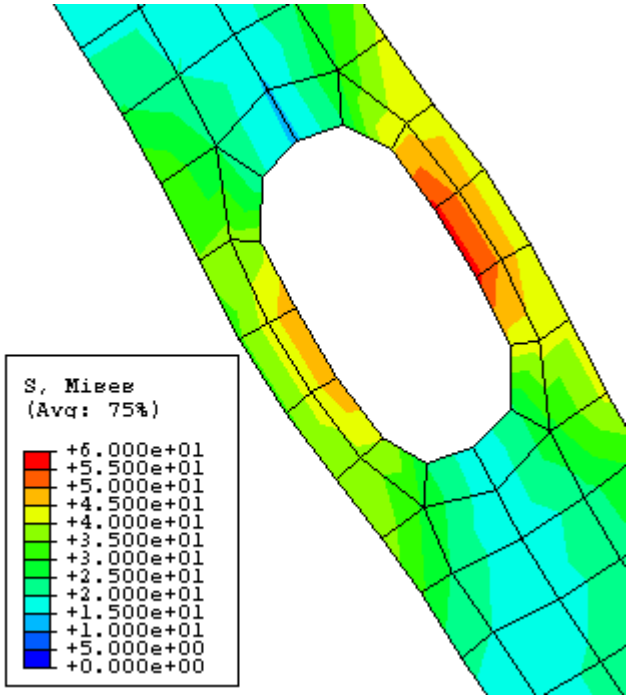

Fig. K99 - Von Mises Stress – Frame “K” with RXS Fuse – Zoom #2.

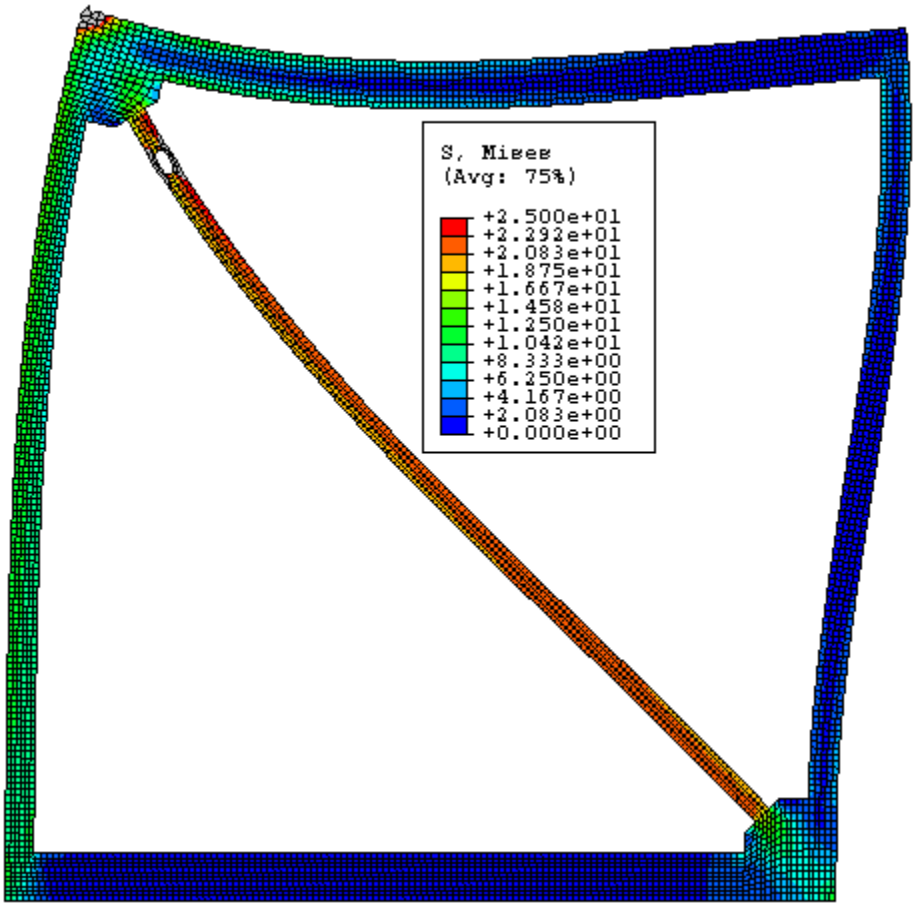

Fig. K100 - Von Mises Stress – Frame “K” with RXS Fuse – Stress Scale #2.

FRAME L

Beam/Column Length Ratio = H/L = 1

Beam-depth/Column-depth = 16”/8”

Brace Angle “ϕ” = 45˚

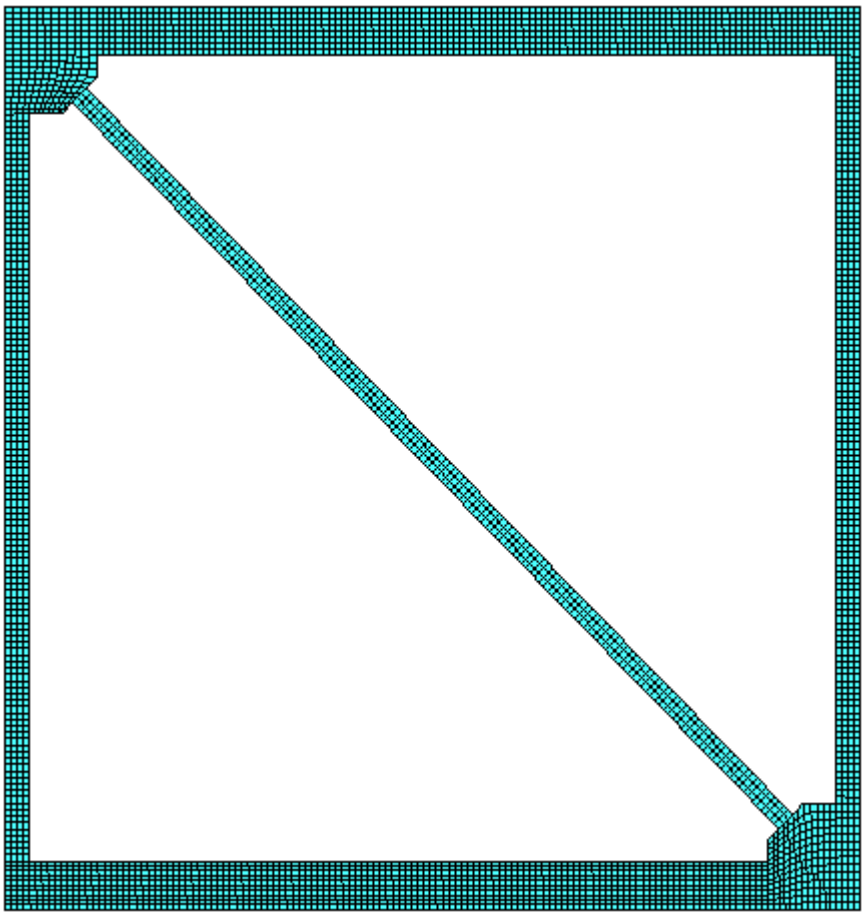

Fig. K101 - FEM Mesh – Frame “L” without RXS Fuse.

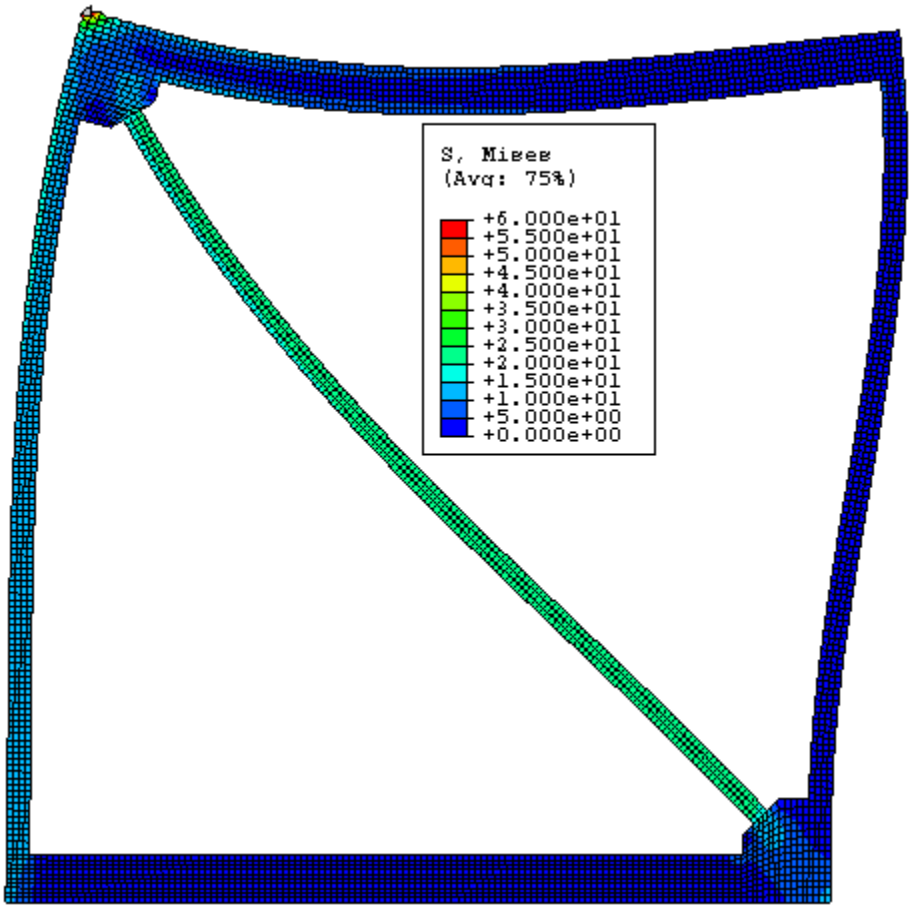

Fig. K102 - Von Mises Stress – Frame “L” without RXS Fuse.

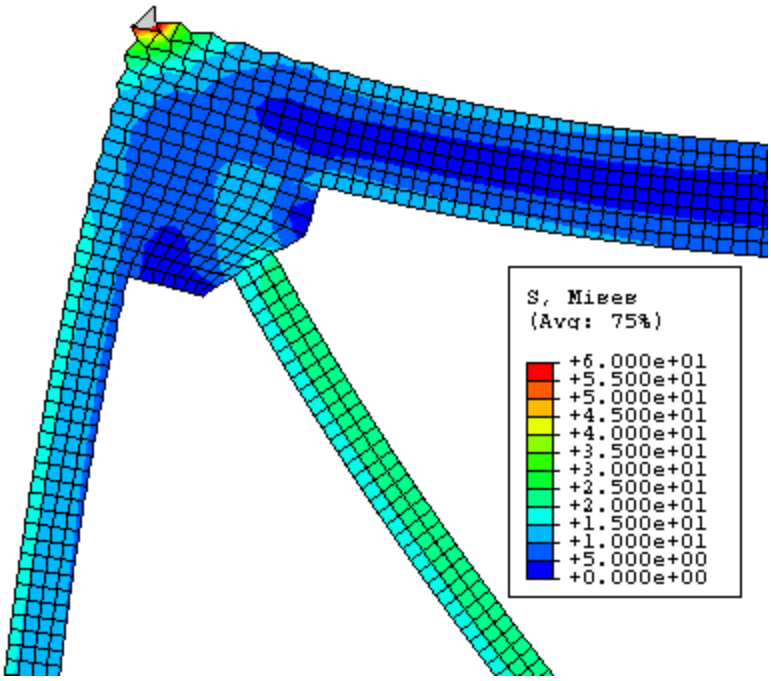

Fig. K103 - Von Mises Stress – Frame “L” without RXS Fuse – Zoom.

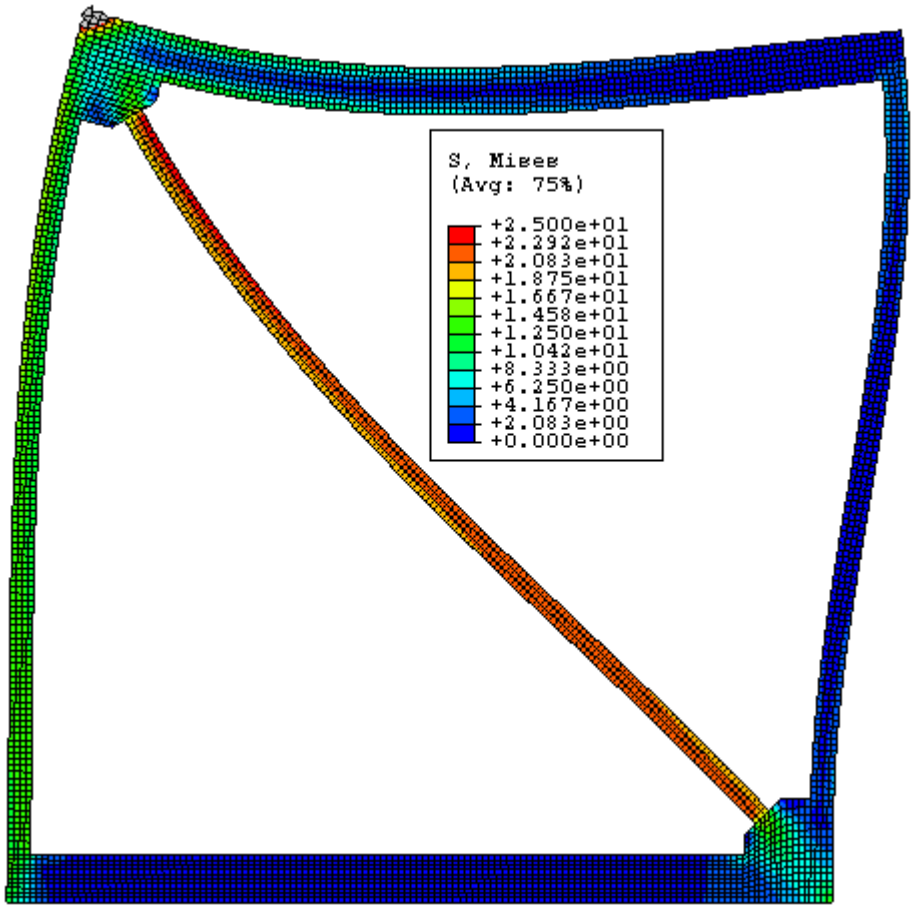

Fig. K104 - Von Mises Stress – Frame “L” without RXS Fuse – Stress Scale #2.

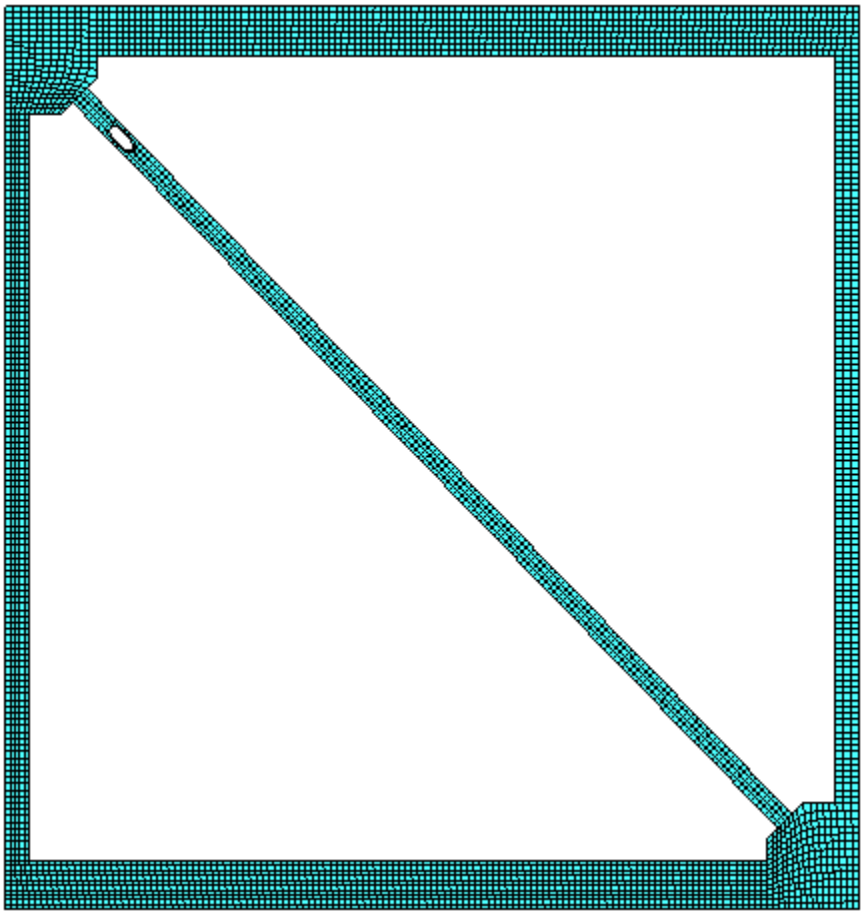

Fig. K105 - FEM Mesh – Frame “L” with RXS Fuse.

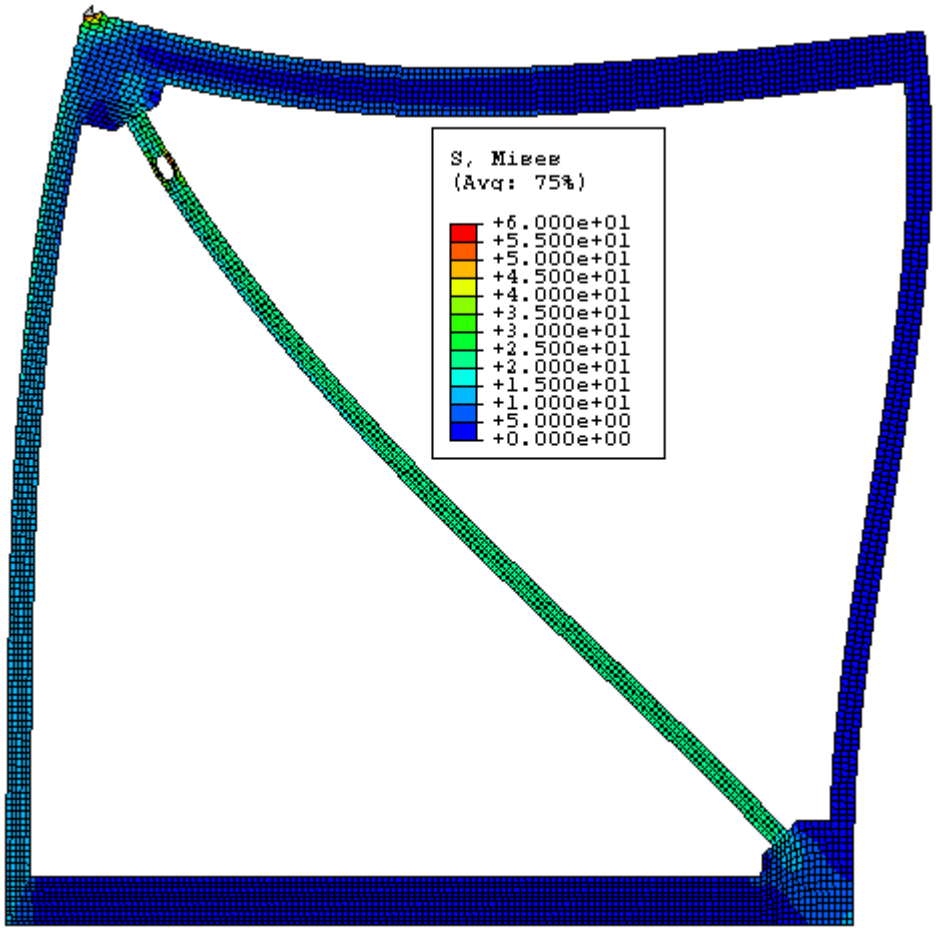

Fig. K106 - Von Mises Stress – Frame “L” with RXS Fuse.

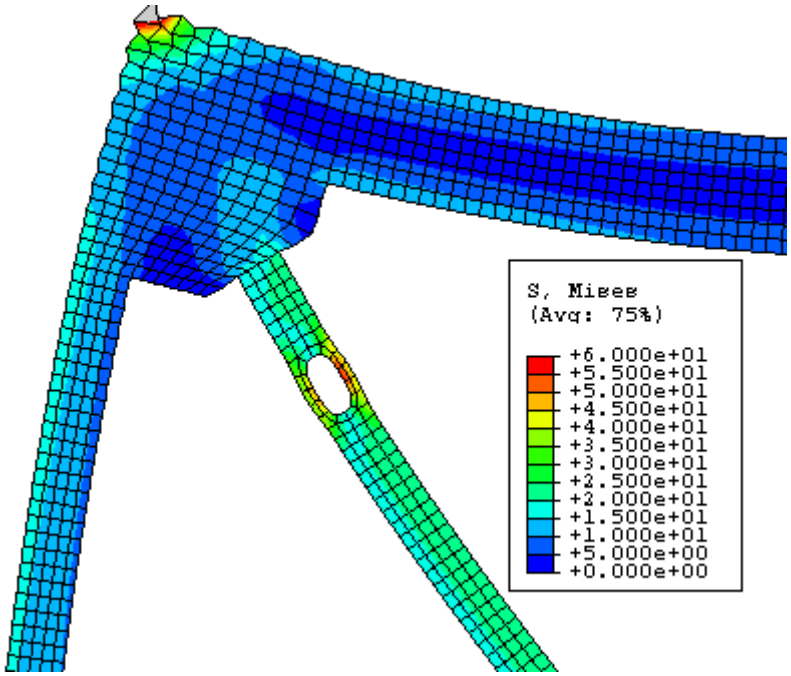

Fig. K107 - Von Mises Stress – Frame “L” with RXS Fuse – Zoom #1.

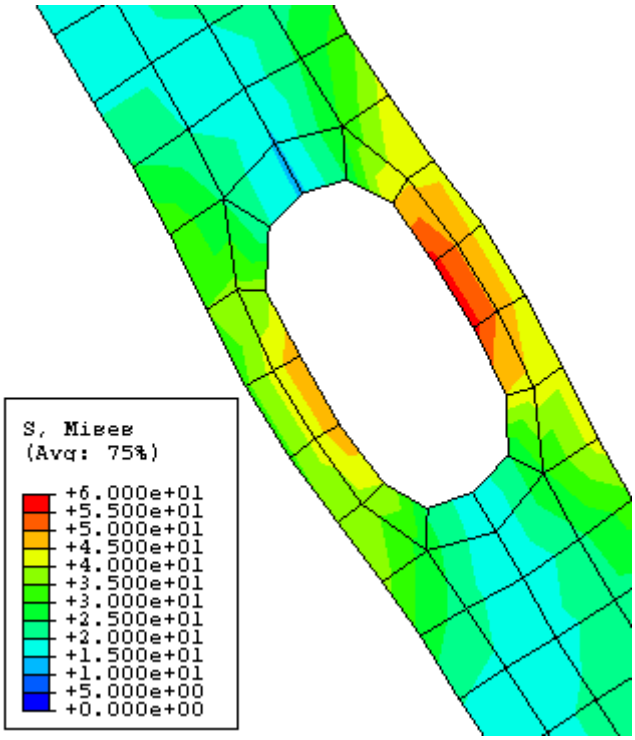

Fig. K108 - Von Mises Stress – Frame “L” with RXS Fuse – Zoom #2.

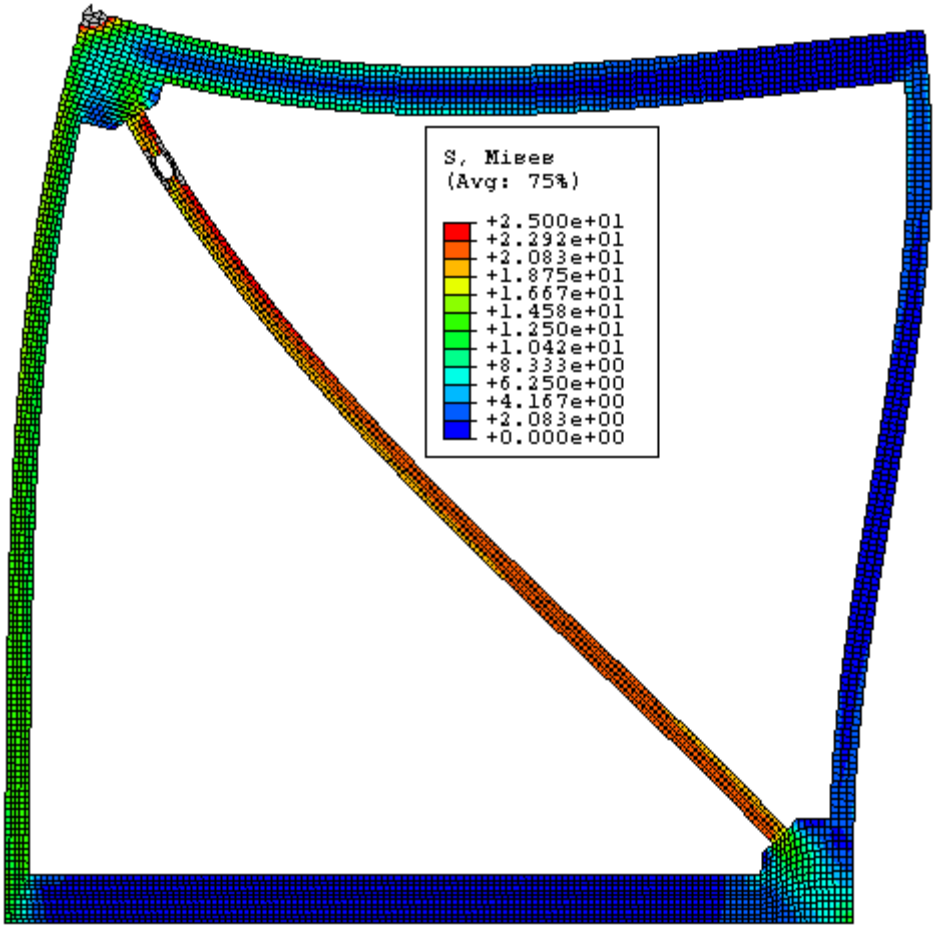

Fig. K109 - Von Mises Stress – Frame “L” with RXS Fuse – Stress Scale #2.

FRAME M

Beam/Column Length Ratio = H/L = 1

Beam-depth/Column-depth = 16”/6”

Brace Angle “ϕ” = 45˚

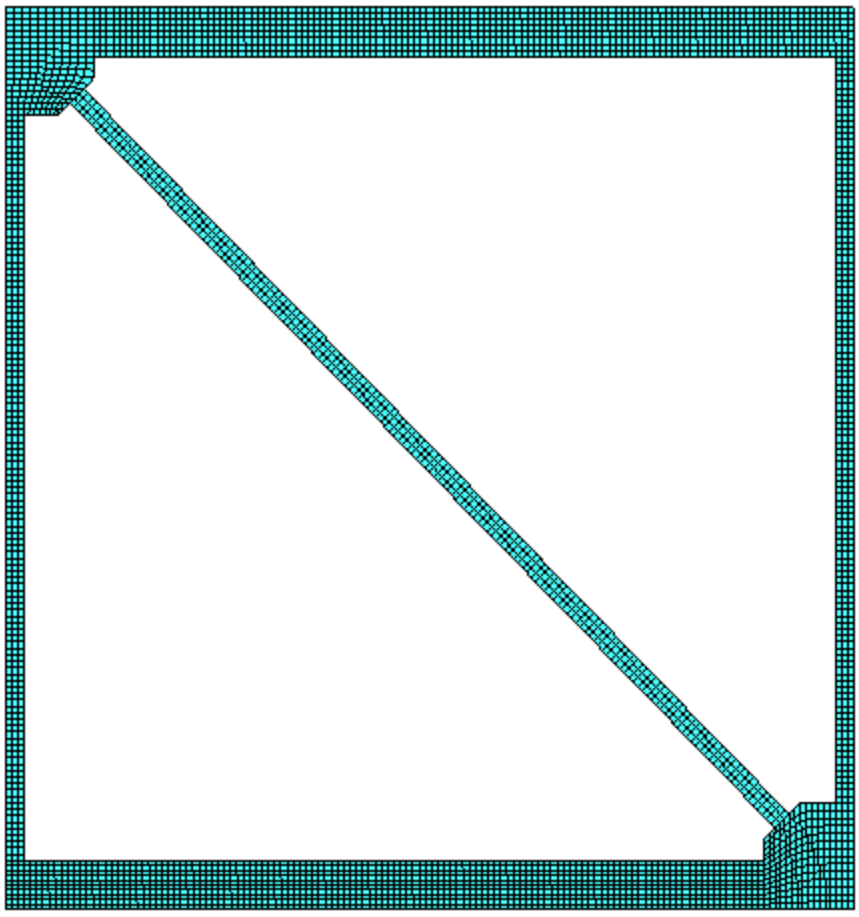

Fig. K110 - FEM Mesh – Frame “M” without RXS Fuse.

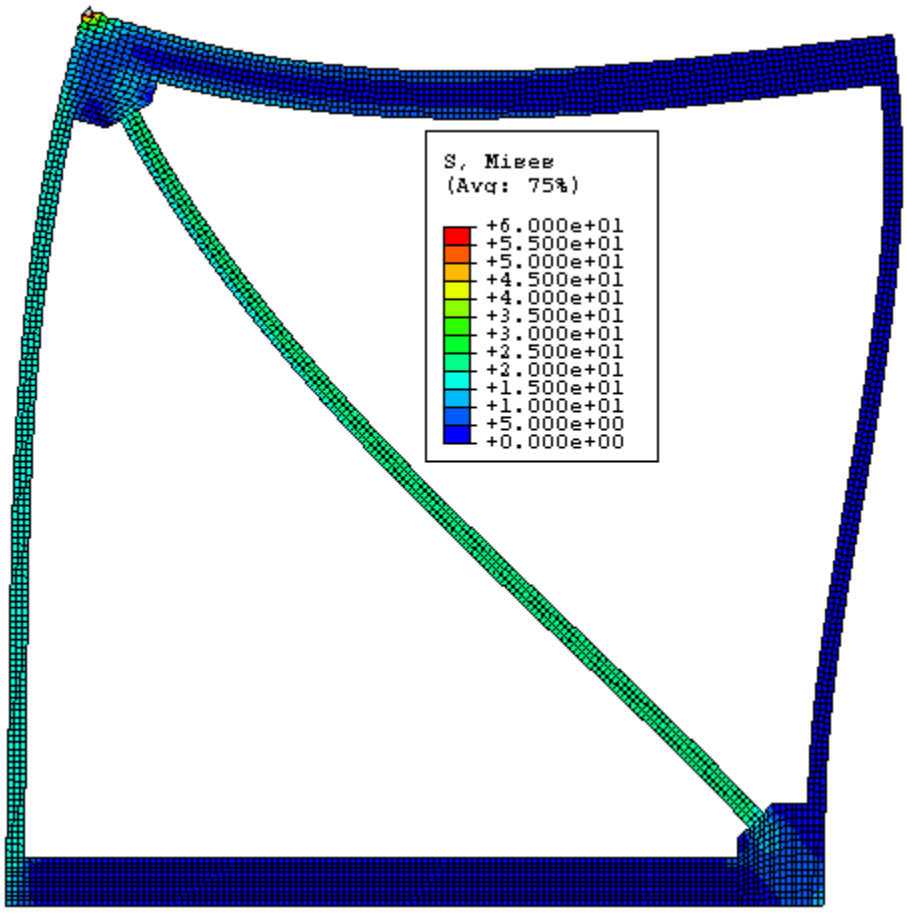

Fig. K111 - Von Mises Stress – Frame “M” without RXS Fuse.

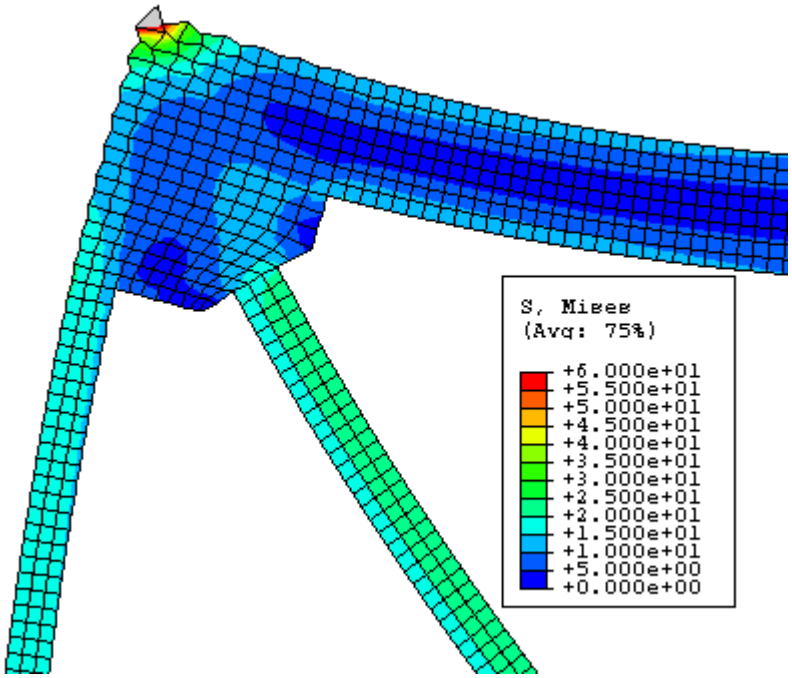

Fig. K112 - Von Mises Stress – Frame “M” without RXS Fuse – Zoom.

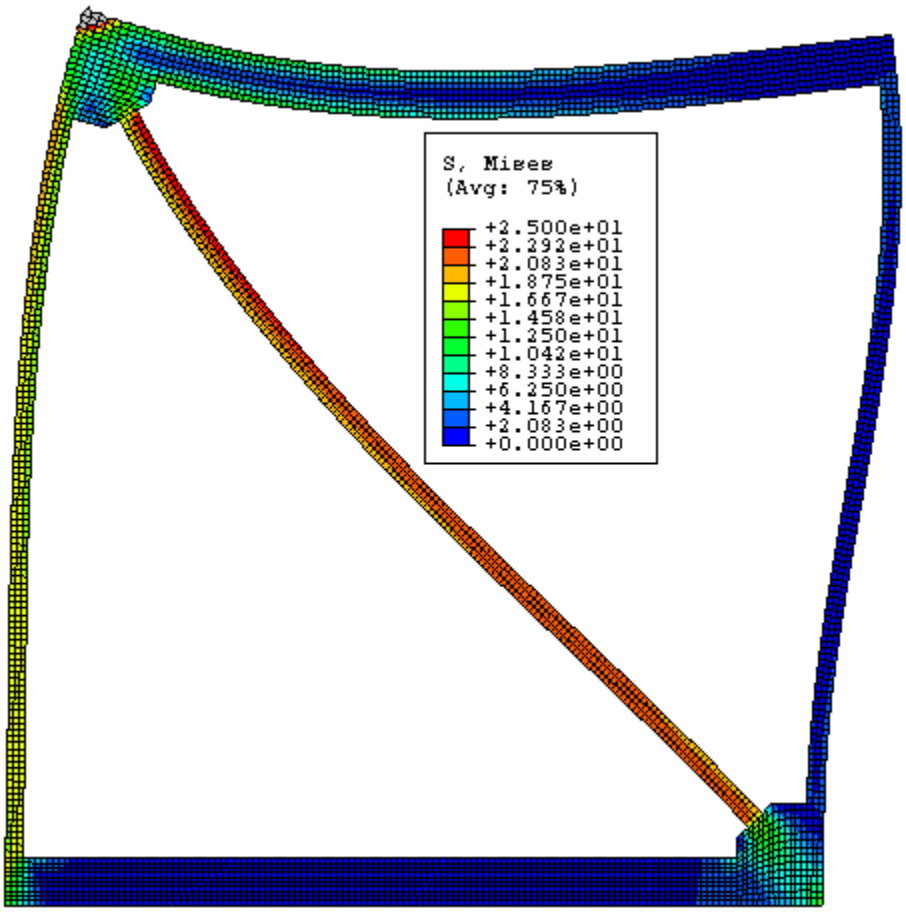

Fig. K113 - Von Mises Stress – Frame “M” without RXS Fuse – Stress Scale #2.

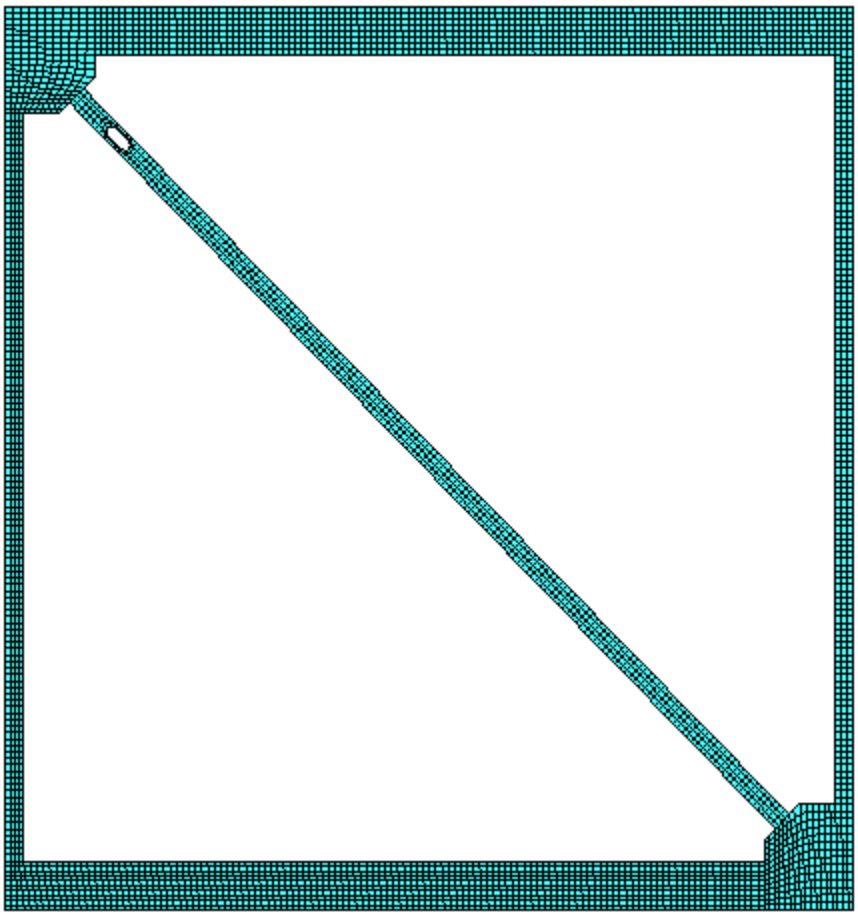

Fig. K114 - FEM Mesh – Frame “N” with RXS Fuse.

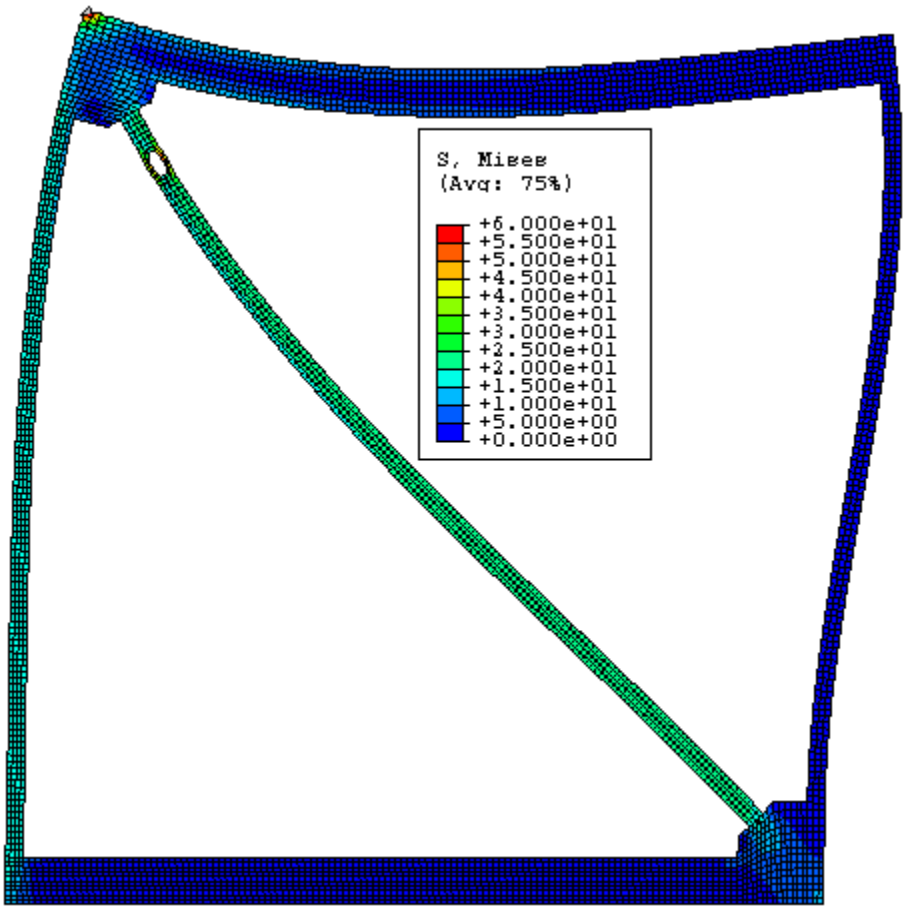

Fig. K115 - Von Mises Stress – Frame “M” with RXS Fuse.

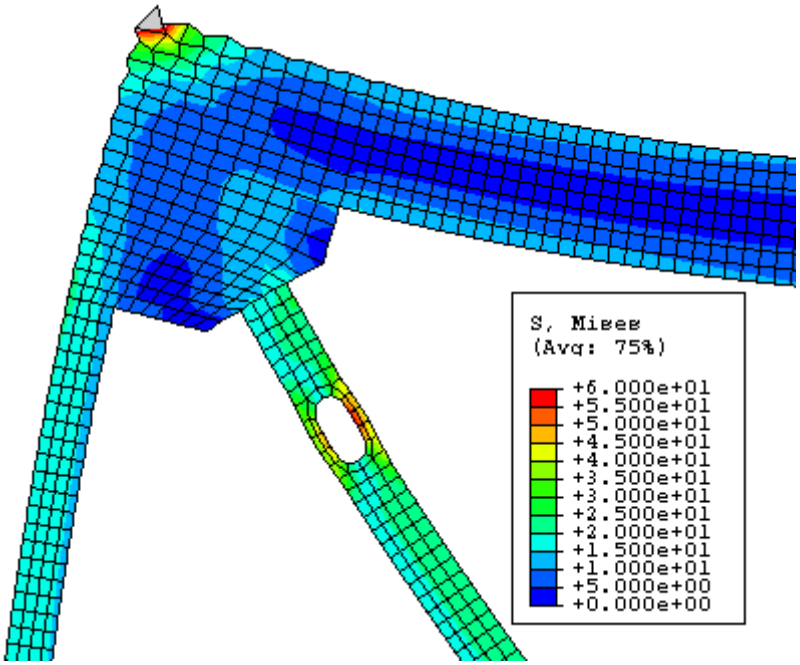

Fig. K116 - Von Mises Stress – Frame “M” with RXS Fuse – Zoom #1.

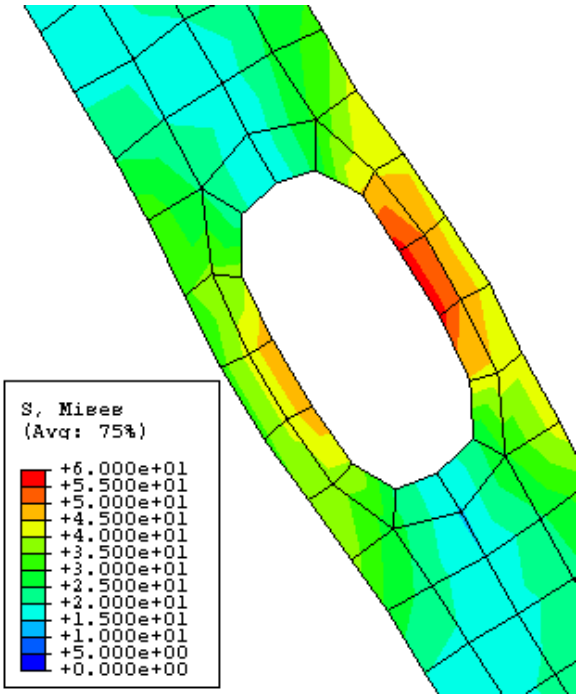

Fig. K117 - Von Mises Stress – Frame “M” with RXS Fuse – Zoom #2.

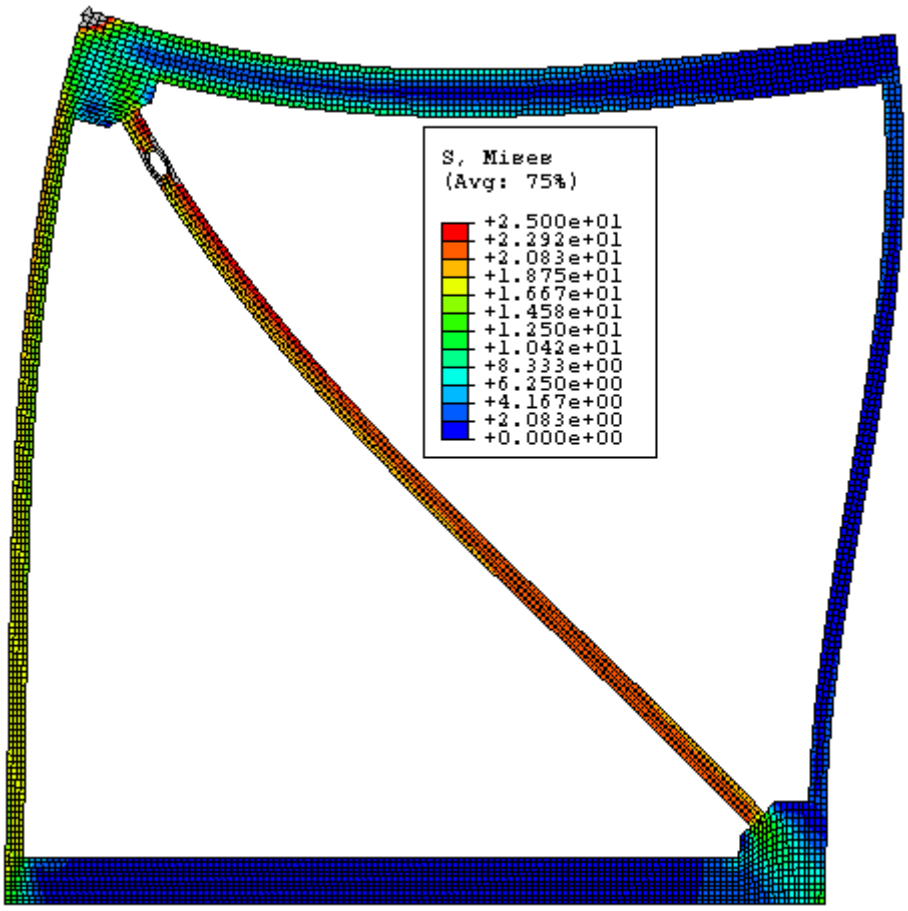

Fig. K118 - Von Mises Stress – Frame “M” with RXS Fuse – Stress Scale #2.

FRAME N

Beam/Column Length Ratio = H/L = 1

Beam-depth/Column-depth = 16”/5”

Brace Angle “ϕ” = 45˚

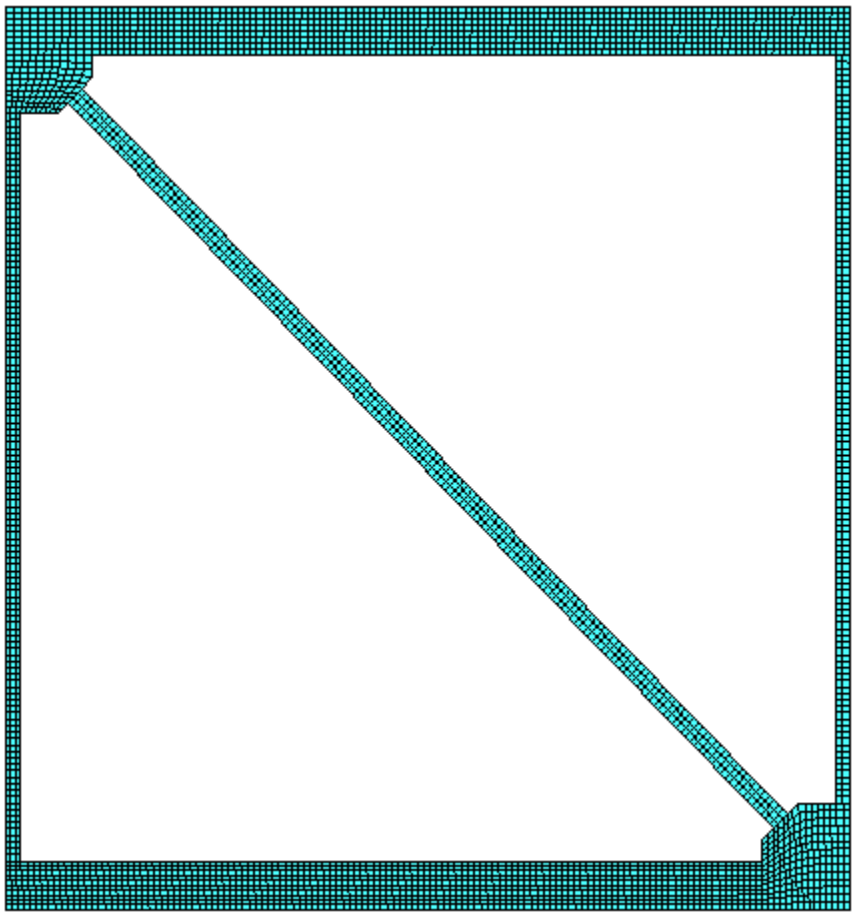

Fig. K119 - FEM Mesh – Frame “N” without RXS Fuse.

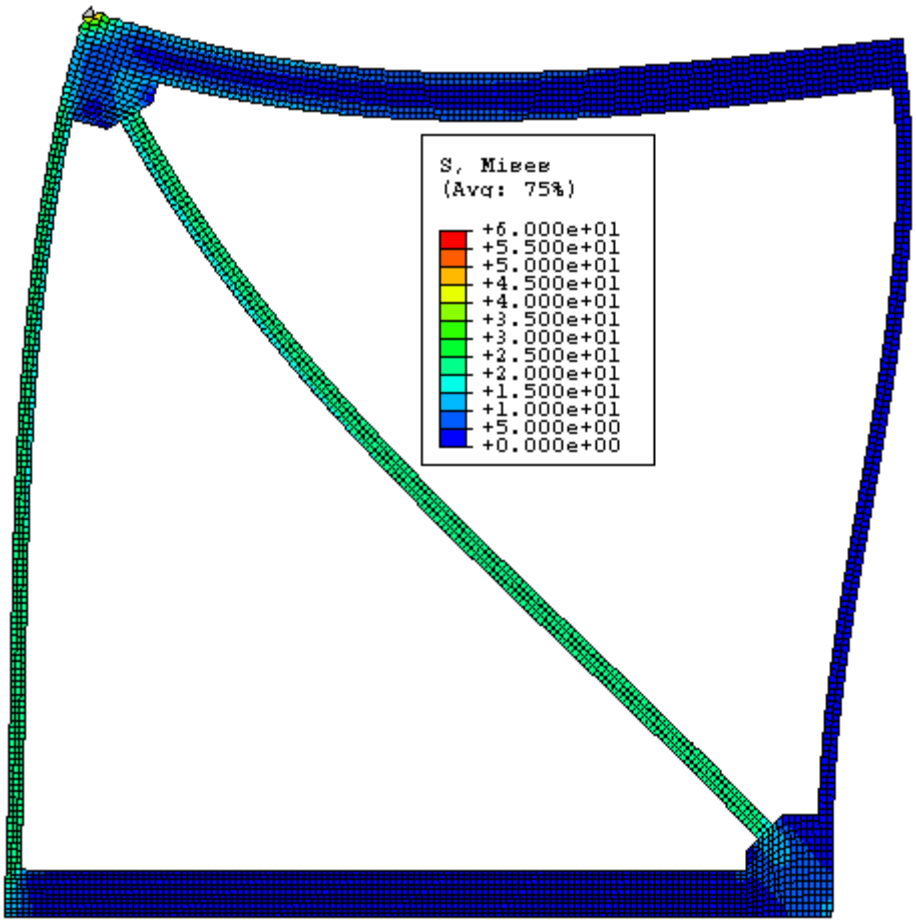

Fig. K120 - Von Mises Stress – Frame “N” without RXS Fuse.

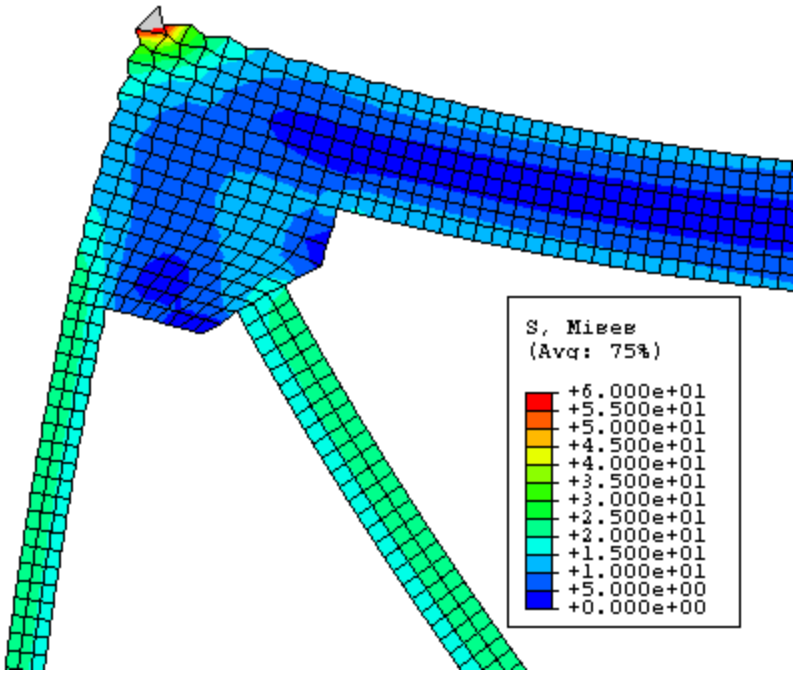

Fig. K121 - Von Mises Stress – Frame “N” without RXS Fuse – Zoom.

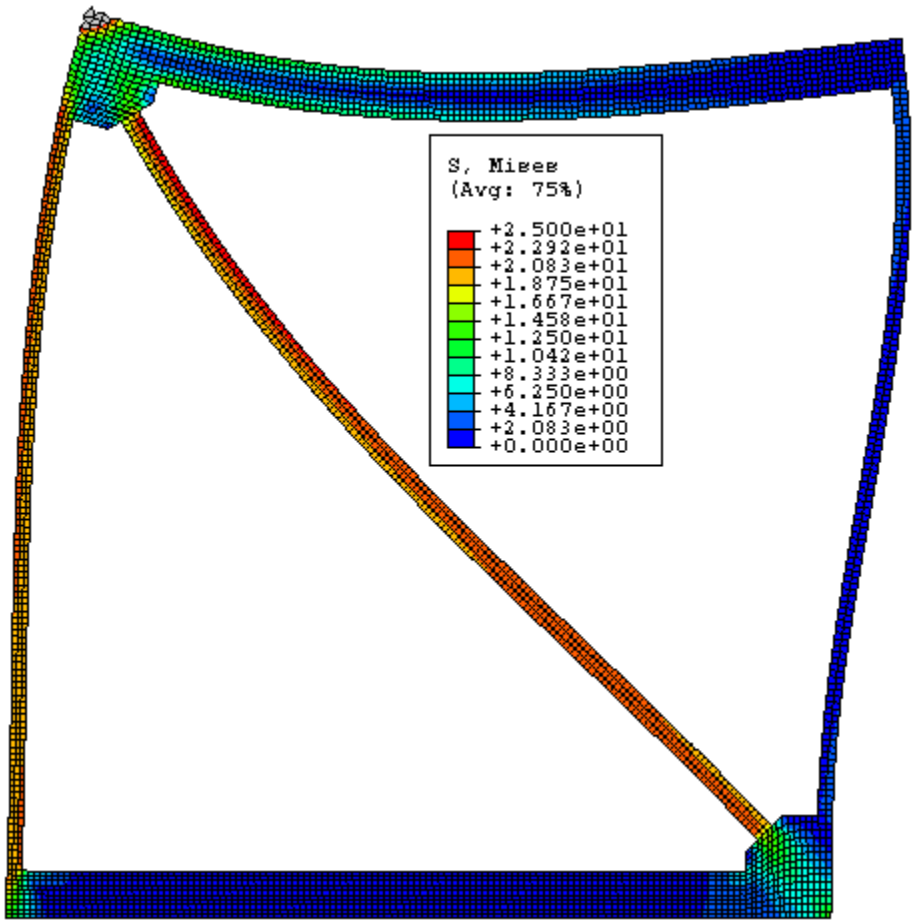

Fig. K122 - Von Mises Stress – Frame “N” without RXS Fuse – Stress Scale #2.

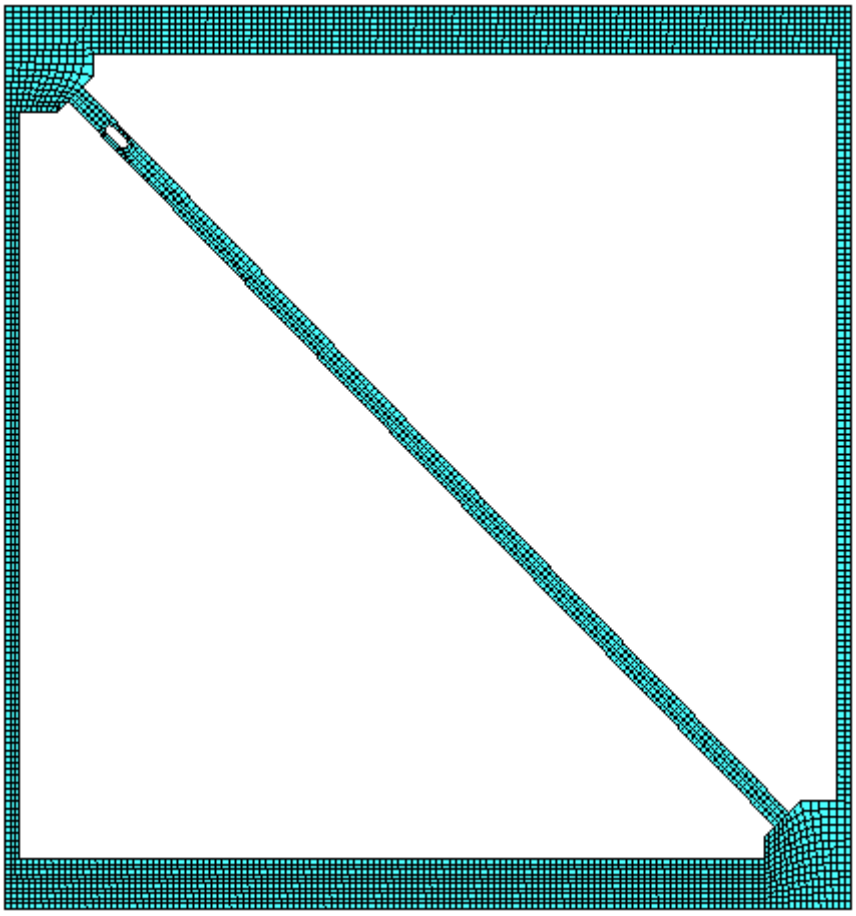

Fig. K123 - FEM Mesh – Frame “N” with RXS Fuse.

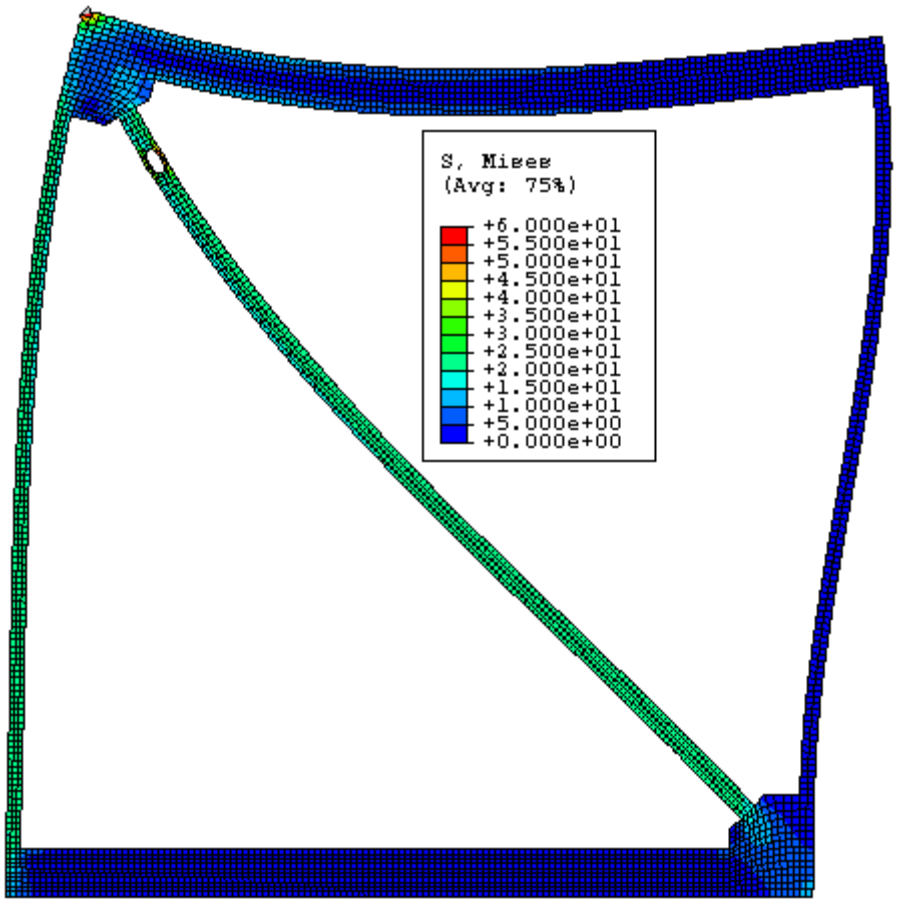

Fig. K124 - Von Mises Stress – Frame “N” with RXS Fuse.

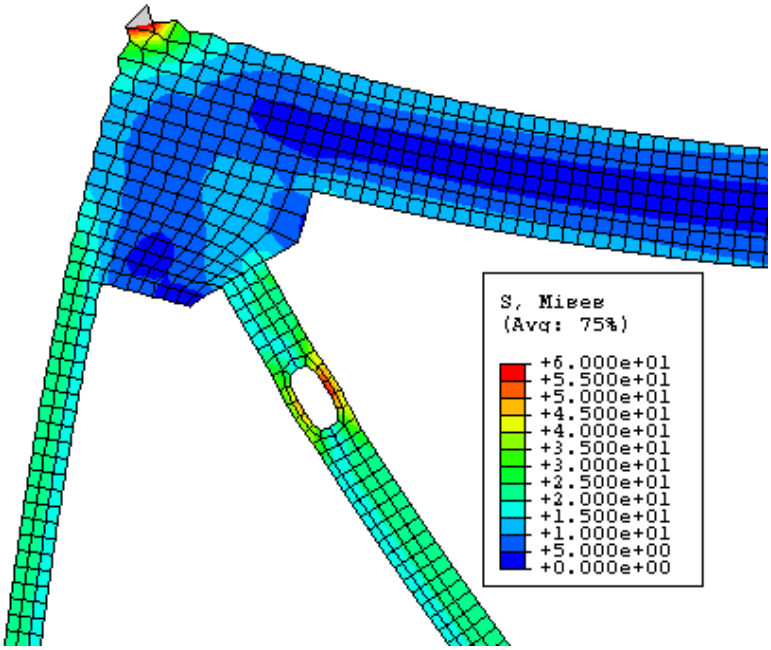

Fig. K125 - Von Mises Stress – Frame "N" with RXS Fuse – Zoom #1.

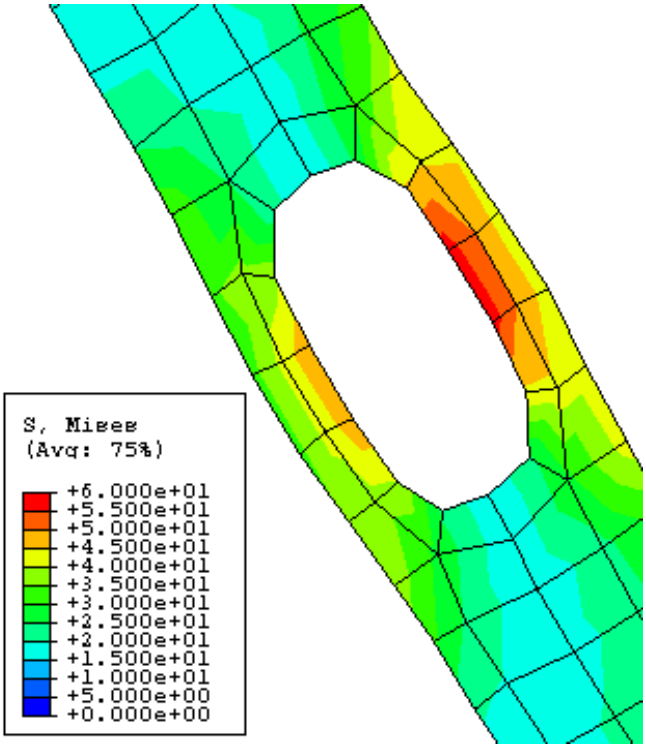

Fig. K126 - Von Mises Stress – Frame "N" with RXS Fuse – Zoom #2.

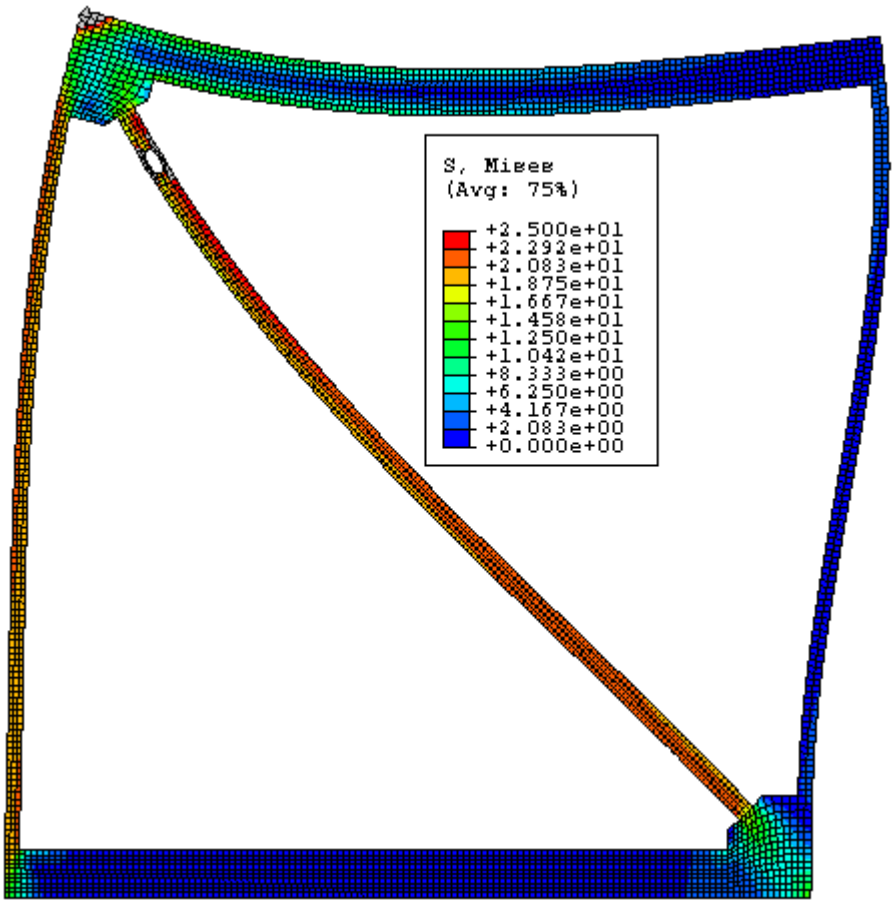

Fig. K127 - Von Mises Stress – Frame “N” with RXS Fuse – Stress Scale #2.

FRAME O

Beam/Column Length Ratio = H/L = 1

Beam-depth/Column-depth = 16”/4”

Brace Angle “ϕ” = 45˚

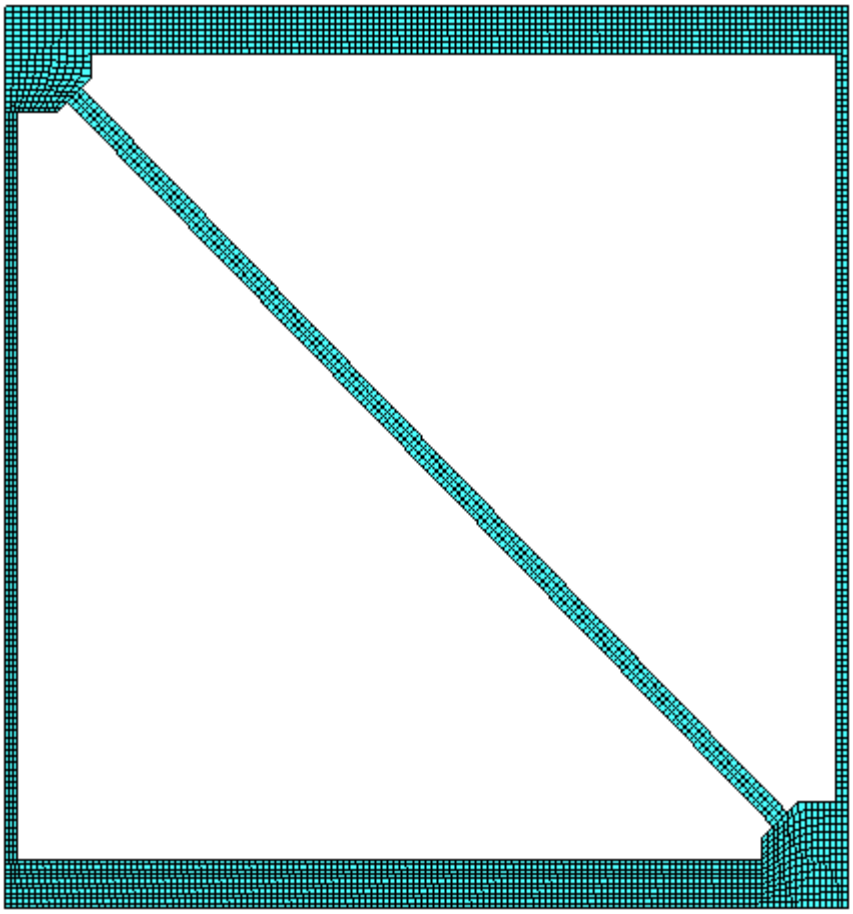

Fig. K128 - FEM Mesh – Frame “O” without RXS Fuse.

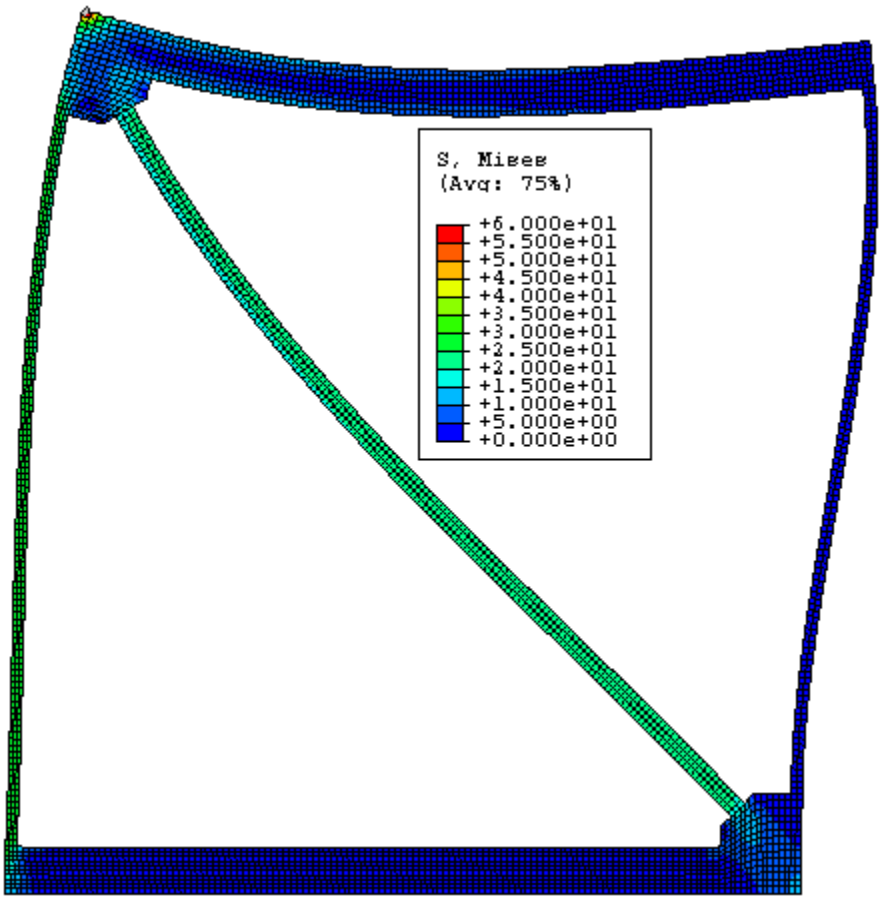

Fig. K129 - Von Mises Stress – Frame “O” without RXS Fuse.

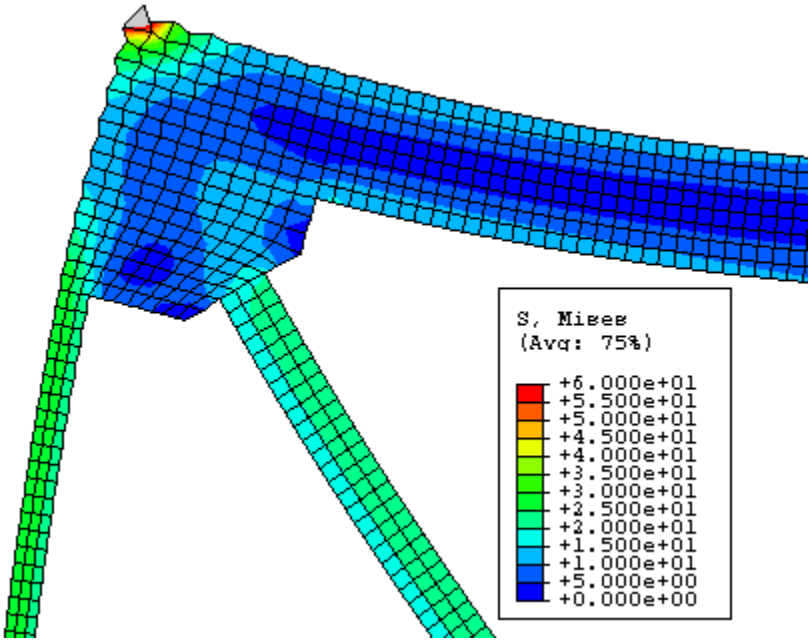

Fig. K130 - Von Mises Stress – Frame “O” without RXS Fuse – Zoom.

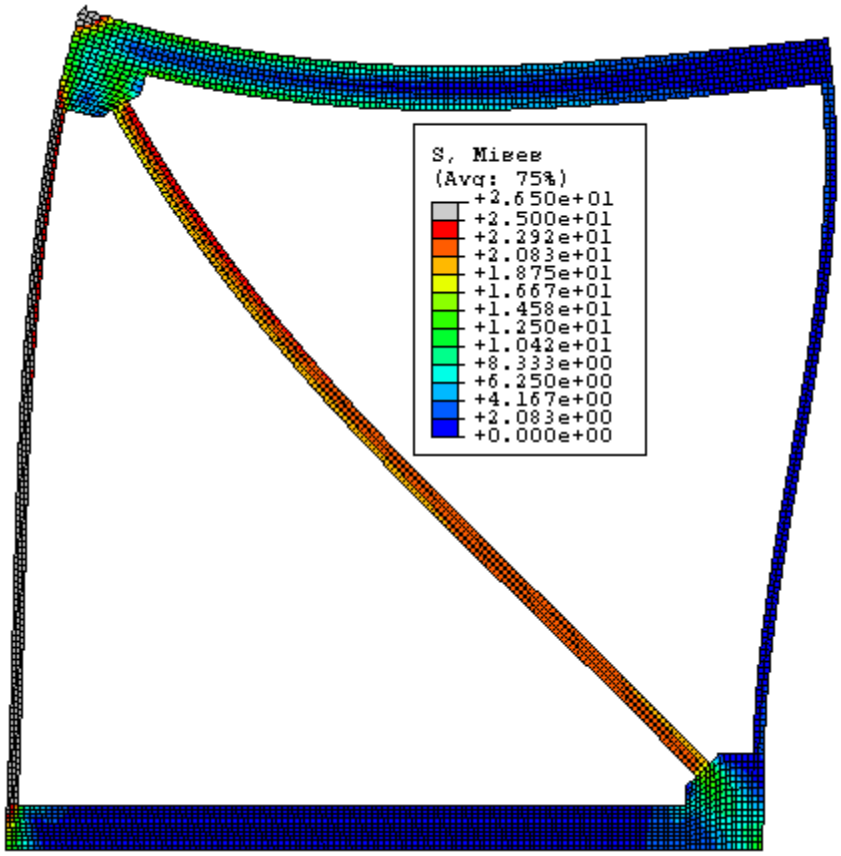

Fig. K131 - Von Mises Stress – Frame “O” without RXS Fuse – Stress Scale #2.

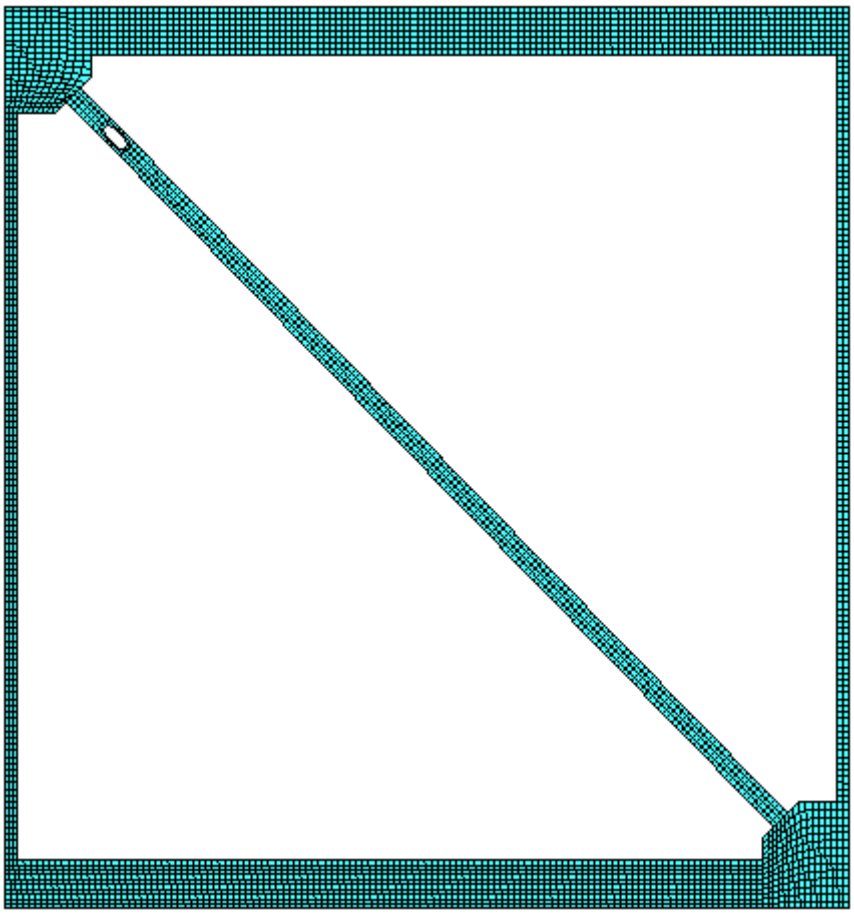

Fig. K132 - FEM Mesh – Frame “O” with RXS Fuse.

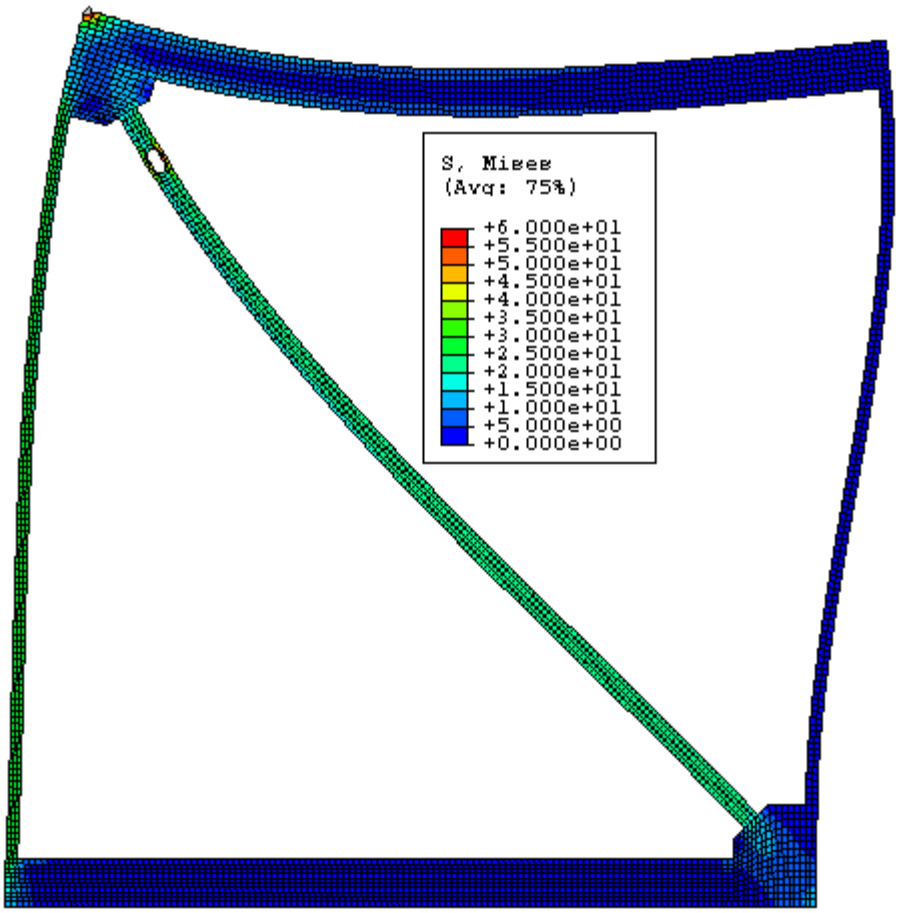

Fig. K133 - Von Mises Stress – Frame “O” with RXS Fuse.

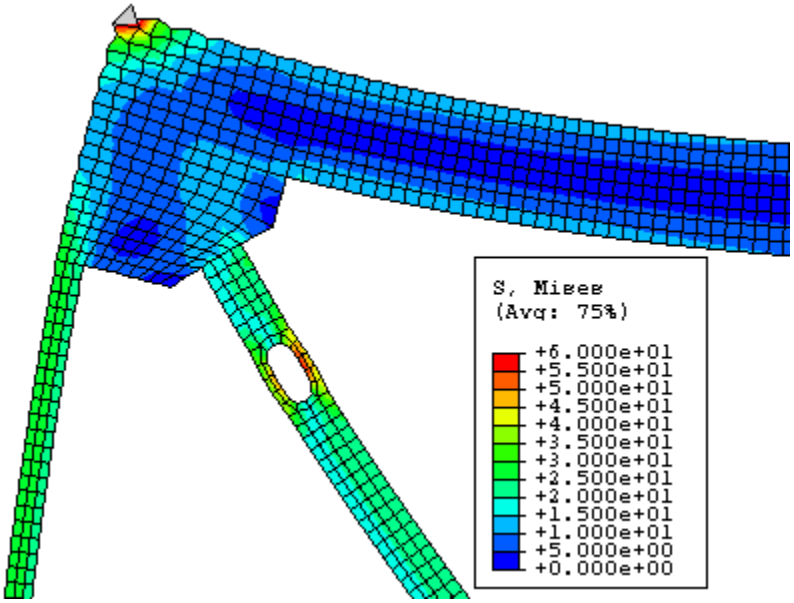

Fig. K134 - Von Mises Stress – Frame “O” with RXS Fuse – Zoom #1.

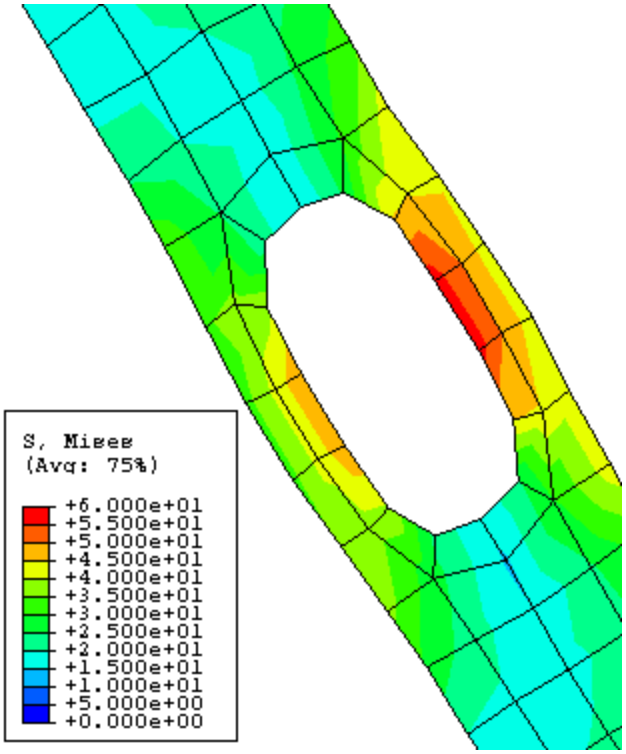

Fig. K135 - Von Mises Stress – Frame “O” with RXS Fuse – Zoom #2.

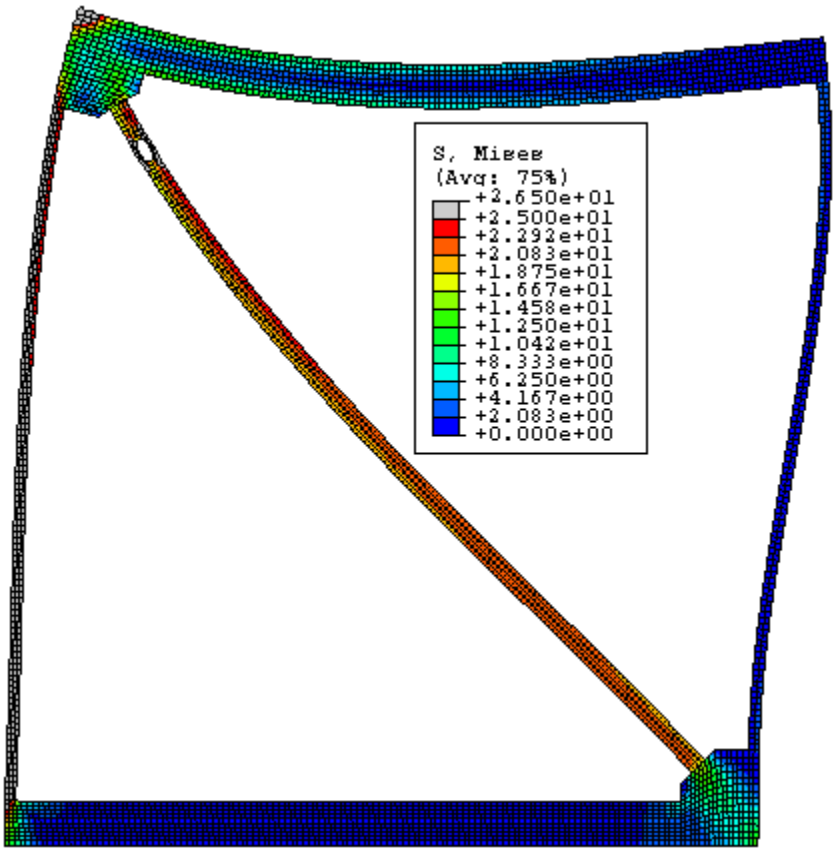

Fig. K136 - Von Mises Stress – Frame “O” with RXS Fuse – Stress Scale #2.

FRAME P

Beam/Column Length Ratio = H/L = 1

Beam-depth/Column-depth = 16”/2”

Brace Angle “ϕ” = 45˚

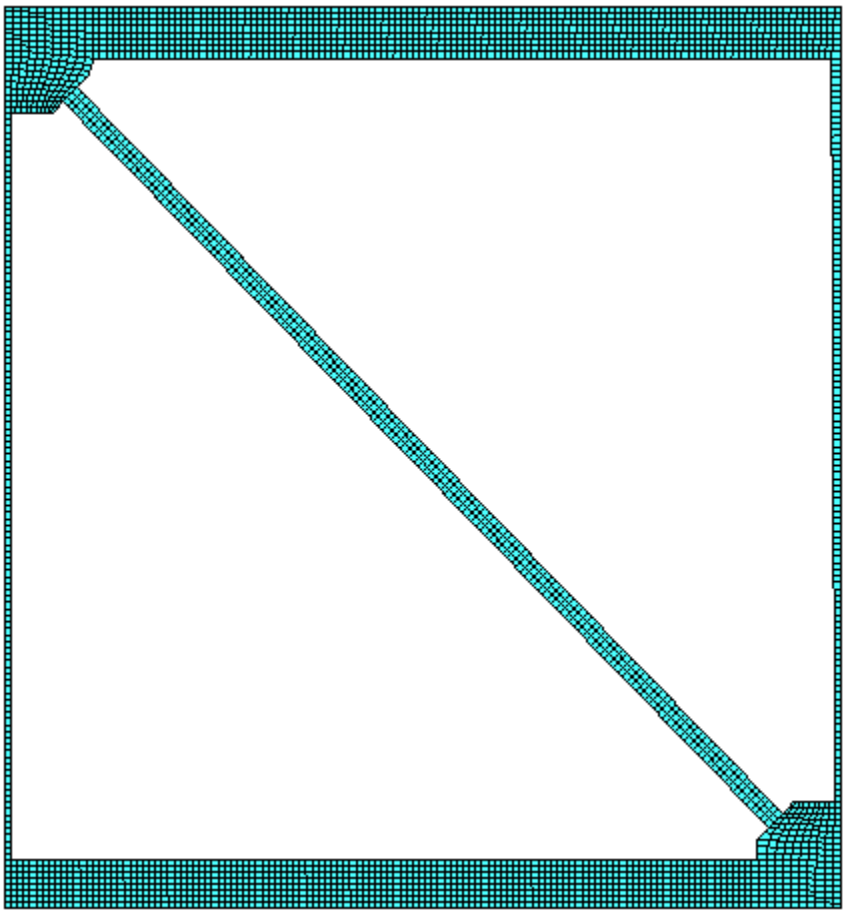

Fig. K137 - FEM Mesh – Frame “P” without RXS Fuse.

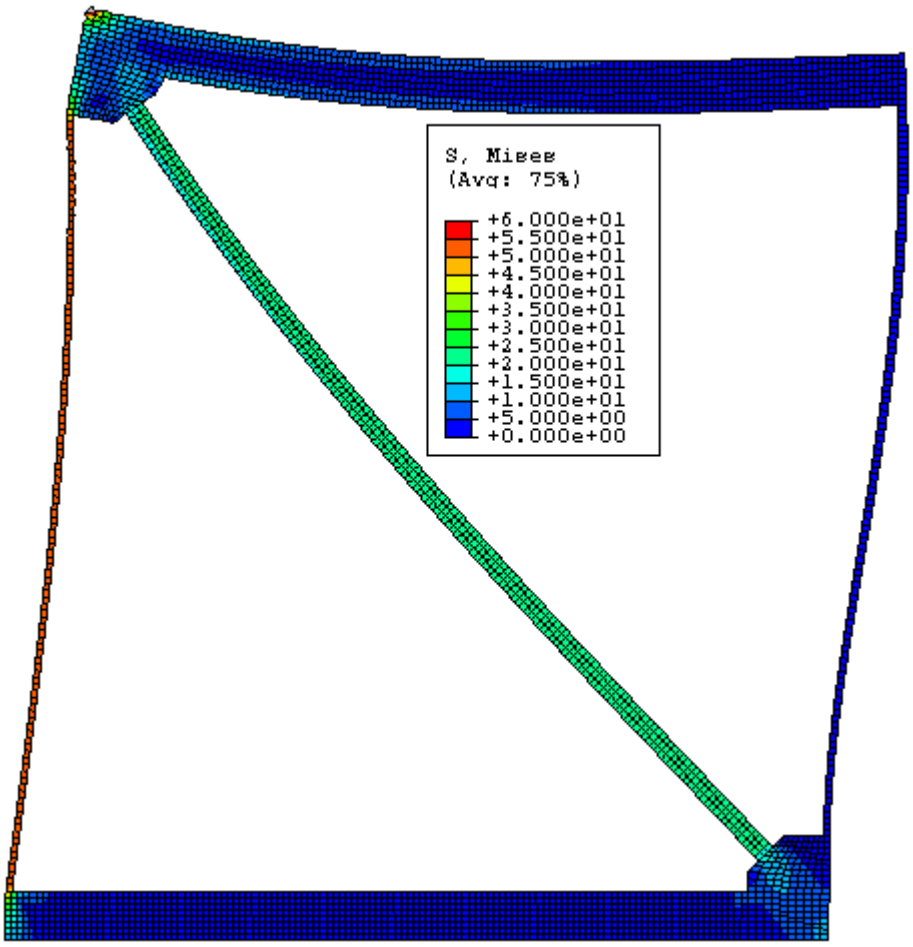

Fig. K138 - Von Mises Stress – Frame “P” without RXS Fuse.

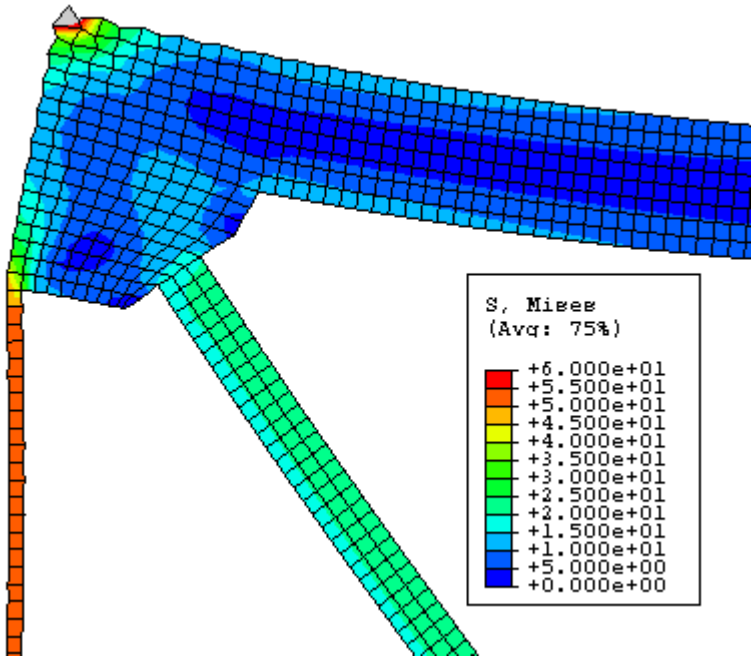

Fig. K139 - Von Mises Stress – Frame “P” without RXS Fuse – Zoom.

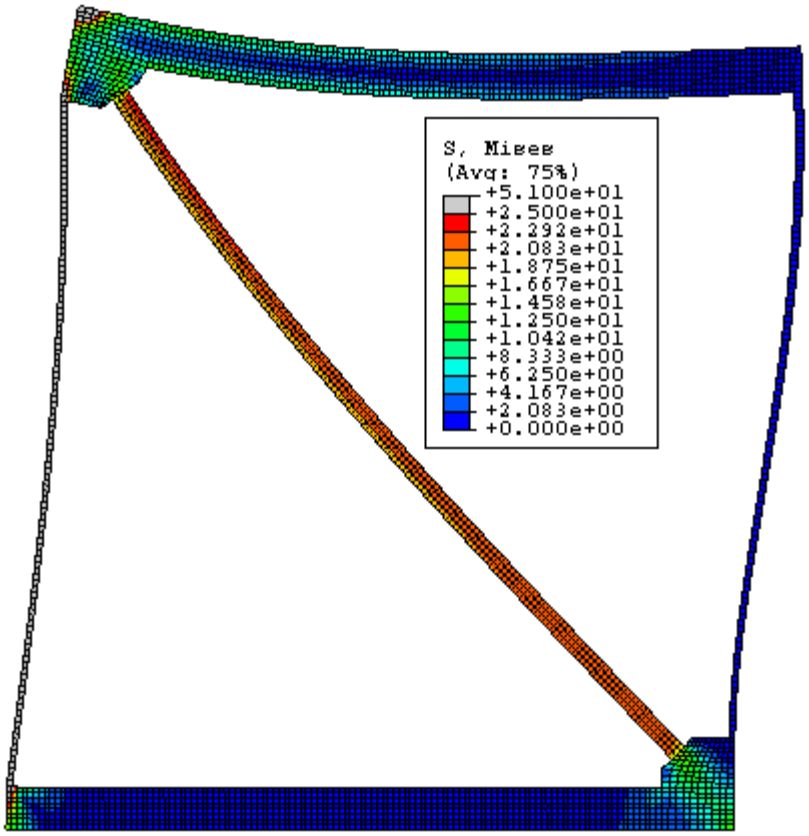

Fig. K140 - Von Mises Stress – Frame “P” without RXS Fuse – Stress Scale #2.

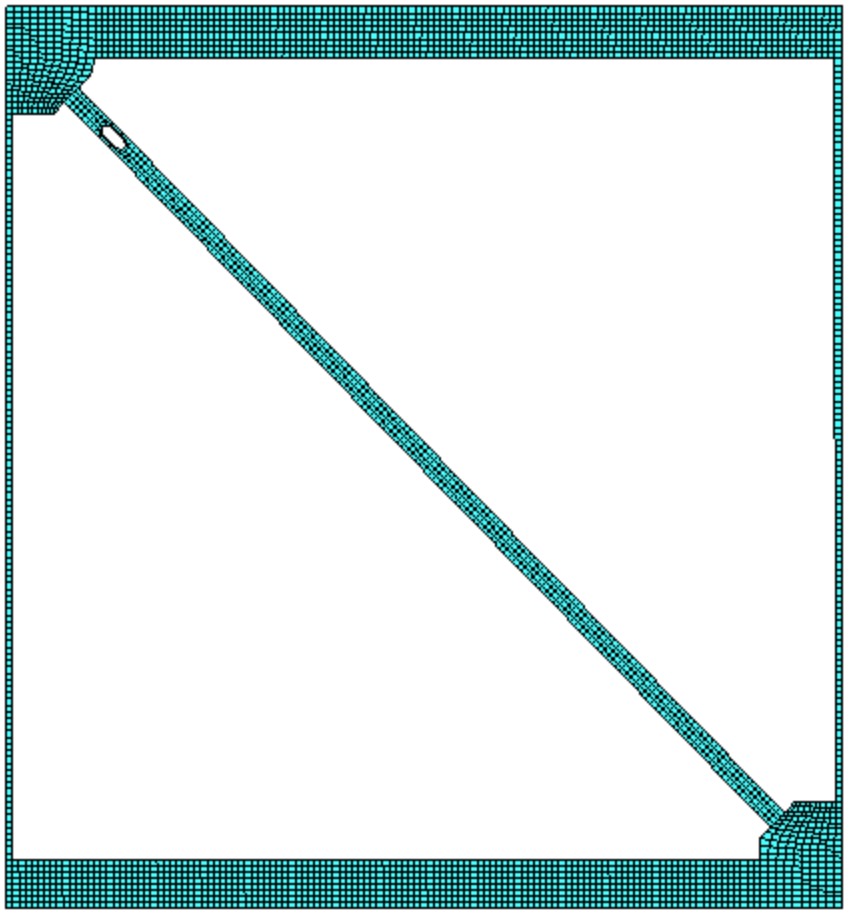

Fig. K141 - FEM Mesh – Frame “P” with RXS Fuse.

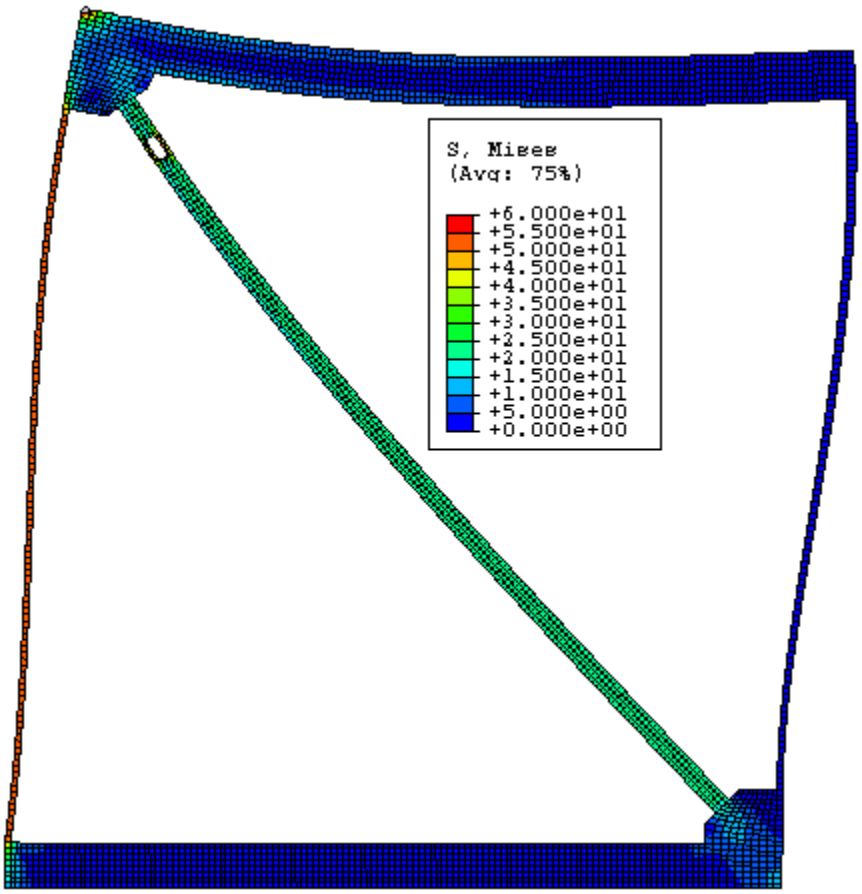

Fig. K142 - Von Mises Stress – Frame “P” with RXS Fuse.

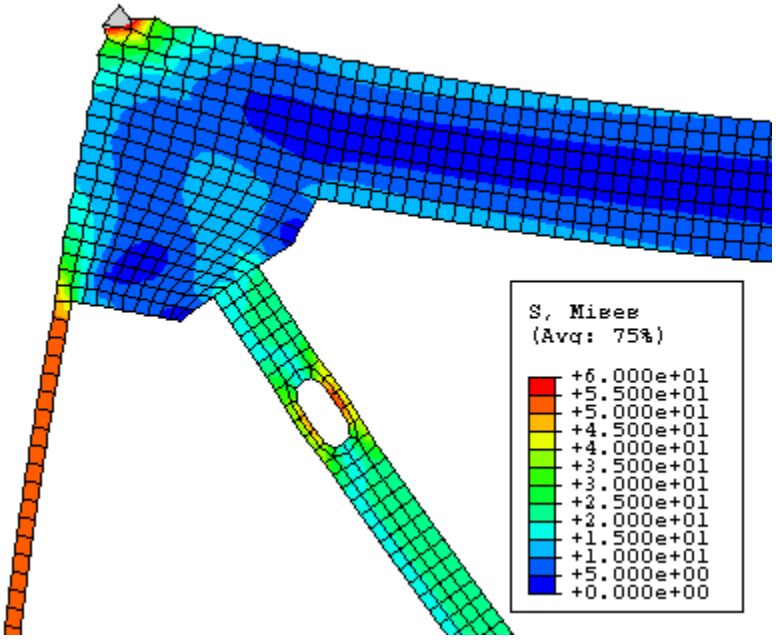

Fig. K143 - Von Mises Stress – Frame "P" with RXS Fuse – Zoom #1.

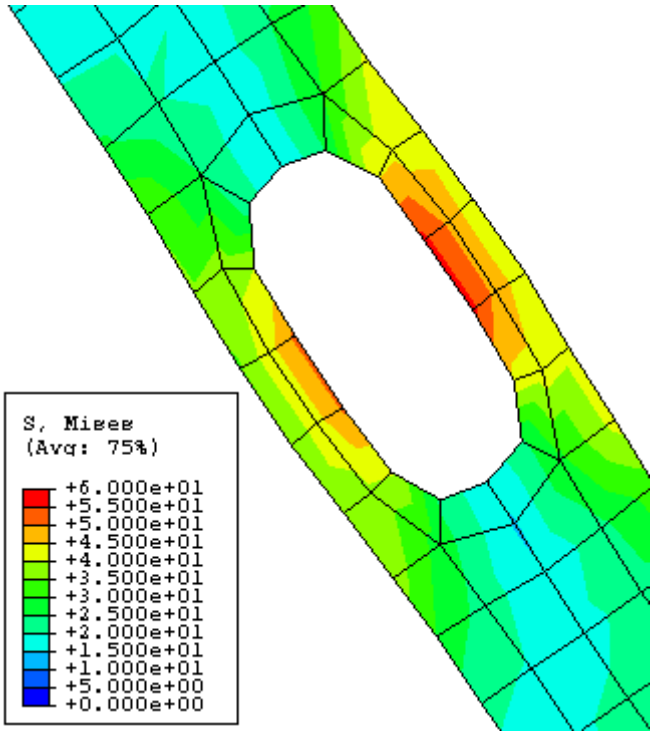

Fig. K144 - Von Mises Stress – Frame "P" with RXS Fuse – Zoom #2.

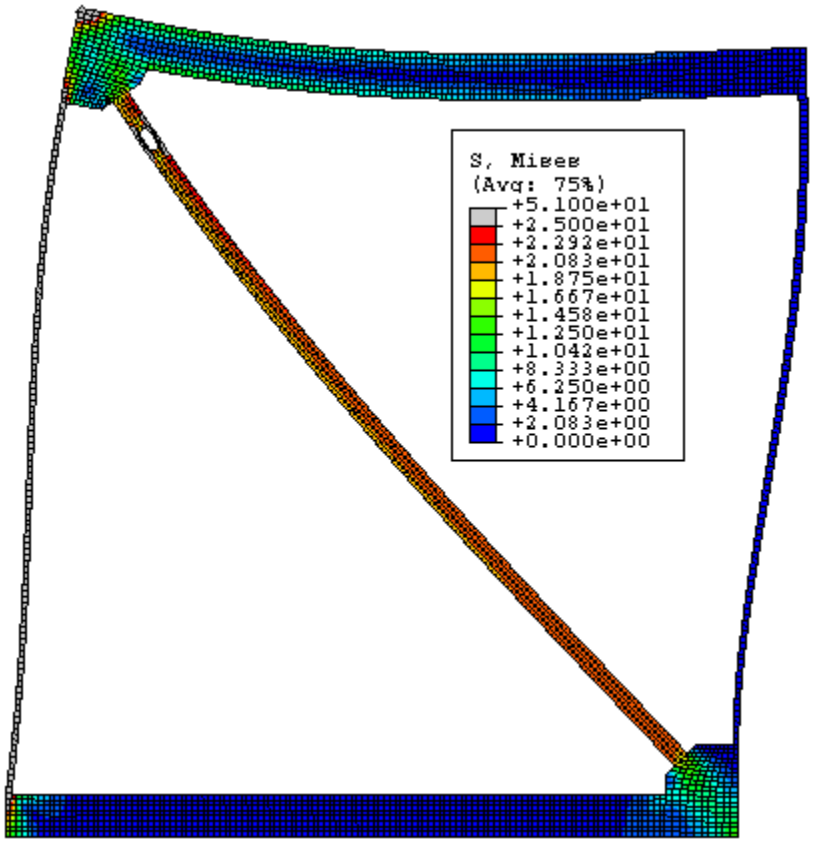

Fig. K145 - Von Mises Stress – Frame “P” with RXS Fuse – Stress Scale #2.

FRAME Q

Beam/Column Length Ratio = H/L = 1

Beam-depth/Column-depth = 16”/16”

Brace Angle “ϕ” = 55˚

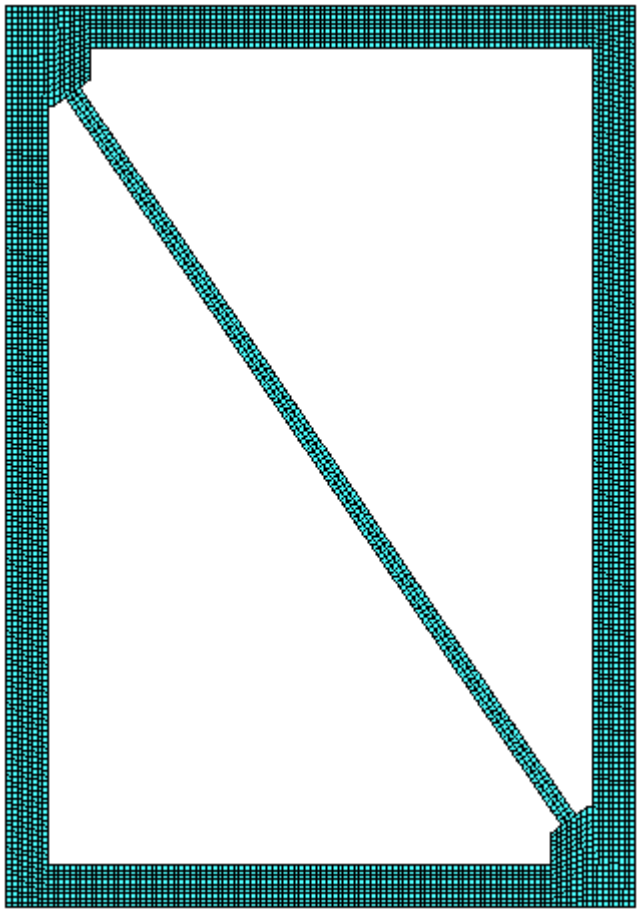

Fig. K146 - FEM Mesh – Frame “Q” without RXS Fuse.

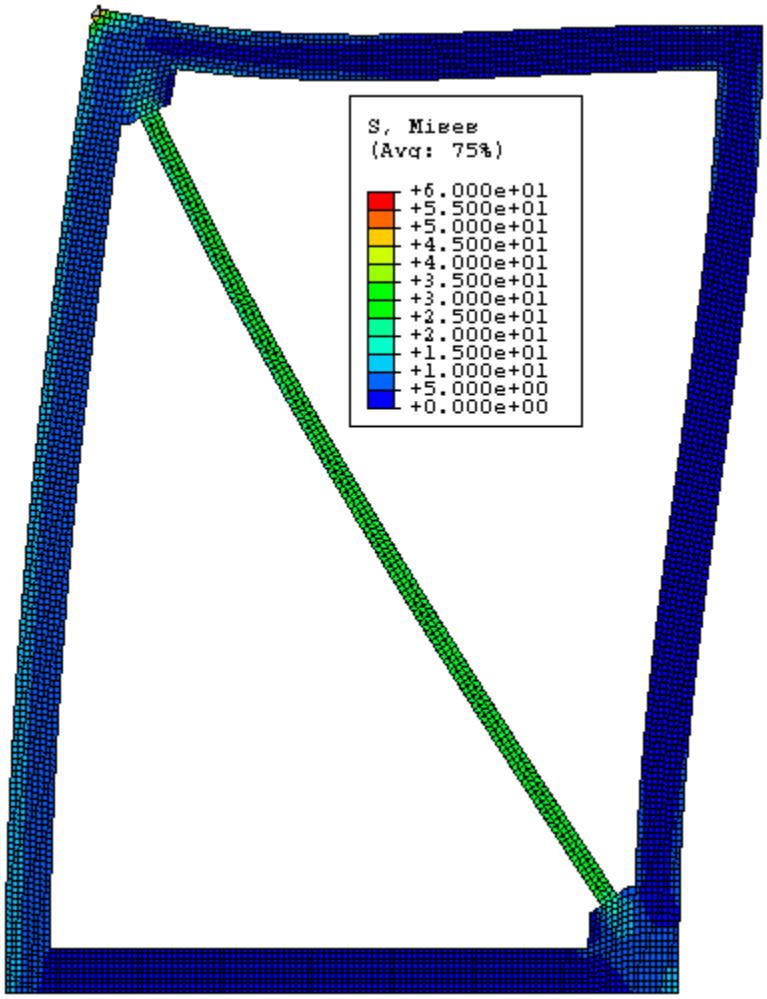

Fig. K147 - Von Mises Stress – Frame “Q” without RXS Fuse.

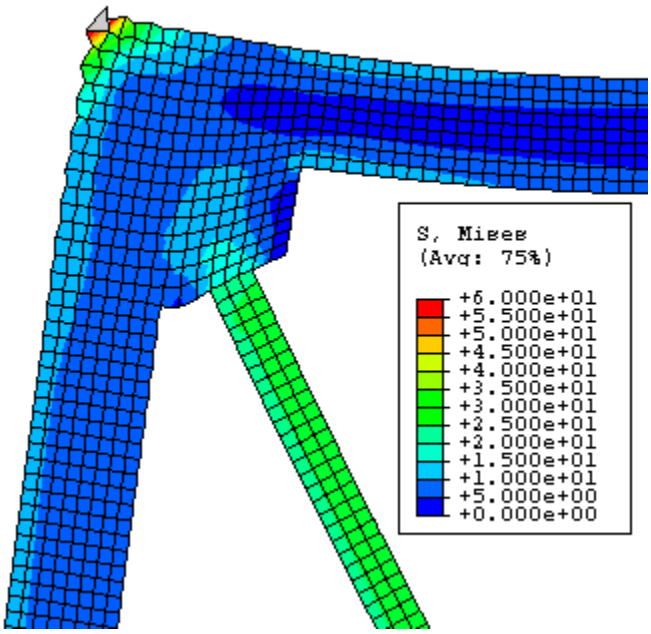

Fig. K148 - Von Mises Stress – Frame “Q” without RXS Fuse – Zoom.

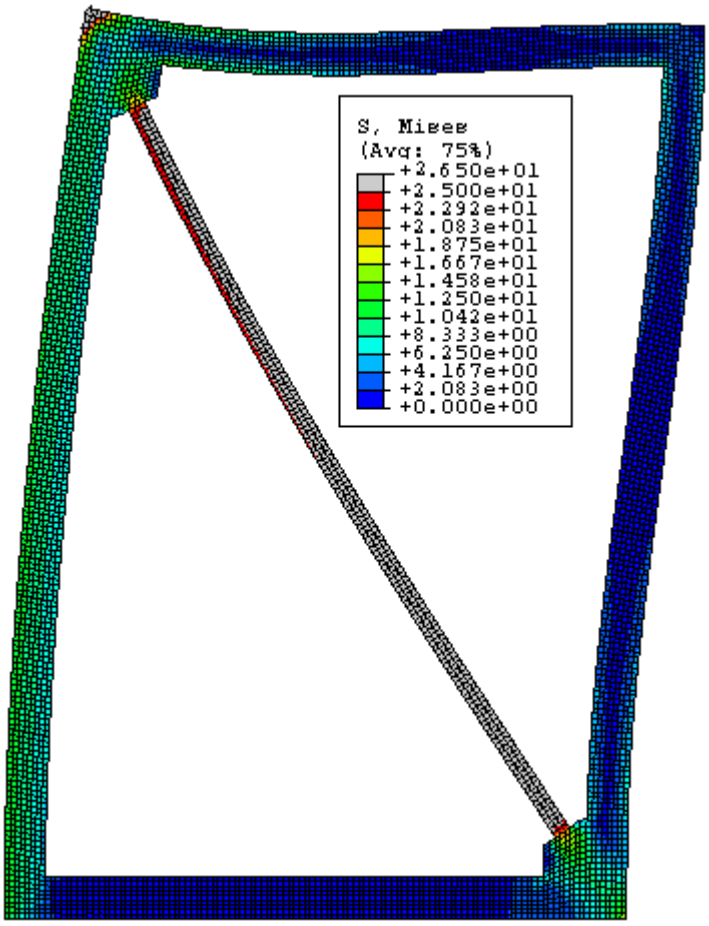

Fig. K149 - Von Mises Stress – Frame “Q” without RXS Fuse – Stress Scale #2.

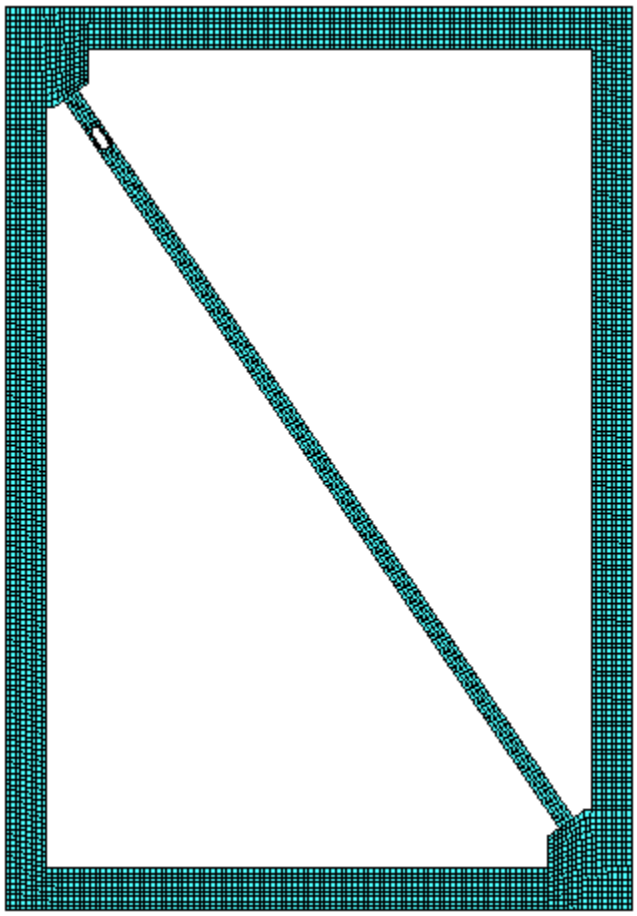

Fig. K150 - FEM Mesh – Frame “Q” with RXS Fuse.

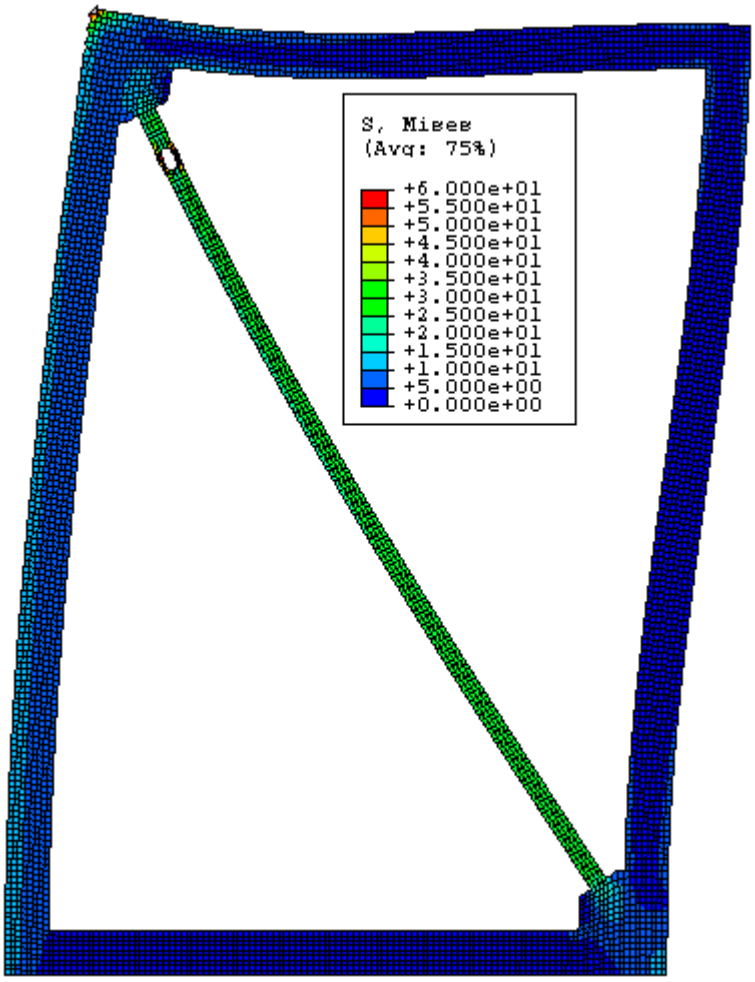

Fig. K151 - Von Mises Stress – Frame “Q” with RXS Fuse.

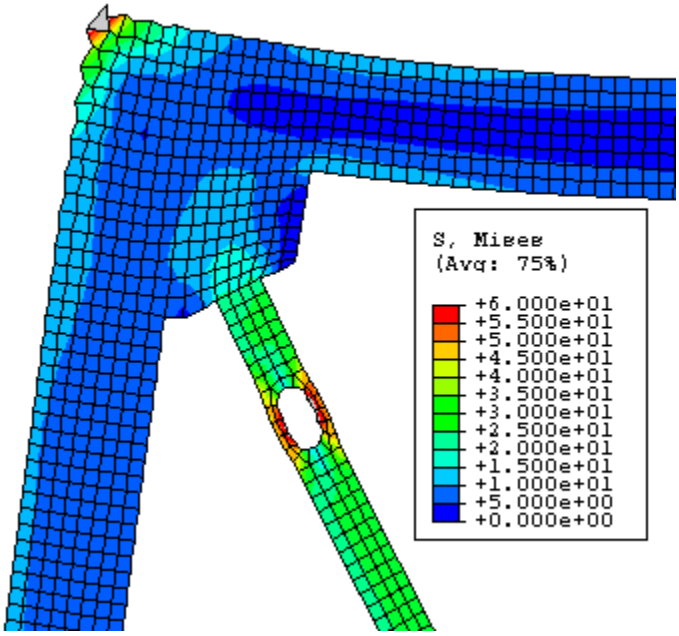

Fig. K152 - Von Mises Stress – Frame “Q” with RXS Fuse – Zoom #1.

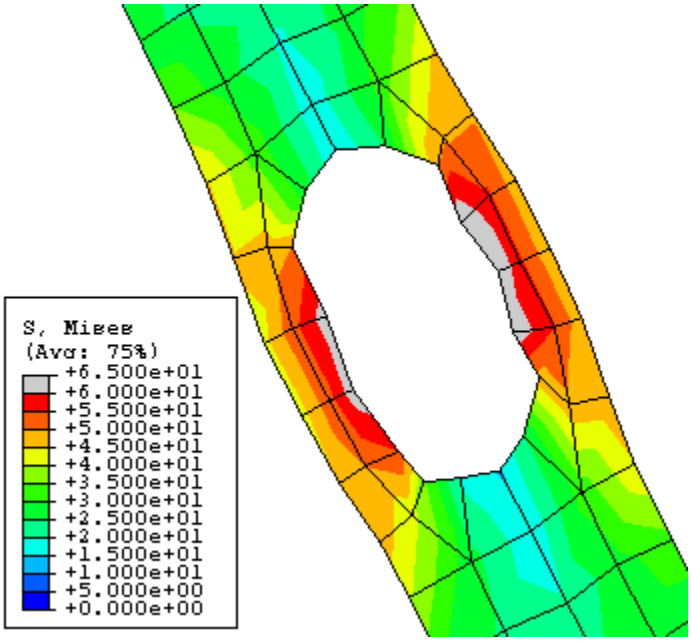

Fig. K153 - Von Mises Stress – Frame “Q” with RXS Fuse – Zoom #2.

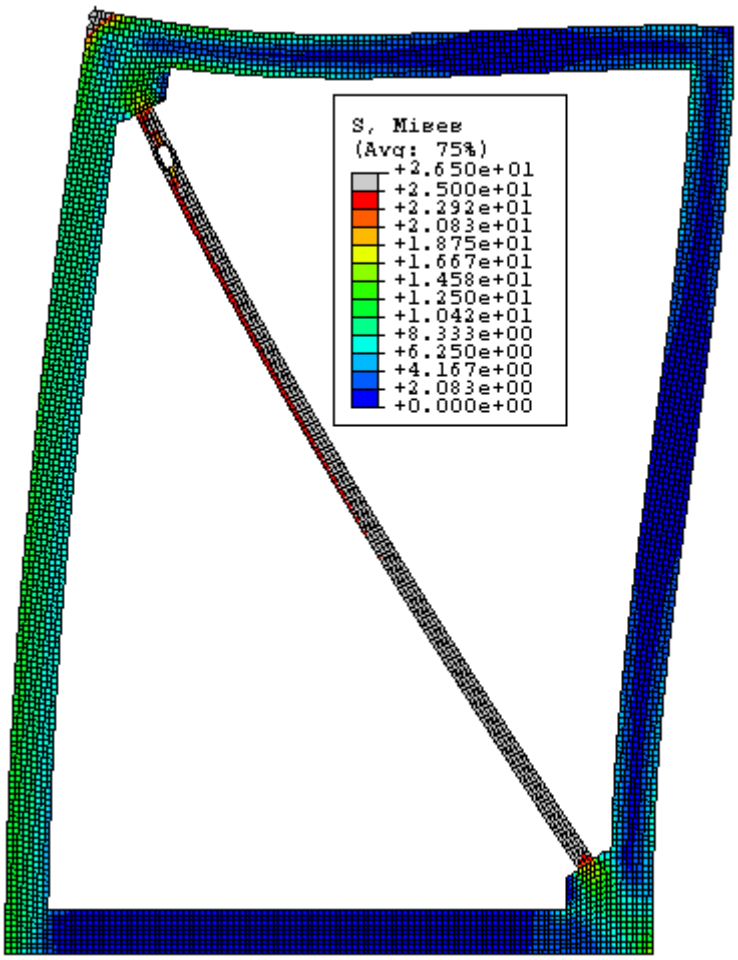

Fig. K154 - Von Mises Stress – Frame “Q” with RXS Fuse – Stress Scale #2.

FRAME R

Beam/Column Length Ratio = H/L = 1

Beam-depth/Column-depth = 16”/16”

Brace Angle “ϕ” = 50˚

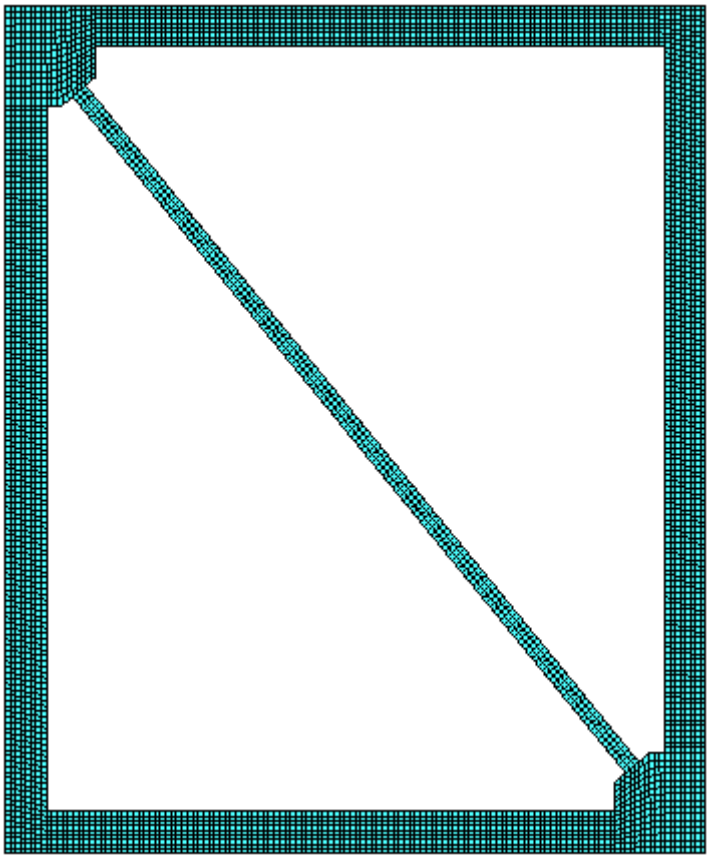

Fig. K155 - FEM Mesh – Frame “R” without RXS Fuse.

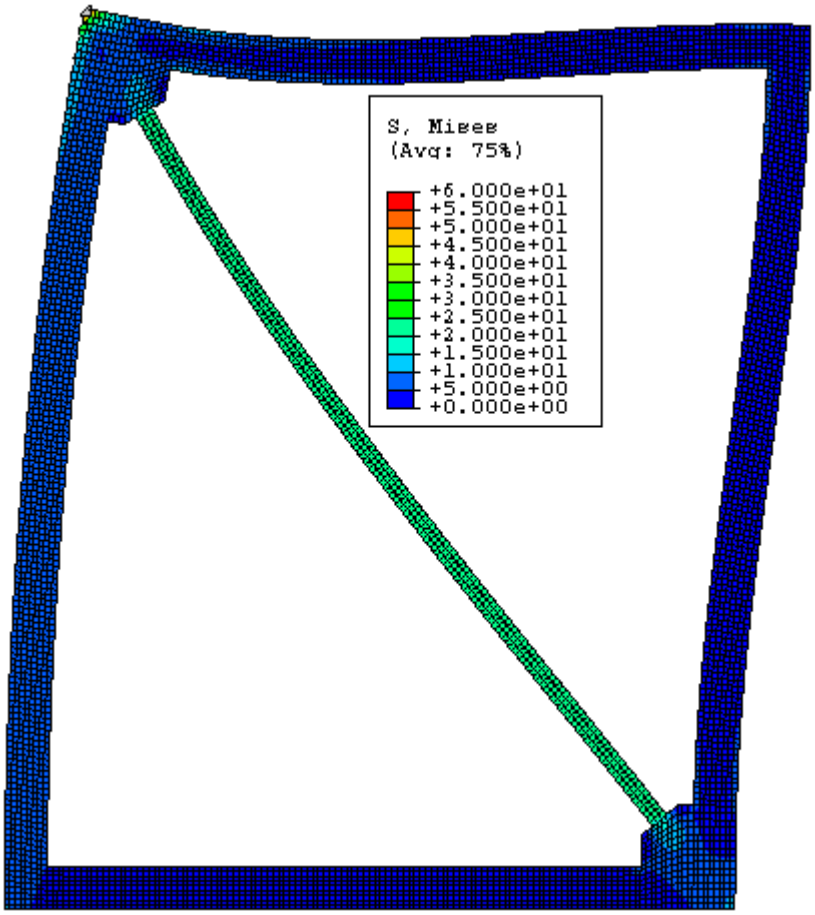

Fig. K156 - Von Mises Stress – Frame “R” without RXS Fuse.

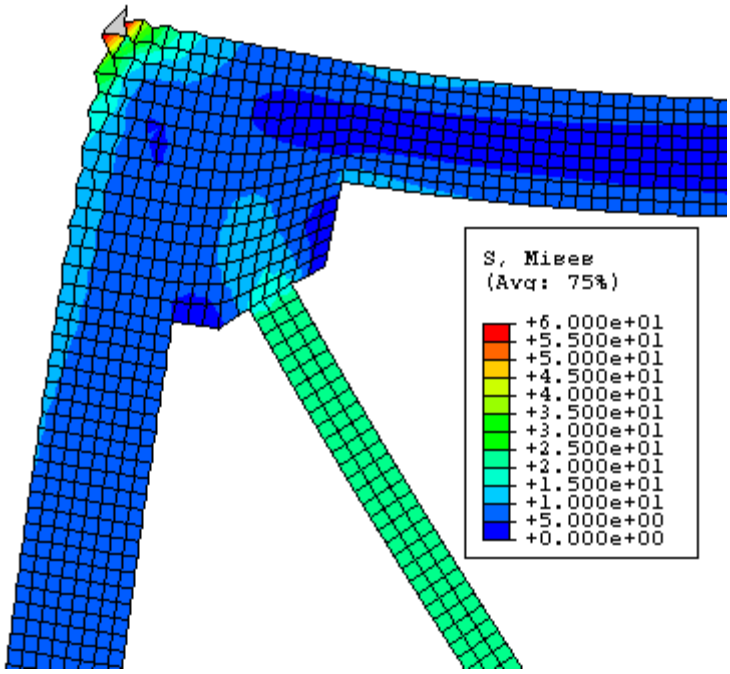

Fig. K157 - Von Mises Stress – Frame “R” without RXS Fuse – Zoom.

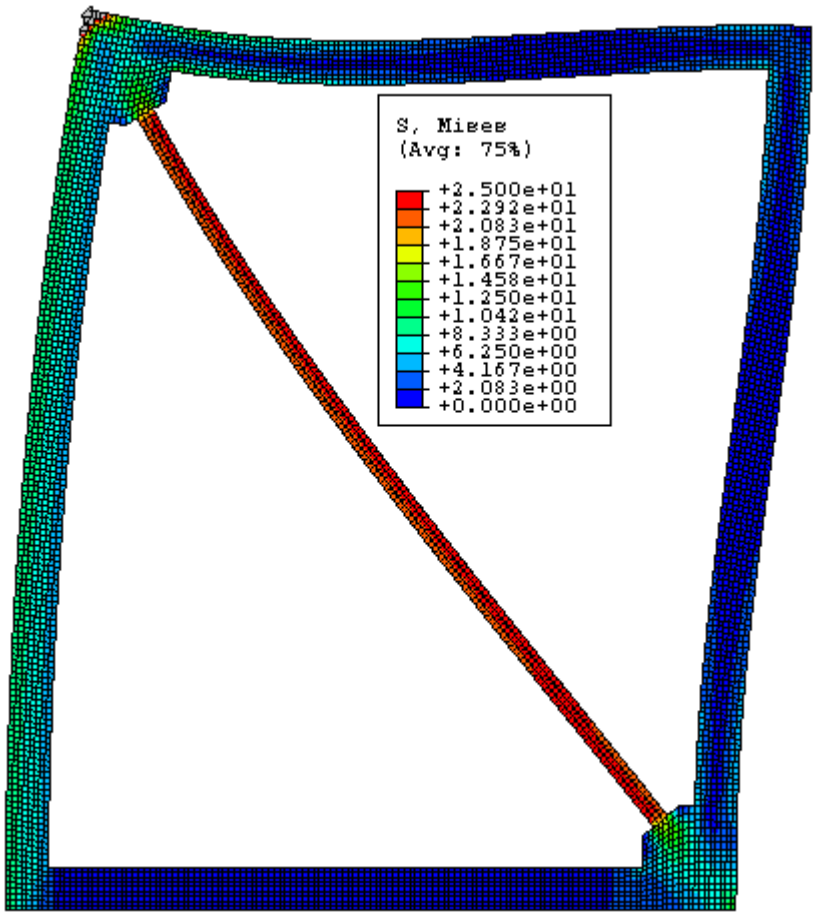

Fig. K158 - Von Mises Stress – Frame “R” without RXS Fuse – Stress Scale #2.

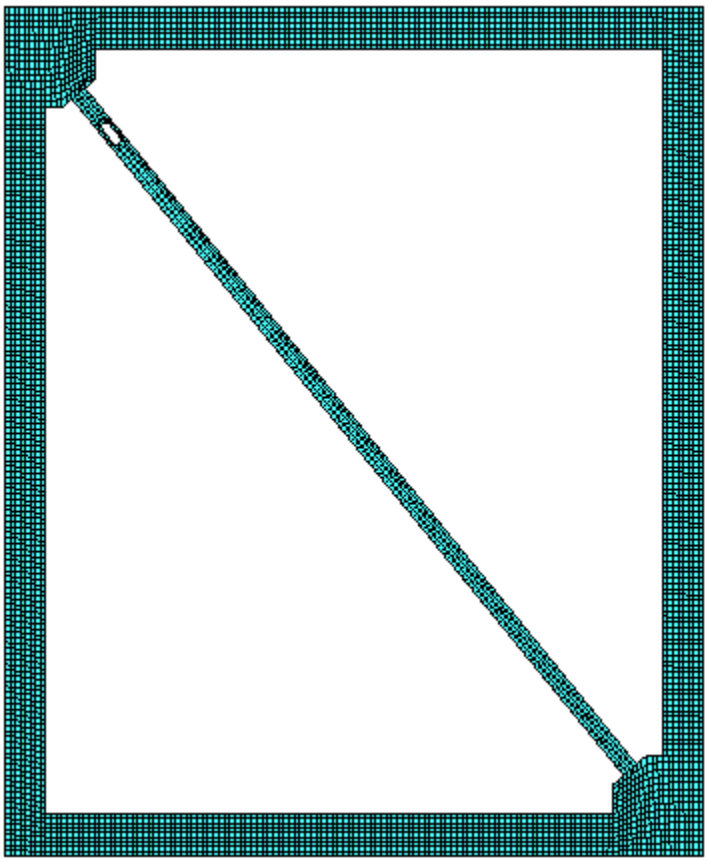

Fig. K159 - FEM Mesh – Frame “R” with RXS Fuse.

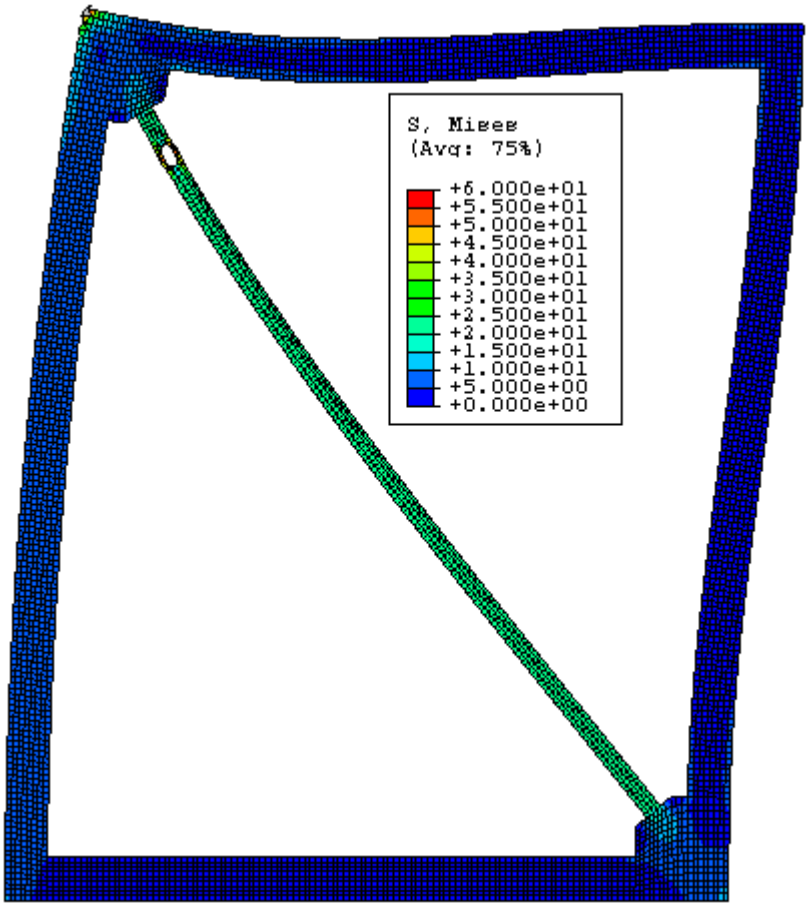

Fig. K160 - Von Mises Stress – Frame “R” with RXS Fuse.

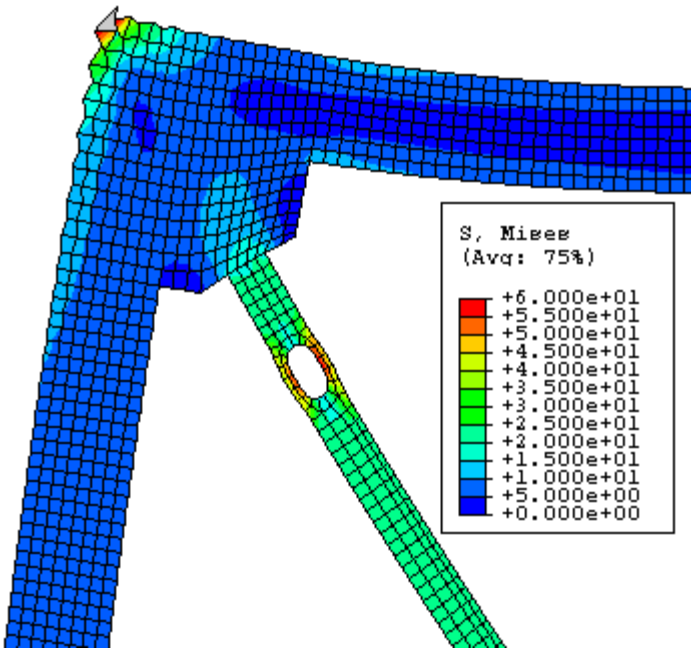

Fig. K161 - Von Mises Stress – Frame “R” with RXS Fuse – Zoom #1.

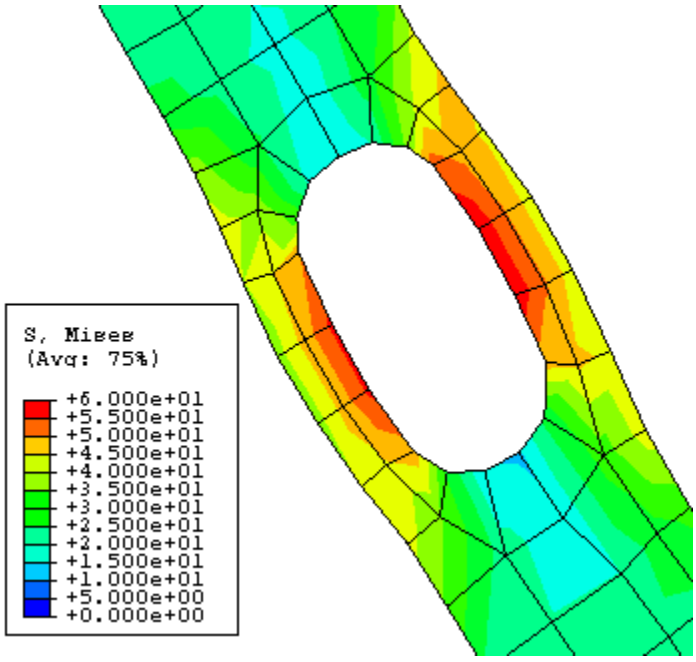

Fig. K162 - Von Mises Stress – Frame “R” with RXS Fuse – Zoom #2.

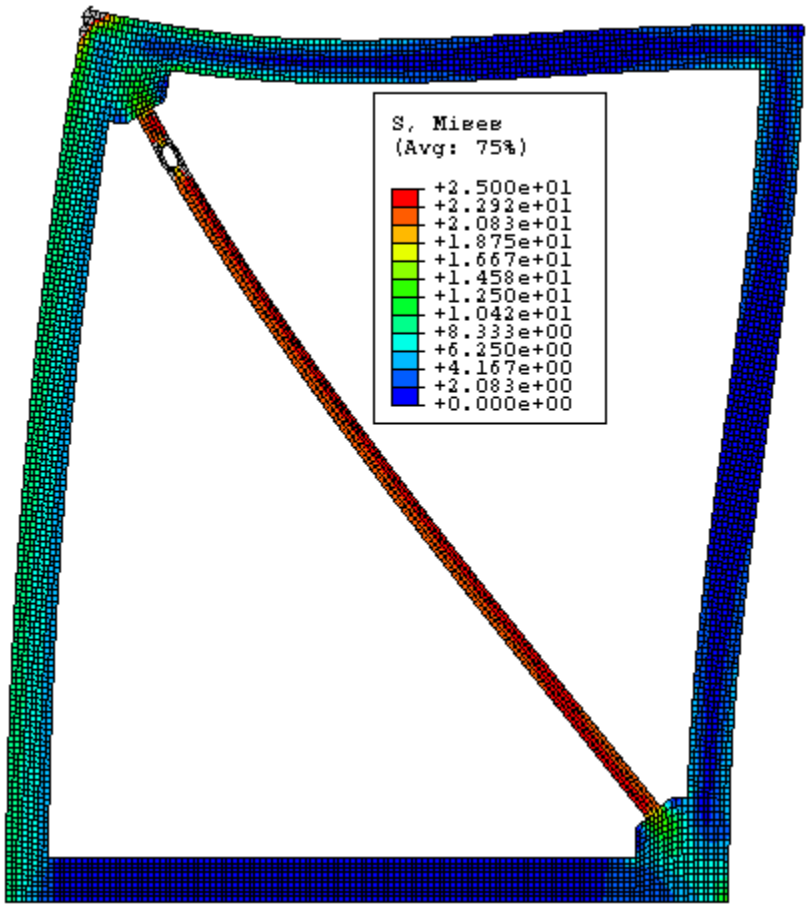

Fig. K163 - Von Mises Stress – Frame “R” with RXS Fuse – Stress Scale #2.

FRAME S

Beam/Column Length Ratio = H/L = 1

Beam-depth/Column-depth = 16”/16”

Brace Angle “ϕ” = 40˚

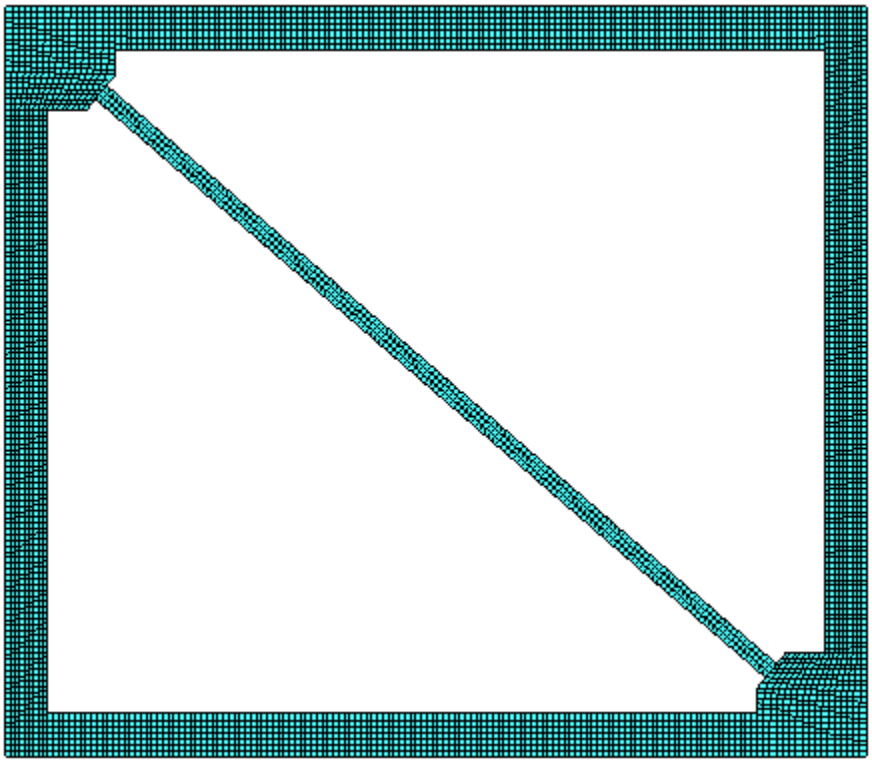

Fig. K164 - FEM Mesh – Frame “S” without RXS Fuse.

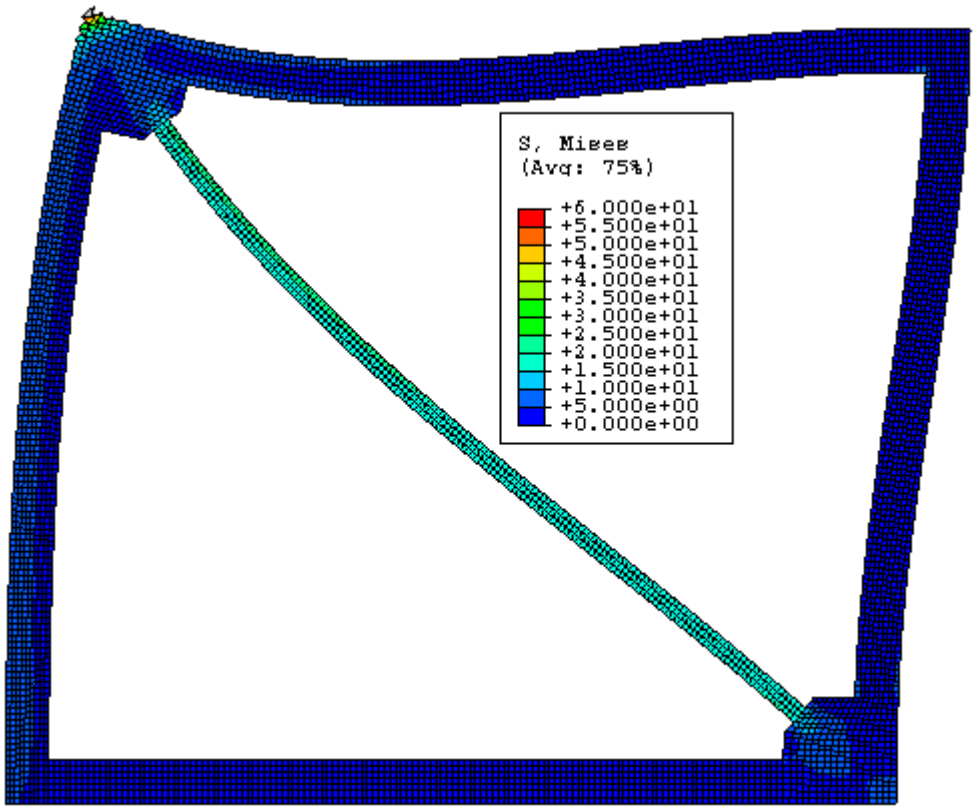

Fig. K165 - Von Mises Stress – Frame “S” without RXS Fuse.

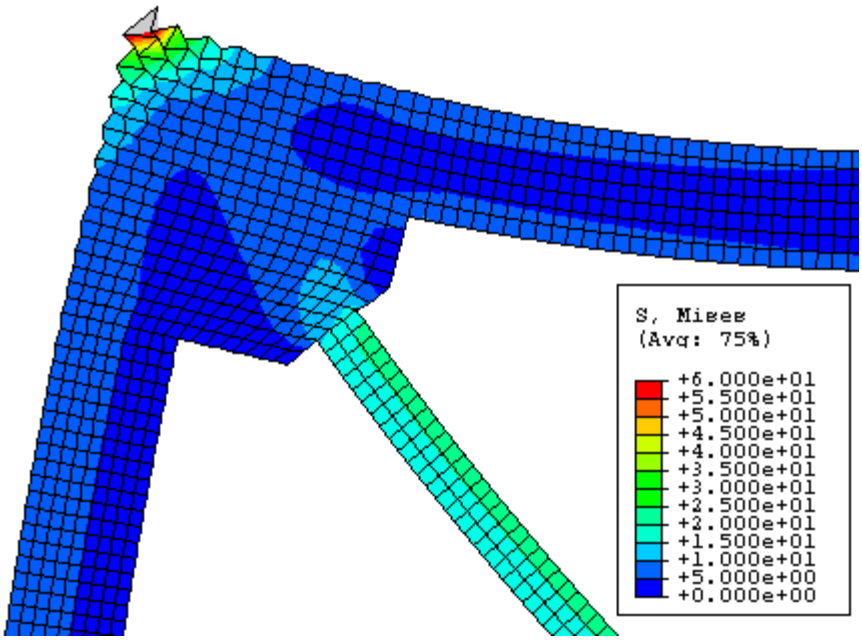

Fig. K166 - Von Mises Stress – Frame “S” without RXS Fuse – Zoom.

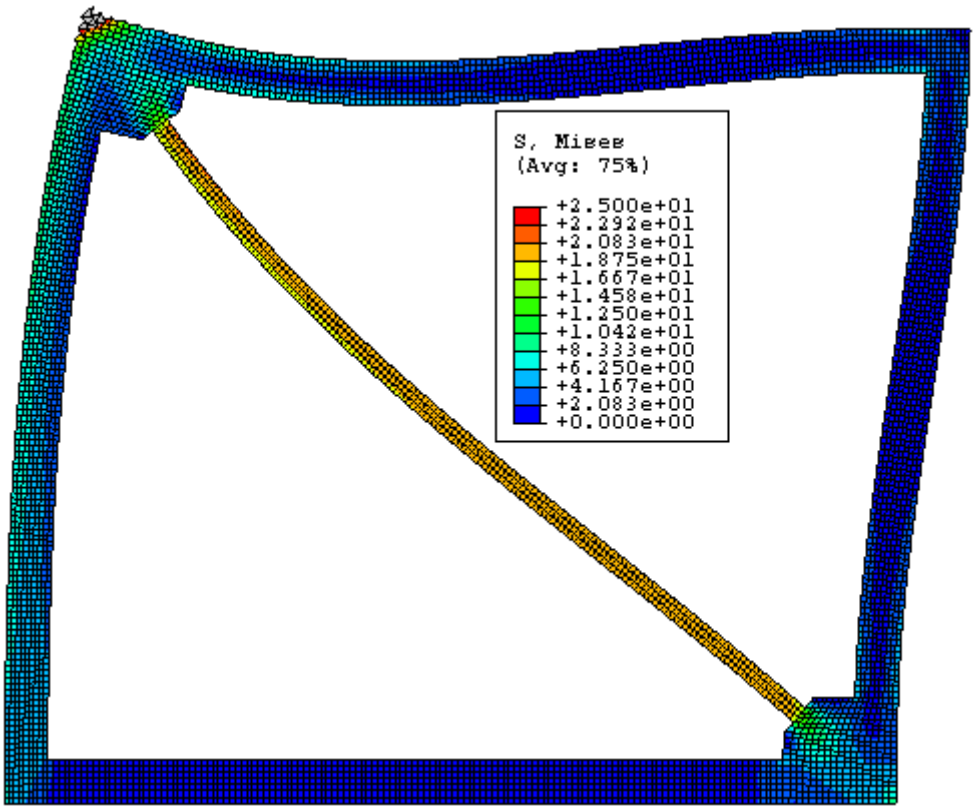

Fig. K167 - Von Mises Stress – Frame “S” without RXS Fuse – Stress Scale #2.

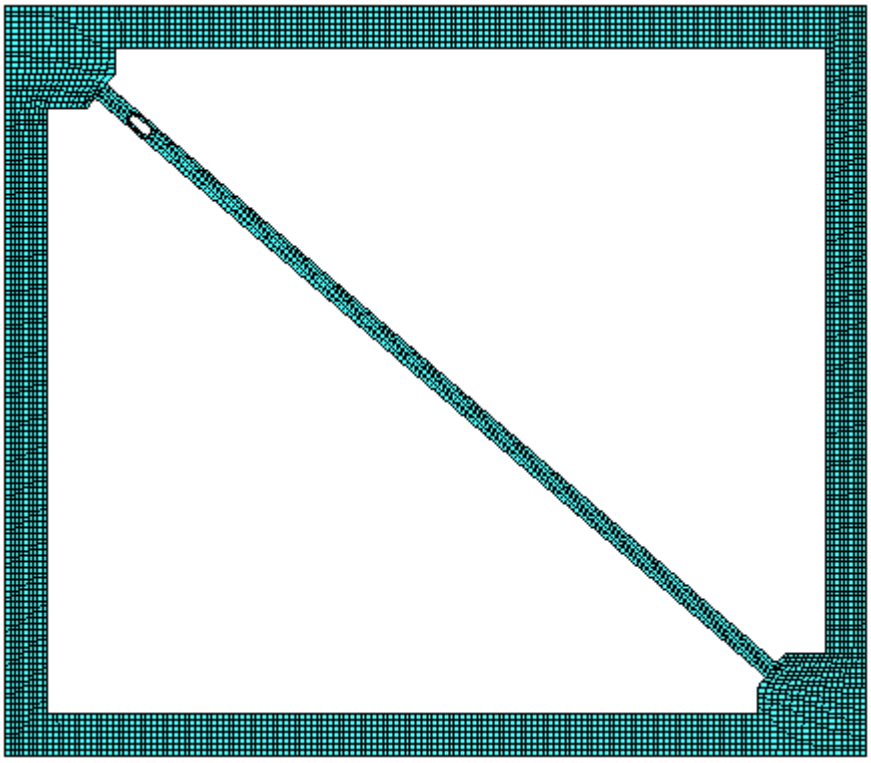

Fig. K168 - FEM Mesh – Frame “S” with RXS Fuse.

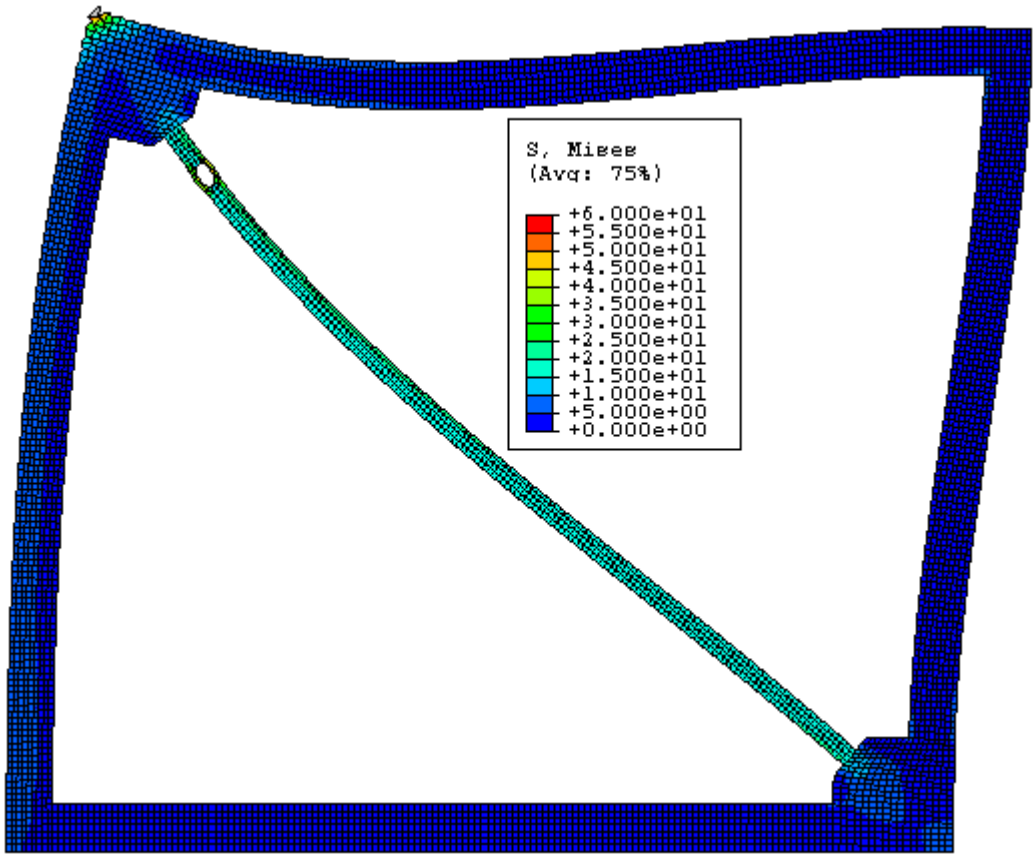

Fig. K169 - Von Mises Stress – Frame “S” with RXS Fuse.

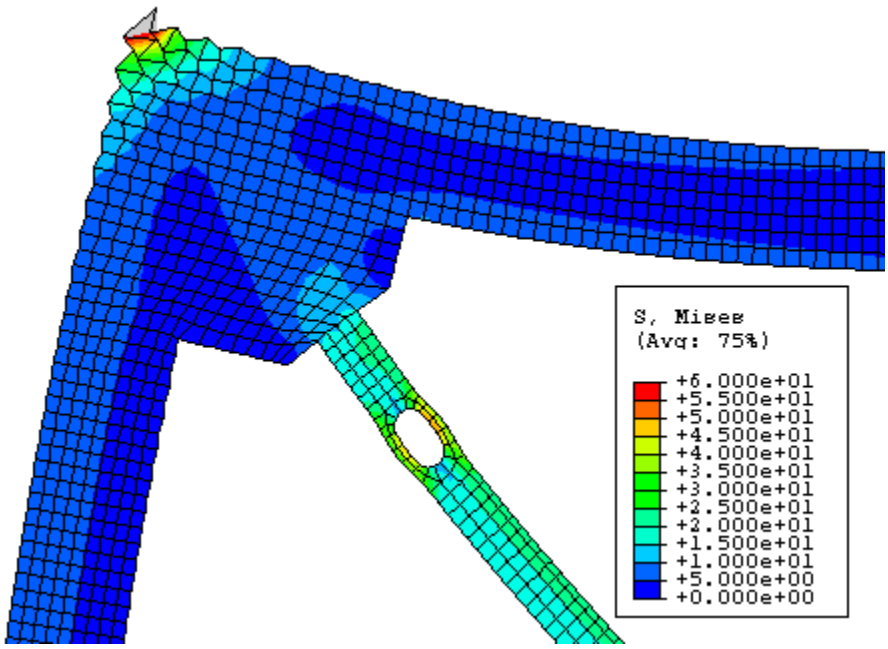

Fig. K170 - Von Mises Stress – Frame “S” with RXS Fuse – Zoom #1.

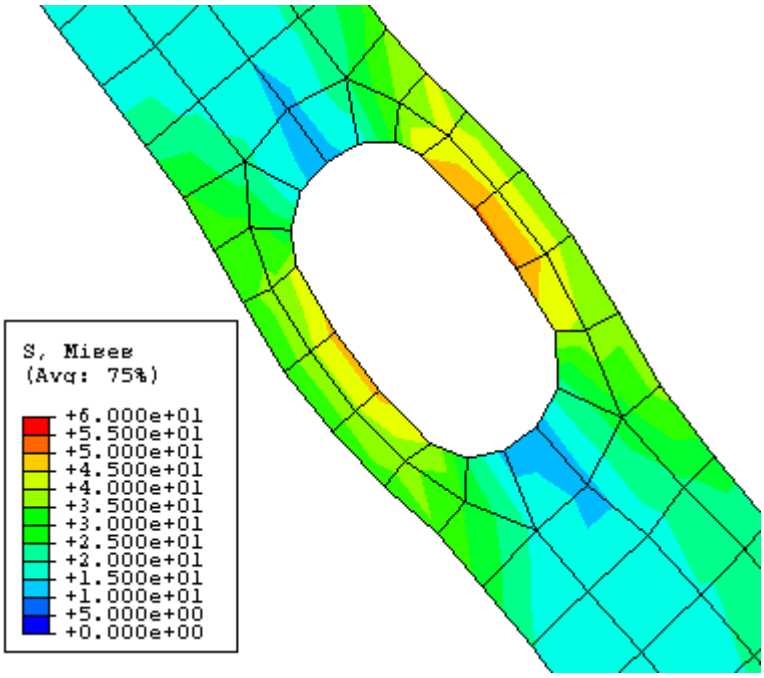

Fig. K171 - Von Mises Stress – Frame “S” with RXS Fuse – Zoom #2.

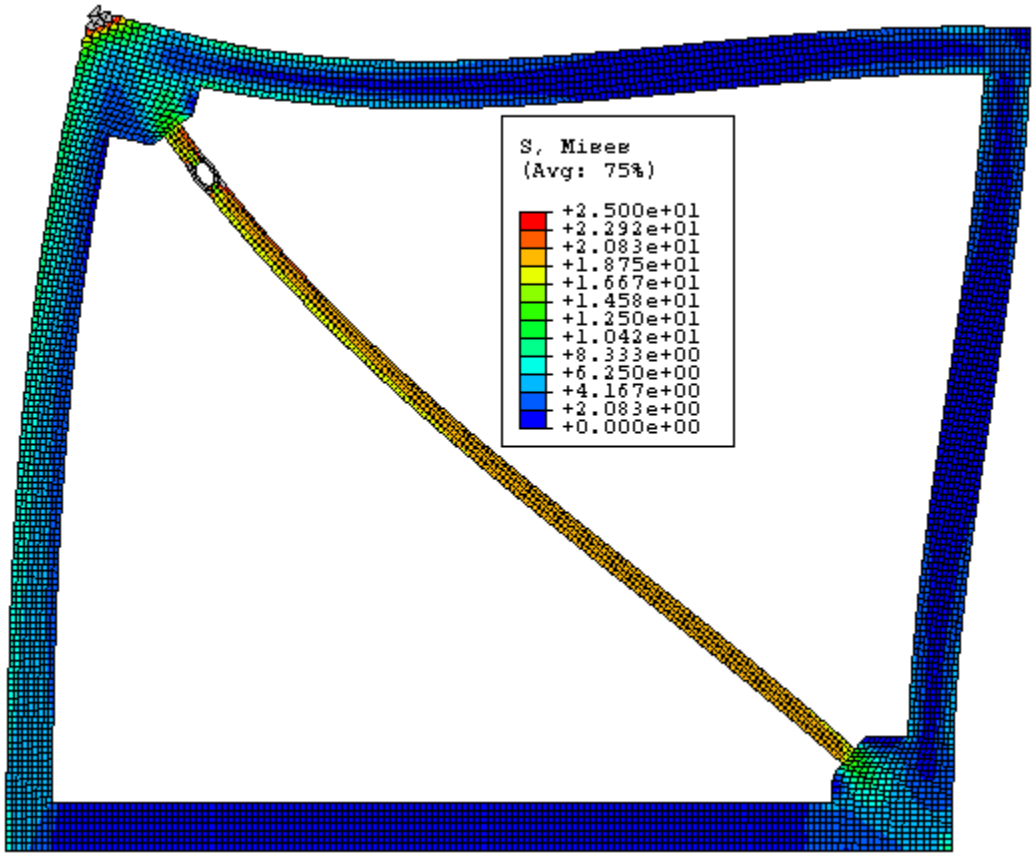

Fig. K172 -Von Mises Stress – Frame “S” with RXS Fuse – Stress Scale #2.

FRAME T

Beam/Column Length Ratio = H/L = 1

Beam-depth/Column-depth = 16”/16”

Brace Angle “ϕ” = 35˚

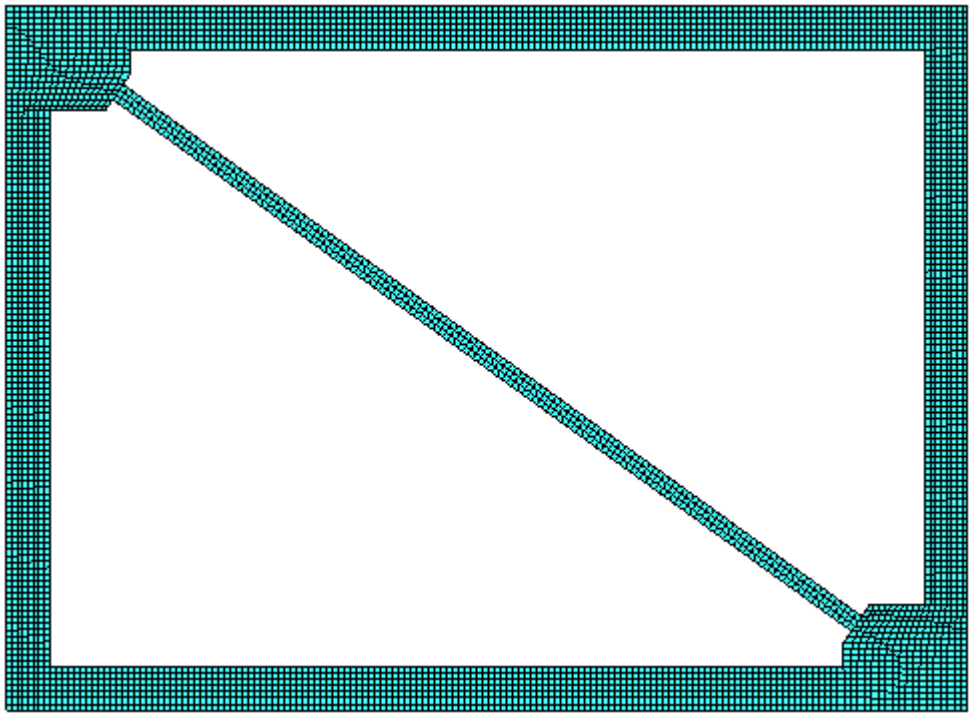

Fig. K173 - FEM Mesh – Frame “T” without RXS Fuse.

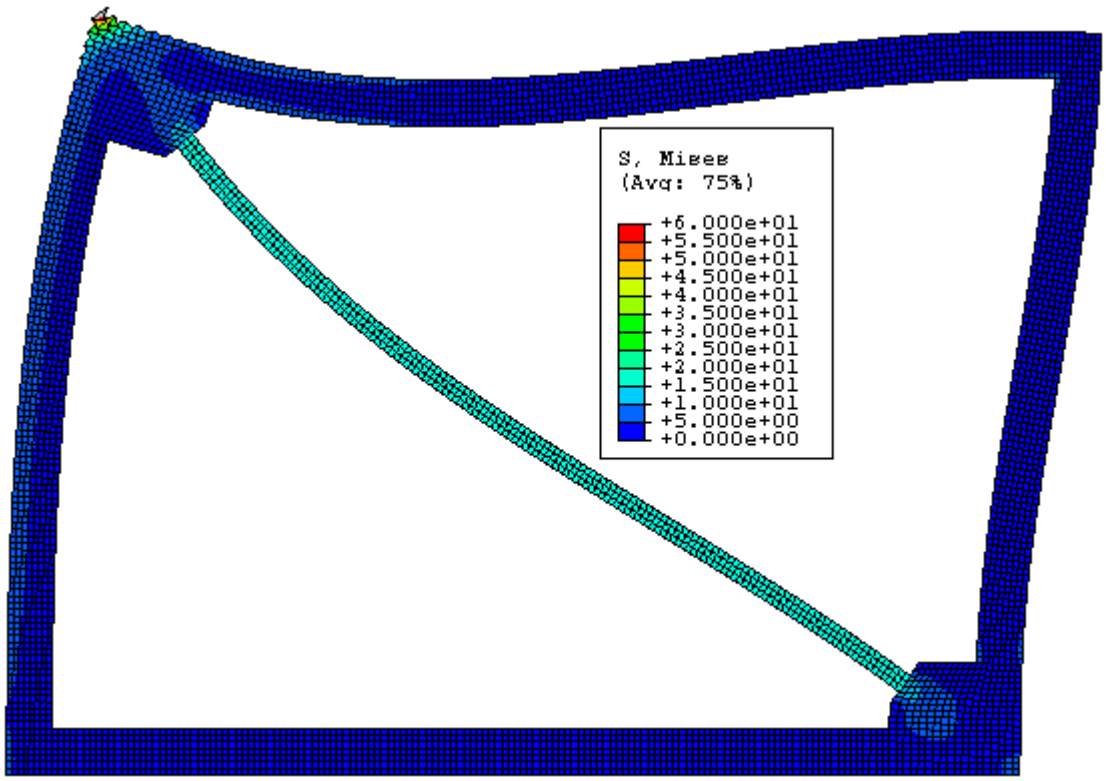

Fig. K174 - Von Mises Stress – Frame “T” without RXS Fuse.

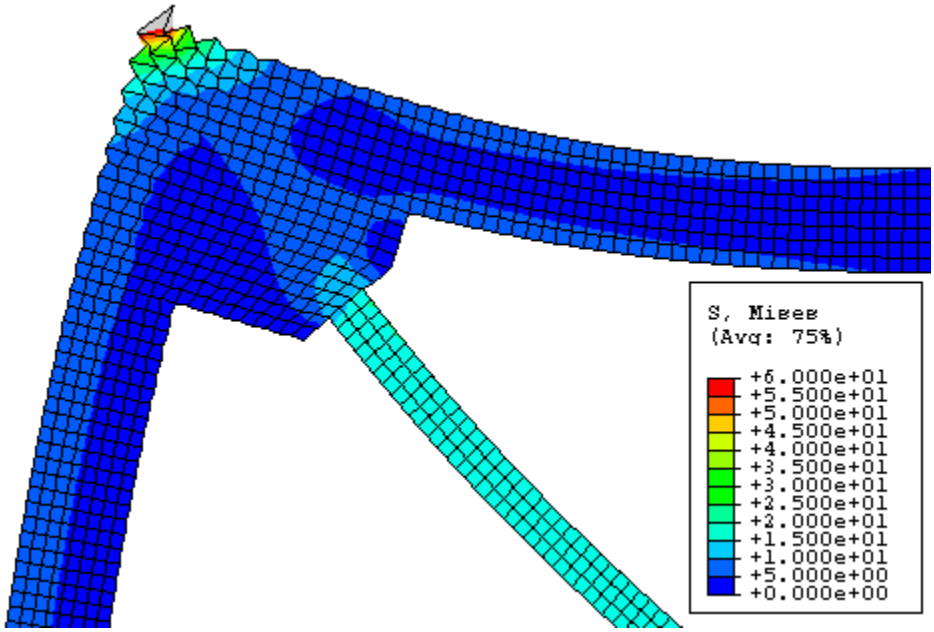

Fig. K175 - Von Mises Stress – Frame “T” without RXS Fuse – Zoom.

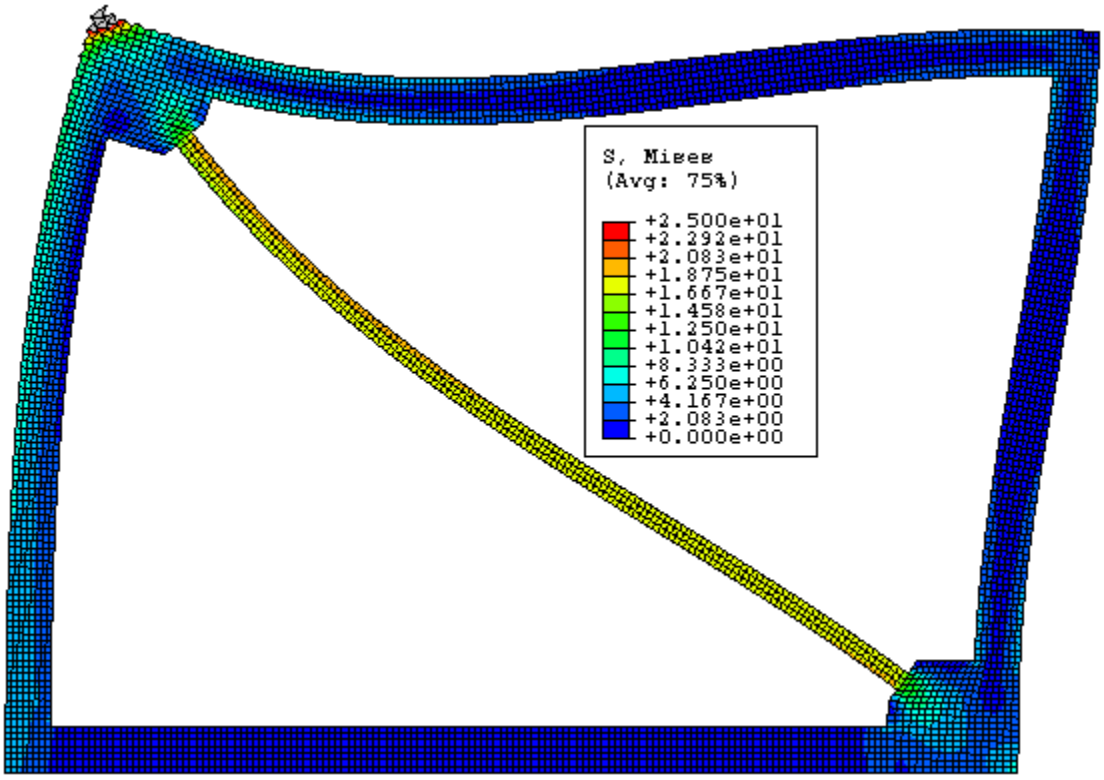

Fig. K176 - Von Mises Stress – Frame “T” without RXS Fuse – Stress Scale #2.

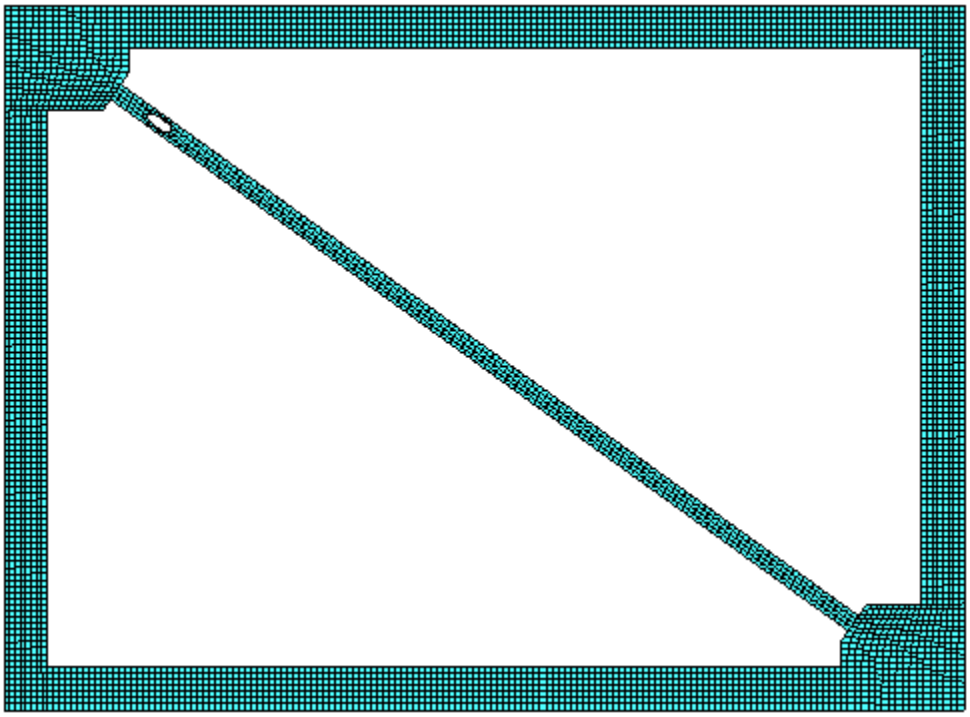

Fig. K177 - FEM Mesh – Frame “T” with RXS Fuse.

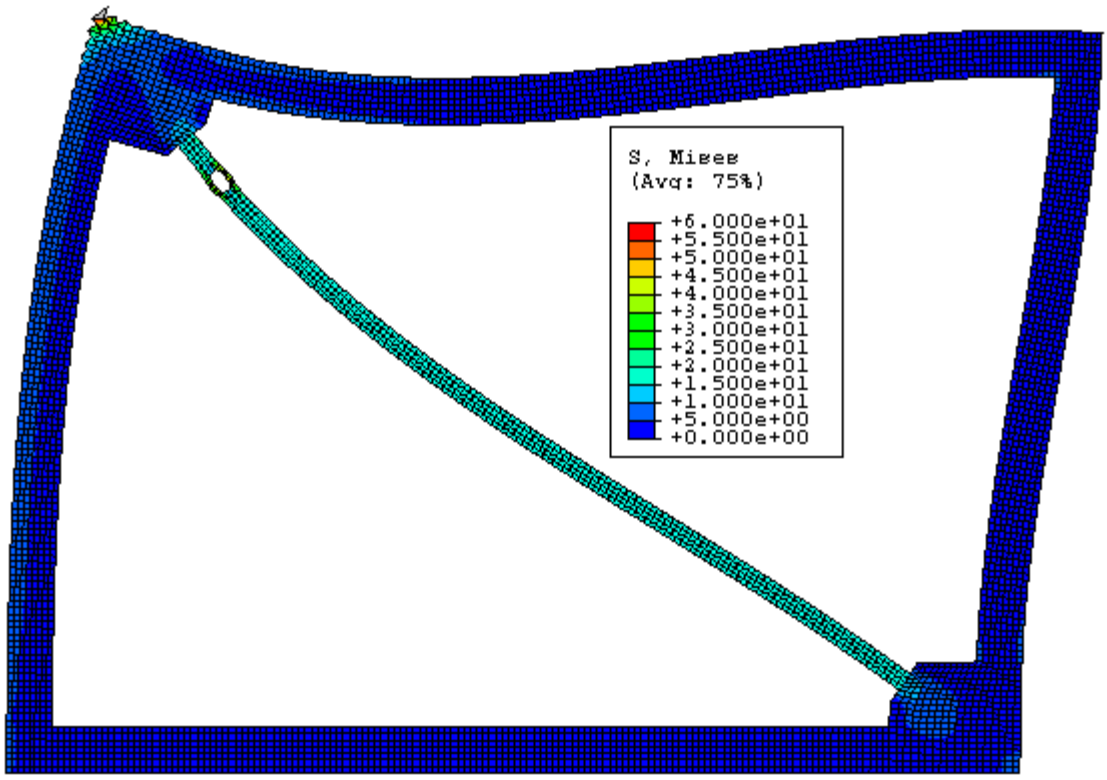

Fig. K178 - Von Mises Stress – Frame “T” with RXS Fuse.

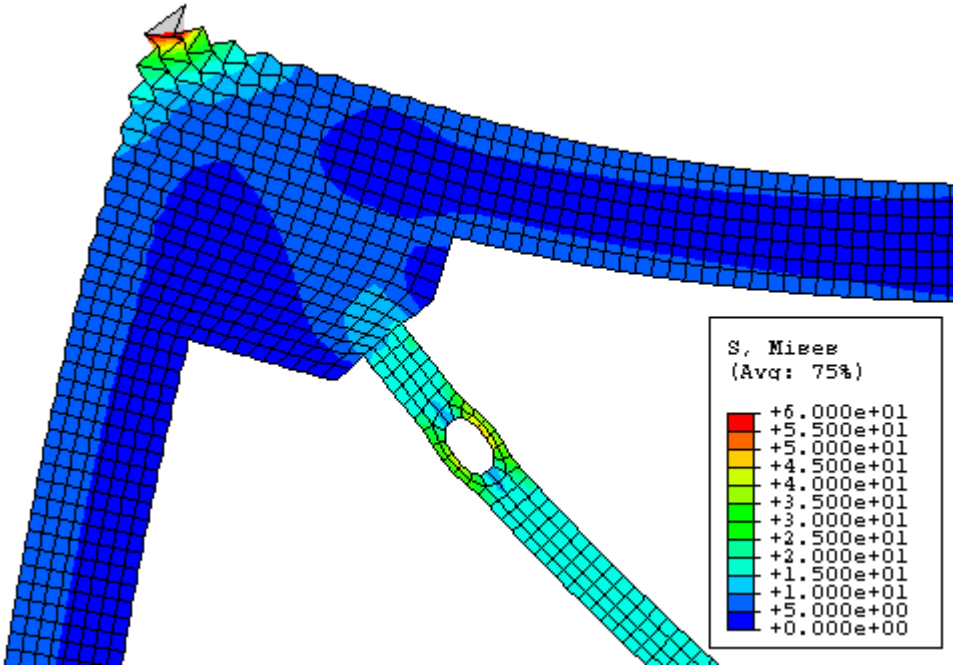

Fig. K179 - Von Mises Stress – Frame “T” with RXS Fuse – Zoom #1.

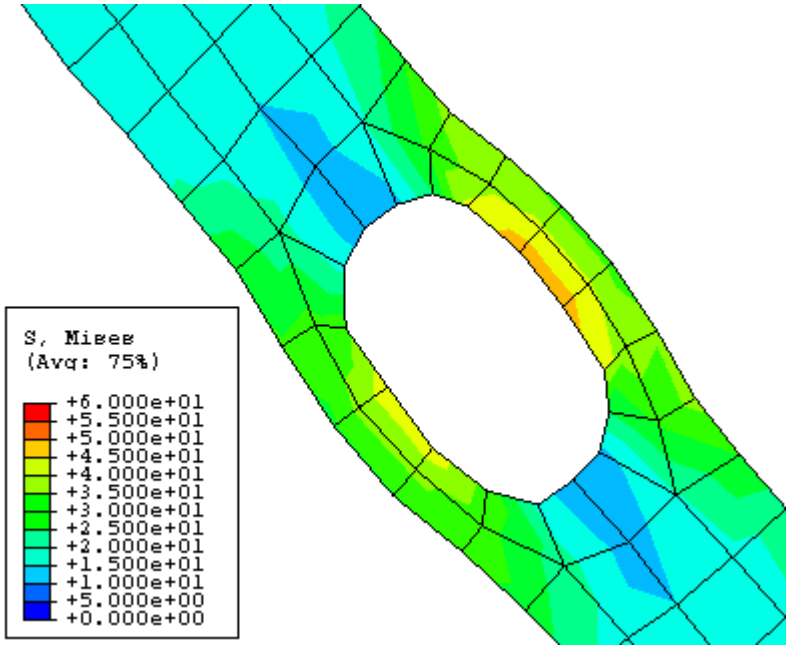

Fig. K180 - Von Mises Stress – Frame “T” with RXS Fuse – Zoom #2.

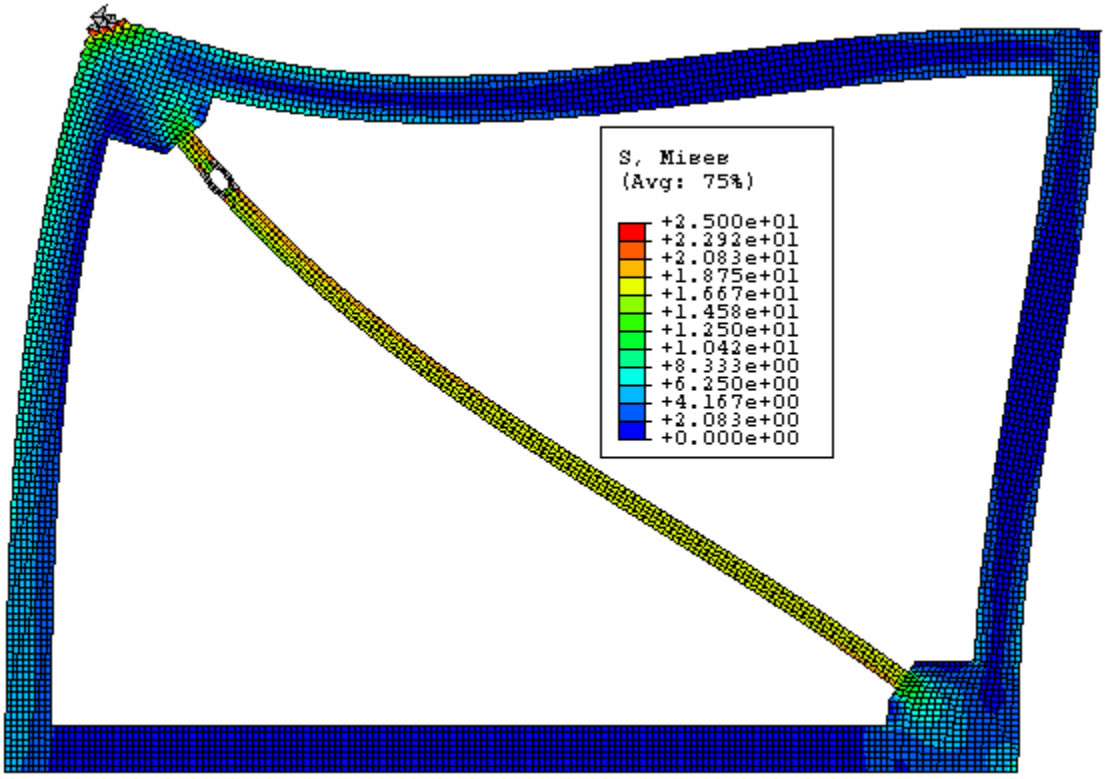

Fig. K181 - Von Mises Stress – Frame “T” with RXS Fuse – Stress Scale #2.

FRAME U

Beam/Column Length Ratio = H/L = 1

Beam-depth/Column-depth = 16”/16”

Brace Angle “ϕ” = 30˚

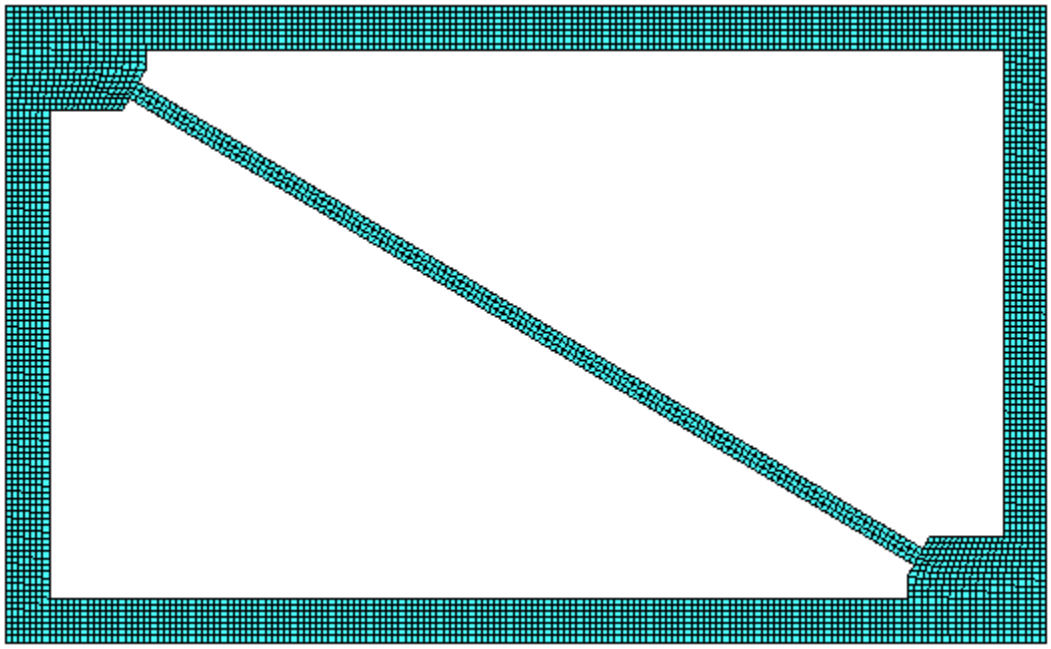

Fig. K182 - FEM Mesh – Frame “U” without RXS Fuse.

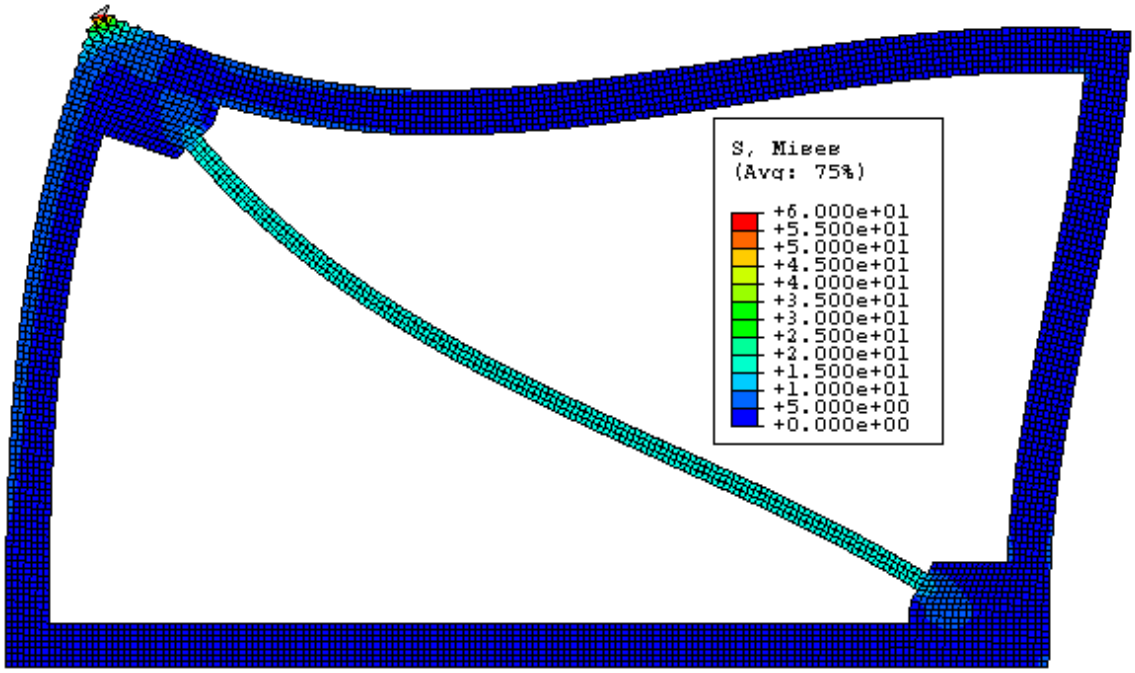

Fig. K183 - Von Mises Stress – Frame “U” without RXS Fuse.

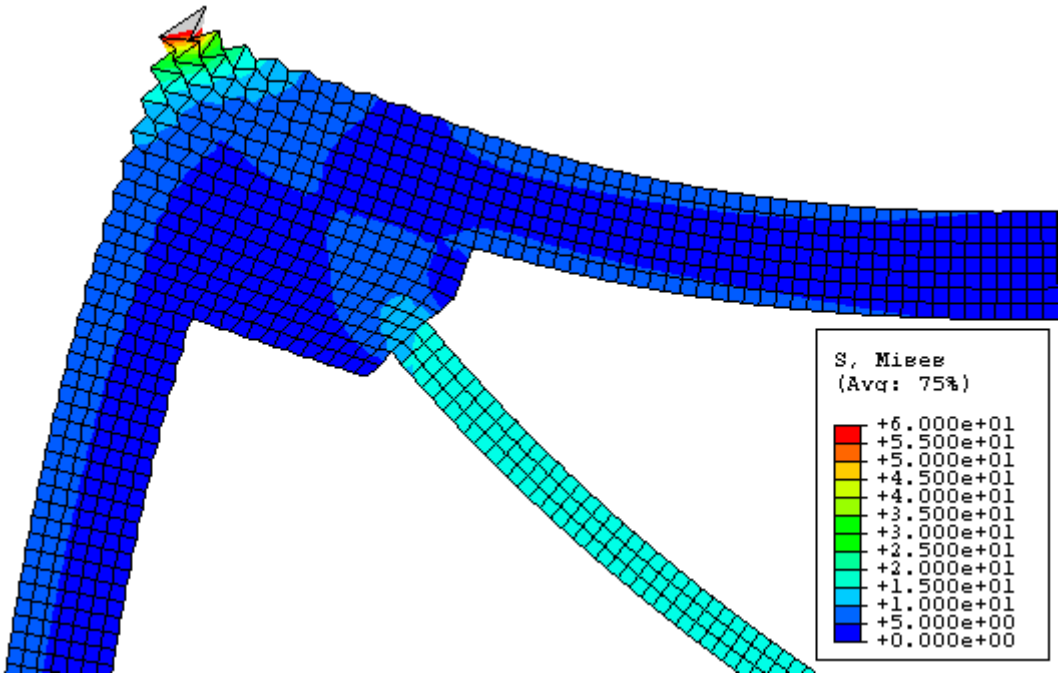

Fig. K184 - Von Mises Stress – Frame “U” without RXS Fuse – Zoom.

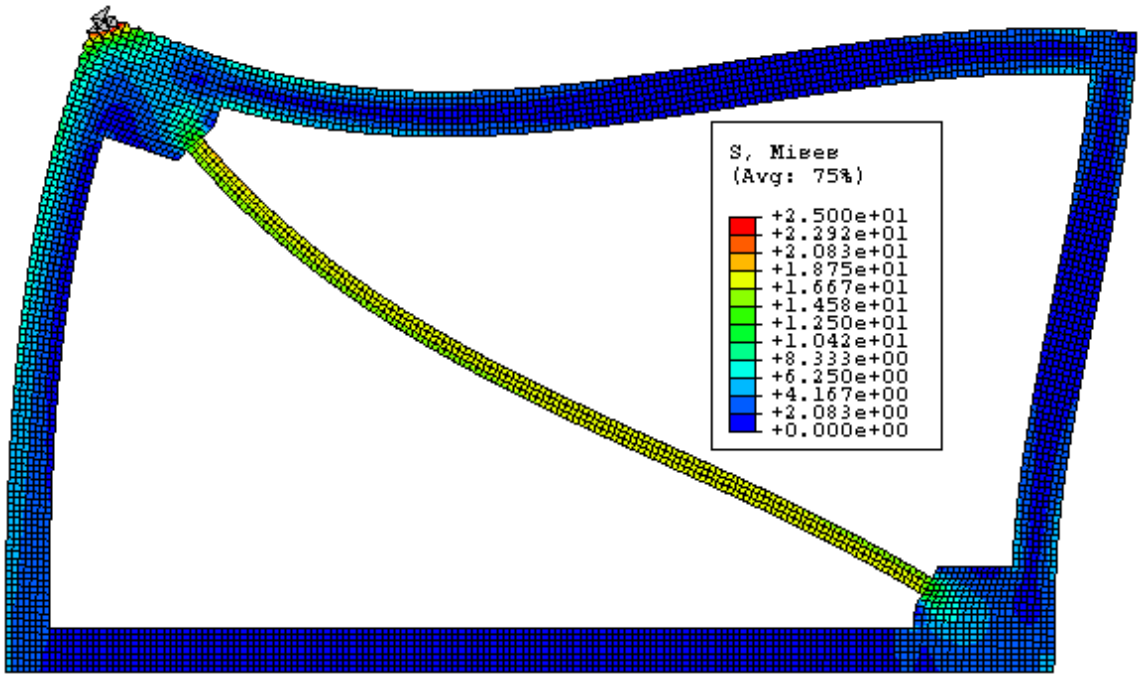

Fig. K185 - Von Mises Stress – Frame “U” without RXS Fuse – Stress Scale #2.

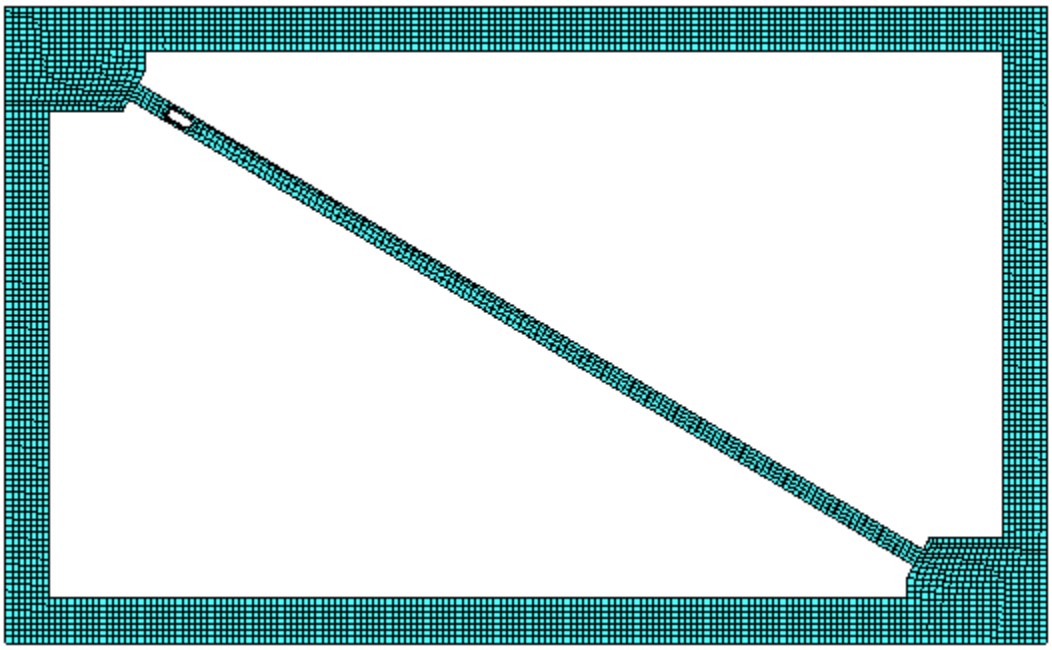

Fig. K186 - FEM Mesh – Frame “U” with RXS Fuse.

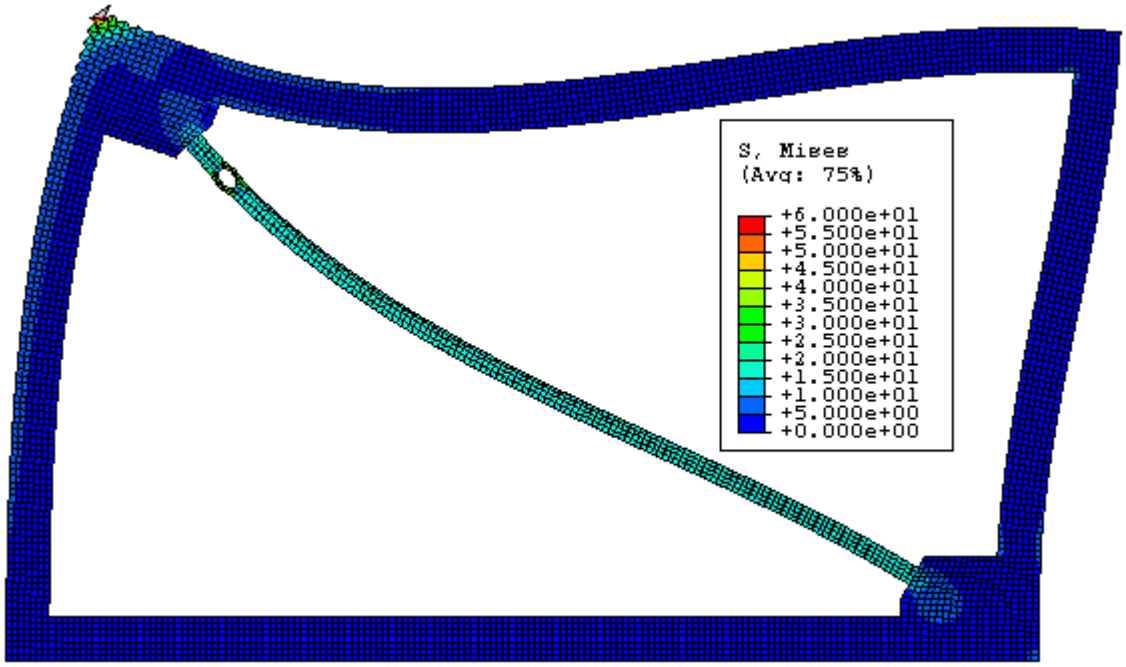

Fig. K187 - Von Mises Stress – Frame “U” with RXS Fuse.

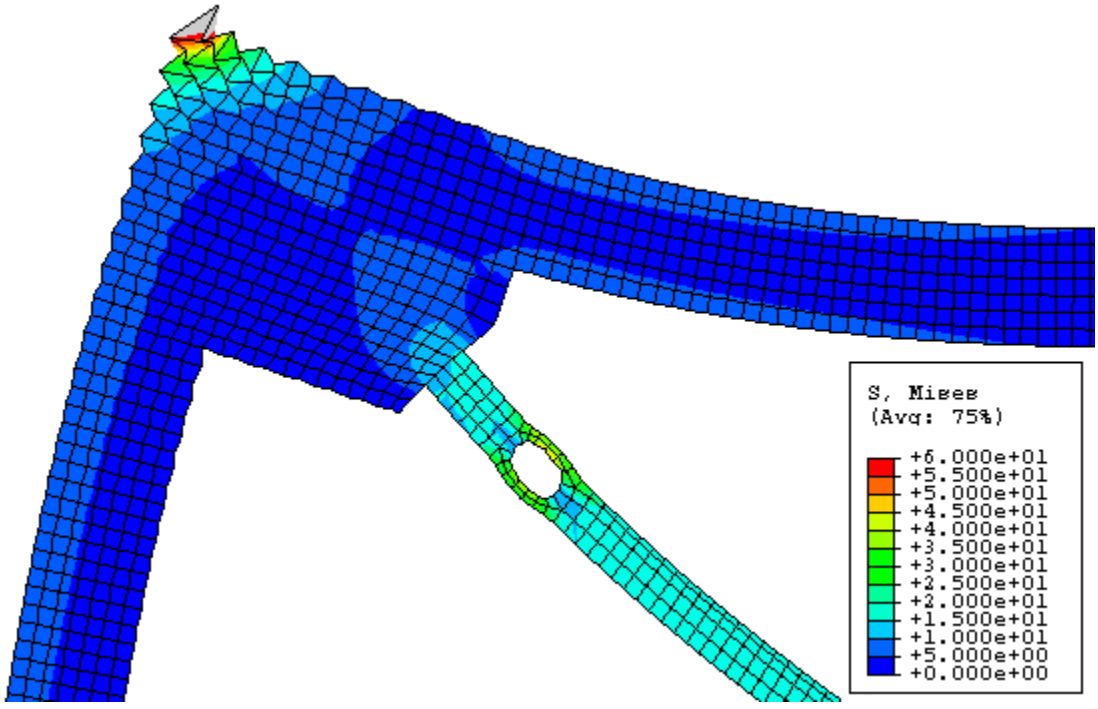

Fig. K188 - Von Mises Stress – Frame “U” with RXS Fuse – Zoom #1.

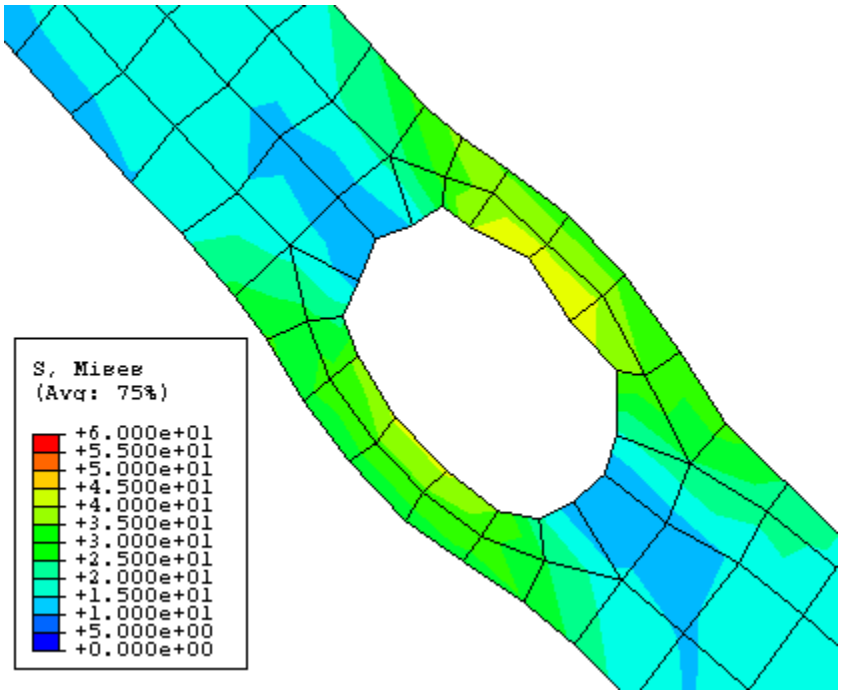

Fig. K189 - Von Mises Stress – Frame "U" with RXS Fuse – Zoom #2.

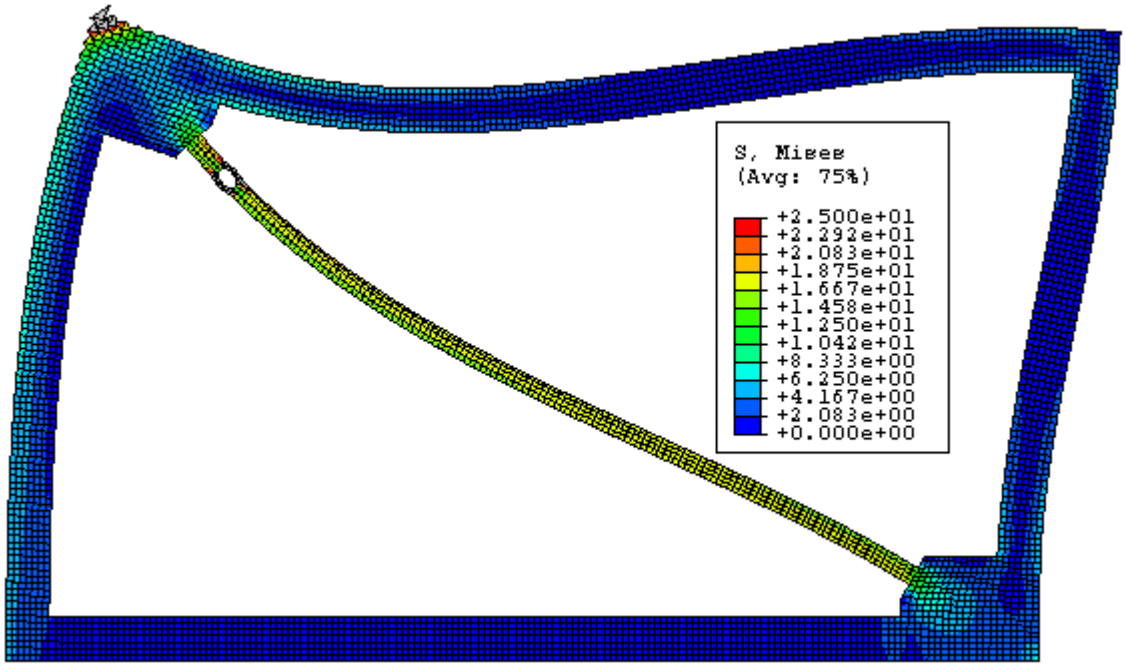

Fig. K190 - Von Mises Stress – Frame "U" with RXS Fuse – Stress Scale #2.

FRAME V

Beam/Column Length Ratio = H/L = 1

Beam-depth/Column-depth = 16”/16”

Brace Angle “ϕ” = 25˚

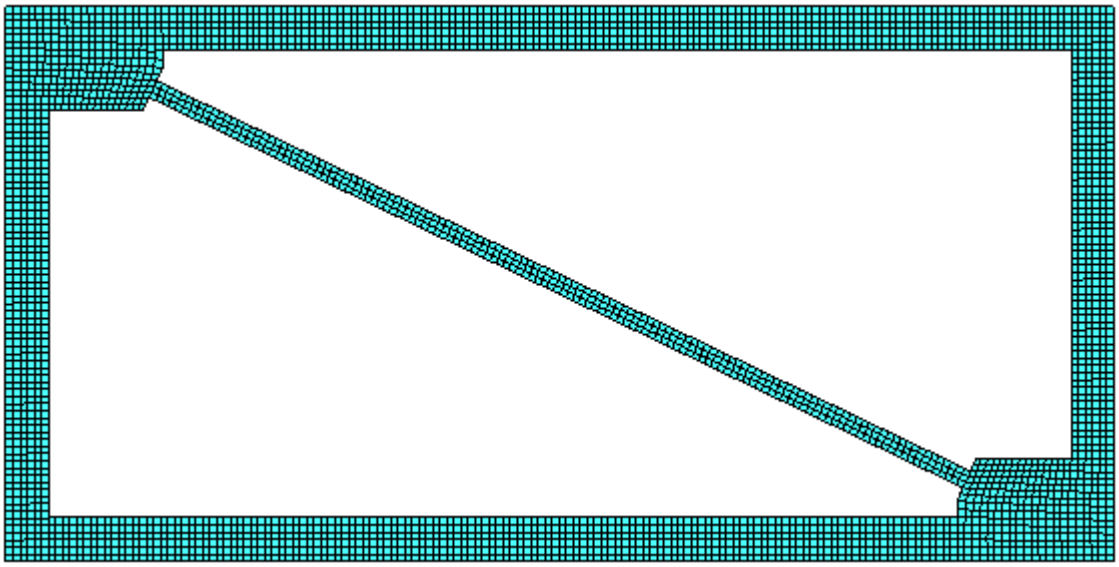

Fig. K191 - FEM Mesh – Frame “V” without RXS Fuse.

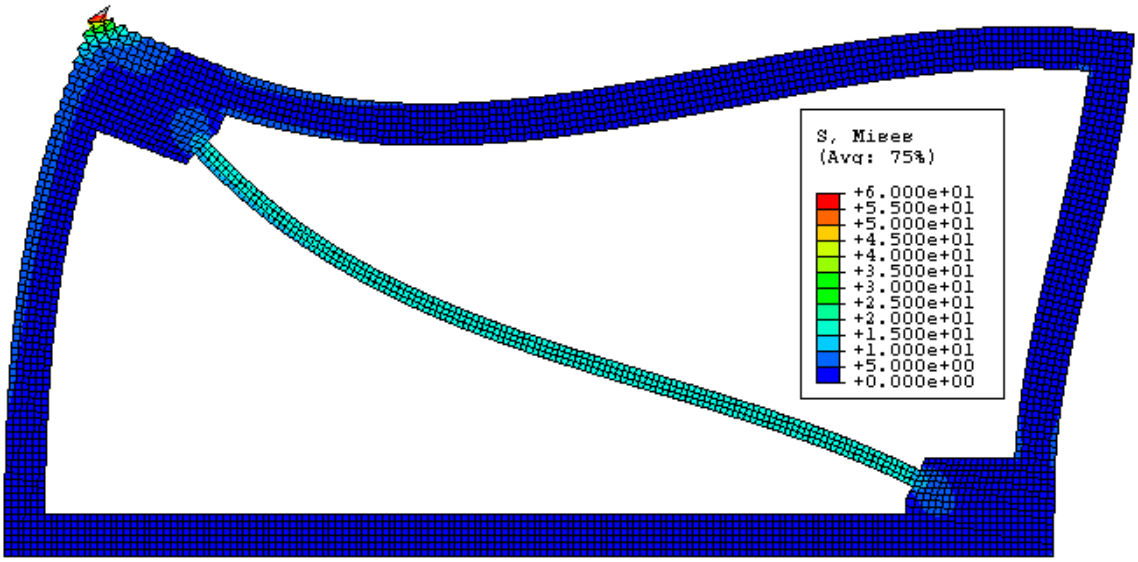

Fig. K192 - Von Mises Stress – Frame “V” without RXS Fuse.

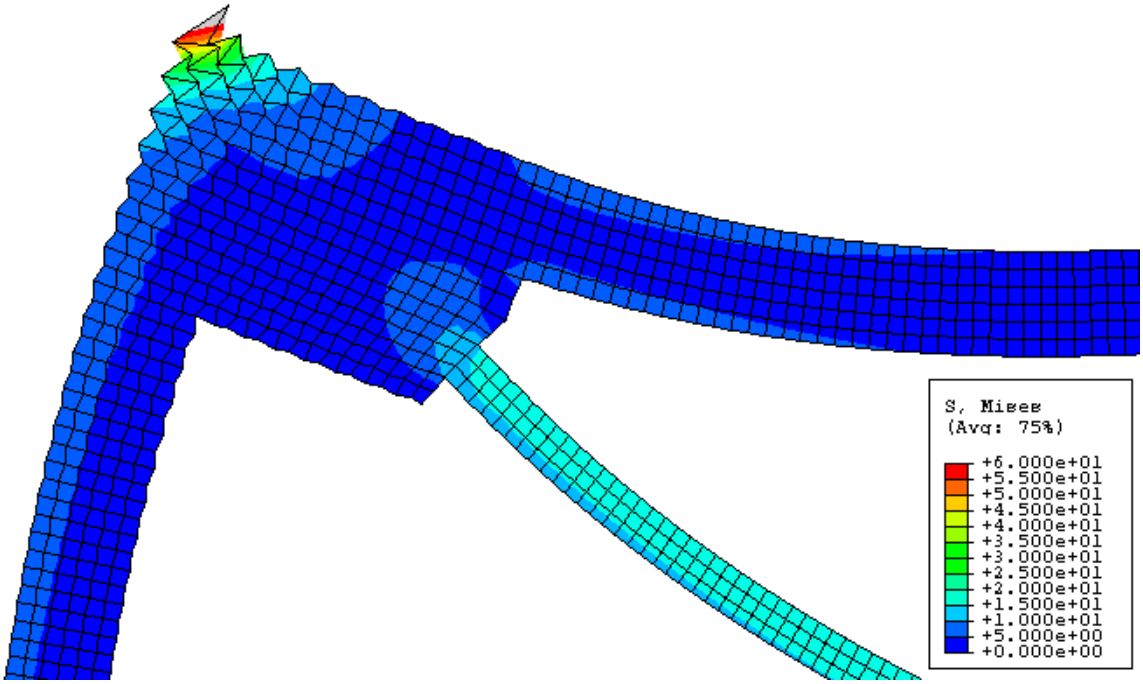

Fig. K193 - Von Mises Stress – Frame “V” without RXS Fuse – Zoom.

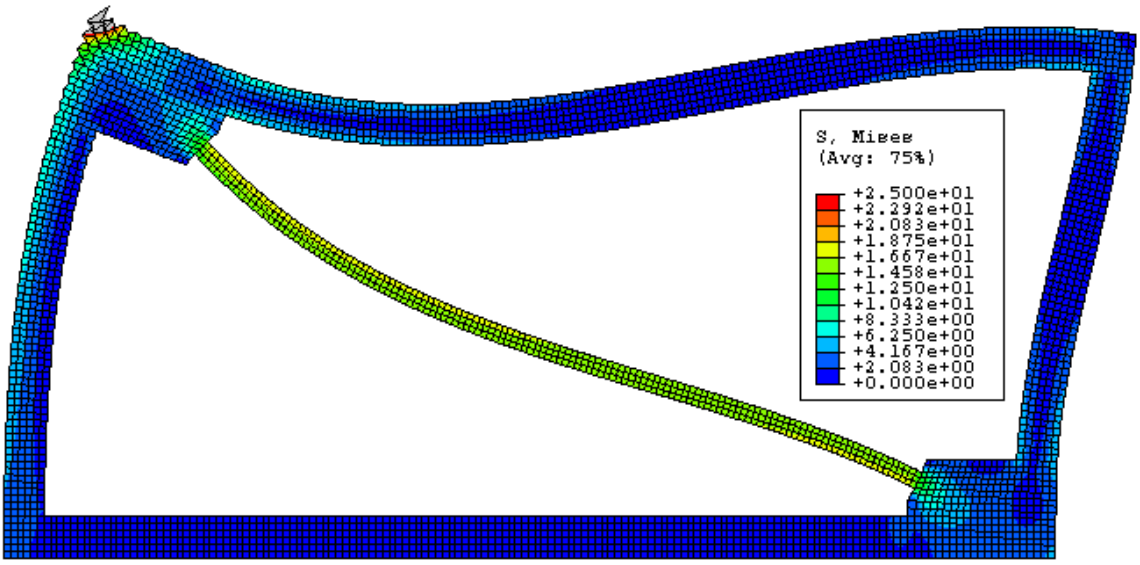

Fig. K194 - Von Mises Stress – Frame “V” without RXS Fuse – Stress Scale #2.

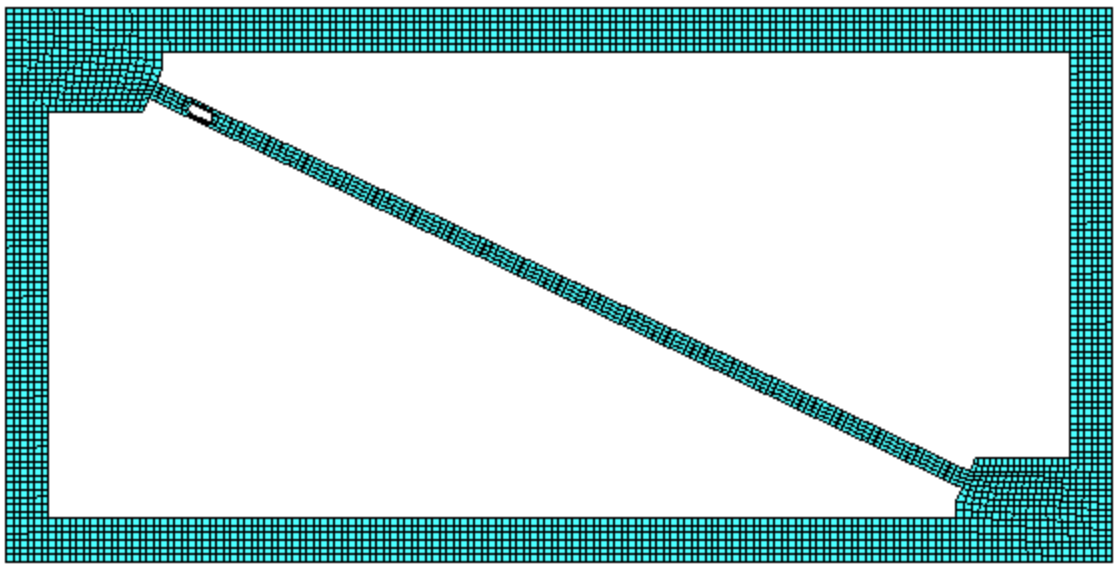

Fig. K195 - FEM Mesh – Frame “V” with RXS Fuse.

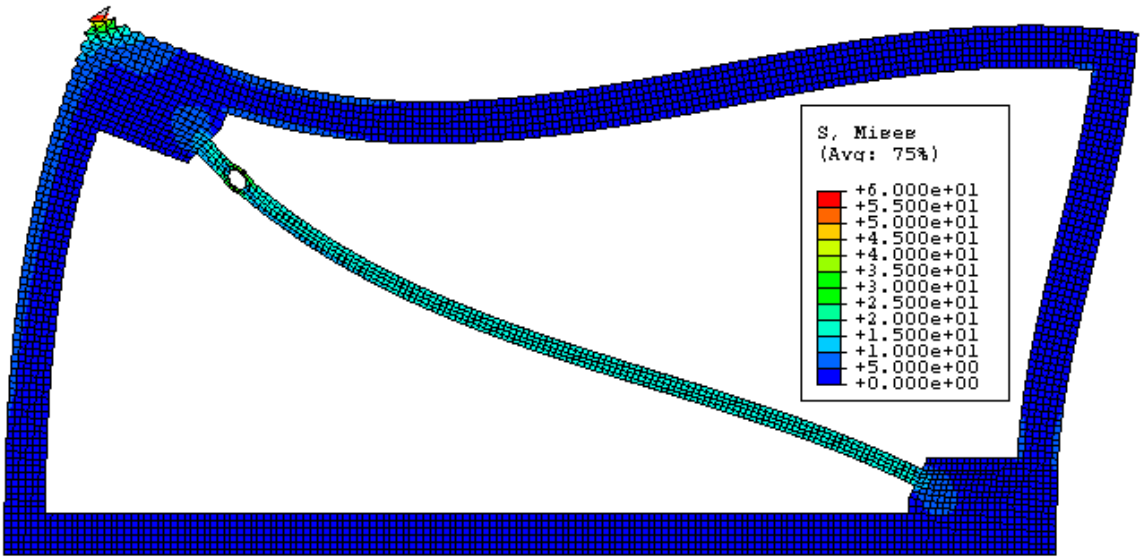

Fig. K196 - Von Mises Stress – Frame “V” with RXS Fuse.

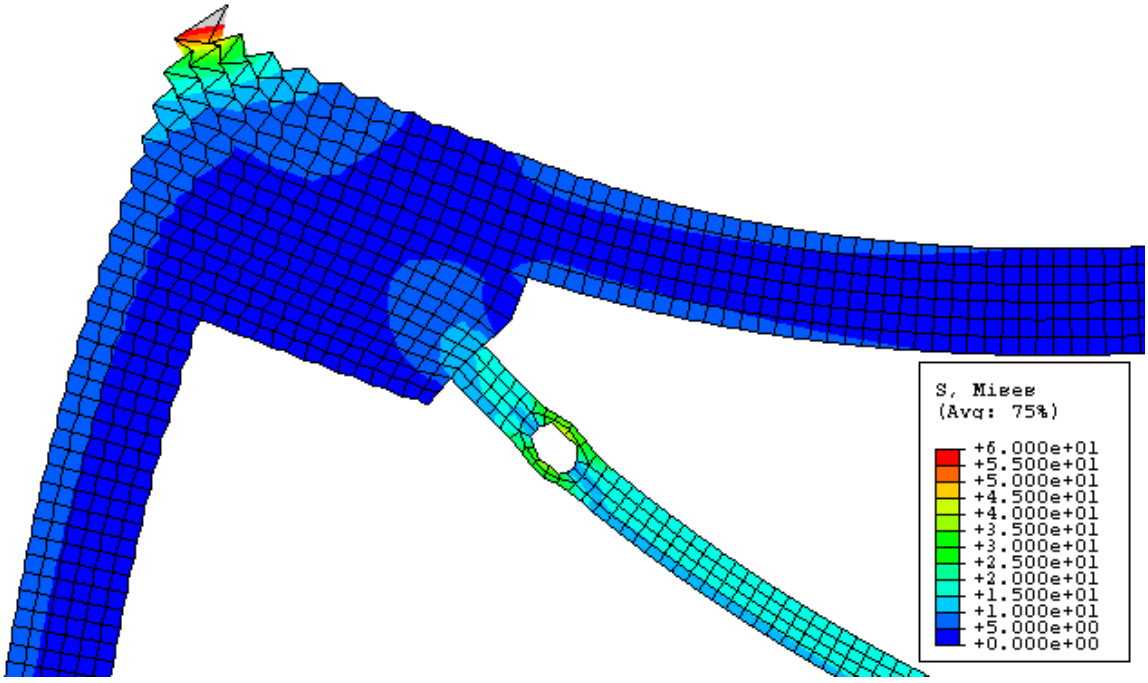

Fig. K197 - Von Mises Stress – Frame “V” with RXS Fuse – Zoom #1.

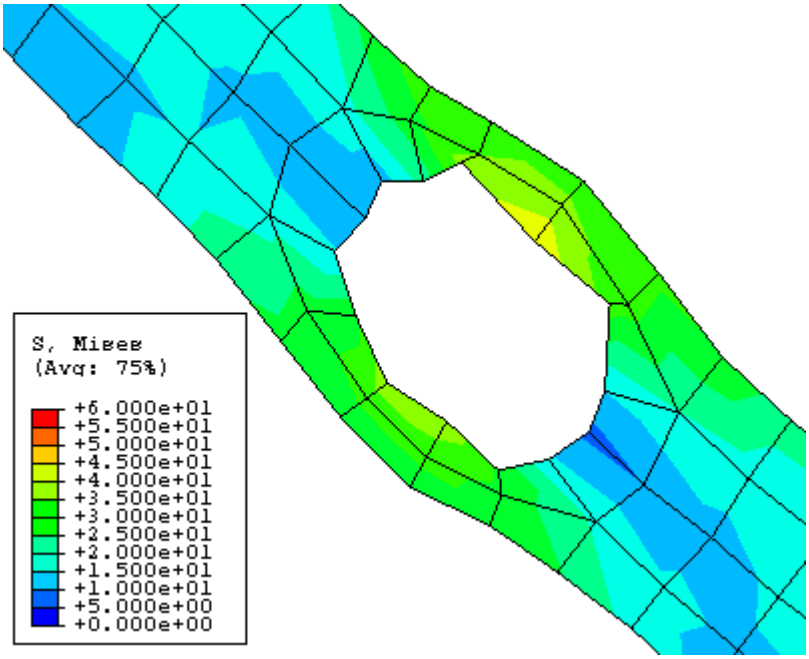

Fig. K198 - Von Mises Stress – Frame “V” with RXS Fuse – Zoom #2.

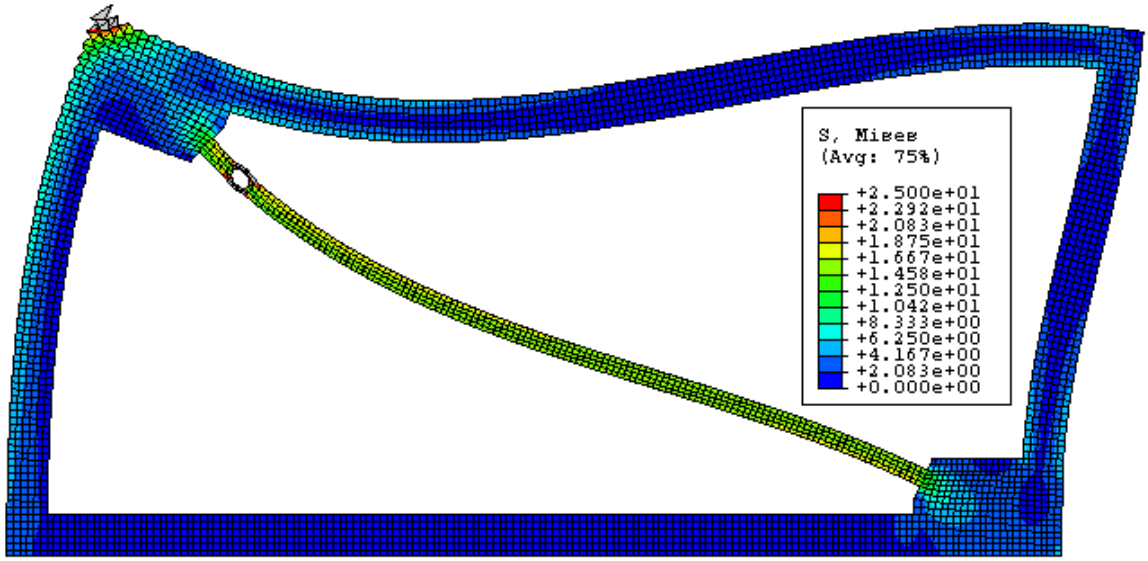

Fig. K199 - Von Mises Stress – Frame “V” with RXS Fuse – Stress Scale #2.

APPENDIX L – ABAQUS INPUTS

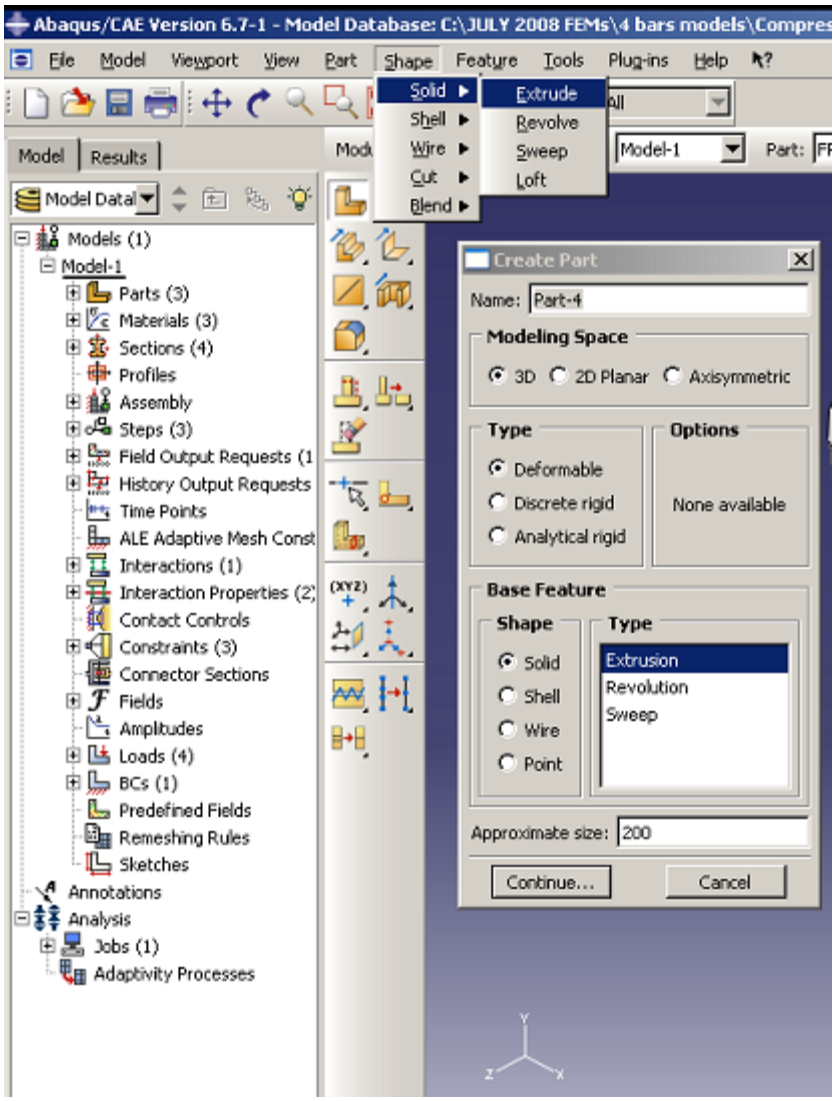

Fig. L1 - Part Module Input.

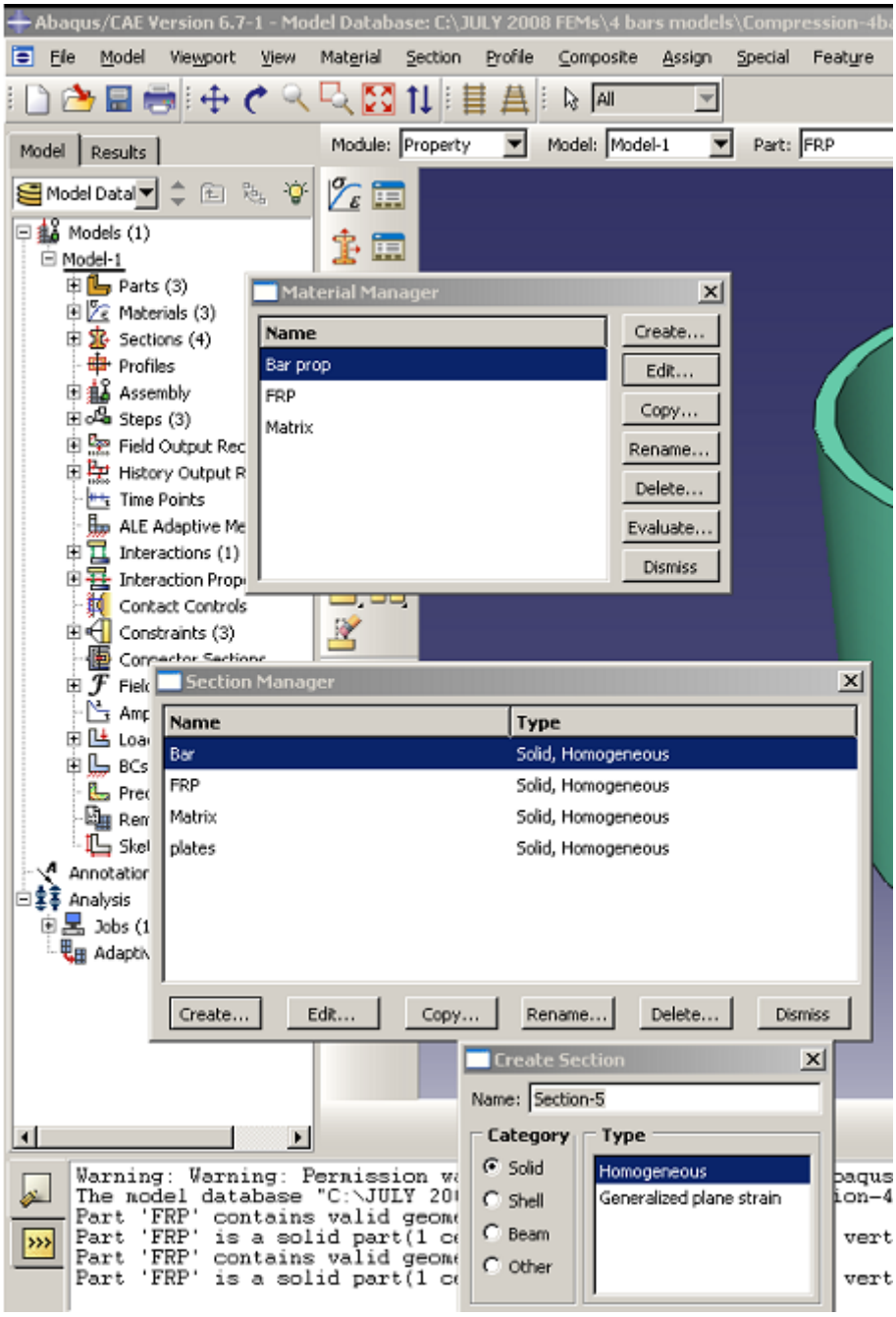

Fig. L2 - Property Module Input.

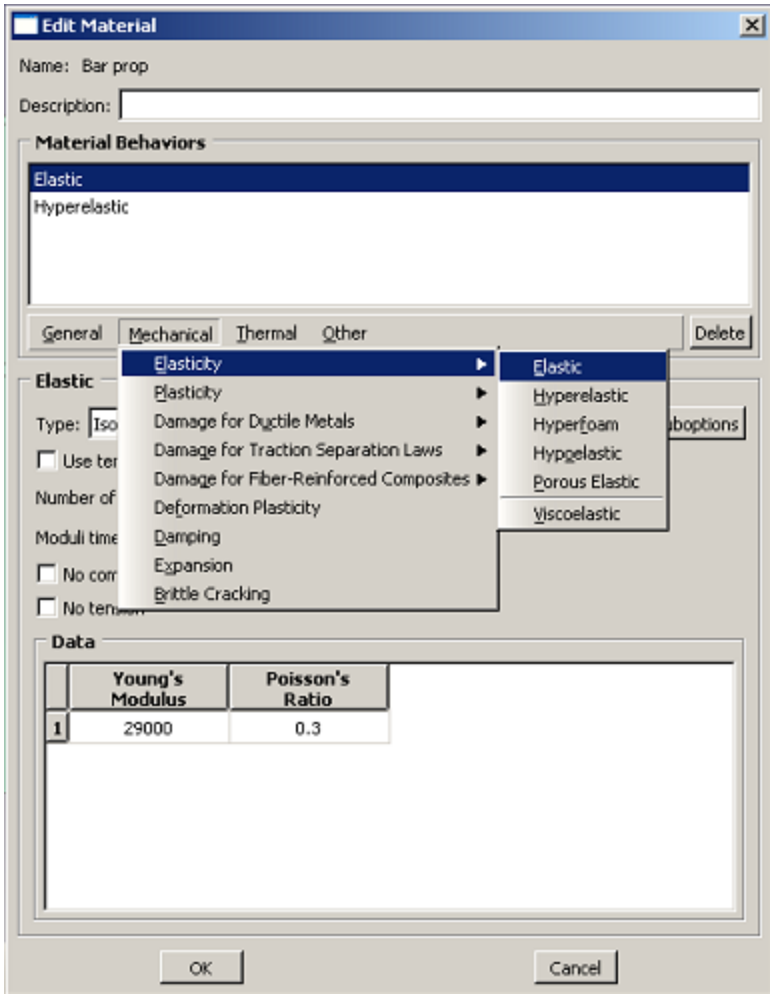

Fig. L3 - Property Module Input – Linear Elastic Properties.

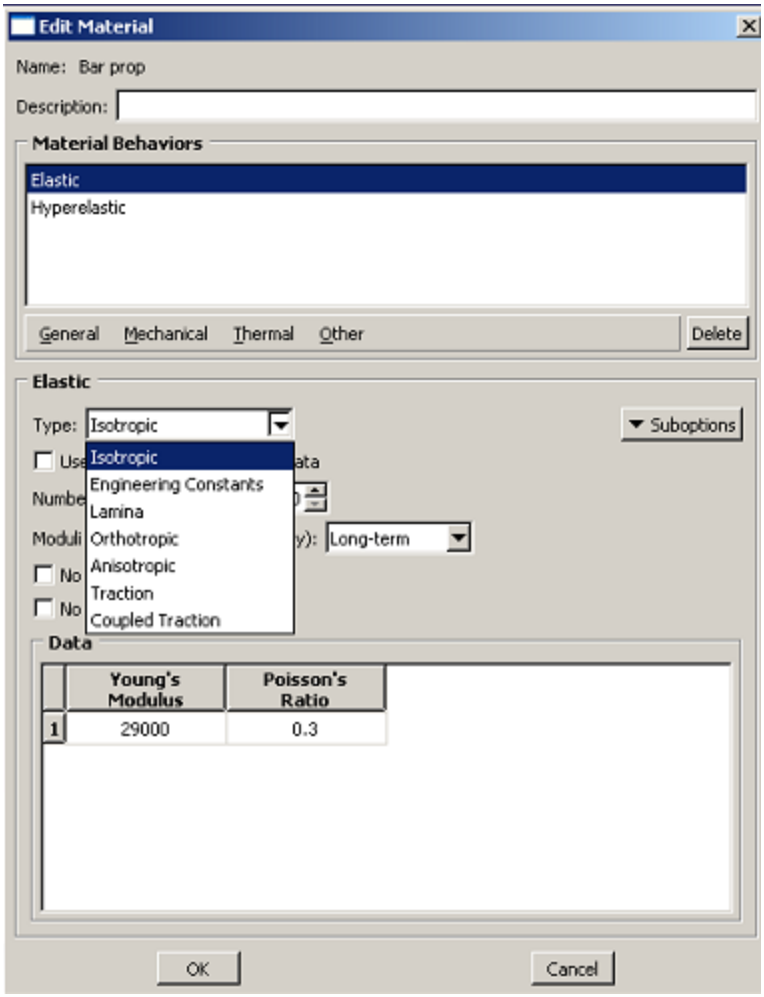

Fig. L4 - Property Module Input – CFRPLayer Isotropic Property.

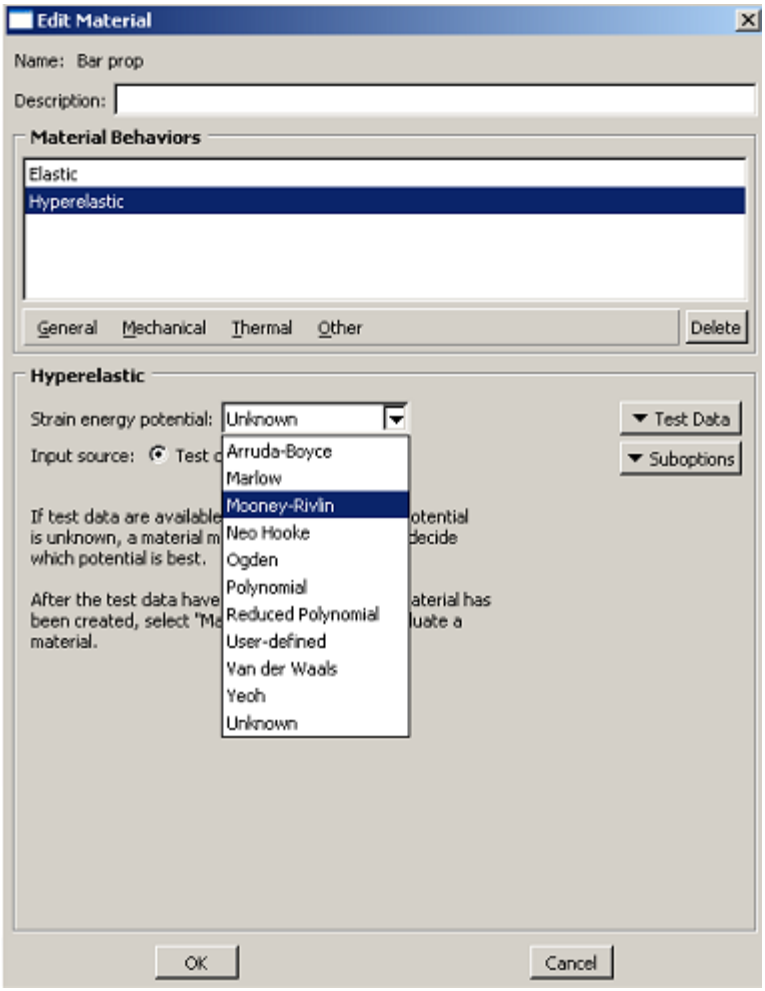

Fig. L5 - Property Module Input – Polyuretahne Matrix Hyperelastic Properties.

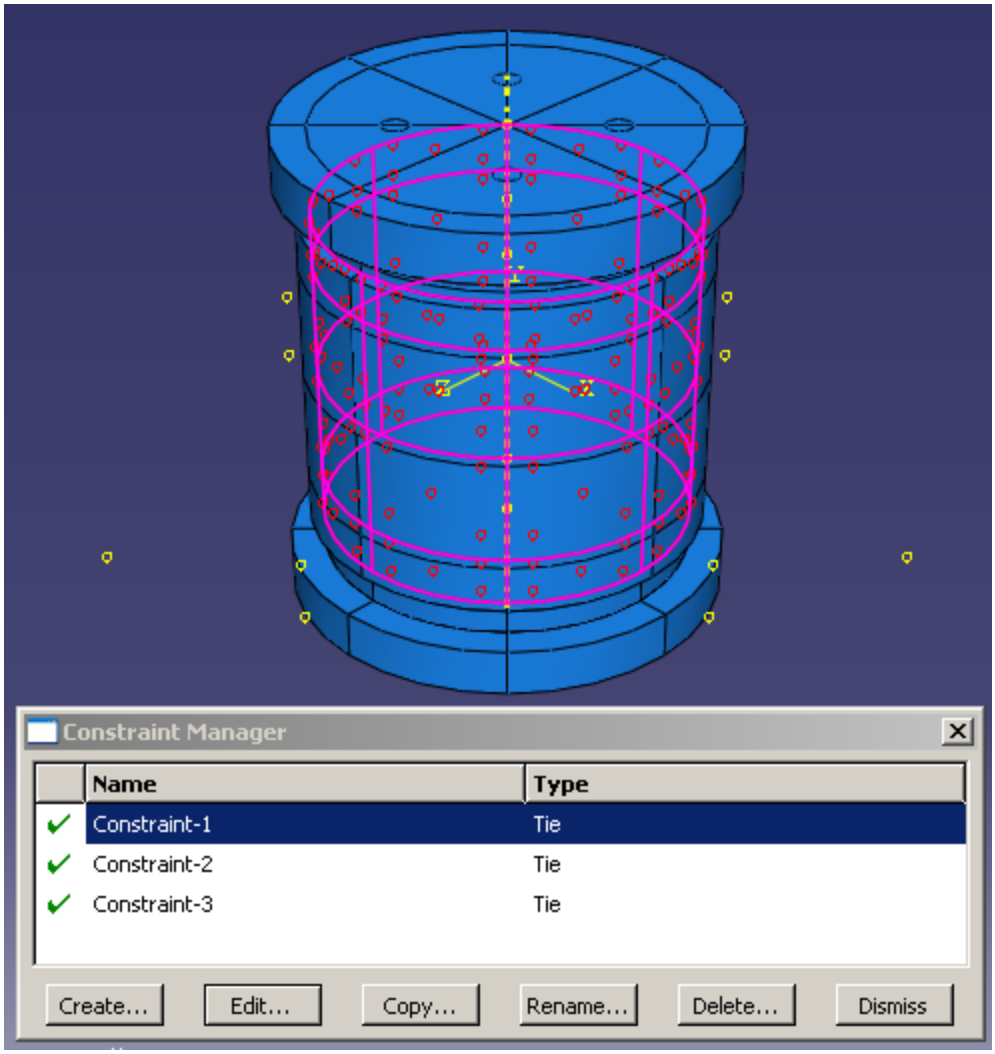

Fig. L6 - Interaction Module Input – Tie Constraint between Polyurethane Matrix and CFRP Layer.

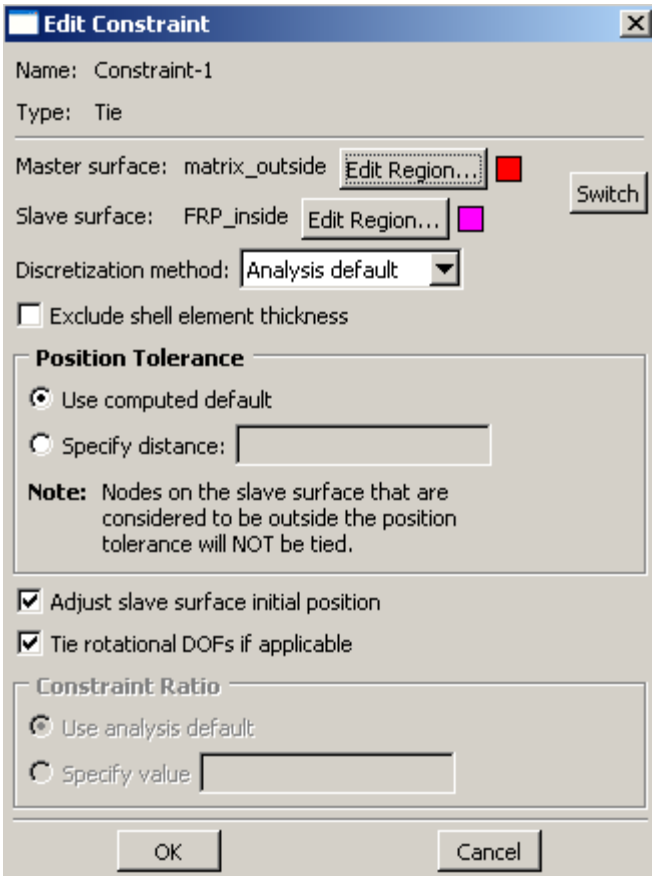

Fig. L7 - Interaction Module Input – Tie Constraint between Polyurethane Matrix and CFRP Layer - Parameters.

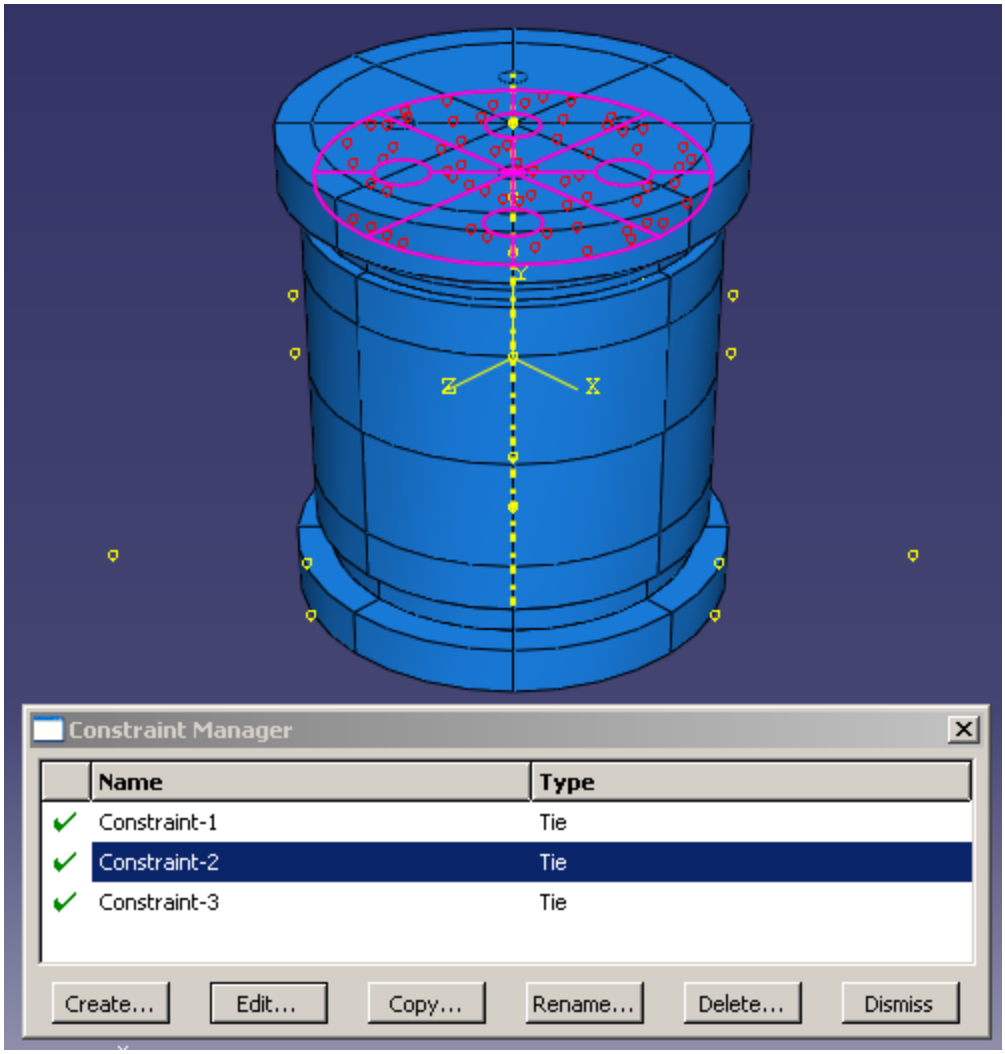

Fig. L8 - Interaction Module Input – Tie Constraint between Polyurethane Matrix and Top and Bottom Plates.

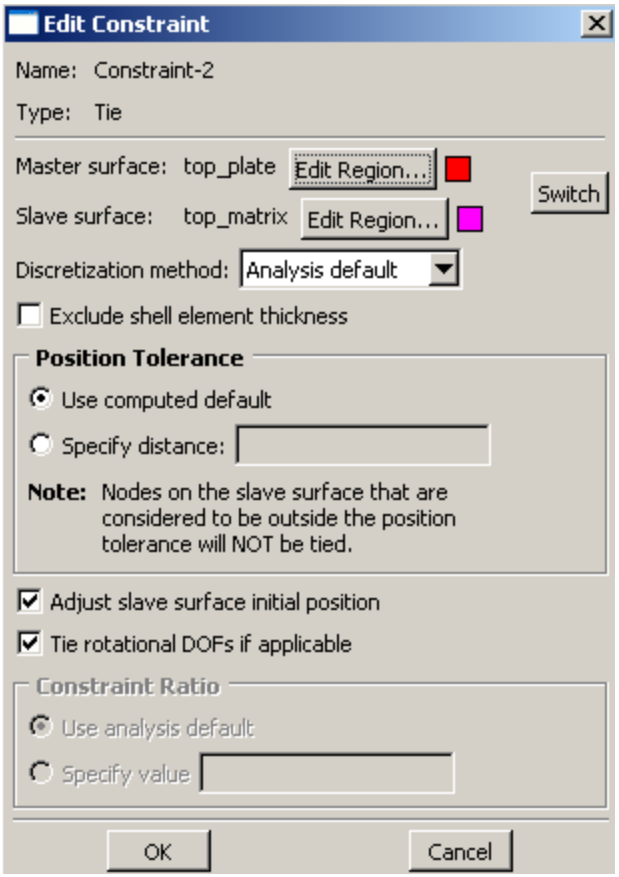

Fig. L9 - Interaction Module Input – Tie Constraint between Polyurethane Matrix and Top and Bottom Plates - Parameters.

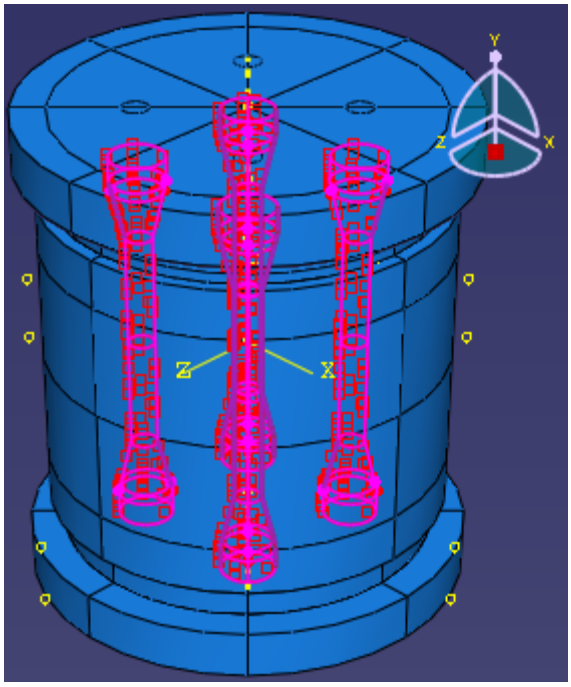

Fig. L10 - Interaction Module Input – Surface-to-Surface Interaction between Polyurethane Matrix and Bars.

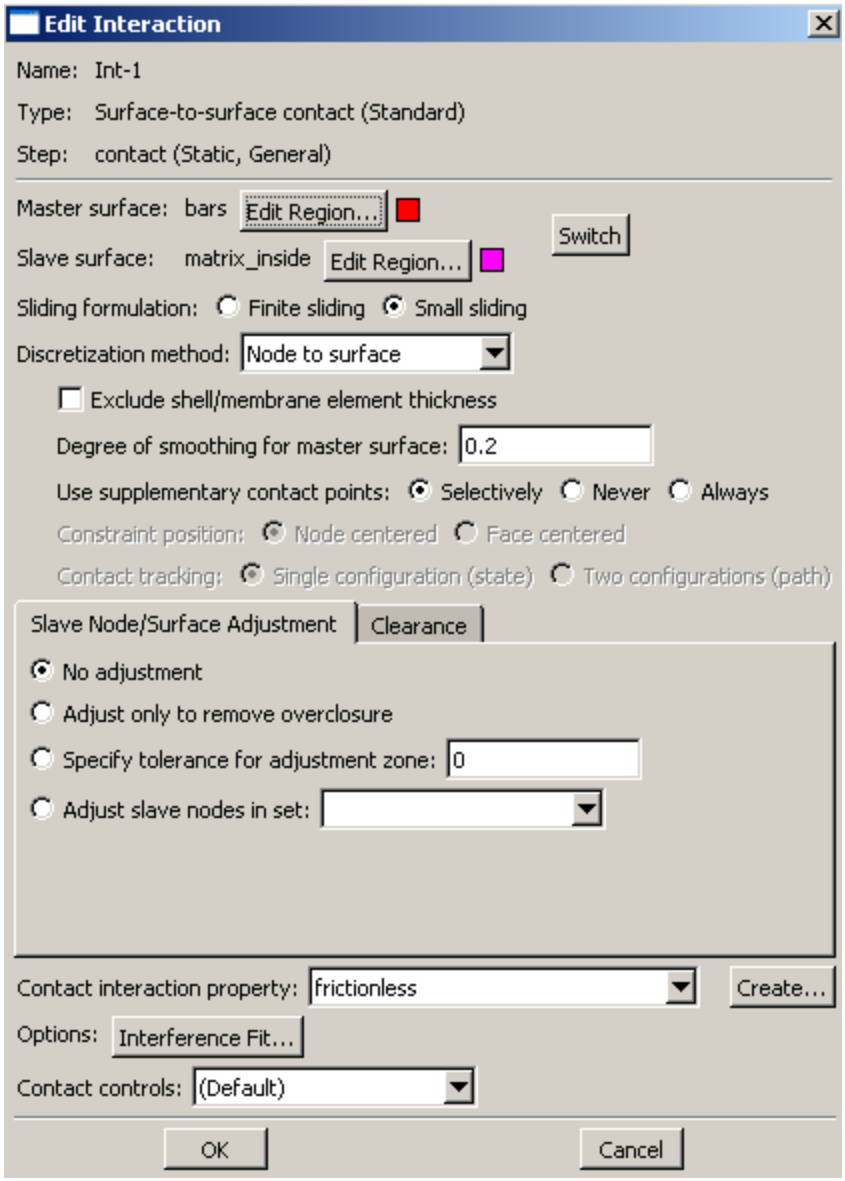

Fig. L11 - Interaction Module Input – Surface-to-Surface Interaction between Polyurethane Matrix and Bars - Parameters.

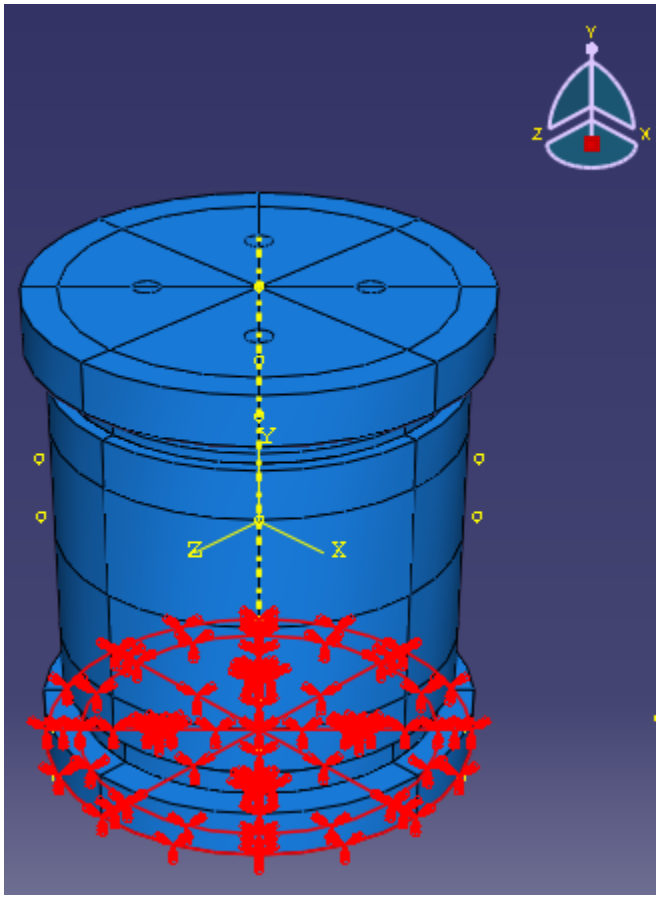

Fig. L12 - Load Module Input – Boundary Conditions – Fixed at Bottom Plate.

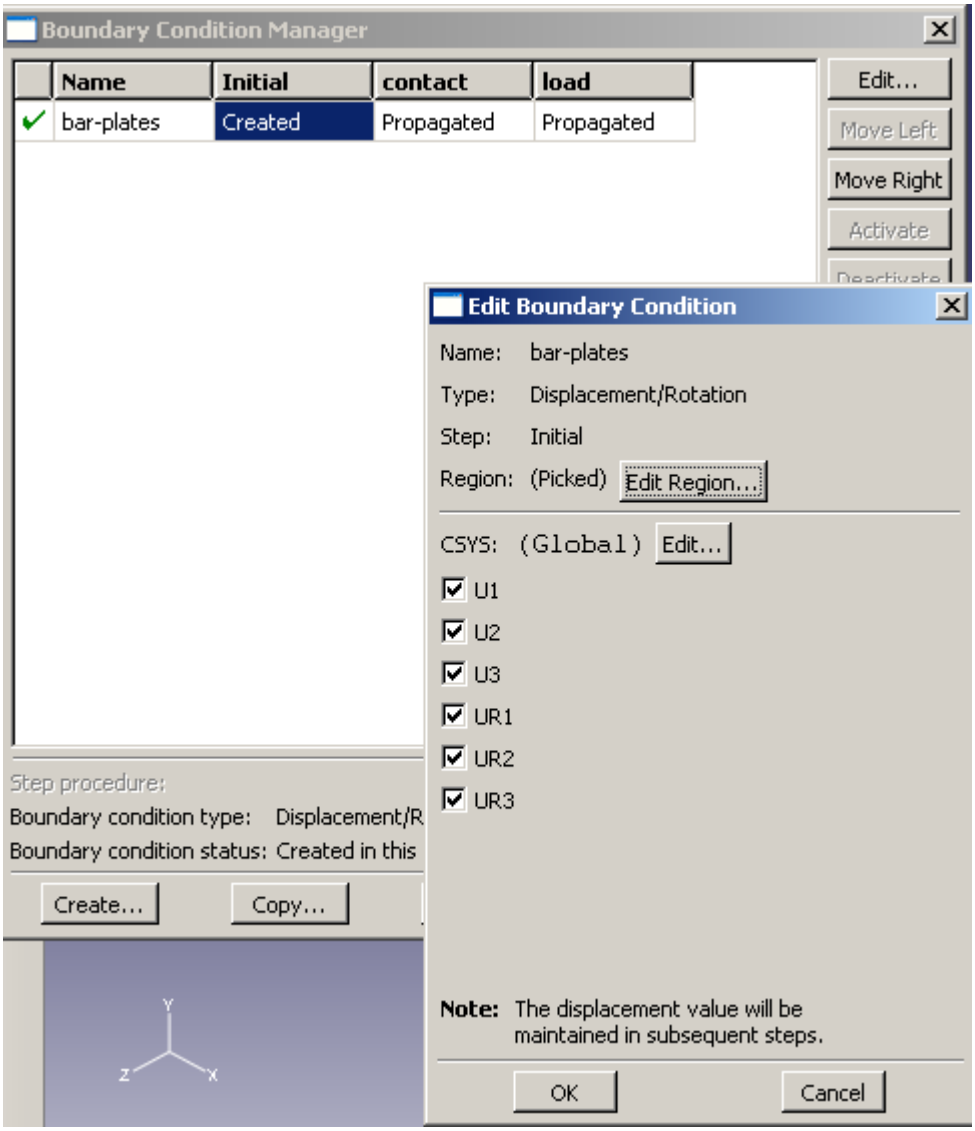

Fig. L13 - Load Module Input – Boundary Conditions – Fixed at Bottom Plate - Parameters.

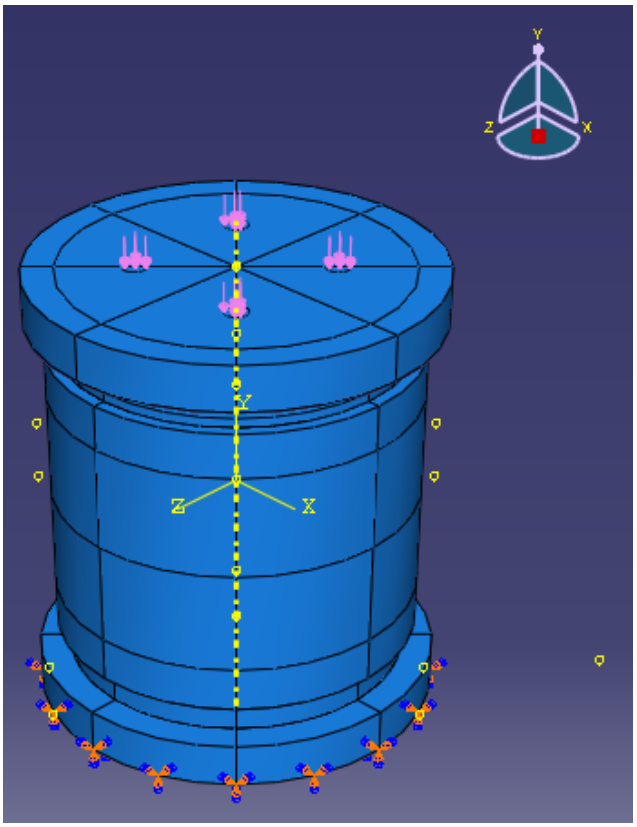

Fig. L14 - Load Module Input – Loads – Applied on Top Plate.

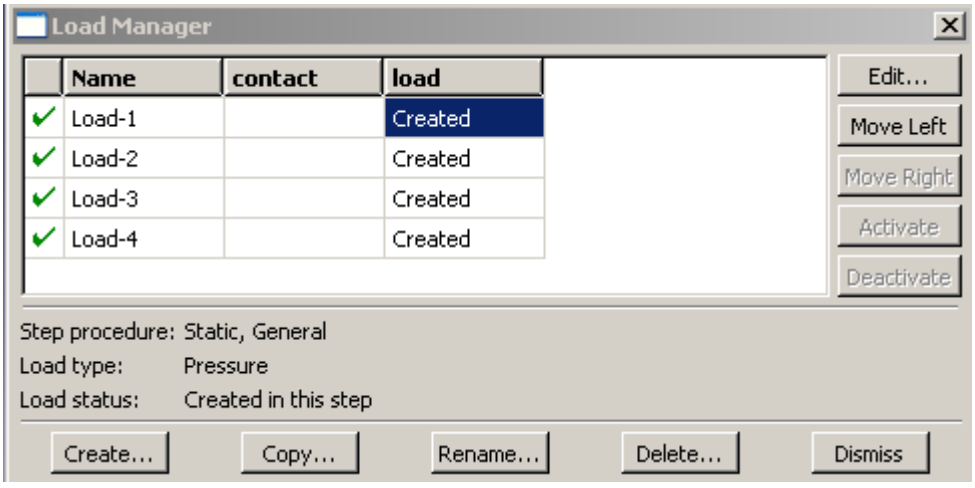

Fig. L15 - Load Module Input – Loads – Applied on Top Plate - Parameters.

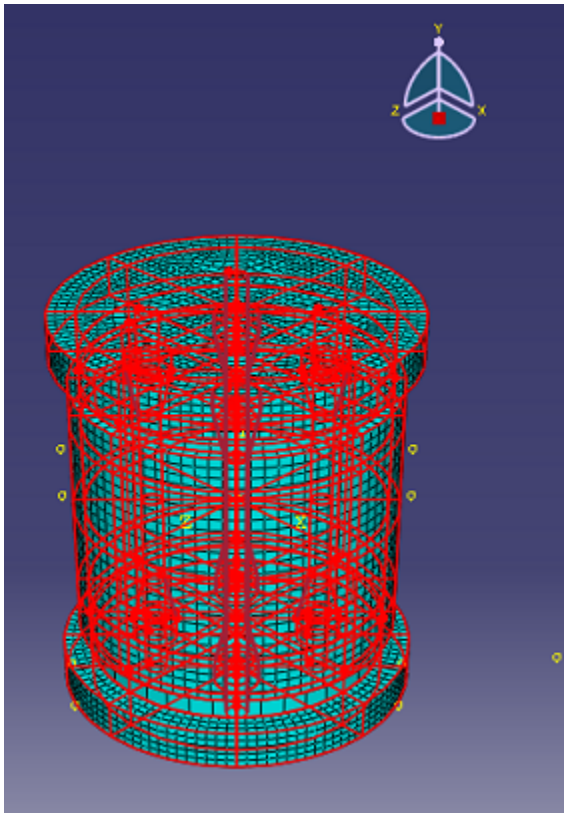

Fig. L16 - Mesh Module Input.

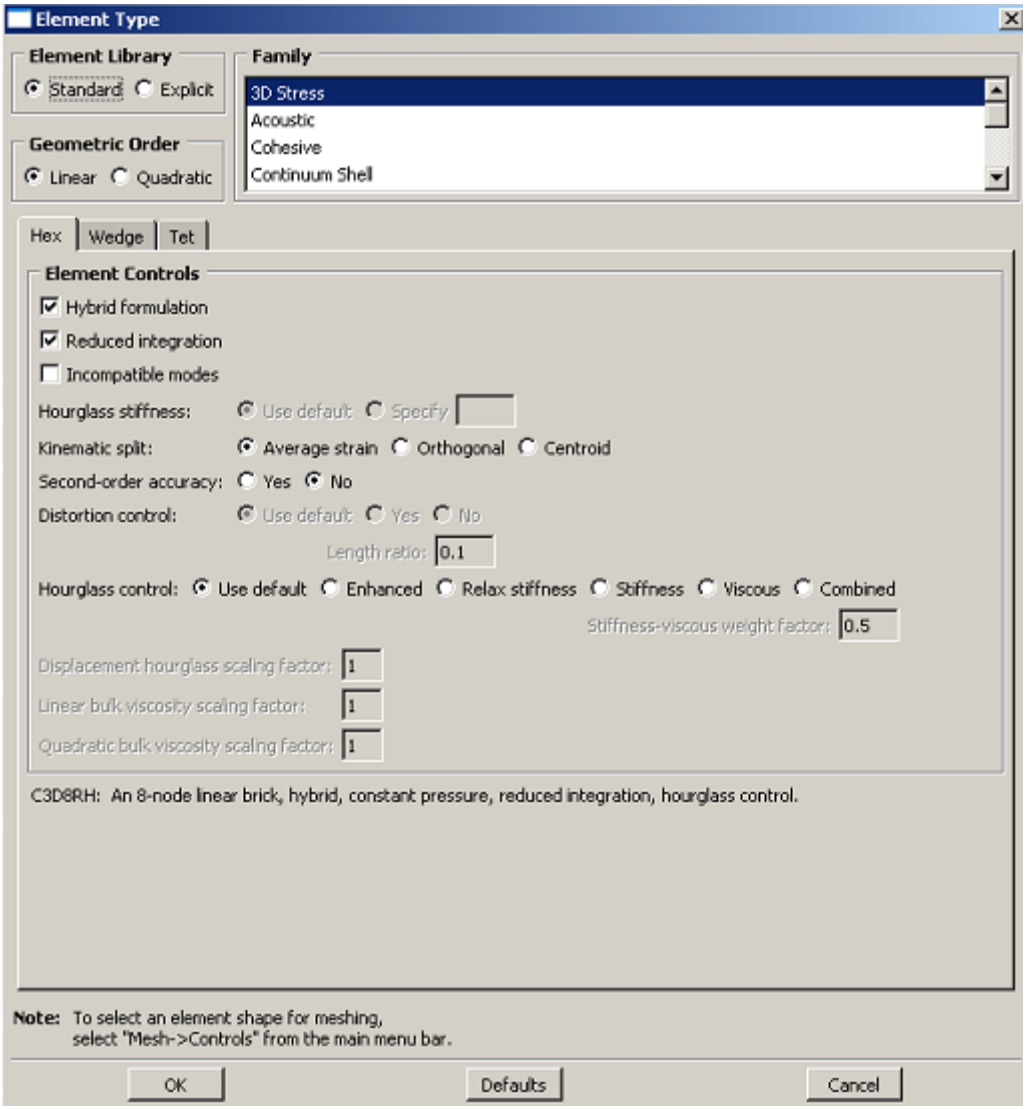

Fig. L17 - Mesh Module Input - Parameters.